# Automated lithofacies predictions from well logs

Richard Martin

B.A. (Hons) Earth Sciences (Oxford) 1998

MSc. Petroleum Geology (Aberdeen) 1999




Thesis submitted for the degree of

Doctor of Philosophy

University of Edinburgh

2004

# Abstract

Discrimination of lithology and sedimentary facies from well logs in any hydrocarbon reservoir is an important requirement in both exploration and production. Traditionally such predictions have been made graphically from log cross-plots by hand or, more recently, by some statistical methods (such as discriminant analysis or fuzzy logic). In the past decade however, neural networks have been used as an alternative technique. The acquired knowledge of any so called 'supervised' neural network is self-generated from given examples, and therefore any interpretation based on this type of network should be consistent and unambiguous. The emphasis of previous studies involving neural networks has been on improving facies classification rather than analysis of factors affecting the data that subsequently influence the results. Also the data incorporated has always been traditional log data, modern image data is rarely incorporated. Moreover, the limitations of using the neural network as a predictive tool are not fully documented, and the actual controls on the outcome are poorly understood.

This PhD study uses two data sets to investigate lithofacies predictions via neural network analysis. A neural network model is developed to predict lithofacies in the Palaeocene submarine fan deposits of the Lomond Field in the Central North Sea. When the results from the optimum model are compared directly to core in many cases a close match is found, even in intervals where the model interpretation does not match the 'human' interpretation. In wells where predictions do not match the core this is shown to be a consequence not of the methodology itself but because of characteristics of the data collected in the training wells. This is due to variations in tool type, interval depth and fluid saturation. When this occurs, prior calibration of logs to the training data, for example through making a correction for fluid saturation, can improve performance. In all cases the observation of the activation levels of all output nodes in the network can qualitatively describe any uncertainty in the results, thus aiding interpretation.

Using a second data set of wells from the deep marine West Delta Deep Concession area, Nile delta, Egypt more neural network models are developed to predict 'image' facies. Model inputs consist of conventional logs and derived logs from statistical and power spectral analysis of the pad data from the Fullbore Formation MicroImager (FMI) tool. Although results are similar, slight improvement is seen if separate networks are trained to predict image facies that belong to specific lithological groups, rather than a single network trained to predict all facies. Where sandy thin beds (<1cm in thickness) occur within thicker shale units further neural networks are needed to discriminate these, trained with different inputs from previous networks. Where there are multiple inputs (which is common when image derived components are incorporated into the methodology) the backpropagation algorithm is able to use the training phase to promote the most useful inputs to be more important in the analysis; inputs that have little discriminatory power are relegated so that they are of lesser importance in the network's decisions. The ranking of inputs in this way can aid future neural network model development and understanding.

## Declaration

I declare that this thesis has been composed solely by myself and that it has not been submitted, either in whole or in part, in any previous application for a degree. Except where otherwise acknowledged, the work presented is entirely my own.

## Acknowledgements

I am indebted to my two supervisors Roger Scrutton and Malcolm Rider. Both have remained enthusiastic and contributed to the evolution of the project over the entire three years. Roger's scientific know-how and ability to ask the right questions at the right time is second to none. Malcolm's well log knowledge is vast and his ability to get the most obscure data files into all types of software has helped make this research go smoothly. This study has also benefited from contributions by Ross Garden and Matt Wakefield at BG Group; Frank Whitehead at Production GeoScience (for help with petrophysics and the software Interactive Petrophysics); Mark Bowers at ExxonMobil (for assistance with petrophysics); Stephen Wolstenhulme (author of the EasyNN neural network program); Roger Hipkin (for use of his spectral analysis programs); Mark Naylor who introduced me to the world of programming, and patiently assisted whilst I attempted to write code for the first time; and Chris Green who assisted in reading the final manuscript.

Finally thanks must go to all those fellow PhD students at Edinburgh who live (and have lived) in the new attic and helped make life enjoyable there.

# Table of Contents


**LIST OF FIGURES** ..... **XVII**

CHAPTER 1 ..... XVII
CHAPTER 2 ..... XVII
CHAPTER 3 ..... XVII
CHAPTER 4 ..... XVIII
CHAPTER 5 ..... XX
CHAPTER 6 ..... XXII
CHAPTER 7 ..... XXIII
APPENDIX 3 ..... XXIII

**LIST OF TABLES** ..... **XXV**

CHAPTER 3 ..... XXV
CHAPTER 4 ..... XXVI
CHAPTER 5 ..... XXVI
CHAPTER 7 ..... XXVII

**LIST OF ENCLOSURES** ..... **XXIX**

**NOTATIONS & CONVENTIONS** ..... **XXXI**

CHAPTERS 3 & 4 ..... XXXI
*Log acronyms* ..... *xxxi*
*Lithofacies columns* ..... *xxxii*
*Keys* ..... *xxxiii*
CHAPTERS 5 & 6 ..... XXXIV
*Log acronyms* ..... *xxxiv*
*Log acronyms- Baker Atlas (in Figure 6.18 only)* ..... *xxxv*
*Lithofacies columns* ..... *xxxv*
*Keys* ..... *xxxvi*

**CHAPTER 1: INTRODUCTION** ..... **1**

1.1 RATIONALE AND BACKGROUND ..... 1
1.2 PROJECT AIMS ..... 7
1.3 NEW CONTRIBUTIONS ..... 8

1.4 DATA ..... 8
1.5 THESIS STRUCTURE ..... 9

**CHAPTER 2: NEURAL NETWORK THEORY, AND PREVIOUS APPLICATIONS TO WELL LOG DATA ..... 11**

2.1 INTRODUCTION ..... 11
2.2 NEURAL NETWORK THEORY AND THE BACKPROPAGATION ALGORITHM ..... 12
*2.2.1 Introduction ..... 12*
*2.2.2 The Perceptron ..... 13*
*2.2.3 The Perceptron Rule ..... 16*
*2.2.4 The Delta Rule ..... 18*
*2.2.5 Training rules for more complex networks ..... 22*
*2.2.6 The Backpropagation algorithm ..... 25*
*2.2.7 Remarks on the Backpropagation algorithm ..... 27*
2.3 STRATEGIES FOR IMPLEMENTING THE ALGORITHM ..... 29
*2.3.1 Introduction ..... 29*
*2.3.2 Local minima ..... 29*
*2.3.3 Encoding of data ..... 30*
*2.3.4 Network architecture ..... 31*
*2.3.5 Stopping criteria ..... 32*
2.4 USE AND LIMITATIONS OF THE BACKPROPAGATION ALGORITHM ..... 33
2.5 OTHER TYPES OF NEURAL NETWORKS ..... 34
*2.5.1 Introduction ..... 34*
*2.5.2 The Hopfield network ..... 34*
*2.5.3 Radial basis functions ..... 34*
*2.5.4 Kohonen networks ..... 35*
*2.5.5 Adaptive Resonance Theory (ART) ..... 35*
*2.5.6 Classification of networks ..... 35*
2.6 THE NEURAL NETWORK PROGRAM USED IN THIS STUDY ..... 36
2.7 NEURAL NETWORK PREDICTIONS IN GEOSCIENCE AND FROM WELL LOGS ..... 36
2.8 SUMMARY ..... 48

**CHAPTER 3 : THE LOMOND FIELD, LITHOFACIES SCHEME & NEURAL NETWORK METHODOLOGY ..... 51**

3.1 INTRODUCTION ..... 51
3.2 THE LOMOND FIELD ..... 51
*3.2.1 Introduction ..... 51*
*3.2.2 Stratigraphy ..... 54*

*3.2.3 Data* ..... 55
3.3 SEDIMENTOLOGY OF THE LOMOND FIELD ..... 56
*3.3.1 Introduction* ..... 56
*3.3.3 Slump sheets and debris flows* ..... 60
*3.3.4 Lobe fringe* ..... 61
*3.3.5 Aerobic / disaerobic basin* ..... 62
*3.3.6 Anoxic basin* ..... 62
3.4 LITHOFACIES DESIGN ..... 63
*3.4.1 Introduction* ..... 63
*3.4.2 Facies architecture* ..... 63
*3.4.3 Reservoir quality of different facies* ..... 65
*3.4.4 Facies quantities* ..... 68
*3.4.5 Log separability* ..... 73
*3.4.6 The lithofacies scheme* ..... 75
3.5 DATA PREPARATION ..... 77
*3.5.1 Introduction* ..... 77
*3.5.2 Input selection* ..... 77
*3.5.3 Data transforms* ..... 79
*3.5.4 Inter-well normalisation of logs* ..... 82
*3.5.5 Depth Shifting* ..... 86
*3.5.6 Training and validation set design* ..... 87
3.6 NEURAL NETWORK METHODOLOGY ..... 90
*3.6.1 Introduction* ..... 90
*3.6.2 Network topology* ..... 90
*3.6.3 Learning and momentum parameters* ..... 93
*3.6.4 Pruning algorithms* ..... 94
*3.6.5 Training with unbalanced data* ..... 98
*3.6.6 Training without derivative logs* ..... 102
*3.6.7 Testing over well 23/21-T8* ..... 103
*3.6.8 Training with different data sets* ..... 107
*3.6.9 Summary of neural network methodology (Section 3.6)* ..... 111
3.7 CHAPTER 3 SUMMARY ..... 113

**CHAPTER 4 : NEURAL NETWORK CRITIQUE BASED ON LITHOFACIES PREDICTIONS IN THE LOMOND FIELD ..... 115**

4.1 INTRODUCTION ..... 115
4.2 FEATURES RECOGNISED IN ALL WELLS ..... 116

*4.2.1 Introduction* ..... *116*
*4.2.2 Thin bed repair* ..... *118*
4.3 MULTIPLE OUTPUTS FROM NEURAL NETWORKS ..... 120
4.4 LITHOFACIES PREDICTIONS IN WELLS 23/21-T8, T5 AND T3 ..... 123
*4.4.1 Introduction* ..... *123*
*4.4.2 Confusion matrices* ..... *123*
*4.4.3 Predicted lithofacies compared to core* ..... *129*
*4.4.4 Lithofacies predictions in wells 23/21-T8, T5 and T3 – summary and discussion* ..... *143*
4.5 LITHOFACIES PREDICTIONS IN WELL 23/21/T4 ..... 145
*4.5.1 Introduction* ..... *145*
*4.5.2 Lithofacies predictions* ..... *145*
4.6 LITHOFACIES PREDICTIONS IN OTHER WELLS ..... 154
*4.6.1 Introduction* ..... *154*
*4.6.2 Predictions in wells 23/21-T1, T2, T6, T9 and T10* ..... *154*
4.7 THE DEPENDENCE OF THE NEURAL NETWORK MODEL ON RESERVOIR FLUID ..... 155
*4.7.1 Introduction* ..... *155*
*4.7.2 Methods for assessing the dependence of the model on various well logs* ..... *156*
*4.7.3 Training without the resistivity log* ..... *165*
*4.7.4 Correcting for fluid* ..... *168*
*4.7.5 Neural network analysis with 'gas-based' logs* ..... *173*
*4.7.6 Summary of Section 4.7* ..... *181*
4.8 CHAPTER SUMMARY ..... 182

**CHAPTER 5 : THE INTEGRATION OF IMAGE LOG DATA INTO THE NEURAL NETWORK PROCESS ..... 185**

5.1 INTRODUCTION ..... 185
5.2 THE WEST DELTA DEEP MARINE CONCESSION AREA ..... 186
*5.2.1 Introduction to the West Delta Deep Marine Concession area* ..... *186*
*5.2.2 Geological evolution of the WDDM channel system* ..... *187*
*5.2.3 Sedimentology of the West Delta Marine Deep Concession area* ..... *190*
*5.2.4 Data* ..... *194*
5.3 IMAGE LOG PREPARATION ..... 195
*5.3.1 Introduction* ..... *195*
*5.3.2 Accelerometer correction* ..... *195*
*5.3.3 Emex (Emmiteur d'exitation) correction* ..... *195*
*5.3.4 Compensation for dead buttons* ..... *196*
*5.3.5 Pad/flap correlation* ..... *196*

*5.3.6 Button equalisation* ..... *197*
*5.3.7 Processing summary* ..... *198*
5.4 QUANTIFYING IMAGE LOG DATA ..... 198
*5.4.1 Published methods for quantifying image log data* ..... *198*
*5.4.2 Statistical pad analysis* ..... *200*
*5.4.3 Spectral analysis of image logs* ..... *209*
*5.4.4 How can these data be used?* ..... *217*
5.5 DATA PREPARATION BEFORE NEURAL NETWORK ANALYSIS ..... 220
*5.5.1 Introduction* ..... *220*
*5.5.2 Input selection* ..... *220*
*5.5.3 Data transforms* ..... *221*
*5.5.4 Inter-well normalisation* ..... *222*
*5.5.5 Training and validation set design* ..... *224*
5.6 PRELIMINARY ANALYSIS ..... 227
*5.6.1 Introduction* ..... *227*
*5.6.2 Image facies prediction with a modular neural network* ..... *228*
*5.6.3 Image facies prediction with a single neural network* ..... *237*
*5.6.4 The identification of thin sandy beds* ..... *242*
*5.6.5 Neural network dependence* ..... *248*
5.7 CHAPTER SUMMARY ..... 251

**CHAPTER 6 : FURTHER ANALYSIS OF IMAGE LITHOFACIES RESULTS ..... 253**

6.1 INTRODUCTION ..... 253
6.2 DETAILED ANALYSIS OF NETWORK PREDICTIONS ..... 253
*6.2.1 Introduction* ..... *253*
*6.2.2 Detailed well analysis* ..... *253*
6.3 LARGE SCALE ANALYSIS OF IMAGE FACIES PREDICTIONS ..... 271
*6.3.1 Introduction* ..... *271*
*6.3.2 Large-scale analysis* ..... *271*
6.4 CHAPTER SUMMARY ..... 276

**CHAPTER 7 : DISCUSSION AND CONCLUSIONS ..... 277**

7.1 INTRODUCTION ..... 277
7.2 CATEGORIES FOR DISCUSSION IN THIS THESIS ..... 278
*7.2.1 Neural network methodology* ..... *278*
*7.2.2 Limitations of the methodology due to data* ..... *284*
*7.2.3 Neural network analysis of deep marine clastic sediments* ..... *286*
*7.2.4 Neural network use with image logs* ..... *287*

*7.2.5 Interpretation of neural network results* ..... 289
7.3 OUTSTANDING QUESTIONS / FURTHER WORK ..... 290
*7.3.1 Backpropagation neural network technique* ..... 290
*7.3.2 Methodologies for integrating image log data* ..... 290
*7.3.3 Use of predictions* ..... 293
7.4 APPLICATIONS & USE ..... 294
*7.4.1 Classification* ..... 294
*7.4.2 Reservoir modelling (both static and dynamic)* ..... 294
*7.4.3 Interpretation of newly drilled wells* ..... 295
*7.4.4 Measurement whilst drilling (MWD)* ..... 295
*7.4.5 Fractures* ..... 296
7.5 MAIN CONCLUSIONS ..... 296
*7.5.1 Prediction of lithofacies and image lithofacies* ..... 296
*7.5.2 Limitations and interpretation* ..... 296
*7.5.1 Incorporation of image data* ..... 297

**REFERENCES** ..... 299

**APPENDIX 1 : TOOL DESIGN AND LIMITATIONS & DERIVATIVE LOG CALCULATIONS** ..... 313

A1.1 INTRODUCTION ..... 313
A1.2 DATA ACQUISITION AND LIMITATIONS ..... 313
*A1.2.1 The gamma ray log* ..... 313
*A1.2.2 The sonic log* ..... 313
*A1.2.3 The density log* ..... 314
*A1.2.4 The neutron log* ..... 314
*A1.2.5 The resistivity log* ..... 315
A1.2 HORIZONTAL WELLS ..... 316
A1.3 DERIVATIVE LOG CALCULATION ..... 316
*A1.3.1 Neutron-density separation* ..... 316
*A1.3.2 Shale volume* ..... 317
*A1.3.3 Total porosity* ..... 317

**APPENDIX 2 : PROGRAMS USED IN THIS THESIS** ..... 319

THIN-BED REPAIR PROGRAM ..... 320

**APPENDIX 3 : CORRECTION FOR FLUID** ..... 329

A3.1 INTRODUCTION ..... 329

A3.2 LOGS AFFECTED BY FLUID ..... 329
A3.3 SONIC ..... 329
A3.4 DENSITY ..... 331
A3.5 NEUTRON ..... 332
A3.6 PARAMETERS USED FOR OTHER WELLS ..... 335
*A3.6.2 Sonic* ..... *335*
*A3.6.3 Density* ..... *337*
*A3.6.4 Neutron* ..... *337*

**APPENDIX 4 : TRAINING INTERVALS FOR THIN-BEDS ..... 341**

4.1 INTRODUCTION ..... 341
4.2 TYPE-I THIN-BEDS ..... 341
4.3 TYPE-II THIN-BEDS ..... 341

**APPENDIX 5 : FULL LOGS AND ELECTRONIC THESIS ..... 343**

# List of Figures


*Chapter 1*

1.1 Cross-plotting logs to determine lithology. 2

1.2 Statistical methods for predicting lithology and facies from well logs. 4

1.3 The conventional way of depicting a neural network. 6

*Chapter 2*

2.1 A simplified neuron. 12

2.2 Pictorial representation of a perceptron. 14

2.3 Graphical representation of a simple neural network. 15

2.4 Graphical representation of the AND and XOR functions. 15

2.5 Perceptron representation of the XOR function. 16

2.6 A simple neural network. 16

2.7 Representative error surface for a perceptron with two weights. 19

2.8 Graphical representation of different sized neural networks. 23

2.9 The sigmoid threshold unit. 23

2.10 Class separability by different sized neural networks. 28

2.11 Graphical representation of calculating three rock components from logs. 28

2.12 Local minima on a complex error surface. 30

2.13 Over-fitting data. 33

2.15 A committee machine. 44

2.16 A modular committee machine. 45

2.17 A recurrent backpropagation neural network. 47

*Chapter 3*

3.1 The position of the Lomond Field in the Central North Sea. 52

3.2 Salt controls on the evolution of the Central Graben. 53

3.3 Stratigraphy of the Palaeogene of the North Sea. 54

3.4 Facies model adapted from Mutti & Ricci Lucchi (1972). 57

| | | |
|---|---|---|
| 3.5 | Sedimentary log representing submarine channel and lobe facies. | 59 |
| 3.6 | Plan view of the three main types of turbidite depositional system. | 59 |
| 3.7 | Sedimentary log representing slump sheet deposition. | 60 |
| 3.8 | Sedimentary log representing thin-bedded submarine lobe fringe. | 61 |
| 3.9 | Sedimentary log representing low energy anaerobic basin. | 62 |
| 3.10 | Porosity and permeability distributions for different facies types. | 67 |
| 3.11 | Facies representing slump sheets and debris flows. | 68 |
| 3.12 | Occurrence of facies in all four cored wells. | 70 |
| 3.13 | Occurrence of facies in well 23/21-T3. | 70 |
| 3.14 | Occurrence of facies in well 23/21-T4. | 71 |
| 3.15 | Occurrence of facies in well 23/21-T5. | 71 |
| 3.16 | Occurrence of facies in well 23/21-T8. | 72 |
| 3.17 | Cross-plots of various logs. | 74 |
| 3.18 | Frequency distribution of the resistivity log. | 80 |
| 3.19 | Frequency distribution of various logs. | 81 |
| 3.20 | The Sele Formation, identified by its gamma-ray log signature. | 83 |
| 3.21 | Frequency plots for the Sele Formation (GR, DT, ILD). | 84 |
| 3.22 | Frequency plots for the Sele Formation (RHOB, NPHI). | 85 |
| 3.23 | Frequency plots for the Forties Sandstone Member (RHOB). | 85 |
| 3.24 | Graph of percentage correct over validation set v network topology. | 92 |
| 3.25 | General relationships between network topology and hit-rate. | 92 |
| 3.26 | Neural networks that have undergone pruning. | 96 |
| 3.27 | The effect of training a neural network with limited examples. | 101 |
| 3.28 | Lithofacies columns predicted by a variety of different networks. | 105 |
| 3.29 | The results of two best performing networks. | 110 |
| 3.30 | Summary of the methodology followed in Chapter 3. | 114 |

*Chapter 4*

| | | |
|---|---|---|
| 4.1 | Raw lithofacies predictions with thin-beds. | 117 |
| 4.2 | Implementation of the thin bed repair program. | 119 |
| 4.3 | Repairing the raw logs with different thin-bed thicknesses. | 120 |
| 4.4 | Comparison of single and multiple output networks. | 121 |
| 4.5 | Graphical representation of the threshold and sigmoid functions. | 121 |

| | | |
|---|---|---|
| 4.6 | Probability density functions of output node activation levels. | 122 |
| 4.7 | Lithofacies results from a section of well 23/21-T8. | 133 |
| 4.8 | Lithofacies results from a section of well 23/21-T8. | 136 |
| 4.9 | Lithofacies results from a section of well 23/21-T5. | 137 |
| 4.10 | Lithofacies results from a section of well 23/21-T5. | 138 |
| 4.11 | Lithofacies results from a section of well 23/21-T3. | 141 |
| 4.12 | Lithofacies results from a section of well 23/21-T3. | 142 |
| 4.13 | Lithofacies results from a section of well 23/21-T4. | 147 |
| 4.14 | Normalising log curves for depth. | 148 |
| 4.15 | Frequency plots for the Sele Formation (DT, ILD). | 150 |
| 4.16 | Section from the logs in well 23/21-T3 (GR, NPHI, RHOB, ILD). | 150 |
| 4.17 | Normalisation of the density log in well 23/21-T4. | 151 |
| 4.18 | Neural network results in well 23/21-T4 for normalised data. | 153 |
| 4.19 | Calculating the contribution of input nodes to the output layer. | 158 |
| 4.20 | Cross-plots of various logs colour coded by lithofacies type, well 23/21-T3. | 160 |
| 4.21 | Cross-plots of various logs colour coded by lithofacies type, well 23/21-T8. | 161 |
| 4.22 | Fluid transition zone in well 23/21-T5. | 162 |
| 4.23 | Fluid transition zone in well 23/21-T1. | 162 |
| 4.24 | Fluid transition zone in well 23/21-T6. | 163 |
| 4.25 | Section from well 23/21-T8. | 164 |
| 4.26 | Sections from wells 23/21-T3, T5 and T8. | 167 |
| 4.27 | Sonic, density and neutron logs after standardising for fluid, well 23/21-T5. | 172 |
| 4.28 | Sections from wells 23/21-T3, T5 and T8. | 176 |
| 4.29 | Section from well 23/21-T5. | 177 |
| 4.30 | Section from the main reservoir in well 23/21-T6. | 178 |
| 4.31 | Section from well 23/21-T8. | 179 |
| 4.32 | Section from well 23/21-T1. | 180 |

*Chapter 5*


| | | |
|---|---|---|
| 5.1 | Location of the West Delta Deep Marine Concession area, redrawn from Samuel *et al.* (2003). | 187 |
| 5.2 | Proposed geological evolution of the West Delta Deep Marine channel system, redrawn from Samuel *et al.* (2003). | 189 |
| 5.3 | Examples of different image facies defined by Baker Atlas. | 193 |
| 5.4 | Image data quality issues. | 194 |
| 5.5 | Pad/flap correlation. | 196 |
| 5.6 | Button equalisation. | 197 |
| 5.7 | Calculating statistics over different moving windows. | 201 |
| 5.8 | Comparison of single and multiple pad statistics. | 202 |
| 5.9 | Variable dip in a single well. | 203 |
| 5.10 | Ambiguity in the defined image facies scheme. | 205 |
| 5.11 | The use of conventional logs in image facies analysis. | 206 |
| 5.12 | Distributions of different calculated statistics via image facies type for well Simian 1, sands. | 207 |
| 5.13 | Distributions of different calculated statistics via image facies type, shales. | 208 |
| 5.14 | Explanation of the theory behind the power spectral method. | 211 |
| 5.15 | Testing the power spectral approach with synthetic data. | 212 |
| 5.16 | Comparison of a FFT over a single pad and over all data. | 213 |
| 5.17 | Comparison of the frequencies contained in the power spectrum of a discrete wave, and the same wave if it repeated. | 214 |
| 5.18 | Horizontal and vertical power spectra of different image facies, well Simian 1. | 215 |
| 5.19 | Horizontal and vertical power spectra of different image facies, well Simian 2. | 216 |
| 5.20 | Horizontal and vertical power spectra of different image facies, well Simian 3. | 216 |
| 5.21 | Modular system for the discrimination of image facies. | 220 |
| 5.22 | Distributions of some input variables. | 222 |
| 5.23 | Calibration between wells Simian 1, 2 and 3. | 223 |
| 5.24 | Training examples from well Simian 1. | 224 |

| | | |
|---|---|---|
| 5.25 | Training examples from well Simian 2. | 225 |
| 5.26 | Training examples from well Simian 3. | 225 |
| 5.27 | The effect of interpolating between data points on the hit-rate over the validation set. | 229 |
| 5.28 | Results of the neural network trained to predict sand, shale and cemented lithological groups from well Simian 2. | 230 |
| 5.29 | Results of the neural network trained to predict sand, shale and cemented lithological groups from well Simian 3. | 230 |
| 5.30 | Results of cemented facies predicted in well Simian 1. | 231 |
| 5.31 | The percentage correct over the validation set for different sized sand networks; three trials per network. | 232 |
| 5.32 | The percentage correct over the validation set for different sized shale networks; three trials per network, trained with image derived inputs only. | 233 |
| 5.33 | The percentage correct over the validation set for different sized shale networks; three trials per network, trained with all inputs. | 233 |
| 5.34 | Results from Simian 1. | 235 |
| 5.35 | Results from Simian 2. | 235 |
| 5.36 | Results from Simian 3. | 236 |
| 5.37 | An example of an edge effect at a sand / shale boundary. | 236 |
| 5.38 | Training a single network. | 238 |
| 5.39 | Comparison of the results from the 'modular' network and single network, well Simian 1. | 239 |
| 5.40 | Comparison of the results from the 'modular' network and single network, well Simian 2. | 240 |
| 5.41 | Comparison of the results from the 'modular' network and single network, well Simian 3. | 240 |
| 5.42 | Comparison of the results from the 'modular' network and single network, well Simian 3. | 241 |
| 5.43 | Thin-bedded levee deposits. | 243 |
| 5.44 | Training intervals for type-I thin beds. | 244 |
| 5.45 | Thin-beds predicted in an area where the log is out of focus. | 244 |
| 5.46 | A successfully predicted type-I thin-bed. | 245 |
| 5.47 | Predictions from well Simian 1. | 245 |

5.48 Type-II thin-bed predictions from well Simian 3. 247
5.49 Bar graphs to show the dependency of the neural network models on various inputs. 248
5.50 Schematic of a two-dimensional cross-section of the hypothesis space in which the neural network is searching for a solution. 250

*Chapter 6*

6.1 Overview of the three wells that make up the data set. 255
6.2 Section of results from well Simian 1, 6945-6965ft. 256
6.3 Section of results from well Simian 1, 6933-7013ft. 257
6.4 Section of results from well Simian 1, 7027.3-7046.8ft. 258
6.5 Section of results from well Simian 1, 7143.7-7150.2ft. 259
6.6 Section of results from well Simian 2, 7018-7046ft. 260
6.7 Section of results from well Simian 2, 7104-7135ft. 261
6.8 Section of results from well Simian 2, 7205-7236ft. 262
6.9 Section of results from well Simian 2, 7318-7345ft. 263
6.10 Section of results from well Simian 3, 6900-6920ft. 264
6.11 Section of results from well Simian 3, 6970-7000ft. 265
6.12 Section of results from well Simian 3, 7067-7096ft. 266
6.13 Section of results from well Simian 3, 7163-7190ft. 267
6.14 Section of results from well Simian 3, 7220-7248.5ft. 268
6.15 Seismic amplitude map of the Simian prospect (from Baker Atlas 2001). 273
6.16 Interpretation of the main depositional environments of the Simian channel system from image facies predicted from a neural network. 274
6.17 Interpretation of the main depositional environments of the Simian channel system from image facies derived manually (from Baker Atlas 2001). 275
6.18 Cartoon showing the widening of the Simian channel system and possible lower net/gross in the downslope direction. 276

*Chapter 7*


| | | |
|---|---|---|
| 7.1 | An advance modular system for the predicting image lithofacies. | 292 |
| 7.2 | An alternative system to Figure 7.1. | 293 |


*Appendix 3*


| | | |
|---|---|---|
| A3.1 | Cross-plot of core porosity against sonic values, gas zone well 23/21-T3. | 331 |
| A3.2 | Cross-plot to determine the hydrogen index of the 'fluid', gas zones, all wells. | 334 |
| A3.3 | Cross-plot of core porosity against sonic values, gas zone, all wells. | 336 |
| A3.4 | Cross-plot of core porosity against sonic values, water zone, all wells, | 336 |
| A3.5 | Cross-plot to determine the hydrogen index of the 'fluid', gas zone, all wells. | 338 |
| A3.6 | Cross-plot to determine the hydrogen index of the 'fluid', water zone, all wells. | 338 |

# List of Tables

*Chapter 3*


| | | |
|---|---|---|
| 3.1 | Ranges used for population of lithofacies dimensions. | 65 |
| 3.2 | The Lomond lithofacies scheme. | 76 |
| 3.3 | The amount of lithofacies available in the data set. | 87 |
| 3.4 | Content of the Primary training set. | 88 |
| 3.5 | Contents of Training set 2. | 88 |
| 3.6 | Contents of Training set 3. | 89 |
| 3.7 | Summary of the contents of all three training and validation sets. | 89 |
| 3.8 | Hit-rate over the validation set after training with different learning rates and momentum parameters. | 93 |
| 3.9 | Hit-rate over the validation set for starting networks with 23 nodes, for different weight and cycle thresholds. | 95 |
| 3.10 | Hit-rate over the validation set for starting networks with 14 nodes, for different weight and cycle thresholds. | 97 |
| 3.11 | The percentage that each lithofacies contributes to the new training set, with unbalanced data. | 98 |
| 3.12 | The percentage correct over the validation set for two different types of network, both trained with unbalanced data. | 99 |
| 3.13 | Percentage of each lithofacies correctly predicted in the validation set, trained with unbalanced data. | 99 |
| 3.14 | The percentage that each lithofacies contributes to the new training set, unbalanced data and with lithofacies 1 artificially reduced. | 100 |
| 3.15 | The percentage correct over the validation set for two different types of network, unbalanced data and lithofacies 1 artificially reduced. | 100 |
| 3.16 | Percentage of each lithofacies correctly predicted in the validation set, trained with unbalanced data and lithofacies 1 in the minority. | 101 |
| 3.17 | The percentage correct over the validation set for two different types of network, all trained without derivative logs. | 102 |
| 3.18 | Lithofacies codes found in Figure 3.28 | 104 |

3.19 Results of six networks trained with training set 2. 108
3.20 Results of six networks trained with training set 3. 108
3.21 The percentage of well 23/21-T3 that were predicted correctly; were predicted as mixed outputs; and as 'none' outputs. 111

*Chapter 4*

4.1 Confusion matrix for well 23/21-T8 before application of the thin-bed repair program. 125
4.2 Confusion matrix for well 23/21-T8 after the thin-bed repair program was applied. 125
4.3 Confusion matrix for well 23/21-T5 before application of the thin-bed repair program. 127
4.4 Confusion matrix for well 23/21-T5 after the thin-bed repair program was applied. 127
4.5 Confusion matrix for well 23/21-T3 before application of the thin-bed repair program. 128
4.6 Confusion matrix for well 23/21-T3 after the thin-bed repair program was applied. 128
4.7 Percentage contributions of input variables to the network output. 158
4.8 Results from training ordinary and pruned networks without the resistivity log. 165
4.9 Results from the best performing network from Table 4.8 when it was applied to wells 23/21-T3, T5 and T8. 166
4.10 Results from training ordinary and pruned networks with the recalculated gas logs. 173
4.11 Results from the best performing network from Table 4.10 when it was applied to wells 23/21-T3, T5 and T8. 174

*Chapter 5*

5.1 West Delta Deep Marine image facies scheme. 192
5.2 Image facies associations, identified and interpreted from resistivity images, after Baker Atlas. 193
5.3 Image facies scheme, based on that defined by Baker Atlas. 219

5.4 Data available to contribute to training and validation sets, by well. 226
5.5 Number of feet of each lithology type used for training for the first (sand / shale / cemented) neural network, and boosting factors. 227
5.6 No of feet of facies used for training for the second (facies 1-4 and facies 5&6) neural networks, and boosting factors. 227
5.7 The percentage correct over the validation set for different sized networks; three trials per network - module 1. 228
5.8 The percentage correct over the validation set for different sized networks; three trials per network, thin-bed network, type-II. 246

*Chapter 7*

7.1 Comparison of different backpropagation networks used by various authors. 279

# List of Enclosures

Enclosure 1 - notations & conventions, Chapters 3 & 4.

Enclosure 2a - notations & conventions, Chapters 5 & 6.

Enclosure 2b - notations & conventions, Chapters 5 & 6.

# Notations & conventions

This thesis contains a number of log acronyms, lithofacies colours, and sedimentary facies codes. Although these are introduced in the main body of the thesis this section contains a summary of these, and relevant keys. They are also listed as two enclosures that should also be used as reference.

## *Chapters 3 & 4*

*Log acronyms*

| | |
|---|---|
| GR | gamma ray log |
| DT | sonic log |
| DT4P | p-sonic (as DT) |
| ILD | deep induction log (resistivity) |
| ILM | medium induction log (resistivity) |
| AHT90 | deep resistivity (from Array Tool) |
| RHOB | density log |
| NPHI | neutron log |
| PORCOR | laboratory measured core plug porosity value |
| KAH (cor) | laboratory measured core plug horizontal permeability value |
| NDSEP | neutron density separation (see Appendix 1) |
| PORLOGT | calculated total porosity (see Appendix) |
| DTgas | sonic log corrected to represent a full gas reservoir |
| RHOBgas | density log corrected to represent a full gas reservoir |
| NPHIgas | neutron log corrected to represent a full gas reservoir |
| P-Train | interval in primary training set (always shown as black flag/bar) |
| Train | interval in primary training set (always shown as black flag/bar) |
| ACT_1 - ACT_5 | activation of output node representing lithofacies 1-5 (from optimum network) |
| ACT_1n - ACT_5n | activation of output node representing lithofacies 1-5 (input data calibrated to training set) |

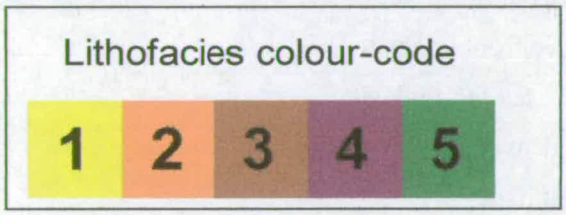
| | |
|---|---|
| ACT_1a - ACT_5a | activation of output node representing lithofacies 1-5 (model not trained with resistivity log) |
| ACT_1G - ACT_5G | activation of output node representing lithofacies 1-5 (when trained with gas corrected logs and no resistivity) |

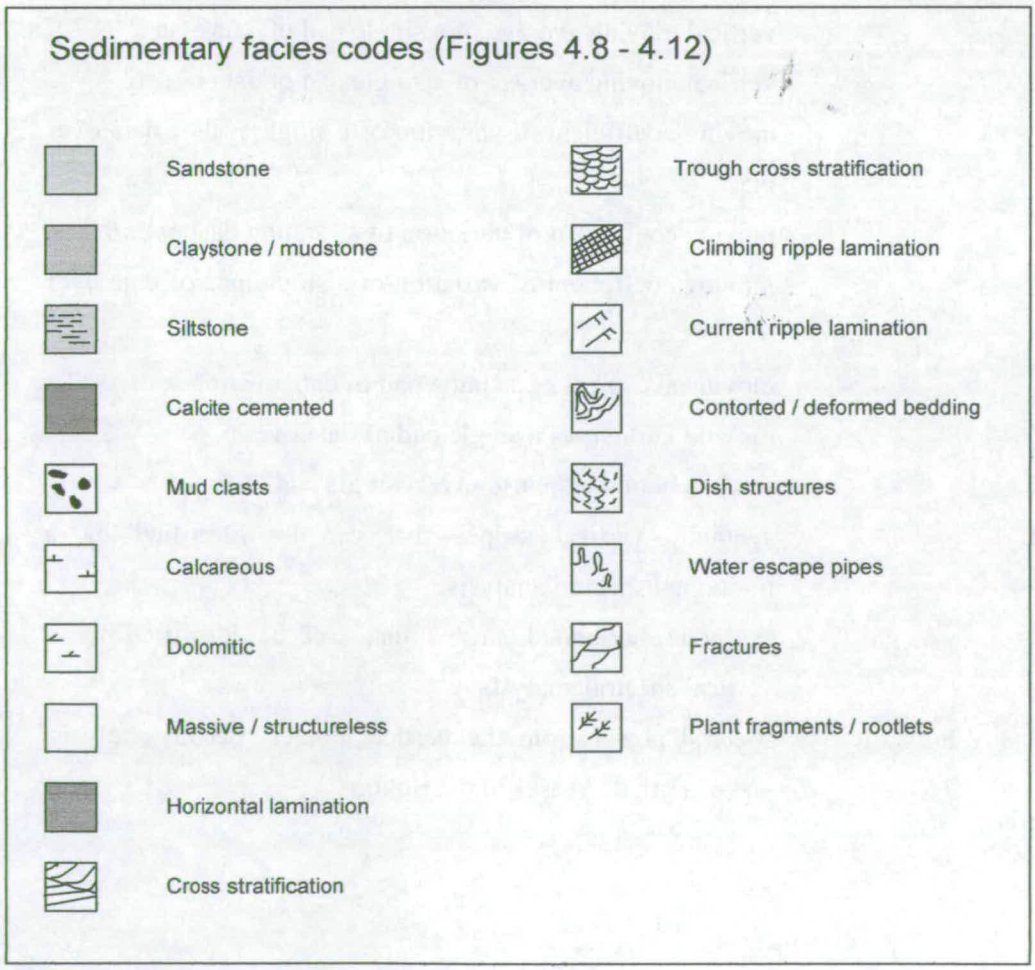
*Lithofacies columns*

| | |
|---|---|
| Lithofacie | core defined lithofacies |
| B | best performing network from topological experiments |
| C | best performing network from experiments with different learning rates and momentum parameters |
| D | best performing network from experiments with pruning algorithm starting with 23 nodes |
| E | best performing network from experiments with pruning algorithm starting with 14 nodes |
| F | best performing network from experiments with unbalanced data |
| G | best performing network from experiments with unbalanced data and lithofacies 1 reduced further |
| H | best performing network from training without derivative logs |
| I | best performing network from training with Training Set 2 |
| J | best performing network from training with Training Set 3 |
| LF_PR | best performing of all networks 'optimum network' (actually same as 'B') |
| PLF_Rep3 | LF_PR after application of thin-bed repair program (with thin-bed defined as 1.5ft) |
| PLF_Rep4 | LF_PR after application of thin-bed repair program (with thin-bed defined as 2ft) |
| PLF_Repair | LF_PR after application of thin-bed repair program (with thin-bed defined as 1.5ft) |
| LF_PRmax | raw lithofacies predictions with maximum activation taken as the output |
| PLF_Rep_m | LF_PRmax but after application of thin-bed repair program |
| LF_PRn | raw lithofacies predicted from normalised data |

| | |
|---|---|
| LF_PRmaxn | raw lithofacies predicted from normalised data with maximum activation taken as the output |
| LF_PRmaxnR | LF_PRmaxn but after application of the thin-bed repair program |
| LF_PRa | lithofacies output from model trained with no resistivity log and the highest activated node as the prediction |
| LF_PRg | lithofacies output from model trained with gas corrected logs and no resistivity log with the highest activated node taken as the prediction |

*Keys*



***Chapters 5 & 6***

*Log acronyms*

| | |
|---|---|
| GR | gamma ray log |
| RHOB | density log |
| RHOZ | density log |
| NPHI | neutron log |
| PHIN | neutron log |
| FMIimage | microresistivity image log, unprocessed |
| FMIimage_P | microresistivity image log, processed (steps described in Chapter 5) |
| C1 | first caliper curve from image tool |
| C2 | second caliper curve from image tool |
| S-PAD | Single pad of data used for analysis |
| AVsp | continuous vertical average of resistivity button responses over a single pad of data |
| A2 | vertical moving average of all button data over 2" |
| A2sp | vertical moving average of a single pad of data over 2" |
| A6sp | vertical moving average of a single pad of data over 6" |
| CV05sp | moving coefficient of variation of a single pad of data over 0.5" |
| CV6 | moving coefficient of variation of all button data over 6" |
| CV6sp | moving coefficient of variation of a single pad of data over 6" |
| Sk6sp | moving skewness of a single pad of data over 6" |
| Kur6sp | moving kurtosis of a single pad of data over 6" |
| Stack_ssp | stacked button response over a single pad of data |
| ARRAY-H | synthetic vertical stripes that can be identified by a horizontal spectral analysis |
| ARRAY-V | synthetic horizontal stripes that can be identified by a vertical spectral analysis |
| POWER-V *or* V-POWER | spectral power from the vertical power spectral analysis, wavelength decreases to the right |

| | |
|---|---|
| POWER-H *or* H-POWER | spectral power from the horizontal power spectral analysis, wavelength decreases to the right |
| FAS2 – FAS12 | individual horizontal power spectral curves; the 2nd lowest frequency sampled – 12th lowest frequency sampled |
| FSP128_2 – FSP128_64 | individual vertical power spectral curves; the 2nd lowest frequency 64th lowest frequency |
| TRAIN_1 | sections from well Simian 1 used for training (black bar) |
| Train2a | sections from well Simian 2 used for training (black bar) |
| Train3a | sections from well Simian 3 used for training (black bar) |
| ACT F1 – ACT F7 | activation levels for image lithofacies 1-7 (activation levels come from module 1 for image lithofacies 7, from module 2 for other facies) |
| thin_bed | raw prediction of type-II thin-beds (packages) |
| T-BED | as for thin_bed except filtered to leave only packages of thin-beds greater than 2ft thickness and those occurring in image lithofacies 1 and 2 |

*Log acronyms- Baker Atlas (in Figure 6.18 only)*

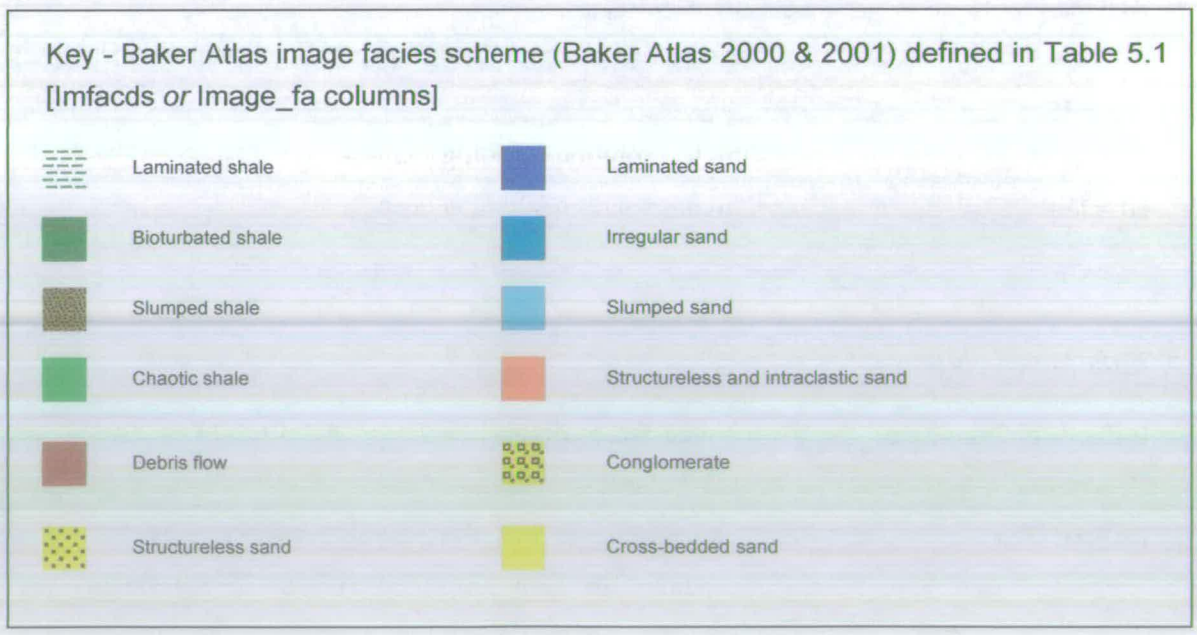
| | |
|---|---|
| TNLW | neutron log |
| RHOB | density log |
| RHOZ | density log |
| AT10 – AT90 | Array resistivity tool (with depth of investigation shown in cm) |
| HLLS | high resolution laterolog shallow |
| HLLD | high resolution laterolog deep |

*Lithofacies columns*

| | |
|---|---|
| Imfacds *or* Image_fa | image facies defined by Baker Atlas (2000 & 2001) – see key below |
| IMFACIESr | facies scheme that the neural networks were trained to predict, this is a simplified version of the Baker Atlas scheme – see key below |

| | |
|---|---|
| Mod1_com | raw results of module 1, used to predict sand, shale and cemented lithofacies |
| Mod1_comb | results of module 1, used to predict sand, shale and cemented lithofacies after thin-bed repair |
| IM_FACall | results from modular system when the shale network in module 2 utilised both conventional and image derived logs as inputs |
| IM_FACal2b | as IM_FACall but after thin-bed repair |
| IM_FACim | results from modular system when the shale network in module 2 utilised only image derived logs as inputs |
| IMFACim2b | as IM_FACim but after thin-bed repair |
| IM_FAC_S | results from a single network trained to predict all 7 image lithofacies at once (non-modular system) |
| IM_FAC_S2 | as IM_FAC_S but after thin-bed repair |
| IMFACal2p | as IM_FACal2b but with type-I thin-beds added |
| IMFACal2q | as IMFACal2p but with type-I thin-beds taken out if caliper curves are above a specific threshold – these are the final results shown in Chapter 6 |

*Keys*



Key - simplified image lithofacies scheme defined in Table 5.3 [IMFACIESr column]


1 - Laminated shale


2 - Bioturbated shale


3 - Slumped and chaotic shale


4 - Shaly SST, debris flow


5 - resistive sand (structureless sand)


6 - Conductive sand (irregular, slumped, intraclastic)


7 - Cemented intervals / conglomerate

# Chapter 1: Introduction

## *1.1 Rationale and background*

Discrimination of lithology and sedimentary facies in any hydrocarbon reservoir is a requirement in both exploration and production. At the exploration stage lithological knowledge allows quantification of net reservoir, assisting in economic appraisal; a sedimentary facies interpretation allows prediction of further reservoir and therefore aids future well emplacement. At the production stage both lithology and facies data are the building blocks of field-wide static geological models. In many cases specific lithologies have distinct petrophysical characteristics allowing the data to also contribute to any dynamic model. In today's environment of targeting very deep sub-sea reservoirs and drilling horizontal wells the coring of wells is very expensive. Therefore only the first few wells drilled in a field are usually cored. Wells logs however are nearly always run in every well drilled. For this reason it is very common to estimate lithology from logs and, by initially correlating log signatures with any available core, to then go on to estimate sedimentary facies from the logs alone.

Traditionally lithology interpretation involves close inspection of all measured wireline logs together with the mud-log (which records descriptions of the drill cuttings). Interpretation is then carried out manually. Certain lithologies such as salt or coal have a specific density and velocity, and are therefore straightforward to interpret. More common lithologies such as shale, sandstone, or limestone have a far greater variety of log readings that are dependent on rock parameters such as porosity, a product of the rock's burial depth and diagenetic history. Thus this type of interpretation requires an experienced geologist, and even then the interpretation can be ambiguous. The use of computers has allowed other methods to complement manual interpretation. By far the most commonly used technique is that of cross-plotting various logs. If the matrix material is known, the neutron-density plot (Figure 1.1a) may distinguish mineral and porosity percentages (Rider 1996). If a shale point can be estimated then fields of sand-shale-porosity or limestone-shale-porosity can be defined, and the percentages of each evaluated. More sophisticated plots exist including the *M-N* plot (Burke *et al.* 1969), (Figure 1.1b), and the *MID* plot (for **M**ineral **ID**entification) (Clavier & Rust 1976). Both use the density, neutron and sonic logs, but algebraically reduce the three

variables to two, effectively eliminating porosity (and therefore fluid). The resulting plots define 'lithology triangles' that can be used to evaluate various matrix components.

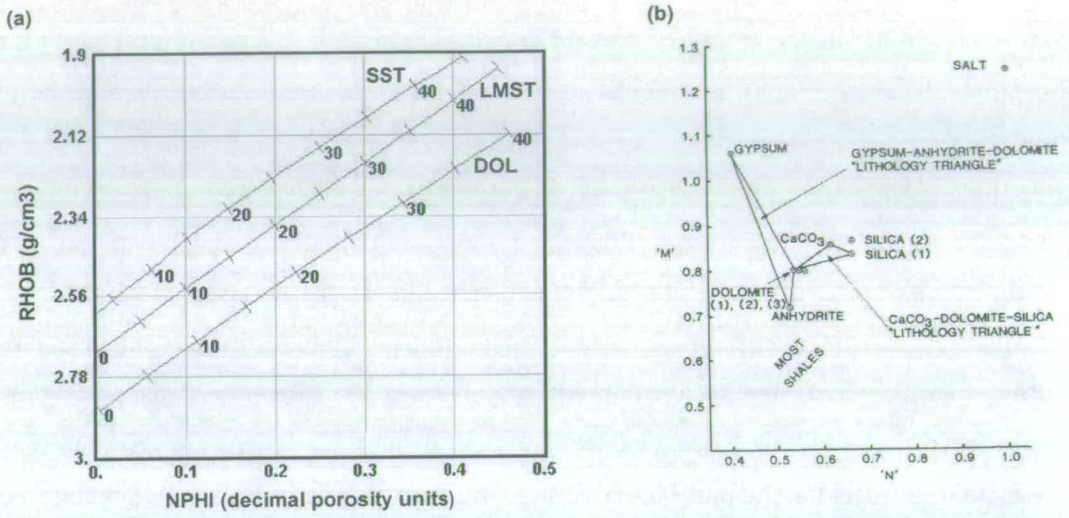



**Figure 1.1** Cross-plotting logs to determine lithology.

(a) Neutron-density plot with defined areas of sandstone (SST), limestone (LMST), dolomite (DOL) and their respective porosities (produced from Interactive Petrophysics software).

(b) The M-N plot (redrawn from Rider (1996), after Burke *et al.* (1969)). M and N are two algebraically derived quantities from the density, neutron and sonic logs.

Although some of these cross-plots have specific disadvantages (such as the co-linear nature of the density and sonic logs), they all suffer from the problem of dimensionality. It is only realistically possible to plot two logs together; three or four can be difficult to visualise. Today many more types of logs are run than in the past and these logs sample the borehole at an ever-increasing resolution. Data is now recorded digitally and any modern technique for lithology or facies prediction from logs must attempt to utilise all data in an efficient manner. In this way lithological-log relationships that previously may not have been known (and could be field specific) may reveal themselves. So-called 'multi-mineral' analysis using simultaneous equations can be used to evaluate more components in the rock matrix, and can utilise as many logs. In fact this type of analysis usually comes as standard in most petrophysical software. The procedure is well known by log analysts, and was used as far back as 1963 (Savre, 1963).

Rider (1996) though, criticises these types of analyses for lithology as being dependent on artificially defined absolutes that have little relation to lithology in the usual sense. A sandstone is not defined solely by its quartz percentage but by its composition and texture, and so 'lithology' defined by the above methods does not always represent true geological 'lithology'.

A different approach for lithology or facies evaluation from logs is via statistical means. These are all classed as 'multivariate' because the data they evaluate is from multiple sources (multiple logs). Doveton (1994) devotes a whole chapter of his book to this type of analysis and Moss (1997) also provides a useful overview. Essentially there are two techniques. The first is where the method is required to discriminate between certain user defined groups (supervised classification); the second is designed to find groups that intrinsically exist within the data (unsupervised classification). These methods represent a completely different philosophy to the cross-plot method. If (in the case of supervised classification) the user defines a class as being 'a mid-channel fluvial sandstone' then that is what it is, and the methodology will try to predict sedimentary facies rather than simply mineralogy. In this case the user should be working within some constraints: he/she should have reasonable confidence that the log signatures of a particular facies enable it to be distinguished from the other defined facies, and that no other facies are expected to be encountered. Therefore these techniques are more specific (e.g. to a particular field or sedimentary environment), whereas the cross-plot and multi-mineral analysis methods are more universal. Discriminant function analysis (for example Doveton (1986)) mathematically defines ellipsoids in n-dimensional space from n histograms (where n is the number of logs) and the resulting equation may classify previously defined populations (Figure 1.2a). Principal component analysis projects logs in dimensional space to axes that account for most variation in the logs (the principal component axes). This is a method of dimensionality reduction, and when data are plotted with respect to the principal component axes specific populations can often be defined more easily. In Figure 1.2b the two principal component axes are shown. By comparison with Figure 1.1a it can be seen that PC1 aligns with porosity and PC2 with grain density. Fuzzy logic (Cuddy 2000) (Figure 1.2c) uses training data to assign statistical distributions to previously defined populations. New data can then be presented and the probability calculated for each log and for each population. The probabilities for all the logs for a single population are combined, and the population with the highest probability is then the assigned class.

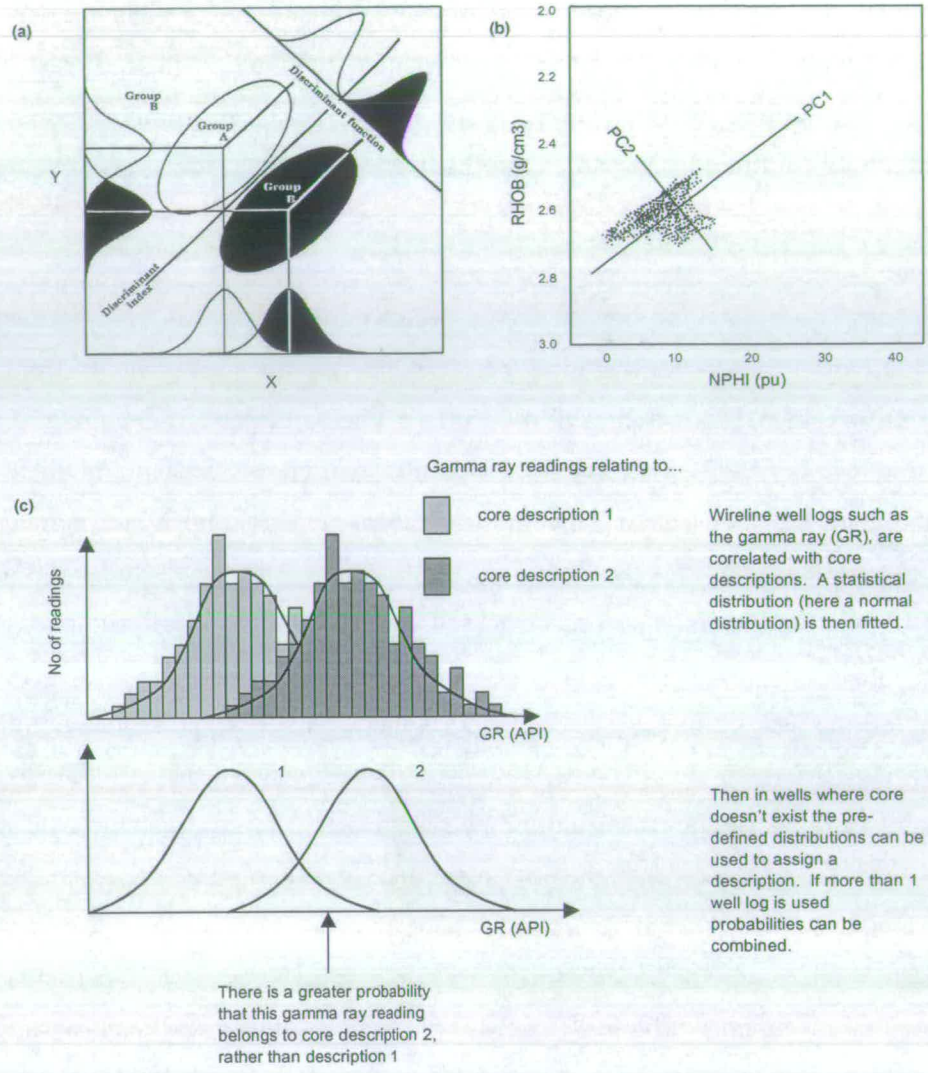



**Figure 1.2** Statistical methods for predicting lithology and facies from well logs.

(a) Discriminant Function Analysis. Two groups, when plotted with respect to a single variable, commonly show overlap in their distributions and thus ambiguity in interpretation. When plotted with two variables separability may improve. The diagram shown shows the 'ideal' where the groups show perfect separation. The discrimination function is the linear equation of the axis shown calculated from the relative contribution of the two variables aiding discrimination. This can be extended to more dimensions. (From Doveton (1994), modified after Davis (1986)).

(b) Principal Component analysis. The first and second Principal Component (PC) axes are shown for data plotted on a conventional neutron-density cross-plot. PC1 has the larger variance and aligns with porosity, PC2 the smaller variance and aligns with the grain density of the rock. (Redrawn from Luthi (2001)).

(c) Fuzzy logic (based on the methodology described by Cuddy (2000)).

When using discriminant function analysis it is common to model the distribution of the populations with a normal distribution; this is also the case when using fuzzy logic. The real distributions can be incorporated, but this is often much more computationally intensive, and many programs lack these capabilities. Consequently some statistical techniques lack universal capabilities. These methods also commonly require a large amount of data – in particular discriminant analysis can be limited in its capability when the training data set is small (Wong *et al.* 1995a). Expert systems (decision trees with IF and OR statements) rely on specific decision thresholds that are therefore inflexible. Dimension reduction techniques can result in parameters that appear far removed from the original input data, making the outcome sometimes ambiguous to interpret.

Mitchell (1997) states that 'neural networks are a powerful classification method for learning relationships between attributes when presented with examples, and for certain types of problems, such as learning to interpret complex real world sensor data, artificial neural networks are amongst the most effective learning methods currently known'. Masters (1993) states that 'neural networks are most likely to be superior to other methods when the data on which conclusions are based is 'fuzzy', for instance the input data are 'human opinions''. They claim to be robust in the presence of noisy data, have the ability to generalise, and can handle data that exists in many dimensions (e.g. many logs). Therefore neural networks offer an alternative to the above methods and appear ideal for interpreting facies or lithofacies where training data are based on interpretation by a geologist. Bhatt & Helle (2002b) note that Poulton (2001) concluded from hundreds of comparisons on a variety of problems that in the worst case neural networks performed as well as traditional methods of classification or function approximation and in most cases they performed significantly better. A definition of a neural network can be found in Gurney (1997): 'A neural network is an interconnected assembly of simple processing elements, *units* or *nodes*, whose functionality is loosely based on the animal neuron. The processing ability of the network is stored in the interunit connection strengths, or *weights*, obtained by a process of adaptation to, or *learning* from a set of training parameters' (Figure 1.3). In this way neural networks differ fundamentally in their design to expert systems. The knowledge of a network is developed from its own making, from a given set of examples, not programmed by a user in the conventional sense.

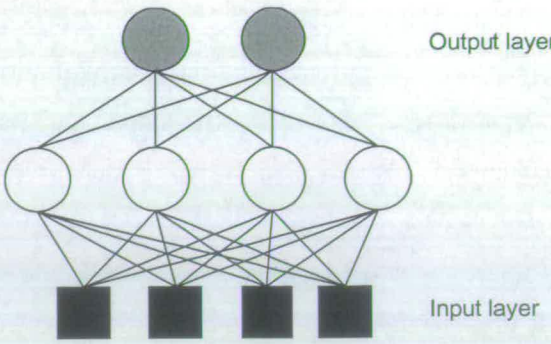



**Figure 1.3** The conventional way of depicting a neural network. More detail and descriptions of neural networks are found in chapter 2.

After the publications of Parker (1985) and Rumelhart & McCelland (1986) and, no doubt in part due to the increase in readily available personal computer power at the time, authors started to use neural networks as a tool to solve specific data analysis problems. Derek *et al.* (1990) were one of the first to use a neural network in geoscience, to discriminate lithofacies. The non-linear discriminatory nature of neural networks meant that many researchers have turned to them to help estimate permeability from logs (e.g. Wiener 1991, Osborne 1992, Wong *et al.* 1995a). Before long many geoscience disciplines were using them for problems of classification, for example copper ore grade distribution (Wu & Zhou 1993) and surface geochemical data analysis to predict subsurface hydrocarbon reservoirs (Doraisamy *et al.* 2000). The most recent advances in using neural networks to analyse data from well logs have been published whilst the research presented in this thesis was carried out. Helle *et al.* (2001) and Bhatt & Helle (2002a) predicted porosity and permeability using a neural network; Helle & Bhatt (2002) predicted fluid saturation from logs and Bhatt & Helle (2002b) attempted to predict sedimentary facies. They claimed that improved performance was obtained by using a 'committee' of networks (many networks connected in parallel), and by having a separate committee dedicated to the prediction of a single lithofacies or permeability/saturation range. They also claim that parameters can be predicted independently of fluid type given a sufficient number of training examples.

Most previous studies have focussed on permeability prediction. Those that predict lithology, lithofacies or facies from well logs have attempted to predict attributes which

would be expected to have very distinct log signatures (e.g. Derek *et al.* (1990) - sandstone reservoir rock; Rogers *et al.* (1992) - limestone, dolomite, shale and sandstone; Wadge *et al.* (1998) - claystone, sandstone and conglomerate; Bhatt & Helle (2002b) - sandstone, shaly sand, shale, coal). Furthermore emphasis has been on improving classification rather than on interpreting what the patterns in the data actually mean (Ali 1994). All authors have attempted to get good classification, but none appear to go on to interpret fully the output of the network and interpret what the misclassifications indicate. Also, although the technique has been applied to conventional log data suites the most modern log data (such as that recorded by imaging tools) is rarely incorporated (some exceptions are Russell *et al.* (2002), Hall *et al.* (1992) and Garden (2001) – see Chapter 2). Imaging tools sample the borehole many times horizontally and vertically and therefore have the potential to provide an exceptional description of a reservoir. Indeed the ability of these tools to reveal the texture of a rock would enable a neural network to discriminate lithofacies on the basis of image texture and lithology. Although, as Delhomme (1992) states 'image texture' is fundamentally different from a geologists 'texture'. The first involves the repetitive occurrence of local patterns in a given region, the latter describes the geometrical aspects of the component particles of a rock. It should be noted that the term 'lithofacies' in this thesis is used to describe lithologies that are genetically related in some way to a specified sedimentary facies. In Chapter 5 the term 'image lithofacies' is defined. This is a lithofacies that is partly defined by attributes derived from image logs.

### *1.2 Project aims*

This thesis attempts to improve lithofacies predictions by attempting to answer the following questions:

- Previous studies do not attempt to make lithofacies predictions from data collected in deep marine clastic sedimentary environments. In particular rocks deposited as the products of submarine fans are especially heterogeneous and therefore difficult to discriminate. Therefore this thesis asks to what extent can lithofacies be evaluated using a neural network from well log data recorded in deep marine clastic sediments?
- What are the most important parameters that influence the outcome? Are they the input data, the output demanded, or the methodology? How is it best to interpret any

outcome from a neural network? Can the methodology express uncertainty in the results?

- Can image log data be incorporated into a neural network model to predict image lithofacies and produce a more acceptable result?

### *1.3 New contributions*

This thesis specifically contributes the following:

- Neural network models for predicting lithofacies in deep marine clastic reservoirs are illustrated;
- It is shown how a combined neural network and knowledge based approach can produce superior results compared to a neural network alone;
- It is shown how uncertainty expressed by the neural network is important in the evaluation of any results;
- It is shown how major limitations of using any neural network model can be practical elements such as tool type and calibration, the depth interval investigated and fluid type;
- In many cases core is only cut in the main hydrocarbon interval and training examples from all fluid zones are not available. A methodology for standardizing logs for a single fluid type is applied to the data enabling predictions to be made in water or gas-water transition zones with the network trained on gas zone examples only;
- It is shown how simple statistics and power spectral analysis of the image data can quantify heterogeneity expressed in these data;
- A methodology is developed to incorporate data from the Fullbore Formation MicroImager (FMI) tool, into the neural network model to predict image lithofacies.

### *1.4 Data*

The data used in this thesis are from two sources:

- The Lomond Field, Central North Sea;
- The West Delta Deep Marine Concession, Nile Delta Egypt.

All data were provided by BG Group plc. The main reservoir in Lomond forms part of the Palaeocene Forties Fan system that extends throughout the Central Graben. A full suite of

conventional well logs was available for ten wells. The West Delta Deep Marine Concession consists of deep marine slope-channels deposited during the Upper Pliocene and originating from the Nile Delta. A suite of conventional logs and FMI logs were available for three wells. Appendix 1 briefly outlines some of the principles behind the acquisition of conventional well log data and documents some of the limitations of the technique. A short discussion then follows on the differences between acquisition in vertical and deviated wells (since Lomond wells are deviated). Chapter 5 includes a section outlining the acquisition and processing of FMI data.

### *1.5 Thesis structure*

Following this introductory chapter the thesis is presented as follows.

**Chapter 2** covers neural network theory. Specifically a justification for using, and explanation of the backpropagation algorithm is given. A detailed section follows on how the backpropagation algorithm should be implemented in practice. Finally a synthesis of geoscience applications using neural networks is presented.

**Chapter 3** contains an introduction to the Lomond Field its sedimentology and available data, followed by a description of the lithofacies scheme that a neural network was trained to predict. The stages involved in the training of the neural network are then described. Experiments are also described that illustrate the effects of training with unbalanced data, derivative logs and different training sets.

**Chapter 4** shows the final results of the optimal network (found in Chapter 3) when applied to all Lomond wells. The results are compared directly to sedimentary descriptions of the core where these are available. In one well lithofacies predictions appear poor. These are illustrated and the reasons for these discussed. The optimal network is then evaluated to see which logs it is most dependent on. The standardisation of logs to single fluid type is then illustrated and after retraining of the network further results are shown.

**Chapter 5** presents an introduction to the West Delta Deep Marine Concession area, its sedimentology and available data. The processing of the image logs is described. Statistical and spectral analysis of image data then takes place. It is shown which specific attributes are

capable of describing different image lithofacies. Data is incorporated into a neural network and comparisons are made between a modular and standard system. Initial results are illustrated.

**Chapter 6** shows results from when the optimal methodology for using the neural network developed in Chapter 5 is applied to the whole data set. Specific detailed well sections are shown that illustrate results adjacent to the image logs. Both are compared and limitations of the neural network methodology to predict image lithofacies are documented.

**Chapter 7** describes the main conclusions of the research and discusses these in light of the current literature. Suggestions are made for further work.

# Chapter 2: Neural network theory, and previous applications to well log data

## *2.1 Introduction*

This thesis uses a program to classify lithofacies that is based on the so called 'backpropagation algorithm'. The algorithm is the most researched, and therefore the most widely understood in neural network studies. It is most suited to problems of classification or prediction where (Masters 1997):

- The target data is represented by many attributes;
- There are abundant potential training examples;
- The target is real (such as a shale volume) or discrete (e.g. sand or limestone);
- Training sets may contain errors - if trained correctly the algorithm will find only the general relationships between attributes;
- Rapid execution of the trained model is necessary.

These are the key reasons why this type of network is suitable for lithofacies predictions and why it is utilised in this study.

Any use of an artificial neural network should be based on sound theoretical principles. This is because many of the strategies employed to successfully train neural networks derive from the algorithm theory and this is especially so with backpropagation. Many papers and textbooks exist that describe the basic theory of neural networks. Gurney (1997) provides a useful conceptual introduction to the topic; Mitchell (1997) provides a detailed account of the backpropagation algorithm; Bishop (1996) provides an overview of neural networks from a statistical and pattern-recognition perspective; and Masters (1993) provides an account of how to successfully implement various algorithms.

This chapter begins with a description of some simple aspects of nodes that are the building blocks of network structures. This leads to a description of the relevant theory behind the backpropagation algorithm (based on that shown in Mitchell (1997)). A section then discusses good practice for implementing the algorithm. A brief summary of other types of neural networks is then given, and a discussion of how they can be classified. Finally a

synthesis of neural network applications in geoscience is presented that specifically focuses on neural network use in deriving attributes from well logs.

## *2.2 Neural network theory and the backpropagation algorithm*

### *2.2.1 Introduction*

An artificial neural network is an information-based processing system that is loosely based on the way the interconnected structure of the human brain processes information. The human brain consists of over 100 billion nerve cells or neurons (Figure 2.1). Neurons are thought to communicate with each other via electrical signals in the cell wall. Interneuron connections are mediated by synapses located at the boundary of the cell.

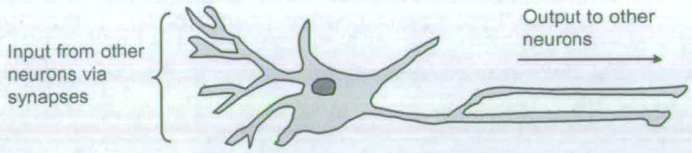



**Figure 2.1** A simplified neuron (redrawn from http://faculty.washington.edu/chudler/cells.html).

Any individual neuron receives thousands of connections from other neurons. In the neuron cell the signals are combined in some way and if the resulting signal exceeds a certain threshold the neuron is said to 'fire' a response. It is thought that some synapses are such that they excite the neuron (act in a way to increase the output) and others may be inhibitors, reducing the neuron's output. It is this style of processing or 'architecture' upon which neural networks are based. The artificial equivalents of neurons are units referred to as perceptrons. Synapses are modelled by a single number or weight so that each input is weighted before being summed at the equivalent of a neuron. Here the weighted signals are summed together to supply the unit with an 'activation'. If the activation exceeds a given threshold, the perceptron is said have fired (i.e. output a 1), otherwise it outputs 0 or -1. The perceptron is the simplest model of a neuron, and is fundamental to the understanding of neural networks.

### *2.2.2 The Perceptron*

McCulloch and Pitts (1943) proposed a model they called a 'Threshold Logic Unit' which is now synonymous with the 'Perceptron' that was developed by Rosenblatt (1958). The perceptron (Figure 2.2) takes a vector of real numbers, calculates a linear combination, and outputs +1 if the number produced is greater than some threshold, and 0 or -1 otherwise.

By re-arranging the equation represented by the perceptron in Figure 2.2, it can be seen that this represents the equation of a straight line. Figure 2.3 illustrates how two points A and B (each representing a different lithology) cannot be separated by the weights that generate the dashed line (line 1). However by changing the weights on the perceptron, the equation of the line the perceptron represents also changes allowing the given points to be distinguished (the dotted line – no. 2). The line which separates the two sets of points is known as a decision surface operating in n-dimensional space. The example shown has two inputs (the gamma ray and density log) and therefore the perceptron representation is drawn in two dimensions.

The very simple example shown above can be thought of as training a very simple system on two depth points in a well that has known gamma ray and density log readings as well as a given lithology. Any subsequent data could be presented to the perceptron and it would output a lithological classification. Any points which lay to the left of the dashed line would be classified as lithology B; points lying to the right of the dashed line lithology A.

A single perceptron can be used to represent many functions. It may classify a range of data, and solve a wide variety of problems. For instance if it is assumed that the Boolean value +1 is TRUE and -1 is FALSE then a single perceptron can classify the logic AND function (see Figure 2.4). However an important limitation of a single perceptron is that it can only classify data that is linearly separable, as the function it represents is a straight line. Thus a single perceptron cannot classify the XOR (one or other not both) problem (Figure 2.4).

However every Boolean function can be represented by some set of interconnected perceptrons. The XOR function can be solved by the system shown in Figure 2.5. This system can be described as a neural network. The term 'network' is used to refer to any system that is made up of connected artificial neurons (usually perceptrons). Usually the neurons are arranged in a layered structure, as in Figure 2.6. This structure is one of many

available and is used to map input patterns into several different classes. Neural networks are able to learn examples just as synaptic strengths are thought to be able to change due to particular stimuli from the brain. In artificial neurons it is the modification of the weights that is the equivalent of this learning. When a set of training patterns is presented to a network and compared to the target outputs the learning is said to be *supervised*. The weights are then changed so that classification is improved. These changes constitute a learning or training rule. A number of algorithms are available to train a single perceptron. The two most commonly cited are the Perceptron rule and the Delta rule. The perceptron rule will train a perceptron to correctly classify all training examples provided those examples are exactly linearly separable (thus a prior requirement is knowledge that the classes in the training set are linearly separable). The Delta rule minimises the *overall* network error, producing a best-fit approximation to the classes; consequently if each group represented in the training set is not exactly linearly separable the algorithm can still work. No prior knowledge of the training set is required.

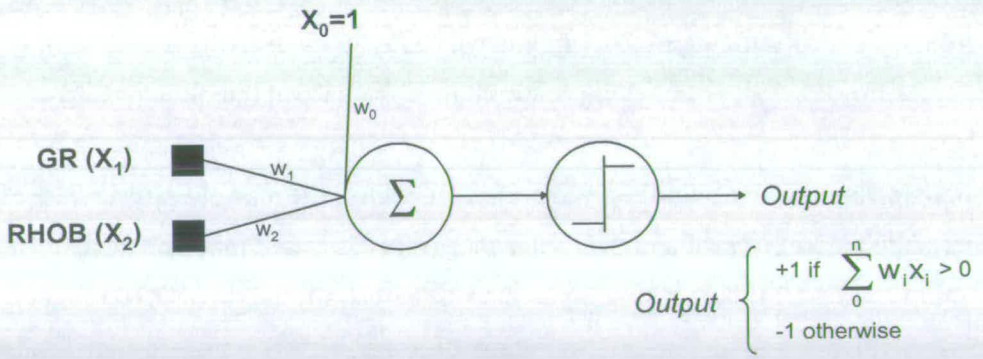



**Figure 2.2** Pictorial representation of a perceptron with a threshold unit of 0 (redrawn from Mitchell (1997)). Real numbers from the gamma ray log (GR) and density log (RHOB) are transferred through the network via multiplication by their respective weights ($W_0$ – $W_2$). The products are summed. If the resulting value is greater than 0 a +1 is output, if less than 0, a -1. The term $X_0$ is known as the bias term and is always fixed at 1. The perceptron shown represents the linear equation $X_0+X_1W_1+X_2W_2=Output$.

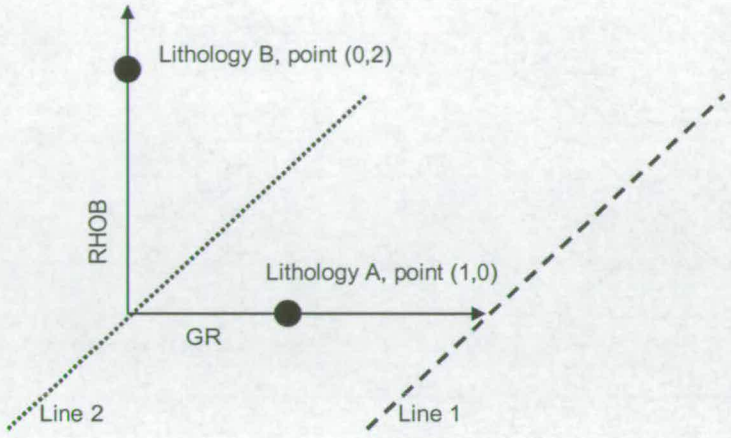



**Figure 2.3** The two points A and B each representing two different lithologies are to be classified by the perceptron shown in Figure 2.2. Inputs to the perceptron are the gamma ray log and the density log. If weights are chosen: $X_0$=-2, $X_1$=+1, $X_2$=-1 the straight line represented is RHOB=GR-2 shown as line 1 (dashed). This is not capable of separating and thus classifying the two lithologies. By selecting different weights: $X_0$=0, $X_1$=1, $X_2$=-1 the perceptron now represents line 2 (dotted) with equation RHOB=GR which is capable of separating the two lithologies.

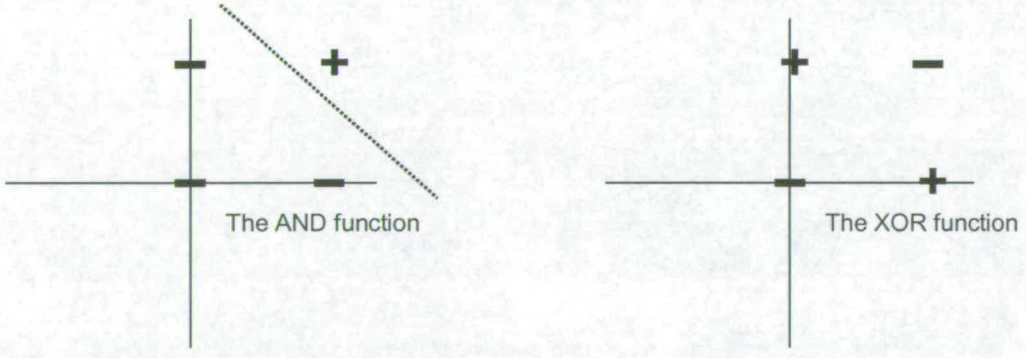



**Figure 2.4** A perceptron is capable of solving the AND function, but cannot solve the XOR problem as the points shown are not linearly separable.

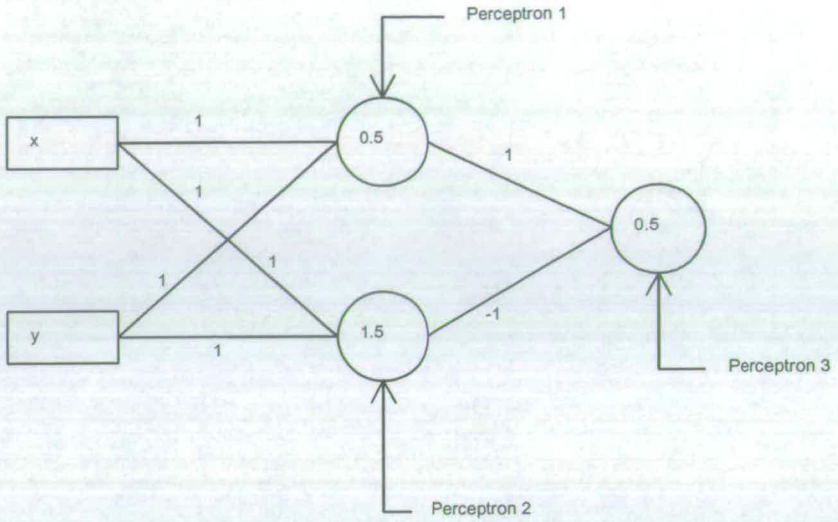



**Figure 2.5** A system of 3 interconnected perceptrons that is capable of solving the XOR problem shown in Figure 2.4. X and Y are inputs, numbers on the connections are weights, numbers on the centre of each perceptron are the threshold of that perceptron. Each perceptron will output a +1 if it is fired, a zero if it is not. Inputs (1,0) and (0,1) will produce a positive output, inputs (1,1) and (0,0) a zero output.

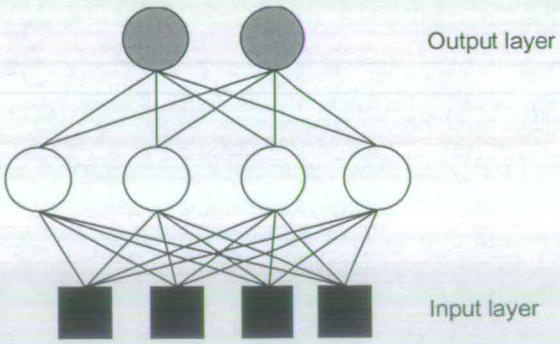



**Figure 2.6** A simple neural network

### *2.2.3 The Perceptron Rule*

The problem is to train a perceptron to produce the correct +1 or -1 output for each given training example. One way for the perceptron to learn an acceptable weight vector is to start

with random weights and iteratively apply the perceptron rule to each training example. If a training example is misclassified then the weight vector must be adjusted so that the misclassified example is more likely to be classified correctly next time. By repeating this process through the training examples the perceptron will eventually classify all the examples correctly and be 'trained'. The perceptron training rule can be described as:

$$\vec{w} \longleftarrow \vec{w} + \Delta\vec{w} \tag{2.1}$$

Where:

$\Delta\vec{w} = \eta(t - o)\vec{x}$;

$\vec{w}$ = weight vector;

$\Delta\vec{w}$ = an amount by which the initial weight vector is modified to produce the new network vector;

$\vec{x}$ = the vector input (training example);

$\eta$ = a constant called the learning rate (this is typically small (between 0 and 1));

$t$ = the target example for a given training example;

$o$ = perceptron output for a given training example.

It can been seen intuitively how this will work. If the target output is the same as the network output (i.e. the perceptron is fully trained already) then *(t-o)* will be zero and the weight vector will not change. If the perceptron outputs a -1 instead of a +1 then $\vec{w} \cdot \vec{x}$ must be increased. The training rule will do this:

$[+1-(-1)]\vec{x}$ i.e. $2\vec{x}$

if $\eta$ =0.2 then $\Delta\vec{w} = 0.4\vec{x}$

Weight vectors are usually normalised to between 0 and 1 before training. So if $\vec{x}$ =0.6 then $\vec{w}$ gets larger and so $\vec{w} \cdot \vec{x}$ will also get larger. It can be proven that this process will converge within a finite number of iterations (Rosenblatt 1962). An important limitation of the perceptron training rule however is that it will only converge if the training class examples are linearly separable (Minsky & Papert 1969).

### 2.2.4 The Delta Rule

This rule provides the basis for more sophisticated training rules that can be more generally applied to supervised neural networks. To understand the Delta rule training an unthresholded perceptron should be considered. This is a linear unit, exactly as the perceptron described above except that no threshold is applied to the output. Thus the output vector ($o$) is simply the input vector ($\vec{x}$) multiplied by the weight vector ($\vec{w}$).

$$o(\vec{x}) = \vec{w} \cdot \vec{x} \tag{2.2}$$

It is known that the overall aim of the Delta rule is to reduce the network error, improving classification as it does so. The minimum error will produce a best-fit approximation for classifying the training examples. It is therefore necessary to specify the training error. One way of expressing the error is:

$$E(\vec{w}) \equiv \frac{1}{2} \sum_{d \in D} (t_d - o_d)^2 \tag{2.3}$$

Where:

$D$ = set of training examples;

$t_d$ = target output for training example $d$;

$o_d$ = the actual output from the perceptron for training example $d$;

$E(\vec{w})$ = the network error during training, which is dependent on the weight vector $\vec{w}$.

It can be seen that if the network output is very different to the target output then the training error is large; if they are the same the training error is zero. The error $E(\vec{w})$ is written as a function of $\vec{w}$ as the output of the perceptron depends on the weight vector only, attached to the perceptron for a given set of training examples.

In order for the perceptron to change its weights, thus moving its output closer to the target it is necessary to minimise $E(\vec{w})$. Figure 2.7 is a schematic visualisation of an error surface for a single perceptron, with two inputs and two weights, $w_o$ and $w_1$. The error $E(\vec{w})$ is a

surface that represents all possible weight vectors for a given set of inputs. This plane is commonly referred to as the 'hypothesis space'.

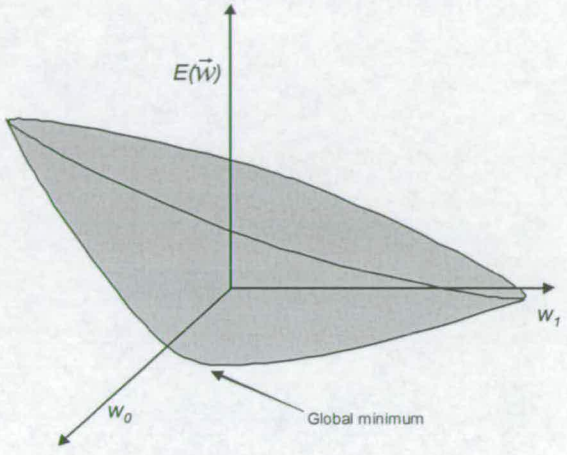



**Figure 2.7** A representative surface of all possible error vectors $E(\vec{w})$ on a perceptron with only two weights, $w_0$ and $w_1$ for a given set of training examples. The plane is often referred to as the 'hypothesis space'. The 'global minimum' is the theoretical minimum error for a given hypothesis space.

In order to minimise $E(\vec{w})$on the above surface one should move down the surface towards the global minimum, and to ensure efficient arrival the steepest descent should be taken. The global minimum is the theoretical minimum error for a given hypothesis space. The direction of the steepest descent can be found by calculating the derivative with respect to each of the components of the vector $\vec{w}$. This is $\nabla E(\vec{w})$ which is the gradient of $E$ with respect to $\vec{w}$. This is a vector whose components are the partial derivatives of $E$ with respect to each of the weights ($w_i$):

$$\nabla E(\vec{w}) \equiv \left[ \frac{\partial E}{\partial w_0}, \frac{\partial E}{\partial w_1}, \ldots \frac{\partial E}{\partial w_n} \right] \tag{2.4}$$

Since Equation 2.4 specifies the direction of steepest increase of $E$ the training rule for gradient descent is:

$$\vec{w} \leftarrow\!\!- \vec{w} + \Delta\vec{w}$$

Where:

$$\Delta\vec{w} = -\eta\nabla E(\vec{w})\,; \tag{2.5}$$

$\eta$ = the learning rate, as for the perceptron rule.

This training rule can be written in its component form:

$$\vec{w}_i \longleftarrow \vec{w}_i + \Delta\vec{w}_i$$

Where:

$$\vec{w} \longleftarrow \vec{w} + \left[ -\eta \frac{\partial E}{\partial w_i} \right] \tag{2.6}$$

The new weight vector ($\vec{w}$) is the previous weight vector minus the gradient vector multiplied by the learning rate. As for the perceptron rule $\eta$ is usually small, and here represents the step size as one moves iteratively down the error surface. The negative sign is present, as the error needs to decrease. The above rule is the Delta rule. The process by which the delta rule works by iteratively moving down an error surface is called 'gradient descent'.

It can be recalled that the error of a perceptron can be expressed by:

$$E(\vec{w}) \equiv \frac{1}{2}\sum_{d\in D}(t_d - o_d)^2$$

Therefore by the chain rule for differentiation:

$$\frac{\partial E}{\partial w} = \frac{1}{2}\sum_{d\in D} 2(t_d - o_d)\frac{\partial}{\partial w}(t_d - o_d)$$

The vector output of the perceptron $o_d$ is dependant on the weight vector (Equation 2.2), and input vector for all training examples $d$:

$$\frac{\partial E}{\partial w} = \sum_{d\in D}(t_d - o_d)\cdot\frac{\partial}{\partial w_i}(t_d - \vec{w}\cdot x_d)$$

$$\frac{\partial E}{\partial w} = \sum_{d \in D} (t_d - o_d) \cdot (-x_d) \tag{2.7}$$

Thus substituting equation 2.7 into 2.6;

$$\vec{w} \longleftarrow \vec{w} + \left[ -\eta \sum_{d \in D} (t_d - o_d)(-x_d) \right]$$

$$\vec{w} \longleftarrow \vec{w} + \eta \sum_{d \in D} (t_d - o_d) x_{id} \tag{2.8}$$

The new weight vector is the old weight vector added to the learning rate $\eta$, multiplied by the sum of the target vector minus the perceptron output $o_d$, multiplied by the input vector $x_{id}$ for all training examples, $d$, in the training set $D$. Equation 2.8 is known as the gradient descent algorithm.

The error surface $E(\vec{w})$ is specific for a given training set, and therefore to calculate a true gradient all the training examples have to be presented. This can be computationally intensive so often the weights are updated based on gradients found on presentation of each example individually, so that:

$$\frac{\partial E^p}{\partial w_i} = -(t^p - o^p) x_i^p$$

Where:
$p$ = a specific example number.

Training now works in a pattern training regime whereby weight vectors are updated after every example presented in the training set. As this is an estimator for the gradient, the minimisation of $E$ is noisy, and the weight changes may even increase $E$. Overall though, there should be a systematic decrease in the error.

Training with the Delta rule was first proposed by Widrow & Hoff (Widrow & Hoff 1960), so the rule was originally known as the Widrow-Hoff rule. Only more recently has it

become known as the Delta rule (the term $t_d$-$o_d$ being referred to as $\partial$ or difference). Other accounts of the Delta rule can be found in Widrow & Stearns (1985), and Widrow *et al.* (1987).

The gradient descent algorithm for linear perceptrons works first by picking a random weight vector. Equation 2.8 is then applied and the weight vector is updated incrementally. If $\eta$ is sufficiently small it can be shown (Widrow & Stearns 1985) that the delta rule will converge whether the example training data is linearly separable or not. This is the main way in which the perceptron and delta rules differ. The perceptron rule would produce oscillating weight vectors if an exact solution did not exist, whereas the delta rule will converge to the minimum error (albeit with some examples possibly misclassified).

### *2.2.5 Training rules for more complex networks*

Single perceptrons can only express linear decision surfaces. What would be much more useful is a system that could be trained to classify groups of data by expressing different non-linear decision surfaces. Multi-layer networks trained with the backpropagation algorithm are capable of doing this (see Figure 2.8). When multiple inputs are present the decision surface operates in multi-dimensional space, and the surface is often referred to as a 'hyperplane'.

At this point in order to prevent confusion some nomenclature should be introduced. A typical network (of the type used in this thesis) would be that of Figure 2.8-right. There are many inputs (shown in red), and a 'hidden layer' shown in yellow. Each of the circles can be described as a node (or neuron), with the hidden and output nodes operating in a similar way to the perceptrons illustrated above. The output nodes signal the response of the network to any input. Many authors refer to such a network as a two layer network (referring to the hidden and output layers); others would refer to it as a single layer network (referring to the hidden layer of nodes). In this thesis such networks are described as having a single layer of hidden nodes. Both the input and output layers are assumed.

Units for constructing multi-layer networks like those of Figure 2.8 are similar to the linear units described as perceptrons. However multiple layers of linear units can only represent linear functions (Mitchell 1997). What is required is a unit that expresses its outputs as a

non-linear function of its inputs that also has a differentiable threshold unit (as this allows gradient descent to take place). Most multi-layer networks are based on a 'sigmoid unit' (Figure 2.9). As for the perceptron the unit calculates a linear combination of its inputs and applies a threshold to the result. The key difference is that the threshold function is a non-linear function of the inputs.

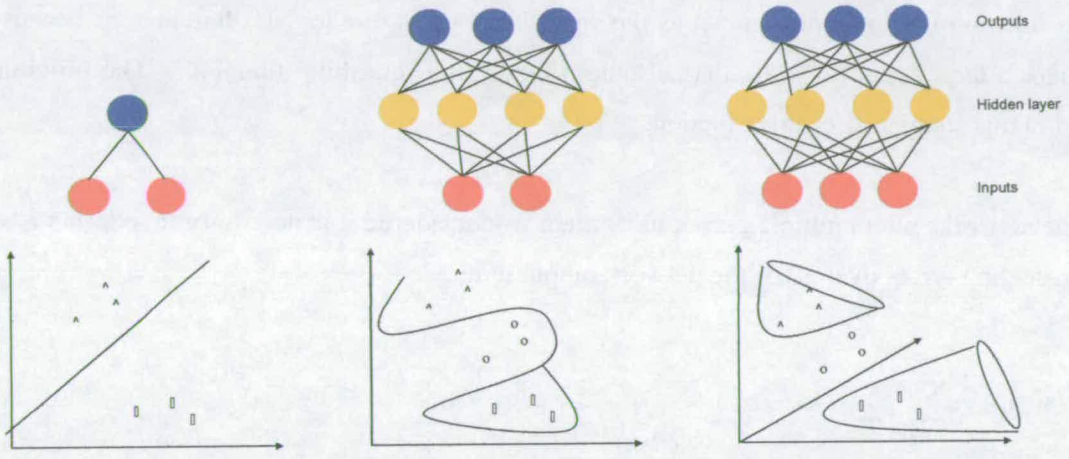



**Figure 2.8** Schematic picture to illustrate the classification capability of different sized networks. Inputs to the networks are red, nodes in a hidden layer are yellow, and outputs are blue. A single node (left) can only express a linear decision surface. Multiple nodes can express non-linear decision surfaces (middle). With three inputs (right) the decision surface is represented by a plane. Decision surfaces in higher dimensions are often referred to as 'hyperplanes'.

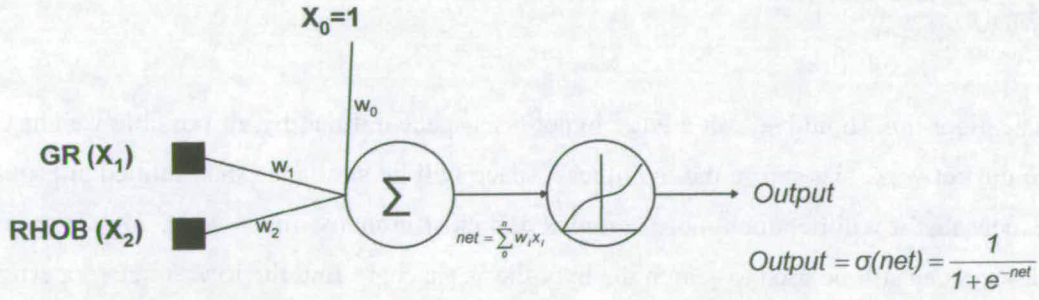



**Figure 2.9** The sigmoid threshold unit (redrawn from Mitchell 1997).

The sigmoid unit computes:

$$o = \sigma(\vec{w}_i \cdot \vec{x}_i)$$

Where:

$$\sigma(net) = \frac{1}{1+e^{-net}}$$

This function is commonly known as the sigmoid function, the logistic function, or because it maps a large input range to a small output range 'the squashing function'. The program used in this study utilises this function.

Since networks with multiple output units are now considered it is necessary to redefine $E$ as representing errors over all of the network output units:

$$\sum(\vec{w}_i) = \frac{1}{2}\sum_{d\in D}\sum_{k\in outputs}(t_{kd} - o_{kd})^2$$

Where:

*outputs* = set of output units;

$t_{kd}$ = the target value for the $k^{th}$ output unit for training example $d$;

$o_{kd}$ = the output value for the $k^{th}$ output unit for training example $d$;

$\sum_{k\in outputs}$ represents the sum over the output nodes;

$\sum_{d\in D}$ represents the sum over all the training data (all examples $d$ in set $D$).

The algorithm should search a large hypothesis space defined by all possible weight vectors in the network. Therefore the hypothesis space will be similar to that defined in Figure 2.7, except that it will be much more complex and exist in many dimensions. However gradient descent can still be used to search the hypothesis space, to find the lowest network error.

### 2.2.6 The Backpropagation algorithm

The following rules apply to networks that contain two layers of sigmoid units (i.e. one hidden layer and one output layer, as in Figure 2.8 right), with all units interconnected:

- Create a network where $n_{in}$ is the number of input units, $n_{out}$ the number of output units, the input from unit $i$ to unit $j$ is denoted by $x_{ji}$, and the weight from i to j denoted as $w_{ji}$;
- Initialise all weights to small random numbers;
- Until a specified termination condition is met
  - For each target vector ( $\vec{w} \cdot \vec{x}$ ) in the training examples
    1. Propagate forward through the network
       a. Input $\vec{x}$ and compute output $o_x$ for all output nodes
    2. Propagate errors back through the network
       a. Calculate the network error from output unit $k$, e.g.

       error from unit $k_1 = \delta_1$

       error from unit $k_2 = \delta_2$

       $$\delta_k \longleftarrow o_k(1-o_k)(t_k - o_k)$$

{note that this is the same as Equation 2.1 for the perceptron rule, but the $\delta_k$ is more complex. $o_k(1-o_k)$ is the derivative of the squashing function.}

       b. For each hidden unit $h_i$ calculate its error term $\delta_h$

       $$\delta_h \longleftarrow o_h(1-o_h) \sum_{k \in outputs} w_{kh}\delta_k$$

{No target values will exist to indicate the error of the hidden units. Error terms are therefore calculated by summing the error terms $\delta_k$ that have been influenced by the hidden unit. Each $\delta_h$ is weighted by the weight connecting the hidden node in question to the output node. This essentially characterises the degree to which a hidden unit $h$ is responsible for the error in the output unit.}

       c. Update each network weight $w_{ji}$ by

       $$w_{ji} \longleftarrow w_{ji} + \Delta w_{ji}$$

       Where:

       $$\Delta w_{ji} = \eta \delta_j x_{ji}$$

This algorithm updates all the weights following each training example. To obtain true gradient descent of $E$, it is necessary to sum $\delta_j x_{ji}$ over all training examples before updating weights, as for the Delta rule. The way in which the algorithm works - by propagating errors back through the network gives rise to the name 'the backpropagation algorithm'. Full derivation of the above algorithm can be found in Mitchell (1997).

The most widely used variation of the original backpropagation algorithm is the addition of so called 'momentum'. The weight update rule above is adapted so that the $n^{th}$ update rule depends on the update rule from the $(n-1)^{th}$ iteration:

$$\Delta w_{ji}(n) = \partial_j x_{ji} + \alpha \Delta w_{ji}(n-1)$$

Where:

$\Delta w_{ji}(n)$ = weight update at $n^{th}$ iteration;

$\alpha$ = a constant (usually between 0 and 1) called 'momentum'.

If gradient descent is thought of as a ball rolling down an error surface, then the momentum term is analogous to the size of the ball. The larger the ball the more chance it has of rolling over small bumps in the surface (avoiding so-called local minima – see section 2.3.2). Avoiding local minima is important in order to reach the true global minimum of the error surface. Adding momentum helps to achieve this. The momentum term is used in this thesis and is discussed in more detail in Sections 2.3.2 and 3.6.3 concerning the appropriate size of the parameter.

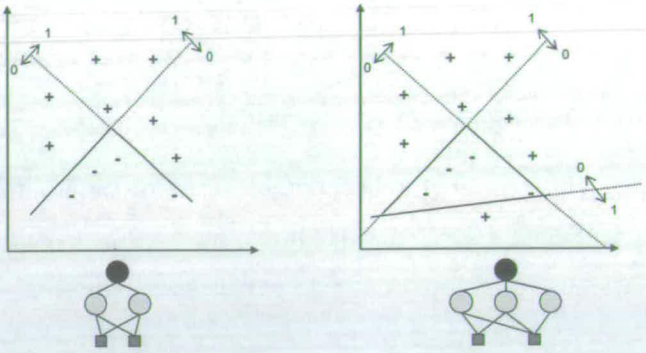
The definition of the backpropagation algorithm described above is true for all networks with one hidden layer of nodes and one output layer. The algorithm can be adapted to many hidden layers by repeating steps 1 and 2 above. If a hidden layer is not connected to the output layer then $\delta_h$ for that layer is calculated from the next layer of hidden units downstream (i.e. closer to the output layer).

The papers of Parker (1985) and Rumelhart & McCelland (1986) are usually credited with the popularity of the backpropagation algorithm, although the idea can be traced back to Werbis (1974). Clearly the introduction of powerful personal computers since the middle of

the 1980s has also played an important role in the use and development of the algorithm since then.

### *2.2.7 Remarks on the Backpropagation algorithm*

Figure 2.8 introduced the fact that more complex networks are needed to solve more complex problems. In Section 2.2.2 it was shown how a single perceptron or node could represent a straight line and therefore delineate two classes. Consider however Figure 2.10-left. The two classes shown need a network with a minimum of two hidden nodes (representing the two planes needed for separation), and an output node that will signal a 1 for positive and 0 for negative. The right hand diagram requires three hidden nodes (to represent the three lines needed for classification) and a single output node. It can therefore be seen that the number of hidden nodes needed depends on the complexity of the decision surface required to separate out the classes (which is not usually known beforehand), and also the actual number of classes to be defined. A backpropagation network can recognise many groups from only a few inputs, as long as they can be distinguished in pattern space. An example of this can be found in Rogers *et al.* (1992). Here four outputs (shale, sandstone, limestone and dolomite) were predicted from only three inputs (gamma-ray, neutron and density logs). This differs from classical compositional analysis from logs, which revolves around solving simultaneous equations. Here if the number of unknowns exceeds the number of knowns then the problem is said to be underdetermined and cannot theoretically be solved (see Figure 2.11). In the type of problem that concerns this study discrete boundaries are drawn in pattern space on the basis of training examples. A discrete section of space then defines a particular class, and there is no continuum of compositions. The problem can be underdetermined if there are too few hidden nodes (as discussed above) or too few training examples. It is intuitive that if there are too few training examples then the network will not learn properly. Baum & Haussler (1989) theoretically discuss the number of training values required to prevent no indecision by a single output network (it depends on the number of weights, the number of hidden units, and the fraction of correctly classified training patterns). The number is generally huge and for most practical applications totally unrealistic. Usually overcoming these issues requires some user knowledge i.e. the creation of a good training set by representing the expected range of input values for all classes. Too few nodes can be recognised by a network that will not learn.



| Hid 1 | Hid 2 | Out | Class |
|---|---|---|---|
| 0 | 0 | 0 | - |
| 0 | 1 | 1 | + |
| 1 | 0 | 1 | + |
| 1 | 1 | 1 | + |

**Figure 2.10** Class separability by different sized neural networks, adapted and redrawn from Gurney (1997). In the left diagram the two classes are nonlinearly separable and because of the nature of how they exist in the pattern space, two lines are required for classification. Therefore a backpropagation solution will require at least two hidden nodes (yellow). The matrix below illustrates how the firing of each node results in the correct output. In the right diagram there is a more complex arrangement of the classes in space, and so three lines are needed for classification. A backpropagation solution therefore requires three hidden nodes.

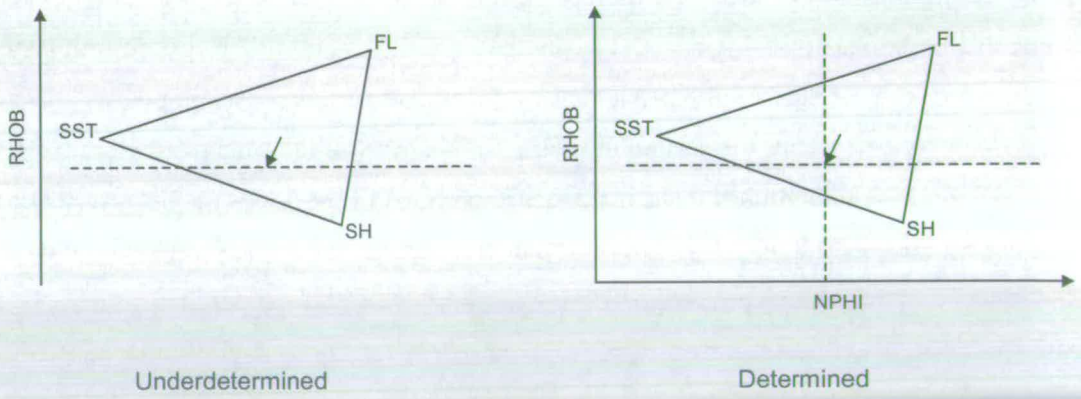



**Figure 2.11** Graphical representation of attempting to calculate three components (SST- sandstone, SH – shale, FL – fluid) from well logs. In the left example there are two knowns, a density log value and the fact that all three components must sum to unity. The solution could lie anywhere along the dotted line, cannot be solved and is said to be underdetermined. In the right example, with the introduction of the neutron log there are now three knowns attempting to evaluate three components, and the problem is said to be determined. The mathematical representation of this problem takes the form of simultaneous equations. Adapted from a similar diagram in Doveton (1994).

## *2.3 Strategies for implementing the algorithm*

### *2.3.1 Introduction*

So far the basic theory of neural networks and the backpropagation algorithm have been discussed. An understanding of the theory is critical for the correct implementation of the algorithm. This section discusses the practical implications of the theory.

### *2.3.2 Local minima*

Figure 2.7 showed a representative error surface for a network with only two weights. The object of gradient descent is to move down the error surface to the global minimum. A consequence of larger networks with many weights is an error surface that operates in many dimensions and is exceedingly complex. These surfaces may have many so-called 'local minima' (Figure 2.12). Backpropagation with large networks is only guaranteed to converge to a local minimum, not necessarily the global one (as gradient descent will simply proceed until the gradient is zero). However the problem of getting stuck in local minima may not be as problematic as some authors suggest. Since a network with lots of weights will have an error surface in many dimensions, if gradient descent falls into a local minimum with respect to a particular weight it will not necessarily be at a minimum with respect to other weights - there will be many 'escape routes'. But because complex error surfaces are very poorly understood, and at present there is no known way to determine whether you are at a local or global minimum there exist a number of important strategies to overcome ending up in a local minimum:

- Use a momentum term, this can help step out of small minima;
- Update after presentation of every training example (this provides only an estimate of the true gradient, and therefore a noisy descent, which can help overstep minima);
- Train a number of networks using the same data, but from a different starting set of weights. Each network is likely to end up at a different minimum. The network that performs best on a validation set should be chosen.

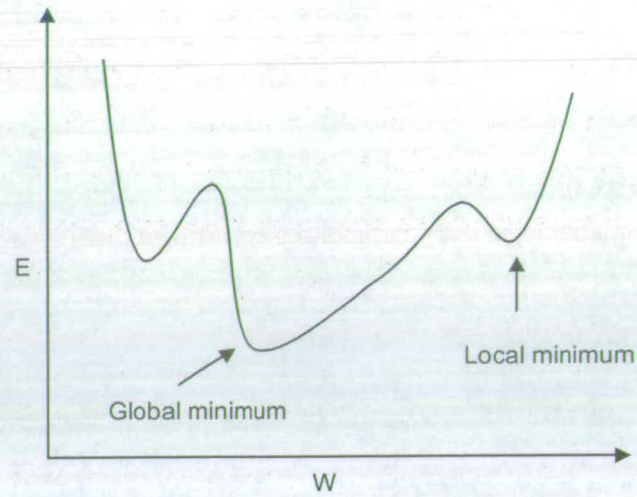



**Figure 2.12** Local minima on a complex error surface. E represents the value of the overall error, and W a particular weight value.

### *2.3.3 Encoding of data*

The backpropagation algorithm accepts inputs that are linearly scaled to between 0 and 1. This means that input units have values in the same interval as hidden and output units. Most neural network programs will perform the 0 to 1 scaling automatically. However it is pertinent for the user to check that each input parameter is operating in a linear way. This is discussed further with respect to resistivity logs in Chapter 3.

As discussed, the output from each of a neural network's output nodes should be a zero or one depending on whether it is fired or not. In reality this is a real number between 0 and 1, and a threshold is applied (often 0.5). If the output is greater than 0.5 the node is fired, if it is less than 0.5 then the node is off. This means that if three classes are to be predicted there could be one output node (with thresholds of say, <0.3 for one class, 0.3-0.6 for the second class, and >0.6 for the third class), or three output nodes each with a single threshold (say of 0.5). In both cases a network will train. However the former case should only be used where some order exists - for instance, if the three classes to be predicted are cold, warm and hot. If there is a chance that there is no order then the second type of arrangement of output nodes should be used.

There are still many users (especially in industry) that use a single output (Matthew Wakefield pers. comm.). A single output could be used if predicting an ordered sequence such as sand, shaly sand, shale but this is often not the case. There are two advantages of having multiple outputs for each class:

- There are more weights in the network and thus more degrees of freedom available to represent the target;
- Differences between the output nodes can give the user a measure of confidence in the output (i.e. if two output nodes are fired then there is clearly some ambiguity in the networks decision). This information is extremely useful. It is surprising how often this is overlooked. This type of analysis is discussed in much more detail in Chapter 4.

Having multiple output nodes suggests binary encoding of output training data such as [100] for facies 1, [010] for facies 2, and [001] for facies 3. Usually however, training a network to predict 0 and 1 can grow the weights very quickly and create instability during training. This appears to be more of a problem when using a threshold function such as tanh rather than a sigmoid function (Stephen Wolstenhulme pers. comm.).

### *2.3.4 Network architecture*

The term 'network architecture' refers to the shape and size of a neural network, specifically the number of hidden layers and hidden nodes. The problem of how many layers or nodes to use to achieve optimum classification is non-trivial and depends entirely on the problem at hand. This was touched on in Section 2.2.5, where it was shown that, generally speaking the more complex the decision surface the more hidden nodes required. Although there is no specific way to find the optimum number, researchers have come up with some guidelines: every Boolean function can be represented exactly and every bounded continuous function can be approximated using only one hidden layer (Cybenko 1989); any function can be approximated by a network with two hidden layers (Cybenko 1988). So for the majority of problems (including lithofacies prediction from well logs) one hidden layer should be sufficient, in theory. However this does not mean that memory or training requirements will dictate that two hidden layers is more practical. In general the optimum number of nodes in hidden layers is more difficult to estimate. Too many hidden nodes can lead to over-fitting of the training data (see Section 2.3.5). Therefore the fewest nodes that can solve the problem is best. This study donates some time to finding the optimum number of nodes for the specific problem (see Chapter 3).

### *2.3.5 Stopping criteria*

The general backpropagation algorithm has no stopping criteria - it could continue indefinitely. However a very common problem with backpropagation is that it can over-fit data (see Figure 2.13). This happens when the network attempts to fit a decision boundary that will very accurately classify the training data but misses the 'general' relationships in the data (that the user wishes the network to learn). Over-fitting is usually overcome by monitoring training with a validation set. After each iteration an independent validation set is presented to the network. The error is calculated. The network should be saved if, after each iteration, the error decreases. The final network selected for use should be the one corresponding to the lowest error over the validation set (Figure 2.14). In this study the percentage correctly classified in a validation set is always monitored during training. Each time the percentage classified correctly increases the network is saved. Monitoring in this way essentially equates to monitoring the error.

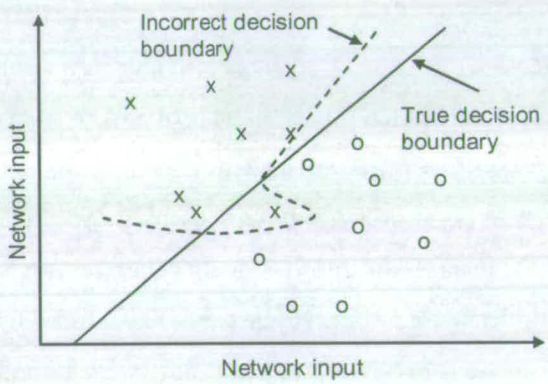



**Figure 2.13** Over-fitting data. Two classes are to be discriminated. The true decision surface (straight line) is shown, but the network has over-fitted its decision line (dashed). This problem could have been solved by a single perceptron. Too many nodes in the network can contribute to over-fitting. The diagram also illustrates that extrapolation of a boundary beyond the range of the training data can be dangerous.

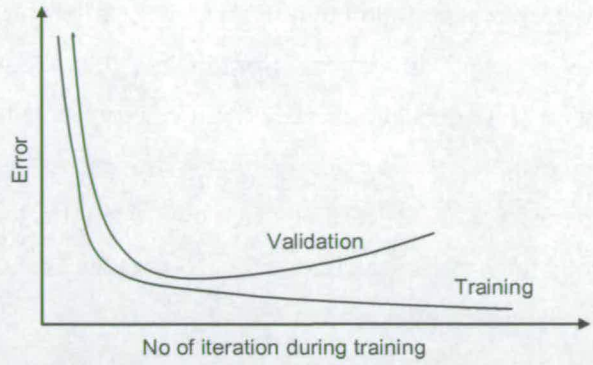



**Figure 2.14** Training with a validation set. The error over the validation set is monitored during training. Training should be terminated at the lowest error over the validation set. Continuing to train can result in over-fitting.

## *2.4 Use and limitations of the backpropagation algorithm*

So far neural networks and their representation in pattern space, and thus their value in classifying groups of data in multi-dimensions have been considered. Clearly this is the role of the neural network used in this study. The key reasons for using the backpropagation algorithm for classification were stated in the introduction to this chapter. However backpropagation can also be used for function fitting (indeed one of the main uses in geoscience is permeability prediction from logs). In classification problems the nodes are described as 'saturated', usually outputting very close to 0 and 1. When function fitting the network simply creates a non-linear combination of its inputs, and outputs a function of them scaled between 0 and 1.

Although there are many books and papers that promote the use of these networks for the tasks described it is critical to understand their limitations. In many cases backpropagation networks require a considerable amount of training data to ensure efficient learning. This may not always be available. Also if classes are differently represented in a training set then the network can learn the discrepancies. Thus a network may find a class that only has a few representatives difficult to classify. This type of problem would not occur with a decision-tree (rules-based) approach to the problem. Experimentation with different training sets and amounts of representation by different classes takes place in Chapter 3. Also predictions from the network can be constrained to lie in the range defined by the training data; data that lies very close to, but outside the range may not be predicted. In many cases it is how data is

encoded that can be problematic (although this is also a problem in other statistical applications). If a network is to learn patterns from images then the image must be encoded to the network so that it can understand the key features represented. This is a problem of feature extraction, which this thesis tackles in relation to image logs, in Chapter 5. The actual algorithm itself can be slow at learning often converging in local minima. This type of network is not good at precise calculations. A network may be able to predict a permeability range but could be a poor predictor of the actual value (Bhatt & Helle 2002a).

## *2.5 Other types of neural networks*

### *2.5.1 Introduction*

So far the backpropagation network has been described. However this is only one of a number of neural network types available. This section describes the most common other types of neural networks and attempts (briefly) to classify neural networks in general.

### *2.5.2 The Hopfield network*

This is a type of feed-forward network (like backpropagation). This network however is trained with data that constitutes both the inputs and outputs. Therefore the network is described as 'associative memory' since from an imperfect copy of the training data it will 'recall' or 'remember' the final output from which it was obtained. Analogous feed-forward networks can perform this task, but Hopfield nets are designed as recurrent, meaning that many nodes are connected to other nodes, so that there is feedback in the network and nodes are used repeatedly to process information. The network iteratively processes the input pattern to provide a version that grows more like the output pattern that is in the 'stored memory'. These types of networks were originally described by John Hopfield (1982).

### *2.5.3 Radial basis functions*

Radial basis functions refer not to a different type of network (although see how networks can be classified – Section 2.5.6 below), but to an alternative node structure in which the activation is determined from a vector that has the same dimensions as the inputs. Whereas the most common activation function is the sigmoid threshold that simply uses the weighted sum of inputs (a single value) to evaluate the threshold, a radial basis function is a Gaussian

surface with dimensions the same as the input vector. The use of this type of node enables complex decision surfaces to be built up with comparatively few nodes.

### *2.5.4 Kohonen networks*

The Kohonen network is a single layer network based on rules first documented by Teuro Kohonen (Kohonen 1982 & 1984). This type of network attempts to group data into a pre-defined number of classes, by having each node (representing a class or cluster) compete for the data. The type of learning is 'unsupervised', as there are no predefined classes or target data. Each node has a start position in the n-dimensional space of vector inputs. Data is then effectively plotted in the space, and the node which is closest is moved an increment towards that data point. Data is continually presented until the node positions are stable. New data applied to the network is simply plotted in the n-dimensional space and is assigned to the cluster represented by the closest neuron.

### *2.5.5 Adaptive Resonance Theory (ART)*

These types of networks are similar to Kohonen type networks in that they are self-organising and cluster pattern data. However, they are far more complex both in their architecture and the way they train. ART networks overcome some of the problems associated with simpler competitive networks; they should not end up in a state of flux - stability after learning should be reached and; they have the capability to define the optimum number of clusters present for themselves (rather than being specified by the user). The first member of the ART family was ART1 (originally presented by Carpenter & Grossberg (1987a)). There are now other variations known as ART2 and ART3 (Carpenter & Grossberg 1987b, Carpenter & Grossberg 1991). Carpenter *et al.* (1991) combined supervised and unsupervised methods for mapping known input-output patterns called ARTMAP. This was used by Wong (1995c) to predict lithofacies (see Section 2.7).

### *2.5.6 Classification of networks*

The world of neural networks can appear very complex with similar terms often used loosely or to describe different phenomena. Below a short classification of neural networks is presented. Networks can be grouped as follows.

- *Task.* The most common tasks that neural networks are used for have been discussed. Feed-forward networks are most often used for classification and function fitting. Recurrent networks are used for associative memory tasks, noise filtering, and signal processing.
- *Node type.* Within different network types there exist a huge number of node types that have differing activation forms and different output functions. Single perceptrons calculate a simple linear combination of its inputs and apply a threshold step function as the output function. This is used in simple Boolean applications. The node used for backpropagation used a linear weighted sum of its inputs and the sigmoid squashing function to calculate its output.
- *Architecture.* This can be described in terms of whether the network is feed-forward, recurrent, or competitive; whether there are any hidden units; or whether connectivity is fully complete.
- *Training algorithms.* These can be supervised or unsupervised. If supervised they can have a complex error feedback such as backpropagation or simple feedback such as in recurrent systems.

## *2.6 The neural network program used in this study*

The neural network package Easynn (http://www.easynn.com) is used throughout this study. This program implements the backpropagation algorithm with a sigmoid squashing function, as described above. The program is extremely flexible in all aspects of its design. All parameters can be displayed during and after training. All weights and relevant parameters can be exported after training so the neural network can be implemented within a user written program or spreadsheet. The program has been continually developed over the past few years by author Stephen Wolstenhulme who also provides online support.

## *2.7 Neural network predictions in geoscience and from well logs*

After the resurgence of interest in neural networks in the mid-eighties, it wasn't long before a variety of disciplines were turning to them to help solve specific scientific problems. One of the earliest publications attempting to use a neural network in conjunction with well logs was Derek *et al.* (1990). They trained a backpropagation neural network to recognise sandstone lithofacies from gamma ray, density and neutron logs and compared their results to those gained from using the linear discrimination function and Bayes classifier. This

paper is not only significant because it is one of the first to use neural networks with logs but also because it documents the actual implementation of the algorithm in detail. Derek *et al.* found that network convergence did not seem particularly susceptible to variation in the learning rate, although a learning rate of greater than 0.5 did appear to give slightly poorer results. The momentum parameter did however seem to be more important, and significant variations in classification could result depending on its size (even more so when training with two hidden layers of nodes). A momentum parameter of greater then 0.9 produced sub-optimal results. Overall five lithofacies were predicted, but the network was optimised so that reservoir rock was predicted very well, with prediction of the other lithofacies of secondary importance. On testing the resulting models the neural network produced classification success of 90.5% for reservoir rock, linear discrimination function 94.1% and Bayes classifier 86.5%. Robinson (1991) showed that backpropagation networks could offer an alternative to traditional linear regression by using artificial data generated from four variables. Linear regression restricted the output to defining a very simple linear relationship whereas the neural network was more flexible and defined a more complex non-linear relationship between the inputs and single output. The root mean squared error gained from testing the neural network was a factor of ten better then that gained from linear regression. Robinson also pointed out that finding the optimum network for a particular task required experimentation, and that training data and network size were both very important variables in determining network performance.

Permeability is notoriously difficult to predict from well logs. Traditionally it is done using linear regression, cross-plotting core derived permeability values with porosity or from equations such as the Wyllie and Rose equation (Wyllie & Rose 1950). Cross-plot methods often work when the reservoir rocks are very simple (e.g. a clean sandstone) but often the relationship between porosity and permeability is much more complex (it is well known that permeability is actually dependent on pore throat geometries which can be unrelated to porosity). Authors realised the potential of neural networks for describing non-linear systems and using them to predict permeability values from well logs. Wiener *et al.* (1991) attempted this in Texaco's Stockyard Creek field, North Dakota (a carbonate reservoir). The target data was laboratory derived core-plug air permeability values. After much experimentation they found a network with two hidden layers (relatively large and complex), and log inputs of deep and shallow resistivity, neutron, sonic, density, porosity, water saturation, and bulk volume water performed best. It is noteworthy that some of the inputs

were derived from the raw log suite (for instance water saturation would have been derived from the deep resistivity log and probably the density log, and the porosity log from the density log or a density-neutron combination). Nevertheless using all these logs did increase performance; Wiener stated that his results 'illustrate the value of incorporating all of the wireline measurements and their interrelationships when analysing carbonate permeability from logs.' His results showed a correlation coefficient of 0.96 when testing the network, compared to 0.61 for linear regression and 0.7 for polynomial regression.

In a widely cited paper Rogers *et al.* (1992) attempted to predict limestone, dolomite, shale, and sandstone lithologies, using a backpropagation neural network. Input logs were gamma-ray, neutron and density. The importance of this paper is that it promoted use of a single output for each lithology, and binary encoding of data. No threshold was applied to the network's output - the node with the highest output was simply taken as the assumed lithology (even if this was very small). However if two nodes had similarly high values then the lithology was taken to show characteristics of both (e.g. a shaly sand or a dolomitic limestone). Training sets appeared to have specific values attached to each lithology (rather than lots of data for the given lithologies).

Neural networks were applied to permeability prediction once again, this time in the Wasson Field, Texas (Osborne 1992). The sedimentary environment was a carbonate platform. The paper is notable as inputs used for the study were depth, porosity, flow unit number (labelled 1-7) and geographic well location (x and y coordinates). In this case the spatial distribution of the reservoir appeared to control its permeability. It therefore illustrates the ability of neural networks to use a variety of input types simultaneously, in this case petrophysical and geographical. Osbornes's final network had 30 nodes in one hidden layer (quite large). The output consisted of isopermeabilty maps. Neural network permeability values produced a correlation coefficient of 0.81 when compared with core plug values. Linear regression from porosity produced a coefficient of 0.44.

Wong *et al.* (1995a) compared discriminant analysis and a backpropagation network when predicting lithofacies, porosity and permeability, in the Carnarvan Basin, Australia (a sand/shale reservoir). Wong noted that previous authors had not paid much attention to input parameters and so experimented considerably with these. He predicted four lithofacies (mudstone, sandy mudstone, sandstone and carbonate cemented beds), using three inputs,

(sonic, density, and acoustic impedance calculated from the sonic and density log). Wong states that 'indeed the consequence of using acoustic impedance was to improve training time' (thus implying easier classification). Overall recognition of lithofacies reached 94.5% which was the same as for discriminant analysis. Wong then attempted to predict porosity using inputs of density, sonic, acoustic impedance and the previously predicted lithofacies. Using lithofacies as an input appeared to improve performance. When porosity predictions were compared to core values the network produced a correlation coefficient of 0.86; discriminant analysis achieved 0.82. Permeability prediction was then carried out using density, sonic, acoustic impedance, lithofacies, and porosity as inputs. On comparison with core the neural network produced a correlation coefficient of 0.81, whereas discriminant analysis produced 0.52. Wong noted that the neural network method benefited from having specific ranges in which predictions had to fall (defined by the training set). This prevented totally unrealistic predictions that sometimes occurred using regression (where predictions are unlimited). Wong also suggested that performance could be improved by making sure the training set was free from errors such as outliers, and ambiguous log values such as those that measure thin beds or shoulder effects. No author would dispute that it is important to remove outliers (due to bad-hole for instance), but some may dispute whether one should leave out data that is related to shoulder effects. Many researchers in neural network studies believe that a large majority of a training set should be devoted to borderline cases (ones that will be close to the decision boundary) and only a few 'easy' examples are needed (e.g. Masters 1993). This should enable the decision boundary to be more carefully placed by the network. However the discussed paper is significant for two main reasons:

- Improved performance was demonstrated when derivative logs were used and;
- It was the first paper that took previous predictions and iterated them into another network to make further predictions.

It is logical to think that if one can predict porosity from density, sonic, acoustic impedance and lithofacies, then one should be able to make predictions straight from density and sonic alone. It appears though that some networks can produce superior results given a larger number of inputs. Experimentation with varying inputs takes place in Chapter 3.

In another paper of the same year (Wong *et al.* 1995c) compared the use of a simplified version of Fuzzy ARTMAP (SFAM), a backpropagation network and discriminant analysis to predict 6 lithofacies (that covered the range from mud-sandstone as well as carbonate cemented beds and concretions). It was found that both the backpropagation algorithm and

Fuzzy ARTMAP performed better than discriminant analysis. Results from these two methods gave comparable results. However the authors conclude that the SFAM was advantageous because it did not suffer from problems such as excessive training time and prior specification of the network topology. They also note that if the amount of time and effort required to fine tune backpropagation parameters is acceptable then this network can offer significantly improved performance, although this requires some experience and skill.

Mohaghegh & Ameri (1996) followed previous authors in attempting to use a network for permeability prediction in the Cranny field, West Virginia. Inputs were gamma ray, density, and deep induction logs, x-y coordinates and some 'geological interpretations' (which appear to be a lithofacies number derived from bulk density variations). So this is again an example of using input logs derived from the raw data. Their results compared well with laboratory measurements and the neural network was once again promoted as a viable procedure to complement other reservoir characterisation tools.

Up until the late nineties the majority of neural networks used for log interpretation utilised the backpropagation algorithm. Saggaf and Nedrija (2000) however used three different approaches to predicting lithology and facies in some Saudi Arabian wells – unsupervised, supervised and semi-supervised systems, none of which used the backpropagation algorithm. The first method used a Kohonen network. Six logs were used as inputs. The system enabled distinct clusters that were inherent in the data to be defined. Four clusters, which were then refined to three, were found. These appeared to match a geologist's interpretation of a short well interval; however the well interval appeared to contain only a limited number of beds that were all relatively thick. The supervised analysis made use of nine core defined carbonate facies and a network with two layers of nodes. The first layer took the input vectors and separated them into several subclasses just as for the unsupervised system. The second layer combined the subclasses in a linear way and associated them with the predefined core facies. The semi-supervised analysis worked as the unsupervised system did, clustering the data. Log values of the cluster centres were then compared to the average values for the predefined clusters and labelled accordingly. Semi-supervised analysis was demonstrated in a single well predicting limestone and dolomite only, and achieved good results. This paper is important because it considers the confidence of results from the networks, something that can routinely be obtained from other methods e.g. fuzzy logic (Cuddy 2000). Three types of confidence measures were generated: 'distinction', 'overall

similarity' and 'individual similarity'. Distinction is the measured distance of a data point in vector space to its closest cluster centre compared to the next closest cluster. Overall similarity is the distance from a data point to its cluster centre, and individual similarity is the same except that the distance from each facies type (a cluster centre) is computed. For lithology prediction (as in the limestone and dolomite example) two distances of comparable size could indicate a mixed composition.

So far the application of neural network analysis to lithofacies and permeability predictions from well logs has been discussed. However neural networks have also been used in a variety of other geoscience applications. Wu & Zhou (1993) modelled the spatial variation and distribution of copper ore grade using a backpropagation network. The network had two inputs (x and y coordinates) and two hidden layers each with 28 nodes, (which is incredibly large!). Overall, results were reported as good, but Wu & Zhou noted that the network appeared to learn that samples with high grades are few compared with medium grades, as seen by the fact that the network under predicted high grade values which had fewer training cases. This implies that classes that are underrepresented in a training set can be underpredicted.

Wong *et al.* (1997) used a special type of radial basis function network to interpolate porosity values in unknown locations, in a fluvial sandstone reservoir from Asia. Sixty-nine representative wells were used for training, with the object to interpolate well porosity values to other cells for which no porosity values were available.

Trappe & Hellmich (2000) used a self-organising feature map (an extension of a Kohonen unsupervised network) to predict porosity thickness from seismic attributes in Rotliegend Sandstone, in the North German Basin. Although the authors noted that over twenty attributes were available, and, in theory, the network should be able to distinguish which ones were discriminatory by itself, only three were chosen as inputs (acoustic impedance, amplitude, and 'lateral homogeneities'). Training data consisted of 14 patterns from 14 wells. The subsequent network was applied to 100km$^2$ of seismic survey. The results were compared to earlier work by Trappe and Hellmich (1998) which attempted to predict the same outcome using linear regression and co-kriging (a statistical interpolation technique) from acoustic impedance only. All the methods gave reasonably good agreement except linear regression that did not perform well when the porosity thickness was close to zero.

The authors suggest that neural networks could be used in the first stage of analysis as they are good at handling different data sources, both qualitative and quantitative. The outputs from networks could then be used as 'soft' data in geostatistical calculations.

Doraisamy *et al.* (2000) used backpropagation to determine whether sample sites of geochemical data were located above a known hydrocarbon reservoir. Inputs to the network were soil descriptions and environmental parameters, including absorbed ethane concentration. The output was simply a yes or no as to whether the site was above the reservoir. On testing the network predicted 95% of sites correctly.

The most recent advances in using neural networks to make predictions from well logs have come from Hans Helle and Alphana Bhatt, working in Norsk Hydro and Trondheim University respectively. They published a suite of papers during 2001 and 2002 that make predictions of porosity, permeability, fluid saturation and sedimentary facies from well logs.

Helle *et al.* (2001) used backpropagation to predict porosity and permeability in Jurassic reservoirs in the Viking Graben, North Sea. Their porosity network had three logs as inputs (sonic, density and resistivity), and used seven hidden nodes in one layer. Training examples were taken from a number of wells and from water, oil and gas zones. It was claimed that the resulting network was able to predict accurate porosity values across all fluid types, indeed the reported average error (core porosity minus network porosity) was less than 1%. Their permeability network attempted to overcome the problems of permeability anisotropy by only choosing training data from near vertical wells and horizontally measured air permeability that had been Klinkenberg corrected. Training data was again taken from water, oil and gas zones (but by far the majority was from water and oil zones). Input logs were density, gamma-ray, neutron and sonic, and the network had 1 hidden layer with 12 nodes. Results of the network were much more scattered than for the porosity network. The resulting errors were put down to errors in core measurement, correction to overburden, and the different sampling volumes of core plugs versus well logs. The largest errors were found in the tested well that contained gas. However both porosity and permeability results were thought useful enough to be used in conventional petroleum engineering applications, given the limitations of measurement.

Bhatt & Helle (2002a) followed their previous work by using backpropagation networks to predict porosity and permeability, this time though focussing on network design. They developed what they describe as *committee networks*, which consist of a number of individually trained backpropagation neural networks, the results of which are combined to produce the final output (Figure 2.15). Work was carried out on synthetic data for both porosity and permeability, before applying to the real data used in Helle *et al.* (2001). The synthetic porosity network was developed with input logs of density, sonic and resistivity. Differing degrees of random noise were added to the data. Twenty networks were trained and nine were chosen to go into the committee. Generally it was found that equipping each of the networks with ten hidden nodes reduced the bias and variance optimally. When only 2.5% of noise was added no improvement in prediction was seen with more than 150 sample data points. With 5 or 10% noise prediction success improved with more than 150 samples. This illustrates the need for more training samples in datasets which are known to be noisy, or in datasets where user uncertainty exists in the relationships between inputs and outputs. The porosity committee used a combiner which produced a linear combination (weighted sum) of the outputs (after Hashem (1997)) which is equivalent to a multi-linear regression of the network outputs and the target data. Overall the committee was shown to reduce both the bias (which is in fact automatically reduced to zero by the combiner) and variance of the resulting errors (expressed as predicted porosity minus core porosity). The porosity committee was then applied to the North Sea data. The results shown are good and comparable to those of Helle *et al.* (2001). Porosity appeared to be predicted independent of pore fluid type. However although the error bias was reduced to zero by the committee, the variance showed no improvement (unlike the synthetic data). A significant amount of the error was considered due to fine layering in the reservoir that the logging tools could not resolve. The permeability committee log inputs consisted of density, neutron, gamma-ray, and sonic. The committee for permeability prediction took on a different and more complex nature (Figure 2.16). The authors noted that it was important to encode permeability as the logarithm of permeability, as it had to be mapped to the [0,1] domain for entry into the neural network. This meant that resolution was lost. To overcome this, the final architecture of the committee consisted of a number of smaller committees each dedicated to the task of predicting permeability over a small range. A 'gate' was also trained over the whole permeability range, with the task of identifying the appropriate range for prediction, and thus effectively switching on the appropriate committee. It was found that training with soft overtraining and using a linear combiner (as for porosity prediction) was not appropriate, as

it appeared to amplify noise. Training with conventional validation and simple averaging of the outputs produced acceptable results. The final architecture had three modules (three ranges of permeability values) each consisting of a committee of five networks. Each individual neural network had 10 nodes in one hidden layer. It was shown that over 300 data samples were needed during training to cope with moderately noisy data - more than porosity because of the intrinsically more complex nature of permeability. Training with the real data took place with less than 300 examples because of a lack of training parameters. On application to the data used in their previous study the authors highlighted small areas of improvement in one well using the modular committee compared with a single neural network. However examining all the errors shows that the single network produced a smaller mean error, and only a slightly larger standard deviation (single neural network bias 0.08, and standard deviation 1.3, modular committee bias -0.11, standard deviation 1.10) in the well interval illustrated.

In summary the main contribution of this work is to the design of neural networks. It is reported that a committee of networks produced a smaller overall error than a single network, and the breaking of the problem down into subtasks (modules) also improved predictions (in this case the resolution of predicted permeability).

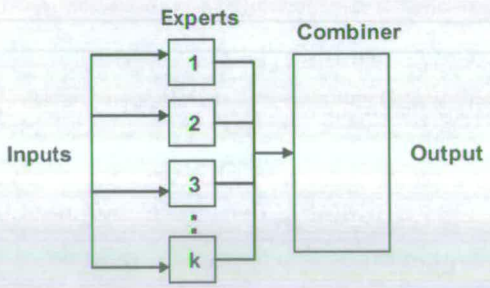



**Figure 2.15** A committee machine. Each of the experts is an individual neural network trained on the same data, but from different starting positions. The results are linearly combined to produce the final output. Redrawn from Bhatt & Helle 2002a.

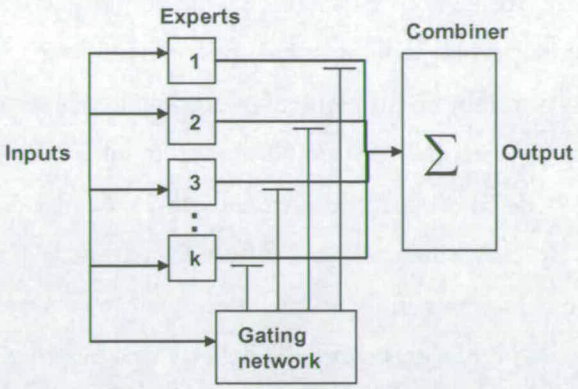



**Figure 2.16** A modular committee machine. Each of the experts is a committee machine (as in Figure 2.15) with a dedicated task of predicting within a specific permeability range. The gating network weights the output from the experts. Results are then simply averaged to produce the final output. Redrawn from Bhatt & Helle 2002a.

In another paper of the same year Helle & Bhatt (Helle & Bhatt 2002) created a committee neural network to predict partial fluid saturations from well logs. The paper followed the theme of their porosity and permeability paper by first testing the performance of the network on synthetic data and then applying it to real data from the North Sea. The reason for using neural networks for the fluid saturation calculation is that any derived model could potentially be universal (eliminating the problems with core plugs encountering only a small volume of rock for instance), and can also take into account field wide variations. A neural model could account for a varying cementation factor, for which a single value is usually chosen when calculating water saturation from empirical relationships such as the Archie equation (Archie 1942). Helle & Bhatt calculated four synthetic logs (sonic, density, neutron, and resistivity) from chosen fluid saturation values and added varying percentages of noise up to 10%. One of the main difficulties to be overcome was whether to design a network to output all three saturations (water saturation Sw, oil saturation So, and gas saturation Sg), a network to calculate two saturations (the third automatically assigned) or to create three networks to calculate the three parameters individually. Experimentation with different networks showed that similar errors resulted from all three of the situations above. In this case the third type was preferred (individual networks for each task) as this meant fewer training examples would be needed, in theory. A committee network was then applied to the synthetic data. A linear combination of the individual networks was used (as in the porosity example of Bhatt & Helle 2002a). It was reported that the errors of the committee

output compared to single networks was an order of magnitude lower. However analysis of the results reveals that the variance of the errors for the committee was similar to that of the individual networks - it was simply the bias that was reduced to zero (a consequence of the linear combination, not of training multiple networks). On application to real data the target training data was based on computer processed interpretation (CPI) logs (calculated by the contractor using models such as Archie (Archie 1942) or Poupon *et al.* (1971)), the hydrocarbon indicated by the contractor, and repeat formation test pressures (RFT). This implies that the training data was derived in part from well logs, via empirical relationships, and thus, in some ways also represents synthetic data (which one might automatically expect a neural network to be able to predict). The results are shown in wells that pass through the Tarbert, Ness and Broom formations, and generally the results match the contractor's interpretation. Some gas spikes occur in the Tarbert and Ness. These represent coal and were predicted as high gas saturation because of low density and sonic readings.

It is apparent that by far the majority of neural network use with well logs is in the prediction of permeability and porosity. By comparison little has been written about lithology and facies prediction. However, Bhatt & Helle (2002b) developed their previous work and predicted facies from well logs, first using synthetic data, before applying to the Jurassic Ness formation in the Oseberg Field (North Sea). An additional focus of this study was the application of so called recurrent neural networks (see Figure 2.17). These take samples from multiple depth levels with the aim of improving predictions at bed boundaries (due to shoulder effects in logs) and from noisy data. Note this system is different from classic 'recurrent' systems described in neural network literature where the outputs are connected to the inputs (as in a Hopfield network). The type of approach used by Bhatt & Helle was also used by Yang *et al.* (1996), by Jenner & Baldwin (1994) and Goncalves, Harvey & Lovell (1997). The recurrent system was incorporated into the modular committee system of Bhatt & Helle 2002a. Using synthetic data the authors created pseudo resistivity, gamma-ray, sonic, neutron and density logs. Data distributions were created for each facies (three in total), with a small overlap between them. Experimentation with an individual neural network which made up a component of the committee showed that the optimal architecture had four nodes and needed a minimum number of training parameters of 10-15. This though applies to the synthetic data, and was carried out on only two facies (which were the furthest apart in the log space). On the basis of these findings the authors used this architecture to experiment with the recurrent system. Experiments revealed that using data from three depth

levels (one above, one below) increased the hit rate from 90% to 93%, and increasing to five depth levels increased the hit rate further to 96%. The results appear to show this clearly. However the synthetic data had 3 layers (i.e. beds) which constituted transition zones on the logs. When the number of beds was increased to 17 the number of miss-hits increased more than 3-fold. However the authors state that 'for any practical purpose the number of transition zones seems not to be a main issue'. The recurrent neural networks were placed in a committee, and although the results were reported as improved, they appear to be similar to the best performing individual network. On application to real data four lithofacies were predicted from the fluvial-lacustrine environment: channel sand; crevasse splays (shaly sands); lake (shaly); and coal, and data was chosen over a range of pore filling types. Results are shown over four wells with the training well performing best. Some intervals of coal were misinterpreted. The authors compare their predictions with other authors who use a variety of techniques for lithofacies predictions. Comparison is in terms of number of facies and hit rate. There is no mention of the sedimentary environment. It should be noted that the system described by Bhatt & Helle (2002b) is fairly large. Each backpropagation committee has 9 networks. Each lithofacies has one dedicated committee. Four lithofacies implies 36 networks (4x9). Each of these systems predicts at 5 depth levels so the final number of networks used is at least 180 (4x9x5).

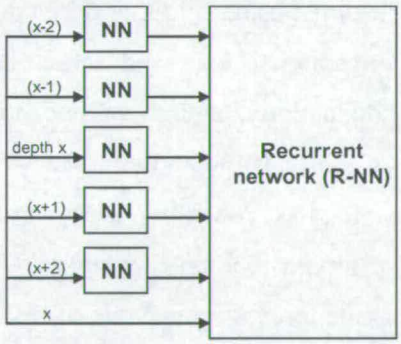



**Figure 2.17** A recurrent backpropagation neural network. Individual networks are trained on data from different depth levels and combined to make the recurrent system. Nine of the above recurrent systems are joined together in a committee with the dedicated task of predicting one specific facies. Then the committees are combined to produce the overall prediction. Redrawn from Bhatt & Helle (2002b).

The key to the integration of image logs into the neural network process is feature extraction – the techniques used to quantify patterns that are seen in the images and encode them in a

suitable way so that statistical learning algorithms are capable of utilising them. This topic is discussed in Chapter 5.

Few studies however have gone on to use extracted features with neural networks. Hall (1996) extracted textures using mathematical morphology and used an unsupervised network for cluster analysis. Garden (2001) calculated statistics (the average, standard deviation and coefficient of variation) from a single button from each pad and integrated these with interpolated coarser logs. A single network was used to predict 3 image facies associations. Results were good, with the network capable of mimicking the variation of sand content in the boreholes studied. Thin-beds of predicted sand tended to be thinner than those recognised in core – this was described as an artefact due to the resolution of the conventional logs. Overall net sand content matched that manually derived from the image logs, and that derived from core. There was however an appreciable difference from net sand that was derived from a porosity and permeability cut-off. Also Garden found an appreciable improvement in the results when image logs were interpolated to be the same resolution as the conventional logs. Russell (2002) examined heterogeneity in a carbonate reservoir. Different biofacies were recognised in core each of which were dominated by different fauna. On the basis of these facies different reservoir rock types were identified that had different petrophysical characteristics. The aim of the paper was to improve characterisation of these rock types using textures derived from high-resolution dipmeters and image logs. Three conventional logs and three image-derived components were available (the background conductivity, and the proportions of resistive and conductive components). The contrast of the resistive and conductive components strongly correlated with permeability. Both unsupervised and supervised learning took place, and results were found to match core derived reservoir rock types well (using inputs from both dipmeters and image logs). It was noted that the tools were capable of resolving heterogeneity that was not typically captured in the core descriptions.

## *2.8 Summary*

This chapter introduced the field of neural networks and discussed their use in geoscience. It began with a justification for the use of the backpropagation algorithm that is used in this thesis. Perceptrons, which represent the fundamental building blocks of neural networks, were then introduced as well as rules that are capable of training them (the Perceptron and

Delta rules). This lead to a detailed explanation of the backpropagation algorithm. At its simplest the algorithm consists of multiple layers of nodes that process input data and map them to known outputs. By a complex feedback mechanism the algorithm changes the weights in the network so that input vectors are moved closer to target data. This learning enables the network to classify large groups of data in multi-dimensional space. A section then followed detailing strategies for the implementation of the algorithm – most of these are a consequence of the actual algorithm itself. With the knowledge of nodes and network architectures other types of networks were then discussed.

Finally the last section gave a historical account of neural network use in geoscience. By far the most commonly cited application of neural networks (using well logs as inputs) is in the prediction of permeability. Lithology has also been predicted, and, more recently lithofacies. In most reported cases neural networks perform at least as well as other statistical techniques. The most recent applications of neural net analysis to this type of problem use large committees' of networks that are averaged to produce the final output. Classification is also reported to be improved by having networks specifically predicting an individual class. Very recently image logs have been integrated into the neural network process.

# Chapter 3 : The Lomond Field, lithofacies scheme & neural network methodology

## *3.1 Introduction*

This chapter describes the methodology used to develop and train a neural network to discriminate lithofacies. Section 3.2 introduces the Lomond Field and data set studied in this thesis. Section 3.3 describes the sedimentology of Lomond in terms of depositional processes, the lithologies, their 3-D architecture, and their petrophysical properties. These factors, along with the facies quantities and their discrimination by the logs are carefully considered before the lithofacies scheme that the neural network will be trained to predict is designed (Section 3.4).

Section 3.5 outlines how log and lithofacies data were prepared before application in the network. This includes input selection, data transforms, inter-well variation, depth shifting and training and validation set design.

Finally, Section 3.6 describes various experiments that took place with the neural network to firstly, define the optimum network for classification and, secondly, to determine some of the main influences on the network output. Preliminary results of these experiments are shown and discussed. The optimum network design was then applied to all cored wells that had sedimentary log descriptions. These results and their subsequent analysis are presented in detail in Chapter 4.

## *3.2 The Lomond Field*

### *3.2.1 Introduction*

The Lomond field is situated in the North Sea 233 km from Aberdeen. It lies in block 23/21 on the east side of the East Central Graben (Figure 3.1). Although the discovery well in 1972 tested hydrocarbon the first appraisal well in 1974 was suspended. Ten years later a second appraisal well was drilled and in 1993 production started. Participants in the field are BP, BG Group and Amerada Hess.

A description of the tectonostratigraphic evolution and associated development of hydrocarbon plays in the Central Graben can be found in Hodgson *et al.* (1992) and is summarised in Figure 3.2. After Zechstein salt deposition in the Permian, salt withdrawal created accommodation space for Triassic and Jurassic continental sediments. Late Jurassic rifting reactivated salt movement with the eventual creation of salt ridges on the margins of remnant half-grabens. Early Tertiary clastic deposition around these salt ridges and diapers followed by basement subsidence eventually created dome play structures, of which the Lomond Field is one.

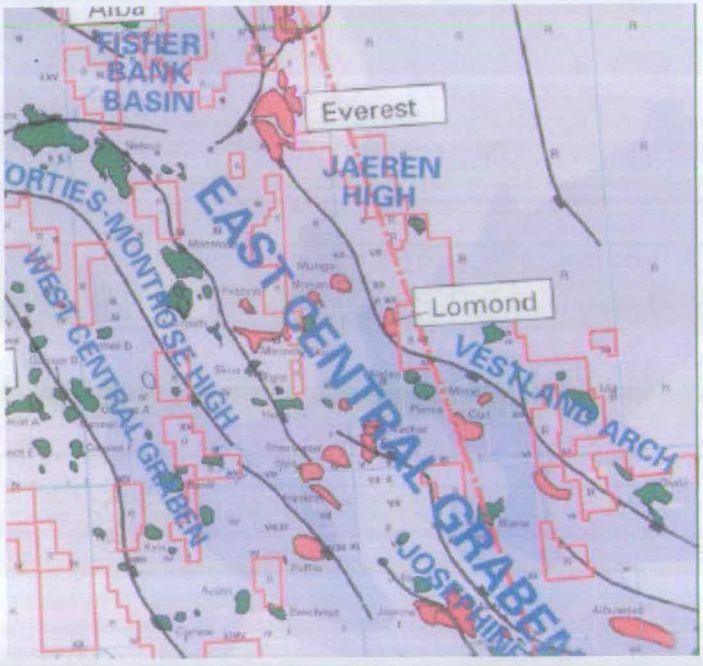



**Figure 3.1** The position of the Lomond Field in the Central North Sea. Oil fields are shown in green, gas and condensate fields in red. The red dashed line represents the division between the UK and Norwegian sectors. (Taken from the Petroleum Exploration Society of Great Britain (PESGB) North Sea map, 2000).

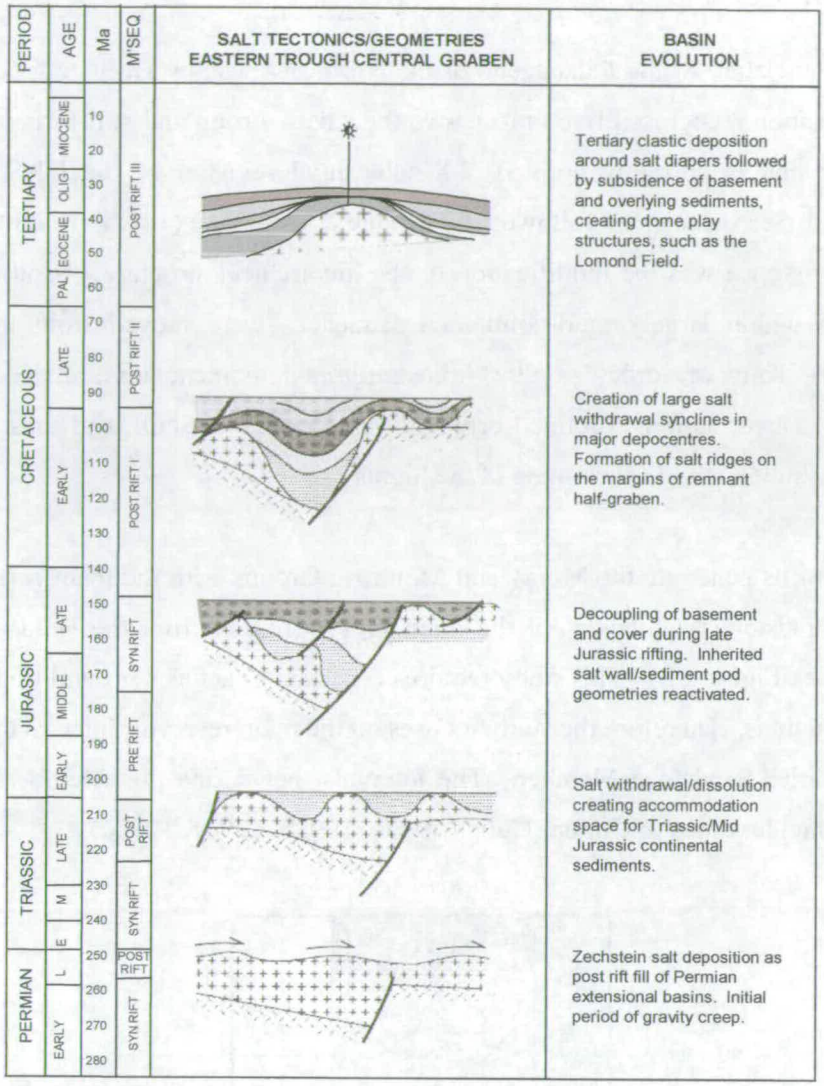



**Figure 3.2** Salt controls on the evolution of the Central Graben, and the development of the Lomond Field. Redrawn from Hodgson *et al.* (1992).

Hodgson *et al.* (1992) consider that clastic deposition was mainly sourced from the Caledonian Highlands resulting in large fluvial deltas building out into the Moray Firth and onto the East Shetland Platform. These deltas are then thought to have developed into extensive submarine fans which prograded into the Central Graben and now form the main reservoir rock in Lomond (The Forties Sandstone). At the end of the Palaeocene clastic input was probably halted by a basin-wide transgressive highstand resulting in the deposition of hemipelagic clays and tuffs of the Sele and Balder Formations of the Rogaland Group. These form the reservoir seal.

### 3.2.2 Stratigraphy

The first nomenclature of the Palaeogene of the North Sea was by Deegan & Scull (1977). Their classification recognised five units above the Chalk Group and still forms the basis of nomenclature that is currently applied. A substantial revision of the UK Central and Northern North Sea Palaeogene followed, by Mudge & Copesake (1992a, 1992b). The most significant difference was the modification of the hierarchical structure. Sandstone bodies that occurred within largely mud-dominated sequences were moved from formation to member status. Knox & Cordey's (1992) lithostratigraphic nomenclature retained the Lower Moray and Montrose Groups (defined originally by Deegan & Scull, and most relevant to this study) but subdivided further some of the higher groups.

All Lomond wells penetrate the Moray and Montrose Groups with the main reservoir target the Forties Sandstone Member. All the main logs were run from the Balder Formation downwards (see Figure 3.3). This study requires core data to act as a ground truth for neural network predictions. Therefore the study focuses on the main reservoir interval that has been cored: the Forties Sandstone Member. The intervals that define this Member were taken from the sedimentary logs of Cullen (Cullen 1993a, 1993b, 1993c, 1993d).

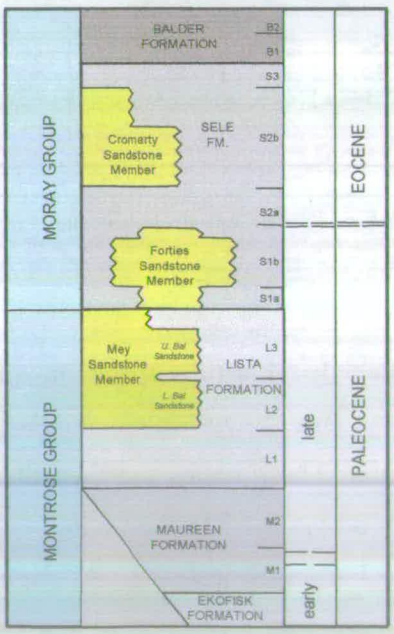



**Figure 3.3** Stratigraphy of the Palaeogene of the North Sea (redrawn from Knox & Cordey, 1992) with the Forties Sandstone as Member status, contained within the Sele Formation. In the Lomond Field well logs were run from the Balder Formation downwards, and sometimes as far as the Ekofisk Formation (e.g. well 23/21-T8).

### 3.2.3 Data

The available data set consists of ten appraisal and production wells (23/21-T1 to 23/21-T10). All are horizontal. Most wells contain a full suite of conventional log data. If a neural network model is created and trained on a specific log then that log must be available in subsequent wells if predictions are to be made. Common logs available in all the wells are:

| | |
|---|---|
| Gamma–ray | GR; |
| Sonic | DT; |
| Deep induction | ILD; |
| Medium induction | ILM; |
| Density | RHOB; |
| Neutron | NPHI. |

(N.B. a full explanation of all symbols used in this thesis is contained in the notations and conventions section preceding Chapter 1.)

The exception to this is 23/21-T7, where no sonic or density log were available due to tool failure (Walsgrove 1996). This well is therefore excluded from this study.

Core was cut in six of the available wells (23/21-T1, 23/21-T2, 23/21-T3, 23/21-T4, 23/21-T5 and 23/21-T8). Detailed core descriptions (1.50 scale logs) and subsequent interpretation were carried out on four wells (23/21-T3, 23/21-T4, 23/21-T5, 23/21-T8) by Brian Cullen (Cullen 1993a, Cullen 1993b, Cullen 1993c, Cullen 1993d). It is these descriptions that provide most of the understanding of Lomond's sedimentology (Section 3.3), and upon which the lithofacies scheme (which the neural network is trained to predict) is partly based on (see Section 3.4).

## 3.3 Sedimentology of the Lomond Field

### 3.3.1 Introduction

Information on Lomond's sedimentology is derived from core descriptions made by Brian Cullen (Cullen 1993a, 1993b, 1993c, 1993d). The facies scheme used to describe the core was adapted from that described by Mutti & Ricci Lucchi (1972) and is shown in Figure 3.4. All parts of the four wells described were interpreted as part of a turbidite depositional system (with the exception of a small interval in well 23/21-T3, which is part of the Maureen Formation and therefore excluded from this study). In total fifty-nine facies codes were used to classify the core. The main facies classes were distinguished primarily on the basis of grain size (facies A-E), and internal organisation (facies F). Subgroups of these (e.g. A1, A2 etc.) were based on internal structures, bed thickness, and composition. Within the core it was noted that many of the sediments showed evidence of post-depositional slumping, and these were denoted by an F prefix or suffix (e.g. B1F, FB1) depending on the degree of alteration of the original facies characteristics. F before a facies code indicates a high degree of alteration and after a lower degree of alteration. What follows is a description of, and evidence for, the main sub-environments of deposition in Lomond. Sedimentology is an important consideration in any lithofacies scheme: the different environments shape the lithologies, and determine their different properties.

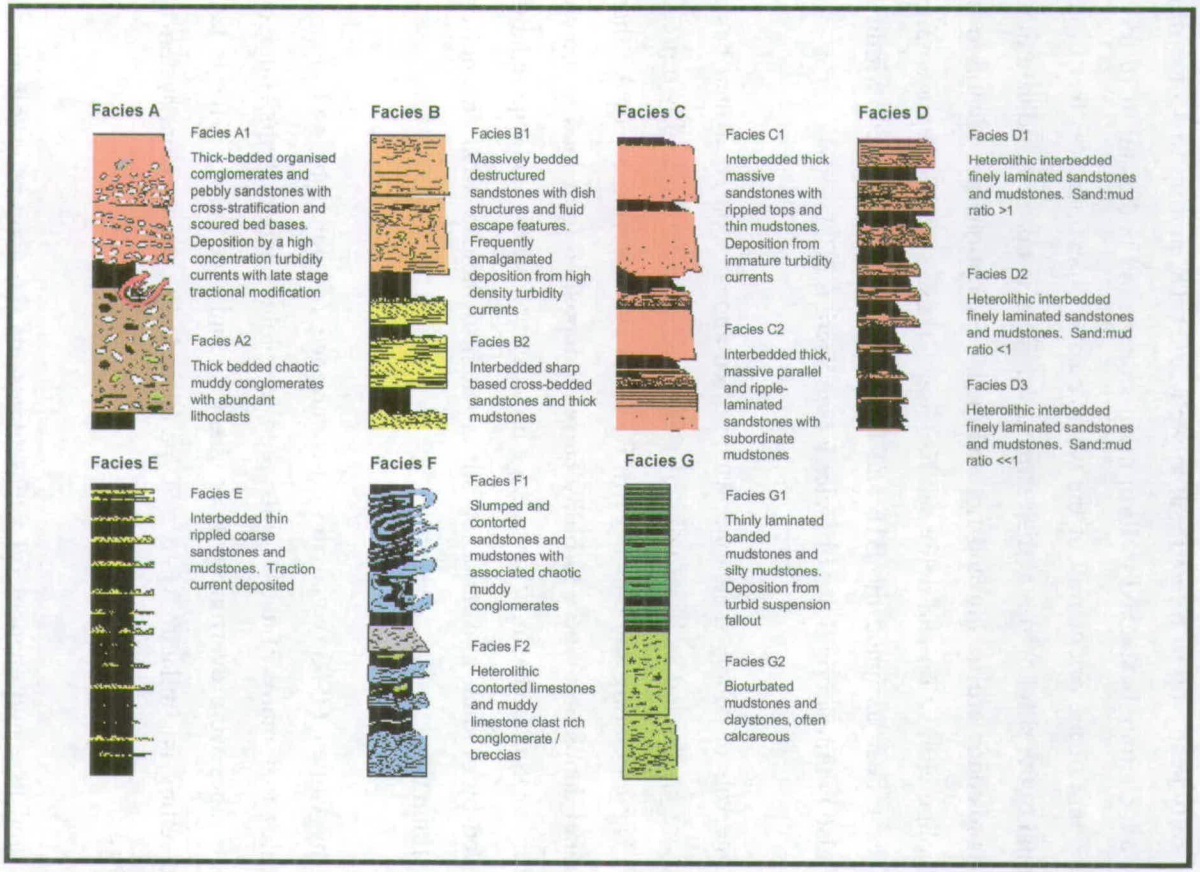



**Figure 3.4** Facies model adapted from Mutti & Ricci Lucchi (1972)

### *3.3.2 Submarine sand lobe and channel fill*

These facies consists of thick-bedded relatively homogeneous sandstone the majority being described as facies B1 (Figure 3.5). Dish structures, and water escape pipes are common, indicating dewatering and rapid deposition. The rocks are interpreted as being deposited by high density turbidity currents. In most cases the lack of an erosive base and fining upward sequences means that these sandstones were interpreted as lobes rather than channel fill. Individual beds are typically up to 6 feet thick in well 23/21-T8, and up to 15 feet thick in 23/21-T3. They are commonly stacked to form multi-storey sand bodies up to 70 feet thick in total. Measurement of the orientation of the water escape pipes indicates that in general they are orthogonal to the sub-horizontal dish structures. This is taken to indicate that most of the massive sandstones are in situ and not slumped. Exceptions are identified by the presence of convolute lamination and deformed bedding. These slumped representations of the main facies have been assigned the B1F and FB1 notation. They occur within larger sand bodies and also within debris flows of facies F (see Section 3.3.3).

Much rarer are intervals of pebbly sandstone, which often appear scoured at their bases (A1 and A2). These are interpreted as basal units of submarine channels, possibly representing initial stages of channel cutting and channel fill. B1 intervals overlying A1 or A2 therefore represent in-channel deposition where turbidity currents deposited their load in the channel before passing further into the basin. The passage upward into parallel and ripple laminated sandstone followed by grading into mud and silt is taken to indicate final channel or lobe abandonment (C1 and C2).

It is suggested by Cullen (1993a) that the co-occurrence of sand lobe and channel fill sequences indicates that many of these units represent lobe–channel transitional bodies, where prograding lobes were overrun by later channels and vice-versa. This is taken to indicate that the setting is similar to Mutti's 'Type II' turbidite depositional system (Mutti 1985) and Figure 3.6.

The submarine sand lobe and channel fill facies represents the main reservoir intervals in Lomond.

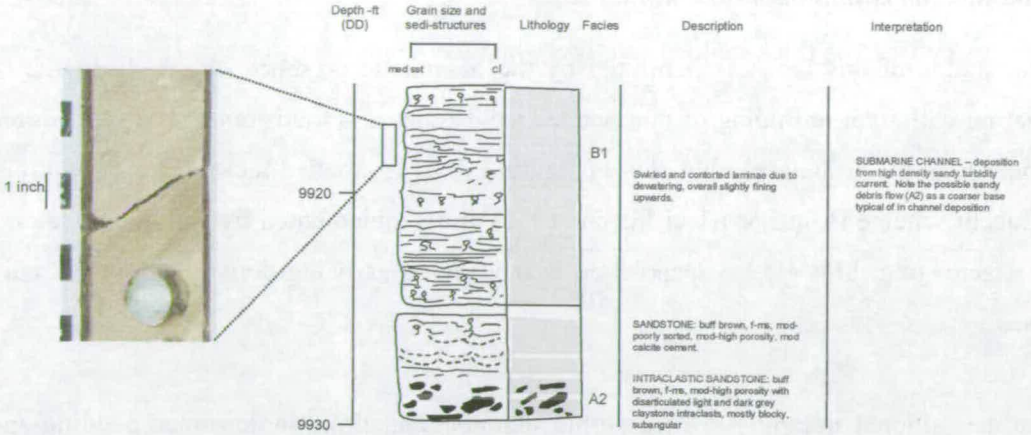



**Figure 3.5** Typical section interpreted as representing submarine channel and lobe facies. Intraclastic sandstone representing a possible channel base, grading upwards into medium sandstone with de-watering structures. Taken from Cullen (1993a), well 23/21-T3. Photograph taken from well 23/21-T5, 9354ft (DD) but typical of this facies.

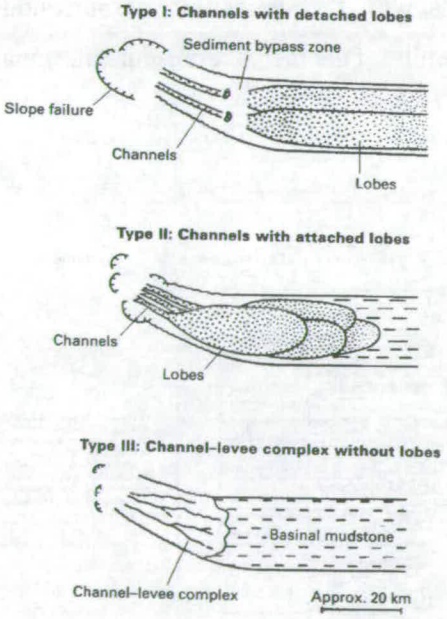



**Figure 3.6** Plan view of the three main types of turbidite depositional system of Mutti (1985). Lomond was interpreted by Cullen (1993a) as a type II system due to the co-occurrence of channels and lobes. Picture taken from Reading (1996), after Mutti (1985).

### *3.3.3 Slump sheets and debris flows*

Characterisation of this facies is permitted by the diagnostic presence of a high degree of deformation with intense folding of interbedded sandstones and mudstones, or poorly sorted sandstones with dis-articulated mud clasts (Figure 3.7). It is labelled facies F in the Mutti & Ricci Lucchi scheme (Mutti & Ricci Lucchi 1972) and supplemented by slump equivalents of other facies (e.g. FB1 etc.). Deposition is interpreted as being derived from two main processes:

- Post-depositional slumping of heterolithic sediments resulting in deformed bedding and folding;
- Deposition by muddy debris flows resulting in poorly sorted sediment with mud clasts.

On occasion individual slump units occur as discrete packages up to twenty feet thick (e.g. in well 23/21-T4). Most common however are intervals of much smaller units stacked together. Slump sheets commonly occur at the top of lobe and channel sand bodies (especially in well 23-21-T5), and are interpreted as the products of lower energy environments during phases of reduced turbidity current activity. Debris flow emplacement was probably contemporaneous with the deposition of surrounding sequences, but also occurs at the base of sand lobe units. This facies represents marginal reservoir rock.

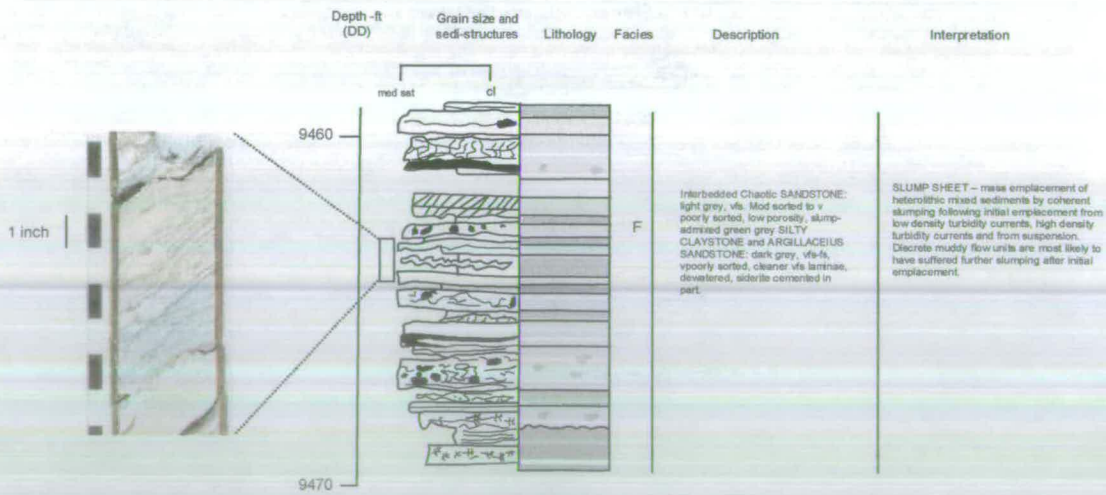



**Figure 3.7** Typical section interpreted as representing deposition by slump sheet emplacement. Taken from Cullen (1993c), well 23/21-T5. Photograph taken from well 23/21-T5, 9336 ft (DD) but typical of this facies.

### *3.3.4 Lobe fringe*

This facies is characterised by thin interbedded mudrock (laminated or bioturbated), and sandstone which is often ripple-laminated, Figure 3.8. The mudrock is interpreted as a suspension fallout deposit and the sand component from low density evolved distal turbidity currents. These rocks belong to facies D1 and D2. Down current facies D3 associated with facies G represents the transition to the outer basin. Up-current a transition to mid-fan sand lobes would be expected. Although these rocks contain thin sandy intervals, overall reservoir quality is poor.

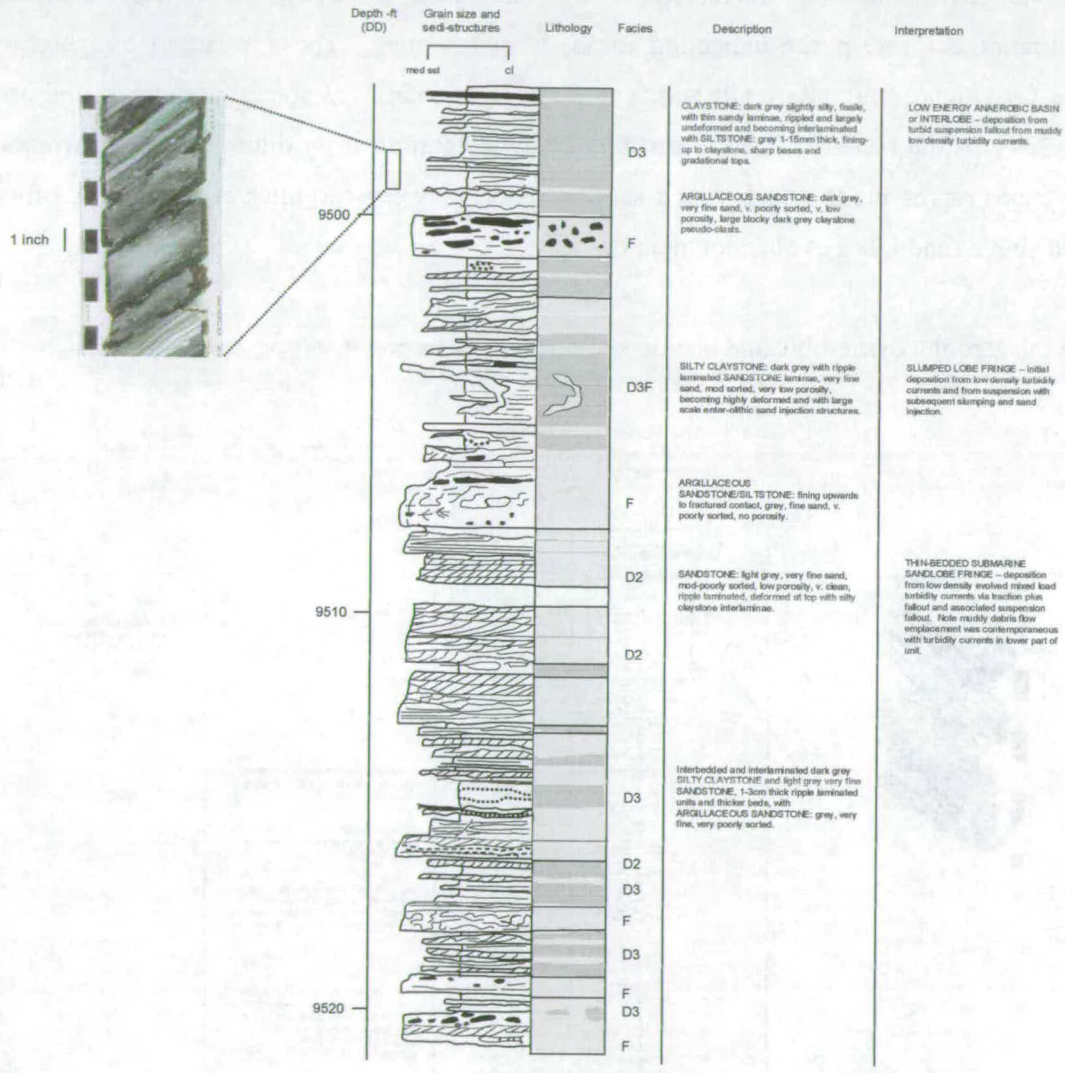



**Figure 3.8** Typical section interpreted as representing a thin-bedded submarine lobe fringe. Taken from Cullen (1993c), well 23/21-T5. Photograph taken from location indicated.

### 3.3.5 Aerobic / disaerobic basin

This facies consists of bioturbated mudstone. Trace fossils recognised in core are *Zoophycos* and *Chrondrites*. These are typical of deposition in a marine setting on a quiet low-energy outer slope with aerobic or disaerobic (restricted oxygen) bottom waters. These rocks are classified as G2. This facies is often associated with minor sand injections and slumping (especially in well 23/21-T4). When this occurs facies F has been assigned.

### 3.3.6 Anoxic basin

This sub-environment is characterised by laminated mudstone sequences, lack of bioturbation and rare pyrite indicating anoxic bottom waters. These rocks are assigned to facies G1 (Figure 3.9). Rare silt and sand laminae of facies D3 sometimes occur, and are interpreted as the result of traction and fallout sedimentation from dilute turbidity currents. This facies represents the background sedimentation between turbidity events, and is often found above sand lobes as abandonment drapes.

Both the aerobic, dysaerobic and anoxic settings represent non reservoir rocks.

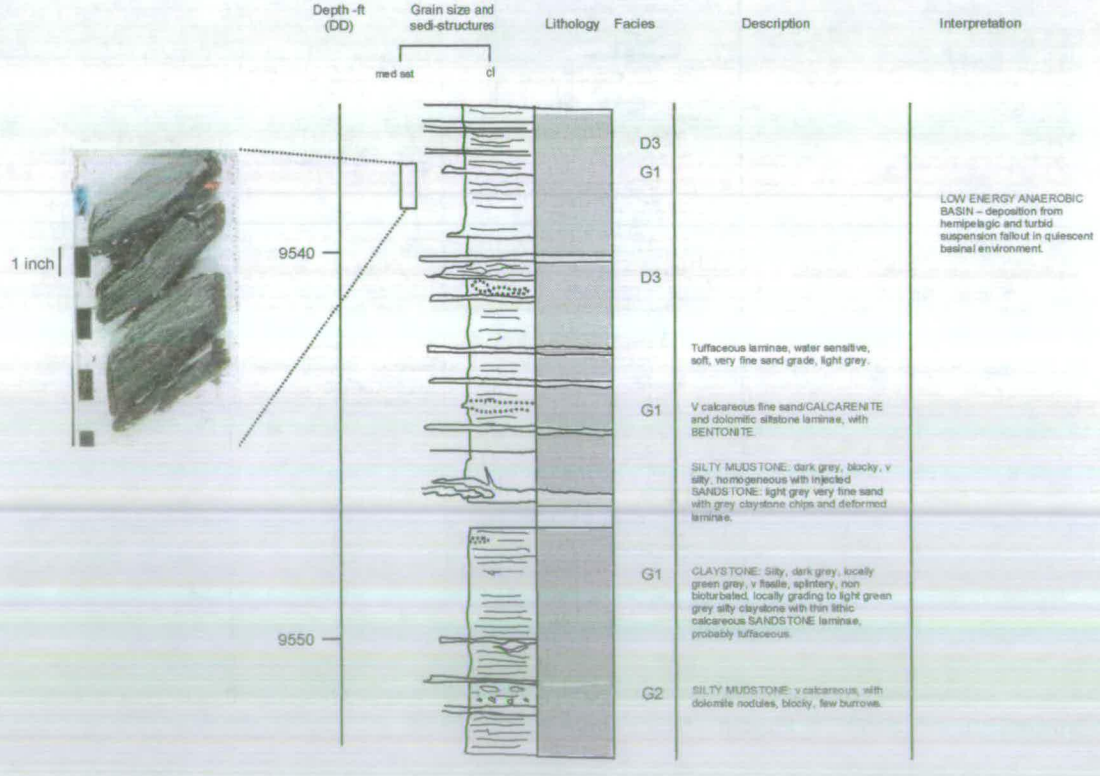



**Figure 3.9** Typical section interpreted as representing a low energy anaerobic basin. Taken from Cullen (1993c), well 23/21-T5. Photograph taken from well 23/21-T5, 9495ft (DD) but typical of this facies.

## *3.4 Lithofacies design*

### *3.4.1 Introduction*

The sedimentology of the Lomond Field was discussed in the previous section. It can be recalled that the core had been divided into fifty-nine possible facies and sub-facies. Clearly if a neural network was trained to predict all these then the results would be expected to be poor. Indeed the sedimentary facies of Mutti & Ricci Lucchi (1972) are based on internal organisation and texture, as well as grain size and composition. Therefore it is necessary to develop a rationalised lithofacies scheme. The term lithofacies is described in the Oxford Dictionary of Earth Sciences (Allaby & Allaby 1996) as 'rock noted for a distinctive group of characteristics, e.g. composition and grain size'. A more formal definition could be a rock noted for a distinctive group of lithological characteristics that are genetically related to a specifically defined facies.' In general a lithofacies is a lithology that occurs in or relates to a particular facies and this is the definition that used here. This is distinct from an electrofacies. Serra & Abbott (1980) define an electrofacies as 'the set of log responses that characterises a sediment and permits the sediment to be distinguished from others.' Clearly if the lithofacies scheme is to be successfully predicted then it must in some ways relate to an electrofacies scheme. This is discussed further in Section 3.4.6.

It was stated in Chapter 1 that one of the main goals of neural network analysis of lithofacies from well logs is the ability to rapidly predict lithofacies in many wells thus providing constraints for both static and dynamic geological reservoir models to aid hydrocarbon field development. For this reason and the reasons stated above the following criteria were considered in the design of the lithofacies scheme:

- Facies architecture;
- Reservoir quality of different facies;
- Occurrence of different facies;
- Log separability.

Each of these is discussed in the following sections.

### 3.4.2 Facies architecture

A typical methodology for creating a 3-D geostatistical model would be similar to that described by Wardell (1996). Models are generally generated at three hierarchical levels. Initially the large-scale architectures such as the channel fairway or mid-channel are identified using interpreted (usually 3-D) seismic sections and seismic attribute maps. The second stage involves stochastically distributing lithofacies within the identified high level architecture; the third involves populating the assigned lithofacies with porosity and permeability data. Clearly any neural network prediction of lithofacies contributes to the second stage, as the distributions of lithofacies are always constrained by wells. At this stage variograms that define lithofacies' geometry are used to populate lithofacies' dimensions, and this must also occur at the wells (thickness can usually be directly derived from core or log data, but the x-y and x-z dimensions must be stochastically assigned). These dimensions are usually gathered from outcrop analogues. If two lithofacies have very different dimensions then they will contribute differently to the geostatistical model. Therefore if it is thought that the logs are capable of distinguishing each of these then is useful to keep them separate for neural network prediction.

Wardell (1996) used five lithofacies to populate his model - the horizontal ranges used are shown in Table 3.1. The dimensions shown were estimated from outcrop analogues (e.g. Hazeu *et al.* 1988; Kleverlaan & Cossey 1993; Schuppers 1993) and from inter-well correlation. No specific well correlations were available for the Lomond data set. However this table serves to provide a useful indication of the dimensions of various lithofacies. For instance Table 3.1 suggests that the highest permeability channel sandstone is not as laterally extensive as moderate permeability channel sandstone. In-channel shales appear much less extensive than interchannel shales. If it is possible for the logs to distinguish these lithofacies then these could act as direct inputs to a geostatistical model.

| Lithofacies | Lithofacies description | Lithofacies variogram (dimensions in m) | | |
|---|---|---|---|---|
| | | Axis parallel | Axis perpendicular | Vertical |
| 1 | Low-moderate permeability channel sandstone | 550 | 275 | 5.6-20.1 |
| 2 | High permability channel sandstone | 365 | 183 | 0.7-2.3 |
| 3 | In-channel shales and doggers | 750 | 375 | 0.4-2.1 |
| 4 | Interchannel shales and siltstones | 2744 | 2744 | 0.5-1.7 |
| 5 | Interchannel sheet sandstones | 2744 | 2744 | 0.5-1.0 |

**Table 3.1** Horizontal and vertical ranges used for population of lithofacies dimensions (turbidite reservoir North Sea). Redrawn from Wardell (1996). Note the dimensions of lithofacies 1 & 2 represent the maximum dimensions of individual preserved sand bodies that were correlated between wells. In-channel shales were artificially assigned slightly larger ranges then channel sandstones to compensate for their low target proportions, which were observed to reduce their size in the final realisations.

### *3.4.3 Reservoir quality of different facies*

It has been stated that a lithofacies scheme can contribute to a dynamic reservoir model. Consequently it is useful to keep separate those lithofacies that have different petrophysical characteristics. Core measurements were available throughout the cored interval in wells 23/21-T3, 23/21-T4, 23/21-T5, and 23/21-T8, enabling the study of the porosity and permeability ranges of specific facies.

Figure 3.10 illustrates porosity and permeability ranges for varying facies types. Figure 3.10(a) the B-type facies (mid channel and mid-lobe, black line) has almost exactly the same porosity and permeability ranges as C-type facies (taken to indicate lobe and channel abandonment), and would consequently behave similarly in any dynamic model. This information can be used as justification for combining these facies into a single lithofacies.

Figure 3.10(b) compares the best reservoir sand (B-type facies, black line) with its slumped equivalent (e.g. B1F, red line, indicating minor local post depositional slumping of B1 facies). The porosity in the slumped intervals remains very high, but the permeability is reduced by an order of magnitude compared with the B-type facies. This indicates differing

petrophysical behaviour and provides justification for keeping these facies separate in the final lithofacies scheme, if the logs permit.

Figure 3.10(c) compares B-type facies (black line) with A-type facies (red line representing pebbly sandstone and commonly indicating channel bases). Petrophysically these are similar, although it should be noted that there are very few examples of A-type facies (see Section 3.4.4), so the distribution shown may not be fully representative.

Figure 3.10(d) compares the slumped equivalent of the channel and lobe sands (e.g. B1F, C1F, black line) with F-type facies (red line, representing slump sheets and debris flows). A lower average porosity and larger range is seen for the F-type facies, and a very large permeability range compared to the channel and lobe slumped units.

It is now appreciated that in many cases raw core porosity and permeability values can be a poor indicator of reservoir behaviour, and this has prompted researchers to develop new models to predict reservoir behaviour (e.g. Amaefule *et al.* 1993). Viewing of core indicates that for F-type facies the permeability would be expected to change rapidly on a centimetre/millimetre scale (see Figures 3.7 and 3.11). Although it is possible for F facies horizons to have a very high permeability, it is most likely that these intervals would behave poorly as a 'flow unit', as adjacent to a measured core plug the permeability could fall dramatically (Figure 3.11). This is in contrast to B1F-type facies that represents minor slumping and would therefore tend to have a narrower range of porosity and permeability values (as shown) and be adjacent to better quality sands. Therefore from a petrophysical perspective it would be useful to keep F-type facies separate. Conventional logs cannot resolve individual sand/shaly horizons that make up intervals of F-type facies, so if this is to be predicted as a single lithofacies then it would have be resolved by its 'bulk' characteristics.

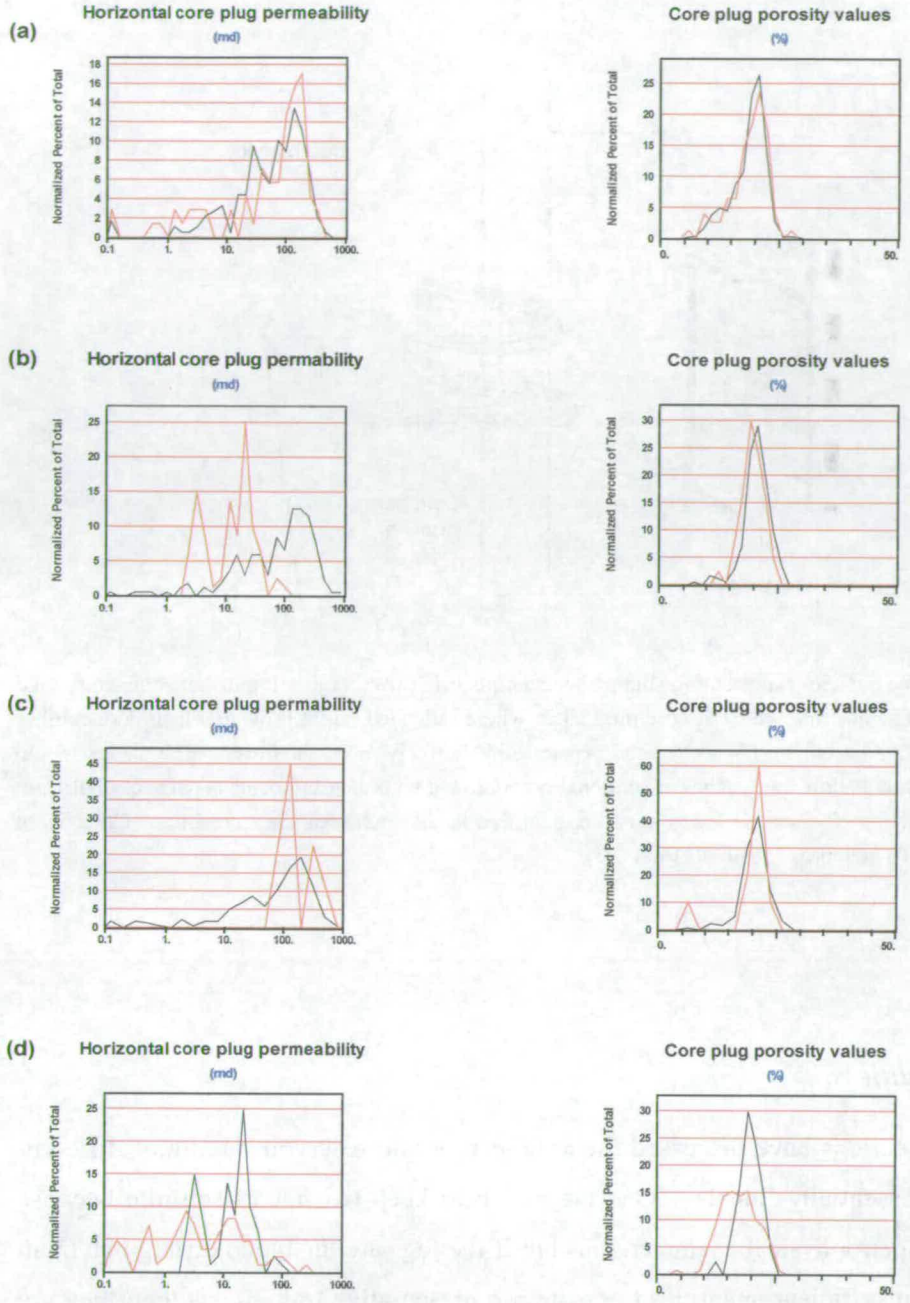



**Figure 3.10** Porosity and permeability distributions for different facies types.

(a) Black – B-type facies, Red – C-type facies, well 23/21-T5. Permeability graph made from 366 B-type measurements, 69 C-type measurements. Porosity graph made from 407 B-type measurements, 78 C-type measurements. See text for graph interpretation.

(b) Black – B-type facies, Red – BF and CF-type facies, well 23/21-T3. Permeability graph made from 167 B-type measurements, 81 BF and CF type measurements. Porosity graph made from 259 B-type measurements, 87 BF and CF-type measurements. See text for graph interpretation.

(c) Black – B-type facies, Red – A-type facies, well 23/21-T3. Permeability graph made from 167 B-type measurements, 9 A-type measurements. Porosity graph made from 176 B-type measurements, 10 A-type measurements. See text for graph interpretation.

(d) Black – BF and CF-type facies, Red – F-type facies, well 23/21-T3. Permeability graph made from 81 BF and CF-type measurements, 86 F-type measurements. Porosity graph made from 87 BF and CF-type measurements, 139 F-type measurements. See text for graph interpretation.

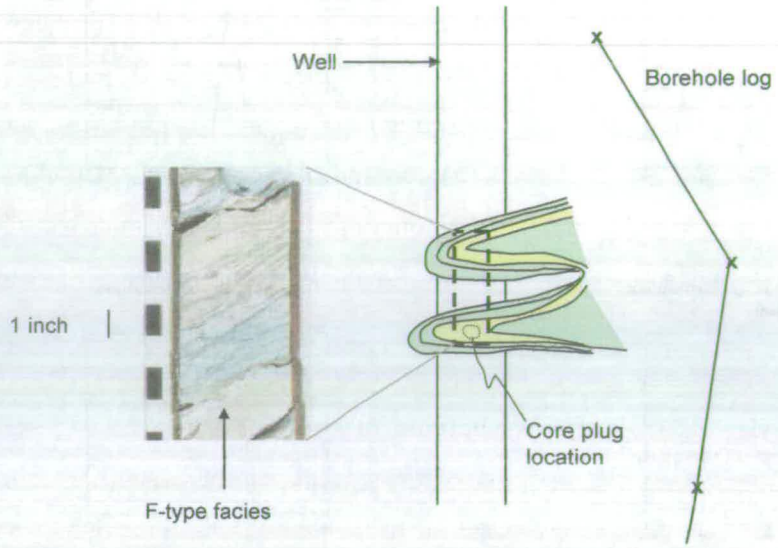



**Figure 3.11** Typical type-F facies representing slump sheets and debris flows: consisting of heterogeneous sand and shale sequences on a cm - mm scale. A core plug taken where indicated might provide a high permeability measurement. However adjacent to this section the permeability is likely to be far lower. This facies would therefore behave poorly as a 'flow unit'. The conventional borehole log with measurements taken every half-foot cannot resolve the heterogeneity, so this facies must be identified by its 'bulk' log characteristics. Core photo taken from well 23/21-T5 at approximately 9336ft (DD).

### *3.4.4 Facies quantities*

The previous two sections have discussed the architecture and reservoir quality of different facies. These are essentially 'ideals'. One may wish to keep two facies separate because they have different petrophysical characteristics but if the logs are unable to distinguish them or if they occur in insufficient quantities to create a representative training set then they are unlikely to be predicted successfully.

Figure 3.12 shows the amount in feet of each facies that occurs in the Forties Sandstone Member of all four cored well intervals. By far the most common facies is B1 (mid lobe and channel sand), its slump equivalent (B1F), and facies F (slump sheets and debris flows). This is not surprising given that the target of the four wells would have been the mid-channel/lobe intervals that would have been previously imaged on seismic. Only a limited amount of core is ever cut and then always in the main reservoir interval.

Figure 3.13 illustrates the abundance of facies in well 23/21-T3. This shows the same pattern (with the majority being B1, B1F and F) as Figure 3.12. Well 23/21-T4 (Figure 3.14) contains large amounts of AF facies (slump equivalent of pebbly sandstone), which the other wells do not. Well 23/21-T5 (Figure 3.15) contains a large amount of C-type and D-type (distal lobe fringe) facies, and also a small amount of G1 (laminated mudrocks). Well 23/21-T8 (Figure 3.16) contains some G2F that is essentially locally slumped bioturbated shale produced from suspension fallout.

Clearly if it is possible to make predictions of the mid channel/lobe sand, its slump equivalent, and debris flows, then most of the expected facies in other wells should be captured (given the limited core information available, and the knowledge that the other wells drilled would have been drilled with the same strategy as the cored wells). However it is likely that other facies types will be encountered in other wells, even if in limited quantities (e.g. G-type facies). Thus in order to create a model capable of predicting these, then, given the data available, training sets must be designed utilising data from more than one well. From Figures 3.12-3.16 it is also seen that facies which occur fairly rarely (such as A-type facies) may not be representative in the data set. Masters (1993) (see also Chapter 2 of this thesis, and Section 3.6.5) states that neural networks are sensitive to the abundance of training data. This implies that neural network models may find it difficult to discriminate lithofacies that make up minor sections of the training data.

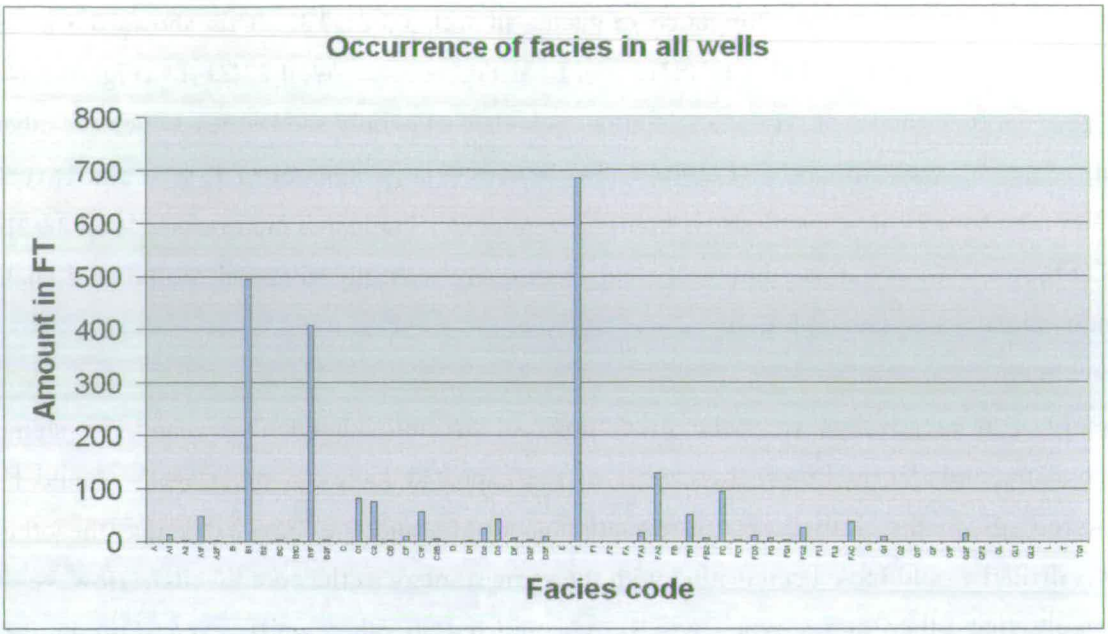



**Figure 3.12** Occurrence of facies in all four cored wells (in feet). The highest columns are, from the left B1, B1F and F.

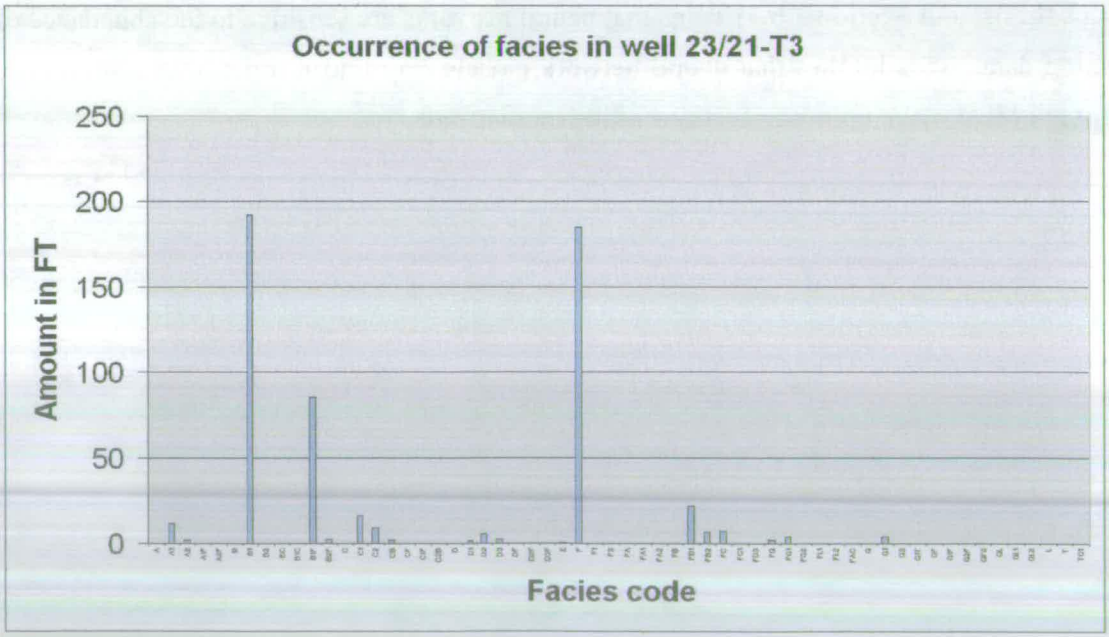



**Figure 3.13** Occurrence of facies in well 23/21-T3 (in feet). The highest columns are, from the left B1, B1F and F.

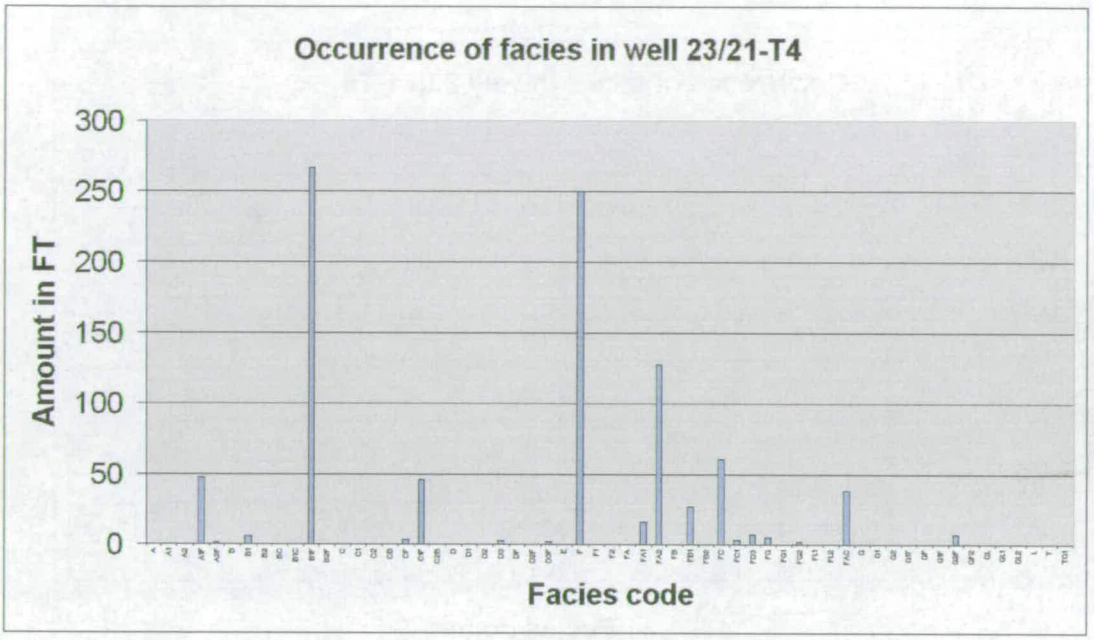



**Figure 3.14** Occurrence of facies in well 23/21-T4 (in feet). The highest columns are, from the left B1F, F, and FA2.

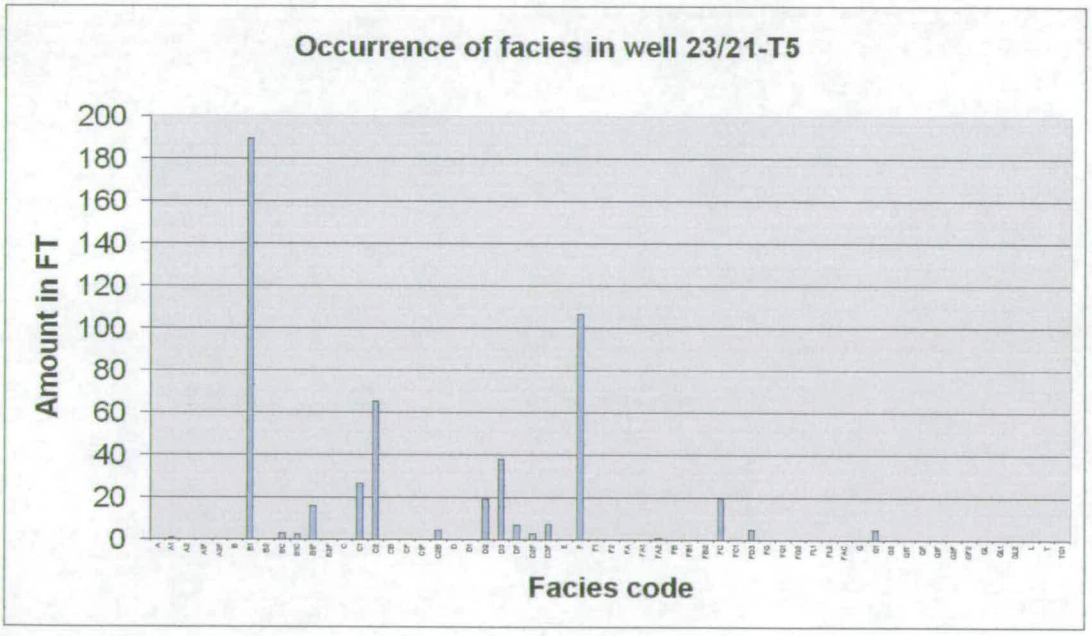



**Figure 3.15** Occurrence of facies in all well 23/21-T5 (in feet). The highest columns are, from the left B1, C2 and F.

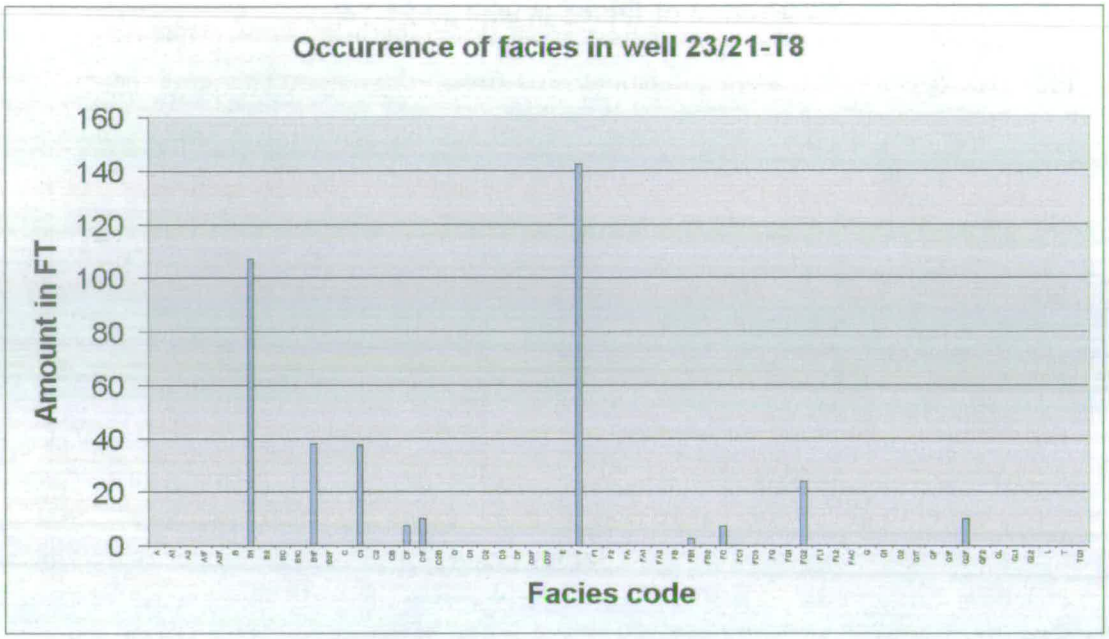



**Figure 3.16** Occurrence of facies in well 23/21-T8 (in feet). The highest columns are, from the left B1, B1F, C1 and F.

### *3.4.5 Log separability*

One of the most important factors to consider when designing a lithofacies scheme is log separability. The logs must be able to distinguish different lithofacies. It can be useful to study cross-plots of different logs to indicate which groups are separable. This is simply a 'quick check' to guide and *partly* justify the lithofacies design. Clearly it is not possible to visualise all the logs cross-plotted together (that is why a neural network is used) and all relationships are not expected to be seen – it is hoped that the neural network may highlight relationships that we were unaware of before.

Figure 3.17 shows two common types of cross-plot used to highlight relationships between facies. Figure 3.17 (a) is a traditional neutron-density cross-plot. It shows that facies B1 (black representing lobe and channel sand with gas) tends to have a low density and neutron porosity. Facies B1F (orange, slumped equivalent of B1) tends to have a higher neutron porosity and density. This could be due to B1F being more poorly sorted than facies B1, having a lower permeability and consequently lower gas saturation (all data are from the gas leg). Facies F (brown, slump sheets and debris flows) covers most of the 'shaly area' on the neutron-density plot. This highlights the heterogeneous nature of this facies. It is mostly 'shaly-sand' and rarely has a very low density or high neutron, and so can generally be distinguished from B1 and B1F. Figure 3.17 (b) is a cross-plot of the gamma-ray and resistivity log. A distinct change can be seen at about 60API where effective porosity starts to influence the log readings. The majority of facies B1F and all of facies B1 fall below this line, and their resistivity readings are heavily influenced by gas. Facies F, having a higher gamma-ray value than B1 and B1F is much more shaly. Figure 3.17 (c) shows that both facies G (pelagic mud) and D3 (suspension fallout) are extremely shaly and cannot be distinguished by the gamma-ray or resistivity log, whereas facies D1 and D2 are much more sand rich. However these tend to have a low resistivity, and as these examples are from the gas zone a low porosity (see Figure 3.8). Although facies F is often shaly and can have a huge variety of log readings, they are rarely as shaly as facies G, which along with facies D3 have the highest gamma-ray values (Figure 3.17 (d)). Figure 3.17 (e) illustrates that facies B1 (best sand) and A (pebbly sandstone often indicating channel base) plot in a similar area on a neutron-density plot and therefore cannot be distinguished by the logs.

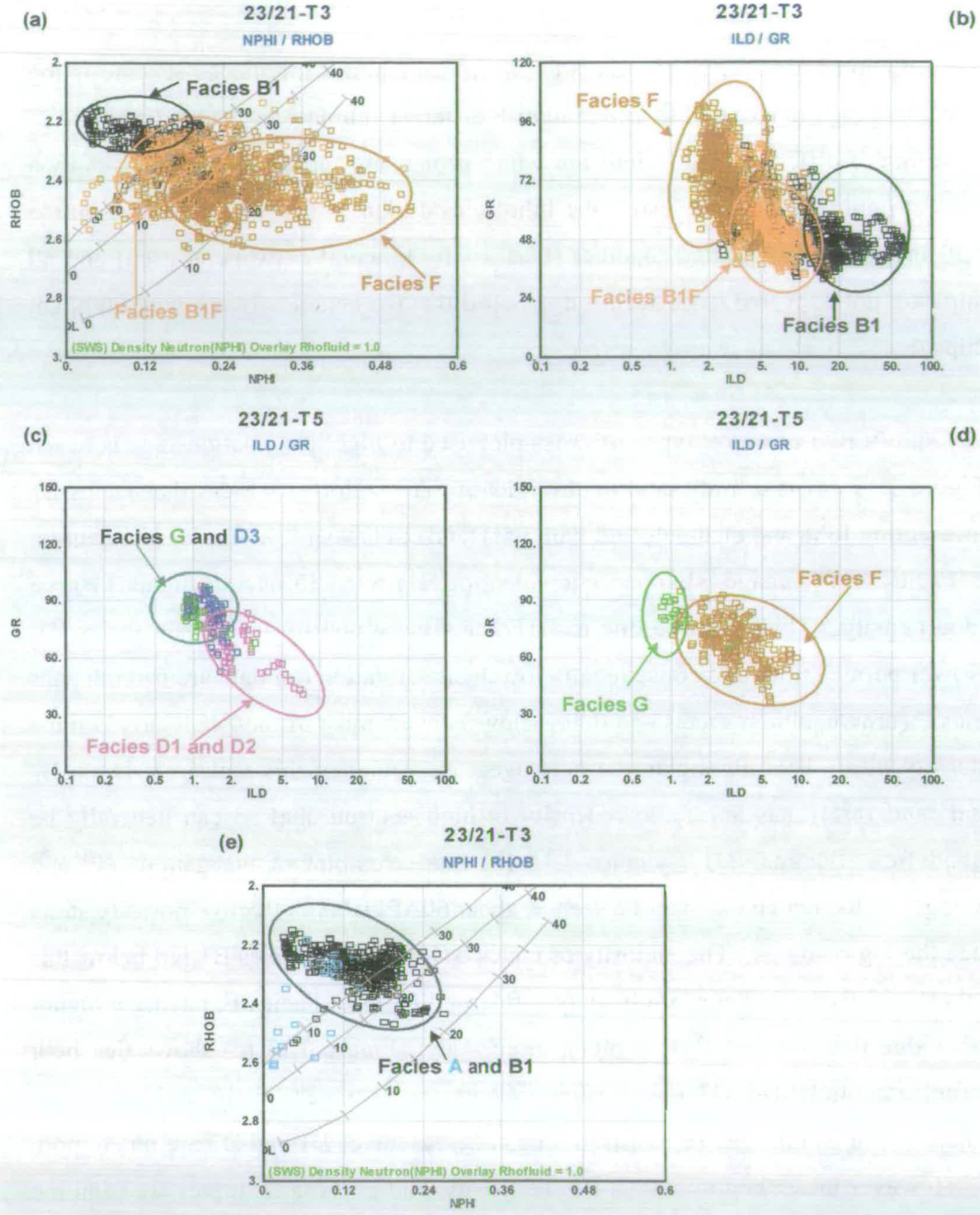



**Figure 3.17** Cross-plots of various logs:

(a) Neutron-density plot, well 23/21-T3. Facies B1 shows low density and high neutron values. Facies B1F has higher density and higher neutron values. Facies F, the most heterogeneous facies, shows a very large data spread. These two logs appear to be able to separate these facies in log space.

(b) Gamma ray-resistivity plot, well 23/21-T3. B1 shows the highest resistivity values, followed by B1F. Facies F is much more shaly (higher gamma-ray) than B1 or B1F.

(c) Gamma ray-resistivity plot, well 23/21-T5. Facies G and D3 both have very high gamma-ray values; these are the most shaly facies and appear to be inseparable by these logs. Facies D1 and D2 (more sandy) show distinctive lower gamma-ray readings.

(d) Gamma ray, resistivity plot, well 23/21-T5. In general facies G has a higher gamma-ray and lower resistivity than facies F.

(e) Neutron-density plot, well 23/21-T3. Neutron and density logs cannot separate facies A and B1.

### *3.4.6 The lithofacies scheme*

Table 3.2 describes the lithofacies scheme on which the neural network models were trained.

If the scheme was designed solely on log separability (i.e. groups of log data that are separate/distinguishable) then this could be called an 'electrofacies' scheme. If the scheme was designed specifically on the basis of porosity and permeability ranges this could be called a 'petrofacies' scheme. If it was based solely on sedimentary facies it would simply be a 'facies' scheme. All of these elements have been incorporated, and therefore the more generic term 'lithofacies' is used. The scheme is loosely based on sedimentary facies that have been shown to have some specific petrophysical characteristics. Clearly the scheme must incorporate elements of 'electrofacies' otherwise the groups would never be distinguishable by the logs. Thus the scheme is useful for making predictions that could be used in reservoir modelling or as a first pass through data acquired from a newly drilled well. At this point it can be said that if, at a particular depth level in a well, 'lithofacies 2' is predicted, then the interpretation might be 'medium-coarse sand, which usually has high porosity and permeability, commonly representing turbidite sand lobes or channels'. If this were overlain by 'lithofacies 6', the interpretation could continue '...that rapidly fines up into shale indicating lobe termination'. Neural networks are good at identifying previously unknown relationships in data; the techniques described above merely indicate 'generally' what the network might achieve. The results of the neural network predictions and their subsequent interpretation can be found in Chapter 4.

This section described the purpose for designing a lithofacies scheme and the criteria that were borne in mind when designing it. The next section describes how the data were prepared before neural network analysis.

| Lithofacies number | Description | Log character | Commonly related sedimentary facies | Petrophysical characteristics |
|---|---|---|---|---|
| 1 | Homogeneous, usually well sorted sandstone, and (much rarer) pebbly sandstone. Best reservoir. | Low GR, low RHOB, high NPHI-RHOB separation. | A1, B1, C. Generally interpreted as representing channel and lobe sand deposited from high density turbidity currents. | Very high permeability (50-800md) Very high porosity(15-25%). |
| 2 | As lithofacies 1 but with minor slumping / deformed bedding. Generally high quality reservoir sand. | As lithofacies 1 but commonly lower NPHI-RHOB separation. | B1F, C1F, CF. As for lithofacies 1 but with minor (and therefore usually post depositional) slumping. | High permeability (3-80md) Very high porosity(15-25%). |
| 3 | Deformed, interbedded sandstones and mudstones / poorly sorted sandstone with mud clasts. | Extremely variable log signatures. But generally higher RHOB than lithofacies 1 and 2. Intermediate GR. | F, FC, FAC, FB1,FC1. Interpreted as being deposited via muddy debris flows, and slumping of other heterolithc sediments. | Highly variable permeability (0.1-80md). Expected to behave poorly as a flow unit. |
| 4 | Sandstone with thin interbedded mudstone. | Very close (but usually shale) NPHI-RHOB separation. Intemediate GR. | D1, D2. Commonly interpreted as being deposited from evolved distal turbidity currents. | Low permeability and porosity. |
| 5 | Shale, laminated or bioturbated. Silt and sand laminae are common. | High GR, high RHOB, high NPHI. | G1, G2, D3. Background pelagic & hemipelagic sedimentation between turbidity events, and dilute turbid suspension fallout. | Very low permeability and porosity. |

**Table 3.2** The Lomond lithofacies scheme

## *3.5 Data preparation*

### *3.5.1 Introduction*

Before neural network analysis can take place a number of important operations must be carried out on the data. Some of the more obvious and most important are:

- Input selection;
- Training / test set design.

Some of the less obvious are:

- Data transforms;
- Inter-well log normalisation;
- Depth shifting.

These are discussed in turn, starting with input selection. Training and test set design is discussed last.

### *3.5.2 Input selection*

All the logs described in Section 3.2.3 were available as possible inputs to the neural network, as well as two derivative logs (total porosity and neutron-density separation – see Appendix 1 for an explanation of how these were calculated):

Gamma-ray;
Sonic;
Neutron;
Density;
Neutron-density separation;
Total porosity;
Resistivity.

Clearly it is possible to use all the logs or just some of them. The derivative logs should inherently carry the same amount of information as the logs that they were derived from.

Each additional input to a neural network adds another dimension to the hypothesis space in which the data resides. Since the role of the neural network is to fit a surface between classes in the data, there must be sufficient data to populate the space densely enough so that the true surface can be 'seen' by the neural network. The amount of data needed to do this increases with increased dimensionality (Baum and Haussler 1989). This implies that the fewer the number of inputs the better, and therefore suggests that derivative logs should be left out. It is possible to use standard tests to determine the best inputs, or to experiment with the network to see which ones improve classification. Goldberg (1989) shows how genetic algorithms can be used to search different combinations of inputs to eliminate interdependence and select the most appropriate for classification. A commonly used technique is Principal Component Analysis (see Chapter 1), used to reduce dimensionality whilst retaining most of the useful information in the data.

However this thesis uses the backpropagation algorithm, which suffers less from the dimensionality problem than many other types of network as it has the ability to concentrate on a lower dimensional section of the high dimensional space (www.trajan-software.demon.co.uk). This is because the backpropagation algorithm can learn to set the output weights from input variables to zero, thus totally ignoring those inputs, if it so wishes. In reality the initially small weights from those inputs will not grow. Thus the backpropagation algorithm effectively 'sorts' the input variables into those that contribute to classification and those that do not. It is therefore expected that the neural network will sort the input logs and only allow useful logs to contribute to classification. Indeed this extremely useful aspect of the algorithm can inform the user which logs are most important for certain classifications, and implies that initially *all* logs should be used. Wong *et al.* (1995a) showed that a neural network trained to predict porosity resulted in faster training times and improved classification when using sonic density and acoustic impedance (calculated from the other logs) rather than sonic and density alone.

For these reasons all seven of the above logs were initially used as input variables into the neural network. Experimentation without the derivative logs was also undertaken (Section 3.6.6).

It is known that many logs are affected by the borehole size – e.g. the density log is affected by washouts. For this reason no data was exported for training or testing if the caliper log

reading was >10", or the DRHO curve was less than –0.15 or greater then 0.15 (values from Gruping, 1998) where the density log becomes uncertain.

### *3.5.3 Data transforms*

Most neural network programs, including EasyNN used in this study, apply a linear normalisation procedure to input variables, scaling between 0 and 1. This brings all data into the same range, essentially equalling the importance of all variables before learning takes place. Masters (1993) states that in order for input data to be useful as a discriminator:

- The variance of each input should be approximately the same (known as homoscedasticity);
- Input data distributions should be approximate ly symmetrical.

The measurement of resistivity results in data that have a skewed distribution. The range of values encountered is typically large, and small but important variations are compressed into a narrow area. In this case non-linear transforms are appropriate to 'linearise' the data. In order to illustrate this, an equal number of resistivity data points from lithofacies 1 and 5 (the most sandy and shaly lithofacies respectively) were taken from the Primary Training and Validation set (an explanation of which well sections make up these sets can be found in Section 3.5.6). They were normalised in the usual way (between 0 and 1). The resulting distribution is seen as Figure 3.18(a). A natural log transform of the same data was taken, and the data then scaled to between 0 and 1, as before. The resulting distribution is shown as Figure 3.18(b).

In Figure 3.18(a) the distribution is compressed towards the lower end. In Figure 3.18(b) the distribution is much more spread out, filling the hypothesis space. Indeed, it is now possible to see the distinct peaks representing lithofacies 1 (sand with gas), and 5 (shale). These two lithofacies could not have been determined very easily using non-transformed data. Thus the transformed resistivity data will be used as an input variable, instead of the raw data.

The distributions of the other input variables were then plotted using same example data as for the resistivity plots. The results are shown in Figure 3.19. The spread of these data are similar, indicating that no further transformations are necessary.

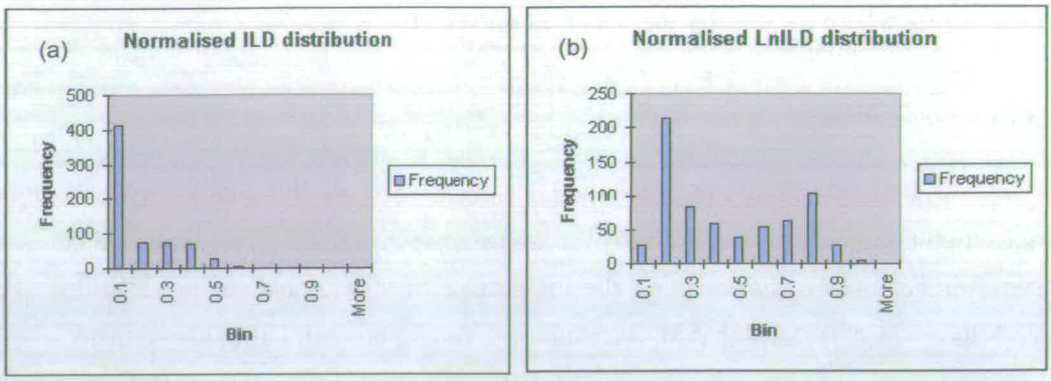



**Figure 3.18**

(a) Frequency distribution of sand and shale raw resistivity data linearly scaled between 0 and 1.

(b) Same data as in (a) with a natural log transform of the raw data before linear scaling. Two peaks can now be seen representing sand and shale.

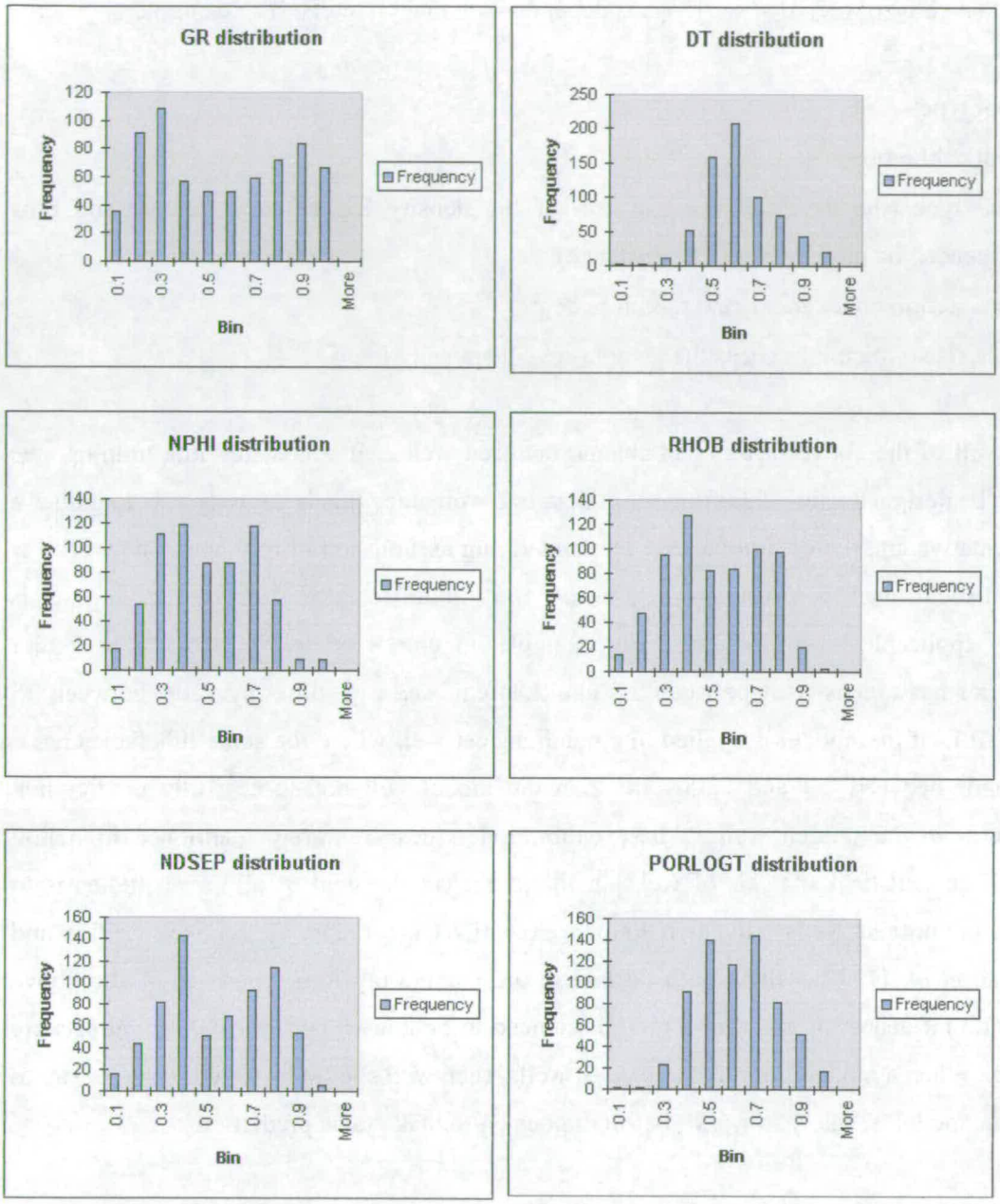



**Figure 3.19** Frequency distributions for sand and shale data for six input logs, gamma ray, sonic, neutron density, neutron density separation, and total porosity. All data is scaled between 0 and 1.

### 3.5.4 Inter-well normalisation of logs

The actual value of recorded well logs is dependent on many factors. For example:

- Tool type;
- Tool calibration;
- Mud type (the depth of investigation of the density log is very shallow and thus influenced by mud invasion, for instance);
- Compaction of sediment, and therefore depth;
- Hole size (which influences the gamma-ray and density logs).

Clearly all of the above factors can change between wells. It was stated that training sets need to be designed using data from more than one well since this is the only way to gather a representative amount of lithofacies. The underlying assumption of any neural network (or any statistical or cross-plot technique) is that the 'model' created from the training set is directly applicable to unseen data. For example imagine a model finds that a particular lithofacies has a density of between 2.2 and 2.3g/cm$^3$ and a gamma-ray value between 35 and 55API. If that model is applied to a much deeper well where the same lithofacies has a density of between 2.3 and 2.35g/cm$^3$ then the model will not successfully predict that lithofacies in the unseen well. These calibration issues are rarely mentioned in neural network or statistical analysis of well-log literature, yet the goal of all these studies is to predict in 'unseen wells' (the two known exceptions are Gupta & Johnson (2001) and Vaughan *et al.* (1999), which both normalise the gamma-ray log). If some of the above factors do influence log signatures then these need to be known before any training sets are created. When a model is applied to unseen wells, each well should be tested in some way to see if the model is 'likely to work', before it goes on to make false predictions.

A way to approach this problem is to study a standard interval that can be recognised by a specific well log signature. This should be shale. Shales are more generally laterally extensive, more easily correlated and are less influenced by porosity or fluid. The assumption is that the same shale interval should show similar log values in all wells. If the log values are very different then this indicates that there is inter-well variability, possibly due to some of the above factors, and suggests that some sort of calibration may be required.

Since the interval can be recognised by well-log signatures alone, this test could be quickly applied to unseen wells, without core to test if any model is 'likely to work'.

The shaly section of the Sele Formation above the Forties Sandstone Member (S2 and S3 in Figure 3.3), is easily characterised by, and therefore identified from its high gamma-ray log signature. Figure 3.20 shows this interval in wells 23/21-T3, T4, T5 and T8.

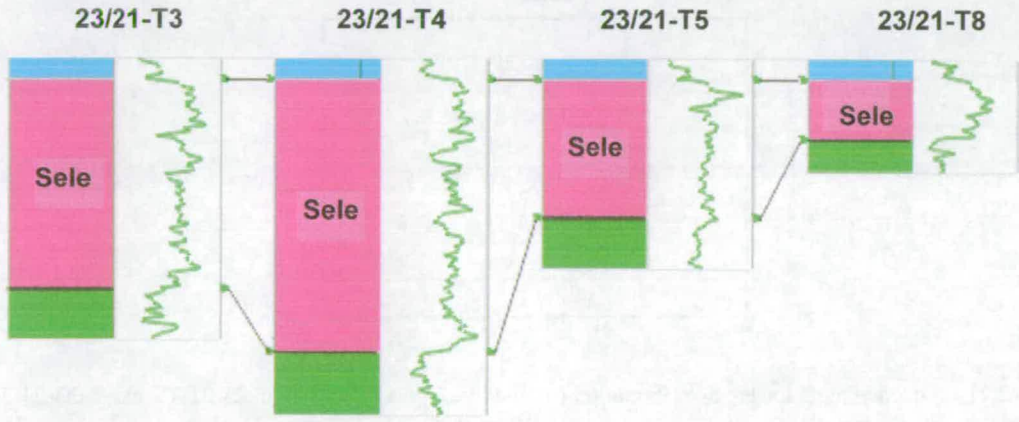



**Figure 3.20** The Sele formation (section above the Forties Sandstone Member – green, but below the Balder Formation – blue, see Figure 3.3), identified by its gamma-ray log signature.

Frequency curves for each of the logs were plotted for this interval in each well (Figures 3.21 and 3.22). The gamma-ray distributions show very slight inter-well variation. The sonic and resistivity show significant deviations from the other wells in well 23/21-T4 (red), with the sonic transit time much lower (higher velocity) and the average resistivity higher.

The neutron and density logs were not recorded through this interval in well 23/21-T4. Figure 3.22 therefore shows neutron and density frequency plots for this interval for wells 23/21-T3, T5 and T8 only. These logs appear to record similar values in all wells.

It is possible to normalise for minor inter-well variability. However any model created should attempt to be as flexible as possible, and encounter a wide a range of values for a given lithofacies as is possible, within reason. Also the more steps involved in pre-processing the data, the more removed the data becomes from that recorded and the more

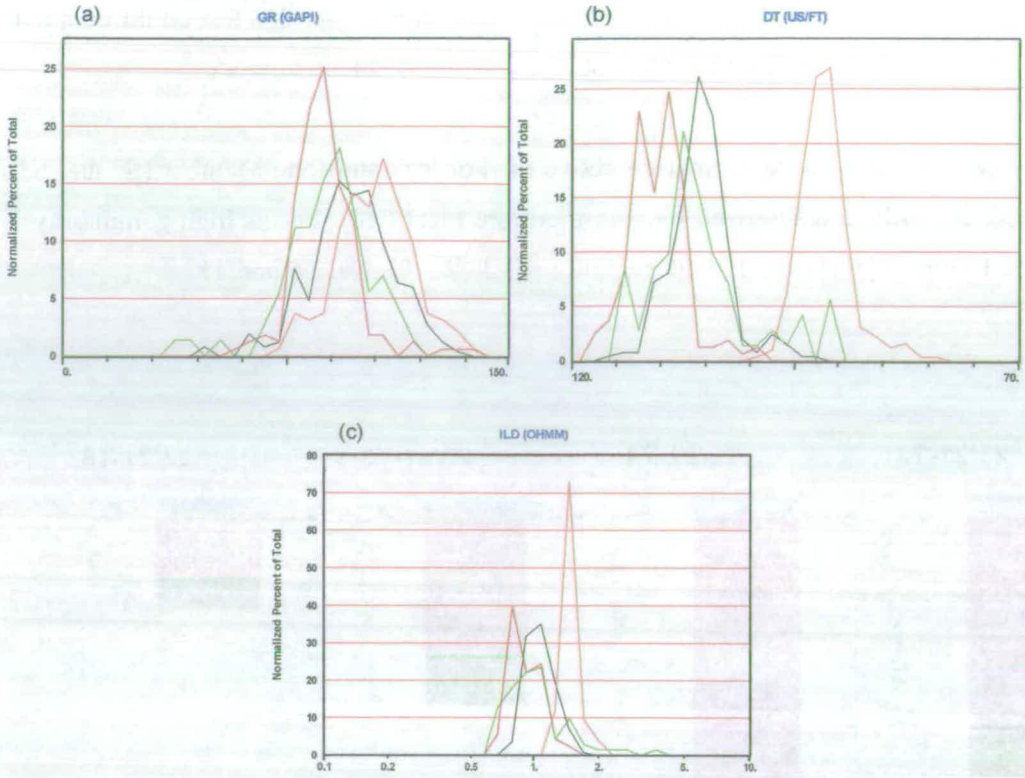



**Figure 3.21** Frequency plots for the Sele formation (defined in Figure 3.20). Well 23-21-T3 black, 23-21-T4 red, 23/21-T5 brown, 23/21-T8 green

(a) GR

(b) DT

(c) ILD

The average sonic transit time is lower and the average resistivity higher for well 23/21-T4 than for all other wells. All curves are normalised so the area beneath them is equal, for comparison.

difficult it can be to interpret the network's output. So for the minor differences between wells 23/21-T3, T5 and T8 no normalisation was carried out. This analysis has simply highlighted that well 23/21-T4 is fundamentally different in its log readings. It is now appropriate to ask the question 'Why?'

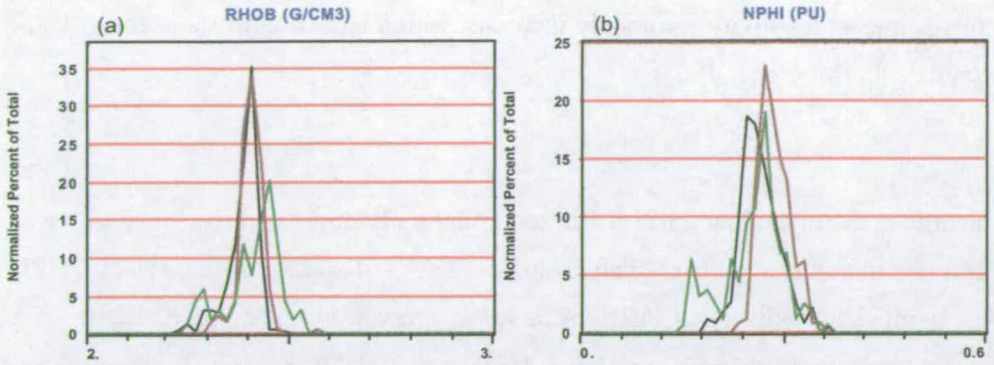



**Figure 3.22** Frequency plots for the Sele formation (defined in Figure 3.20). Well 23-21-T3 black, 23/21-T5 brown, 23/21-T8 green:
(a) RHOB
(b) NPHI
All curves are normalised so the area beneath them is equal, for comparison.

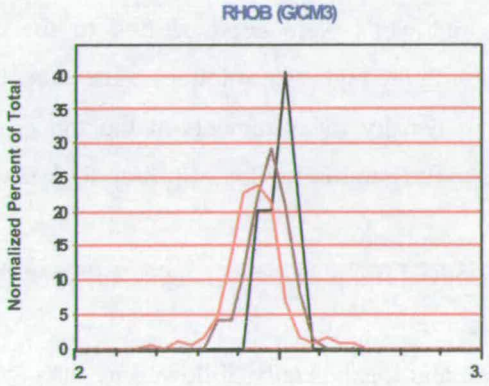



**Figure 3.23** Frequency plot of the bulk density log for the Forties Sandstone Member of the Sele Formation. Black curve is well 23/21-T3 and lithofacies 5 only (most shaly facies). Brown curve is well 23/21-T5 and lithofacies 5 only. Red curve is well 23/21-T4 and lithofacies 1 and 2 only (the most sandy facies). The sandy facies in well 23/21-T4 is as dense as the most shaly facies in the other wells. A model incorporating data from 23/21-T4 may potentially not be able to distinguish sand from shale. All curves are normalised so the area beneath them is equal, for comparison.

Logs in well 23/21-T4 were logged whilst drilling (LWD), the others were not. This could be one reason. However another, more likely reason is depth. Well 23/21-T4 is on average 600-700ft deeper than the other wells and so the sediments are expected to be more compact resulting in a lower measured sonic transit time (higher velocity). The resistivity log also

suggests this is true as resistivity commonly increases with a reduction in shale porosity and therefore with depth (Mcgregor 1965).

It could be argued that including 23/21-T4 in the training set might create a more universal model However in this study it is unlikely as log properties of specific facies in well 23/21-T4 overlap significantly with other different facies in other wells (see Figure 3.23). It is possible to calibrate for depth differences (e.g. Vaughan *et al.* 1999). Initially this was not carried out and therefore well 23/21-T4 was not included in any training sets. The final model was applied to this well though, and the results interpreted (Chapter 4), in the context of the above information.

### *3.5.5 Depth Shifting*

All cored intervals in all cored wells were depth shifted to the density log (the Shell convention, this being the log with the highest resolution). The exception was well 23/21-T4 where, because of the lack of density measurements at the top of the Forties Sandstone Member, the core was shifted to the gamma-ray log. Shifting took place in two stages:

- Approximate bulk depth shifting using a single shift per core. The shifts were provided by the contractor;
- Correlation of the core and logs visually, followed by interactive depth shifting, bed by bed.

Although this step has been described in the data preparation section, this clearly took place before some of the earlier steps (e.g. log separability) that relied on accurate core-log shifts.

### *3.5.6 Training and validation set design*

A standard way to test 'learning from data' methods is to use small subsets of data, train on each one and test on all the others. The well data being studied does not lend itself to creating many subsets. Simply, there is not enough, especially of some of the less frequently occurring lithofacies. Therefore only three training sets were created from a combination of wells 23/21-T3, T5 and T8. Table 3.3 shows the amount of each facies from these three wells.

| Lithofacies | 1 | 2 | 3 | 4 | 5 | core gap | Total |
|---|---|---|---|---|---|---|---|
| Well T3 | 234 | 88 | 220.5 | 7 | 12.5 | 21 | 583 |
| Well T5 | 293.5 | 16 | 126 | 29 | 55.5 | 14 | 534 |
| Well T8 | 144.5 | 55.5 | 152 | 0 | 34 | 11 | 397 |
| % of whole data set | 45.8 | 10.9 | 34.0 | 2.5 | 6.9 | | 100 |

**Table 3.3** The amount of lithofacies available in the data set. Lithofacies 1 and 3 (shaded) make up the vast majority of the dataset; lithofacies 4 and 5 are minority lithofacies. All values are in feet.

The core is dominated by certain lithofacies types (especially 1 and 3) and therefore training sets have to be created from more than one well. Table 3.4 shows well sections contained in the Primary Training Set. This set is mainly based on well 23/21-T3, but some of the minority lithofacies (4 and 5) have been 'borrowed' from wells 23/21-T5 and T8. However even after this, lithofacies 4 and 5 are still very much in the minority. The quantities were therefore boosted so that the amounts of each lithofacies were approximately equal: lithofacies 4 was boosted seven-fold, and lithofacies 5 three-fold. The consequence of training with boosted data versus the original data is investigated in Section 3.6.5.

| Lithofacies | | 1 | 2 | 3 | 4 | 5 | Total ft |
|---|---|---|---|---|---|---|---|
| | Depth interval (in ft, MD) | | | | | | |
| Well T3 | 9796 - 9974 | 119.5 | 0 | 36.5 | 7 | 6.5 | 169.5 |
| | 10174 - 10351 | 0 | 65.5 | 87 | 0 | 2 | 154.5 |
| | 10371 - 10374.5 | 0 | 0 | 0 | 0 | 3.5 | 3.5 |
| Well T5 | 9011.5 - 9042 | 14 | 4.5 | 2 | 1.5 | 7 | 29 |
| | 9428.5 - 9534 | 19.5 | 0 | 43.5 | 13.5 | 25.5 | 102 |
| Well T8 | 9488 - 9513 | 7.5 | 8 | 2.5 | 0 | 6.5 | 24.5 |
| % of whole training set | | 33.2 | 16.1 | 35.5 | 4.6 | 10.6 | 100 |
| Boosting factor | | x1 | x2 | x1 | x7 | x3 | |

**Table 3.4** Content of the Primary Training Set. All values are in feet.

From the remaining data a validation set (to be used to monitor training) was created consisting of approximately 12.5ft of each lithofacies. Hence no boosting of the validation set was required.

The second training set consisted of 52.5ft of each lithofacies, all from well 23/21-T5 (see Table 3.5). For validation when training with this set, approximately 75ft of data was randomly selected from the Primary Training Set, excluding that used in Training Set 2. The validation set contained an equal number of lithofacies.

| Lithofacies | 1 | 2 | 3 | 4 | 5 | Total Ft |
|---|---|---|---|---|---|---|
| | 52.5 | 11.5 | 52.5 | 14 | 23 | 153.5 |
| Boosting factor | x1 | x4.5 | x1 | x3.7 | x2.3 | |

**Table 3.5** Content of Training set 2. Lithofacies that initially had less than 52.5 ft of data were boosted to make up to that amount. All values are in feet.

Training Set 3 also consisted of 52.5ft of each lithofacies, mostly from well 23/21-T8. However because lithofacies 4 does not occur in this well data were borrowed from well 23/21-T5 (Table 3.6). For validation whilst training, approximately 57.5ft of data were randomly selected from the second training set, excluding the lithofacies 4 'borrowed' for the training set. The validation set contained an equal number of lithofacies.

A summary table of the main sections that make up the training and validation sets is shown in Table 3.7.

| Lithofacies | 1 | 2 | 3 | 4 | 5 | Total Ft |
|---|---|---|---|---|---|---|
| | 52.5 | 50 | 52.5 | 14 | 27.5 | 196.5 |
| Boosting factor | x1 | x1.1 | x1 | x3.7 | x1.9 | |

**Table 3.6** Content of Training set 3. The lithofacies 4 data was taken from well 23/21-T5, the rest from 23/21-T8. Lithofacies that initially had less then 52.5 ft of data were boosted to make up to that amount. All values are in feet.

| | Approximate size (ft) | Boosting | Composed of | Validation set |
|---|---|---|---|---|
| Primary training set | 795 | Initially, followed by experimentation without boosting in section 3.6.5. | Mostly well T3 with some additions of lithofacies from T5 and T8. | Randomly selected from wells T5 and T8, but those intervals not used for training. |
| Training set 2 | 262.5 | ✓ | All from well T5. | Selected from the Primary Training Set. |
| Training set 3 | 262.5 | ✓ | Mostly from well T8 with some lithofacies 4 from well T3. | Selected from Training Set 2. |

**Table 3.7** Summary of the contents of all three training and validation sets.

## 3.6 Neural network methodology

### 3.6.1 Introduction

Most users of neural networks allow themselves a degree of experimentation with the network during training so that they are sure that they definitely have the optimum network. Networks can be tweaked indefinitely; different parameters can be tried, different training sets, input logs, training times etc. Indeed these aspects could themselves produce enough results to fill an entire PhD thesis. What is presented here is a short description of some of the main experiments that were carried out in order to determine the optimum network for this study. Indeed this illustrates some of the main influences on the results and therefore some of the conclusions from this section will be returned to in Chapters 7 and 8. The optimum network was applied to all Lomond wells. These results are presented and discussed in detail in Chapter 4.

The main influences on the network discussed in this section are:

- Network topology (i.e. number of nodes and layers);
- Momentum and learning parameters;
- Pruning algorithms;
- Training with unbalanced data;
- The use and influence of derivative logs;
- Different training sets.

### 3.6.2 Network topology

In order to determine the best topology for the problem a number of networks of different sizes were trained. In general one network layer should be sufficient (Cybenko (1989), see Chapter 2 of this thesis). However experimentation took place with one and two layer networks (28 different topologies in total). In order to prevent networks getting stuck in local minima each network was trained three times (therefore 84 were run in total), and also trained with momentum (in fact the momentum was set at 0.8, and the learning rate at 0.6 – the program defaults). All networks were trained on the Primary Training Set, and validated accordingly, as described in the previous section. Networks were run for a maximum of 15000 cycles through the data, and automatically saved if the percentage correct over the validation set increased. Out of the three networks trained for each specific topology the one

with the highest percentage correct over the validation set (the validation set 'hit-rate') was taken for comparison with other topologies. Figure 3.24 shows a graph of the percentage correct (for the highest of the three networks) versus topology.

It can be seen (on the left side of the graph) that for 1-layer networks there is an increase in the hit-rate with an increase in the number of nodes. Clearly 1, 2, and 3 nodes in 1-layer is very restrictive: the hit-rate struggles to get above 50%. A peak is seen at 11 nodes where the percentage correct is 69%. Further addition of hidden nodes appears not to increase the ability of the network to classify the data.

When training with two hidden layers the smaller networks (3,2, 3,8 & 3,13) appear fairly restrictive, suggesting that it is the nodes in layer 1 that are the limiting factor. As the number of nodes in the first layer increases the hit-rate increases, but plateaus at a threshold that is close to that originally defined by the 1-layer 11 node network. Figure 3.25 shows the general relationships that have been found.

In general the smallest network should be selected that gives the best results; thus the single layer 11-node network was selected for further testing (Section 3.6.7).

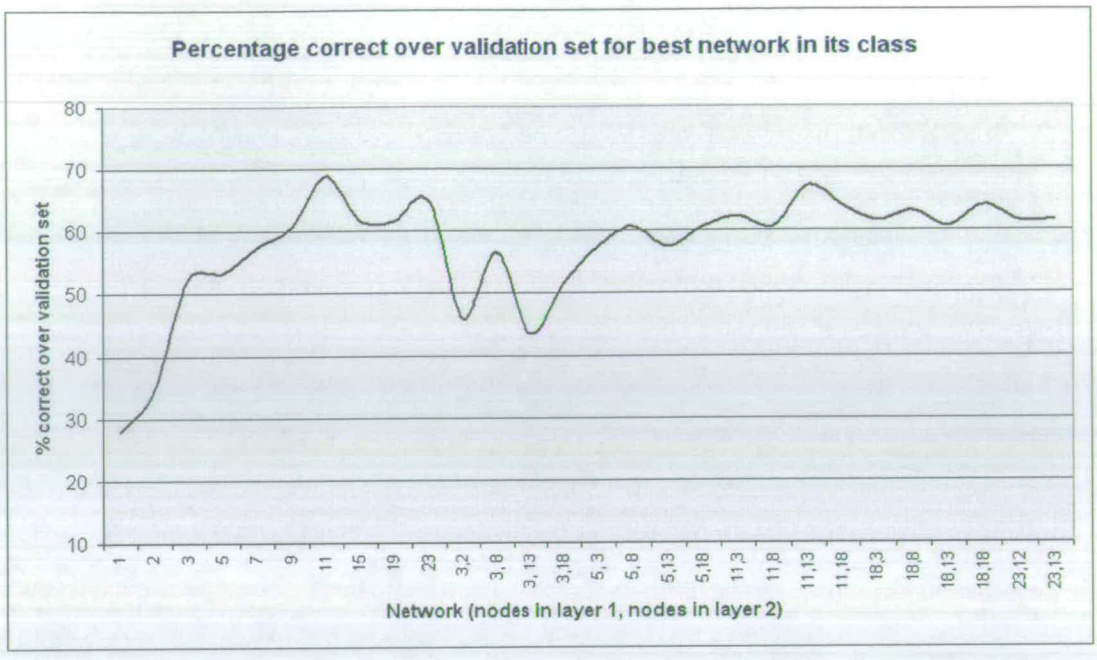



**Figure 3.24** Percentage correct over validation set versus topology for the best out of three trained networks. A gradual percentage increase is seen as the number of nodes is increased in the first hidden layer, until there are 11 hidden nodes. There is no percentage increase after then. On the introduction of a second layer, the percentage correct decreases – the small number of nodes initially in the first layer appear to restrict the network. With two hidden layers, as the number of nodes in the first hidden layer increases the hit-rate increases, to a threshold that appears to be that defined originally by the 1 layer 11 node network.

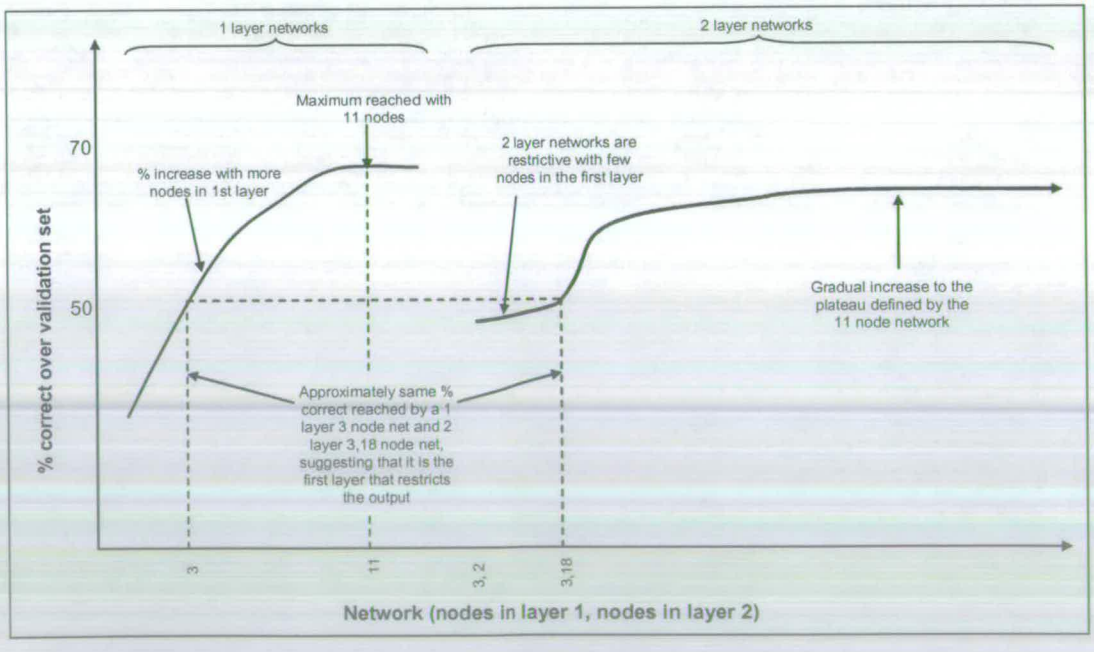



**Figure 3.25** General relationships between network topology and hit-rate over the validation set.

### *3.6.3 Learning and momentum parameters*

The learning rate is the step size taken by the network as it moves down the error surface. In general larger steps are expected to take less time to arrive at the global minimum. However if the rate is especially large the weight vector may roam erratically around the error surface (Gurney 1997). Small learning rates will take longer to reach the global minimum but will have more chance of ending up in the exact global minimum. Momentum is the term that helps jump over small 'bumps' in the error surface, thus preventing the network converging in a local minimum of the error surface. The larger the term the more chance it has of succeeding. In general the momentum parameter is usually larger than the learning rate. More details are in Chapter 2.

So far it has been found that a 1-layer 11-node network appears to be the optimum configuration for the problem. A number of these networks were trained with varying momentum and learning rates. Table 3.8 shows the different sizes of the parameters chosen. In total 12 different combinations were attempted in addition to the program defaults that were used in the previous topological experiments (0.6 and 0.8 respectively). In order to elude local minima, each of these combinations were trained three times, as in the previous topological experiments. All combinations were trained on the Primary Training Set and validated accordingly. For each combination the highest percentage reached of the three trained networks was taken and compared with the other combinations (also Table 3.8).

| | | Learning rate | | | |
|---|---|---|---|---|---|
| | | 0.3 | 0.5 | 0.6 | 0.9 |
| Momentum | 0 | 54.92 | 59.84 | | 57.38 |
| | 0.3 | 54.92 | 54.1 | | 60.66 |
| | 0.6 | 55.74 | 59.02 | | 59.02 |
| | 0.8 | | | 68.85 | |
| | 0.9 | 60.66 | 59.02 | | 55.74 |

**Table 3.8** Maximum percentage reached over validation set for different combinations of learning rates and momentum parameters for networks with 1 layer and 11 hidden nodes. The 0.6, 0.8 combination was that from the previous section.

The above results show very few trends. All combinations produce results of between 50 and 70%. For the networks trained in this study the size of these parameters does not appear to conclusively or consistently affect the results.

### *3.6.4 Pruning algorithms*

The networks discussed so far have assumed a fixed structure. A defined number of inputs are connected to a defined number of hidden nodes, which are in turn connected to a defined number of outputs. One problem was to find the best topology for the given problem. A high number of networks were trained in order to find the optimum one. An alternative strategy aimed at eliminating this step and improving training efficiency is to dynamically modify the network as it is learning. There are essentially two approaches:

- Begin with a small network and dynamically make it bigger during training e.g. the Cascade-Correlation algorithm (Fahlman & Lebiere 1990). This begins with the inputs connected directly to the outputs; training then takes place. If after a while there is a residual error that is above a specified threshold, then a single hidden node is added. Training restarts and the process is repeated until the network error is below the acceptable level. One obvious difficulty to overcome is the determination of the acceptable error level;
- Begin with a large network and dynamically make it smaller ('prune' it) during training. This may be done by identifying those weights that, after a certain amount of training are close to zero. These weights will contribute very little to the networks final output, and can therefore be pruned (or in reality fixed at this small value). An alternative, more complex way, is to identify small weights close to zero that do not appear to change and see the effect of the network error by varying these weights (e.g. LeCun (1990), who refers to this as the 'optimal brain damage approach'). The weights that have little effect on the error are then pruned.

The second method above was investigated as an alternative to training many networks. A number of networks were created, all slightly larger than the size known capable of classifying the data (i.e. larger than a 1-layer 11-node network). A weight threshold and a number of cycles were specified. Once training commenced if any network weights stayed below the specified threshold for the specified number of cycles then these were fixed and no

longer updated during subsequent training. The other weights go on to grow, thus influencing the network output more. In this way the network should be reduced to the minimum size needed for optimum classification, and is less likely to overtrain, as many weights are fixed early on in training.

Initial weights in EasyNN are set to between -0.5 and +0.5. Experimentation was carried out starting with a single layer 23-node network and a single layer 14-node network with differing pruning thresholds. Pruning does not help elude local minima, so for each network that had different parameters three of them were trained and the best performing over the validation set was compared with other pruned networks. All networks were trained on the Primary Training Set and validated accordingly. Table 3.9 shows the different thresholds used for a 23-node starting network, and the validation percentage reached, from the best of three.

| | | No of cycles for which weights must stay below threshold | | | | | | |
|---|---|---|---|---|---|---|---|---|
| | | 100 | 250 | 500 | 1000 | 5000 | 10000 | 50000 |
| Weight threshold | 0.01 | 45.08 | 53.28 | 58.2 | 60.6 | 59.02 | 55.74 | 60.66 |
| | 0.03 | 40.98 | 41.8 | 54.1 | 54.92 | 57.38 | 59.02 | 60.66 |
| | 0.08 | 45.08 | 37.7 | 52.46 | 47.54 | 57.38 | 61.48 | 61.48 |
| | 0.14 | 36.07 | 31.97 | 44.26 | 40.98 | 53.28 | 58.2 | 60.66 |
| | 0.2 | 32.79 | 50.82 | 39.34 | 49.18 | 56.56 | 59.84 | 55.74 |

**Table 3.9** Percentage reached over the validation set for starting networks with 23 nodes, for different weight and cycle thresholds. The yellow area approximately represents the area where too much pruning has taken place, the green area where too little has taken place. See text for more details.

The first thing to notice is that for a low number of cycles (e.g. 100), as the weight threshold increases the percentage correct decreases dramatically. This is because many of the weight connections will stay below say 0.2 for the short amount of cycles and are therefore pruned early on. The network is so heavily pruned that it cannot train at all (Figure 3.26 (a)). For networks that have a low weight threshold but a large number of cycles, very few weights stay that low for that length of time, and therefore very little pruning takes place (Figure 3.26(b)). In this case the pruning has no effect at all.

The results show that training with a threshold of 0.08 and a 10,000-cycle limit appears to give optimum results. However for a single layer 23-node network with 7 inputs and 5 outputs there are 276 weight connections (7x23 + 5x23). The 10,000 cycle, 0.08 threshold network pruned 57 connection weights in total. The optimum network (found in Section 3.6.2 with 11 hidden nodes) had 132 weight connections. So although the 10,000 cycle 0.08 threshold network appeared the optimally pruned one, the pruning algorithm has not managed to get close to the optimum network found via experimentation.

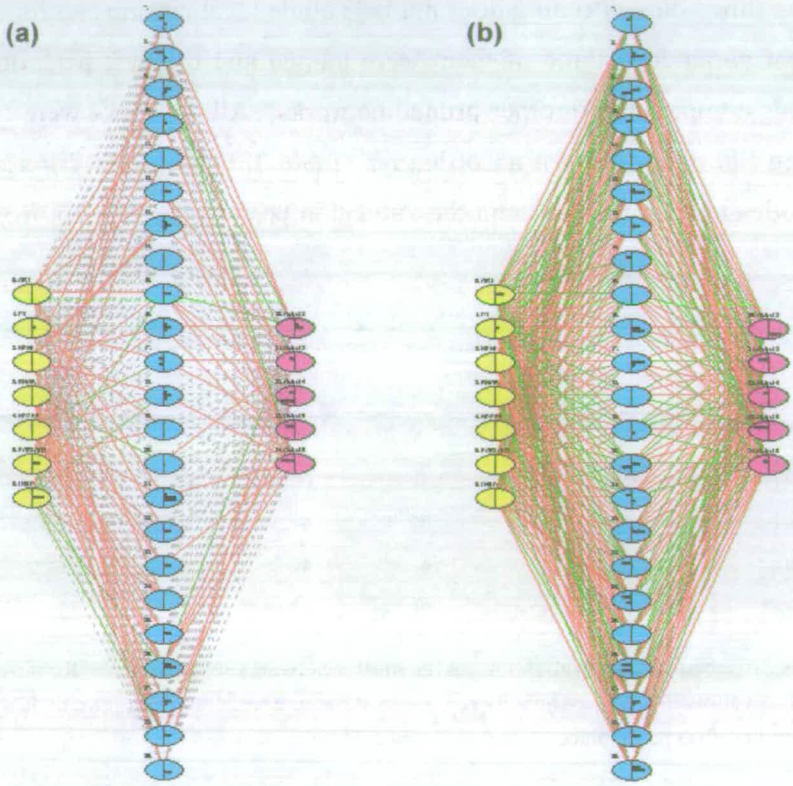



**Figure 3.26** Neural networks that have undergone pruning. Red and green lines represent non-pruned connections. Dashed lines represent pruned connections.

(a) Threshold of 0.2 for 100 cycles. Lots of pruning has taken place, so much that the network cannot learn and the resulting validation percentage is very low (32.79%).

(b) Threshold of 0.2 for 50,000 cycles. No pruning has taken place as no weights have stayed that low for that amount of time.

Table 3.10 shows the same results as above except that all networks were started with 1 layer and 14 nodes. In general these show similar results to those for the 23-node starting networks. For a small number of cycles and a large threshold (e.g. 100 or 250 cycles and 0.14 or 0.2) the percentage correct is low, for the same reason suggested above. However in this matrix a high percentage can be seen with the 250, 0.03 thresholds (66.39%). Also the

percentage correct values generally appear to be higher throughout the table. This is presumably because a 14-node starting network is very close to the optimum 11-node starting network. Even if very little pruning takes place it is still quite close to the optimum network. The optimum pruning parameters for a 14-node starting network appear to be about 10,000 cycles and a threshold of 0.03 (a compromise between too much and too little pruning). For larger networks a bigger threshold should be sought to make sure that more pruning actually takes place (e.g. 0.08 for the 23-node starting network).

| | | No of cycles for which weights must stay below threshold | | | | | | |
|---|---|---|---|---|---|---|---|---|
| | | 100 | 250 | 500 | 1000 | 5000 | 10000 | 50000 |
| Weight threshold | 0.01 | 52.46 | 52.46 | 58.2 | 60.66 | 63.93 | 61.48 | 61.49 |
| | 0.03 | 59.84 | 66.39 | 58.2 | 62.3 | 59.84 | 63.11 | 63.93 |
| | 0.08 | 43.44 | 51.46 | 53.28 | 54.1 | 56.56 | 59.02 | 59.02 |
| | 0.14 | 39.34 | 45.9 | 45.08 | 48.36 | 54.92 | 51.64 | 63.11 |
| | 0.2 | 42.62 | 44.26 | 46.72 | 48.36 | 58.2 | 56.56 | 58.2 |

**Table 3.10** Percentage reached over the validation set for starting networks with 14 nodes, for different weight and cycle thresholds. The yellow area approximately represents the area where too much pruning has taken place, the green area where too little has taken place.

This is by no means an exhaustive study of pruning algorithms. What the results appear to show is that for a standard implementation of the backpropagation algorithm pruning in the way described cannot substitute for exhaustive experimentation with different topologies to find the optimum size. Where top-down pruning algorithms are implemented they benefit from a starting topology that is not always too far from the optimum one. The optimum one is obviously unknown beforehand.

### 3.6.5 Training with unbalanced data

So far all implemented networks were trained on the Primary data set. The data in this set were artificially boosted (especially lithofacies 2, 4 and 5) so that each lithofacies made up approximately the same amount in the training set (see Section 3.5.6). There was good reason for doing this. Multi-layer feed-forward networks cannot adjust for unbalanced training sets; when a network learns by minimising the mean error across the entire training set the proportional representation in the training set can have a profound influence on the network's performance (Masters 1993). If a particular class makes up a high proportion of the training set, then the network will strive to optimise its performance at classifying that class. Classes that are very poorly represented may subsequently not be classified correctly when the network is implemented.

Although data boosting is generally accepted as good practice, it is possible that a user may wish to take advantage of the property of unbalanced data. For instance if it is known beforehand that lithofacies A is twice as likely to occur as lithofacies B, this could be used as justification for using a training set with twice as many A examples than B.

In order to investigate this phenomenon a number of networks were implemented with the training set made up of the raw unbalanced data (Table 3.11). Clearly lithofacies 2, 4, and 5 are in the minority.

| | Lithofacies | | | | |
|---|---|---|---|---|---|
| | 1 | 2 | 3 | 4 | 5 |
| % in training set | 33.2 | 16.2 | 35.5 | 4.5 | 10.6 |

**Table 3.11** The percentage that each lithofacies contributes to the new training set. No balancing of the classes has taken place.

Although training is now with a different data set, the relationships between the classes in the multi-dimensional log space should be exactly the same as the Primary Training Set. Therefore three 1-layer 11-node and three 1-layer 14-node networks were created and trained on the new data set. The weight connections in the 14-node networks were pruned if they

stayed below 0.03 for 10,000 cycles. Networks were validated on the same data as before (see Section 3.5.6), which was made up of equal amounts of lithofacies.

The results from the training of these networks are found in Table 3.12.

| Trial | Ordinary 1-layer 11-node network | Pruned 1-layer 14-node network |
|---|---|---|
| 1 | 64.75 | 58.2 |
| 2 | 59.84 | 62.3 |
| 3 | 62.3 | 57.38 |

**Table 3.12** The percentage correct over the validation set for 2 different types of network; three trials per network type. All training data were unbalanced (see Table 3.11).

Validation percentages in the above table appear similar to the best of the other networks trained so far (compare with Figure 3.24, Tables 3.8, 3.9 and 3.10). It therefore appears that training with an unbalanced set can produce similar results to those using a balanced set. This is not necessarily expected. To interpret these data further it is necessary to study the actual percentage of each lithofacies that are predicted correctly. Table 3.13 shows the percentage of each lithofacies predicted correctly for the validation set.

| | Lithofacies | | | | |
|---|---|---|---|---|---|
| | 1 | 2 | 3 | 4 | 5 |
| % predicted correctly | 76 | 76 | 92 | 0 | 80 |

**Table 3.13** Percentage of each lithofacies correctly predicted in the validation set. Network trained with unbalanced data.

The percentage of each lithofacies predicted correctly is fairly high (all above 75%) except for lithofacies 4. This could be because it is a minority lithofacies, or because the logs that were used were unable to resolve it. Lithofacies 5 was also a minority lithofacies, so why is its classification not affected so much? Lithofacies 5 is the most shaly lithofacies. Perhaps although it did not make up a large proportion of the training set, its log signatures are so distinct that the network is able to distinguish it anyway. For the same reasons it can be argued that lithofacies 1 (best quality sand with gas) should also be very distinctive. Given that its log signature is so distinctive and it made up a large proportion of the data set why

isn't its percentage higher than lithofacies 5? It may well be that some of lithofacies 1 gets mixed up with lithofacies 2, as they appeared fairly close in the log space (see Figure 3.17). In order to determine whether the prediction successes of minority lithofacies really are affected by the amount of training data, the prediction of minority lithofacies that have very distinct log signatures should be investigated. In order to do this the number of data points representing lithofacies 1 was reduced to a fifth of the original amount. The make-up of this data set is seen in Table 3.14. Once again three 1-layer 11-node and three 1-layer 14-node networks were trained. The 14-node networks were pruned as before. The results of these networks are shown in Table 3.15. The best performing of these is the first of the 14-node pruned networks (57.38%). The percentage of each lithofacies predicted correctly for this network's validation set is seen as Table 3.16.

Figure 3.15 shows that the percentage correct in the validation set over all implemented networks appears lower than for other networks (for instance none get above 60%). Is this because lithofacies 1 is predicted poorly? Table 3.16 shows that there has indeed been a reduction in the success of lithofacies 1 prediction. It also seems that the inability of the network to accurately place its decision line has also adversely affected the classification of the other lithofacies (e.g. 2 and 3).

| | Lithofacies | | | | |
|---|---|---|---|---|---|
| | 1 | 2 | 3 | 4 | 5 |
| % in training set | 7.2 | 22.4 | 49.4 | 6.3 | 14.7 |

**Table 3.14** The percentage that each lithofacies contributes to the new training set. Lithofacies 1 has been artificially reduced so it is now a minority lithofacies.

| Trial | Ordinary 1-layer 11-node network | Pruned 1-layer 14-node network |
|---|---|---|
| 1 | 55.74 | 57.38 |
| 2 | 53.28 | 55.74 |
| 3 | 54.92 | 56.56 |

**Table 3.15** The percentage correct over the validation set for 2 different types of network; three trials per network type. Training data in proportions described in Table 3.14.

| | Lithofacies | | | | |
|---|---|---|---|---|---|
| | 1 | 2 | 3 | 4 | 5 |
| % predicted correctly | 52 | 64 | 88 | 0 | 96 |

**Table 3.16** Percentage of each lithofacies correctly predicted in the validation set; network trained with unbalanced data and lithofacies 1 in the minority.

These results should be evaluated in the correct context: a limited number of trials are presented, from a limited amount of data. However the findings do appear to show that the classification of lithofacies is indeed affected by their occurrence in the training set (as the theory suggests). However if a lithofacies is very 'distinct' in the multi-dimensional space it can be successfully predicted even if it is in the minority (lithofacies 5 is always predicted successfully, and even when the quantity of lithofacies 1 was reduced it was still predicted correctly more than 50% of the time). This implies that if a class is extremely poorly predicted (e.g. lithofacies 4) then this is not totally due to it being in the minority. It must also be because the logs cannot resolve it. In fact these two aspects are related. If very few data points exist for a particular class then it is unlikely that there is a representative sample, and its 'class' boundaries cannot be defined very easily (Figure 3.27). This implies that the user should make some educated decisions about data balancing. If the user has 10,000 examples of one lithofacies and 1000 of another, then it can be imagined that 1000 may define the hypothesis space with reasonable accuracy, even though it is in the minority. In this case partial boosting, or no boosting would be appropriate. If there were 100 examples of one lithofacies and 10 of another then it may be that these 10 can define the hypothesis space, or that they may not (Figure 3.27). In the latter case boosting will not improve

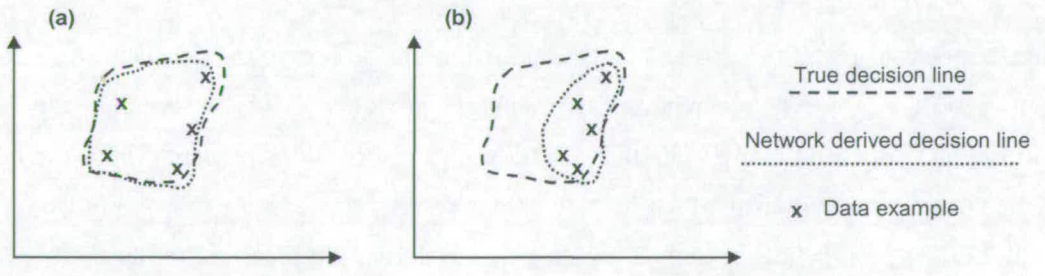



**Figure 3.27** A lithofacies that has very few examples may or may not be classified correctly by a neural network:
(a) Five examples approximately define the true decision line.
(b) The same number of examples does not define the true decision line. When the network is presented with new data this lithofacies would be poorly predicted. In this case data boosting would not help.

performance.

### *3.6.6 Training without derivative logs*

Seven input logs including two derivative logs (Section 3.5.2) were initially justified by the fact that backpropagation networks are able to sort input variables in order of importance and therefore effectively ignore those that have little influence on the output. This is done by setting the weights attached to those inputs close to zero. In this section the effect of using these derivative logs is investigated by leaving them out. Networks were trained on the five raw logs (GR, RHOB, NPHI, DT and ILD).

It would be expected that networks with only five inputs need a smaller topology. Therefore three 1-layer 10-node and three 1-layer 13-node networks were trained. The 13-node networks were pruned if the weight connections stayed below 0.03 for 10,000 iterations. All were trained on the Primary Training Set (as described in Section 3.5.6), and validated accordingly. The results are displayed in Table 3.17.

| Trial | Ordinary 1-layer 10-node network | Pruned 1-layer 13-node network |
|---|---|---|
| 1 | 54.92 | 58.2 |
| 2 | 56.56 | 58.2 |
| 3 | 50 | 54.1 |

**Table 3.17** The percentage correct over the validation set for 2 different types of network; three trials per network type. Networks run with five inputs only; see text for details.

All trials appear to result in a lower hit-rate than some of the previous best networks - none get above 60%. However the resulting percentages are only 8-10% lower than the best performing network, and many trials that used 7 inputs did result in percentages in the high fifties. Therefore a criticism of citing the above results as showing that 7 inputs (with derivative logs) perform better than 5 inputs with no derivative logs, is that the number of trials does not indicate whether the performance difference is significant. For now it can be stated that using derivative logs does not result in poorer performance from the network, and that using them may increase the accuracy of prediction. It can be recalled (Chapter 2) that

Wong *et al.* (1995a) showed how using derived logs can decrease training times and sometimes improve performance when predicting lithofacies, porosity, and permeability from logs with a neural network. The best performing network in Table 3.17 was run over the blind interval of well T8. These results are shown in the next section.

### *3.6.7 Testing over well 23/21-T8*

So far a variety of different networks have been evaluated in order to study the main factors that control training of a backpropagation neural network. The success of these networks was calculated by assessing their prediction over a simple validation set. This formed a method of rapid analysis of all networks and could be implemented during training. In order to get more precise ideas about the output from different networks, it is necessary to apply them to a well section of unseen data, and evaluate the predicted lithofacies columns next to the supposed 'real' column defined from core. Geologists are used to looking at predictions in this way, and so it provides a final measure of network performance before application to wells across the entire field. The cored interval 9120-9530 in well 23/21-T8 provides a blind test for network performance (with the exception of the section 9488-9513, which made up part of the Primary Training Set). Table 3.18 contains a summary of Figure 3.28, which provides lithofacies columns for various networks that have been discussed in this section. It should be noted that the various columns have gaps. These gaps represent areas where the network did not output a lithofacies (i.e. no output nodes were activated) and where the network defined mixed lithofacies (i.e. 2 or more output nodes were activated). Therefore the displayed columns represent only those intervals where the network made a single lithofacies prediction. More details on interpreting multiple and 'none' outputs can be found in Chapters 2 and 4.

The first thing that one notices when looking at the lithofacies columns is that they appear fairly 'spiky'. Predictions change due to rapidly changing data (from one well log value to the next), and due to inflexion points in the logs at bed boundaries (e.g. at 9330ft and 9340ft). These are general issues that affect all columns. These are discussed in detail in Chapter 4. This section is reserved for a simple comparison of the different columns.

All networks have made a good attempt at discriminating the main well sections. The main reservoir intervals (9240-9320ft, 9330-9340ft, 9440-9355ft) have been successfully defined

(albeit with some slight mix up of lithofacies 1 and 2). The top half of the plot (9120-9230ft) contains mostly lithofacies 3, the most heterogeneous of the sediments, and most predictions attempt to populate this section with lithofacies 3. The lowest section (9460-9530ft) consists of interbedded sand and shale. In most cases this is defined correctly by the different neural networks.

| Lithofacies code | Network | Relevant section | % correct over validation set | % correct over well 23/21-T8 |
|---|---|---|---|---|
| B | Best performing network from topological experiments. | Section 3.6.2<br>Figure 3.24 | 68.85 | 56.9 |
| C | Best performing network with different learning rate and momentum parameter from above network (LR 0.3. Mom 0.9). | Section 3.6.3<br>Table 3.8 | 60.66 | 53.37 |
| D | Selected pruned network, starting with 23 nodes in 1 hidden layer. Pruned if weights stayed below 0.08 for 10,000 cycles. | Section 3.6.4<br>Table 3.9 | 61.48 | 53.2 |
| E | Selected pruned network, starting with 14 nodes in 1 hidden layer. Pruned if weights stayed below 0.03 for 10,000 cycles. | Section 3.6.4<br>Table 3.10 | 63.11 | 53.24 |
| F | Trained with unbalanced data. | Section 3.6.5<br>Table 3.12 | 64.75 | 66.45 |
| G | Trained with unbalanced data, and with lithofacies 1 reduced further. | Section 3.6.5<br>Table 3.15 | 57.38 | 43.78 |
| H | Trained with 5 inputs (the raw logs) only. | Section 3.6.6<br>Table 3.17 | 58.2 | 41.17 |
| Lithofacie | Real lithofacies defined from core. See Table 3.2. | n/a | n/a | n/a |

**Table 3.18** Lithofacies codes found in Figure 3.28, next page; and summary of the networks that defined the various columns.

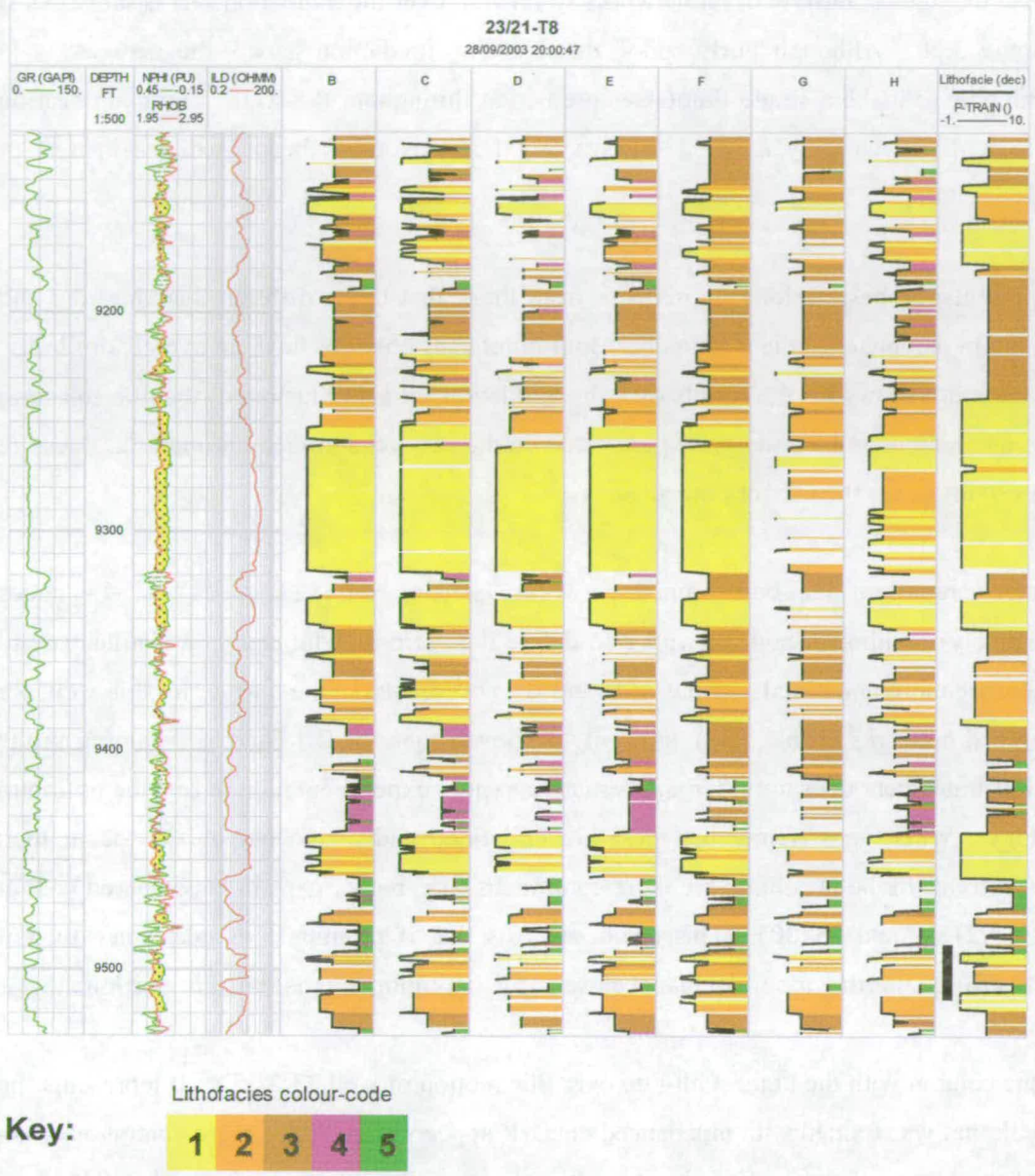



**Figure 3.28** Lithofacies columns predicted by a variety of different networks, well 23/21-T8. See Table 3.18 for lithofacies symbols. All log headers are contained in the notations and conventions section. The black bar (track 12) represents data that was used for training.

The best network found when experimenting with different topologies (and indeed the one that had the highest hit-rate of all networks so far run, over the validation set) is shown as B in Figure 3.28. Although fairly spiky, this has few prediction gaps - the network is in general able to make a single lithofacies prediction throughout the well. The main section that is predicted wrongly is at 9430ft, where lithofacies 4 has been predicted instead of lithofacies 3.

C represents the best performing network from those that had a different learning rate and momentum parameter to the B network. Both lithofacies columns have an overall similarity. This therefore shows (as the results over the validation set also illustrated) that the selection of the momentum and learning rate parameters in the networks trained on this data, does not appear to influence the network outcome.

D and E represent the best pruned networks (starting with 23 nodes and 14 nodes respectively). Although both networks do define the various sediments in a similar way to B, there are more undefined sections in D and E. This results in the hit-rate for this well, for the pruned networks (Table 3.18), to be slightly lower than for B. Therefore pruning in the way illustrated here does not offer an alternative to pure experimentation to find the optimum topology. When gaps (remember these are undefined and mixed outputs) do occur then these intervals in the D column are more continuous (e.g. bigger gaps in D compared to E at 9170ft, 9215ft, and 9528ft). This again suggests that if pruning does take place then it benefits from a starting topology that is close to the optimum one (as stated in Section 3.6.4).

F is the column with the highest hit-rate over this section of well 23/21-T8. It represents the network that was trained with unbalanced data. It appears to be much more continuous than any of the other columns. The hit-rate is high because it predicts the interval at 9430ft as lithofacies 3, whereas most other networks predict it as lithofacies 4. It can be seen that this network has predicted a lot of lithofacies 1 and 3, which occurred most in the training set. Since these are the most common lithofacies in this well the hit rate is artificially high. It would be questioned whether this network is capable of predicting lithofacies 4 at all.

G represents the network trained with unbalanced data, but with lithofacies 1 artificially reduced. The striking element of this column is that lithofacies 1 is hardly ever predicted. The gaps around 9300ft represent areas where both lithofacies 1 and 2 were predicted,

presenting some ambiguity. Clearly the reduction of lithofacies 1 in the training set has had a huge influence on the ability of the network to define this lithofacies correctly. It can be concluded that the occurrence of a lithofacies in the training set is an important influence on the network outcome. If a lithofacies contributes a tiny amount to the training set, that lithofacies is unlikely to be predicted correctly. Where it is in the minority, but there are a 'fair' number of points, and it is very distinct, it can successfully be predicted.

H shows the results from the best performing network that was trained with five inputs and no derivative logs. The predictions are much worse than for the best network with seven inputs (B). There are many more gaps, and the network appears to specifically mix up lithofacies 1 and 2 (e.g. around 9280ft). The hit-rate over this section is therefore very low (41.17%, in fact the lowest of all the columns shown). The inclusion of total porosity and neutron-density separation logs appears to assist the network in defining lithofacies 1. It is certain that all information contained in the derivative logs is contained in the raw logs. However the network makes more accurate predictions when all logs are included.

### *3.6.8 Training with different data sets*

So far many different aspects of neural network design and implementation have been analysed. A common test to define whether the network is capable of finding relationships that exist across the entire data set is to train with subsets of data, whilst testing the resulting networks on other subsets. It was already stated that the data type studied does not lend itself to creating many subsets. Some lithofacies occur in such small proportions that this is not possible. Therefore a Primary Training Set (used so far) and two smaller training sets were created (see Section 3.5.6). Training set 2 was all taken from well 23/21-T5. Training Set 3 was taken mostly from well 23/21-T8, with some data borrowed from 23/21-T5 (see Table 3.7). In this section networks are trained with both of these smaller training sets, and then predictions assessed in light of those results already achieved.

Training Set 2 was used to train three fixed, 1-layer, 11-node networks, and three 1-layer, 14 node networks. The 14-node networks were pruned if weights stayed below 0.03 for 10,000 cycles. All networks were validated during training with validation data selected from the Primary Training Set (see Table 3.7). The results of training these networks are shown in Table 3.19.

| Trial | Ordinary 1-layer 11-node network | Pruned 1-layer 14-node network |
|---|---|---|
| 1 | 34.27 | 44.06 |
| 2 | 40.56 | 34.27 |
| 3 | 30.07 | 40.56 |

**Table 3.19** Results of six networks, all trained on Training Set 2; three trials per network.

Training Set 3 was also used to train three fixed 1-layer 11-node networks, and three 1-layer, 14 node networks. The 14-node networks were pruned if weights stayed below 0.03 for 10,000 cycles. All networks were validated during training with validation data selected from Training Set 2 (see Table 3.7). The results of training these networks are shown in Table 3.20.

| Trial | Ordinary 1-layer 11-node network | Pruned 1-layer 14-node network |
|---|---|---|
| 1 | 48.45 | 44.33 |
| 2 | 46.39 | 42.27 |
| 3 | 43.3 | 48.45 |

**Table 3.20** Results of six networks, all trained on Training Set 3; three trials per network.

Both sets of results appear poor when compared to the hit-rates of previous networks. The maximum hit-rate reached for the best network trained on Set 2 was 44.06%, and for Set 3 48.45%. Also the results from training with Set 3 are consistently better than those from Set 2. Why is this? Both of these data sets were much smaller than the Primary Training Set, so is it because the full range of data examples is not represented, and the decision lines formulated by the networks were consequently incorrect? Or are the actual data values for each lithofacies different across the training sets?

In order to visually test how the networks have performed and determine whether the hit rate is particularly low due to certain lithofacies being predicted wrongly, networks can be

applied to well 23/21-T3 and the results displayed as a lithofacies column, similar to those in the previous section (Figure 3.29).

I represents the column that was produced by the best network trained with Set 2 (mostly taken from well 23/21-T5). This appears to have performed particularly well at predicting lithofacies 1 – the main reservoir intervals. The network has also predicted lithofacies 3 in generally the correct intervals (e.g. 10140-10180, 10280-10300). Lithofacies 2 is very rarely predicted correctly (it commonly predicts lithofacies 1 instead of lithofacies 2). Lithofacies 4 and 5 hardly ever occur in this well, and are hardly ever predicted. Referring back to Table 3.5 it is seen that there is only a small amount of lithofacies 2 in the training set - it consequently was heavily boosted. Therefore this is probably the reason for the poor prediction of lithofacies 2. What is also significant is the number of data gaps that occur. These represent areas where the network predicted mixed lithofacies or no lithofacies. If the data is analysed further (Table 3.21) it is found that 7.1% of the time mixed lithofacies were predicted, 10.1% no lithofacies were predicted and 47.5% of lithofacies were predicted correctly. If all unsure and mixed outputs were predicted correctly then the hit-rate for this well would be approximately 65%, which is in-line with some of the highest hit-rates gained so far. This suggests that there are insufficient training examples to accurately define the true decision boundaries between lithofacies.

J represents the column that was produced by the best network trained with Set 3 (mostly from well 23.21-T8). This network has also accurately predicted the best reservoir, although in places it sometimes gets mixed up with lithofacies 3 (e.g. at 9930ft). Lithofacies 3 is generally predicted in the correct place and in more continuous sections than I. Once again lithofacies 2 is hardly ever predicted. However lithofacies 2 was not heavily boosted, as it was for Training Set 2. This indicates that even more data points are needed to properly define lithofacies 2 or the distribution of the logs for lithofacies between wells 23/21-T5 and T8 are fundamentally different. Referring to Figure 3.28, B the best network trained primarily on well 23/21-T3, when applied to well 23/21-T8 does have some success at predicting lithofacies 2 (e.g. at 9370ft and 9500ft). This implies that simply having more examples of lithofacies 2 might improve performance. Table 3.21 shows that lithofacies were predicted correctly 49.9% of the time in this well, 0.4% were predicted as mixed outputs, and for 22% of the time there were no predictions. This again suggests that there is not a representative sample of data to correctly define all the lithofacies.

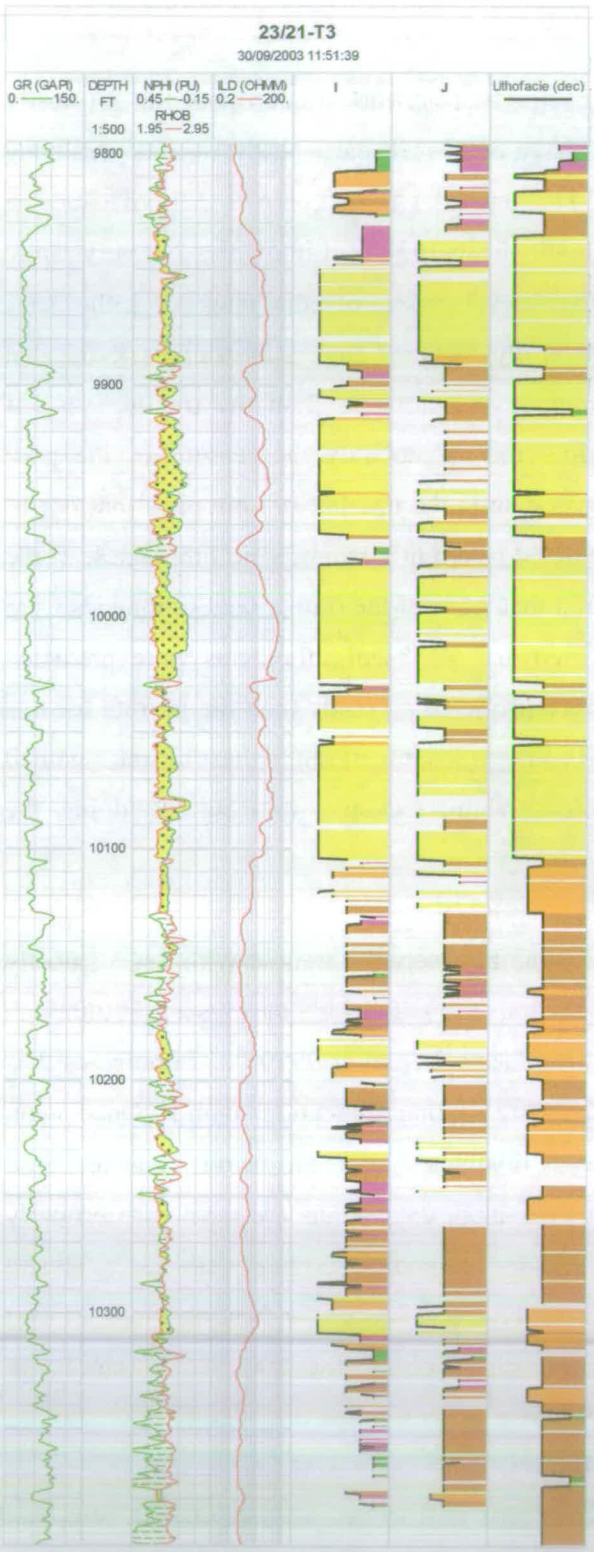






**Figure 3.29** Best performing networks from Tables 3.19 and 3.20 applied to well 23/21-T3.
I Best network trained on Set 2.
J Best network trained on Set 3.

| | Best network trained on set 2 | Best network trained on set 3 |
|---|---|---|
| correct prediction (%) | 47.5 | 49.9 |
| mixed lithofacies prediction (%) | 7.1 | 0.4 |
| no lithofacies prediction (%) | 10.1 | 22 |

**Table 3.21** The percentage of well 23/21-T3 that were predicted correctly, were predicted as mixed outputs, and as 'none' outputs.

In this short study neural networks were trained with three different data sets. Training with the Primary Training Set produced overall success rates of approximately 60% when applied to unseen wells. When training with smaller sets, on subsequent application to unseen well data many of the data were unable to activate any of the network output nodes, resulting in no lithofacies being predicted; or more than one of the output nodes was sufficiently activated so the network made mixed predictions. This ambiguity in the network's decision reduces the overall hit-rate, without reducing the percentage that is classified wrong. This suggests that there is a lower limit to the amount of data that are needed to successfully train a neural network.

### *3.6.9 Summary of neural network methodology (Section 3.6)*

This section provided a description and discussion of various experiments that were undertaken with different neural networks. The aims were to determine the optimum network capable of predicting the lithofacies scheme over Lomond data, and to determine some of the main influences on the network output. A summary of the findings are given below:

- A neural network with one hidden layer and 11-nodes provides the best topology for predicting the lithofacies scheme. Larger networks can provide similar classification hit-rates. When two layers are present in the network, the degree of classification appeared to be strongly dependent on the number of nodes in the first layer;

- Although it is noted that, in general, training with a momentum parameter is good practice as it can assist in eluding local minima during training, and that a small learning rate is more likely to result in a network that is truly at the global minima, these parameters did not appear to significantly affect the classification of lithofacies in this study;
- Pruning in the way described in this section cannot substitute exhaustive experimentation with different topologies to find the optimum size. When top-down pruning algorithms are implemented they benefit from a starting topology that is not too far from the optimum one;
- Classification of lithofacies from well logs via a neural network is influenced by the lithofacies quantities that make up the training set. If a lithofacies is in the minority, this could result in poor classification of that lithofacies. However if the log signature of a particular lithofacies is very distinct, and where there are sufficient examples to approximately define the decision lines around that lithofacies in the multi-dimensional log space, it can be successfully predicted even if it is in the minority;
- Training with derivative logs does not result in poorer classification of lithofacies. Using them may actually improve classification;
- Sufficient examples must be present in the training set to properly define lithofacies. Therefore networks trained on small training sets are often not capable of good classification. When training with small sets, the limiting factor of training set size can be recognised from studying the percentage of test examples that activate more than one output node, or activate no output nodes, rather than the percentage that are classified incorrectly.

These results are discussed further, in the light of other author's findings in the discussion chapter (Chapter 7).

### *3.7 Chapter 3 summary*

This chapter described the methodology employed to generate and train a neural network for lithofacies prediction (see Figure 3.30). It started with an introduction to the Lomond Field, and a discussion of its sedimentology. If a lithofacies scheme is to be developed to describe new log data (as a first pass), or to help populate geological reservoir models, then an understanding of the sedimentology of a field is an important consideration in designing such a scheme. The different processes that deposit the sediment influence lithology type, 3-D architecture, and petrophysical properties. All of these factors, along with the facies quantities and their separation by the logs (that would eventually predict them), were carefully considered. On the basis of these parameters a lithofacies scheme was designed. The neural network was then trained to predict lithofacies in the context of this lithofacies scheme.

It was important that actual log and lithofacies data were prepared correctly in order to give the network as good a chance as possible to correctly define the lithofacies classes. Therefore it was necessary to consider the different possible inputs, and whether these data needed to undergo any non-linear transforms to aid discrimination. It was necessary to consider inter-well variability and to exclude well 23/21-T4 (which was considered to show different relationships between its lithofacies and logs than the other wells). Finally training and validation sets were carefully designed.

Different topologies, learning and momentum parameters were attempted and a pruning algorithm was used to test if this could find the optimum topology automatically. Experiments took place to test the effects of training with unbalanced data, with derivative logs and different training sets (summarised in Section 3.6.9).

This chapter presented some preliminary results and discussion. These were presented to give an insight into the workings of the neural network, and to help determine the optimum one. The 1-layer, 11-node network trained with all inputs on the Primary Training Set with balanced data appeared to give optimum classification. This network was applied to all cored wells that had sedimentological descriptions. These results and their subsequent analysis are presented in detail in Chapter 4.

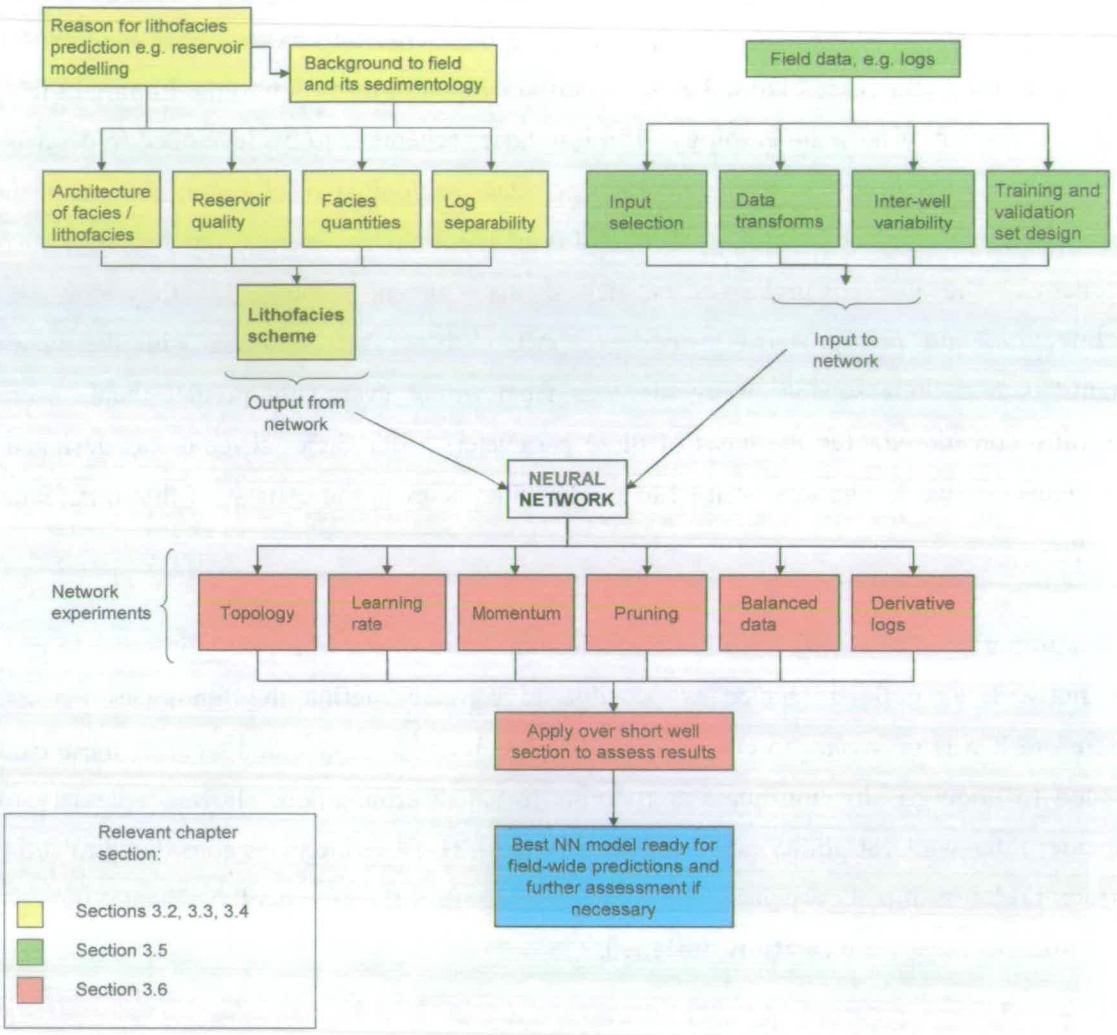



**Figure 3.30** Summary of the methodology followed to create and train a neural network for lithofacies prediction.

# Chapter 4 : Neural network critique based on lithofacies predictions in the Lomond Field

## *4.1 Introduction*

Chapter 3 described the method that was used to generate and train a neural network to predict lithofacies from Lomond log data. Various experiments took place with different networks with one aim being to determine the optimum one. A 1-layer 11-node network trained with all inputs, and on the Primary Training Set appeared to give optimum results. This was determined by its performance over a small validation set and also (albeit very briefly) by studying the network's predictions in well 23/21-T8. This Chapter presents and analyses in detail the results of this network when it was applied to all Lomond wells. The results are used to evaluate the inner workings and limitations of the network and attempts are made to develop techniques to overcome some of the limitations.

There are some features that can be quickly recognised in all predictions, such as small intervals of possible 'noise' and indecision by the network at log inflexion points. It is possible to implement techniques to eliminate these. Therefore well sections that illustrate these features and the methodology used to eliminate them are shown in Section 4.2. Also, in Chapter 2 it was stated that the best way to encode the outputs from a neural network was in a binary fashion, having multiple output nodes. A key advantage of this is that differences between output nodes can be used as a measure of confidence. This aspect of network design is briefly discussed in Section 4.3, before presentation of the results.

The Lomond wells 23/21-T3, T5 and T8 were used to create the Primary Training Set since very detailed sedimentological descriptions of the core (Cullen 1993a, Cullen 1993c, and Cullen 1993d) were available. The intervals in these wells that were not used for training can be used to test the model. Therefore a major part of this chapter (Section 4.4) is devoted to studying these intervals, and comparing predictions to the core defined lithofacies and the actual core itself. Section 4.5 describes the results when the model was applied to well 23/21-T4; in Chapter 3 this well was found to have different relationships between its log signatures and lithofacies to the other cored wells and therefore it was not included in any training sets. Results from all the remaining wells are presented in Section 4.6.

Since core is usually only taken from the reservoir interval and therefore the hydrocarbon zone, training data are often restricted to this interval (and this is the case for Lomond). Therefore because some well logs are influenced by reservoir fluid any model created is usually fluid specific. The dependence of the model on the different input logs, and hence the fluid is discussed in Section 4.7 and a methodology is implemented in an attempt to create a more 'universal' model.

A brief summary of this chapter is Section 4.8. The results are discussed further, in the context of the current literature in Chapter 7.

## *4.2 Features recognised in all wells*

### *4.2.1 Introduction*

There are some features that are recognisable in all lithofacies predictions. In Chapter 3, figures 3.28 and 3.29, it was observed that the predicted lithofacies columns tended to be fairly variable in places. This is due in part to rapidly changing data as a result of very heterogeneous sediments. However well logs record data that is derived from a large volume of rock, the actual volume of which is partly related to the emitter-receiver spacing of the tools (Rider 1996). As data is recorded the tools are of course moving. Therefore well log tools have a minimum bed thickness that they are capable of fully resolving. Of the logs that were used as inputs to the neural network model the density log has the highest resolution of approximately 2ft under normal logging conditions, and the resistivity (induction) and gamma ray logs the lowest resolutions, 4ft and 3ft respectively (values from Rider 1996, after Hartmann 1975). Therefore the well logs that acted as inputs into the neural network model in theory cannot fully resolve beds of less then 2ft. Beds that are predicted by the network and are less than 2ft thick may not be predicted correctly as the logs are not reading the true values of that particular facies. Studying the predicted lithofacies in Lomond data, it appears possible to divide predicted thin beds up into two categories (Figure 4.1):

- Thin beds occurring at the edge of thicker beds due to log inflexion points at bed boundaries;
- Thin beds that occur within thicker beds simply due to a thin bed that is not fully resolved (i.e. although a prediction is made it may not be the correct prediction).

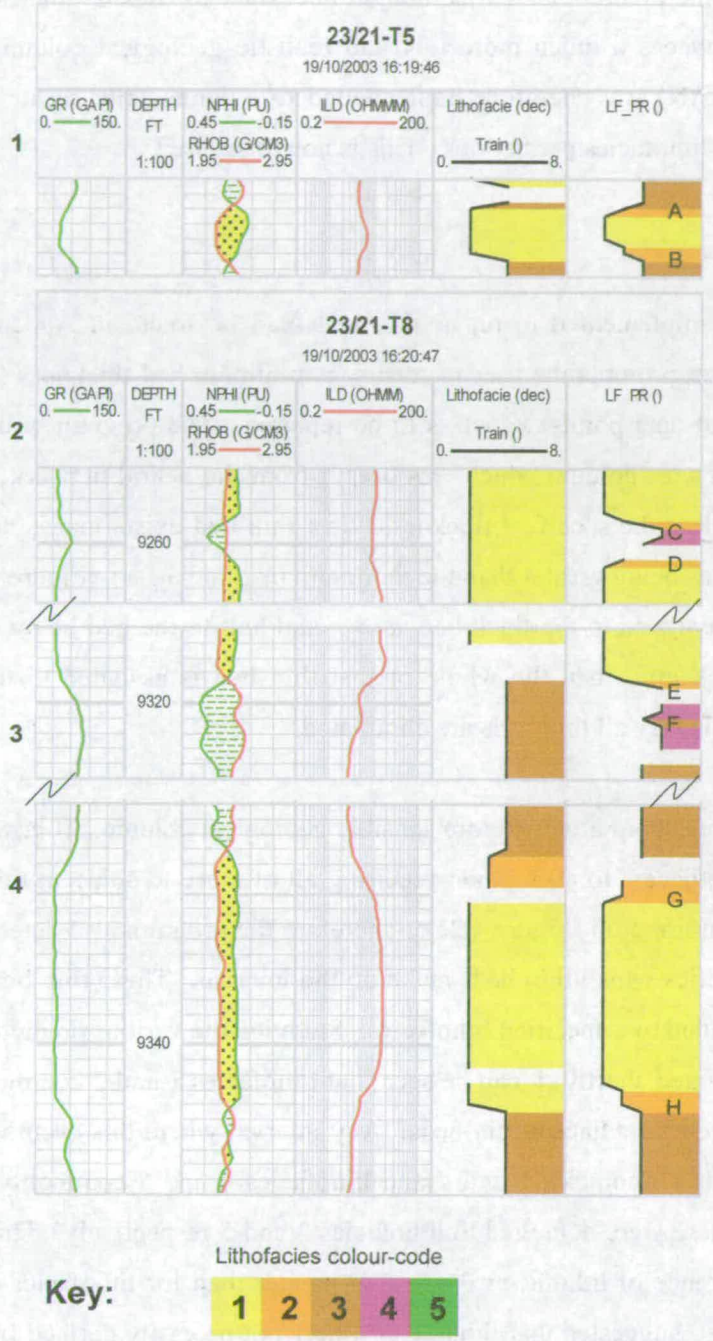



**Figure 4.1** Raw lithofacies predictions (LF_PR, track 6) commonly contain thin-beds. These can be classified into two categories:

(i) Thin beds occurring at the edge of thicker beds due to log inflexion points at bed boundaries;

(ii) Thin beds that occur within thicker beds.

Sections 1, 2 & 3, wells 23/21-T5 and 23/21-T8, lithofacies 2 occurs as edge effects around a thicker bed of lithofacies 1 (A, B, C, D, E), due to inflexion points in the neutron and density logs.

Section 4 well 23/21-T8, lithofacies 2 occurs as edge effects around a thicker bed of lithofacies 1 (G & H) due to inflexion points in the gamma ray and resistivity logs.

Section 3 well 23/21-T8 lithofacies 3 occurs within a thicker bed of lithofacies 4, (F).

In order to tidy up the predictions it was thought necessary to 'repair' thin beds when they occurred. This produces a much more tidy and realistic geological column. A program (written in FORTRAN) was therefore implemented to automatically repair thin beds that occurred within the lithofacies predictions. This is now discussed.

### *4.2.2 Thin bed repair*

The program code implemented to repair thin beds can be found in Appendix 2. When executed the program prompts the user to specify a minimum bed thickness (it is actually a minimum number of data points) which is to be repaired. The program will then read the raw predicted lithofacies column which was output from the neural network, and eliminate all beds that are below the specified thickness. If a thin bed exists that is adjacent to two thick beds (defined as being greater than the minimum bed thickness), (Figure 4.2a) then half of that thin bed is assigned to the thick bed above, and half to the bed below. If a thin bed exists within a thick unit, then the whole of that thin bed is assigned to the thicker bed (Figure 4.2b). In this way all thin beds are eliminated.

In most cases this results in a much more sensible geological column. If however there are multiple thin beds adjacent to each other, repairing all of these to adjacent thicker units can result in a loss of information (Figure 4.2c). Therefore the program also detects thin bedded intervals, and identifies which thin beds make up the interval. These thin beds can then be automatically defaulted to a specified lithofacies. Studying the various predictions across the Lomond logs (presented shortly) it can be seen that lithofacies 1 and 2 commonly get mixed up and therefore occur as adjacent thin beds. Any interval where this occurs was defaulted to lithofacies 1. Also lithofacies 3 and 4 and lithofacies 4 and 5 commonly occur as thin bedded intervals; these were defaulted to lithofacies 3 and 5 respectively. This was because the expected occurrence of lithofacies 3 and 5 is greater than for lithofacies 4 (see Section 3.4.4) and it was also suggested that lithofacies 4 may not be easily defined by the logs (see Section 3.6.5).

The network is also capable of making mixed decisions and no decision (see next section). These, until now have been left as gaps in the resulting column. These can also be repaired in the same way (Figure 4.2d), whether they occur as thin beds or thick beds.

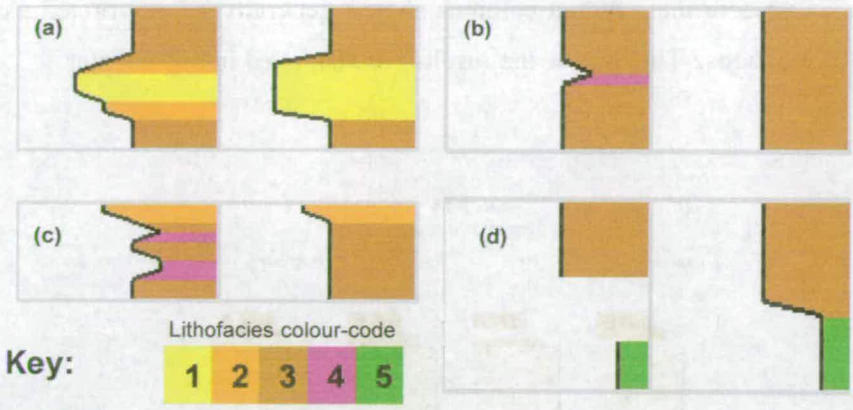



**Figure 4.2** Implementation of the thin bed repair program. In each example the raw lithofacies column is on the left, the repaired column on the right.

(a) Thin beds that occur as edge effects around thicker beds. The program assigns half of the thin bed to the bed above and half to the bed below.

(b) Thin beds that occur within thicker beds. The thin bed is automatically assigned to the thicker bed.

(c) Multiple thin beds that make up a thin bedded interval. In this case if half of this interval was assigned to the thicker bed above (LF 2) and half to the thicker bed below (LF 3) this would incorrectly extend the thickness of the lithofacies 2 bed above. In this case the thin bedded interval is defaulted to lithofacies 3.

(d) The gap represents an area of ambiguity by the network (in actual fact the output nodes of both lithofacies 3 and 5 are highly activated). In this case half of the gap is assigned to the bed above and half to the bed below, even though the gap is 'thick'.

So what size should the minimum bed thickness be? From the logs used as inputs the one with the highest resolution is the density log (approximately 2ft, Rider 1996, after Hartmann 1975). If repair takes place over this thickness it may well be that edge effects still exist as a consequence of the poorer resolving power of other logs. The issue is that logs with different resolutions have been combined; repairing over small thicknesses could result in many thin-beds being left in, repairing over larger thicknesses could result in a loss of detail. Therefore it is useful to repair over different thicknesses and assess the results. Figure 4.3 shows examples of repairing over 1.5ft and 2ft (3 and 4 data points respectively). In many cases repairing over 1.5ft preserves important beds (i.e. good reservoir) that appear to match the 'real lithofacies'. A coarser repair eliminates these. Therefore all repaired columns subsequently shown in this chapter were repaired, with a minimum bed thickness of 1.5ft.

A criticism of repairing the logs in the way described is that, if a log shows a small deviation (as the result of a real thin bed, cemented band, nodule etc.) but it is not fully resolved (and therefore the wrong lithofacies is assigned) the fact that there is an anomaly at all is useful

information. Therefore the repaired columns should generally be interpreted alongside the original raw predictions. This is how the results are displayed in this chapter.

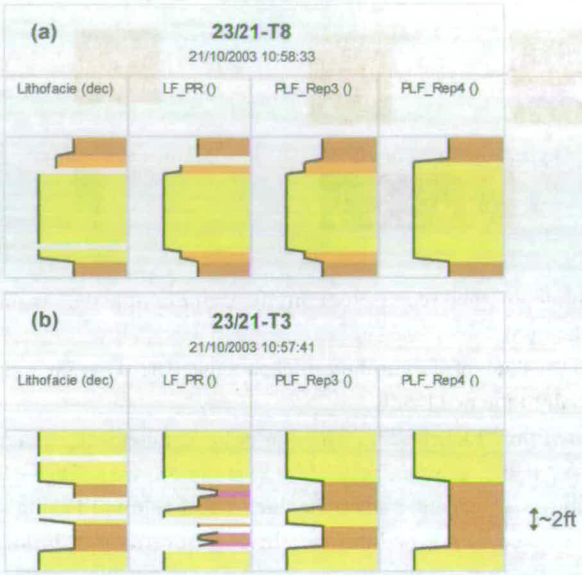



**Figure 4.3** In each example track 1 is the core defined lithofacies, track 2 the raw neural network prediction, track 3 the raw prediction repaired over 1.5ft (3 data points), track 4 the raw prediction repaired over 2ft (4 data points). Although repairing over 1.5ft can allow edge effects to remain in the column, whereas repairing over 2ft would eliminate these (example a), repairing over 1.5ft also preserves some thin beds that are important (i.e. good reservoir), whereas repairing over 2ft would eliminate these (example b). There is a suggestion that the edge-effect in (a) could in fact be a correct prediction. Therefore, repairing over 1.5ft is to be preferred.

## *4.3 Multiple outputs from neural networks*

In Chapter 2 it was stated that having multiple outputs in a backpropagation network for lithofacies prediction was to be preferred. In this case each lithofacies has a dedicated output node (Figure 4.4). It can be recalled that one of the advantages of designing the network in this way was that the differences between the outputs given by each node can provide the user with a measure of confidence in the predictions. This is especially useful when interpreting all results. Although output nodes are generally on or off in a well trained network (termed 'fully saturated') in fact they can be on 'to a degree'. Recall that the neural network program EasyNN uses a sigmoidal squashing function as its 'threshold function' (Figure 4.5). A threshold logic function (see also Figure 4.5) would enable the nodes to be

just on or off. However networks with these functions cannot be trained via the gradient descent algorithm. The use of the sigmoidal function means that outputs can be any value between 0 and 1. In EasyNN an output node is deemed to be on if its activation is greater than 0.5; a prediction is then made. If all the activations are below 0.5 then no predictions are made. But what if all the activations are less than 0.5 but one is 0.4 and the rest are zero. Clearly this is useful information and can aid interpretation. Therefore interpretation should be made in the presence of the activation levels for all output nodes.

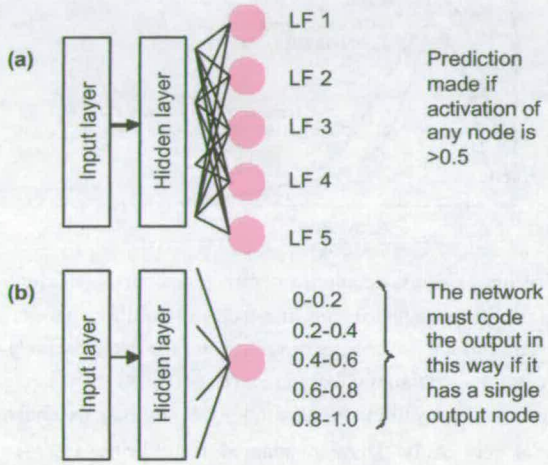



**Figure 4.4** When multiple outputs are used (a) the network will make a prediction if any of the nodes output a value greater than 0.5. The difference between activations can provide the user with a degree of confidence in the networks prediction. When one output node is used (b) the network must code in the way illustrated. Activations of different lithofacies cannot be compared.

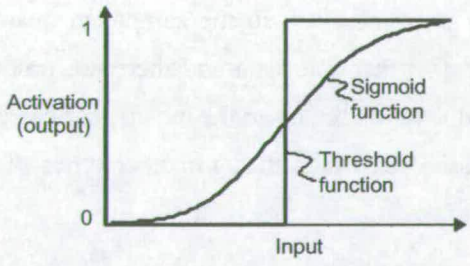



**Figure 4.5** A threshold function allows the output nodes to be on or off. A sigmoid function allows the output to be any real number between 0 and 1.

It should be noted however that although the term 'confidence' is used these values are not confidence limits in the usual sense and should be interpreted with this in mind. Just because

the activation of the lithofacies 1 output node is 1, this doesn't mean that there is a 100% chance that that prediction is lithofacies 1. Discussion of how to convert activation levels into confidence is discussed in Masters (1993). He states that 'in practice the answer (to converting activation to confidence) is generally discouraging or possibly even dangerous due to overconfidence in our abilities.' In general, confidence can be estimated if the distributions of different activation levels are known (Figure 4.6).

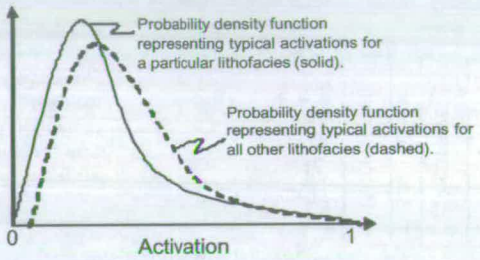



**Figure 4.6** Probability density functions are required to convert network activations to true confidence. In the example shown one might think that for the particular lithofacies in question, an activation of 0.3 suggests a high probability that it is actually this lithofacies as activations around 0.3 are extremely common (solid). However activations of 0.3 are also extremely common for activations of other lithofacies (dashed). Therefore it is necessary to study the distribution of activations for all lithofacies. In the case shown the network is not capable of discriminating this lithofacies very easily. Diagram adapted from Masters (1993).

Computing the probability distributions in Figure 4.6 is far more difficult than some researchers like to admit (Masters 1993). It relies on correct sampling of the activation levels, and all cases must be represented in the sample in quantities proportional to their expected occurrence. The fact that core data and therefore training data and consequently activation levels are biased towards the reservoir means that correct sampling is much more difficult to achieve with lithofacies data than for other types of data. This was however, discussed in Chapter 3.

Therefore in this chapter the activation levels of all nodes are presented and used to indicate indecision in the network. If both lithofacies 1 and lithofacies 2 output nodes are highly activated then at least a sandy lithofacies is predicted, and this information can be evaluated in the context of the predictions made in beds above and below.

## *4.4 Lithofacies predictions in wells 23/21-T8, T5 and T3*

### *4.4.1 Introduction*

This section describes the results in detail obtained when the optimum neural network was applied to wells 23/21-T8, T5 and T3. All three wells contain core and this acts as the 'ground truth'. Section 4.4.2 illustrates confusion matrices for all these wells that show the hit-rates for all lithofacies types. Section 4.4.3 then goes on to compare the results directly to the sedimentary logs that closely describe the core.

### *4.4.2 Confusion matrices*

One way of illustrating lithofacies predictions is via confusion (often also called coincidence) matrices. These tables show the number of data points that were correctly predicted by lithofacies type. They also highlight which lithofacies commonly get mixed up with each other. Table 4.1 shows the matrix for well 23/21-T8 before the thin-bed repair program was applied. Note how the matrix specifies the number and percentage of data points that were predicted as 'uncertain' (no output from the network), and mixed (more than one output from the network). In this matrix if all data points had been predicted correctly the grey boxes would contain high numbers and the other boxes would be empty. Table 4.2 shows the confusion matrix for results after the thin-bed repair program was implemented. In this case the matrix is simpler as the uncertain and mixed predictions have been eliminated. Since only a very small part of well 23/21-T8 was used in the training set (6%) this well can essentially act as a blind test well.

Overall before repair 56.9% of points were predicted correctly, the overall hit-rate. 4.0% were predicted as mixed (most of these were twin outputs of lithofacies 1 and 2); 2.2% were predicted as uncertain. The low percentage of uncertain prediction indicates that the well log responses in well 23/21-T8 generally fall in to the log ranges set by the network during training, and consequently the network is able to make predictions. Table 4.1 shows that the best reservoir (lithofacies 1) is correct only 58.1% of the time; the reason this is not higher is that it often gets mixed up with lithofacies 2. Lithofacies 2 is predicted correctly only 45.9% of the time. Again this is because of mix up with lithofacies 1 and also lithofacies 3. Lithofacies 3, the most heterogeneous of all the rock types is predicted correctly 54.3% of the time. It gets mixed up with lithofacies 2, 4 and 5, and the majority of the uncertain and

mixed network predictions actually belong to lithofacies 3. These figures themselves indicate the heterogeneous nature of this rock type. Lithofacies 4 is not predicted very successfully at all. Since this well is essentially acting as a blind test, this can for the moment be taken to indicate that the logs are not capable of resolving this particular rock-type. However, in the next section a comparison is made between specific intervals that contain lithofacies 4 to the sedimentary logs. The only lithofacies that is predicted very successfully is lithofacies 5 (80.9%). This could be because some of the training data for this lithofacies was taken from this well. However as the next section illustrates, there are many areas that are not in the training set where this lithofacies is predicted correctly; therefore it is predicted successfully because its log signatures are very distinct.

Comparing Tables 4.1 and 4.2 it is possible to estimate the action of the thin-bed repair program on the results. Overall the percentage correct has risen to 60.5%. The success of lithofacies 1, 3 and 5 has also improved. The most significant improvement is seen in lithofacies 3, the most heterogeneous lithofacies; hit-rates for this lithofacies have increased by approximately 6%. Thus these tables indicate that not only does the thin-bed repair program result in a more continuous and geological looking column but it also acts to actually improve predictions, and specifically improves the predictions of the most heterogeneous lithofacies.

Tables 4.3 and 4.4 show the same type of matrices as Tables 4.1 and 4.2, except for well 23/21-T5. Studying Table 4.3 it can be seen that the overall hit-rate is 70.1%. This is higher than for well 23/21-T8. This could be a consequence of more of this well making up the training set (25%). Lithofacies 1 is predicted fairly successfully (73.9%) but, as in well 23/21-T8 gets mixed up with lithofacies 2 and 3. Lithofacies 2 is poorly predicted because of mix up with lithofacies 1 (although in general there isn't actually much of lithofacies 2 at all in this well). Lithofacies 3 is correct in 62.7% of cases and, as for well 23/21-T8 most uncertain predictions were made in intervals of this lithofacies. Lithofacies 4 is predicted correct 41.4% of the time, much higher than for well 23/21-T8. However many of these data were contained in the training set, and therefore actually define the hypothesis space of that lithofacies, so it is no surprise that the percentage correct is higher in this well. The hit-rate of lithofacies 5 is very high, as for well 23/21-T8.

| | Predicted Lithofacies | | | | | | | | |
|---|---|---|---|---|---|---|---|---|---|
| Real Lithofacies | | 1 | 2 | 3 | 4 | 5 | uncertain | mixed | % of real lithofacies predicted correctly |
| | 1 | 168 | 76 | 26 | 6 | 0 | 2 | 11 | 58.1 |
| | 2 | 21 | 51 | 28 | 5 | 0 | 2 | 4 | 45.9 |
| | 3 | 2 | 25 | 165 | 54 | 30 | 12 | 16 | 54.3 |
| | 4 | 0 | 0 | 0 | 0 | 0 | 0 | 0 | - |
| | 5 | 0 | 0 | 1 | 11 | 55 | 1 | 0 | 80.9 |
| Overall % correct | | | | | | | | | 56.9% |
| Mixed, uncertain predictions (%) | | | | | | | 2.2% | 4.0% | |

**Table 4.1** Confusion matrix for well 23/21-T8 before the thin-bed repair program was applied. The grey boxes indicate how many data points were predicted correctly by lithofacies type. These are translated into percentages in the right hand column. The overall hit-rate for the well is shown, as well as the number and percentage of uncertain and mixed predictions.

| | Predicted Lithofacies | | | | | | |
|---|---|---|---|---|---|---|---|
| Real Liothofacies | | 1 | 2 | 3 | 4 | 5 | % of real lithofacies predicted correctly |
| | 1 | 176 | 75 | 32 | 2 | 4 | 60.9 |
| | 2 | 28 | 47 | 30 | 4 | 2 | 42.3 |
| | 3 | 12 | 19 | 183 | 47 | 43 | 60.2 |
| | 4 | 0 | 0 | 0 | 0 | 0 | - |
| | 5 | 0 | 0 | 1 | 6 | 61 | 89.7 |
| Overall % correct | | | | | | | 60.5% |

**Table 4.2** Confusion matrix for well 23/21-T8 after the thin-bed repair program was applied. Note this matrix is simpler than Table 4.1 since the program has eliminated all uncertain and mixed predictions.

Table 4.4 shows that the action of the thin-bed repair program in this well is to increase the overall hit-rate once again. All lithofacies have improved, apart from lithofacies 4 (that stays the same) and lithofacies 2 which decreases very slightly. Lithofacies 3 has improved by 6%.

Tables 4.5 and 4.6 show the same matrices again but for well 23/21-T3. 56% of this well made up 67% of the training set. This is no doubt the reason for the overall hit-rate being 74.9%, higher than for wells 23/21-T5 and T8. Lithofacies 1 and 3 have high hit-rates (85.6% and 79.2% respectively): these by far make up the majority of this well. Lithofacies 2 is again poorly predicted, even though many of these data contributed to the training set. In most cases in this well it is mixed up with lithofacies 3. Lithofacies 4 is predicted correctly in 57.1% of cases, the highest of the three wells. All of these data though do contribute to the training set. Lithofacies 5 is predicted correctly 70.1% of the time, which is in general high, but slightly lower than for the other wells (although there isn't actually very much of it at all in this well). Table 4.6 again illustrates the action of the thin-bed repair program. The overall hit-rate increases. However this is at 2.6%, far lower than for the other wells. Since this well makes up most of the training set there are fewer 'wrong' predictions and therefore less noise for the program to remove. But it may also be due to the bed thicknesses in this well. In general in well 23/21-T3 beds are thick, and continuous, resulting in less log inflexion points and thin beds.

| | Predicted Lithofacies | | | | | | | | |
|---|---|---|---|---|---|---|---|---|---|
| Real Lithofacies | | 1 | 2 | 3 | 4 | 5 | uncertain | mixed | % of real lithofacies predicted correctly |
| | 1 | 434 | 83 | 39 | 7 | 0 | 24 | 0 | 73.9 |
| | 2 | 13 | 9 | 5 | 5 | 0 | 0 | 0 | 28.1 |
| | 3 | 5 | 23 | 158 | 16 | 16 | 29 | 5 | 62.7 |
| | 4 | 0 | 5 | 17 | 24 | 8 | 4 | 0 | 41.4 |
| | 5 | 0 | 0 | 2 | 4 | 104 | 1 | 0 | 93.7 |
| Overall % correct | | | | | | | | | 70.1% |
| Mixed, uncertain predictions (%) | | | | | | | 5.6% | 0.5% | |

**Table 4.3** Confusion matrix for well 23/21-T5, before the thin-bed repair program was implemented.

| | Predicted Lithofacies | | | | | | |
|---|---|---|---|---|---|---|---|
| Real Liothofacies | | 1 | 2 | 3 | 4 | 5 | % of real lithofacies predicted correctly |
| | 1 | 472 | 70 | 41 | 4 | 0 | 80.4 |
| | 2 | 16 | 7 | 2 | 7 | 0 | 21.9 |
| | 3 | 25 | 24 | 172 | 15 | 16 | 68.3 |
| | 4 | 0 | 6 | 19 | 24 | 9 | 41.4 |
| | 5 | 0 | 1 | 0 | 5 | 105 | 94.6 |
| Overall % correct | | | | | | | 75.0% |

**Table 4.4** Confusion matrix for well 23/21-T5 after the thin-bed repair program had been applied to the results.

| | | Predicted Lithofacies | | | | | | | |
|---|---|---|---|---|---|---|---|---|---|
| Real Lithofacies | | 1 | 2 | 3 | 4 | 5 | uncertain | mixed | % of real lithofacies predicted correctly |
| | 1 | 399 | 18 | 35 | 4 | 0 | 1 | 9 | 85.6 |
| | 2 | 15 | 68 | 68 | 3 | 0 | 0 | 22 | 38.6 |
| | 3 | 11 | 7 | 319 | 9 | 40 | 0 | 17 | 79.2 |
| | 4 | 0 | 0 | 0 | 8 | 5 | 0 | 1 | 57.1 |
| | 5 | 0 | 0 | 4 | 3 | 16 | 0 | 0 | 69.6 |
| Overall % correct | | | | | | | | | 74.9% |
| Mixed, uncertain predictions (%) | | | | | | | 0.1% | 4.5% | |

**Table 4.5** Confusion matrix for well 23/21-T3, before the thin-bed repair program was implemented.

| | | Predicted Lithofacies | | | | | |
|---|---|---|---|---|---|---|---|
| Real Liothofacies | | 1 | 2 | 3 | 4 | 5 | % of real lithofacies predicted correctly |
| | 1 | 404 | 17 | 40 | 5 | 0 | 86.7 |
| | 2 | 17 | 79 | 80 | 0 | 0 | 44.9 |
| | 3 | 19 | 7 | 329 | 2 | 46 | 81.6 |
| | 4 | 0 | 0 | 0 | 11 | 3 | 78.6 |
| | 5 | 0 | 0 | 7 | 0 | 16 | 69.6 |
| Overall % correct | | | | | | | 77.5% |

**Table 4.6** Confusion matrix for well 23/21-T3 after the thin-bed repair program had been applied

Using well 23/21-T8 as a blind test well indicates that the overall hit-rate that the neural network appears capable of is approximately 57%. However this figure must be quoted with caution. Different lithofacies are predicted with different degrees of success and therefore the percentage hit-rate in any one well is determined by the amount of each lithofacies in that well, and the thickness of the beds (i.e. the number of bed boundaries etc.). Lithofacies 1, 3 and 5 are predicted with a fairly high success rate (60%, 60% and 70-90% respectively). Lithofacies 2 however does not appear to be predicted very successfully at all, even in wells where some of that data were used for training. It is most commonly mixed up with lithofacies 1 and 3. Lithofacies 4 does not appear to be able to be predicted very well at all. It is only ever predicted relatively successfully in those intervals that were used for training. This suggests that the logs are incapable of resolving this lithofacies. As mentioned in Chapter 3 this could be due to insufficient data to correctly define this lithofacies.

The action of the thin-bed repair program was to eliminate very thin beds that were not fully resolved, and to eliminate those beds that occurred at log inflexion points, between thicker beds. In all cases this improves the overall hit-rate and specifically it appears to significantly improve the prediction success of lithofacies 3, the most heterogeneous lithofacies.

### *4.4.3 Predicted lithofacies compared to core*

The matrices presented so far indicate the hit-rate by lithofacies type for all three wells. This is the most widely quoted statistic when attempting to determine the success of any methodology that allows rock-type prediction from well logs (e.g. Derek *et al.* 1990). Many papers also present well sections that show predicted lithofacies next to the 'real lithofacies' (e.g. Bhatt & Helle 2002b). However it is the author's opinion that many papers that do show the results in this way devote only a limited well section and small paragraph to this type of analysis. Chapter 1 stated that the main focus of recent work has been on improving the hit-rate and not on understanding and interpreting the output of neural networks. No publications show the network predictions, and the real core defined lithofacies alongside the core description and interprets the results in this context.

It is possible to show all the results bed by bed. It is more productive however to illustrate multiple key sections. Therefore this section illustrates various key well intervals (at a fairly high scale) and compares the results of the neural network directly to the sedimentary facies

column that closely describes the core. Two sections from each well are shown. Figures 4.7 and 4.8 are from well 23/21-T8, Figures 4.9 and 4.10 from well 23/21-T5, and Figures 4.11 and 4.12 from well 23/21-T3. All sections were deliberately chosen as they represent areas where the network commonly appears to have made incorrect predictions. In each case the gamma-ray, neutron, density and deep resistivity logs are shown on the left. The left lithofacies column is the 'real' core defined lithofacies, the centre column is the raw lithofacies predictions, and the right column the repaired lithofacies, with thin-beds removed. The next two tracks show core plug porosity and permeability values respectively. The final five tracks show the activation levels of all five output nodes as described in Section 4.3. On the far right are various sections of sedimentary logs from Cullen (1993a, 1993c and 1993d). These are correlated with the logs and specific areas of interest within each section are highlighted with a dashed line. When a particular section was contained in the training set this is indicated by a black bar in Track 5 (see Figure 4.11). These sections are now discussed. Predictions over other areas of these wells can be found in Appendix 5.

Figure 4.7 shows a 120ft section from well 23/21-T8, mid-way through the Forties Sandstone Member. Overall it can be seen that the neural network predictions do approximately follow the 'real' core defined lithofacies: there is more sand predicted at the top and bottom of the section, the centre is characterised by mostly lithofacies 3. There are many discrepancies though. Figure 4.7 (a) shows an interval where the 'real' lithofacies was described as lithofacies 1, the best reservoir. However the neural network predicts a mixture of lithofacies 1, 2 and 3 (the raw predictions also contain some lithofacies 4). Indeed the actual logs in this interval do not show a 'typical' signature of lithofacies 1, as described in Table 3.2. The sedimentary logs show an interval of facies C1 grading into facies F. Facies C1 consists of interbedded claystone and argillaceous sandstone, which is poorly sorted and has a low porosity (note, sedimentary log symbols were described in Section 3.3). Near the base (i) there is a bed of dolomitic siltstone which is very hard. This corresponds with an increase in the density log, and the neural network predicts lithofacies 1. Lithofacies 1 usually represents sandstone with the highest porosity and permeability, and therefore this rock-type has totally different petrophysical properties. At this point it should be highlighted that some sections of well 23/21-T3 that were very well cemented were interpreted as lithofacies 1, and used for training (e.g. 9853.0 in well T3, see Appendix 5). Therefore horizons that are totally cemented are predicted as lithofacies 1. This is a product of the lithofacies scheme being designed on the basis of general properties (described in Chapter

3). By far the majority of lithofacies 1 cases represent very good quality sand. A very small percentage represent cemented horizons. This therefore presents a limitation of using lithofacies 1 predictions to represent high quality sand in a reservoir model. However since it is only totally cemented horizons (with very little porosity) that are predicted as lithofacies 1 then these could easily be screened using a cut-off on the density and sonic log (these areas are also highlighted in Figures 4.20 and 4.21). The rest of section (a) in Figure 4.7 represents quite heterogeneous sediments that are fairly argillaceous and have variable porosity and permeability. Therefore the neural network predictions appear much closer to the original core than the actual 'real lithofacies'. Figure 4.7 (a, ii) shows a bed that is coarser than much of the rest of this interval and there is evidence of dewatering structures, indicating rapid sandy deposition. This section was predicted as lithofacies 2 which appears reasonable. One final note on this section should point out that the raw lithofacies column predicted some thin beds of lithofacies 4, which is supposed to represent interbedded sand and shale, the sands having a low porosity and permeability. This also appears reasonable.

Figure 4.7 (b) shows a section that is Facies F. A small section in the centre (i) has reduced clay pseudoclasts compared to the rest of this section, and appears sandier. There is also evidence of water escape pipes. The prediction of lithofacies 2 here is reasonable.

Figure 4.7 (c) shows an interval, the whole of which is described as lithofacies FB1, characteristic facies F which shows some elements of facies B1. Clearly the description of FB1 can span nearly the whole spectrum from facies F to B1, and therefore the final interpretation can be ambiguous. Figure 4.7 (c, i) shows a sandy horizon with dish structures and water escape pipes, with high porosity and quite high permeability, predicted as lithofacies 1. Figure 4.7 (c, ii) shows a sandy horizon with high porosity and slightly lower permeability, predicted as lithofacies 2. The slumped admixed claystone interval is predicted as lithofacies 3. Clearly the neural network interpretation is good.

In Figure 4.7 (d) the neural network predicts lithofacies 2 rather than lithofacies 1. At point (ii) the real core was interpreted as facies B1. The porosity is high, however the permeability is moderate. To some extent, in terms of permeability, these predictions are reasonable (i.e. lithofacies 2 should have lower permeability than lithofacies 1). However further down in (e) lithofacies 1 is predicted and the porosity and permeability are similar. However in (d) the resistivity log is lower than at (e) indicating a lower gas saturation. The

neural network model in this instance appears dependent on the resistivity log. Another point to note is that at (d, i) detail is picked out by the network that is missed in the original lithofacies column.

Figure 4.7 (e) shows lithofacies 1 predicted successfully (corresponding to facies B1). Some detail is picked out by the network that is overlooked in the 'real' lithofacies column (i). At this point the raw lithofacies column predicts thin beds of lithofacies 2 as edge effects, and lithofacies 3 and 4 (shown more easily by the activations of lithofacies 2, 3 and 4). After repair by the thin bed-repair program, lithofacies 3 is predicted. The sedimentary logs indicate this interval to be a carbonaceous claystone. This should really be lithofacies 5. The limitation appears to be the resolution of the tools, thus this limitation is obviously contained within the neural network model too. However a change of facies is indicated by the network which was overlooked in the 'real' lithofacies column.

The rest of this page is deliberately left blank

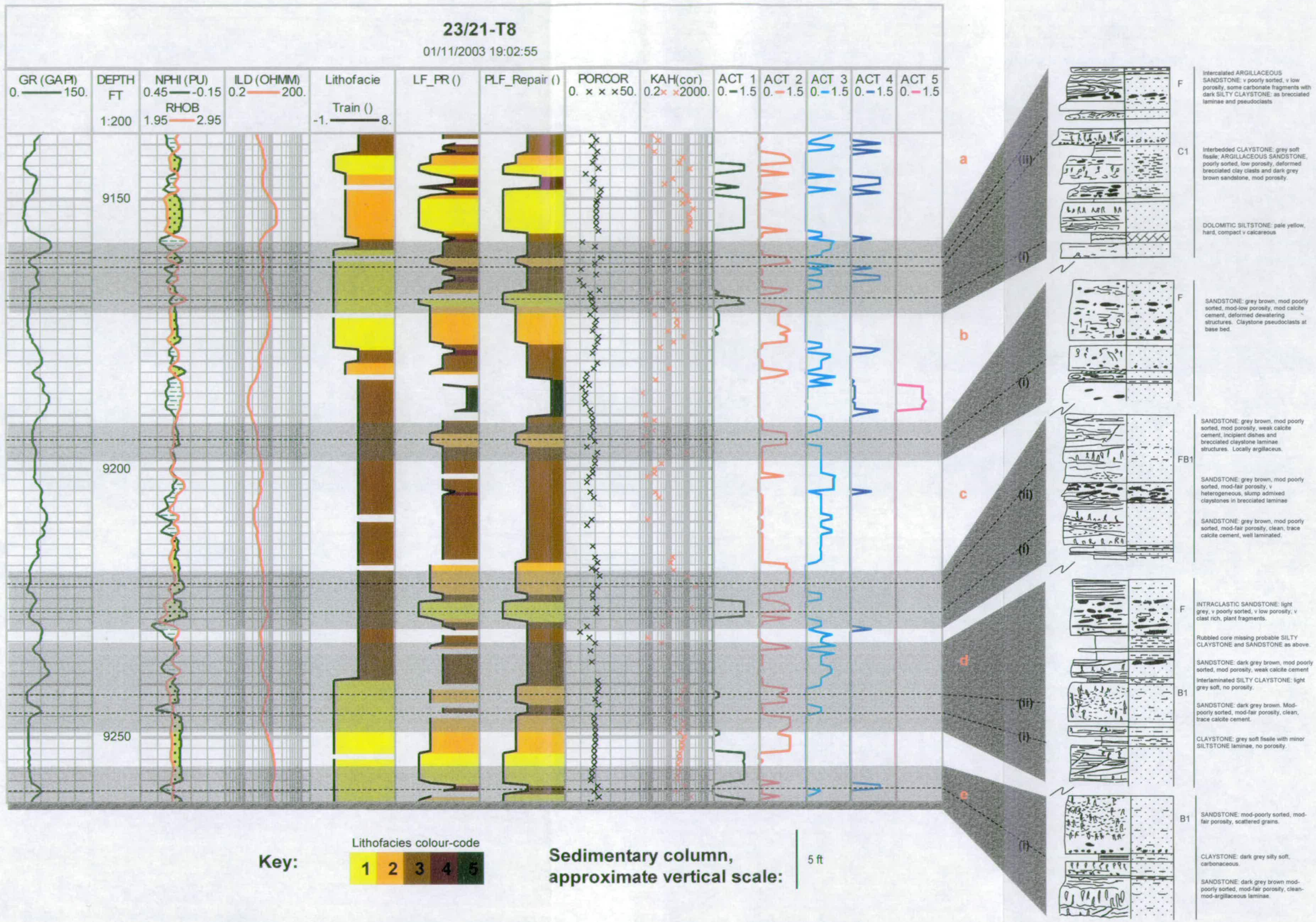



**Figure 4.7** Section from well 23/21-T8. Log headers and sedimentary facies symbols can be found in the notations and conventions section preceding Chapter 1. See text for picture explanation.

Figure 4.8 shows another section from the Forties Sandstone Member of well 23/21-T8. Section (a) shows a similar phenomenon to that of Figure 4.7 (a). The lower part of this section (i) is sandstone that has a very low porosity due to interstitial clay, and dolomite cement. This is indicated by a kick in the density log. The neural network predicts lithofacies 1. A similar prediction of lithofacies 1 at a cemented horizon can also be seen at approximately 9387ft.

Figure 4.8 (b) shows a section that is generally predicted quite successfully. From the top facies FG2 is predicted successfully as lithofacies 5; below this facies F is predicted successfully as lithofacies 3. In this case F is sandy, but has scattered clay grains and claystone laminae and consequently although the porosity is high the permeability is low-moderate. However the sandy nature of facies F is indicated by the activation levels – both lithofacies 2 and 3 output nodes are activated at this point (at ii). Below facies F is bioturbated mud (facies FG2) so the prediction of lithofacies 5 is good. Within this interval of lithofacies 5 the raw lithofacies column predicts some very thin beds of lithofacies 4 (at i). These appear to correspond to kicks in the neutron log to the right (more sandy). Close inspection of the sedimentary log indicates that there are some thin injected sandstones in the mudstone, as well as a very low porosity sandstone bed. The logs appear to respond very slightly to them, enough for the neural network to pick them out. They do however disappear in the repaired column. It is therefore very important for detailed work to view both columns side by side.

Figure 4.8 (c) shows a section of supposedly lithofacies 1 that has been predicted as lithofacies 1 and lithofacies 2. The activation levels for lithofacies 1 and 2 show that in places both output nodes are highly activated throughout this interval, indicating that the logs show elements of both lithofacies. The porosity is high throughout, but the permeability is higher at the top of the section at point (ii). There is therefore some justification for the network's decision. These rocks are essentially on the boundary between lithofacies 1 and 2. If the results were to be used in a dynamic model then maybe the permeability and porosity variograms could be combined and used to populate regions like this.

Figure 4.8 (d) shows bioturbated claystone (lithofacies 5) predicted successfully. Once again the raw lithofacies column predicts some small amounts of lithofacies 4 (at i), that appear to correspond to some very thin injected sands, as in (b).

Figure 4.9 shows a section from well 23/21-T5. As indicated none of this section was used for training. Interval (a) shows an area where at (ii) the network is unable to make a decision between lithofacies 3 and 4 (shown by the activation levels). Unfortunately the lithofacies repair program has eliminated all of this bed and repaired it to be lithofacies 1. A similar type of scenario is seen at (i). Here the sedimentary log indicates an argillaceous sandstone with no visible porosity. The neural network predicts lithofacies 2. Clearly this horizon is not fully resolved by the logs. However the network prediction does appear more accurate than the 'real' column.

Figure 4.9 (b) shows a large section. Towards the base (i) a clay horizon is not fully resolved but is picked out by the network in its raw predictions. This also occurs higher up at (ii) where the gap in the raw prediction represents no output from the network (indicated by the activation levels). The lack of output indicates that it is not typical lithofacies data here. The interval that is b (iii) is predicted correctly. Interval b (iv) corresponds to facies C2, consisting of interbedded sand and shale; some of the sands have tight calcite cement. The neural network predicts beds of lithofacies 1, 2 and 3, which appears a more accurate estimate then the simplified lithofacies 1 that is indicated by the 'real' lithofacies column.

Figure 4.10 is also from well 23/21-T5, and not from the training set. Section (a) shows a section where the core interpretation consists of B1 sand at its base, followed by argillaceous sandstone (facies F), B1 sand again, and then C1 sand on top of this. The neural network predictions indicate the whole interval to be sandy. The activation levels show that the network estimates this interval to be mostly lithofacies 2, with small amounts of lithofacies 1 3, and 4. The repaired column simplifies this so that the whole section is lithofacies 2. Although the porosity is high, the permeability is variable ranging from 5 to 100md (approximately) with most in the 20-50md range representing the moderate-poor sorting and weak cement in this interval. These permeability values fall into the typical range of BF and CF facies, and lithofacies 2 (see Figure 3.10). Therefore the predictions are perfectly reasonable even though they do not match the 'real' lithofacies column.

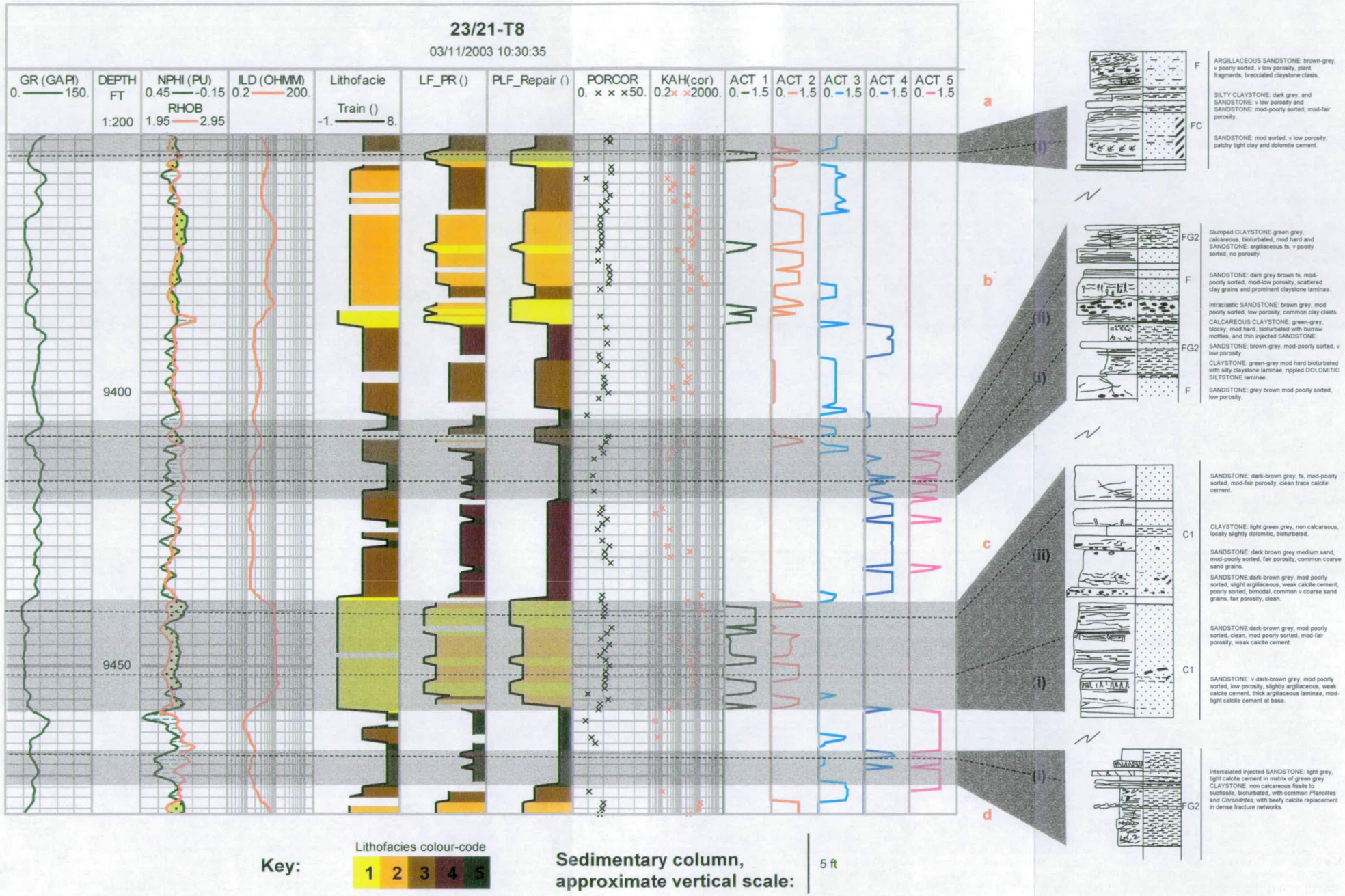



**Figure 4.8** Section from well 23/21-T8. Log headers and sedimentary facies symbols can be found in the notations and conventions section preceding Chapter 1. See text for picture explanation.

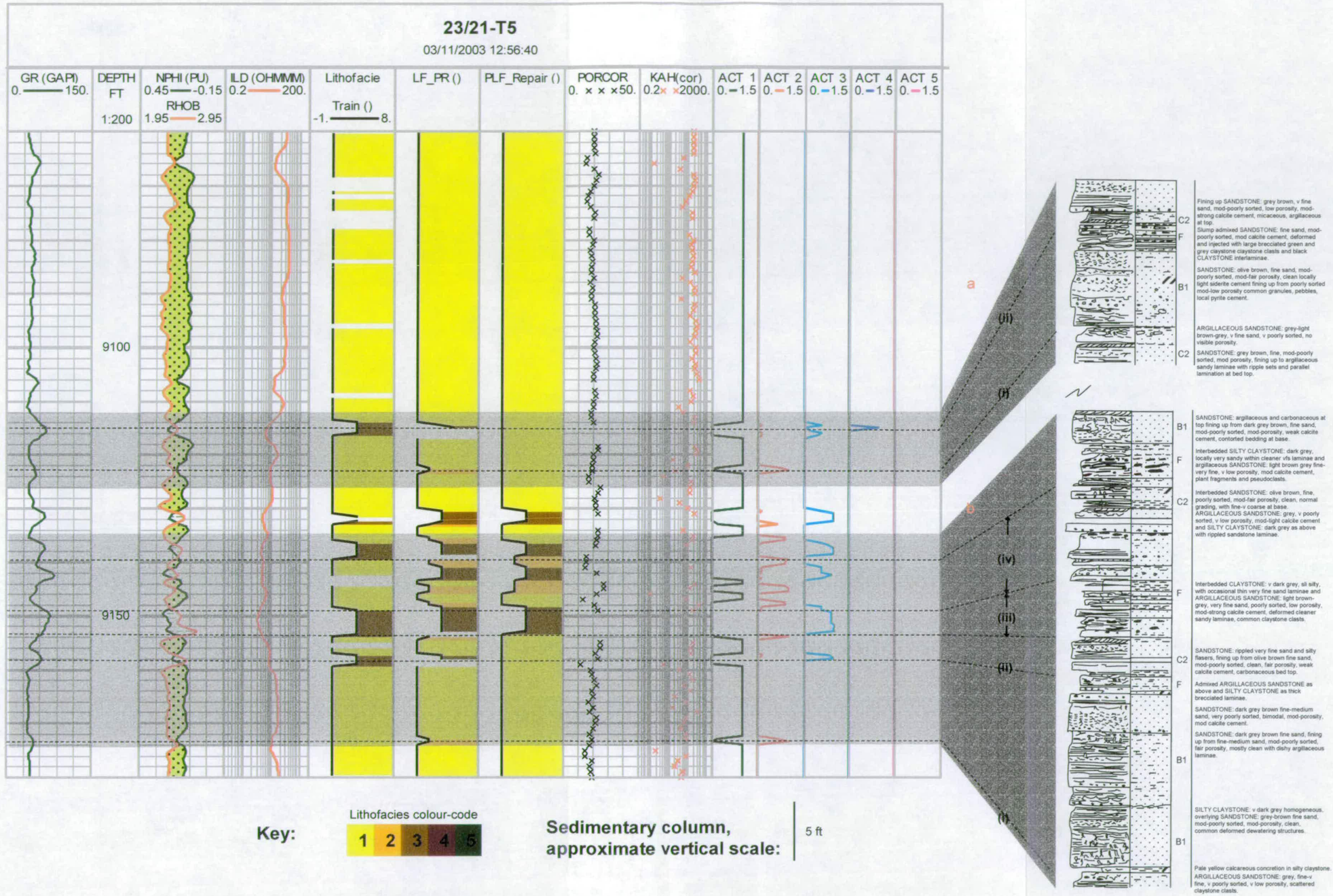



**Figure 4.9** Section from well 23/21-T5. Log headers and sedimentary facies symbols can be found in the notations and conventions section preceding Chapter 1. See text for picture explanation.

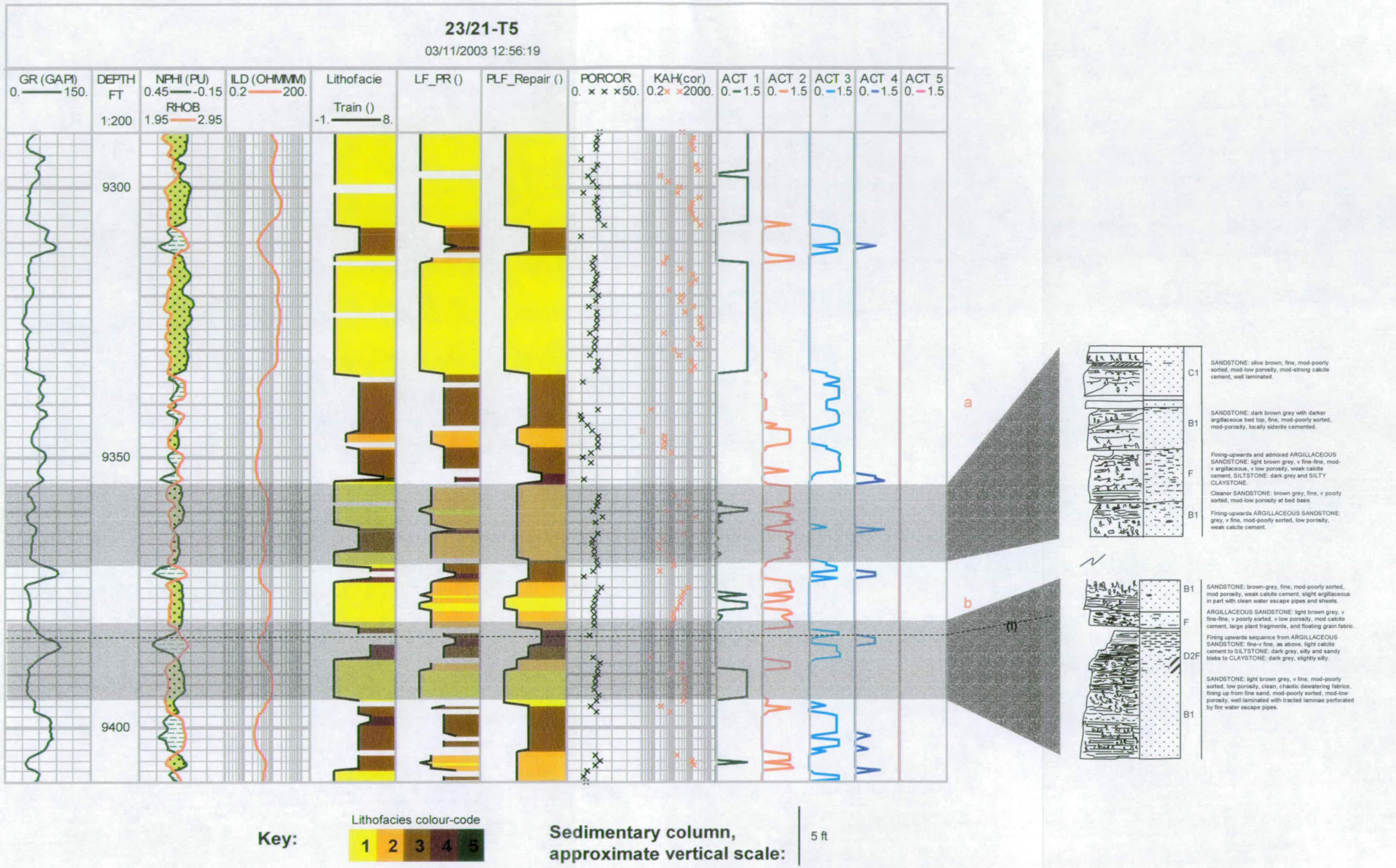



**Figure 4.10** Section from well 23/21-T5. Log headers and sedimentary facies symbols can be found in the notations and conventions section preceding Chapter 1. See text for picture explanation.

Figure 4.10 (b) shows a section with B1 sands at its base that grades into sandstone with cement, and then into siltstone and claystone. The neural network predictions show lithofacies 1 and then 2 above this, and then lithofacies 3 a more heterogeneous and argillaceous rock on the top. A porosity or permeability profile based on these lithofacies predictions would result in a section showing reduced porosity and permeability upwards. This is exactly what is present. The interval of lithofacies 4 (i) above the fining upwards sequence corresponds to facies F in the sedimentary log. Facies F here has a very low porosity, and so the network estimate here is also reasonable.

Figure 4.11 is a section from well 23/21-T3. The majority of this section was contained in the training set (indicated by the black bar in track 5). Up until now suspicion has been drawn upon evaluation the networks performance from sections that were used for training. They generally tend to be predicted very well (probably the most likely reason why the confusion matrices of wells 23/21-T3 and T5 indicated higher overall hit-rates than well 23/21-T8). This is because this data actually defined the exact place where the neural network places its decision line, and therefore this is partly to be expected. However this section shows data that was contained in the training set, but where the neural network has predicted different lithofacies to the 'real' core defined lithofacies. In Figure 4.11 (a, i) the neural network has predicted lithofacies 1, good quality sand, and it can be seen that there is a high porosity and permeability (most core values are above 100md), so the prediction is correct. Below this although the facies was described as B1 and CB, the B1 sands contain large claystone clasts. These result in a lower and more variable porosity, and a much lower permeability. The neural network predicts lithofacies 3. Clearly this is a reasonable estimate of the lithofacies type. Above the good sand at the interval labelled (ii) the B1 sand is described as having a slumped top. This along with the C2 shaly bed means that the neural network has predicted lithofacies 3. The porosity and permeability values are all very high, suggesting that it should in fact be lithofacies 1 that is predicted. However these measurements were taken from very small core plugs and clearly from the more sandy parts (i.e. not in the shaly bed labelled C2). The neural network predictions are from the logs that are reading the 'bulk' rock signature (albeit with some smoothing). Therefore the predictions suggest more complexity in the rocks than is seen by the 'real' lithofacies column and the porosity and permeability values. This complexity is observed in the sedimentary log.

Figure 4.11 (b) shows lithofacies 5 predicted when the core defined lithofacies is 4. However this represents the very shaly bed within the facies F interval in the core. Since this is probably close to one of the most shaly intervals expected to be found (illustrated by the gamma ray and neutron logs as well as the sedimentary log), the network prediction seems reasonable.

These two last sections show that even though intervals that are contained in the training set are generally predicted correctly, the network has captured the 'general' relationships between the lithofacies and is not overtrained (see Chapter 2 for an explanation of this). If part of the training set does not fit into the general pattern, the network will highlight these sections by predicting a different lithofacies.

The final figure in this section is Figure 4.12 from well 23/21-T3 and not contained in the training set. In section (a) the raw predictions are fairly noisy. The nodes of lithofacies 1, 2, 3 and 4 are all activated to some extent, indicating uncertainty in predictions. In this example the thin-bed repair program does a good job of tidying up the predictions. The repaired column matches the real column, but more importantly also matches the actual core. Where the lower B1 sands represent high quality typical sand they have been assigned to lithofacies 1 (at i). The interval on top of the B1 sands (base of interval labelled ii) has mostly been assigned with facies FB1 above. Intervals have been indicated whereby facies FB1 appears closer to lithofacies 2 (lithofacies 1 with some slight slumping). However in this case the network has made its judgement and decided that it is most like lithofacies 3. The internal slumping and abundant claystone clasts appear to validate the networks decision. Above this (at iii) the network has predicted the B1 sands correctly, and above these (at iv) lithofacies E (low porosity sand) and F have been predicted as lithofacies 3.

Figure 4.12 (b) shows an interval where the network is uncertain. The activations of all the nodes are very low and consequently the raw lithofacies column shows a thin gap. Unfortunately this detail is lost when the thin-bed repair program tidies up the predictions.

Figure 4.12 (c) shows a section that is similar to that in (a ii) above. The core is described as facies FB1, but here the network has decided that this interval is quite sandy and the heterogeneity is less than in (a, ii) and consequently predicted lithofacies 2. This appears a reasonable estimate, as there appears less clay pseudoclasts than in (a, ii).

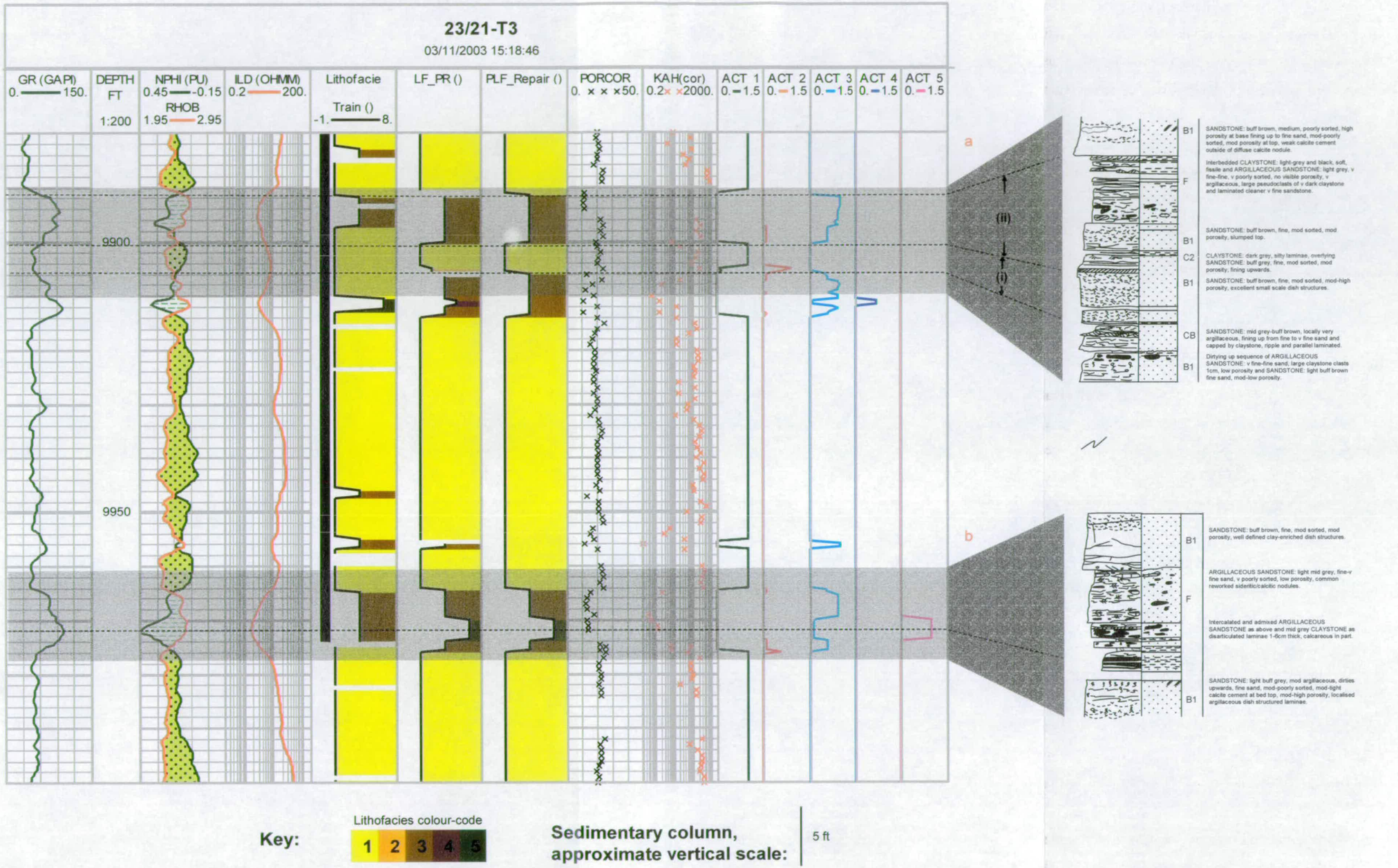



**Figure 4.11** Section from well 23/21-T3. Log headers and sedimentary facies symbols can be found in the notations and conventions section preceding Chapter 1. See text for picture explanation.

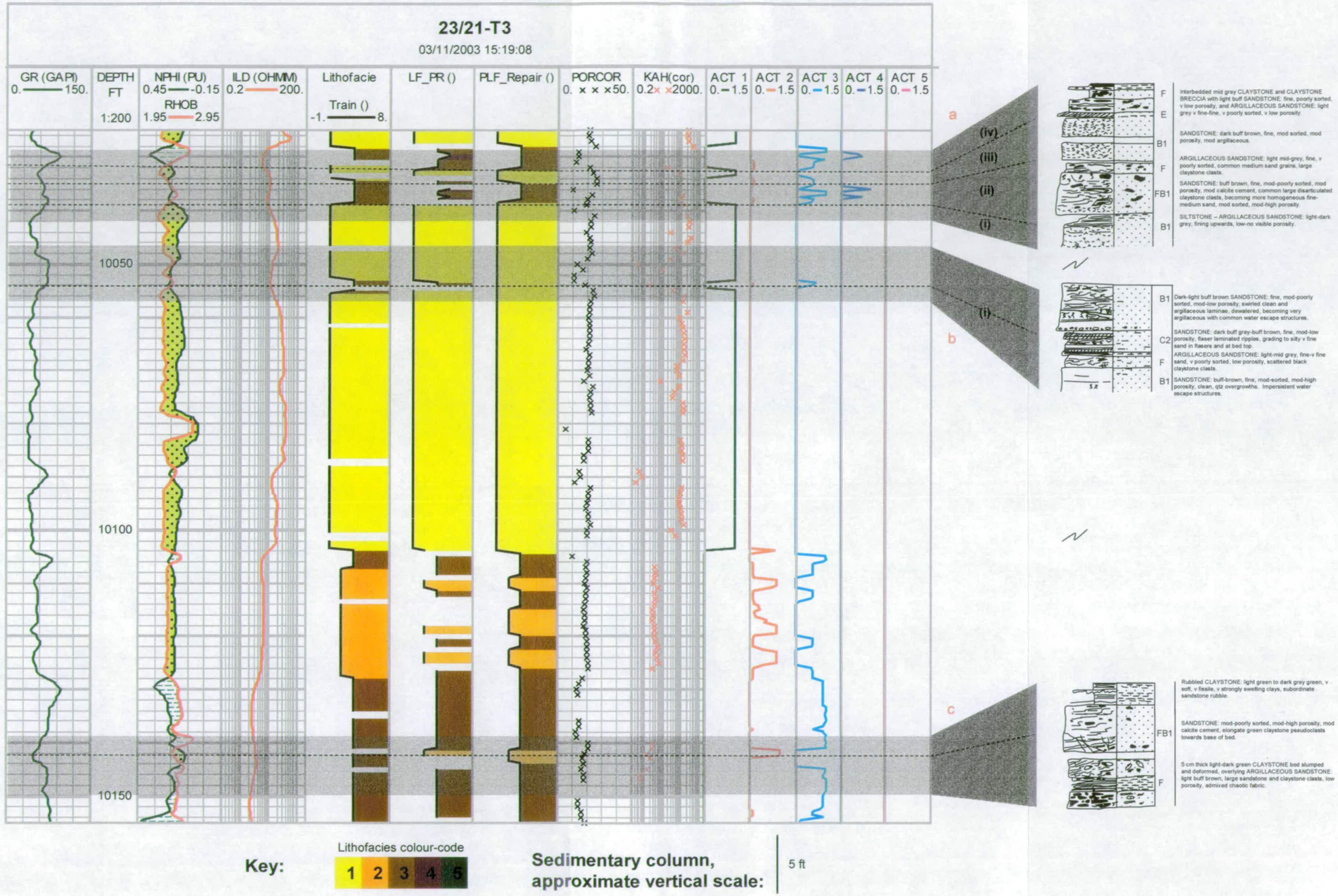



**Figure 4.12** Section from well 23/21-T3. Log headers and sedimentary facies symbols can be found in the notations and conventions section preceding Chapter 1. See text for picture explanation.

### *4.4.4 Lithofacies predictions in wells 23/21-T8, T5 and T3 – summary and discussion*

The confusion matrices indicated that the network was capable of predicting lithofacies correctly approximately 60% of the time overall. Lithofacies 1, 3 and 5 tended to have success rates of 60-90%. Lithofacies 2 tended to get mixed up with 1 and 3 a lot, and this reduced its hit-rate significantly. Lithofacies 4 did not appear to be predicted correctly at all. However comparison to core indicated that in many places where the neural network did not match the 'real' lithofacies column the predictions actually seemed reasonable. The network appeared to have learnt *typical* properties of each of the different lithofacies. The typical properties (defined by the network) appear as follows. Lithofacies 1 represents high porosity and permeability sandstone deposited from high density turbidity currents *or* areas that are cemented and have no porosity (this is commonly calcite or dolomite cement). Lithofacies 2 is more heterogeneous than lithofacies 1, the porosity is high but the permeability tends to be lower. This is because the sediments are generally more poorly sorted due to the sandstone having an argillaceous component or because of scattered clay grains or minor shale clasts. Lithofacies 3 represents heterogeneous argillaceous sediments with highly variable porosity and permeability. These commonly contain clay pseudoclasts in a sandy matrix, deformed and claystone laminae or frequent scattered clay grains. Siderite or calcite nodules are also commonly present. Lithofacies 4 appears to represent thin sands, usually with low porosity and permeability occurring within thicker shale units. Sometimes these sands are interpreted as being injected. Although it cannot be suggested that lithofacies 4 is predicted very well overall, in these instances, predictions appear reasonable. The hit-rate suggested in the confusion matrices for this lithofacies could be a lower limit. Lithofacies 5 represents intervals of shale and claystone, bioturbated or laminated. This facies can also represent beds of sand that are totally dominated by claystone clasts, although this is rare. Although lithofacies 1, 2 and 3 do tend to get mixed up, generally where they are predicted the above descriptions hold true.

The viewing of the results adjacent to the core descriptions has also revealed many other features. It was noted that lithofacies 1 was predicted in a number of places where the core was very well cemented. This represents a limitation if these results were to be used to populate any dynamic reservoir model. This is a consequence of some small intervals that were all consistently cemented being assigned to lithofacies 1 in the training set. Since it appears that all totally cemented horizons are predicted as lithofacies 1, and these are easily

identified by the density log, then it would be possible to screen these out using a density and sonic log cut-off, before the results were used in any dynamic model.

The results also illustrated some of the limitations of using the thin-bed repair program. For overview work, quick-look interpretations, correlation of intervals between wells, and bulk upscaling for instance, the repaired column is much more useful; it is smoother and more geologically consistent. However many places were observed where the raw column picked out detail that was lost after the thin-bed repair step was implemented. Thus it is useful to keep the raw predictions (and the activation levels), if detailed interpretation is necessary.

The core results also showed that when predictions are made in intervals used for training the network is not restricted to predicting the 'real' lithofacies that it was trained on. This shows that the network is not overtrained, and that it has found 'typical/general' relationships for each lithofacies.

Many sedimentary facies descriptions in the logs were assigned codes such as FB1. This means that the rocks are facies F. i.e. slump sheets or debris flows, with highly variable porosity and permeability. The B1 notation means that the rocks also show elements of facies B1, for instance maybe the rocks have a fairly high sand content and there are dewatering structures present. Some intervals are described as facies B1F, which is clearly a typical B1 facies that shows elements of facies F (maybe there is some minor slumping for instance). There is a whole spectrum of rocks between a typical B1 and F type facies and the assignation of a facies code is very subjective. Also the facies codes assigned by Cullen (1993a, 1993c, and 1993d) are *sedimentary* facies codes, and relate to process of deposition not to log values. In Chapter 3 a lithofacies scheme was designed that was partly based on sedimentary facies. Similarities and differences in petrophysical properties and the log values of different facies were also considered. The lithofacies scheme it was hoped could then be used in a 'sedimentary' way – i.e. if the lithofacies were to be used to populate a reservoir model they could be assigned specific 3-dimensional properties. Many of the facies obviously overlap in their properties. What the network has achieved is that it has found the *typical* properties of the different lithofacies. In the vast majority of cases the network model picks out finer detail that *is* actually present in the core. It has been shown that some intervals of facies F are much more like typical facies 1 and 2 rather than 3. If they are then the network will predict 1 or 2, not 3. If a section of B1 sands (usually

lithofacies 1) has a slightly lower permeability and it is predicted as lithofacies 2 then this is probably closer to the truth than if the network had predicted lithofacies 1. A variety of sections have been shown that illustrates this. Thus the author believes the overall hit-rate to be much higher than that suggested by the confusion matrices (75%?). The results tend to show sensible results in all wells, and at all levels. These findings are discussed further in the context of other literature in the discussion chapter.

## *4.5 Lithofacies predictions in well 23/21/T4*

### *4.5.1 Introduction*

In Chapter 3 it was recognised that well 23/21-T4 was fundamentally different in its log signatures than other wells. This was found this by studying the shaly section of the Sele Formation (S2 and S3 in Figure 3.3), and plotting histograms of log distributions by well. The sonic log showed a much lower transit time (higher velocity), and the induction log a higher resistivity. Unfortunately the neutron and density logs were not recorded through this section of the Sele Formation. Possible reasons cited for this were: the intervals of interest (the Sele Formation, and the Forties Sandstone Member with it) occurring much deeper in this well than in wells 23/21-T3, T5 and T8; the logs were acquired using LWD (logging whilst drilling), rather than conventional wireline (so logs that read close to the well bore such as the density log would read the true formation rather than the invaded zone (Ellis 2003)); also the density data were uncalibrated due to rotation of the stabiliser (Walsgrove 1996). It was shown that the log properties of different lithofacies in this well overlapped significantly with each other, and for this reason this well was not included in any of the training sets. In this section well 23/21-T4 is studied in more detail. The model is applied to the well and the results assessed in the light of the above information.

### *4.5.2 Lithofacies predictions*

The optimum neural network model was applied to well 23/21-T4, and the results are shown as Figure 4.13. The neutron and density logs were recorded from 13463ft downwards (within the Forties Sandstone Member), so the predictions run from this depth down to the base of the Forties Sandstone Member at 13915ft (taken from Cullen 1993b).

In Figure 4.13 the neutron, density and resistivity logs are shown on the left. The left most lithofacies column is the 'real' core defined lithofacies. The next column (LF_PR) is the raw lithofacies prediction. The first characteristic that one recognises in this column is that there are significant gaps in the predictions, especially towards the base of the section. These are areas where no predictions or mixed predictions have been made. The last five tracks show the activation levels of output nodes 1 to 5, and it can be seen that in many cases more than one node is highly activated at any one depth level (towards the bottom output nodes 3 and 5 are often highly activated together for instance). In all previous well sections shown in this thesis, multiple outputs were left blank in the raw predictions; in these cases the gaps tended to be small. In this well the gaps are significant. For this reason a new column is presented (LF_PRmax) *L*itho*F*acies *P*redicted *R*aw, from the *Max*imum activation level. In this column the highest activation of all the outputs is accepted as the predicted lithofacies (usually only if the activation is > 0.5 this results in a prediction). This column is the third lithofacies column. The fourth lithofacies column is the raw predicted lithofacies from the highest activation level after the thin bed repair program had been implemented (with a thin bed having a maximum thickness of 1.5ft as for earlier wells). Core porosity and permeability values are also shown.

At the top the results appear reasonable. At point A the predictions appear to match the 'real' column, and the neural network has made a single prediction. The porosity is moderate and the permeability variable, thus these predictions appear reasonable. At B the network predicted interbedded lithofacies 2 and 3 which again appears reasonable especially in the light of the results of the previous section. However the density log is exceptionally low around point B (as low as 1.95g/cm3). Considering the low gamma-ray the rocks appear sandy, but the resistivity is low-moderate indicating that there is very little gas. The measured core porosity is not exceptionally high either, so the density values appear erroneous when compared to other sections of this well.

At C is one of the few sections where the logs appear to record fairly 'normal' results. There is a small but reasonable neutron-density separation, the gamma-ray is low, and the resistivity is responding to gas. The permeability is in the 20-50md zone which is approximately correct for the predicted lithofacies 2.

However further down at D is where there are significant errors in the predictions. The gaps in the second lithofacies column indicate that the network was having difficult making a decision. The activation levels show that the network is having difficulty choosing between lithofacies 3 and 5. However in most cases lithofacies 5 has the highest output. The gamma ray is low so that conventional log interpretation would indicate that this is not shale. If the predictions were a mix of lithofacies 2 and 3 this would appear reasonable. However the network is clearly wrong as it is mixing up the sandiest and shaliest lithofacies. The reasons

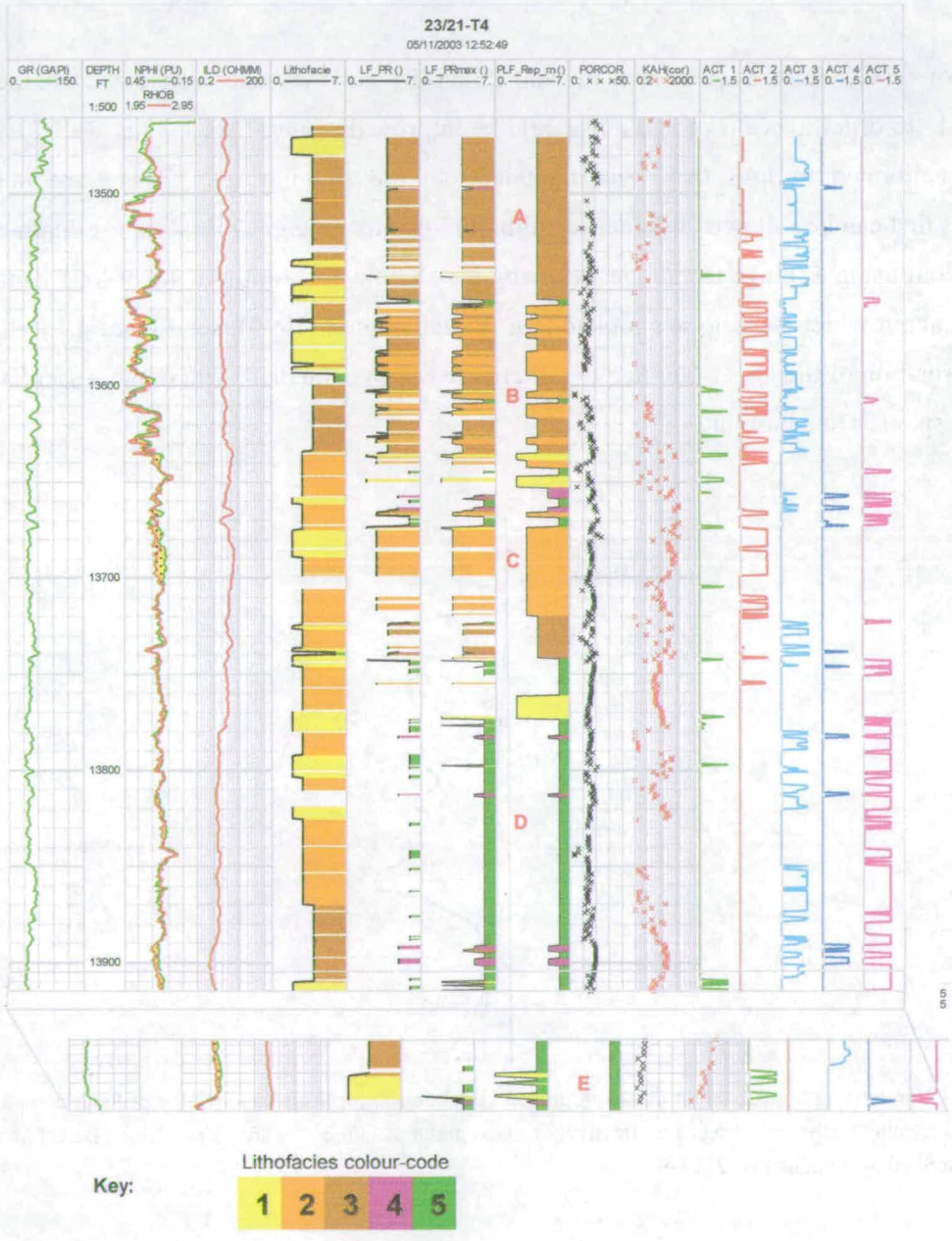



**Figure 4.13** Results obtained when the optimum model was applied to well 23/21-T4. See text for more details.

for this could be due to any of those already mentioned. However, the model was unavoidably trained on data taken from the gas interval. Thus good sand tended to have a high resistivity. Therefore poor predictions could be because of low resistivity values. Around point D in Figure 4.13 as the resistivity is fairly low, indicating a transition or water zone. However at point E some lithofacies 2 has been predicted in the raw column. The resistivity is low and approximately the same value as around D. A low resistivity cannot be singly responsible for the erroneous predictions. Discussion about the dependency of the model on fluid and its possible limitations are discussed in Section 4.7.

So far poor results have been shown in well 23/21-T4 but the exact cause has not been established. In order to see if predictions could be improved some of the logs in well 23/21-T4 were calibrated to logs that were contained in the training set. There are many procedures that can be followed in order to calibrate log curves: e.g. calibration for depth can be carried out using a 'hinge technique' whereby the shallowest point in a set of logs is used as a hinge about which the logs are rotated (e.g. Vaughan *et al.* 1999), see Figure 4.14. The degree of rotation of the logs is applied to effectively remove the drift with depth, essentially aligning responses to a baseline.

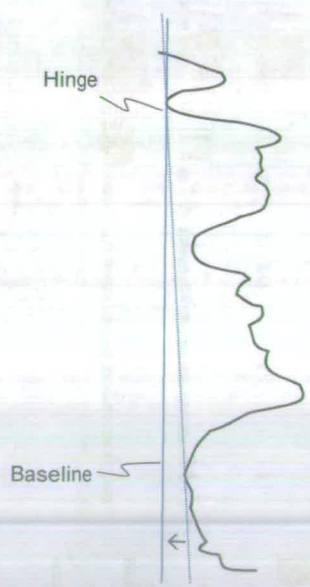



**Figure 4.14** Normalising log curves for depth. A greater correction is applied to a log value at depth compared with the same value further up. Logs are effectively rotated about a 'hinge' towards a base line. Based on the method described by Vaughan *et al.* 1999.

Since the exact reason why the log values in well 23/21-T4 are different from other wells was uncertain a very simple calibration procedure was applied. For the sonic and resistivity logs the histograms of the log readings in the shaly interval of the Sele Formation were taken (Figure 3.21) and the median value was calculated. The median was then calculated for well 23/21-T3 (that made up the bulk of the training set). The difference between these two medians was the bulk shift that was then applied to the relevant curve in well 23/21-T4 (see Figure 4.15). As stated already the neutron and density log values in this section of the Sele Formation were not recorded. How can these logs be normalised? An attempt was made to normalise these curves by choosing the most 'typical' sandy interval in well 23/21-T4 - for instance the interval approximately at point C in Figure 4.13 (13675-13693ft). This represents data that 'looks' most similar to data in other wells. The gamma-ray is low, there is a reasonable neutron-density separation, and the resistivity is at its highest, indicating a response to gas. The neutron and density values in this interval were compared to a similar interval in well 23/21-T3. This interval is shown in Figure 4.16. It was chosen not only because it is in the training set but also because its gamma-ray value is very low, and its resistivity value similar (the same order of magnitude) as the original resistivity curve and the new normalised resistivity curve, thus the gas saturation may be similar. Figure 4.17 shows histograms of the neutron and density log values corresponding to these two intervals. The histograms are revealing in that the neutron responses are very similar. It is the density logs that are different, 23/21-T3 having a lower reading than in 23/21-T4. This appears to correlate with the fact that the density log was uncalibrated when the data were recorded (Walsgrove 1996). The density log was normalised via a single bulk shift as described in Figure 4.17.

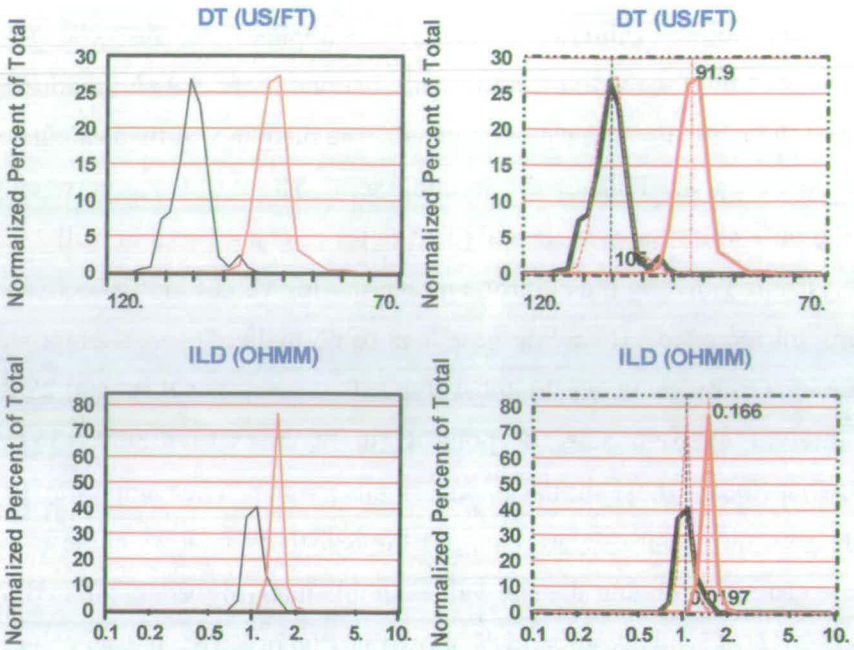



**Figure 4.15** The top left histogram shows the distribution of sonic log values in the shaly section of the Sele Formation in wells 23/21-T3 (black) and 23/21-T4 (red). Also shown (top right) are the calculated medians of both (91.9 for T4, 105 for 23/21-T3). The difference between these values was the bulk shift applied to the sonic log in well 23/21-T4. The lower histograms show the same relationships but for the resistivity log (the medians are 0.166 for well 23/21-T4 and 0.097 for well 23/21-T3; note that these are the log of the actual median values).

This method is similar to a normalisation procedure used by Vaughan *et al.* (1999) to normalise for different logging environments and tools. In that case, for cored wells, core photos were used to 'match' similar rock types; for uncored wells the procedure was the same as described here. The neutron log in well 23/21-T4 was not normalised.

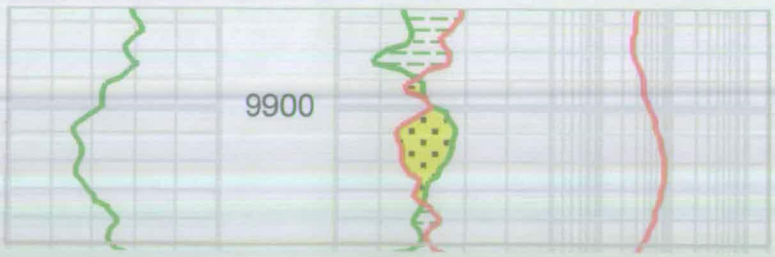



**Figure 4.16** Section from well 23/21-T3. From the left, gamma-ray, neutron (green) and density (red) and resistivity logs. The sandy interval shown was taken and a similar interval in well 23/21-T4 was normalised to this – see below, Figure 4.17. Each vertical box represents 2ft.

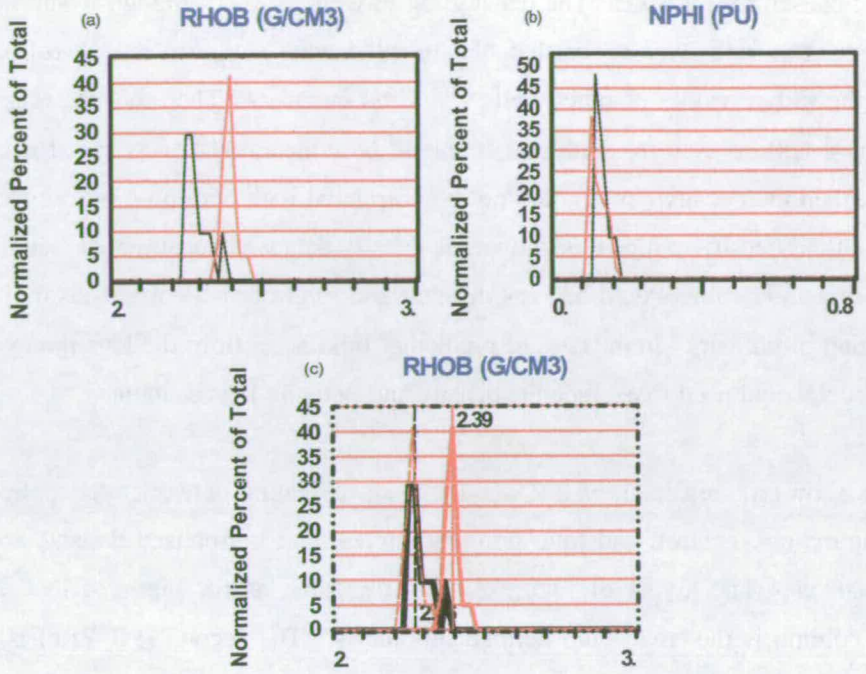



**Figure 4.17** Normalisation of the density curve in well 23/21-T4.

(a) The distribution of the density log values for the intervals described in the text and in Figure 4.16. The discrepancy of the density readings, compared with the neutron readings (b) could be because the density log was uncalibrated.

(b) The distribution of neutron log values for the same intervals as in (a).

(c) The normalisation of the density log. The median value in well 23/21-T4 is 2.39, in well 23/21-T3 2.26. The difference is the bulk shift that was applied to the density log in well 23/21-T4.

Other logs required for input into the neural network model are a total porosity curve and a neutron-density separation curve. A new neutron-density separation curve was calculated using the new normalised density (see Appendix 1 for the methodology). The total porosity curve was left the same, rather than being recalculated from the new normalised density log. This was because initially fluid density values (needed to calculate porosity – see Appendix 1) were taken from Walsgrove (1996). When estimating porosity Walsgrove divided the well up into three zones based on the density log, and correlated these data to core plug values. Thus if this procedure was done with the new normalised density log the fluid density would change and the resulting total porosity would be the same as before. It should be noted though that this does produce a dilemma; if well 23/21-T4 was uncored then how would the total porosity be estimated? A fluid value would have to be determined by the petrophysicist based on an estimation of the hydrocarbon type and density (that may be based on information from other wells). In the case of Lomond in all uncored wells the same

values were chosen for all wells. The density log in well 23/21-T4 though would have read the true formation resistivity rather than the invaded zone (because it was collected via LWD), so the filtrate values of other wells would be incorrect. Therefore the original total porosity curve will be used for analysis. It should be understood however that if core was unavailable then the density curve could not be correlated with core plug porosity values to estimate the fluid density. Since it is known the density data was uncalibrated then the actual estimation of a fluid value would be very difficult and might provide a serious limitation to the calculation of porosity. In the case of predicting lithofacies from the logs it may well be that any model would need to exclude the density and porosity logs as inputs.

Figure 4.18 shows the results in well 23/21-T4 when the neural network was applied to the original gamma-ray, neutron and total porosity curves, and normalised density, sonic and resistivity curves. The layout of Figure 4.18 is the same as for Figure 4.13. The first lithofacies column is the 'real' core defined lithofacies. The second (LF_PRn) is the raw lithofacies predictions from the normalised data. The third (LF_PRmaxn) is the same but with the maximum activated node taken as the predicted lithofacies. The final column LF_PRmaxnR is the third column but after the thin bed repair program had been implemented.

One can see immediately that the normalisation of the density log has meant that the neutron density separation is much greater, indicating a much more sandy interval overall. This corresponds with the gamma-ray that is generally low throughout. It can be seen that the raw column has much fewer gaps than in Figure 4.13. This means that there are fewer multiple outputs and fewer 'none' outputs. Clearly the normalisation procedure must have brought some of the data into the hypothesis space defined by the network. There is less ambiguity in the results. The top part of the section is similar to before – the results are reasonable with mostly lithofacies 3 predicted. At A some thin beds of sand are predicted that correspond approximately with the real lithofacies. At B lithofacies 2 predictions now correspond with a high permeability zone, and the interval around C appears closer to the 'real' core than the previous predictions; now the network predicts mostly lithofacies 2 (rather than 3 and 5).

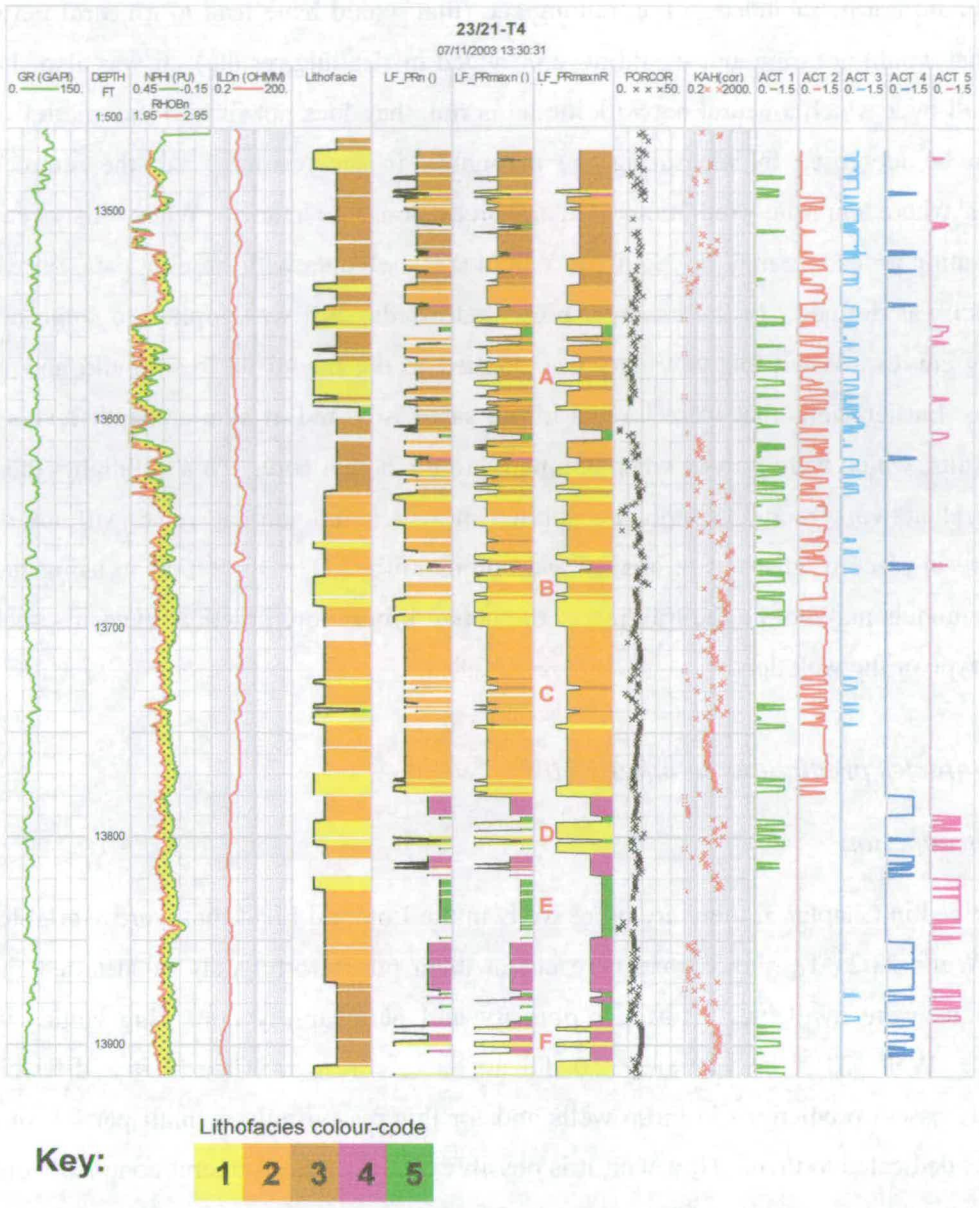



**Figure 4.18** Neural network results in well 23/21-T4, for normalised data.

Also at F some lithofacies 1 is predicted (before this was lithofacies 4 and 5) which corresponds to a high permeability zone. There are though still problems at E where mud is predicted in an area of low gamma ray, and the real core indicates the rocks to be sandy. Potential reasons for this were discussed and the exact reasons for the ambiguity were not resolved. Using a simple procedure it was possible to highlight well 23/21-T4 as being different from other wells before generating any training sets. This was clearly a very important step in the procedure as it highlighted the well for special treatment, and indicated

that it should not be included in the training set, (that would have lead to a neural network model that would not train and would have provided misleading results). It was also shown that a well over which a neural network model is run, that does not fit into the 'model' very well can be identified by measuring the ambiguity in the results – i.e. the number of instances where multiple predictions and no predictions are made. When this occurs a normalisation procedure may be required to align that well data with training data, on which the model was defined. In the example presented a bulk shift was applied to some of the input log curves. When this new data was applied to the model the results did appear to improve. Earlier wells that were logged in the same way and at similar depth levels had good results, which were proved when compared to the actual core. This highlights the fact that neural network models cannot be applied at will to numerous wells, without some procedure in place to check data quality and compatibility. The limitation in using neural network models may not be the training of the network but more practical elements such as the tool type or the well depth.

## *4.6 Lithofacies predictions in other wells*

### *4.6.1 Introduction*

As described in Chapter 3, there are more wells in the Lomond Field that were available for study. Wells 23/21-T1 and T2 had core cut in them but unfortunately no detailed facies descriptions were available. However porosity and permeability core plug values were available. Wells 23/21-T6, T9 and T10 did not have core cut. Clearly it is difficult to accurately assess predictions in these wells and for this reason only a small portion of this chapter is dedicated to them. However, it is possible to make some general comments on the predictions, which are presented below. Wells 23/21-T1 and T6 are also discussed further in Section 4.7.

### *4.6.2 Predictions in wells 23/21-T1, T2, T6, T9 and T10*

The shaly section of the Sele Formation was identified in all these wells, and histograms of the logs in this interval created. These were compared to the histograms of wells 23/21-T3 and T5 that contributed most to the training set. It was found that all the log signatures of wells 23/21-T1 and T2 showed similar distributions to wells 23/21-T3 and T5. However as for well 23/21-T4 the sonic and resistivity logs of wells 23/21-T6, T9, and T10 showed

significant deviation. In the case of well 23/21-T6 this could be because this well occurred deeper than the training wells (the Top Sele is approximately 400ft deeper than 23/21-T3 and T5), however the density log does not show any deviation. Well 23/21-T9 occurs at a similar depth to the training wells, but 23/21-T10 is approximately 300ft shallower. The deviation in these wells could be due to tool type. Both 23/21-T9 and T10 (the most recently drilled wells) use DT4P (compressional wave from P and S wave sonic tool) and AHT90 (array induction tool) rather than the conventional DT and ILD, as in the older wells. The optimum model was run on the raw data in all these wells; the results can be found in Appendix 5.

Despite the above comments wells 23/21-T9 and T10 appear to show good results. There are very few mixed and 'none' outputs and the main reservoir intervals are predicted successfully as lithofacies 1. Non-reservoir intervals with the highest gamma-ray values are predicted as lithofacies 5 with some thin horizons of lithofacies 4. Areas with intermediate sand/shale signatures and rapidly changing logs are predicted as lithofacies 3.

Wells 23/21-T1 and T2 to a certain extent show similar results. The main reservoir intervals appear in the correct place. What is noticeable (especially in 23/21-T1) is that the amount of lithofacies 2 increases and lithofacies 1 decreases towards the base of the reservoir interval, where the resistivity log is lower. This could be due to reduction in gas saturation and therefore the resistivity log value with depth. Towards the base of the Forties Sandstone Member lithofacies 4 is predicted, interbedded with lithofacies 5.

Most noticeable of the predictions in well 23/21-T6 is that most of the main reservoir interval is predicted as lithofacies 2. It can be questioned whether this is correct as the majority of the other wells' reservoir intervals are made up of lithofacies 1. The reasons for these predictions are discussed further in the next section.

## *4.7 The dependence of the neural network model on reservoir fluid*

### *4.7.1 Introduction*

This section attempts to answer the question: 'which logs in the neural network model contribute most to the final outcome?' This question can be difficult to answer exactly, and is why some potential users of neural networks for log analysis prefer to use other methods.

The next subsection illustrates a number of methods that can be utilised to answer this question. It will be shown that the network is very dependent on the resistivity log, and consequently on the gas saturation in the rocks. This is because the majority of the training data was drawn from the gas legs of the various wells used (this is where the core was cut). Therefore a serious limitation of using the model is that it may not work very well in water zones or transition zones. These sections make up important parts of any geological model. Bhatt & Helle (2002b) illustrate how a neural network model can be trained to predict lithofacies irrespective of fluid type when sufficient training data (i.e. core) is available from all fluid zones. Core is always cut in the reservoir interval but then generally only in the hydrocarbon zone. Assessment of the model dependence on the resistivity log is followed up by the training of a new model without this log (although other logs are affected by fluid type, the resistivity is by far the most affected log). An attempt is then made to improve performance by standardising all input logs to a single fluid type. Discussion of the method used and results from this analysis are also contained within this section.

### *4.7.2 Methods for assessing the dependence of the model on various well logs*

Since it is the weights on the connections between various nodes in the network that actually describe the decision surfaces and therefore the output from the network it is these that one should turn to assess the dependence of a model on various input logs. Wong *et al.* (1995b) modified the presentation of so called weight-visualisation curves (previously described by Bischof *et al.* (1992)). Essentially they explain how the weight values can be used to calculate the average contribution of a node in a layer to a specific node in the next layer:

$$P_{ij} = \frac{|W_{ij}|}{\left|\sum_{k=1}^{n} |W_{ik}|\right|} \bullet 100\% \qquad (4.1)$$

Where $P_{ij}$ is the contribution of a node $i$ in a layer to a node $j$ in the next layer. $W$ is the weight on the connection, and $n$ is the number of nodes in the first layer.

Since weight values can be negative the absolute values of the weights are used. The resulting value can be multiplied by 100 if the contribution is required as a percentage. A

similar expression can be used to measure the average contribution of a specific node in a layer to the next layer:

$$A_i = \frac{\sum_{j=1}^{n_2} |W_{ij}|}{\sum_{k=1}^{n_1} \sum_{j=1}^{n_2} |W_{kj}|} \bullet 100\% \qquad (4.2)$$

Where $A_i$ is the contribution of a specific node in a layer to the whole of the next layer; $n_1$ and $n_2$ are the number of nodes in the first and second layer respectively (including bias).

Further explanation can be found in Figure 4.19. By combining these equations it is possible to calculate the contribution of a single output node to the output layer. Firstly using equation 4.1, it is possible to calculate the contribution of a single input node to each of the nodes in the hidden layer. Then using equation 4.2 the average contribution of each hidden node to the output layer is calculated. For each node in the hidden layer the contribution of the input node (to a hidden node) is multiplied by the contribution of that hidden node to the output layer. These values are then summed over all of the hidden nodes. Wong *et al.* (1995b) used this type of measurement during training. If an input variable was found to contribute very little to a model then it was dropped, before retraining. This method is used to assess the final model. The first column in Table 4.7 shows the percentage contribution calculated for each input variable as described for the optimum network (1 hidden layer with 11 nodes).

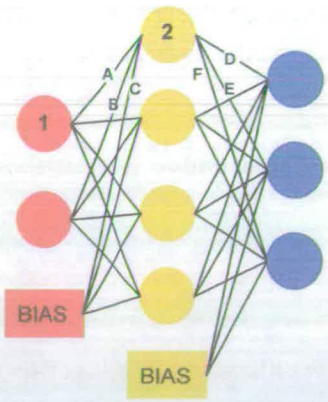



**Figure 4.19** Calculating the contribution of input nodes (variables) to the output layer. The diagram shown illustrates a conventional backpropagation network, with the bias terms drawn in (see Chapter 2). The contribution of input variable 1 to node 2 in the hidden layer is simply A / (A+B+C). The contribution of node 2 in the hidden layer to the output layer is (D+E+F) / (sum of all weights connecting the hidden layer to the output layer, including bias). These equations can be combined as discussed in the text so that the contribution of an input variable to the output layer can be calculated.

| Input variable | % contribution to final output (calculations illustrated in Wong *et al* 1995b) | % contribution to final output (simplified method, described in text) |
|---|---|---|
| BIAS from input layer | 7.9 | 7.7 |
| GR | 12.1 | 14.8 |
| DT | 12.8 | 11.2 |
| NPHI | 10.7 | 11.8 |
| RHOB | 11.7 | 13.6 |
| NDSEP | 10.2 | 11.3 |
| PORLOGT | 10.2 | 13.3 |
| LN (ILD) | 16.2 | 16.3 |
| BIAS from hidden layer | 8.2 | n/a |
| Total | 100% | 100% |

**Table 4.7** Percentage contributions of input variables to the network output - calculated from the two methods described in the text. All log symbols can be found in the notations and conventions section preceding Chapter 1.

Another approximate method for assessing the contribution of an input variable to the output is to sum the absolute values of the weights from that input variable. By doing this for all input variables it is possible to calculate each sum as a percentage of all weights from the input layer. Effectively this ignores all weights, except those from the input layer. The second column in Table 4.7 shows the percentage calculated this way.

It can be seen that each log contributes a similar amount – between 10 and 17%. The order of importance is not the same for both methods but in general the amounts are similar. An important conclusion can be draw from this – that it is the weights from the input variables that are most influential in the outcome, and, that assessing the weights from the input layer *only* (a much simpler task especially for large networks) can provide a good approximate measure of the contribution to the final result of different variables (this method will be used further in Chapters 5 and 6).

The results also indicate that the most influential input variable is the resistivity log. In Chapter 3 many different networks were trained with different numbers of hidden layers and nodes etc. The author can report (although this is not illustrated) that *all* trained networks reported the resistivity log as being the highest contributor to the output (using the second, simpler method above). But Table 4.7 only suggests that the resistivity log was a *slightly* higher contributor than the other logs. So is there evidence in the actual results for high dependency on the resistivity log? Figures 4.20 and 4.21 show cross-plots of various logs (for wells 23/21-T3 and T8 respectively). The data are colour-coded by *predicted* lithofacies type. These indicate networks decision surface in a two-dimensional cross-section of the 7 dimensional log space that the network was working in.

In Figure 4.20 specific groups of defined lithofacies can be seen. Lithofacies 1 (yellow) can be seen to have a low gamma ray and density, and high resistivity. Lithofacies 5 by contrast has a high gamma-ray, density and neutron, and a much lower resistivity. The position of lithofacies 1 on the neutron-density plot indicates the area where sand with gas normally plots, obviously indicated by the resistivity log too. What it is also possible to see are points that have a low neutron and high density and velocity, that represent cemented zones. These are the zones that were discussed earlier that would need to be screened out before entry into any geological model (this would be simple, as these data do not overlap with any other lithofacies).

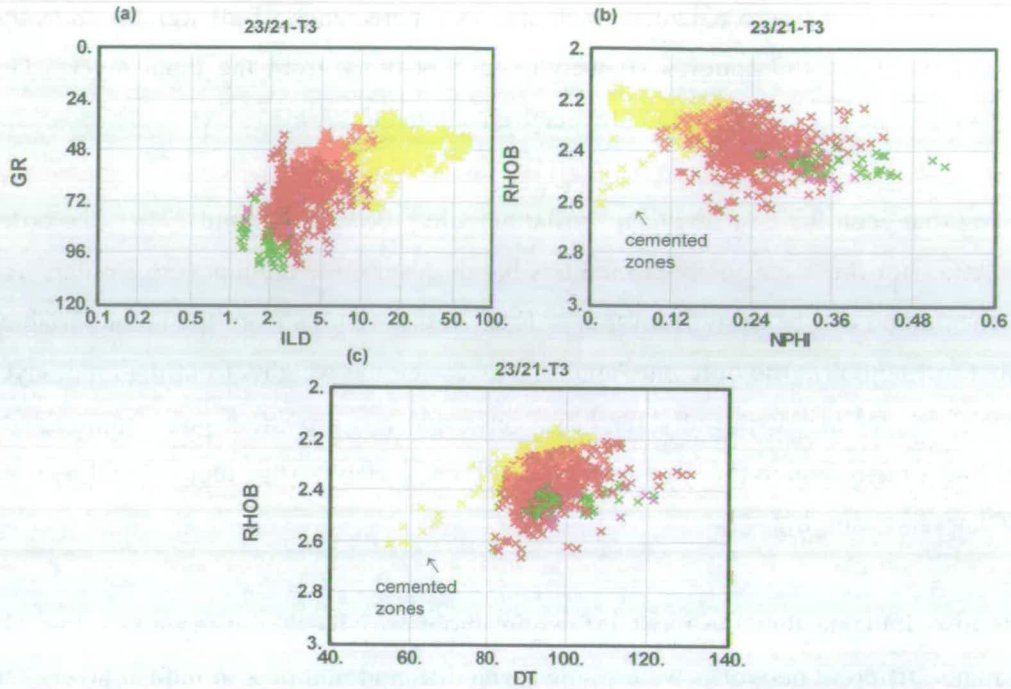



**Figure 4.20** Crossplots of various logs, that are colour coded by the predicted lithofacies type for well 23/21-T3: lithofacies 1 (yellow); lithofacies 2 (red); lithofacies 3 (brown/maroon); lithofacies 4 (purple); lithofacies 5 (green). These show the definition of the decision line created by the network. Cemented zones that were discussed earlier in the chapter are indicated. The resistivity log is seen to have high discriminatory power.

This figure also shows that the resistivity log has quite a lot of discriminatory power in its one single dimension. Figure 4.21 shows the same relationships but for well 23/21-T8. The neutron-density plot (b) shows a much greater overlap between the lithofacies than for well 23/21-T3. The resistivity-gamma-ray plot showed the resistivity to have a good degree of discriminatory power. It can be noted that these plots show some slightly unexpected results. There are some lithofacies 5 data (green) that are predicted as having a very low density and gamma ray. These actually represent bed boundaries as shown, so are not 'typical' lithofacies. So it has been shown that the resistivity log is consistently a good discriminator but is it possible to find some predictions by the network that are thought to be wrong because the resistivity log is not high enough? Figure 4.22 shows the lower part of well 23/21-T5. The sand beds at the top of the section have a very high resistivity indicating gas, and these are predicted correctly as lithofacies 1.

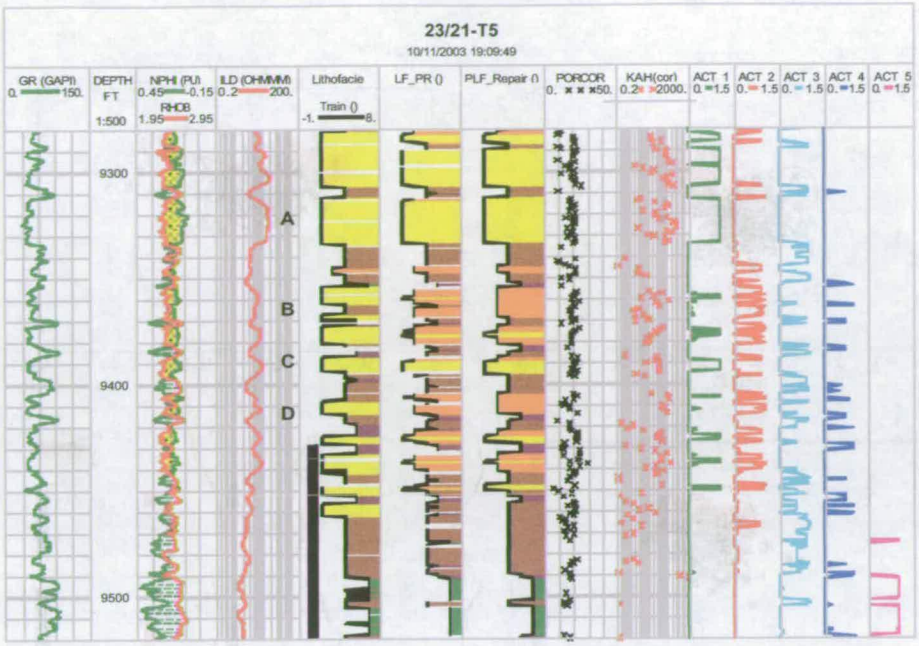



**Figure 4.22** Transition zone in well 23/21-T5. Good sands at A have a high permeability and are predicted correctly as lithofacies 1. Further down at B and D where the resistivity is slightly lower lithofacies 2 is predicted. At D though, the permeability is high. At C the resistivity is higher than at B and D and lithofacies 1 is predicted. See the notations and conventions section for log acronyms and colours.

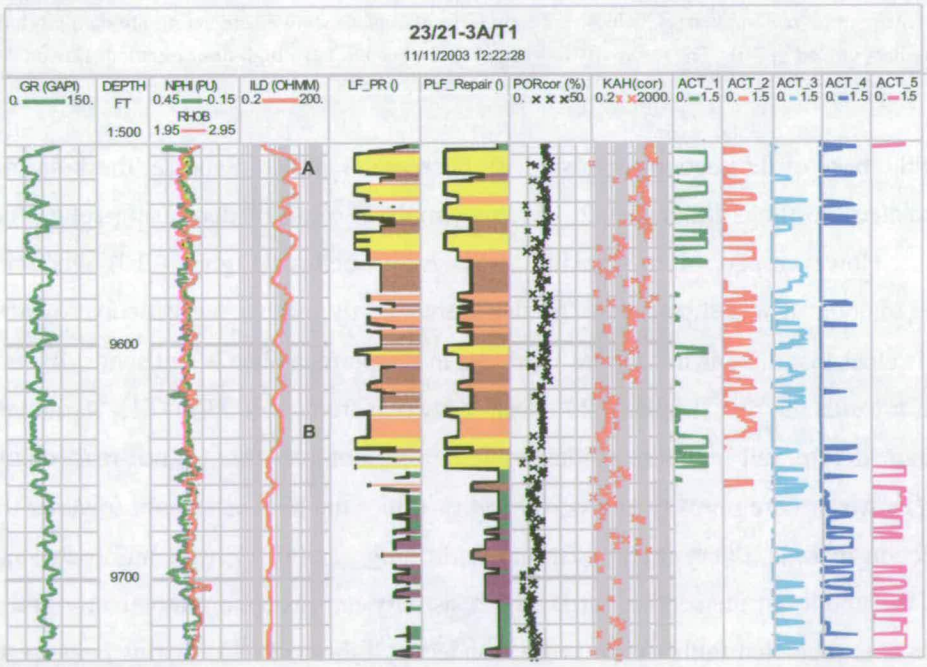



**Figure 4.23** Transition zone in well 23/21-T1. Good sands at A have a high permeability and are predicted correctly as lithofacies 1. Further down at B the resistivity is lower and lithofacies 2 is predicted. At B the permeability is lower so again this could be a 'correct' prediction. See the notations and conventions section for log acronyms and colours.

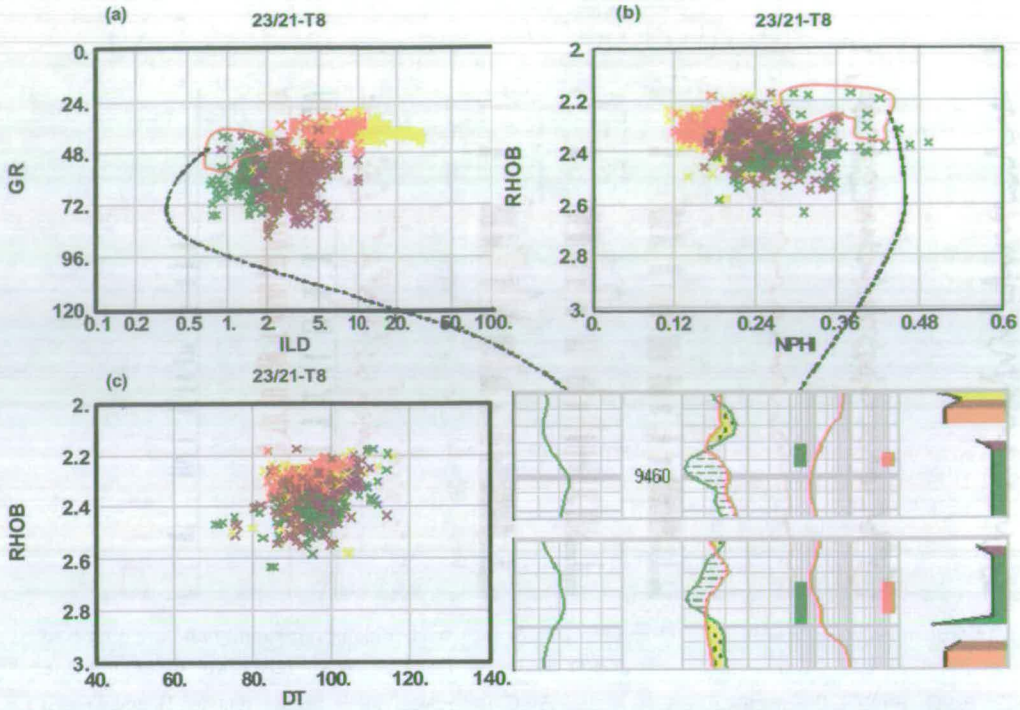



**Figure 4.21** Crossplots of various logs, that are colour codes by the predicted lithofacies type for well 23/21-T8: lithofacies 1 (yellow); lithofacies 2 (red); lithofacies 3 (brown/maroon); lithofacies 4 (purple); lithofacies 5 (green). These show the definition of the decision line created by the network. Some lithofacies 5 data that have unusually low gamma-ray and density values represent edge effects, as shown (green flag are data circled in (a), red flag are data circled in (b)). The resistivity log can again be seen to have high discriminatory power.

Towards the base of the section the resistivity decreases rapidly. Sands at the bottom have been predicted mostly as lithofacies 2 – is this simply because of decreasing saturation? It could be. However part of this section was shown before (Figure 4.10) when it was compared to core. It was shown how the sands are slightly more heterogeneous towards the base. It is clear that there is a lot more variation in the permeability of the sands towards the base than towards the top. Figure 4.23 shows a section from well 23/21-T1. Although this well contained core, full sedimentary descriptions were not available, so no 'real' column is defined. However core porosity and permeability values are shown. Again towards the top of the section there is a very high resistivity, indicating gas (at A), with high permeability. Towards the middle of the section (at B) the resistivity has dropped dramatically and some lithofacies 2 is predicted (although it is surrounded by lithofacies 1). Is this because of the low resistivity? The permeability is much lower at B so it may well be that that the rocks are poorer quality sand so they should be lithofacies 2.

Figure 4.24 shows a section from well 23/21-T6. No core was cut in this well. Virtually all of the sands in the reservoir interval are predicted as lithofacies 2. The resistivity log is generally lower throughout this interval then in the reservoir intervals of other wells. It is not possible to tell if the sand is of poorer quality than 'usual' lithofacies 1; but what can be established is the *fact* that lithofacies 2 makes up most of the reservoir interval and the resistivity is lower than in other reservoir sections. Although this well is deeper than the training wells, normalising for depth would act to decrease the resistivity value, (and increase the sonic transit time) – this procedure does not allow lithofacies 1 to be predicted in this interval.

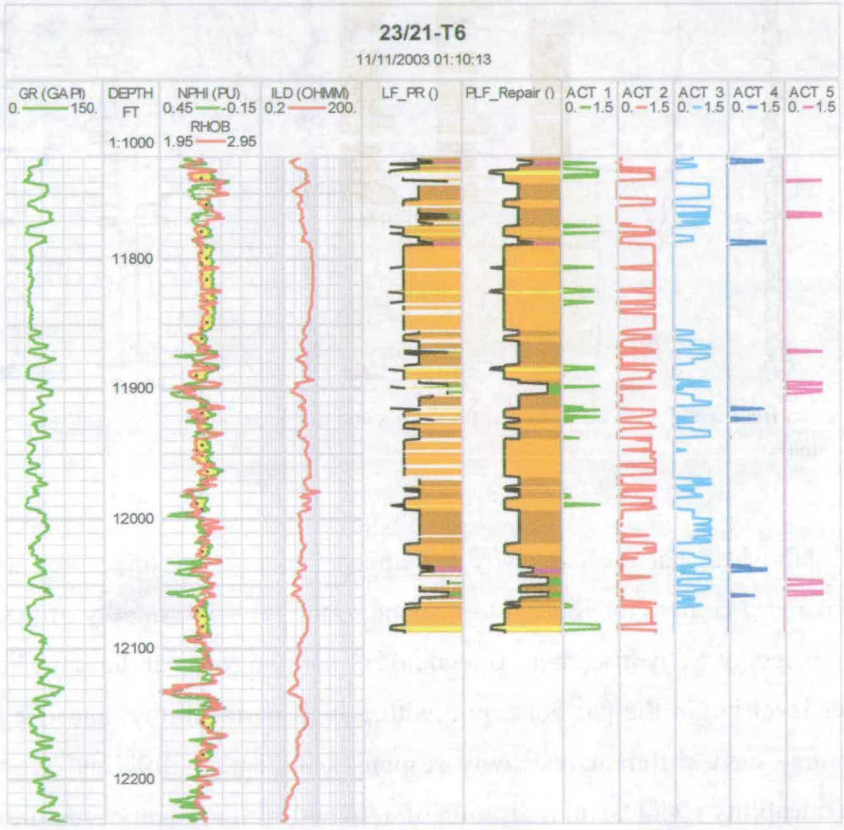



**Figure 4.24** Transition zone in well 23/21-T6. Most of the reservoir interval is predicted as lithofacies 2. The resistivity is lower than reservoir sections in other wells. See the notations and conventions section for log acronyms and colours.

Figure 4.25 shows a small interval from well 23/21-T8. At A the resistivity decreases and lithofacies 2 is predicted rather than lithofacies 1. All other logs have similar values to the lithofacies 1 bed below (including the total porosity and sonic log which are not shown).

The reservoir quality is similar to the bed below (although the permeability is very slightly lower). The resistivity decreases over about 10ft so this is well within the resolution of the tool. The resistivity log therefore appears to be responding to this slight permeability change.

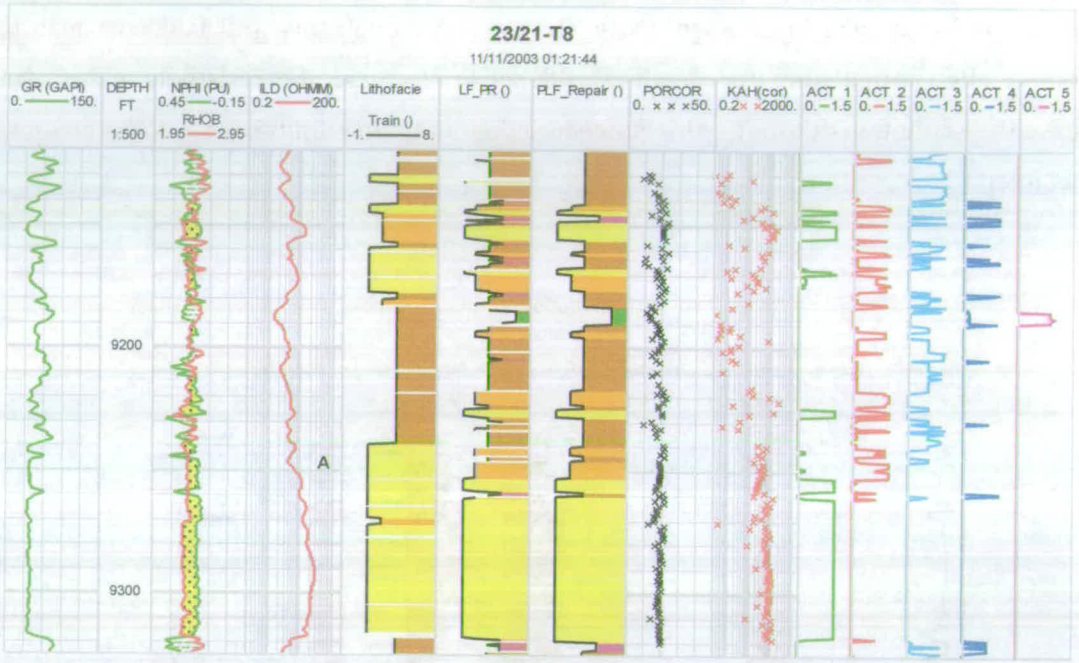



**Figure 4.25** Section from well 23/21-T8. See text for details and the notations and conventions section for log acronyms and colours.

It has been established that the resistivity log appears to be very important in lithofacies discrimination and it commonly appears to respond to the reservoir quality of the rocks. The resistivity log responds to hydrocarbon so it could be that two rocks at the same height above the free water level i.e. in the gas zone, one with a high permeability, and one with a low permeability may have different resistivity responses indicating different gas saturations. The lower permeability could be an indication of a higher capillary entry pressure and so this rock would have been charged less with gas. This relationship has not been proved, however results have been presented that show this could be true indicating that the neural network will give good rock discrimination but only in the gas zone. Outside of the gas zone this relationship will probably break down. Unfortunately this has proved difficult to establish in the Lomond data set. What is required is an interval that is definitely below the free water level. If it were established that some rocks that were definitely lithofacies 1 were being consistently predicted wrong this would help prove this relationship. In this case the figures

presented occur in transition zones and the rocks are of variable quality, so it is not possible to be absolutely sure that the predictions are not true. In order to establish the real value of using the resistivity log the next section illustrates results from when a new neural network was trained on exactly the same data as before but without the resistivity log.

### *4.7.3 Training without the resistivity log*

A number of neural networks were trained on exactly the same data (and validation set) as for the optimum network. Three fixed networks were trained each with 11 hidden nodes in one hidden layer. Three pruned networks were also trained that started with 14 hidden nodes in 1 hidden layer. These topologies represent the same as those used in Chapter 3. Although there is now one less dimension it was decided to use these topologies as it was known that the size would definitely be adequate to solve the problem. They could be slightly too large but any overtraining should be eliminated by the use of the validation set. Connections in the pruned networks were pruned if they stayed below 0.03 for at least 10,000 iterations. The results from the training of these networks are found in Table 4.8.

| Trial | Ordinary 1-layer 11-node network | Pruned 1-layer 14-node network |
|---|---|---|
| 1 | 43.44 | 44.26 |
| 2 | 38.52 | 33.61 |
| 3 | 47.54 | 45.08 |

**Table 4.8** Results from training ordinary and pruned networks without the resistivity log. The numbers all represent the % hit-rate over the validation set. This is the same validation set that was used to train the optimum network in Chapter 3.

The highest percentage achieved for a network that is trained without the resistivity log is approximately 48%. This is considerably lower than the equivalent result for the optimum network that was trained with the resistivity log (68.85%). Indeed most of the previous networks that were trained (with different numbers of nodes etc.) managed to achieve hit-rates of above 55% and many above 60%. This therefore suggests that the resistivity log is indeed very important in discriminating the different lithofacies. The best performing network in Table 4.8 (trial 3, ordinary network) was applied to wells 23/21-T3, T5 and T8,

and the results are shown in the first column in Table 4.9. In this column the results are displayed in the usual way – an activation of greater than 0.5 from any output node is interpreted as a prediction. The percentage correct can be seen to be far lower than the values seen in the second column (from the previous optimum network that was trained with the resistivity log). It is also clear that the percentage where no prediction was made (i.e. all

| Trial | | Best network with normal threshold of 0.5 | Comparable result from the optimum network that was trained with the resistivity log | Best network with highest activation taken as prediction |
|---|---|---|---|---|
| 23/21-T3 | Correct | 39.1 | 74.9 | 52.5 |
| | No prediction | 32.1 | 0.1 | - |
| | Mixed prediction | 1.0 | 4.5 | - |
| 23/21-T5 | Correct | 51.1 | 70.1 | 57.5 |
| | No prediction | 14.2 | 5.6 | - |
| | Mixed prediction | 1.1 | 0.5 | - |
| 23/21-T8 | Correct | 26.6 | 56.9 | 34.6 |
| | No prediction | 20.6 | 2.2 | - |
| | Mixed prediction | 1.6 | 4.0 | - |

**Table 4.9** Results from the best performing network in Table 4.8 when it was applied to wells 23/21-T3, T5 and T8. All numbers shown are percentages. The first column shows the results if a prediction is taken as representing activation of an output node above 0.5 (the most common way). The second column shows the comparable results from when the previous optimum network that was trained with the resistivity log and was applied to these wells. The third column shows the results of the same network as for the first column but if the highest activation of all the output nodes is taken as the prediction.

activations were less then 0.5) is very large. This indicates that there is a lot of uncertainty in the output from the network. When the highest activated output node is taken as a prediction then the hit-rate increases. However in each of the three wells it is still considerably lower then the hit-rate from the previous optimum network (centre column). It can be concluded that training without the resistivity log does indeed decrease the prediction capability of the neural network; and, since in many cases activations are low there is more uncertainty in the results.

Figure 4.26 shows predictions from the best network from Table 4.8 applied to wells 23/21-T3, T5 and T8. It can be seen that a consequence of training without the resistivity log is that the network finds it very difficult to separate lithofacies 1 and 2 from each other. In well

23/21-T3 (top) the permeability is variable, but even when it is very high (as in well 23/21-T5, centre) there is still some mix up.

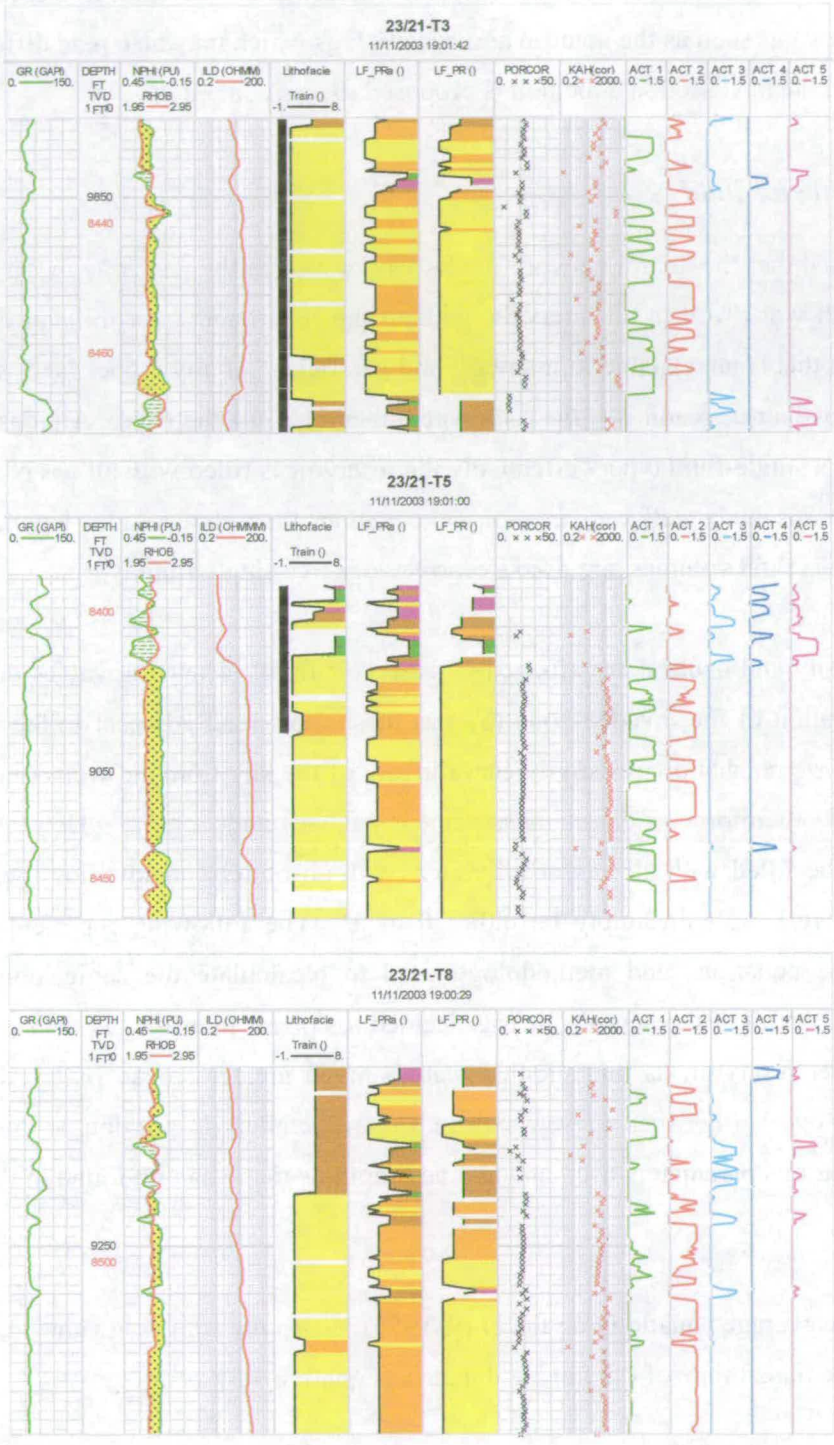



**Figure 4.26** Sections from wells 23/21-T3, T5 and T8. The first lithofacies column is the 'real' core defined lithofacies, the second the raw predictions from the network trained with no resistivity log (LF_PRa) with the highest activation taken as the prediction, and the third the predictions from the previous optimum network, trained with the resistivity log (LF_PR). The activation level curves (ACT_1a-ACT_5a) represent the activation levels corresponding to the centre lithofacies column.

Therefore it is clear that if the original model that had the resistivity log included as an input was applied to transition zones or water intervals then the predictions would probably be poor. The influence of the resistivity has only been investigated here, but in fact many logs are influenced by gas such as the neutron and density logs which may also read differently in water zones. In the next section a method is proposed to overcome this.

### *4.7.4 Correcting for fluid*

It was recognised that the neural network model works well in the gas zone, but a model is needed that will work well in all intervals, without the requirement for training data from water zones, as this is unavailable in many oil and gas fields. If any model is to work then the logs must give a true reading of the rock type rather than just the fluid. All logs must be standardised to a single-fluid type – effectively the reservoir is filled with all gas or all water for instance. In this study well-known empirical equations that relate various log readings to porosity, and thus fluid volumes, are used to correct logs to a single fluid type.

The sonic, density and neutron are affected by reservoir fluid. Their log values depend on the water saturation of the invaded zone ($S_{xo}$) as these tools read adjacent to the borehole wall. There exists no shallow resistivity curve in any of the key Lomond wells (e.g. 23/21-T3, T5 and T8) therefore no direct measurement can be made of $S_{xo}$. However if the reservoir is to be filled with all gas or all water (with absolutely no invasion by the mud filtrate whatsoever) $S_{xo}$ will simply be either 0 or 1. The following represents a brief summary of the equations and methodology used to recalculate the sonic, density and neutron logs for a 'full gas' reservoir. It was decided to correct to a full gas reservoir rather than a full water reservoir, as this should create a much greater spread of log data with potentially less overlap between facies. A much more detailed description of the method including the various parameters used and any assumptions made can be found in Appendix 3.

The Wyllie time average equation (Wyllie *et al.* 1956) relates the sonic log value to the rock porosity, and the transit time of the fluid and matrix (Equation 4.3).

$$\Delta t = \phi.\Delta t_{fl} + (1-\phi).\Delta t_{mat} \qquad (4.3)$$

Where:

$\Delta t$ = sonic log value;

$\Delta t_{fl}$ = travel time in invaded zone fluid (mud filtrate, residual water and gas);

$\Delta t_{mat}$ = travel time in matrix;

$\phi$ = porosity.

This equation can incorporate a shale correction:

$$\Delta t = \phi \ .\Delta t_{fl} + V_{sh}(\Delta t_{sh}) + (1 - V_{sh} - \phi \ ).\Delta t_{mat} \tag{4.4}$$

Where:

$V_{sh}$ = shale volume from gamma ray;

$\Delta t_{sh}$ = sonic transit time in shale.

The above Wyllie time average equation was used to find the average sonic values for fluid and matrix respectively via a cross-plot of sonic values against core porosities corrected to reservoir conditions (this was done both for the gas and water zones separately). Values were only plotted if shale content was less than 10% (in order to get a clean matrix point). Using the transit times for matrix and fluid and an estimation of the sonic transit time in shale, porosity was calculated from the sonic log using the above equation but re-arranged:

$$\phi = \frac{\Delta t - \Delta t_{mat} + V_{sh}(\Delta t_{mat} - \Delta t_{sh})}{\Delta t_{fl} - \Delta t_{mat}} \tag{4.5}$$

By using the calculated parameters it is possible to back-calculate the sonic transit time for an all gas reservoir, using equation 4.5. This involves substituting the fluid transit time by the equivalent value for gas.

The following equation can be used to calculate the effective porosity from the density log:

$$\phi_e = \frac{\rho_{mat} - \rho_b - V_{sh}(\rho_{mat} - \rho_{sh})}{\rho_{mat} - \rho_{fl} S_{xo} - \rho_{hc}(1 - S_{xo})} \tag{4.6}$$

Where:

$\phi_e$ = effective porosity;

$V_{sh}$= shale volume from gamma ray;

$S_{xo}$ = water saturation in the invaded zone;

$\rho_{mat}$ = matrix density;

$\rho_{hc}$ = hydrocarbon density;

$\rho_{fl}$ = mud filtrate density;

$\rho_b$ = bulk density;

$\rho_{sh}$ = average shale density.

The above equation can be simplified to:

$$\phi_e = \frac{\rho_{mat} - \rho_b - V_{sh}(\rho_{mat} - \rho_{sh})}{\rho_{mat} - \rho_{fl}} \tag{4.7}$$

Where:

$\rho_{fl}$= density of the fluid in the invaded zone.

Effective porosity from the density log was calculated using parameters from Walsgrove (1996). These were determined from a cross-plot of density log values and core porosity values (which provide the fluid and matrix densities). This was carried out separately for the gas and water zones. The equation for calculating a new density curve with a standard fluid type becomes:

$$\rho_b = \rho_{mat} - \phi_e(\rho_{mat} - \rho_{fl}) - V_{sh}(\rho_{mat} - \rho_{sh}) \tag{4.8}$$

A shale density was estimated and a new density curve calculated for an all gas reservoir by replacing the fluid density value by the equivalent gas density.

The neutron log is affected by all hydrogen in the formation. It is therefore affected by water, oil, gas, mud filtrate and shale (that contains clay, which consists of hydrogen in the crystal lattice or as bound water). Relevant equations that describe the neutron tool's response to a formation are:

$$\phi_N = \phi_e\left[HI_{mf}.S_{xo} + HI_{hc}(1 - S_{xo})\right] \tag{4.9}$$

$$\phi_N = \phi + V_{sh}\phi.N_{shale} \tag{4.10}$$

From Gruping (1999) and Schlumberger (1972) respectively, where:

$\phi_N$ = porosity as read by the neutron log (for pure water in the second equation);
$S_{xo}$ = water saturation in the invaded zone;
$HI_{mf}$ = hydrogen index of the fluid (mud filtrate, gas and residual water);
$HI_{hc}$ = hydrogen index of the hydrocarbon;
$\phi N_{shale}$ = the neutron reading when $V_{sh}$ is equal to 1.

These equations essentially state that the neutron response is made up of the hydrogen index of the mud filtrate multiplied by the volume of this material, summed with the volume of shale multiplied by the hydrogen index of shale, summed with the hydrogen index of the hydrocarbon multiplied by the volume of hydrocarbon. This is valid for limestone formations as the hydrogen index of limestone is zero (Rider 1996). As the matrix is sandstone any neutron readings must be corrected. The HI of quartz is 0.01 (from Rider (1996), after Serra (1979)). Therefore the above equations can be re-written to express the mud filtrate, gas and residual water as 'fluid', and for a quartz matrix:

$$\phi_N = 0.01V_{mat} + \phi_e HI_{fl} + V_{sh} HI_{shale} \tag{4.11}$$

Where:
$HI_{fl}$ = hydrogen index of the fluid.

In general when gas is present the hydrogen content per unit volume is lower than in water. Accordingly the neutron log, calibrated for water filled formations reads porosities that are too low. The reduction in neutron porosity is substantially greater than would be expected if the hydrogen content alone is taken into consideration. This is because for an equivalent water filled formation (of equal hydrogen content), there will be more solids per unit volume of formation – and the solids contribute to the slowing down of neutrons (Schlumberger, 1972). This is known as the 'excavation effect'. If it is assumed that close to the borehole wall (where the neutron log reads) there is little gas (argued by the fact that the density of the fluid adjacent to the borehole wall is close to that expected for oil based mud), then the HI of the 'fluid' can be estimated from the above equation. For clean formations the $V_{sh}$ part of the equation drops to zero. Therefore the above equation can be rearranged so that:

$$\phi_N - 0.01 = \phi_e \left(HI_{fl} - 0.01\right) \tag{4.12}$$

Thus a cross-plot of (neutron-0.01) against effective porosity (which will approximate the core measured total porosity in very clean formations) reveals the hydrogen index of the fluid. The hydrogen index of shale was estimated from a common neutron-density plot. Therefore it is possible to estimate porosity from the neutron tool, and once this has been calculated substitute the hydrogen index of the fluid by a value representing gas so that the neutron tool response can be estimated for a gas filled reservoir.

The resistivity log was not recalculated for a gas-filled reservoir. The Archie equation relates resistivity values to hydrocarbon saturation via porosity. However if the resistivity log was recalculated using the Archie equation this would simply equate to a rescaling of the density log in resistivity units (if density had been used to evaluate porosity). For this reason the resistivity log will be left out in any subsequent analysis that is undertaken. Further explanation of the fluid substitution procedure can be found in Appendix 3. Figure 4.27 shows the result of applying the above equations to the sonic, neutron and density log. The lower part of the diagram represents the transition zone in well 23/21-T5 while the top part is in the gas zone. It can be seen that the new 'all gas' logs read approximately the same for similar lithofacies types (notably the sands) despite their position in the reservoir.

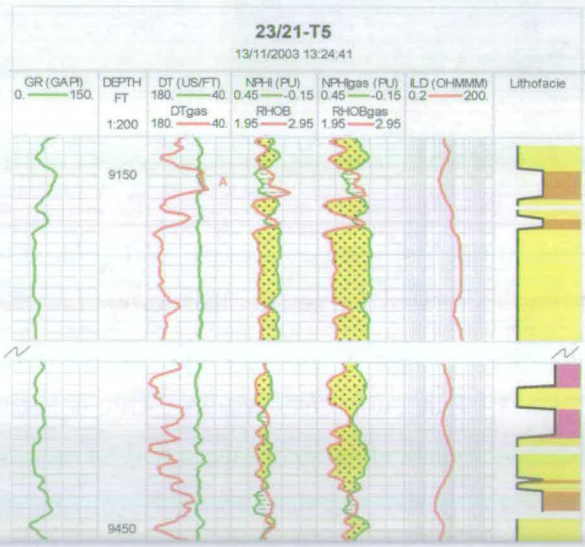



**Figure 4.27** The result of standardising for fluid - the sonic, density and neutron logs. Track 3 shows sonic logs. Green is the original log, and red the new log for the gas filled reservoir. Since gas has such an extremely high transit time the new log is much more sensitive to porosity changes than the original sonic log that was mostly reading invaded fluid. It is shown (at A) that the sonic log is working as expected as in this interval it is very shaly, and therefore there is no effective porosity, and little or no gas saturation, thus the original and new curves approach each other. Track 4 shows the original neutron and density, track 5 the new neutron and density logs. There is a much greater neutron density separation for the all gas logs than for the original logs. The lower section represents the transition zone in this well (note the resistivity is lower). All the new logs in the transition zone approximate their gas zone contemporaries.

### *4.7.5 Neural network analysis with 'gas-based' logs*

A new neural network model was created and trained on the new logs that had been standardised for gas. The resistivity was excluded, but the original gamma-ray log was used as this should not be affected by gas saturation. Also a new neutron-density separation log was calculated (see Appendix 1) and total porosity log. The total porosity log was found to be the same as the original log (as expected). Therefore since the same inputs that were used in the previous analysis (that excluded the resistivity log) are used here the results can be directly compared.

The training set used to train the new network was made up of exactly the same intervals that made up the data set that the optimum network was trained on (the Primary Training Set), and was also boosted in the same way. From the remaining data 125 examples were selected to make up a validation set (with each lithofacies making up 20%). Therefore although the validation set was made up in the same way as the optimum network's validation set it did not consist of exactly the same data.

Three fixed networks were trained each with 11 hidden nodes in one hidden layer; and three pruned networks were also trained that started with 14 hidden nodes in 1 hidden layer. The results from training these networks can be seen in Table 4.10.

The best performing network is able to classify the validation set correctly approximately 44.26% of the time. The network that did not utilise the resistivity log classified its validation set correctly 47.54% of the time (Section 4.7.3, Table 4.8). So on this basis there

| Trial | Ordinary 1-layer 11-node network | Pruned 1-layer 14-node network |
|---|---|---|
| 1 | 42.62 | 41.8 |
| 2 | 44.26 | 35.25 |
| 3 | 39.34 | 39.34 |

**Table 4.10** Results from training ordinary and pruned networks with the recalculated gas logs. The numbers all represent the % hit-rate over the validation set.

is no improvement. However the validation sets did not contain exactly the same data and most of the validation data is from the gas leg, as this is where core exists. However, is there any improvement in specific areas of interest such as transition zones?

The hit-rates over wells 23/21-T3, T5 and T8 will be investigated before the results from specific well sections. Table 4.11 shows the hit-rates over these three wells. It can be seen that there is still a reasonably high percentage of cases where the neural network is unable to make a decision (for instance in 23/21-T8 it is 15.3%), which illustrates a degree of uncertainty in the results. However these percentages are lower than the model that was trained without the resistivity log (Section 4.7.3 Table 4.9). When the highest activated node is taken as the network prediction, then the percentage correct is increased, as expected; and

| Trial | | Best network with normal threshold of 0.5 (trained on gas logs) | Best network with highest activation taken as prediction (trained on all gas logs) | Best network that was trained without the resistivity log (with highest activated node taken as the prediction) | Comparable result from the optimum network that was trained with the resistivity log |
|---|---|---|---|---|---|
| 23/21-T3 | Correct | 46.6 | 51.2 | 52.5 | 74.9 |
| | No prediction | 9.3 | - | - | 0.1 |
| | Mixed prediction | 1.3 | - | - | 4.5 |
| 23/21-T5 | Correct | 69.1 | 72.5 | 57.5 | 70.1 |
| | No prediction | 5.8 | - | - | 5.6 |
| | Mixed prediction | 1.0 | - | - | 0.5 |
| 23/21-T8 | Correct | 37.6 | 47.3 | 34.6 | 56.9 |
| | No prediction | 15.3 | - | - | 2.2 |
| | Mixed prediction | 3.6 | - | - | 4.0 |

**Table 4.11** Results from the best performing network in Table 4.10 when it was applied to wells 23/21-T3, T5 and T8. All numbers shown are percentages. The first column shows the results if a prediction is taken as representing activation of an output node above 0.5 (the most common way). The second column shows the results of the same network as for the first column but if the highest activation of all the output nodes is taken as the prediction. The third column shows the best network results from training with the original logs without the resistivity, and the final column is the hit-rate from the optimum network (all original logs including resistivity). If the resistivity is excluded then training with the gas logs shows improvement over training with the ordinary logs. However both of these models perform worse than the model that was trained with the resistivity log.

in all cases the hit-rates are approximately equal to or higher than the network trained without the resistivity log. However all networks do not perform as well as the original 'optimum' network that was trained with the resistivity log. So how does the new network that is corrected for gas perform over specific intervals? Figure 4.28 shows the predictions over sections of wells 23/21-T3, T5 and T8. They are the same sections as in Figure 4.26 for comparison. The various columns are explained in the figure caption. The top section that is 23/21-T3 shows a section where a lot of lithofacies 2 is predicted by the 'all gas' network rather than lithofacies 1. The network trained without the resistivity log also predicted quite a lot of lithofacies 2 rather then 1. The original optimum network managed to predict this interval correctly. Although the core is not studied directly it can be seen that at A and B where lithofacies 2 is predicted by the 'all gas network' this does in fact relate to areas where there is a slight reduction in permeability. So the 'all gas predictions' might not be totally incorrect – maybe the original optimum network was more incorrect. This section in well 23/21-T3 is partly responsible for the low hit-rate in this well. Unfortunately it appears that the 'all gas network' is not totally consistent though. At C in the middle section (well 23/21-T5), the permeability is very high and lithofacies 2 is predicted. From the logs shown this area does not appear any different to the surrounding intervals of lithofacies 1, implying that these data may just lie on the boundary between lithofacies 1 and 2. The lithofacies 1 output node is activated slightly at C so the network does actually indicate this. The lower section (well 23/21-T8) shows a very large sand bed that is predicted as lithofacies 2 rather than lithofacies 1 (at D). It is this bed that causes the hit-rate for the 'all gas' network in this well to be much lower than for wells 23/21-T3 and T5. The prediction though does agree with the network that was trained without the resistivity log.

Figure 4.29 shows a transition zone in the lower part of the Forties Sandstone Member in well 23/21-T5. What is clear from this plot, is that the new lithofacies column from the 'all gas' network has predicted lithofacies 1 beds approximately in the correct place, that match the real core defined lithofacies. No other network was able to predict these beds in this horizon. In the original optimum network the resistivity log was cited as being too low to allow lithofacies 1 predictions (that usually higher up in the reservoir has a much higher gas saturation). When a network was trained without the resistivity log it was still not able to predict lithofacies 1. Therefore other logs must have been highly affected by gas too, and prevented lithofacies 1 prediction. The exaggeration of the logs to emulate a fully saturated gas reservoir has meant the logs appear similar to their compatriots higher up in the

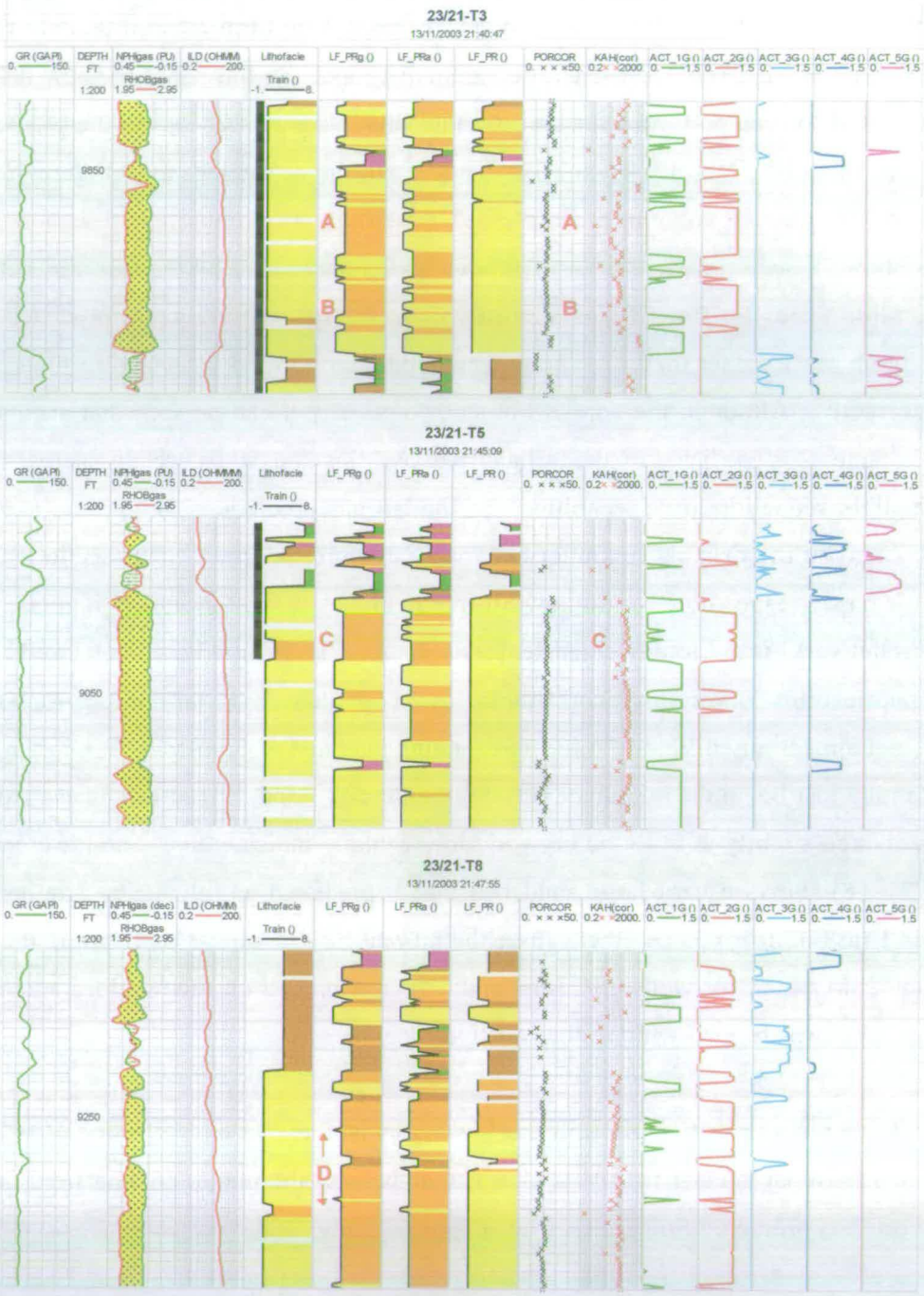



**Figure 4.28** Sections from wells 23/21-T3, T5 and T8. The first lithofacies column is the 'real' core defined lithofacies, the second the raw predictions from the network trained on the gas logs (LF_PRg) with the highest activation taken as the prediction, the third the predictions from the network trained without the resistivity log (LF_PRa), and the fourth the optimum network that was trained with the resistivity log (LF_PR). The activation level curves (ACT_1G-ACT_5G) represent the activation levels corresponding to the second lithofacies column. See text for a discussion of this figure.

reservoir, and so are able to be predicted correctly via a model that is trained on gas zone

examples. It was already stated that in this interval the permeability values are variable. Previously these data were used to suggest that the prediction of lithofacies 2 could have in fact been correct. It was stated that the resistivity log could be responding to the fluid saturation that could be related to the reservoir quality of the rocks. This still could be true. By eliminating the resistivity log some ability to discriminate lithofacies 1 and 2 may have been lost, and in fact it could be the case that the original model was closer to the truth. However what has been shown is that by leaving out the resistivity log, and rescaling the other inputs to represent a fully saturated gas reservoir, it is possible to create a model that can be trained on gas zone data but still has the ability to predict the highest quality sands in transition zones.

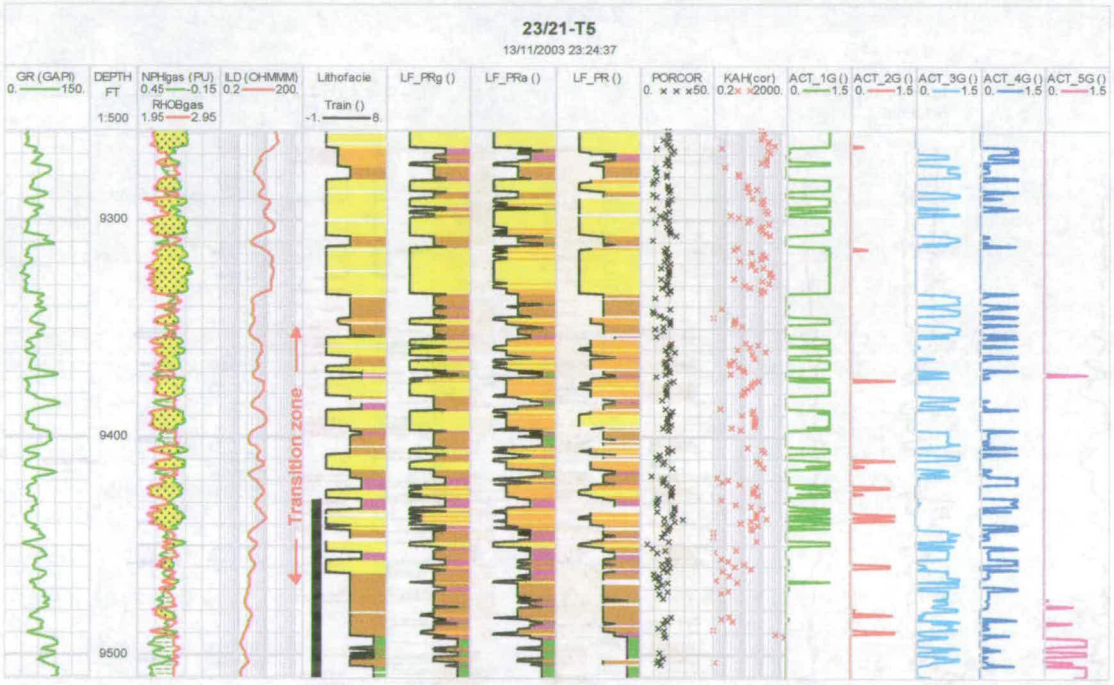



**Figure 4.29** Section from well 23/21-T5. The lithofacies columns are the same as those described in the previous figure. The transition zone is labelled where the resistivity log is decreasing with depth. The 'all gas' network is able to predict the best sand in the transition zone, the other networks do not appear capable. See text for more discussion.

Figure 4.30 also shows the effect of applying the all gas model to well 23/21-T6. This figure represents the main reservoir interval in this well. There was no core cut in this well and consequently no porosity or permeability core plug measurements are available. The resistivity log is lower than in the main reservoir sections in equivalent wells, and this was cited as to why possibly the thick-bedded sands that make up this interval were predicted as lithofacies 2. If the resistivity log is responding to the reservoir quality then these could be perfectly correct predictions. However as in the previous example when the 'all gas' model was applied to this interval lithofacies 1 was predicted. This again illustrates that this model does have the ability to predict high quality sand in intervals when the gas saturation is lower, even though the model was trained in highly saturated intervals.

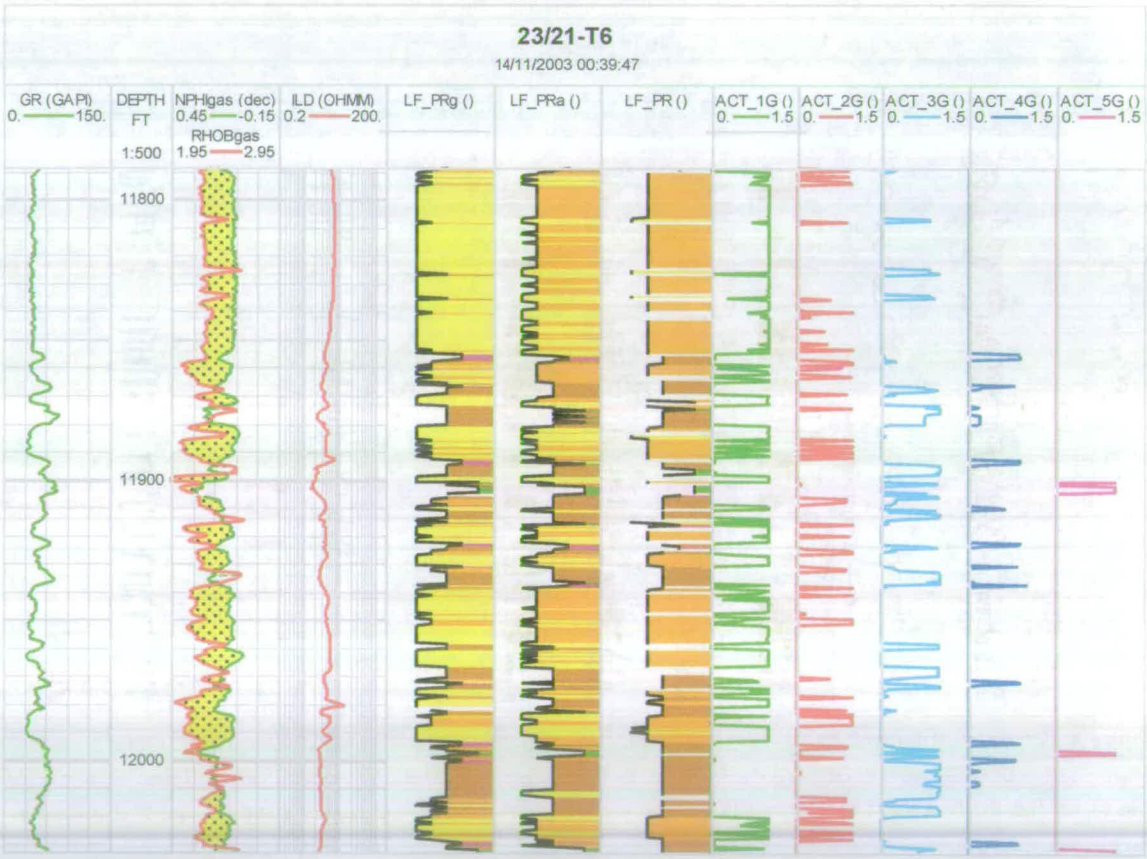



**Figure 4.30** Section from the main reservoir in well 23/21-T6. The lithofacies columns are the same as those described in the previous figures. The lower section represents the transition zone as the resistivity log gently decreases with depth. The 'all gas' network is able to predict the best sand in the reservoir interval and transition zone. The other networks do not appear capable. See text for more discussion.

The above examples that illustrate the use of the gas-corrected logs were taken from transition zones or wells that appear to have a lower gas saturation than equivalent intervals in the training set. All these are from the Forties Sandstone Member, where the training data came from. Nearly all Lomond wells show a large and complex transition zone. This means that the true water zones are fairly deep and lower down in the stratigraphy. Figure 4.31 shows a well section just below the assumed fluid contact (taken from Cook (2000)) from the Mey Sandstone Member (see Figure 3.3). Although this is outside of the Forties Sandstone Member that this study has so far concentrated on, the rocks (in terms of depositional environment) are similar to those higher in the well (Cullen 1993d), and so this can aid as a test interval for the new gas-corrected model. The columns shown are the same as previous figures in this section, except that the neutron and density logs are the original ones. Although there are some similarities between the three columns (for instance at A sand is predicted in all three), there are specific differences. The gaps in the column defined by the optimum model (LF_PR) illustrate uncertainty in this model. Around B this model also predicts lithofacies 5 in an area of low-moderate gamma ray. The model trained without the resistivity log provides a better result, but the area around B incorrectly contains a lot of lithofacies 1. The core plugs indicate this to have variable porosity and low permeability. The model trained with gas corrected logs populates this interval with mostly lithofacies 3 which appears the correct interpretation.

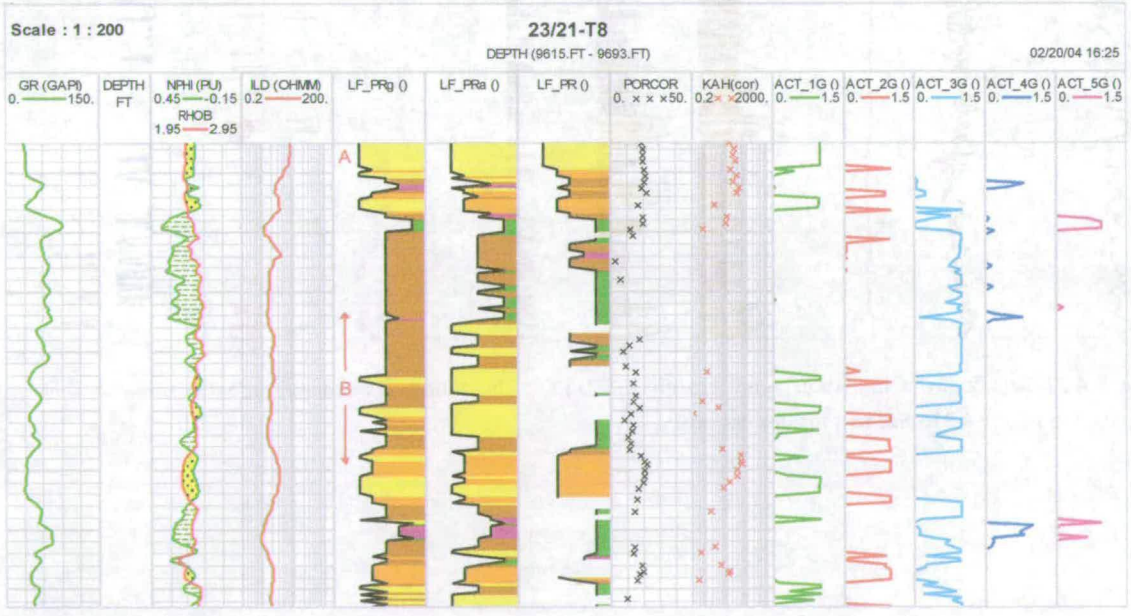



**Figure 4.31** Section from the water zone in well 23/21-T8. The lithofacies columns are the same as those described in the previous figures, except the neutron and density are the original logs. See text for discussion.

Figure 4.32 shows an interval from the base of the Forties Sandstone Member in well 23/21-T1. This interval is well below the fluid contact (taken from Cook (2000)). Right at the bottom of the section the rocks have a fairly high porosity and permeability, yet the resistivity remains low. The right hand lithofacies column (LF_PR) is the interpretation from the optimum model. This is restricted to predicting only lithofacies 5 and 6, and the gaps indicate uncertainty in the interpretation. The centre column (LF_PRa) is from the model trained without the resistivity log. The interpretation appears better since there are some beds of lithofacies 4 predicted. However around B some lithofacies 1 is predicted that appears incorrect (although this could be a slightly cemented horizon since the density log is fairly high). The model trained with gas corrected logs however (LF_PRg) manages to predict mostly lithofacies 3 throughout this interval (at A and B). This appears the correct interpretation given the moderate-high porosity, and low but highly variable permeability. This model also predicts sandy lithofacies in response to a low gamma ray.

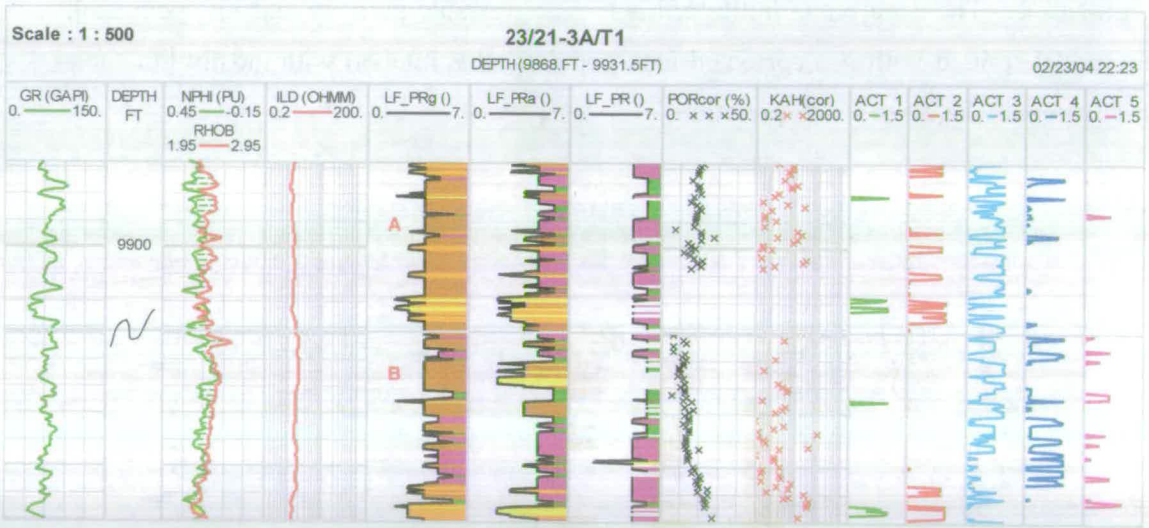



**Figure 4.32** Section from the water zone in well 23/21-T1. The lithofacies columns are the same as those described in Figure 4.31. See text for discussion.

### 4.7.6 Summary of Section 4.7

This section began with an analysis of different approaches available to evaluating the influence of various logs on the final network prediction. An analysis of the weights, in a similar manner to Wong *et al.* (1995b) showed that all the logs contributed a similar amount, with the resistivity log slightly more important than the rest. A simpler analysis of the weights showed similar results. Analysis of two-dimensional sections of the hypothesis space also supported the view that the resistivity log showed a higher degree of discriminatory power. The reason for this was because the majority of the training data was taken from the gas zone (where virtually all the core was cut). In the sandy lithofacies especially, the resistivity log appeared particularly important in discriminating lithofacies 1 (the best reservoir quality sandstone), where the resistivity is usually very high. Various sections were shown (e.g. towards the base of the Forties Sandstone Member in well 23/21-T5 and the reservoir interval in 23/21-T6) where the resistivity was lower than the main reservoir rocks in the training set. These horizons were predicted as lithofacies 2. It was questioned whether the predictions should be lithofacies 1, and whether it was simply the hydrocarbon saturation that was lower implying that a main factor in the control of predictions is actually the fluid content. However some of the sections that were illustrated (e.g. well 23/21-T5) showed lower permeability values than typical lithofacies 1 reservoir. It therefore appeared that although the resistivity log was responding to bulk fluid content this was indirectly describing the reservoir quality. It was suggested that the lower permeability sandstone would have lower capillary entry pressures, and thus at the time of logging would have contained less hydrocarbon. In order to fully assess the dependence of the resistivity log, a new model was created that excluded this log. In all cases the new model performed worse than the previous model.

A consequence of the dependence on the resistivity log is that the model would not be expected to perform very well if applied to a water, or transition zone, or a well that had an overall lower gas saturation than the training data. In order to overcome this limitation all the logs that are known to be affected by fluid were re-calculated so that they represented a 'full gas' reservoir. This involved filling the effective porosity of the rocks with gas and training on the subsequent log readings. Models were created with the new logs trained on exactly the same data as before; the resistivity log was excluded. When tested (on gas zone data) the new models showed improvement over the models that excluded the resistivity log,

but were still poorer than the previous 'optimum' model that was trained with the resistivity log. Since all the gas zone logs were calculated via filling the effective porosity with gas, this essentially skips the relationship between permeability and fluid content (although very recent work by Wu & Berg (2003) shows relationships between effective porosity, permeability and capillary pressure). This was illustrated when some of the lower permeability sand zones (previously predicted as lithofacies 2) were predicted as lithofacies 1 with the new model. This suggests that the model has the ability to predict good reservoir quality sandstone independent of fluid type. In the true water zone the model trained with the gas-corrected logs showed definite improvement over the previous optimum model and the model trained without the resistivity log.

It should be stated though that the Lomond data set may not be the ideal data set to test the 'all fluid' model and therefore the generality of the conclusions needs to be tested on other data.

It is thought that the variable free water level in Lomond and the complex transition zone is controlled by the distribution of facies (Neil McCulloch pers. comm.). This work supports this view.

### *4.8 Chapter summary*

This chapter began by illustrating some general features that could be recognised in all wells, such as unresolved thin-beds and edge effects at log inflexion points. A method was implemented to remove these that subsequently produced a more geologically consistent lithofacies column. It was also shown how the activation levels of the output nodes could provide a qualitative measure of confidence/uncertainty in any neural network predictions.

The results of the 'optimum' model found in Chapter 3 were then illustrated on three cored wells. The overall hit-rate appeared to be around 60% with different lithofacies having different degrees of success (e.g. lithofacies 1, 3 and 5 were successful, lithofacies 4 was poorly predicted). When the results were compared directly to core it was found that the initial hit-rates shown in the confusion matrices did not illustrate the true success of the network. The nature of turbidite deposits is that they are very heterogeneous and consequently difficult to discriminate. Our network managed to find the *typical* log

signatures of each lithofacies and provided an unbiased estimate of the rock type. Many of the predictions therefore closely matched the core, even though they initially appeared to be incorrect. Thus the true hit rate the author believes to be higher than that suggested by the confusion matrices.

The optimum model was then applied to well 23/21-T4 that was shown in Chapter 3 to have different log signatures to other wells for a variety of possible reasons that were discussed. It was also shown how to identify such wells. Results in this well were initially poor. A normalisation procedure was implemented that improved results. This highlighted the fact that a severe limitation in neural network analysis and its use in populating many wells is commonly very practical elements such as the tool type / depth / calibration etc. rather than the methodology.

Predictions in other Lomond wells (shown in Appendix 5) were discussed in Section 4.6.

Section 4.7 assessed the dependence of the model on different logs, discussed limitations of the model and implemented procedures that attempted to overcome some of them. This section was previously summarised in detail.

The wider implications of the results shown in this chapter are discussed in the context of the current literature in Chapter 7. The next chapter builds on the work presented in Chapters 3 and 4 when neural network modelling is applied to electrical image data.

# Chapter 5: The integration of image log data into the neural network process

## *5.1 Introduction*

Previous chapters have focussed on neural network analysis of conventional log data in a reservoir deposited in a deep marine environment. This chapter presents a methodology for applying neural network analysis to electrical image log data, in a similar sedimentary environment.

Image logging tools were first developed in the 1960s with the acoustic imaging device (the Borehole Televiewer). Resistivity devices first appeared in the 1980s as an extension of the high-resolution dipmeter (Prensky 1999). Electrical resistivity devices can provide an extremely accurate description of any reservoir, as they sample the formation many times both vertically and horizontally via a large array of buttons attached to pads that press against the borehole wall. The data form a dense matrix of measurements, which are conventionally displayed as a computer-generated image. Each measurement defines a pixel the conductivity value of which defines its colour.

The detail captured by image logs allows them to be used in many different ways. Structural information such as strike and dip can be determined; pore spaces can be identified and classified (e.g. Russell *et al.* 2002); sedimentary structures can be identified (e.g. Luthi 1990) aiding in sedimentary facies discrimination; different fracture types can be identified (e.g. Haller & Porturas 1998); the vertical resolution of the data even allows identification of thin-bedded net pay. The fact that images are orientated has also allowed identified fractures to be orientated thus assisting in the deduction of tectonic stress regimes (Lovell *et al.*1998). Excellent accounts of the tool design, data acquisition, processing and all types of interpretation can be found in Schlumberger (1990), Rider (1996), Lofts *et al.* (1997) and Cheung (1999). Prensky (1999) details the current status of the technology. Prensky also includes an excellent bibliography of published literature.

It has already been stated that visually recognisable geological features can commonly be identified in the images such as rock texture and pore structure (in carbonates). If these

features revealed in the data can be quantified this would allow neural network analysis of lithofacies based on compositional (as from conventional logs) *and* textural definition, bringing the result closer to the conventional geological description of lithology and sedimentary facies. This chapter attempts to quantify textural aspects of microresistivity log data and use these as additional inputs in neural network models for lithofacies discrimination.

The next section (5.2) introduces the West Delta Deep Concession - the area where the data originates from, its sedimentology and the actual data that were available for use. Section 5.3 briefly describes the processing of the images that took place before interpretation. Section 5.4 describes a methodology for quantifying textural elements of image log data. Section 5.5 follows with a short section highlighting the preparation of the data before neural network analysis, which takes place in Section 5.6. A Chapter summary is found in Section 5.7. Further results are shown in Chapter 6.

## *5.2 The West Delta Deep Marine Concession Area*

### *5.2.1 Introduction to the West Delta Deep Marine Concession area*

The West Delta Deep Marine (WDDM) Concession sits 50-100km offshore in 500-1000m of water in front of the present Nile Delta (Figure 5.1). The concession for this area is held jointly by BG Group plc and Edison Gas. Early exploration of the area focused on the extension of onshore Messinian incised valleys and known shallow marine reservoirs such as the Rosetta Field (Samuel *et al.* 2003). Since then 3-D seismic data and the latest in drilling and logging technology has helped identify a number of Upper Pliocene slope channels that contain several trillion cubic feet of gas. An excellent description of the depositional architecture of these channels and a model for their deposition can be found in Samuel *et al.* (2003). As an introduction to this area a brief summary of some aspects of this paper are presented.

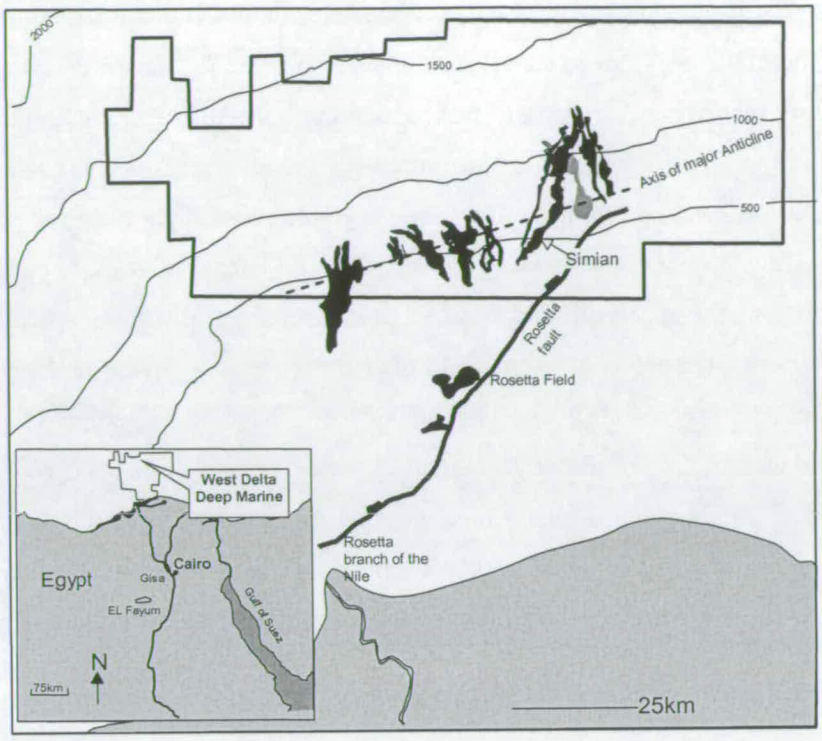



**Figure 5.1** Location of the West Delta Deep Concession area, redrawn from Samuel *et al.* (2003). The WDDM Concession area is shown in bold. The black areas represent submarine channels. The dashed line represents the axis of the anticline that forms the trapping structure. Contours refer to water depth and are in metres. Also indicated is the Simian channel system where the data used in this study were derived from.

### *5.2.2 Geological evolution of the WDDM channel system*

Four key stages in channel development have been identified (Figure 5.2), based on interpretation of core and images.

- Stage 1 - initial valley cut and slumping. The initial valleys are clearly imaged on seismic, with widths 0.5-6km and depths from 50-200m. The bases of these valleys are characterised by mass transport deposits. It is inferred that the initial valleys occurred as a result of erosion from high energy turbidity currents and slumping.
- Stage 2 - initial valley fill. The bases of the valleys consist of sheet like sands that are composed of an amalgamation of intersecting channels. This initial fill is often preserved. It is commonly overlain by a variety of sediments - individual channel sands, thin sequences of sheet sands, thin low density turbidites, slumped shales and hemipelagic shales.

- Stage 3 - re-incision and fill. Re-incision into the lower sheet like units is common and these surfaces are in most cases clearly imaged by seismic. Most commonly infilling the incised valleys are 'nested' sand units (thalweg channels) that appear up to 55km in length. These units are often separated by shales and chaotic units such as debris flows and slumps. They are very sinuous compared to the initial valleys. They show a consistent sense of aggradation and lateral migration, and make up the majority of the reservoir rock. Associated with these channels are levee deposits. The extent of these is sometimes limited by the extent of the original channel re-incision, but some late stage channel deposits have more extensive deposits that extend over the top of the original incised valley. Levee deposits can be identified in core and sometimes on image logs and are commonly slumped and folded. Some channels are overlain by more sheet sands that sometimes erode into the stacked channels. These are similar to the lower sheet-like units in that they are made up of many meandering channels that have low vertical aggregation but high lateral migration.
- Stage 4 - channel abandonment. The sand deposited in the above stages is commonly overlain by slump deposits, or thin-bedded sands that pass into thin bedded turbidites and then finally hemipelagites.

The erosion and depositional phases that make up the channel geometries can be correlated to sea-level change.

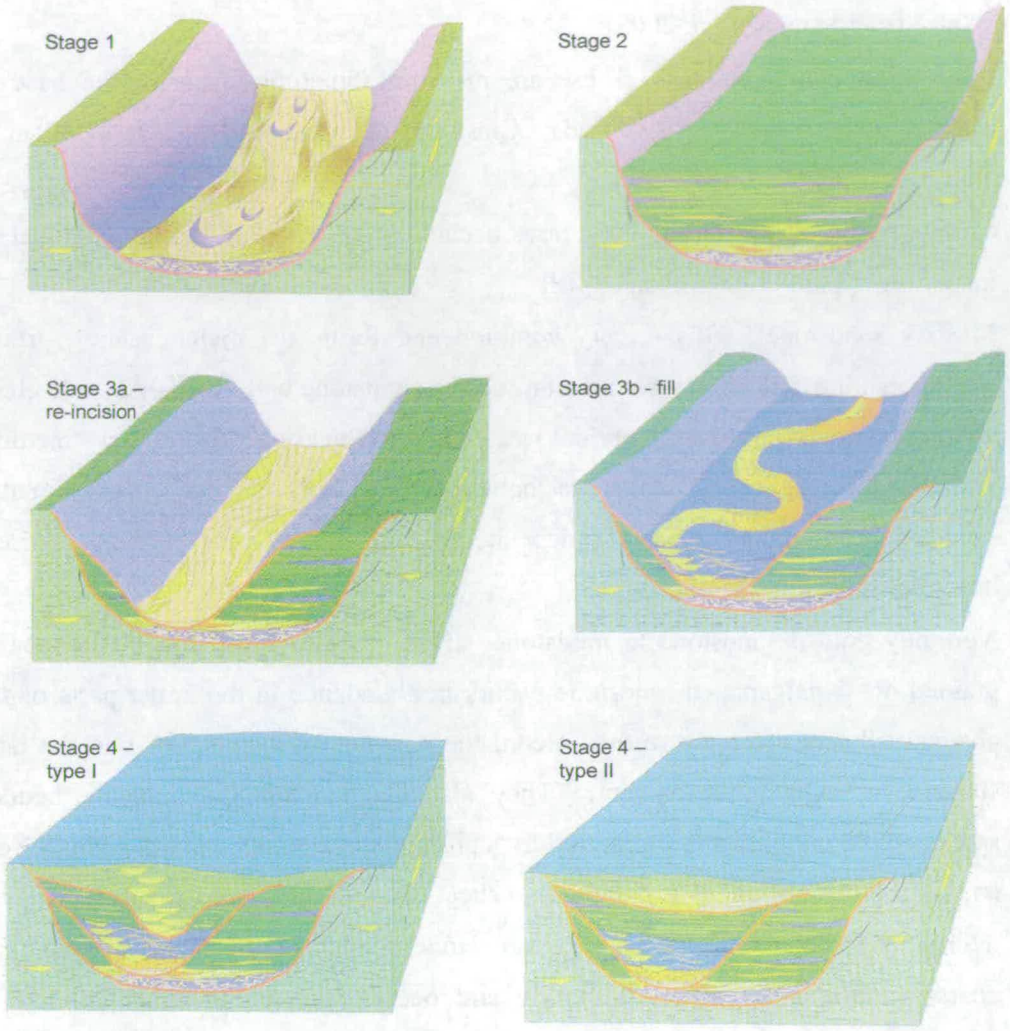



**Figure 5.2** Proposed geological evolution of the WDDM channel system (redrawn from Samuel *et al.* (2003)).

*Stage 1*, initial slope valley cut and slumping that is correlated with a sea-level lowstand.

*Stage 2*, initial valley-fill. Amalgamation of intersecting channels to produce more sheet like bodies. This corresponds with a transgressive stage in the sea-level cycle.

*Stage 3a*, re-incision. The lower sand sheets are eroded into. This is thought to correspond to a sea-level lowstand.

*Stage 3b*, infill. The incised valleys that were created in stage 3a are now filled by stacked meandering thalweg channels and their levee deposits. This is thought to correspond to a transgressive stage in the sea-level cycle.

*Stage 4*, two end members of the final stage in channel development. Type I where thalweg channels are wholly aggradational. Type II where there exists an upper sheet that is similar to the initial valley fill in stage 2. This stage corresponds to a highstand on the sea-level curve.

### 5.2.3 Sedimentology of the West Delta Marine Deep Concession area

The interpretation of core has identified a range of depositional facies that include the following (also from Samuel *et al.* 2003):

- Lithic clast conglomerates. These are rare but sometimes form at the base of channel successions in erosive beds. Clasts are well rounded and up to 40cm in diameter;
- Cross-stratified sandstone. Very rare, occurs at the base of channel sequences, indicating bypass prior to channel fill;
- Massive sandstone. This is very common and forms the main channel –filling sequences. It exists as massive medium-coarse sandstone with lithic and shale clasts interpreted as the product of debris flows, and more thickly bedded massive medium grained to conglomeratic sandstone that often fines upwards into cross-laminated sandstone, interpreted as being deposited from high density turbidity current deposits;
- Normally graded sandstone to mudstone. This medium-thick bedded fine-coarse grained non-amalgamated sandstone occurs in abundance in the upper parts of the channel fill sequences where they record the passage of smaller flows in the later stages of channel abandonment. They also occur within more thinly bedded sequences where they are interpreted as representing crevasse splay deposits. Low angle dips from the image logs indicate a sheet like morphology to this facies;
- Normally graded muddy sandstone to mudstone. This medium-thickly bedded fine-coarse sandstone is extremely muddy and occurs locally. It is interpreted as representing late stage local mud rich turbidity currents;
- Slumps, slides, debris flows. These are characterised by an extremely variable dip (seen on the image logs). They are interpreted as representing mass flow deposits ranging from slide sheets (relatively undeformed) to debris flows;
- Sandy thin beds within thicker shaly units. In many cases these make up a significant amount of the channel fill, and are extremely productive. Their thickness ranges from a few mm to a few cm. Their original depositional fabric is often significantly altered due to bioturbation, soft sediment deformation or re-working from bottom-water currents.

Not all of the wells in the WDDM Concession are cored. There is however an abundance of image logs (Schlumberger's Formation MicroImager (FMI) tool was run in every drilled well). This has led to the establishment of an 'image facies' scheme produced by Baker Atlas (2000 & 2001) when they interpreted the images on behalf of BG Group plc and Edison Gas. Static and dynamic images, (and interpreted dip values from them) were calibrated to core and used to establish a scheme that was applied throughout all the drilled wells. Twelve image facies in total were identified, and these are thought to be representative of the entire area. The image facies do not give direct information regarding depositional process but the grouping of these can reveal depositional units that can be linked to the process of formation. They have also proved useful for determining net/gross estimations. Table 5.1 illustrates the scheme defined by Baker Atlas, and some examples of these are shown as Figure 5.3. Table 5.2 illustrates how the image facies can be related to depositional process.

If a neural network model is to incorporate image logs then the final result could be simply called an 'image facies'. However, both the image facies and conventional logs provide a lithological signature too, so the term 'image lithofacies' is preferred. The image facies scheme designed by Baker Atlas (2000 & 2001) described above, represented the starting point for building training sets on which a neural network could be trained (see later sections).

| Image facies type | Image description | Interpretation |
|---|---|---|
| Laminated shale | Conductive very common. Continuous bedding fabrics traceable across the borehole (laminations). | Suspension fallout, thin low density turbidites and thin muddy turbidites. |
| Bioturbated / structureless shale | Conductive, no obvious structure, plain image , sometimes speckled. | Bioturbated shale |
| Slumped shale | Conductive oversteep - steep definable dip fabric, locally overturned. | Down-slope gravity driven failure of semi-consolidated shale mass. Slumps and slides. |
| Chaotic shale | Conductive, near random dip fabric. | Down-slope gravity driven failure of shale mass, proto debris flow. |
| Debris flow | Conductive, floating to clast supported, with shale clasts, crude bedding fabric. | Cohesive debris flow. |
| Structureless sand | Resistive near uniform image character, no internal fabrics visible. | From high density turbidity current. (Bouma Ta division). |
| Laminated sand | Resistive, laminated. Commonly occurs interbedded with structureless sands. | Bouma Tb division. |
| Irregular sand | Resistive laminated, wavy, and discontinuous bedding. | Locally deformed sand. |
| Slumped sand | Resistive laminated steep bedded and common contorted bedding. | Down slope gravity driven failure of sand mass. |
| Structureless and Intraclastic sand | Resistive near uniformly resistive, floating resistive and conductive clasts. | Sandy debris flow, slurried flows and capping flows to some laminated and structureless sand units. |
| Conglomerate | Resistive, with resistive and conductive patches. Angular to rounded mix of resistive (sand and lithic grains) and conductive (shale intraclasts). | Sandy pebble dominated, high density turbidite. Coarse grained residual deposit, channel base. |
| Cross-bedded sand | Resistive, low-moderately inclined bedding, near unimodal azimuth. Very rare, does not occur in any of the Simian wells. | Either sub concordant infilling of scour site or large scale migrating dune bedform. |

**Table 5.1** WDDM image facies scheme, redrawn from Baker Atlas (2000 & 2001)

| Facies Association | Description | Principal facies | Interpretation |
|---|---|---|---|
| Laminated mud association. | Undisturbed laminated shales. | Laminated mud. | Stable slope or basin floor. |
| Disturbed bedding association. | Thick slumps and slides. | Slumped sand and shale, bioturbated shale, chaotic shale. | Unstable slope. |
| Channel-fill chaotic slumps and debris flow s. | Disturbed bedding or debris flow below base of channel feature. | Laminated mud, slumped sand , bioturbated shale, chaotic shale. | Channel pre-cursor, retrogressive up-slope failure. |
| Channel fill sands. | Stacked sharp based, erosive, shaling and thinning up sand rich interval. | Structureless, laminated, irregular and intraclastic sand, debris flow . | Channel complex. |
| Sheet sands channel and non channel related. | Thick stacking of shales and very common heterolithic bedding. | Laminated and slumped shale. Structureless sand. | Intra-channel sheet fill. Or channel back-filling: no erosion. |
| Thinly interbedded sands and mud association. | Shales, heterolithic bedding, slumps. | Laminated mud, structureless sand. | Inter-channel and/or overbank sediments. |
| Laminated mudstone w ithin sandy channels association. | Undisturbed laminated shales <3m in thickness. | laminated shale, bioturbated shale. | Talw eg channel overbank fines, or background fines associated w ith channel inactivity. |
| Isolated channel / gully sands. | Single or stacked erosional sands on a small scale (<3m total thickness). Surrounded by mudstone lithofacies association | Slumped, bioturbated, and chaotic shale. Slumped sand. | Slope gully erosion and infill. Minor reservoir element. |

**Table 5.2** Image facies associations identified and interpreted from resistivity images, after Baker Atlas (2000 & 2001).

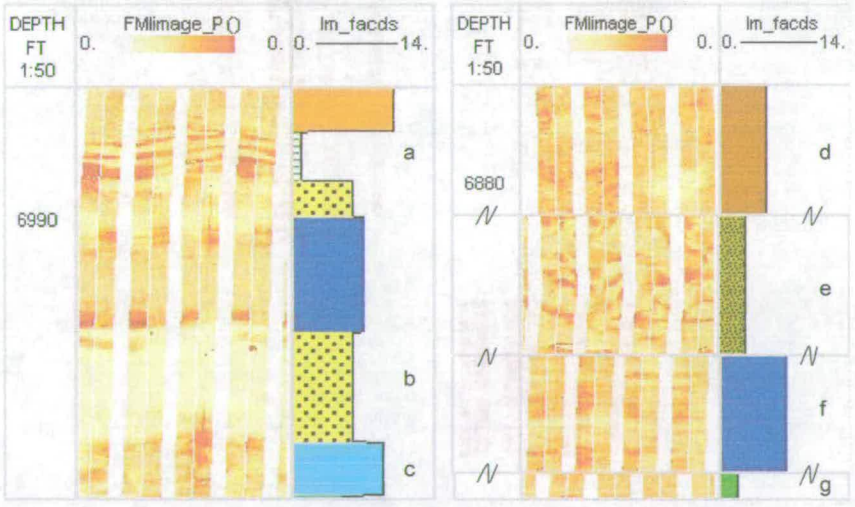



**Figure 5.3** Examples of different image facies defined by Baker Atlas (2000 & 2001). (a) Laminated shale, showing continuous bedding fabrics across the borehole. (b) Structureless sands. Very resistive and uniform image, no visible internal structure. (c) Slumped sand, showing contorted bedding. (d) Debris flow. Overall conductive image, with large speckles that could represent shale clasts. Also present is a more resistive area that could be a sand clast. (e) Slumped shale. Conductive, with steep and variable dip fabrics. (f) Laminated sand. Laminations are faint, but traceable across the borehole. (g) Bioturbated shale. Dull, plain image, little internal fabric, faint speckles. All examples are taken from well Simian 1 and are dynamic images.

### 5.2.4 Data

Data were made available by BG Group plc for three wells Simian 1, 2 and 3 – drilled into the Simian channel system (Figure 5.1). All wells are vertical to sub-vertical. The data set contained a full suite of conventional logs (GR, RHOB, NPHI, ILD, and ILM), FMI logs, and a digital record of the Baker Atlas image facies scheme that had been assigned.

Although it is now recognised that artefacts can commonly form a large amount of many FMI data sets (Cheung 1999, Lofts & Bourke 1999), the image data in the available wells were generally excellent (they were in fact partly chosen for this reason). Some exceptions are in Simian 2 where some borehole washouts cause defocusing of the image (this is easily identified by the caliper log); one of the pads in Simian 2 apparently recording a consistently different range than the other pads and flaps; and, (in all wells) some minor pad/pad, pad/flap mismatch occurs due to incorrect speed correction (see Figure 5.4).

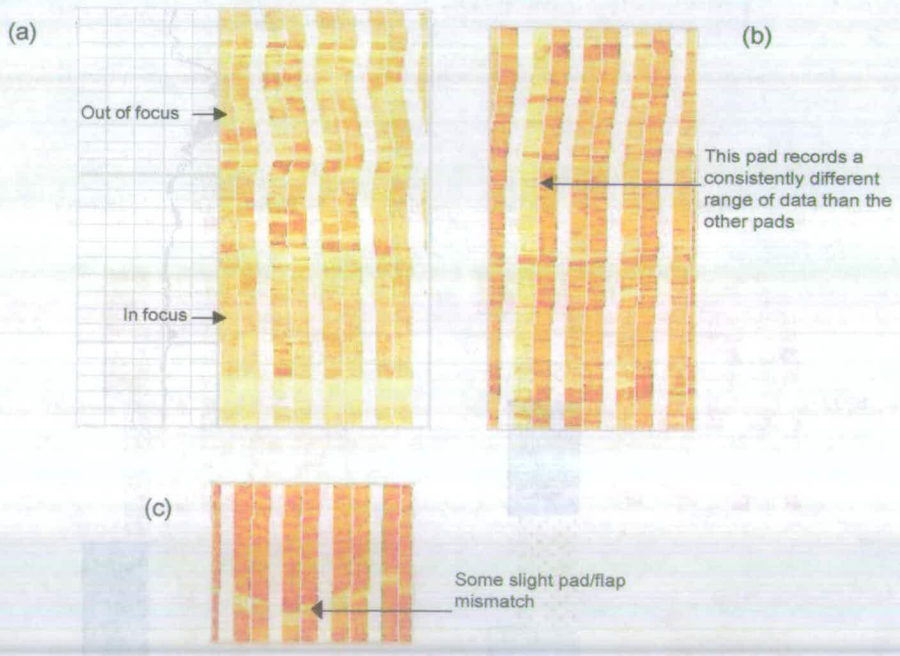



**Figure 5.4** Image data quality issues.
(a) Defocusing of the image data, due to borehole washout, indicated by the two caliper curves (grey). This example is from a processed image.
(b) Pad consistently recording a different data range than the other pads and flaps (this example is from an unprocessed image – see next section).
(c) Some slight pad/flap mismatch due to an incorrect speed correction. The example shown is from a processed image.

## 5.3 Image log preparation

### 5.3.1 Introduction

This section briefly describes a number of processing steps that took place before any interpretation. These apply corrections to the raw data to enhance the final image. All processing took place in TerraStation software. Further information on the processing steps can be found in the TerraStation manual (TerraSciences 2002). Cheung (1999) also gives a useful overview of some aspects of image data processing.

### 5.3.2 Accelerometer correction

The buttons on the various pads and flaps are offset vertically from one another. The result of this is that the tool measures different values that occur at the same depth at different times. If the tool travelled at a constant velocity, the time for the next row of buttons to reach a depth being measured by the first row of buttons would be known. Logs are generally recorded as a function of cable depth. However the velocity of the actual tool does not always equate to the velocity of the cable at the surface since the tool cable can stretch. This occurs if a tool becomes stuck (and is therefore more frequent in horizontal wells). Correction can take place by using the recorded acceleration of the tool (via an accelerometer that is located in the tool body). TerraStation automatically corrects for different tool accelerations, in a similar way to that described by Chan (1984). Essentially the recorded acceleration is integrated which provides an estimate of tool velocity and depth. However as Cheung (1999) points out, these corrections rely on measurements that themselves have limitations and possible errors.

### 5.3.3 Emex (Emmiteur d'exitation) correction

The low frequency signal from the tool may vary during measurement (by the tool operator) – this can help focus the high frequency return of the FMI pad resistivities thus improving resolution over very high or very low resistivity zones (Rider pers. comm.). For this reason the actual readings may not be comparable from one zone to another. This is also the reason why this type of resistivity measurement cannot be used to calculate a shallow water saturation curve. Using the Emex curve (that indicates the applied voltage against depth) the image log was automatically compensated.

### 5.3.4 Compensation for dead buttons

Individual buttons that record the data that make up the image sometimes fail, due to the tool electronics. This failure can be permanent or intermittent. In order to account for this, button values that fell below a specified threshold (in many cases they will represent 'null' values) were replaced by values that were linearly interpolated from adjacent button values at either end of the dead button section on the same pad or flap. If a whole row of dead buttons exists then interpolation is taken from the next line of buttons. A limitation occurs if a whole area of dead buttons exists. In general, because of the high quality of the data this step did not appear to make significant differences to the images.

### 5.3.5 Pad/flap correlation

This is a secondary speed correction that is based on a comparison of the data at the edge of any pad or flap. In theory the data at the edge of a pad should record approximately the same value as the attached flap as they are adjacent to each other. The pad/flap correction correlates all four pad/flap boundaries and weights the offsets accordingly so that adjacent data has approximately similar values. When this was applied images could be seen to be enhanced in a number of areas (see Figure 5.5).

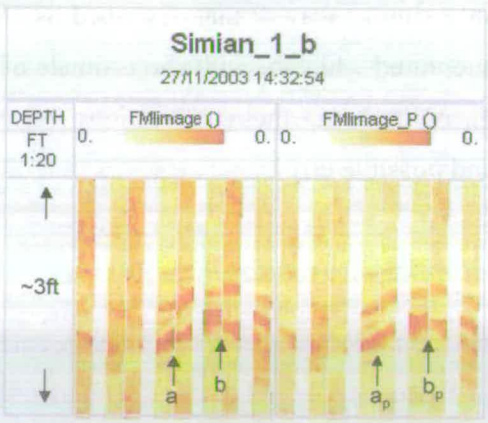



**Figure 5.5** Pad/flap correlation. The left image is unprocessed, the right one processed. The result of the pad/flap correlation step can be seen; there is a greater mismatch between the pad and flap at points a and b than on the processed image at points $a_p$ and $b_p$. Well Simian 1, both images are dynamic.

### 5.3.6 Button equalisation

When recording data, button responses can vary considerably due to factors such as uneven pad contact or mud smear across particular buttons. This processing step attempts to remove this variable response. It involves computing the data distribution of each button over a specific moving window, as well as the distribution of all button data over the entire window. A transform is then applied so that the data distribution of each button is similar to the overall distribution. This step is different than for the compensation for dead buttons step in that all data are considered rather than button responses that are below a given threshold (and therefore considered dead).

Figure 5.4 showed that one of the pads in well Simian 2 recorded a consistently different range of data than the other pads and flaps. This processing step adjusted the data recorded by that pad, bringing the range into line with the other pads and flaps, whilst still preserving the textural elements within the image (Figure 5.6).

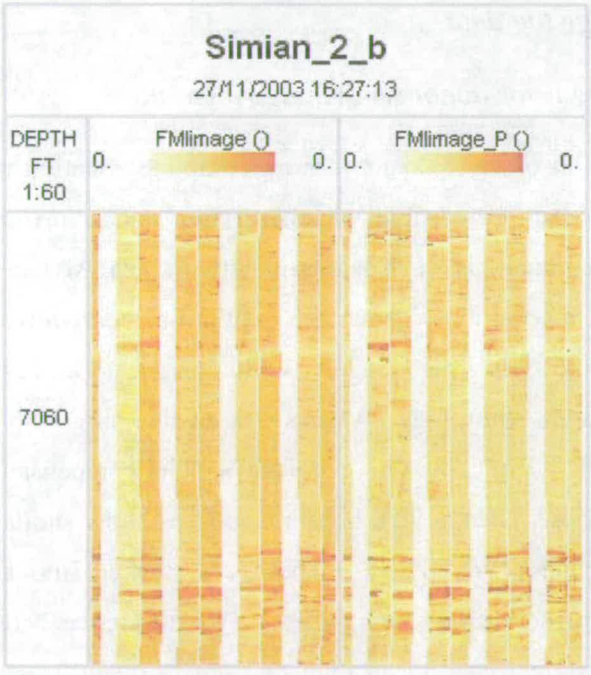



**Figure 5.6** Button equalisation. The left image is the raw image; one pad has recorded a different range of data than the other pads and flaps (it is lighter in colour). After processing (right image) all pads and flaps appear to show similar ranges, and textural elements of the image are preserved. Well Simian 2, both images are static.

### 5.3.7 Processing summary

The processing steps were carried out in the order described above. These steps are especially important for this work, since the images are to be used in a quantitative fashion. Neural network models (in the way implemented in this thesis) respond to the absolute values of the data. Therefore any inputs used should have specific ranges that relate to specific lithofacies. For instance a particular type of sand in one section of a well should have the same range of values (of whatever variable used) as the same sand in a different well section. It is possible to capture elements of the images that do not rely on the absolute value of the data measured. However, if raw values can be incorporated they could prove to be useful discriminating factors. Clearly processing steps such as button equalisation make this a possibility. Other processing steps such as the accelerometer corrections that align buttons, thus improving the sharpness of bed boundaries are also more important in quantitative work. Interpretation by hand can compensate for the miss-alignment of pads and flaps and resulting variable bed boundaries during analysis, quantitative approaches do not have this benefit.

## 5.4 Quantifying image log data

### 5.4.1 Published methods for quantifying image log data

As Luthi (2001) states in order to create a more complete zonation it must be possible to integrate any method that is capable of classifying image textures with other logs. Supervised classification methods (such as neural network analysis) are an obvious tool with which to integrate the observations. What are required are derivative curves that describe specific textural attributes from the image. Schlumberger's BorTex program allows the creation of various image-texture logs. An example of this program's methodology can be found in Luthi (2001). Typically this involves a 'dip compensation' step to produce horizontal bed boundaries. Then, where button responses show similar values these can be taken as the 'background conductivity'. These are stacked into a single channel and inflexion points used to define bed boundaries. The difference between the background conductivity and the original curves can then be used to quantify various heterogeneities. These can be expressed as a percentage of conductive or resistive components. After supervised analysis Luthi (2001) described the resulting classification of these components as 'morphofacies'. Some vertical continuity logic (like the thin-bed repair program

described in Chapter 4) can also be applied. Luthi also stated though, that the method described is rather conceptual as the logs and methodologies are very new. Consequently there are very few case studies. However, Delhomme (1992) and Hall *et al.* (1996) both described ways of classifying zones based on image textures. Delhomme (1992) developed image texture extractors to automatically highlight vugs and fractures in carbonates. Thresholding of the images highlighted specific objects. The objects were then contoured and the contours revealed the connectedness of the objects, with conductive spots equating to local maxima, resistive spots local minima. The percentage of spots that contributed to the image and their apparent size was output as sliding window logs. Vug and fracture connectedness was then correlated with permeability. Hall *et al.* (1996) used Hough transforms to quantify shapes from images. As in Delhomme (1992) images underwent thresholding that revealed objects and their edges. The images were then filtered to preserve only the main objects and remove noise. Shapes were then detected from their edges using a Hough transform (postulated by Wong *et al.* (1989)). The degree of granularity and rock fabric was calculated from co-occurrence matrices that looked away from a particular pixel to see if adjacent ones were similar. Once the various image elements were quantified they were clustered using an unsupervised (Kohonen type) neural network. These techniques were illustrated in a short siliciclastic reservoir section. Luthi (1994) used the concept of 'texture energy' (after Laws' (1984)) to quantify line edges and spots and a vertical sliding Fast Fourier Transform (the mean of the power spectrum) to quantify textures before undergoing principle component analysis and clustering. Garden (2001) used the average, standard deviation and coefficient of variation of button 12 from each pad to characterise turbidite deposits. He recorded that the coefficient of variation decreased upwards through a typical Bouma sequence, and that results were better when the conventional logs were included and interpolated to be the same resolution as the image logs. Results were used for net sand determination. Russell *et al.* (2002) identified the proportion of conductive heterogeneities and used them to assist in the discrimination of biofacies in carbonate rocks. In the data set studied the distribution of the biofacies was a controlling factor on permeability. These case studies are very specific and the ability of their models to predict in large well intervals or in other wells is poorly documented.

A common element in all of these studies is the calculation of statistics followed by comparison of these with the images, to see whether they are capable of describing the images in any way, before classification. Therefore investigation begins with the calculation

of various statistics associated with the images. Another very common way of classifying all different types of images (especially in astronomy and physics) is to transform various aspects of the image into the frequency domain (Will Hossack pers. comm.). Spectral analysis of the data is illustrated in Section 5.4.3.

### *5.4.2 Statistical pad analysis*

Statistical analysis of the microresistivity image log data took place across all three wells. A number of statistics were calculated, in order to assess which were able to describe the different image facies most effectively. The arithmetic mean, standard deviation, covariance, skewness, and kurtosis of the image data were calculated over different vertical moving windows of 0.5", 6", and 12" for all pads and flaps combined *and* for a single pad. Button responses were also stacked in a similar way to reflections in seismic data (this simply involved the summing of all the button responses at a single depth level followed by division by a constant). The equations used to calculate statistics were taken from Press *et al.* (1992):

$$\bar{x} = \frac{1}{N}\sum_{j=1}^{N} x_j \tag{5.1}$$

$$Var(x_1 \ldots x_N) = \frac{1}{N-1}\sum_{j=1}^{N}(x_1 - \bar{x})^2 \tag{5.2}$$

$$\sigma(x_1 \ldots x_N) = \sqrt{Var(x_1 \ldots x_N)} \tag{5.3}$$

$$Skew(x_1 \ldots x_N) = \frac{1}{N}\sum_{j=1}^{N}\left[\frac{x_j - \bar{x}}{\sigma}\right]^3 \tag{5.4}$$

$$Kurt(x_1 \ldots x_N) = \left\{\frac{1}{N}\sum_{j=1}^{N}\left[\frac{x_j - \bar{x}}{\sigma}\right]^4\right\} - 3 \tag{5.5}$$

$$CV = \frac{\sigma}{\bar{x}} \tag{5.6}$$

Where $\bar{x}$ is the mean, *Var* is the variance, *Skew* is the skewness, *Kurt* is the kurtosis, and *CV* is the coefficient of variation (or covariance). The skewness is a quantitative measure of the actual skewness of a distribution and the kurtosis measures the peakedness or flatness, both relative to a normal distribution. The coefficient of variation is a measure of the variation in

a distribution (similar to the standard deviation). It is used in preference to the standard deviation or variance because in many cases the standard deviation is dependant on the mean. To compare variations of distributions correctly the coefficient of variation should be used. These quantities were calculated via a program written in FORTRAN.

Statistics were calculated over a number of different moving windows as it was thought that using values that relate to buttons from individual depth levels would produce spurious results (see Figure 5.7). Clearly there is a compromise to strike, small moving windows pick out too much detail and do not sample the bulk response of the image, a large moving window decreases the absolute resolution (one of the reasons for incorporating the image logs is because they have a very high resolution).

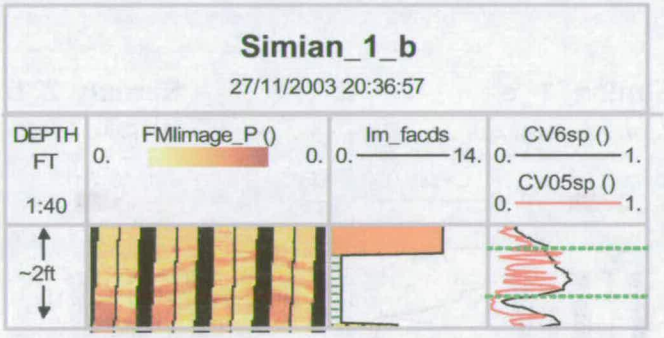



**Figure 5.7** Calculating statistics over different moving windows. The image shows a small interval of dipping laminated shale - continuous bedding fabric can be seen across the entire borehole. The logs on the right show the coefficient of variation calculated over a 0.5" moving window (CV05sp, red) and over a 6" moving window (CV6sp, black) for a single pad. Since the conductivity measurements vary considerably between the laminations the overall 'bulk' response of the CV should be fairly high. The coefficient of variation over 0.5" picks out too much detail, it shows the variation of the logs between the laminae. The curve that was calculated over the larger moving window measures the bulk response of the bed and therefore defines it more accurately – the green lines show where bed boundaries would be drawn on the basis of the CV6sp curve.

Statistics were calculated for all pads and flaps combined *and* for a single pad, since it was noted that many of the wells showed dipping beds suggesting that statistics that represented all the data would be averaged at bed boundaries resulting in ambiguous interpretation (see Figure 5.8). This is especially important where thin beds exist (Figure 5.8b). It is possible to estimate an average structural dip for a particular well and then perform an automated dip correction, as in Schlumberger's BorTex program. However in these data the dip changes rapidly down the wells (Figure 5.9), and in many cases the dips indicated by the image logs

are sedimentary dips. Also the transformation of the image data into the frequency domain is more successful when done on a single pad basis (see next section). Thus single pad statistics are preferred and these are presented from now on. It is also hoped that the application of the thin-bed repair program described in Chapter 4 might improve any ambiguous predictions at bed boundaries.

The various calculated statistics along with some of the conventional logs (GR, RHOB, NPHI) were evaluated to determine those that could offer discrimination of particular image facies. This involved the study of a number of histograms as well as the various statistics plotted adjacent to the images and defined image facies. Not all of the possible permutations that were studied are shown.

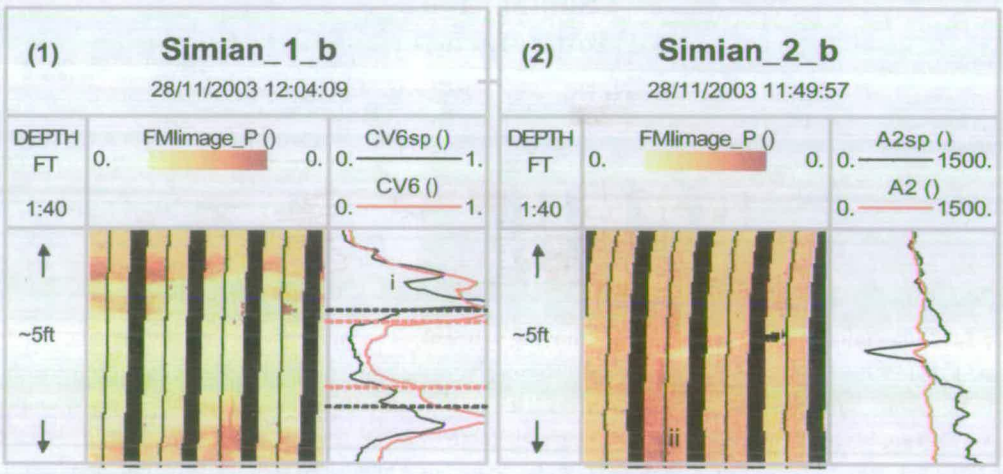



**Figure 5.8** Comparison of single and multiple pad statistics. Example 1 (left) shows a dipping thick bed of structureless sand. The coefficient of variation (CV) is a useful discriminator as the image is plain and therefore there is little variation so the CV is low. When the statistics are calculated for a single pad (CV6sp, black) sharper bed boundaries are defined resulting in more accurate definition of the bed, compared with the same statistic calculated over all the pads and flaps combined (CV6, red). The thin bed at i is also resolved better with the single pad statistics. In example 2 the image shows a thin bed of structureless sand. The average of the button responses for a single pad over 2" (A2sp, black) defines the bed extremely well. The average over all the pad and flaps (A2) does not pick out the bed at all. A disadvantage of single pad statistics is also demonstrated in example 2 – the pad from where the A2sp curve was calculated is indicated (ii), and the recorded conductivity at this point is seen to be higher than many of the other pads, resulting in the average for this pad being higher than the average for the all the data. This could result in an incorrect interpretation. A disadvantage of using the CV statistic can also be seen in example 1. Although this curve has the potential to discriminate the bed shown, the peaks in the curves at the bed boundaries are in effect artefacts because the moving window at this point sees half of the bed above and half of the bed below resulting in maximum variation. The example shown though is the most extreme that is likely to occur (as structureless sand has such different measured conductivity values compared to most other image facies).

What can immediately be seen when the interpreted image facies (after Baker Atlas (2000 & 2001), and defined in Table 5.1) are viewed adjacent to the images is that there is a lot of ambiguous interpretation. Figure 5.10 shows a variety of sections where the author believes the interpretation to be uncertain. In many cases the image does not match the description in Table 5.1 and different image facies appear to have very similar images. This ambiguity may exist for a number of different reasons; human error, or because many of the sections were also interpreted in the presence of core. The neural network model can only utilise the images and conventional logs. If two particular intervals of core have different properties but their images are the same the model will see them as the same. In order to overcome this, a number of zones were created in each well where the interpretation was deemed good. These zones combined represent a database, which was known to contain the key features that define specific image facies. These sections will make up the training sets that models will be trained on (see Section 5.5). Therefore when various statistics are previewed they should come from this database.

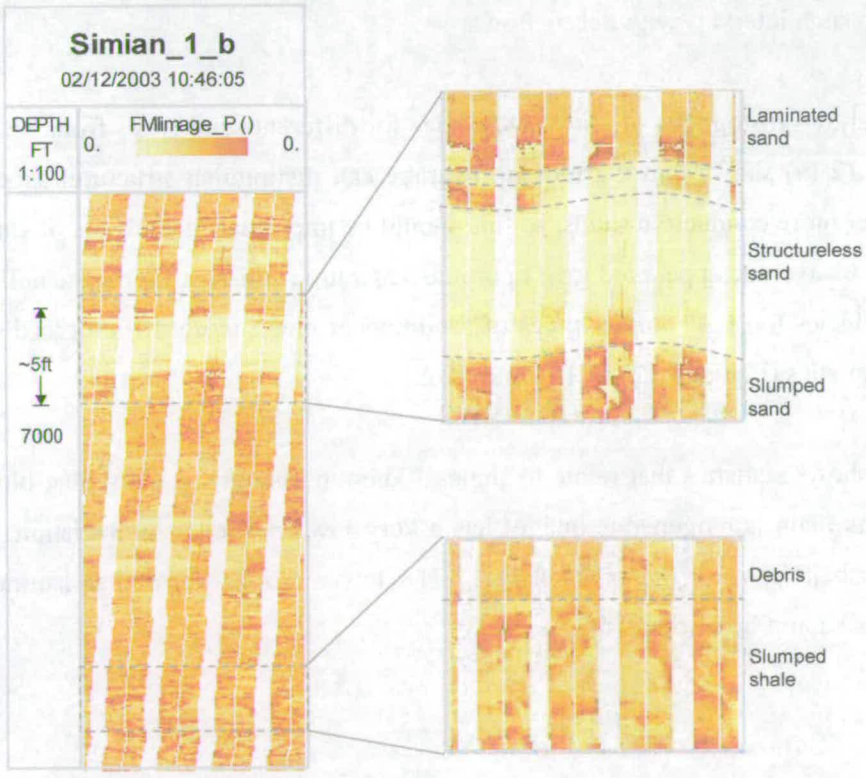



**Figure 5.9** Variable dip in a single well. A well section from Simian 1 is shown, and the image facies defined by Baker Atlas (2000 & 2001) are labelled. In the upper part of the section a definite dip can be interpreted from the amplitude of the bed boundaries. Lower down the boundary between the debris flow and slumped shale appears flat (dashed line). A 'standard' shift to remove the effect of dip would alter the lower boundary and could result in an incorrect interpretation. Correction for dip usually requires some adjustment by hand, which detracts from the automated process.

Figure 5.11 shows the power of the conventional logs in discriminating the defined image facies. The neutron and gamma ray can easily distinguish sand from shale, and the density log can distinguish cemented zones (that often correspond to conglomerate). The use of these logs should not be underestimated (indeed these are always necessary when interpreting image logs by hand to determine whether an interval is a sand or shale (Malcolm Rider pers comm.)). Figure 5.11(c) shows that statistics for sandy and shaly image facies (including simply the average conductivity) overlap significantly. This implies that the conventional logs should be used during analysis.

Figure 5.11 (b) shows how the neutron and gamma ray logs can also define image facies that have been interpreted as debris flows. In virtually all cases the debris flows show a 'shale' neutron density signature (the neutron lying to the left of the density log), but they are very close together. The logs appear to be responding to the increased sand content that is usually present in these heterogeneous sediments. Thus these logs are expected to be important in distinguishing debris flows. Shaly intervals are also shown that contain thin sand beds. These also have a very close neutron density separation, so it is possible that the network could mix up such intervals with debris flows.

Figure 5.12 shows histograms of various statistics for different sand types from well Simian 1. Figure 5.12 (a) shows that the moving average can distinguish structureless sandstone from the other more conductive sands, so this should be important in analysis. It can also be seen that the 6" average appears to give optimum separation (this is true for the definition of other image facies too). The other types of sand appear much more difficult to distinguish with these statistics (Figure 5.12 (b), (c), and (d)).

Figure 5.13 shows statistics that relate to shales. The top histograms show that bioturbated shale (with its plain homogeneous image) has a very low coefficient of variation, and this can distinguish it from all the other shales. The lower graphs show that laminated and chaotic shales cannot be distinguished.

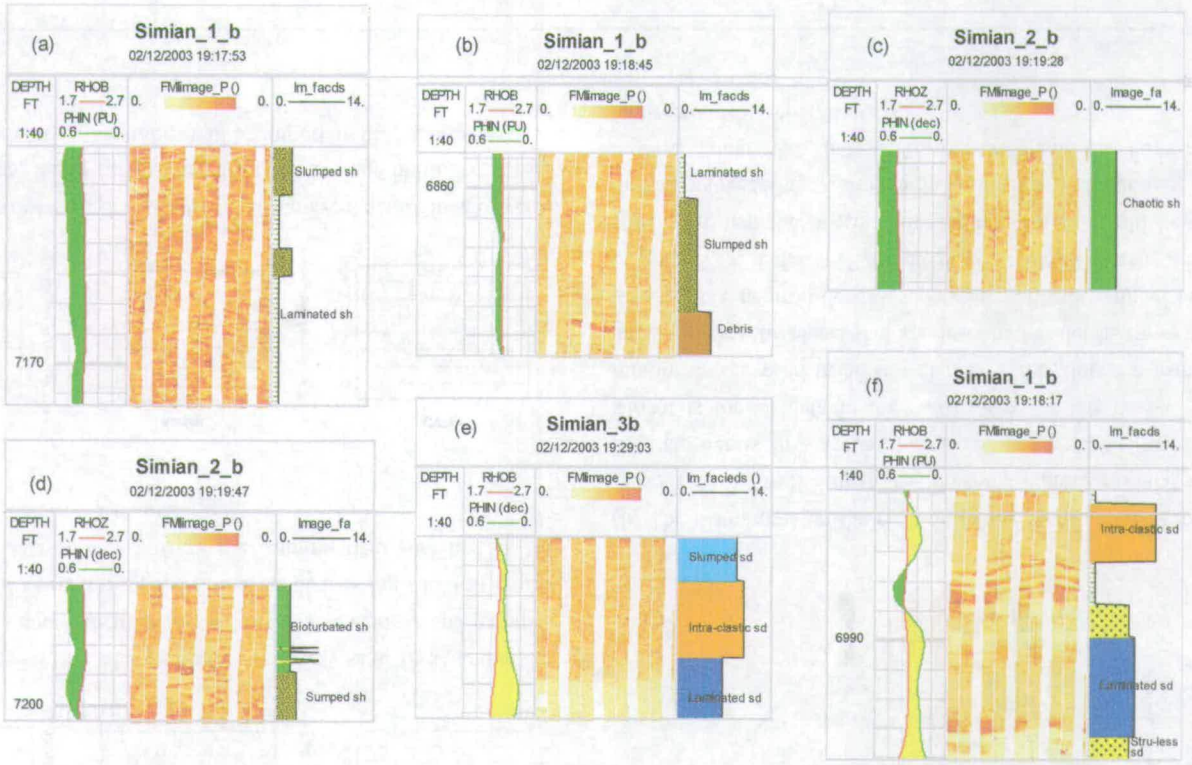
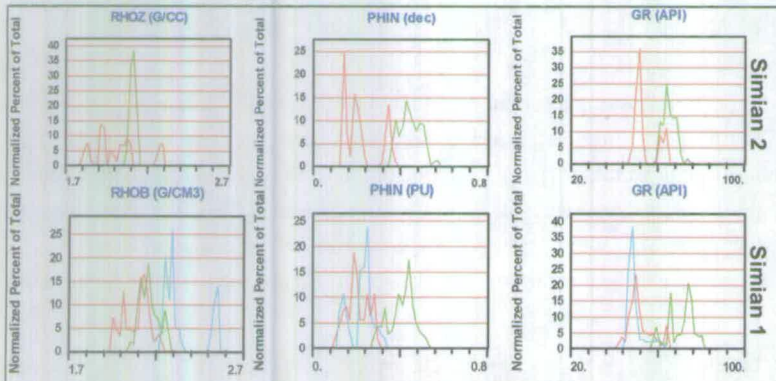
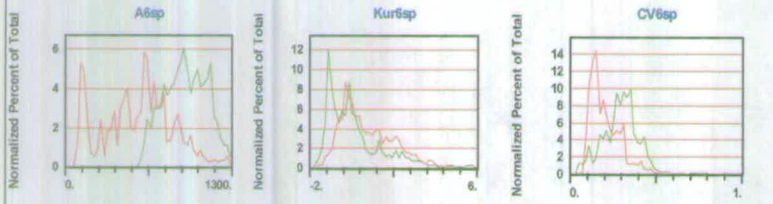


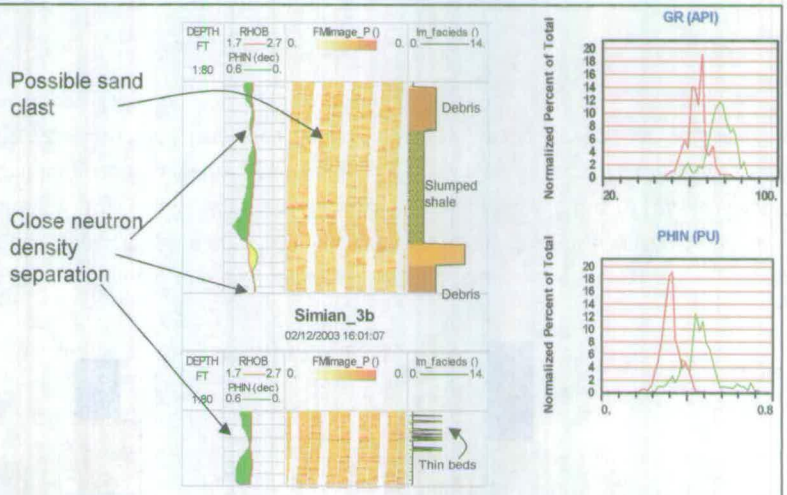

**Figure 5.10** Ambiguity in the defined image facies scheme. In (a) laminated shale has been interpreted but no continuous horizontal bedding fabric exists. Also there is no clear difference in the image between sections interpreted as slumped or laminated shale. (b) Again laminated and slumped shales have been interpreted with no clear difference between them; the plain and speckled nature of the image suggests that this should have been interpreted as bioturbated shale. (c) Chaotic shale which shows a similar image to that of (b). (d) Bioturbated shale that shows some continuous laminations across the borehole. (e) This section shows slumped and intraclastic sand that appear to have very similar images. The laminated sand represents a zone of very high resistance that usually represents structureless sand. (f) In this example intraclastic and laminated sands show very similar images, there appears no particular properties that can tell them apart. All images are dynamic, and in each case 1 vertical square represents 1ft.




(a) Histograms showing the distribution of different sand (red) and shale (green) image facies and cemented zones (blue). The neutron and gamma-ray logs can distinguish sand from shale, and the density log can distinguish cemented zones. Data shown is from the training data (see text). No cemented zones exist in well Simian 2.

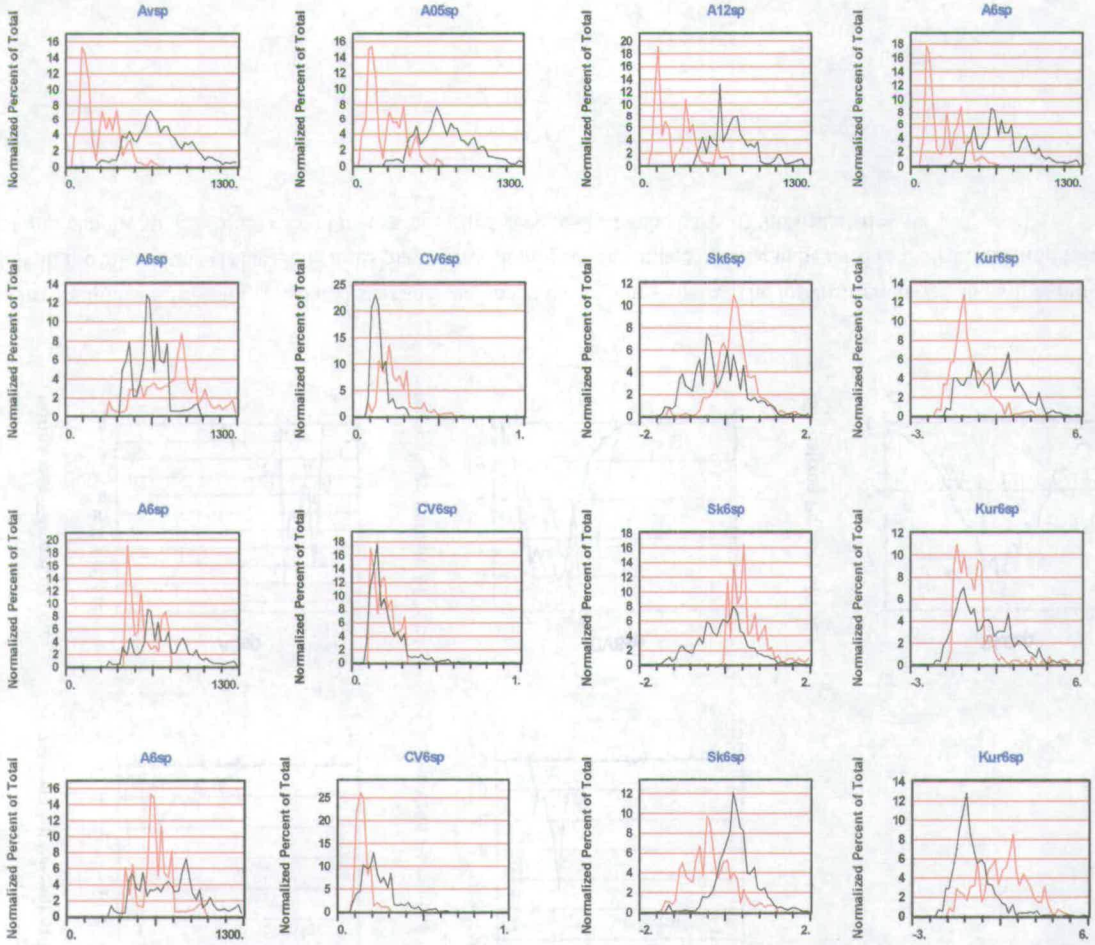



(c) There is much overlap in the statistics that represent sandy image facies (red) and shale image facies (green), even for the average button response. This implies that the conventional logs will be important during analysis.




(b) The histograms on the right show the distribution of log data by image facies type, in well Simian 1 – both the gamma-ray and neutron logs can separate debris flow (brown) from all other shaly image facies (the data shown is for all data in the well). On the left it can be seen that this relationship is valid in other wells too – the plots are from well Simian 3, and show that the places that are described as debris flows consistently have a very close neutron-density separation reflecting higher bulk sand content compared to shales. Highlighted is a possible sand clast on the image suggesting that the debris flow defined above should be extended further down – representing possible ambiguous interpretation (see text). It can also be seen though, that shaly horizons that contain thin beds also show a close neutron density separation.

**Figure 5.11** The use of conventional logs in image facies analysis (a, b). Various image statistics overlap significantly between sand and shale groups (c).




(a) The histograms show that structureless sst (red) can be distinguished from all other sst via the average conductivity. Figure 5.7 described why averages over small moving windows can produce erroneous results (e.g. Avsp and A05sp). The average over 6" is to be preferred as there is less overlap than over 12", and therefore one would expect more accuracy in its definition.

(b) The histograms show overlap between laminated sands (red) and other conductive sands (slumped and intraclastic, black). Some distinction can be seen from the average, the CV and kurtosis. However laminated sands are generally difficult to distinguish.

(c) The histograms show overlap between slumped sands (red) and other conductive sst (laminated and intraclastic, black). These are difficult to distinguish on the basis of these statistics. Note that the slumped sand histogram only represents approximately 1ft of data.

(d) Some distinction can be seen between intraclastic sst (red) and other conductive sst (laminated and slumped, black). However generally these are difficult to distinguish.

**Figure 5.12** Distributions of different calculated statistics via image facies type for well Simian 1- sands. Note that there is no slumped sand at all in this well. For acronyms please refer to the notations and conventions section preceding Chapter 1.

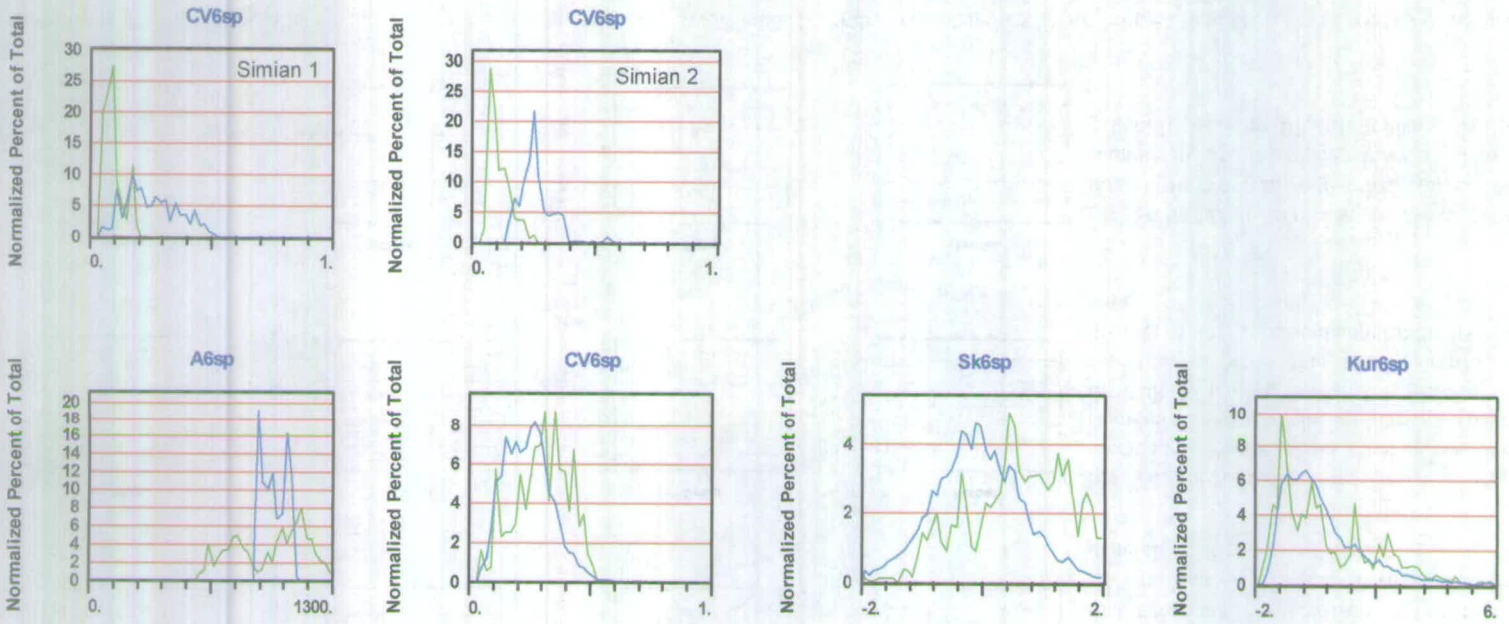



**Figure 5.13** Distributions of different calculated statistics via image facies type - shale. The top histograms (a) show that bioturbated shale (green) has a low coefficient of variation compared with all the other shales (blue), due to its plain fairly homogeneous image. This can be used as a discriminating factor. The lower histograms (b) show that laminated shales (green) and slump/chaotic shales (blue) cannot be distinguished very easily on the basis of these statistics.

### 5.4.3 Spectral analysis of image logs

Power spectral analysis of the image data took place in both the vertical and horizontal directions. An introduction to some of the theory behind this approach can be found in Figure 5.14. Log analysts are familiar with this type of analysis as it is commonly used to recognise repeating sedimentary cycles (e.g. Worthington 1990). However, Luthi (1994) was possibly the first author to use the power spectral method to quantify what he describes as 'macro-textures' from image logs. A macro-texture is defined by Luthi as a repetitive pattern of two or more textures (textural elements that show a specific pattern down the borehole). Luthi carried this out in the vertical direction only and computed the mean frequency over lengths of 32 and 64 pixels (approximately 8cm and 16cm respectively). The resulting mean frequency was then used with other textural measures to evaluate lithofacies, over a short 10m well section.

The programs used in this study were provided courtesy of Roger Hipkin at the School of Geosciences, Edinburgh University. The result of implementing the programs with synthetic data can be seen in Figure 5.15. These show the expected results if vertical or horizontal repeating stripes are present in the images. The stripes shown represent a pure sine wave with a single frequency, and so the resulting power spectrum is a single spike. This work not only illustrates what kind of results one can expect, but also serves as a test of the programs, and illustrates how power spectra data are conventionally illustrated.

The power spectra were calculated vertically with moving windows of 32, 64, 128, and 256 pixels (3.15" to 2.1ft) and for the 64 pixel moving window over all the data, and over data from a single pad. Figure 5.16 compares the results of calculating the spectrum over all data and a single pad of data. It is seen that in general different beds are differentiated more easily in the spectrum from a single pad of data. This is in part from dipping bed boundaries, which appear much fuzzier when the spectrum is applied to all the data. It is also because of very slight misalignment of textures from one pad/flap to another. Imagine a section of laminated shale (e.g. near the top of Figure 5.16) in which the laminations do not line up across the entire image (i.e. they are not perfect horizontal stripes as in Figure 5.15). This is partly because of pad/flap misalignment and tool response but also simply because of natural variation and variable dip. Therefore for all subsequent analysis over all wells the vertical power spectrum was calculated over a single pad of data only. For the power spectrum in

the horizontal direction this was also calculated over data from a single pad. This was for two reasons. Firstly a transform across all the data does not equate to a true azimuthal transform, because the data is not continuous around the borehole, as there is a gap between each pad/flap combination. To calculate a true azimuthal transform is more complex. The second reason (and more important) is that already mentioned in relation to the vertical transform – that textures across the borehole do not always line up very well. A very slight change in the data from one pad to another, discontinuous laminae, are all strongly highlighted by the horizontal transform. For these reasons the horizontal transform was also restricted to a single pad. This meant that the length of the array that underwent the discrete transform was fairly short (24 pixels). In order to make the data more continuous (and the program more efficient) the transform was carried out with the mean button values of the relevant pad attached to the end of the signal (see Figure 5.17). A sample of frequencies from the lower frequency end of the spectrum was selected for analysis. It can be seen that the low frequency sample corresponds closely to the full spectrum, if it were calculated over 24 points only. In the case of the vertical power spectrum a moving window of 128 points appeared to produce the best results. This again is a compromise - shorter moving windows may not capture the full image texture (the extreme would be if the window was smaller than the distance between laminations for instance), longer moving windows produce more frequency components and are therefore numerically more difficult to handle, and also produce more fuzzy bed boundaries. All vertical spectra shown from now on were calculated over a 128 point data window.

Physical data can be described in the time domain with the quantity in question e.g. *(h)* being a function of time *t* e.g. *h(t)* or else in the frequency domain where by the quantity is specified by its amplitude *H* (which is usually a complex number that also indicates phase as a function of frequency) e.g. *H(f)*. Essentially these are two ways of representing the same function. The discrete Fourier transform is the way in which the function *h(t)* is transformed between these two domains when it is *sampled*. The discrete Fourier transform of *N* sample points $h_k$ is *Hn*:

$$H_n \equiv \sum_{k=0}^{N-1} h_k e^{2\pi i k n / N}$$

for *k*=0, 1,2...N-1. If *h* is a measure of distance then *H* is a function of inverse wavelength (in cycles per unit distance). If *h(t)* is sampled at regularly spaced intervals and the distance between the samples is Δ then the Nyquist critical frequency *(fc)* can be defined as:

$$f_c \equiv \frac{1}{2\Delta}$$

The sampling of a wave at its Nyquist frequency represents a data point at a peak, and then a trough, repeated – *'critical sampling of a sine wave is two sample points per cycle'* (Press *et al.* 1992). This is important because when the power spectral density of a function is evaluated (see below) the maximum frequency that it is possible to sample is the Nyquist frequency. Larger frequencies than this are *aliased* (falsely translated) into the range (*-fc* , *fc*).

The power spectrum is a method to estimate the amount of power present in the component frequencies of a signal (this is essentially a way of comparing and quantifying the amount of *amplitude* in the fundamental frequencies of any signal). If an N-point sample of the function *h(t)* is taken its discrete Fourier transform computed, then the power spectrum can be defined for N/2+1 frequencies as:

$$P(0) = P(f_0) = \frac{1}{N^2}|H_0|^2$$

$$P(f_k) = \frac{1}{N^2}\left[|H_k|^2 + |H_{N-k}|^2\right]$$

$$P(f_h) = P(f_{N/2}) = \frac{1}{N^2}|H_{N/2}|^2$$

If the power spectrum is taken as a function of distance then the resulting units are $m^4$. It is convention though for the units not to be shown, what is important is the relative power of different frequencies (and therefore no units of power are displayed in this thesis). For the analysis considered here the power spectrum was computed over a vertical moving window of 128 data points (these represented the average button values at each depth). The distance between the button values is 2.5mm (Rider 1996), so the Nyquist frequency is $0.2mm^{-1}$ (a wavelength of 5mm). Thus the application of the spectral power method vertically, resolves the power of component waves with wavelengths ranging from 5mm to 320mm continually along the borehole. Pad buttons are also 2.5mm apart horizontally (Rider 1996) so the application of the power spectral method horizontally resolves the power of component waves with wavelengths 5mm to 60mm. Figure 5.15 shows how the resolved power spectra are conventionally displayed.

**Figure 5.14** Explanation of the theory behind the power spectral method. The description and equations are taken from Press *et al.* (1992). The programs to calculate these quantities were provided courtesy of Roger Hipkin at the School of Geosciences Edinburgh University.

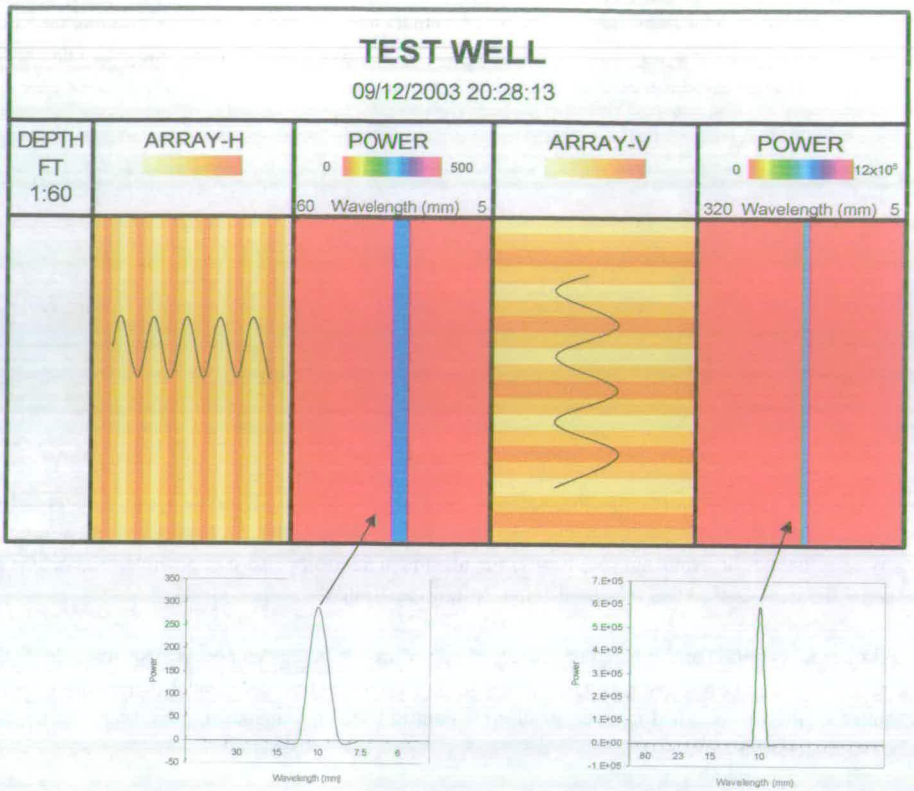



**Figure 5.15** Testing the power spectral approach with synthetic data. The left array shows a series of vertical stripes that are equally spaced. The shading of the stripes represents the value at that point in the array. Each stripe has a width of 1 pixel, so the 24 stripes equate to a single FMI tool pad or flap. The stripes represent a pure sine wave (shown) with a wavelength of 4 pixels (10mm on the tool). This represents the single frequency present in the sine wave. The power spectrum analysed over each row of data, plotted against depth is shown. Since any pure sine wave contains only a single frequency the resulting power spectrum shows a single stripe at a wavelength of 10mm. Power is colour-coded, the blue represents high power, the red very low power. The lower graph illustrates the same result. The right array shows horizontal stripes colour coded as before, and with each stripe once again being a single pixel in width. Data at each depth level was averaged. The power spectrum shown is from the implementation of a sliding power spectral analysis of the average curve over a moving window of 64 pixels. Once again a single peak is seen at a wavelength of 10mm as expected. These results show that that the programs are working properly, and illustrate the type of result to expect if vertical and horizontal features are present in the images. Note the scale of the power of the right-hand array – it is very large. For this reason in all subsequent interpretation on real data the natural log of the power was calculated and used for analysis. The result though is still referred to simply as 'power'.

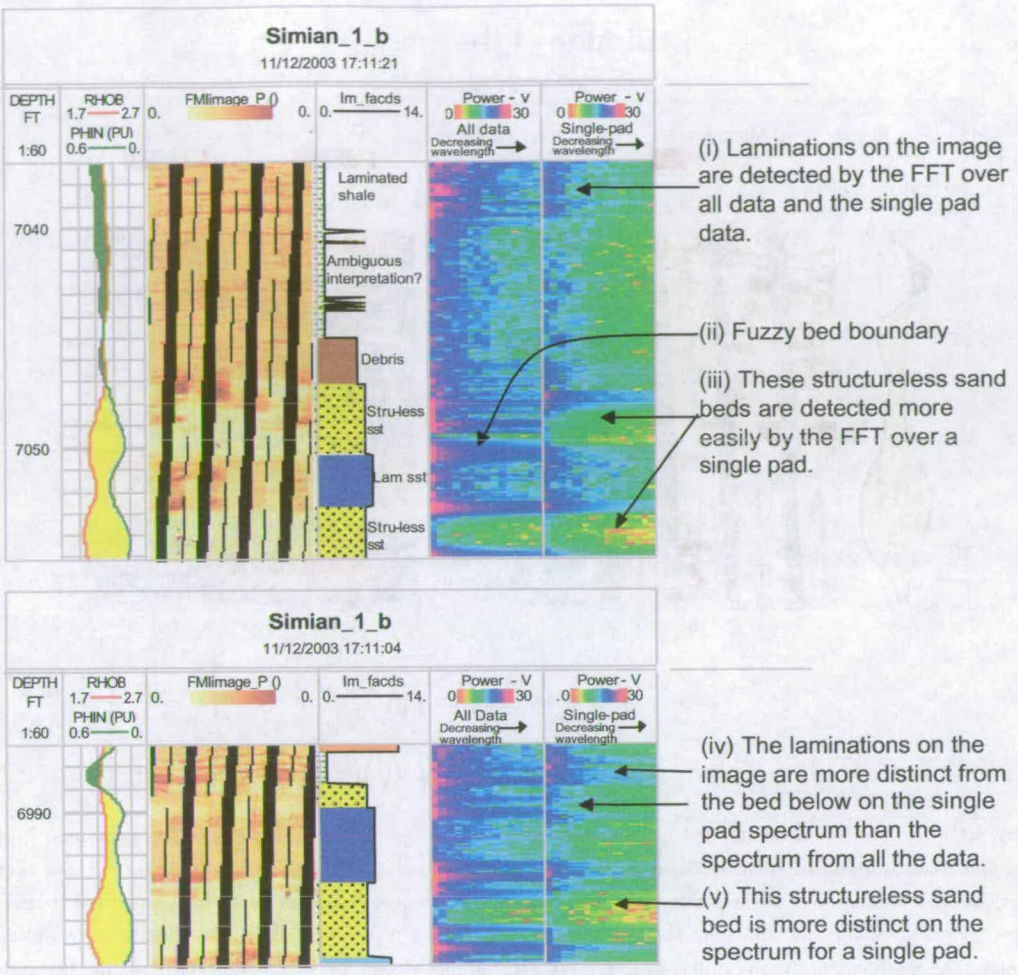



**Figure 5.16** Comparison of spectral analysis of a single pad of data and all data. The left spectrum shows the results of a vertical spectral analysis over a moving window (64 pixels) over the average for all the data (average of 192 button responses). The right spectrum shows the results of spectral analysis over the average of a single pad of data (24 button responses). It can be seen that at (i) both spectrums recognise the laminations in the shale (this is seen as a blue / purple high at the low frequency end of the spectrum). At point (ii) it can be seen that both spectrums pick out the bed boundary (as this represents a point of maximum change); however the bed boundary is less prominent in the single pad spectrum and because of this the laminated sand bed is more distinct in this spectrum. At point (iii) and (v) structureless sandstone beds that are easily identified by their image are much clearer in the single pad spectrum. Point (iv) shows an area that represents laminated shale above structureless and laminated sandstone. The laminations are identified by both Fourier transforms. However because the beds are dipping the shale-sandstone boundary is much sharper in the single pad spectrum than in the spectrum over all the data and therefore the beds are easier to distinguish. The image shown is from Simian 1 and is dynamic. 1 vertical square represents 1 ft.

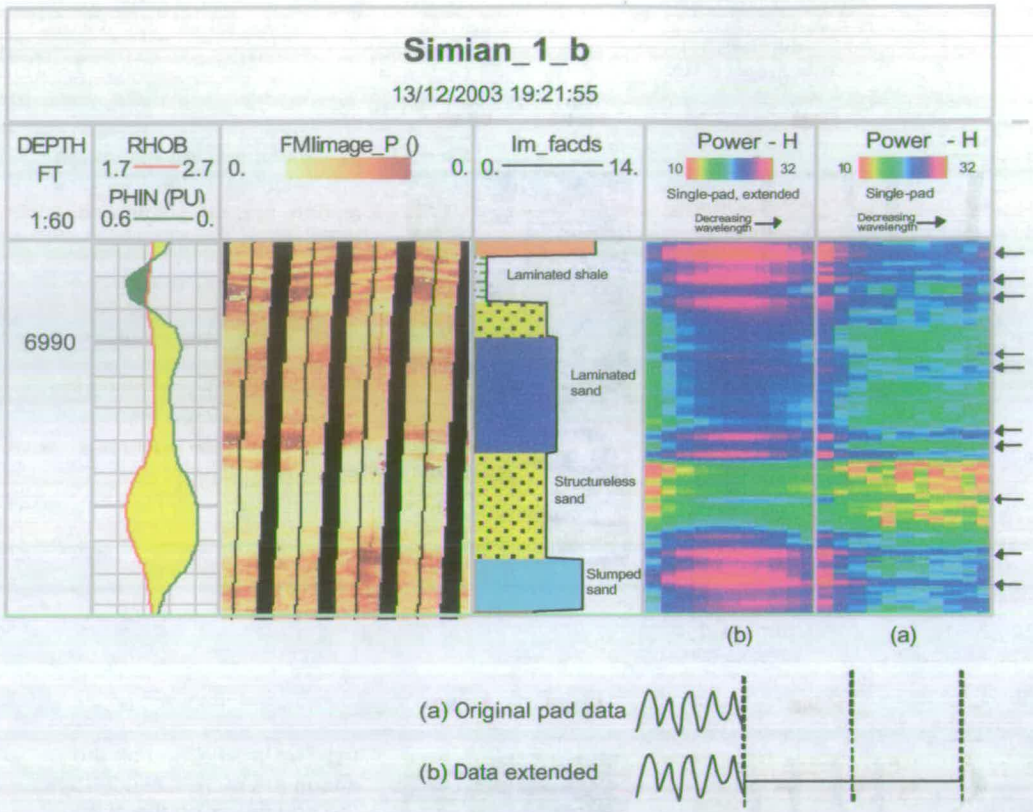



**Figure 5.17** The frequencies contained in the power spectrum of a discrete wave (a) are also contained in the power spectrum of the same wave if it is extended (b). The right hand power spectrum (a) is that from a single pad of data (24 points only). Where the data changes horizontally across the pad there is a purple/red 'high' at the low frequency end of the spectrum (black arrows). The spectrum picks out the slumped sand very well. It also picks out the boundary between the structureless and laminated sand (as this is dipping). As the laminated shales are also dipping this means that there is variation across the pad and the spectrum sees this too. The other power spectrum (b) is of the same data but with the mean button value repeated on the end. As the length of the signal is longer more frequencies are present in the spectrum, however only a sample of the frequencies present are shown – those that contain most information. It can clearly be seen that the detail picked out in spectrum (a) is also present in spectrum (b) and indeed it is much clearer in (b). The image shown is from Simian 1 and is dynamic. 1 vertical square represents 1 ft.

It must now be determined exactly what the vertical and horizontal power spectra are measuring and whether they are able to assist in image facies interpretation. Figures 5.18, 5.19, and 5.20 show the power spectra of the image data adjacent to a variety of different image facies from all available wells. It can be seen that the spectra do not show single frequencies that relate to specific textures, but they do show high/low power contrasts in certain frequency ranges that correspond to specific textural elements that are seen in the images. Laminated shales are clearly distinguished by the vertical power spectrum, as

purple/red highs at the low frequency end. Slumped shales show this feature too, but also have very high horizontal power indicating a higher degree of variation in the image data in this direction. Structureless sand and bioturbated shale have very low power because of their plain image. The power spectral method though does not appear to be able to quantify any differences between slumped and chaotic shale, or between laminated, intraclastic, or slumped sand (although the image interpretation shown in Figure 5.20 could have been misinterpreted). In summary the power spectral method appears to measure and quantify the amount of heterogeneity in the image data. Since this was carried out both vertically and horizontally it provides a measure of *directional heterogeneity*. The next section discusses how power spectral analysis and the calculated statistics can be used as neural network inputs.

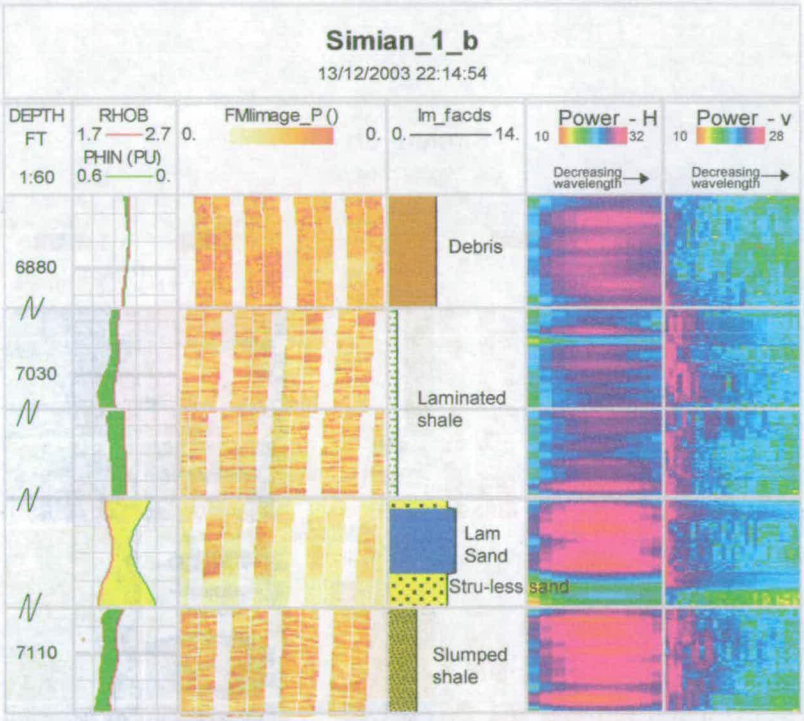



**Figure 5.18** Horizontal and vertical power spectra of different image facies, well Simian 1. Track 5 is the horizontal spectrum, track 6 the vertical spectrum. Slumped shale shows high power in both the horizontal and vertical directions indicating variation in these directions in the image. This is in contrast to laminated shale which shows high power at the low frequency end of the vertical spectrum (due to the horizontal laminations), but slightly lower horizontal power. The image of the debris flow appears to have no vertical pattern and therefore there is low-medium power in the vertical direction. The horizontal power is high. Structureless sand with its plain image is very distinct on both spectrums – with exceptionally low power, in contrast to the laminated shale that has high horizontal power and a reasonably high vertical power. The image is dynamic, and 1 vertical square represents 1 ft.

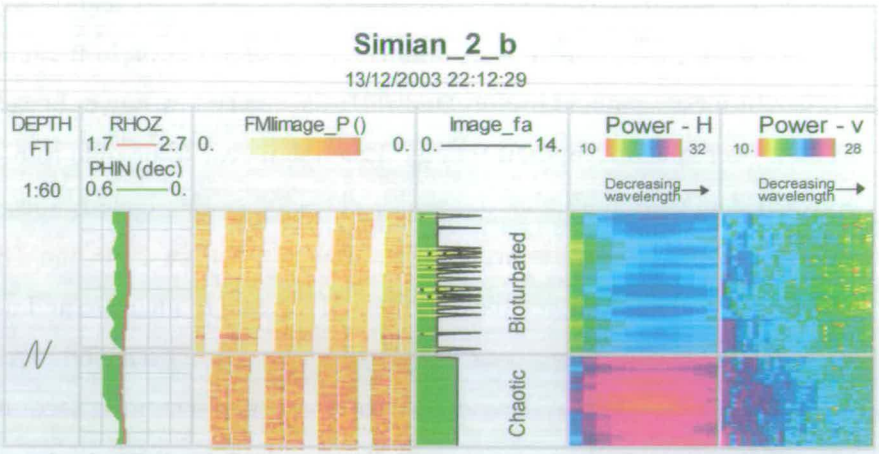



**Figure 5.19** Horizontal and vertical power spectra of different image facies, well Simian 2. The plain image of bioturbated shale has low power in both the vertical and horizontal spectrums. In contrast chaotic shales have high horizontal and vertical power (similar to the slumped shale in Figure 5.18). The image is dynamic and 1 vertical square represents 1 ft.

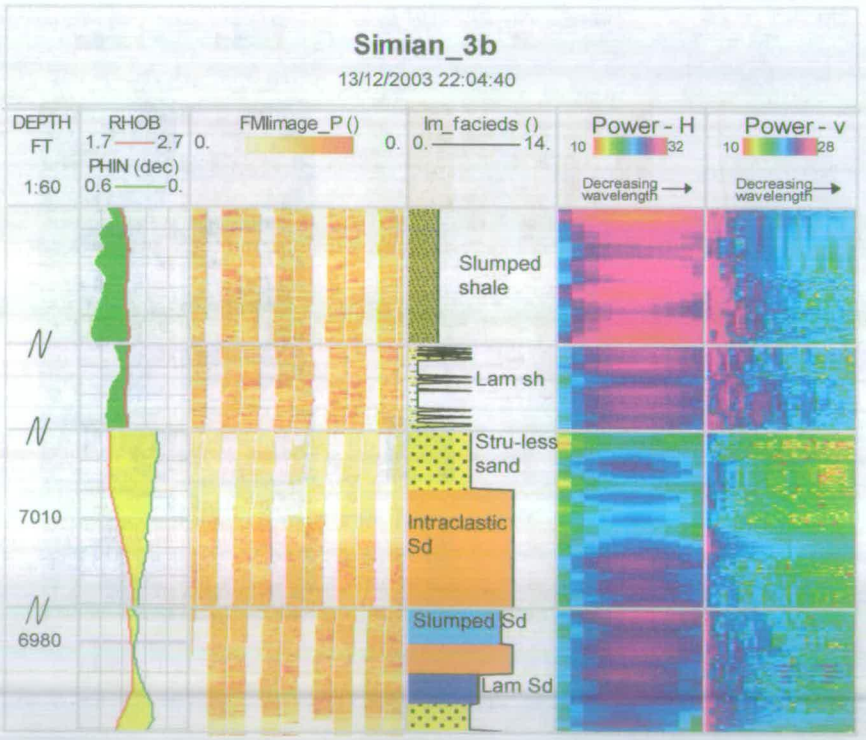



**Figure 5.20** Horizontal and vertical power spectra of different image facies, well Simian 3. Slumped shale can be seen with high vertical and horizontal power; laminated with lower horizontal power. Different types of sand are also shown. The structureless sand is very distinct as it has low power in both spectrums. However there appears no distinction between the laminated, slumped or intraclastic sand. The images actually look the same, so the author believes this to be an area where the interpreted image facies could be incorrect (the speckled nature of the image suggests it is all intraclastic sand). The image is dynamic and 1 vertical square represents 1 ft.

### 5.4.4 How can these data be used?

A variety of image statistics have been calculated and also the power spectrum both vertically and horizontally across a single pad of image data. This means there are many different statistical curves as well as many individual power curves for each frequency represented in the spectrum (for the vertical power spectrum this is 64 curves, for the horizontal spectrum 12 frequencies were sampled). Since there are so many possible inputs, how can these be used? Luthi (1994) used Principal Component Analysis (see Chapter 1) to reduce redundant information in his multivariant data (in this case he reduced ten principal components to three, which accounted for almost 96% of the variance in the data). However in Chapter 3 it was discussed how the backpropagation algorithm is able to effectively 'sort' the input variables into those that contribute to classification and those that do not. Therefore it is proposed that a large number of inputs are selected that are thought to be useful image facies discriminators, and the network is allowed to sort them. Indeed it is fairly common in traditional applications of the backpropagation algorithm to have many inputs, e.g. Pomerleau (1993) who used 960 inputs from a 30x32 input 'retina' to steer a moving vehicle.

Potential inputs were also correlated with various image facies that were described by Baker Atlas (2000 & 2001). The correlations showed which measures were capable of discriminating features present in the images (and they also highlighted places where the Baker Atlas interpretation was thought to be ambiguous or wrong). Specifically no discernable differences could be found between the chaotic and slumped shale. The difference between these shown in Table 5.1 is that chaotic shale is described as being a gravity driven failure of a shale mass, rather than a gravity driven failure of a semi-consolidated shale mass (slumped shale). The slumping in slumped shale is thought to have derived locally whereas the chaotic shale is interpreted as having been transported further before deposition. Also very few differences could be seen on the images between laminated, slumped, and intraclastic sand. There are two exceptions to this – in well Simian 1, where some faint laminations can be seen at approximately 7065ft and slumped sand can be seen at 6997ft (both in Figure 5.3). In all other sections of the three wells where intraclastic/laminated and slumped sand have been interpreted it is very difficult to tell them apart. Baker Atlas (2000 & 2001) actually states that laminations in the sand are below the resolution of the image tool. Irregular sand occurs rarely and when it does this is also

difficult to interpret on the images. A new image facies scheme was therefore defined that neural network models were trained on. This can be seen as Table 5.3 and is loosely based in the Baker Atlas scheme. However the scheme is strictly defined by the conventional and image logs; no correlation is made to core. This scheme effectively partitions the image into various categories that all look different in some way. Once the neural network is trained and applied to unseen sections of wells it should tell us which of the facies in Table 5.3 the image is most similar to. The associations of the image facies will still provide interpretation regarding depositional process (Table 5.2).

A common feature of this particular dataset is that many thin beds of sand occur within thicker beds of shale (interpreted by Samuel *et al.* (2003) as levee deposits). Although a thin-bed is defined as being below the normal resolution of conventional logs they generally occur from a few mm in thickness up to approximately 5cm. The potential discriminators discussed so far are averaged over various vertical intervals (from 6" to 1ft) and it had been shown that this is necessary in order to describe the various textures present in the image logs. Unfortunately this means that these parameters are unable to resolve thin sand beds. These are important economically as they make up a large amount of net pay in these wells, especially in Simian 2 and 3. It will be seen in later sections that some parameters (such as the image log average), calculated over a much smaller moving window are capable of resolving thin beds. This is a problem of utilising logs with very different resolutions. What is proposed, in order to define image facies and the thin beds within them is to break the neural network analysis down into various modules. It has been shown that some sand and shale facies have overlapping log signatures (Figure 5.11c) expressing a need for these two groups of facies to be kept apart, and it is known from recent literature (Bhatt & Helle 2002b) that modular systems can sometimes show improved results compared to their single module counterparts. Therefore the modular arrangement shown in Figure 5.21 was initially used for neural network analysis. Broad sand/shale groups of facies are defined first with the conventional logs. These groups are then divided further on the basis of their lithological and textural characteristics and include image log information. Finally data from those facies that are known to potentially contain thin beds can be analysed, for thin bed detection.

| Image facies number | Lithological description (from conventional and image logs) | Textural description (from image log) | Baker Atlas scheme equivalent | Interpretation examples |
|---|---|---|---|---|
| 1 | Shale | Strongly laminated image. | Laminated mud. | Stable slope or basin floor. |
| 2 | Shale | Plain but sometimes speckled image. | Bioturbated shale. | Can indicate overbank fines, especially when associated with very thin beds of facies 5 (levee deposits). |
| 3 | Shale | Very heterogeneous image, with dipping, discontinuous and chaotic bedding fabrics. | Slumped and chaotic shale. | When occurs with facies 1 indicates inter-channel and/or overbank sediments. |
| 4 | Shaly sandstone (shale signature on neutron/density log (neutron to right of density log), but much closer together than for facies 1-3). | Variable texture, can be plain, but common are 'patches' of resistive and conductive areas (sand and shale clasts). | Debris flow. | When associated with sandstone facies, can indicate a channel complex. |
| 5 | Sand | Very high resistivity, resulting in a very low image conductivity value. Images are generally homogeneous. | Structureless sand. | When occurs thickly bedded with facies 1 and 3 can indicate intra-channel sheet fill. |
| 6 | Sand | Much lower resistivity values measured by the image than facies 5. Image texture is variable but generally heterogeneous. | Laminated, slumped, intraclastic and irregular, sand. | When occurs on a small scale (<3m in thickness) and associated with facies 3, can indicate gully erosion and infill. |
| 7 | Cemented sandstone / conglomerate (high density and low neutron values). | Image can be variable but sometimes shows evidence of pebbles. | Conglomerate. | If occurs with stacked sandstone facies above can indicate a channel base. |

**Table 5.3** Image lithofacies scheme (loosely based on that define by Baker Atlas (2000 & 2001)). This is partly based on lithological information provided by conventional logs, and textural information provided by the image logs.

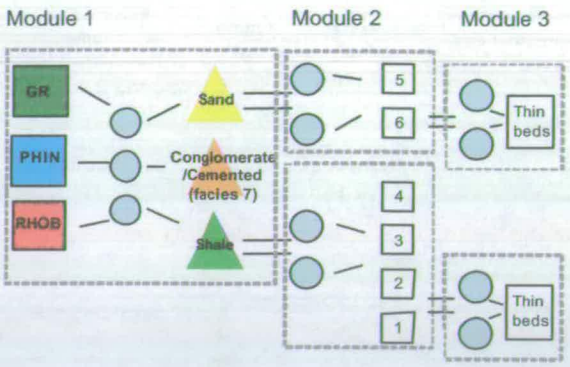



**Figure 5.21** Modular system for the discrimination of image facies. A simple neural network is used to distinguish the sand, shale and conglomerate groups with conventional logs only. The sand and shale predictions are further refined with separate neural networks, with conventional log and image log inputs. Shale facies that are known to contain thin beds are then refined further using higher resolution logs derived from image data only. Different modules are shown as a grey outline. Numbers 1 to 7 refer to facies 1 – 7 in Table 5.3.

## *5.5 Data preparation before neural network analysis*

### *5.5.1 Introduction*

This section describes the data preparation steps that took place before application of the neural network, including input selection, data transforms, inter-well normalisation, depth shifting, and training and validation set design.

### *5.5.2 Input selection*

It was shown that the neutron, density and gamma ray logs are very good at distinguishing sand from shale and that the density log is very important in recognising cemented zones. For this reason, for the first module, these three logs were selected as inputs.

For the second module (for both the sand and shale networks) that introduces image-derived logs, there are many inputs to choose from. It was proposed to simply use the ability of the backpropagation algorithm to sort the input variables during classification, rather than perform a dimension reduction stage. For this reason the vertical moving average, moving coefficient of variation, moving skewness, and moving kurtosis were selected as inputs as well as 14 frequencies from the vertical power spectrum (over a 128 pixel window), and 7 frequencies from the horizontal power spectrum. From the analysis so far it was discovered that it is the lowest frequencies in the vertical direction that appear to provide most

information. By including some higher frequencies these inputs can act as a test to see if the algorithm relegates them to be of lesser importance than other curves. Initially it was undecided whether to include the conventional logs with the image derived components. It was shown that the neutron and density logs both appeared important in defining the 'debris flow' facies (facies 4 in Table 5.3). Excluding these may be detrimental to the prediction of this particular facies. However there are some intervals of other shaly facies (facies 1 and 2) that contain many thin beds of sand. The presence of sand appears to reduce the neutron-density separation. The inclusion of conventional logs could result in the mix up of these particular facies. For this reason, for shaly facies discrimination (module 2 shale network in Figure 5.21) the neural network was run with and without conventional logs for comparison.

### *5.5.3 Data transforms*

The importance of all input data having approximately symmetrical distributions and similar variances was discussed in Chapter 3. Figure 5.22 shows examples of distributions from some of the proposed inputs. It can be seen that the spread of these data are approximately similar, (although it is noted that the kurtosis is slightly skewed). However no transforms of the data took place in this instance. Note however that the natural log of the power spectra has already been taken.

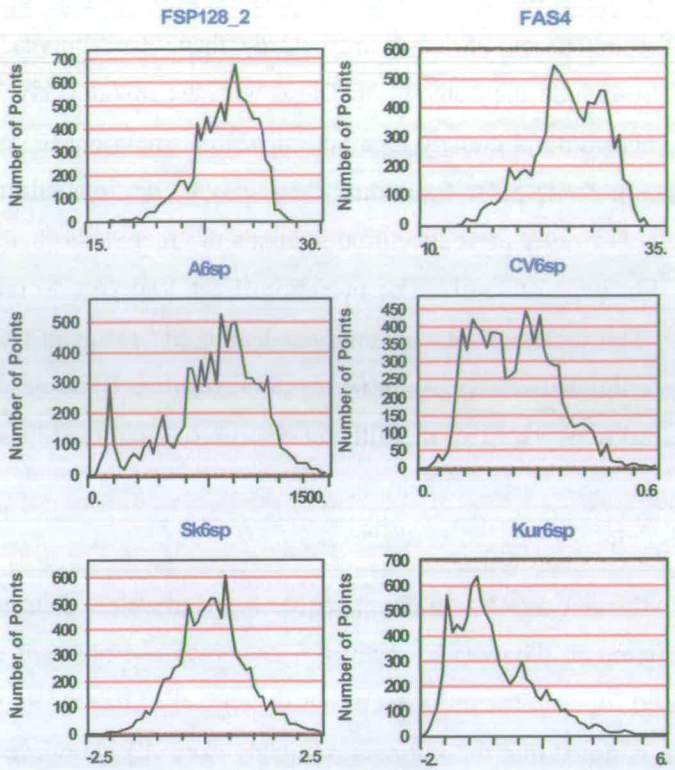



**Figure 5.22** Distributions of some input variables. Shown is the second lowest frequency in the vertical spectrum (FSP128_2), the fourth lowest frequency in the horizontal spectrum (FAS4), and the moving average, coefficient of variation, skewness, and kurtosis over 6" (A6sp, CV6sp, Sk6sp, Kur6sp). Data shown are from the training intervals in well Simian 1. Other input variables (such as other frequency curves in the power spectra), and curves from other wells show similar distributions.

### *5.5.4 Inter-well normalisation*

In Chapter 3 various factors were identified that can vary between wells, and ways were discussed to test if a neural network model is 'likely to work' in any particular well. For the Lomond data set a standard interval (the shaly section of the Sele Formation) was identified and it was used to identify wells that appeared to have fundamentally different log responses to other wells. They were subsequently excluded from the training set. For the Simian wells this step is also important. The majority of the input parameters to be used are not 'absolute' measurements – the coefficient of variation and power spectra for instance all measure variation in logs and these curves should therefore not require any inter-well normalisation. Inputs such as the average button response, the density, neutron, and gamma ray log may require normalisation.

However for the Simian wells it is very difficult to calibrate in the same way as Lomond. There is no 'standard' shale section that can be correlated between the wells. The only possible interval is at the very top of the wells above the main canyon fill that represents general background sedimentation (although it has been interpreted as laminated, bioturbated, and chaotic shale by Baker Atlas (2000 & 2001) suggesting that it may not all be pelagic/hemipelagic sedimentation). In this interval in Simian 1 and 3 though, the borehole is of very poor quality, indicated by the caliper log, so this cannot be used. In general there is no obvious reason why there should be a large degree of inter-well variability. The well intervals all occur at similar depths (Simian 1 6830ft – 7200ft, Simian 2 6880ft -7350ft, Simian 3 6770ft – 7240ft), and all were drilled with similar tool types. However the borehole diameter in Simian 2 is 12" (it is 8" in Simian 1 and 3). This could affect the gamma-ray log (Malcolm Rider pers. comm.). Also the response of the FMI tool can vary due to changes in the input voltage during logging (although an Emex correction was applied in Section 5.3.3). For these reasons some calibration was attempted, shown in Figure 5.23. Some very small intervals of structureless sand (that is very easy to identify on the images), and a short arbitrary interval of 'shale' were identified in all three wells and the log values compared. If a neural network model is to work then these should show similar values.

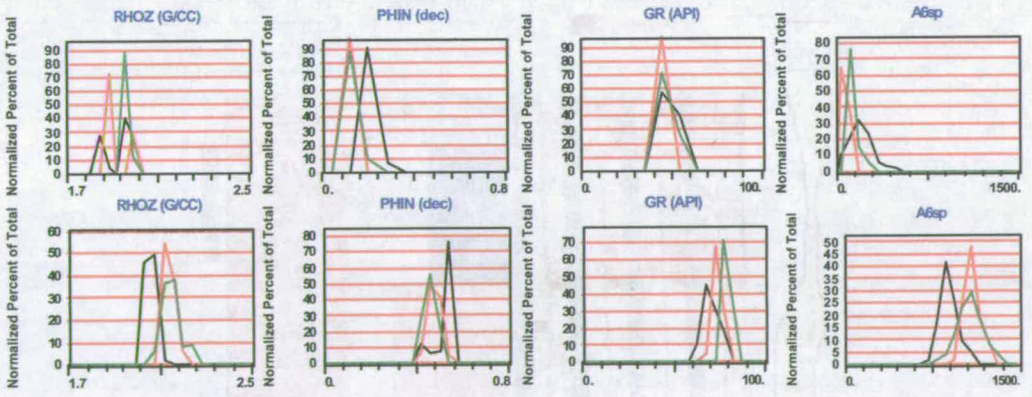



**Figure 5.23** Calibration between wells Simian 1, 2 and 3. Green curves are Simian 1, black Simian 2 and red Simian 3. The top histograms show log distributions for short sections of structureless sand. The lower histograms show the log distributions for a short section of arbitrary 'shale'. Plotted intervals are: Simian 1 6994.6-6995.7ft and 7053.1-7054.9ft for structureless sand, and 7140-7150ft for shale; Simian 2 6975.4-6976.4ft, 6929.6-6930.9ft and 6906.8-6907.6ft for structureless sand and 7322-7329.8ft for shale; Simian 3 7115-7117.5ft and 7049.5-7050.5ft for structureless sand and 7297-7305ft for shale. See text for further details.

Although there is slight variation in the distributions between wells, in general the positions of the histograms are similar. This type of analysis is looking for large discrepancies between log signatures (as is seen for the sonic log in Figure 3.21 for instance). In all the histograms in Figure 5.23 there is some overlap between them. It must also be noted that the histograms represent short intervals, and in the case of the conventional logs therefore represent a small number of measured data points (less than 10 in some cases). For these reasons no normalisation took place. This though is not an ideal way to calibrate wells, as it requires interpretation to be carried out prior to neural network analysis.

### *5.5.5 Training and validation set design*

A single training set was created for each well, and was made up of many small intervals rather than a few large continuous ones. Sections were only included in the training set if they showed the specific characteristics described in Table 5.3 *and* if the author agreed with the Baker Atlas interpretation. This essentially acted as a double check on the interpretation (see Figures 5.24, 5.25 and 5.26). All the training intervals are indicated on the full logs in Appendix 5.

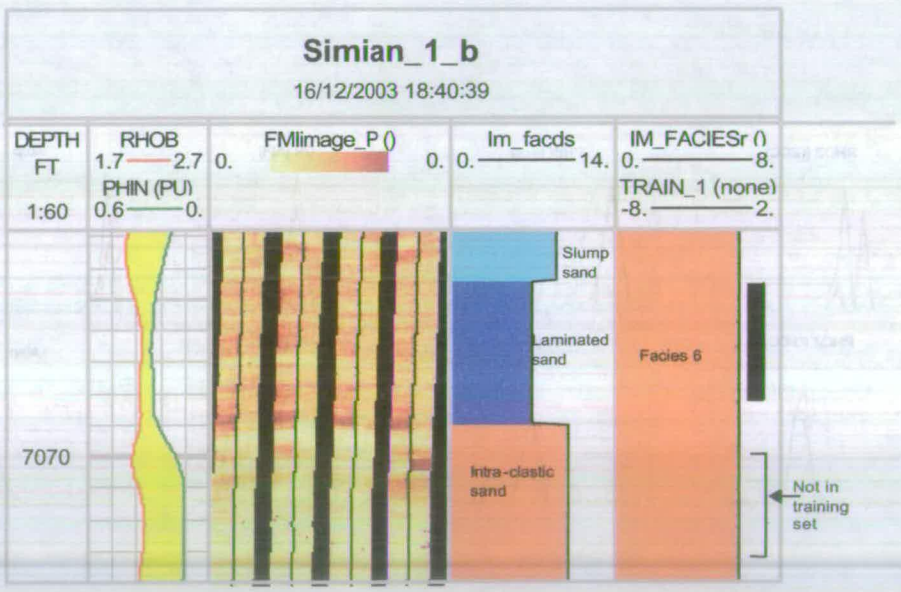



**Figure 5.24** Training examples from well Simian 1. Track 4 shows the Baker Atlas image facies interpretation, track 5 the facies scheme from Table 5.3 (in fact that shown is a simplified version of the Baker Atlas scheme). The black bar indicates an interval that was used for training. The lower interval indicated appears more like facies 5 (structureless sand), rather than conductive sand (facies 6), so this section was not used for training. 1 vertical square represents 1 ft.

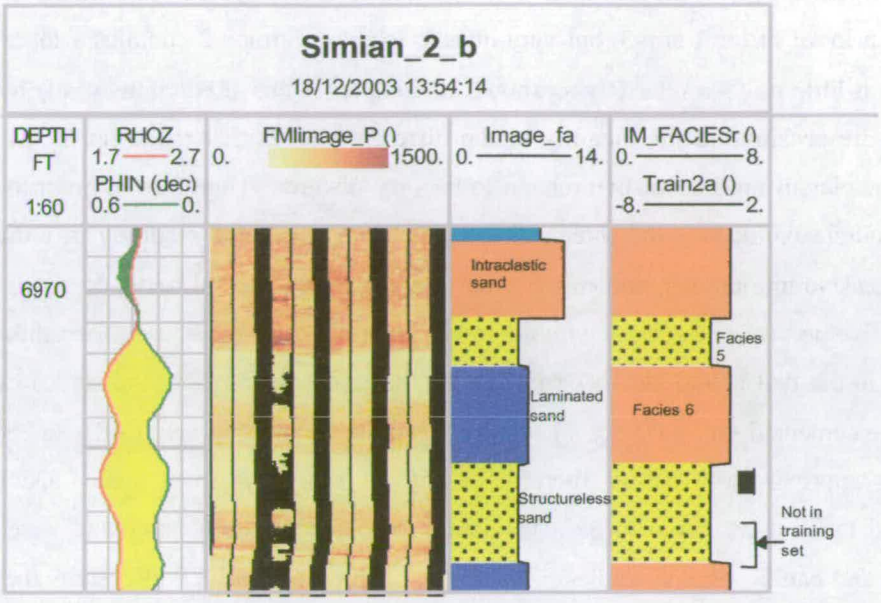



**Figure 5.25** Training examples from well Simian 2. Track 4 shows the Baker Atlas image facies interpretation, track 5 the facies scheme from Table 5.3 (in fact that shown is a simplified version of the Baker Atlas scheme). The black bar indicates an interval that was used for training. The lower interval indicated appears more like facies 5 and 6 (structureless sand interbedded with conductive sand), rather than simply facies 5, so this section was not used for training. 1 vertical square represents 1 ft.

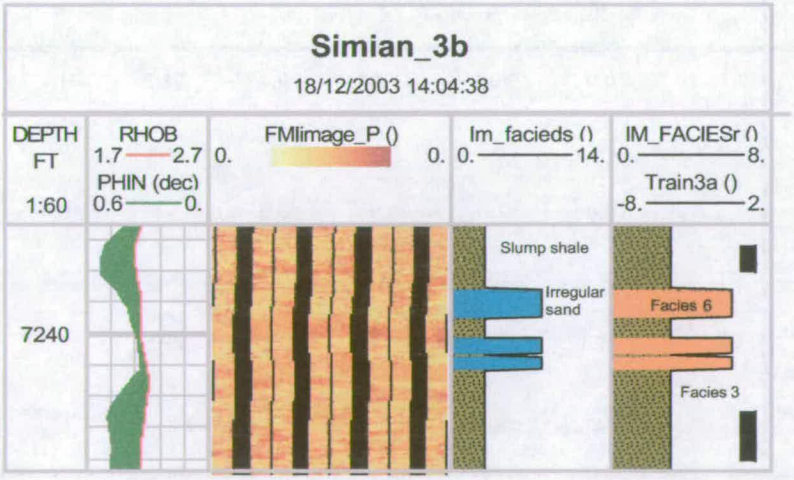



**Figure 5.26** Training examples from well Simian 3. Track 4 shows the Baker Atlas image facies interpretation, track 5 the facies scheme from Table 5.3 (a simplified version of the Baker Atlas scheme). The black bars indicate intervals that were used for training. 1 vertical square represents 1 ft.

The data available to contribute to training and validation sets can be seen in Table 5.4. Certain wells appear to be dominated by particular facies types. For instance Simian 1 contains a lot of facies 1 and 3, but very little 2, whereas Simian 2 contains a lot of facies 2, but only a little of facies 1. It was shown in Chapter 3 that predictions made by a neural network are sensitive to the quantity of the different classes that make up the training set, unless the classes are known beforehand to be very distinct. Therefore in order to facilitate more accurate predictions the three training sets were combined resulting in a much more comprehensive training set, and this is what the subsequent neural network was trained on. Twenty-five percent of the class with the lowest overall amount was used for validation: (for instance in the first neural network (module 1), that can only predict sand shale or cemented facies the cemented facies (facies 7) occurred least in the training set (1.4ft), so 25% of this facies is approximately 0.35ft; therefore 0.35ft of sand, 0.35ft of shale, and 0.35ft of cemented facies were taken to be a validation set). The resulting amounts were used for training, and can be seen in Tables 5.5 and 5.6. Tables 5.5 and 5.6 also show the boosting factors that were used for the training data. For the first sand / shale / cemented network (module 1) it was thought that all these lithologies were very distinct, and so only a very small amount of boosting of the cemented facies took place (Table 5.5). For the second tier of networks (module 2) that predict the different image facies, partial boosting also took place (Table 5.6).

| Lithofacies | 1 | 2 | 3 | 4 | 5 | 6 | 7 | Total |
|---|---|---|---|---|---|---|---|---|
| Simian 1 | 13.7 | 0.9 | 19.2 | 7.0 | 9.4 | 21.2 | 1.4 | 72.8 |
| Simian 2 | 1.2 | 19.9 | 9.1 | 0.0 | 5.2 | 3.9 | 0.0 | 39.3 |
| Simian 3 | 2.6 | 0.0 | 7.0 | 3.5 | 5.0 | 5.4 | 0.0 | 23.5 |
| Total | 17.5 | 20.8 | 35.3 | 10.5 | 19.6 | 30.5 | 1.4 | 135.6 |
| % of whole data set | 12.9 | 15.4 | 26.0 | 7.7 | 14.4 | 22.5 | 1.0 | 100.0 |
| % sand / shale/ cemented | Shale 62.0% | | | | Sand 36.9 % | | Cemented 1.0% | |

**Table 5.4** Data available to contribute to training and validation sets, by well. All values are in feet.

| Lithofacies | Shale | Sand | Cemented | Total Ft |
|---|---|---|---|---|
| No of Ft in Training set | 83.9 | 49.8 | 1.1 | 134.7 |
| Boosting factor | x1 | x1 | x5 | |

**Table 5.5** Number of feet of each lithology type used for training for the first module (sand / shale / cemented) neural network, and boosting factors. See text for more details.

| Lithofacies | 1 | 2 | 3 | 4 | 5 | 6 | Total Ft |
|---|---|---|---|---|---|---|---|
| No of Ft in training set | 15.0 | 18.3 | 32.8 | 8.0 | 19.6 | 30.5 | 124.19 |
| Boosting factor | x1.25 | x1.25 | x0.75 | x2 | x1.25 | x1 | |
| | Shale network | | | | Sand network | | |

**Table 5.6** No of feet of facies used for training for neural networks in module 2, and boosting factors. See text for more details.

## *5.6 Preliminary analysis*

### *5.6.1 Introduction*

In Chapter 3 some experimentation was described that took place to determine the optimum network for predicting the described lithofacies in the Lomond Field. This experimentation allowed conclusions to be drawn about the main influences on the neural network model. The data studied in this chapter presents different challenges. There are many more inputs than before, which are at a far higher resolution (although the majority are vertically averaged). Some of these inputs are conventional logs that have a far lower resolution than their image equivalents, but have been shown to have a large amount of discriminating power. Also, many of the identified facies from the images contain thin beds that sometimes appear resolved by the image logs and sometimes not, and these often change the 'bulk' signature of the conventional logs.

This section describes some experiments that took place to find the optimum way of predicting the image facies described. It is necessary to determine: to what extent neural

networks are capable of discriminating the image facies scheme; whether the neural network ranks inputs in the expected order (given the analysis that has already taken place); what is the best way to integrate logs with different resolutions; and whether thin beds can be resolved?

A methodology was outlined (in Section 5.4.4, and Figure 5.21) that it was hoped could discriminate the various image facies. This is implemented first and described in Section 5.6.2. Results from this analysis are then compared with a non-modular system (combining modules 1 and 2 into a single network) for facies predictions (Section 5.6.3). The ability of the methodology to identify thin-beds is discussed in Section 5.6.4.

### *5.6.2 Image facies prediction with a modular neural network*

Figure 5.21 described a modular system for the prediction of image facies. The first step involves the segregation of the logs into broad sand /shale lithological groups. This is best achieved with the conventional logs (RHOB, NPHI, and GR). Facies 7 that represents cemented zones (which are commonly conglomeratic) can also be distinguished. It was found in Chapter 3 that varying the momentum and learning parameters did not appear to affect the results very much. Also the use of a pruning algorithm was only successful if the starting network was close to the optimum one. Therefore learning and momentum parameters were left constant at 0.4 and 0.6 respectively, and the weight connections not pruned during training. At first a network with two nodes in one hidden layer was trained (justified by the fact that there are only three inputs and the sand / shale / cemented lithologies are known to be fairly distinct). Table 5.7 shows the results of training this and other networks, with different numbers of nodes.

| Trial | No. of nodes in single hidden layer | % correct over validation set |
|---|---|---|
| 1 | 2 | 98.04 |
| 2 | 3 | 98.04 |
| 3 | 4 | 98.04 |

**Table 5.7** The percentage correct over the validation set for different sized networks; three trials per network.

All networks produce the same hit-rate over the validation set, which is very high at 98.04%. The results for all three networks are the same since the validation set is very small (a consequence of having very little cemented facies). Also, the percentage hit-rate should be interpreted with caution. The next step in the procedure (module 2) will be the prediction of the image facies within the sand and shale lithology groups, and it is this step that will involve the integration of the image and conventional logs. For this reason the conventional logs were interpolated so that data existed at the same increments as the image logs. Data used in the above analysis was at this (high) resolution, and therefore this could have lead to an artificially high hit-rate over the validation set (see Figure 5.27). The hit-rate does give us an indication of the networks success, but the results should also be tested by applying the model to unseen sections of the well. Therefore the simplest network was selected for further assessment and applied to the wells in the data set (examples are shown as Figures 5.28, 5.29 and 5.30).

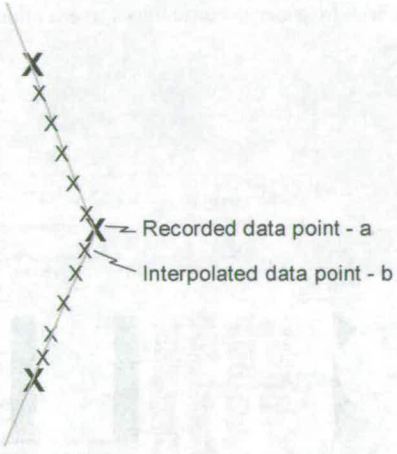



**Figure 5.27** The effect of interpolating between data points on the hit-rate over the validation set. Conventional logs were interpolated so that data existed at the same increments as image logs. In this diagram recorded data points are schematically shown in bold, with the interpolated points between them. Neural network models were trained with all the data. This means that when conventional logs are used a large part of the training set is made up of interpolated data. This may affect the training of the model (see later). It will also affect the hit rate over the validation set – imagine that the recorded data point (a) is included in the training set, but the interpolated point at (b) is included in the validation set. Validating with point (b) is essentially the same as validating with point (a) as the value of (b) is very much determined from (a). This is similar to validating data used for training (see Chapter 2). Therefore caution should be exercised when interpreting hit-rates over validation sets when the data have been interpolated. Any models should be tested over unseen data.

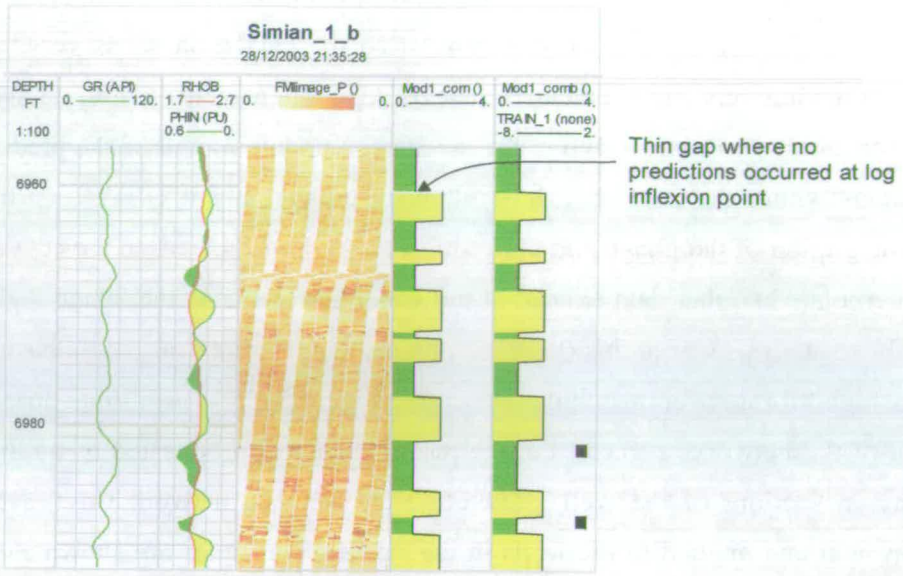



**Figure 5.28** Results of the neural network trained to predict sand, shale and cemented lithological groups from well Simian 1. Track 5 shows the raw predictions which include some very small intervals where no predictions were made – commonly at log inflexion points. Track 6 shows the results after these intervals had been repaired (see text for more details). In general the results are excellent. Note the black bars indicate sections that were used for training.

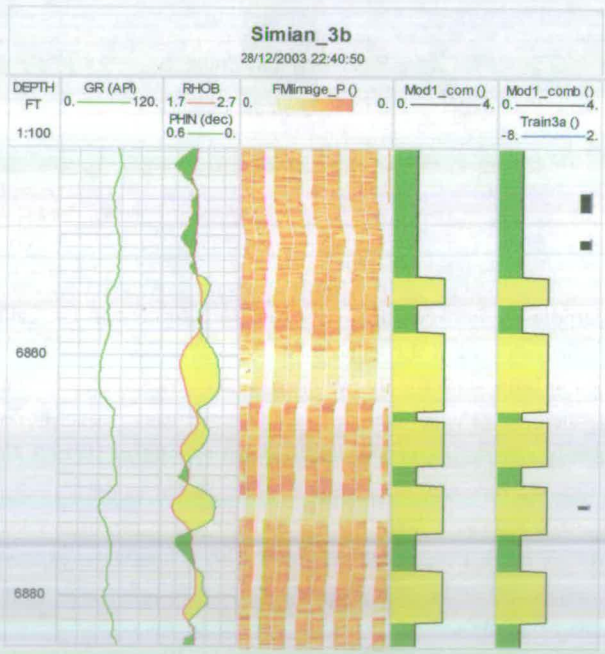



**Figure 5.29** Results of the neural network trained to predict sand, shale and cemented lithological groups from well Simian 3. Track 5 shows the raw predictions and track 6 the results after these intervals had been repaired (see text for more details). In general the results are excellent. Note the black bars indicate sections that were used for training.

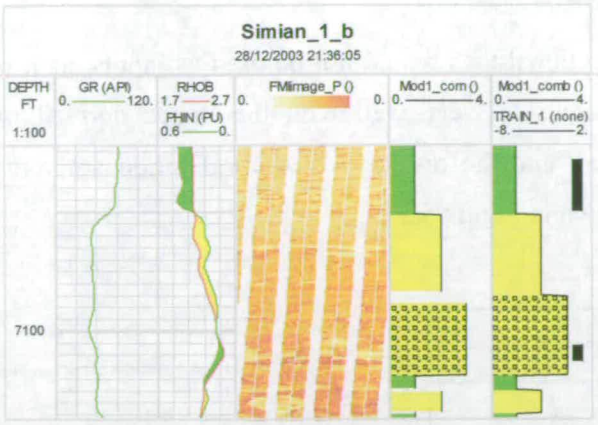



**Figure 5.30** Cemented facies (facies 7) occurs in approximately the correct place (the density log increases and the neutron log decreases). However part of the section shown (where there is a black bar) is the training set. Unfortunately this is the only section of cemented facies in all three wells so it is difficult to properly test the ability of the model to predict this facies. However we can conclude that the model does have the ability to predict this facies. 1 vertical square represents 2ft.

In general the results are excellent. There are a very few number of places where predictions are not made, these tend to occur at log inflexion points (see Figure 5.29). Therefore the 'thin-bed repair' program was implemented, as in Chapter 4 to remove these. The program was run with a thin-bed being defined as having a thickness of 0.5ft. Although this value is smaller than that used in Chapter 4, and below the resolution of the density tool, its use can be justified. In all three wells there are very few thin beds and they always appear to be less than 0.5ft thick. Also there are fewer potential outputs, so if a thin bed of shale that is 1ft thick for example occurs within a larger bed of sand, even though it is not fully resolved by the logs, it may still be correctly predicted (this would probably not be the case if there were more potential outputs). The cemented facies also appeared to be predicted successfully however it is very rare and therefore difficult to test the real ability of the model to predict this facies (see Figure 5.30).

The next step in the implementation of the modular system (module 2) is the segregation of the different lithological groups (sand and shale only – the cemented facies is not separated further) into the different image facies (refer back to Figure 5.21). Different neural networks were trained to predict different types of sand (facies 5 and 6) and different types of shale (facies 1 to 4). The results of the two networks were then combined with the cemented facies to produce the final predictions from module 2. The training sets that these networks were trained on were shown in Table 5.6. As for module 1, it was decided to train networks with fixed learning and momentum parameters, and no pruning. For the sand network it was

decided that the conventional logs would not be used as inputs, as it appeared that facies 5 and 6 could be distinguished very well with the image derived inputs only. Various topologies were trained, and the results over the validation set compared. For the sand networks these are shown in Figure 5.31.

| Trial | No. of nodes in single hidden layer | % correct over validation set |
|---|---|---|
| 1 | 1 | 97.77 |
| 2 | 2 | 97.85 |
| 3 | 3 | 99.23 |
| 4 | 5 | 99.48 |
| 5 | 7 | 99.4 |
| 6 | 9 | 99.23 |
| 7 | 11 | 99.66 |

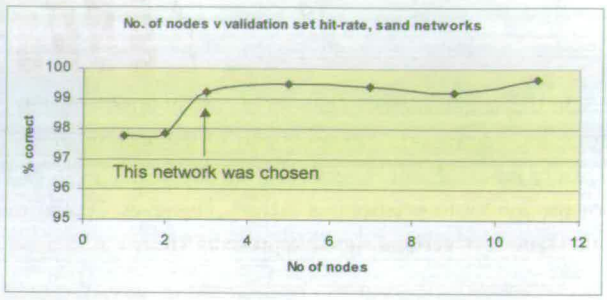



**Figure 5.31** The percentage correct over the validation set for different sized sand networks; three trials per network. The graph on the right shows the network chosen for further analysis – this is the smallest topology with the best results (3 nodes in 1 hidden layer).

The simplest network that shows high results has 3 hidden nodes in 1 hidden layer. The hit-rate is very high at 99.23%. This is very plausible though as the network has only two outputs and both types of sand appear fairly distinct. The fact that many of the image inputs are averaged vertically could affect the hit-rate over the validation set in a similar way to that described in Figure 5.27, but it is thought that the problem is not as significant in this case as the data are not interpolated.

For the shale networks it is difficult to decide whether the conventional logs should be used as inputs as well as the image derived logs. The conventional logs were shown to be potentially important discriminators for facies 4 (which are debris flows – see Figure 5.11b), however other shales that contain sandy thin beds also have a close neutron-density log separation. If the conventional logs are used will the resulting network mix up facies 4 with other shales that contain these thin beds *or* if the conventional logs are left out will the network be able to predict facies 4 successfully at all? Two different networks were therefore trained – one had both conventional log and image derived inputs, the other just the image derived inputs (as for the sand network). For each network type various topologies were trained, and the results over the validation set compared. These are shown in Figures 5.32 and 5.33.

| Trial | No. of nodes in single hidden layer | % correct over validation set |
|---|---|---|
| 1 | 3 | 91.76 |
| 2 | 5 | 94.79 |
| 3 | 7 | 96.97 |
| 4 | 9 | 98.82 |
| 5 | 11 | 99.24 |
| 6 | 13 | 99.66 |
| 7 | 15 | 99.92 |

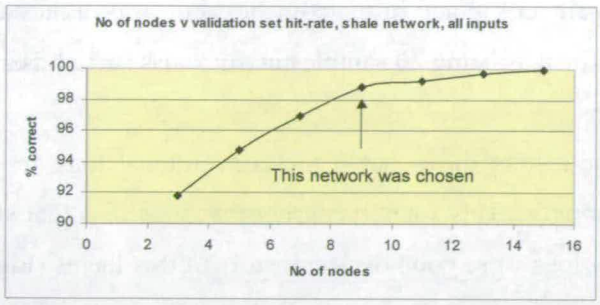



**Figure 5.32** The percentage correct over the validation set for different sized shale networks that were trained with conventional log and image derived inputs; three trials per network. The graph on the right shows the network chosen for further analysis – this is the smallest topology with the best results (9 nodes in 1 hidden layer).

| Trial | No. of nodes in single hidden layer | % correct over validation set |
|---|---|---|
| 1 | 5 | 88.24 |
| 2 | 7 | 92.18 |
| 3 | 9 | 93.45 |
| 4 | 11 | 95.88 |
| 5 | 13 | 96.89 |
| 6 | 15 | 96.97 |
| 7 | 20 | 97.56 |

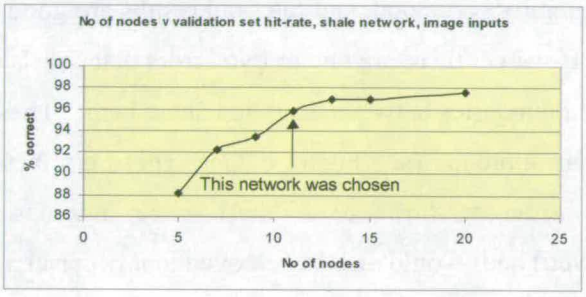



**Figure 5.33** The percentage correct over the validation set for different sized shale networks that were trained with image derived log inputs only; three trials per network. The graph on the right shows the network chosen for further analysis – this is the smallest topology with the best results (11 nodes in 1 hidden layer).

The results are interesting in that they show that in all cases the same size network when trained with the conventional logs results in a higher validation set hit-rate compared to the same network trained without these logs. This is probably due to interpolation of data (Figure 5.27). The results from each of the best shale networks were spliced with those from the sand network, and facies 7 (from module 1), for comparison. These can be seen as Figures 5.34, 5.35 and 5.36.

These figures show that all raw predictions are fairly spiky (as they were when neural network analysis was applied to the Lomond Field data), but generally more spiky in the shale results which utilised the image derived inputs only (compare tracks 6 and 8 in Figure 5.36). Where the conventional logs were also used they appear to have 'smoothed' the results, this no doubt due to the coarser resolution of these logs and the interpolation of the

data. Both sets of predictions though do appear to benefit from thin-bed repair. Thin-bed repair took place in exactly the same way as described in Chapter 4, but with a thin-bed defined as being 20 samples in thickness (which is approximately 2").

The results show that if the conventional logs are left out then facies 4 is often predicted wrongly. This supports earlier investigations that showed the neutron, density, and gamma-ray logs were good discriminators of this facies (Figure 5.11b). What was feared was that if the conventional logs were included facies 4 would be predicted where thin-bedded intervals exist (which have higher bulk sand content and therefore a closer neutron-density separation). This does not appear to be the case, some beds of facies 4 are predicted in these intervals but these are not frequent, implying that the image inputs are also very important in analysis. From the figures shown, the results from the shale networks that used all curves are generally very good, and the sand results are good too, following the image exceptionally well. However there are one or two errors that consistently appear – 'edge' effects that occur on the boundaries between sand and shale beds. These could be a consequence of using the modular approach (see Figure 5.37). These artefacts could be removed with the thin-bed repair program, however if these were automatically removed then other (correctly predicted) beds would also be removed that occur in a single lithological sequence.

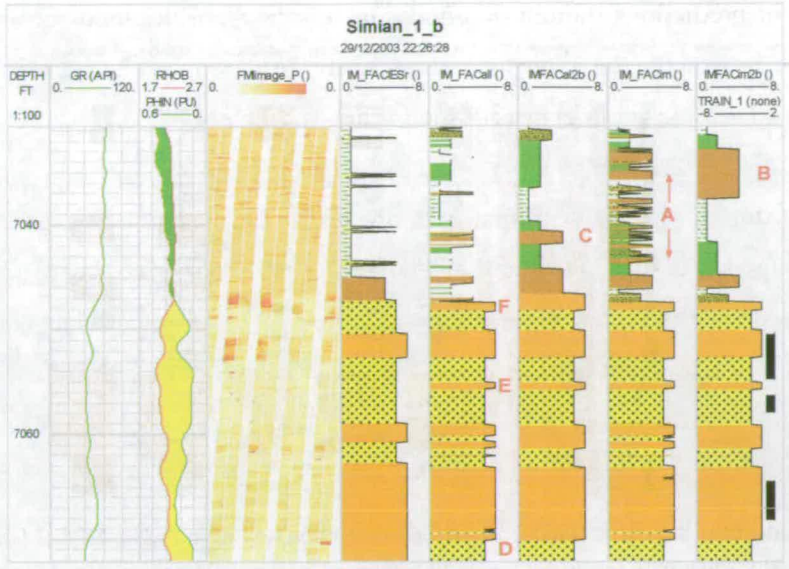



**Figure 5.34** Results from Simian 1. Track 5 shows the 'real' image facies (although this is simply a simplification of the scheme interpreted by Baker Atlas); track 6 are the results when all logs were used as inputs into the shale network; track 7 are the same results as track 6 but after the thin-bed repair program had been run over the data (see text); track 8 are the results when only image derived inputs were used as inputs into the shale network; track 9 are the same results as track 8 but the after the thin-bed repair. When only image derived inputs are used in the shale network, much more facies 4 (brown, at A) is predicted incorrectly, and this often still exists after thin-bed repair (at B). When the conventional logs are also used as inputs for the shale network then there is less facies 4 predicted incorrectly, however some still does occur (e.g. at C). The sands appear to have been predicted very successfully with the facies correlating with the image well (e.g. at D and E, even though this doesn't match the 'real' image facies). There does appear however to be an 'edge effect' at F (see text for more details).

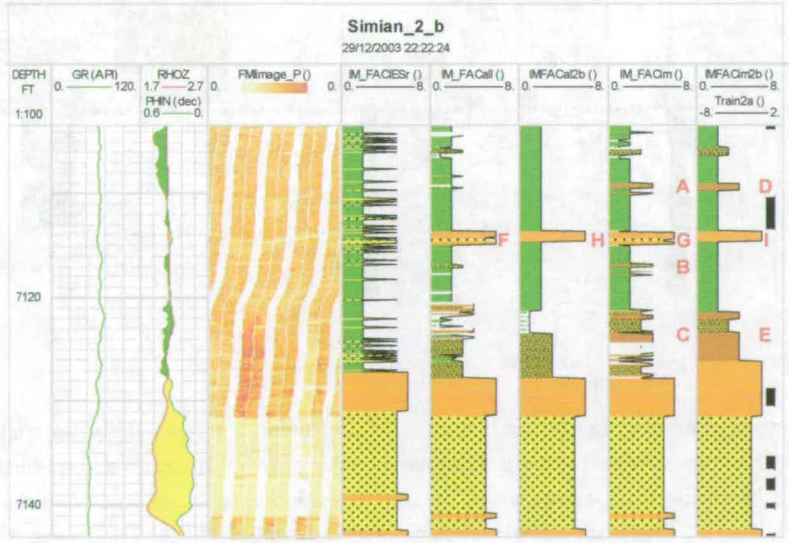



**Figure 5.35** Results from Simian 2. Tracks are set up in the same way as in Figure 5.34. More facies 4 is predicted incorrectly when only image derived inputs are used in the shale network (at A, B and C), and these still exist after thin bed repair (at D and E). Overall the shales appear to be predicted well, as do the sands. However there are some edge effects (at F and G), which are made worse after thin-bed repair (H and I).

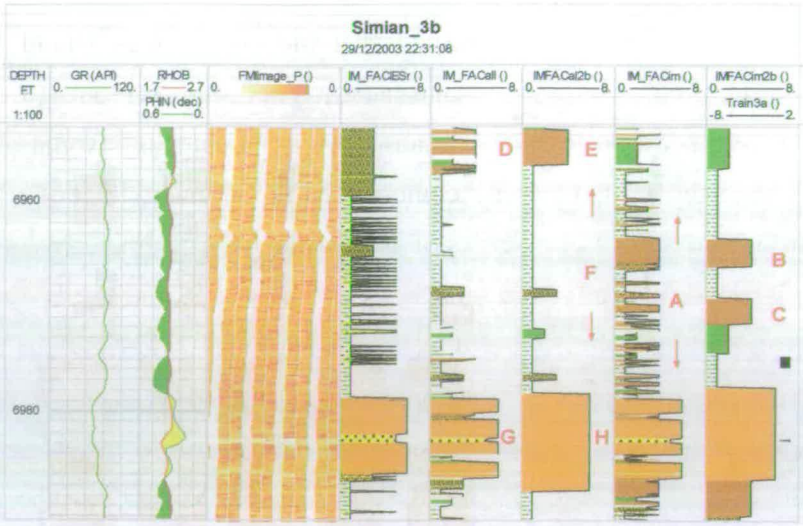



**Figure 5.36** Results from Simian 3. Tracks are set up in the same way as in Figure 5.34. More facies 4 is predicted incorrectly when only image derived inputs are used in the shale network (at A), and these still exist after thin bed repair (at B and C). Although the shales predicted using all inputs show good overall predictions there are some incorrect intervals of facies 4 (e.g. at D). The sands are also predicted successfully, although some thin-beds of high quality sand (e.g. at G) are lost after thin-bed repair. However these should be added back in when thin-beds are identified later, in module 3 (see Figure 5.21).

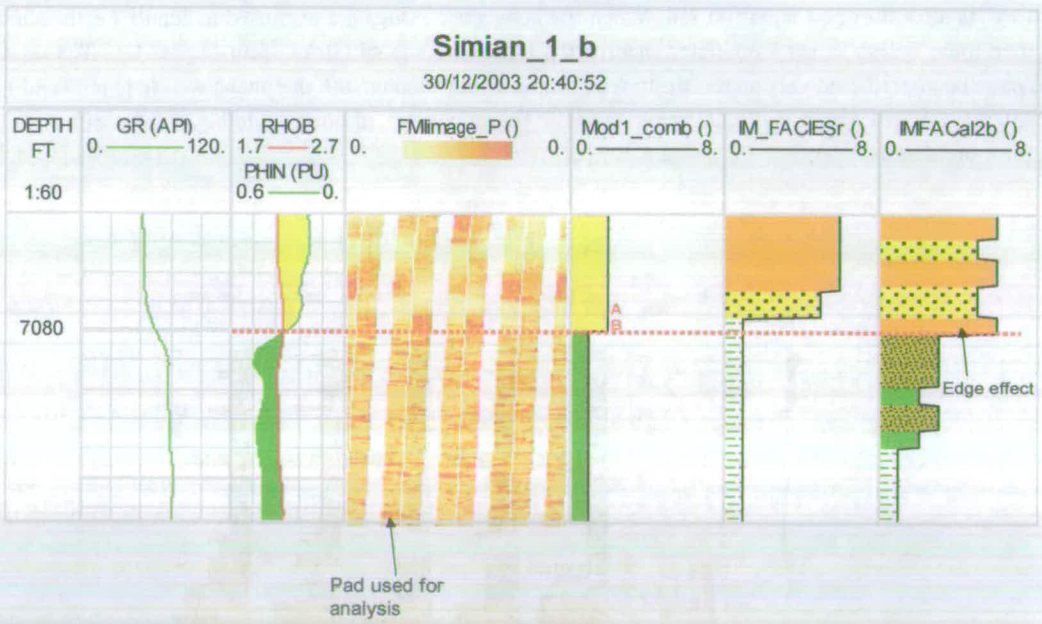



**Figure 5.37** An example of an edge effect at a sand / shale boundary. This could be an artefact derived from integrating curves with different resolutions in the modular system. The results from the first module which defined the broad lithological groups can be seen in track 5. The sand shale boundary has been defined correctly at the GR, PHIN, and RHOB inflexion points (dashed red line). The second 'module' that divided the lithological groups into image facies was forced to predict sand above the red line and shale below it (shown in track 7). However the boundary is defined more accurately by the image, and does not start until around point A which is clearly very resistive sand. Although the model has predicted resistive sand correctly (yellow, dotted), below this it has predicted more conductive sand (orange) between the coarse logs inflexion point and the true sand / shale boundary. 1 vertical square represents 2 ft.

From earlier investigations it was expected that the coarse logs would be important discriminators in the prediction of the image facies. They were kept apart from the image logs resulting in two separate modules because it was thought this would aid prediction. However it has been shown that when it comes to the second module, the prediction of the image facies (in the case of different types of shale) is better when the conventional logs are also included as some of the actual image facies (especially facies 4) have a distinct lithological signature that is discriminated well with these logs. They also act to smooth the results making them more geologically consistent. The question should now be asked whether all the logs could have been incorporated at the same time in a single network that could predict sand and shale image facies (i.e. could modules 1 and 2 have been combined)? If this is so then boundaries between lithological groups might also have been defined by image derived components, and this could remove the artefacts described above in Figure 5.37. The next section describes the creation of a single neural network trained to predict all the image facies. The results are then compared to those of the modular system.

### *5.6.3 Image facies prediction with a single neural network*

The single network created had exactly the same inputs as before (28 in total as described in Section 5.5.2) and 7 outputs corresponding to the seven different image facies described in Table 5.3. A variety of different networks of different sizes were trained, with fixed learning rate and momentum parameters of 0.4 and 0.6 respectively. No pruning took place. The training and validation sets were exactly the same as before (for the second 'module', as described in Section 5.5.5 and Table 5.6). The training sets were partially boosted before so that there were similar amounts of sandy facies, and similar amounts of shaly facies. If the same training sets are used then this means that even though there are similar amounts of, say, facies 5 and 6 (both sand), there will be different amounts of say facies 1 and 6 (1 being a shale, 6 being a sand). However it is known that the sand and shale groups themselves should be fairly distinct and the facies groups within these broad lithological classes have been partially balanced. Also the training set is fairly large consisting of over 15,000 data examples. Therefore the training set was the same size as before. The validation set was created as before with the amount of each facies in it equal to 25% of the least occurring facies (which is facies 7 – cemented).

The results of training the different sized networks can be seen in Figure 5.38. As described earlier one has to be careful when interpreting the hit-rate over the validation set due to the interpolation of the conventional logs. However this can be taken as an indication of the network's performance, before further testing.

| Trial | No. of nodes in single hidden layer | % correct over validation set |
|---|---|---|
| 1 | 2 | 54.63 |
| 2 | 4 | 90.32 |
| 3 | 5 | 93.06 |
| 4 | 6 | 96.68 |
| 5 | 8 | 95.93 |
| 6 | 10 | 98.3 |
| 7 | 12 | 98.34 |
| 8 | 14 | 97.92 |

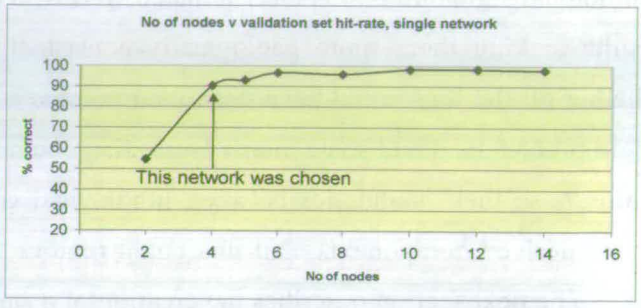



**Figure 5.38** Training a single network. The percentage correct over the validation set for different sized networks; three trials per network. The graph on the right shows the network chosen for further analysis – this is the smallest topology with good results (4 nodes in 1 hidden layer).

The hit-rate can be seen to rise rapidly and flatten off so that all networks that have 4 or more hidden nodes all have hit-rates that are above 90%. Therefore the simplest network, (with 4 hidden nodes, as indicated) was chosen for further testing. This network is only slightly larger than that which predicted the different sand facies in 'module 2' (that had 3 hidden nodes in 1 hidden layer) and in fact smaller than the network that predicted shaly facies in module 2 (that had 9 nodes in 1 layer). But this network has seven outputs so one might have expected the number of nodes needed to be larger. What this simply shows is that there exists a number of different networks of different sizes that are able to classify the same data to a similar degree of accuracy. The reason for validating the network is so that, for instance, the network with two hidden nodes in Figure 5.38, which would be expected do a very poor job of classifying the data is not chosen. The simplest network is to be preferred, as larger networks are more susceptible to overtraining. However if a larger network is properly validated, and then assessed on unseen data there appears no reason why it cannot be used to make predictions. For instance Figures 5.34, 5.35 and 5.36 show that the modular network (when all input curves were used) produces fairly reasonable results outside of the training intervals and therefore there is no reason to choose a smaller network.

The network indicated in Figure 5.38, trained to predict all image facies was compared to the results of the modular system. Comparisons are made in Figures 5.39, 5.40, 5.41 and 5.42.

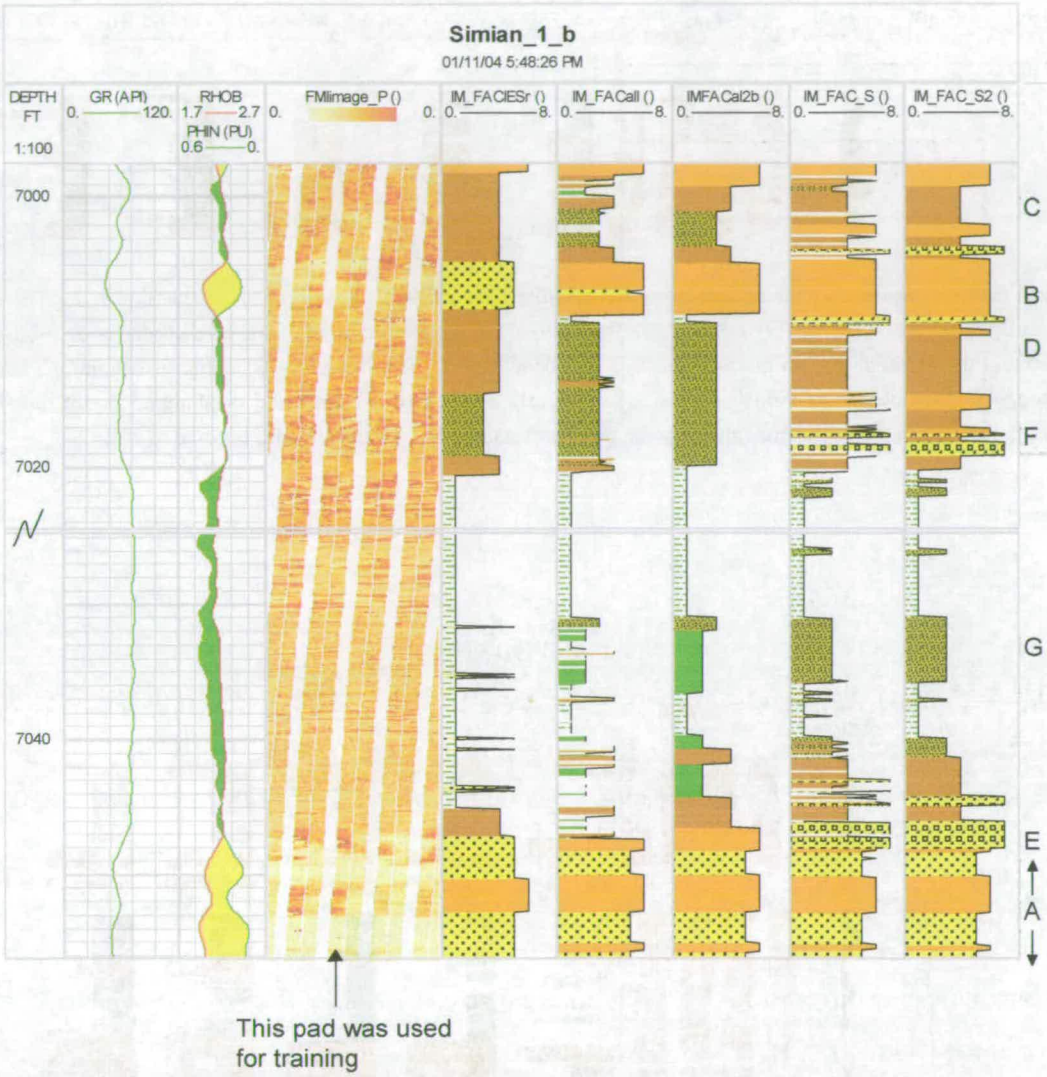



**Figure 5.39** Comparison of the results from the modular network and single network, well Simian 1. Track 5 shows the 'real' image facies (simplified from the Baker Atlas scheme), tracks 6 and 7 show the results from the modular network (raw and repaired respectively), and tracks 8 and 9 the results from the single network (raw and repaired respectively). It can be seen that the single network is similar to the modular one in many respects, the sandy intervals around A and B are almost exactly the same. The prediction of facies 4 (debris flow) at C and D for the single network could actually be a better interpretation than the modular result – although the image at D clearly shows a slumped horizon the neutron-density and gamma-ray response is closer to that of facies 4. However there are some discrepancies in the single network's interpretation: at E and F there are some small intervals of facies 7 (cemented) which shouldn't occur. Also at point G the single network has predicted facies 3 (slump shale). The modular system has predicted facies 2 (bioturbated shale) that appears much closer to the image especially when the pad that the networks were trained on is highlighted.

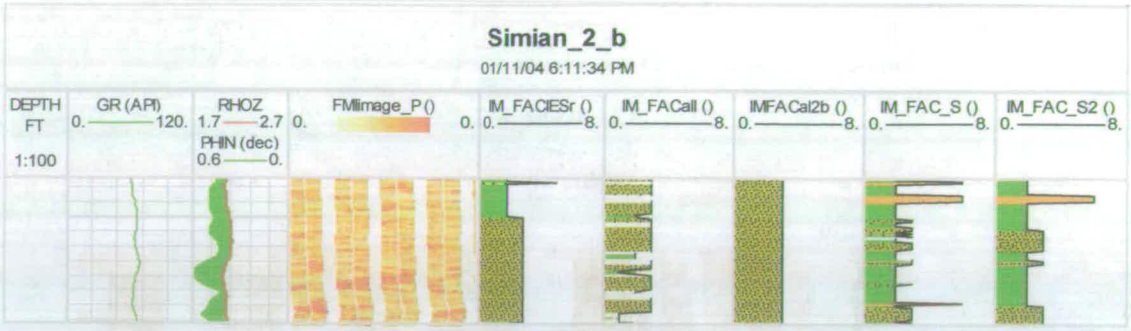



**Figure 5.40** Comparison of the results from the modular network and single network, well Simian 2. The tracks are set up in the same way as Figure 5.39. In the interval shown the single network predicts facies 2 (bioturbated shale) and the modular system predicts facies 3 (slumped shale). The image shows some discontinuous laminae. Although this is not very obviously facies 3, it is clearly either 1 or 3 (laminated or slumped shale) rather than facies 2, thus the modular system appears to be more correct. Note 1 vertical square is equal to 1 ft.

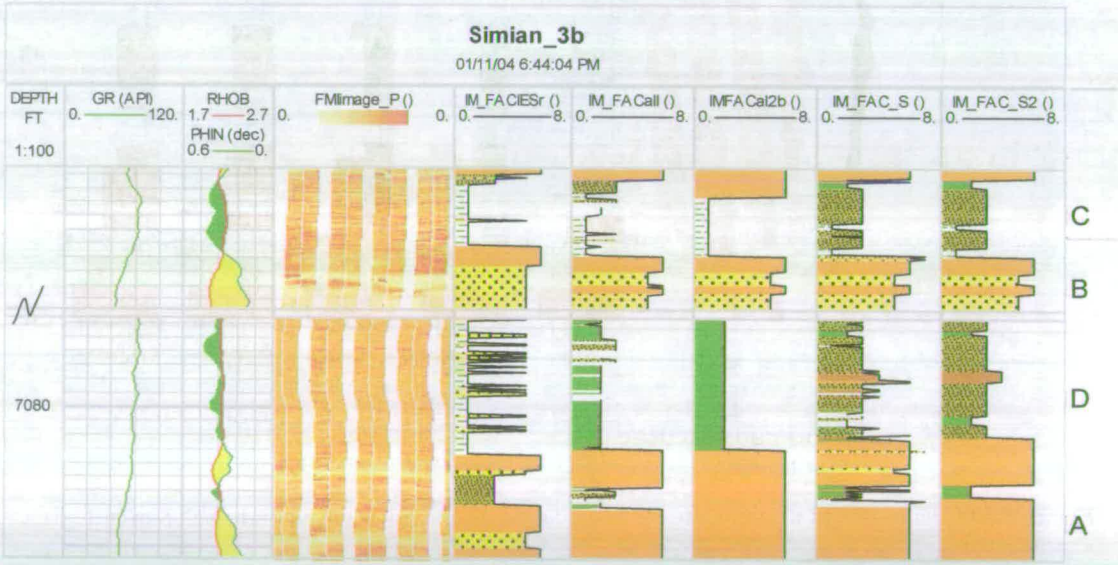



**Figure 5.41** Comparison of the results from the modular network and single network, well Simian 3. The tracks are set up in the same way as Figure 5.39. The prediction of the different sandy facies are very similar for both the modular system and the single network (at A and B for instance). At C the modular system predicts facies 1 (laminated shale), that matches the 'real' facies, the single network predicts facies 3 (slumped shale). The image shows some faint laminations so the modular system appears 'more correct' than the single system. At D there is another example of the single network mixing up facies 2 and 3: 3 is predicted but the image is clearly plain and homogeneous, matching the description of facies 2 (even though the 'real' facies implies that it is facies 1 (laminated shale). Note 1 vertical square is equal to 1 ft.

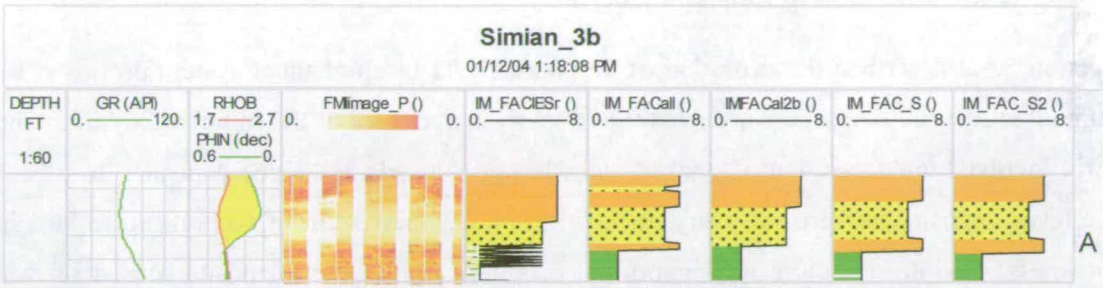



**Figure 5.42** Comparison of the results from the modular network and single network, well Simian 3. The single network results are not immune from 'edge' effects that appear at sand / shale boundaries (A). These are an artefact of incorporating logs at different resolutions into the model, rather then simply the modular approach. 1 vertical square is equal to 1ft.

In many cases the two methodologies produce very similar results, especially in the sandy facies. There are places where the single network may have produced better results, for instance at C and D in Figure 5.39. However, consistently the single network predicts very small sections of facies 7 incorrectly and facies 2 and 3 (bioturbated and slump shale) appear to get mixed up – in all the examples shown the modular system appears to have a preferred interpretation. Also the singular neural network is not immune to edge effects that occur between sand and shale boundaries (Figure 5.42), which are simply the result of using logs with different resolutions.

It is difficult to compare these two methodologies on the basis of these few sections. In many ways they appear very similar. Theoretically they *should* produce similar results – although the single network does have more freedom (as it is not restricted by the first module) it can essentially predict any facies wherever it wants. However it may well be that the division of the problem into smaller tasks allows the network to find the true relationships more easily.

Therefore the results of the modular system will be taken for further analysis – in subsequent sections and Chapter 6.

### 5.6.4 The identification of thin sandy beds

Section 5.5.2 described the evolution of the West Delta Deep channel system proposed by Samuel *et al.* (2003). Stage 3 involved the re-incision and infill of the initial valley fill. The infill involved the deposition of stacked meandering channels and levee deposits. In places the levee deposits are vertically very thick (in Simian 3 they occur in sections up to 30ft in thickness), and are therefore very important economically. Levee deposits consist of thin sand beds a few mm to a few cm in thickness interbedded with shale. Commonly their original depositional fabric is altered due to bioturbation or soft sediment deformation. Since the majority of the thin beds are only a few mm thick the methodologies described so far have not been able to identify them. The inputs used were averaged over vertical moving windows, because it was necessary to quantify the 'bulk' textural elements (see Figure 5.7). If thin-beds are to be identified then the discriminators cannot be averaged to the same degree as the inputs used previously. Examples of some levee deposits in the Simian wells are shown as Figures 5.43 and 5.44. It is shown that some thin-beds are resolved by the image, and when this is so the average or stacked button responses from a single pad are equally good discriminators (calculated in Section 5.4). No other statistics other than these appear to consistently identify them. In many cases though, individual sand beds are not resolved by the image. However it appears (from careful depth shifting of core photographs to the logs) that if they occur in a dense package then the coarser logs such as the neutron and density respond to them measuring the increase in the bulk sand content adjacent to the borehole (see Figure 5.43 (b)).

In order to build the identification of the thin-beds into the automated neural network process further neural networks were trained to identify thin-beds. One was trained to identify those that are resolved by the image logs (type-I thin-beds) and the second to potentially identify those that occur in dense packages but are not seen on the images (type-II thin-beds).

A very simple network was created to identify type-I thin-beds. Since the average button response (over a single pad), and stacked button response appear to equally discriminate these types of thin-beds (Figure 5.43) then only the average was used. The network was created with this single input connected to two outputs (thin-bed or 'not' thin-bed). This network is only capable of describing a decision line that represents a straight line (see Chapter 2), meaning that the network is describing a cut-off below which all data will be

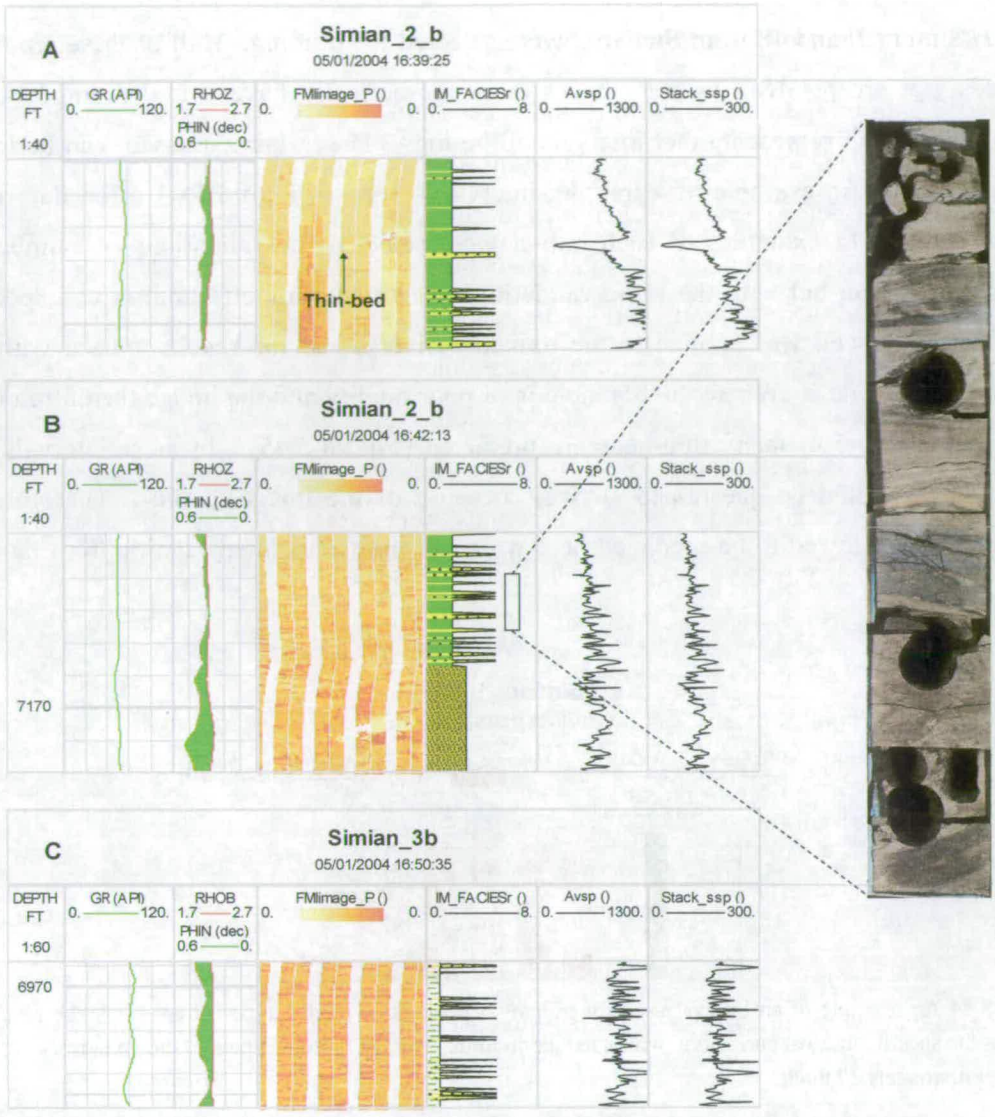



**Figure 5.43** Thin-bedded levee deposits. In many cases individual thin-beds are resolved by the image logs (as in A). When this is so the average button response from a single pad is a good discriminator (track 6), as is the stacked button response (track 7). Many thin-beds though, appear below the resolution of the image logs (it may be that they have been bioturbated to some extent so that the moving image tool 'smears' them into the surrounding shale), for example in B and C. If individual thin-beds are unresolved by the image but they occur in a dense package then it appears that the coarser logs such as the neutron and density log respond to them, measuring the bulk increase in sand content. This relationship appears fairly consistent: example B is from well Simian 2, C is from Simian 3. Note that the image facies shown (with the interpreted thin-beds) is the interpretation by Baker Atlas (2000 & 2001). The cored section shown is 60cm/2ft in height. 1 vertical square represents 1 ft.

classified as a sandy thin-bed (facies 5). If the network's output is not a thin-bed then the original interpretation from module 2 will still be upheld. Although this appears like a very simple problem that doesn't necessarily require a neural network to solve, the benefit of using a network is that it is itself that decides where to draw the decision line based solely on the training data, rather than a line drawn by hand. Therefore 48 data points from Simian 1,

30 from Simian 2, and 48 from Simian 3 were selected for training. Half of these represent thin-beds that are resolved by the images (and consequently have a low average button response), and half represent other intervals of the logs. The training intervals can be found in Appendix 4. An example of a training interval is seen as Figure 5.44. The data were randomised and 15 examples of each output were selected for validation. A number of iterations were run but with the same validation hit-rate each time (93.65%), as expected. Data from each well was applied to the trained network, and the results spliced with the results from module 2. Where the borehole is of poor quality and the image therefore out of focus (see Figure 5.4) many thin-beds are predicted (Figure 5.45). In these intervals any interpretation should be questioned anyway, because of the image quality. Therefore no thin-beds were allowed to be predicted here whatever the facies interpretation from module 2.

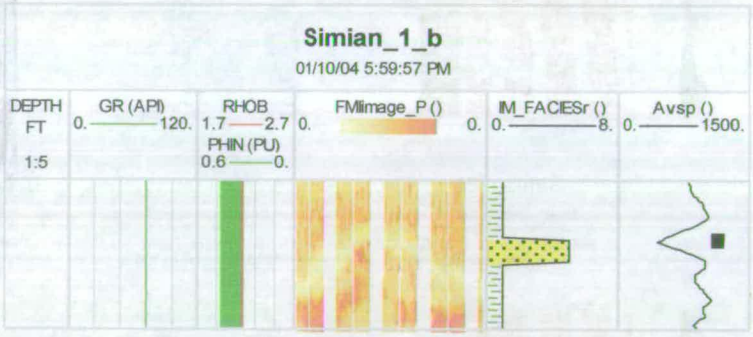



**Figure 5.44** An example of an interval used for training a network to predict type-I thin-beds. The black bar indicates the specific interval correlating with a reduction in the average button response (shown in track 6). The bed is approximately 1" thick.

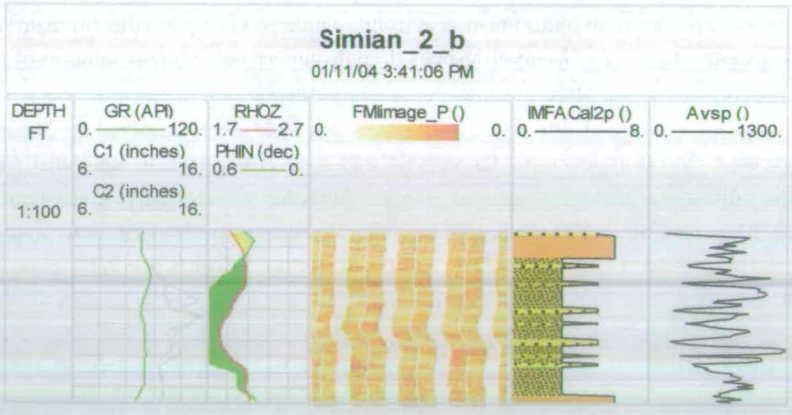



**Figure 5.45** An example of an area from well Simian 2. The image is out of focus, because of the poor quality hole (shown by the calipers) and is therefore extremely variable often recording very low values. The neural network trained to predict type-I thin-beds predicts thin-beds in this interval, which are artefacts. Predictions were therefore not allowed in these intervals (based on a caliper cut-off). 1 vertical square represents 1 ft.

An example of a successfully predicted type-I thin-bed can be seen as Figure 5.46.

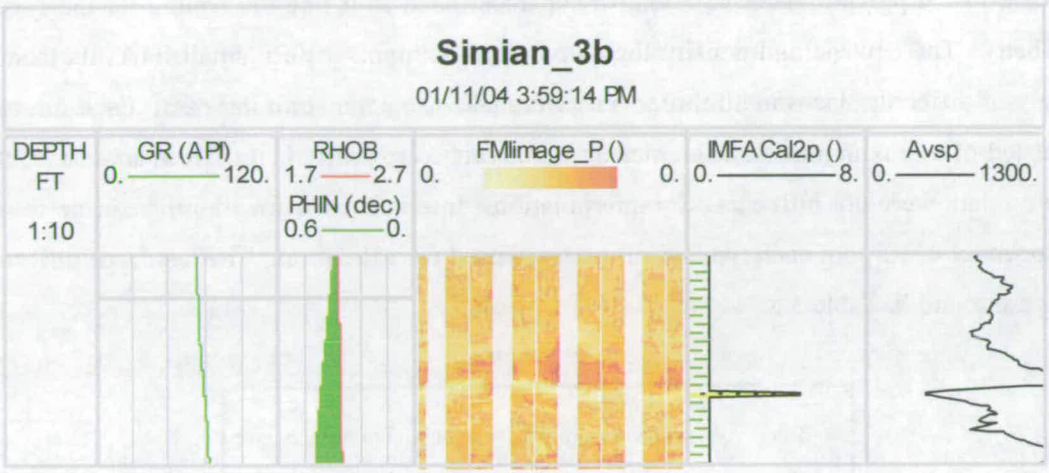



**Figure 5.46** An example of a predicted type-I thin-bed from well Simian 3. It is approximately 1-2" in thickness.

A consequence of predicting thinner sandy beds in this way is that within a sandy interval, where the image shows a mix of facies 5 and 6 (resistive and conductive sand) more detail is revealed (Figure 5.47)

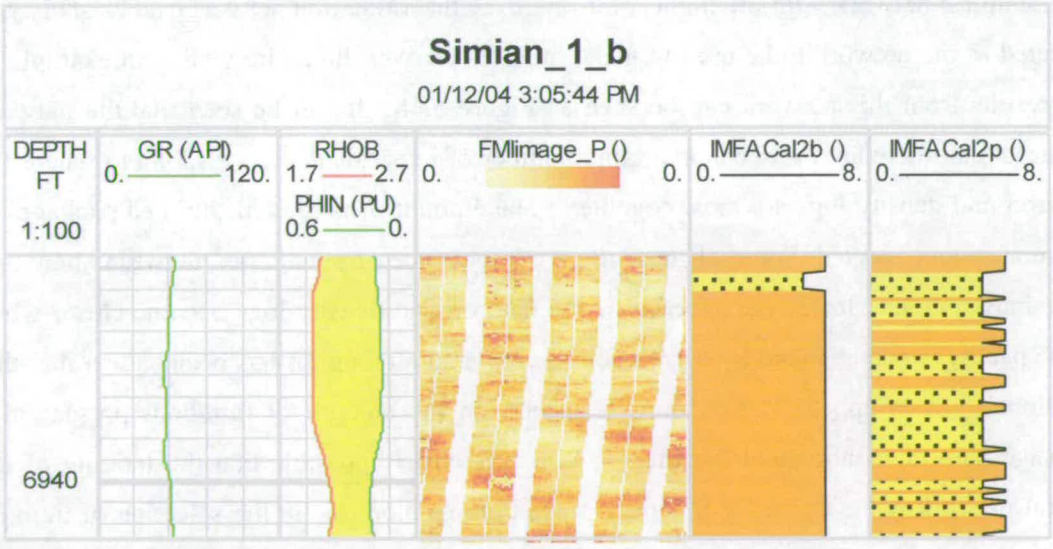



**Figure 5.47** An example of predictions from well Simian 1. The result from module 2 is shown in track 5, where facies 6 has been predicted (conductive sand). However the image is fairly patchy with many light areas indicating more resistive sand. After the prediction of type-I thin-beds much more detail is added to the interpretation, which is seen in track 6. 1 vertical square represents 1 ft.

A second network was created to identify type-II thin-beds. Since these thin-beds are not revealed by the image but are identified as 'packages' by the coarser logs the network result will be a 'flag' that indicates probable thin-bed packages or not. The flag will be plotted adjacent to the previous interpretation, rather than added to it like the results for the type-I thin-beds. The neutron and density logs were used as inputs. Very small intervals from a variety of different places in all three wells were taken to act as training data. Each interval consisted of a maximum of 2 examples and intervals were more than 0.5ft apart so that the training data were not influenced by interpolation. Intervals used for training can be found in Appendix 4. 25% of each type of output were used for validation. The results of different trials are found in Table 5.8.

| Trial | No. of nodes in single hidden layer | % correct over validation set |
|---|---|---|
| 1 | 1 | 83.33 |
| 2 | 2 | 96.67 |
| 3 | 3 | 96.67 |

**Table 5.8** The percentage correct over the validation set for different sized networks; three trials per network.

The simplest network with the highest hit-rate over the validation set was trial 2. This was selected as the network to be used to make predictions over the entire well. An example of the results from this network can be seen as Figure 5.48. It can be seen that the network suggests that there are thin-beds in a large number of intervals that correspond to where the neutron and density logs are close together. The amount of predicted thin-bed packages is far more than expected. Some of these are a consequence of boundaries between shaly and less shaly regions. It was described how the neutron and density logs become closer when these packages occur, found by correlation to core, and although it has been shown that this relationship does appear to exist it will depend on the amount of thin-beds present in a package, and their individual thickness. Also it is clearly possible that the training of the neural network is the cause for this over-prediction, or more likely the selection of training data that the network was trained on. From a commercial point of view the most important thin-bed packages occur in facies 1 and 2 (laminated and bioturbated shale), and occur in packages that are greater than 2ft in thickness. If these packages occur in slumped shale then the slumping will have destroyed the fabric of the beds making them less productive.

Therefore if thin-bed packages are only allowed to occur in the principal facies (1 and 2) and only in intervals that are greater than 2ft in thickness then only the most important levee deposits are identified (see Figure 5.48).

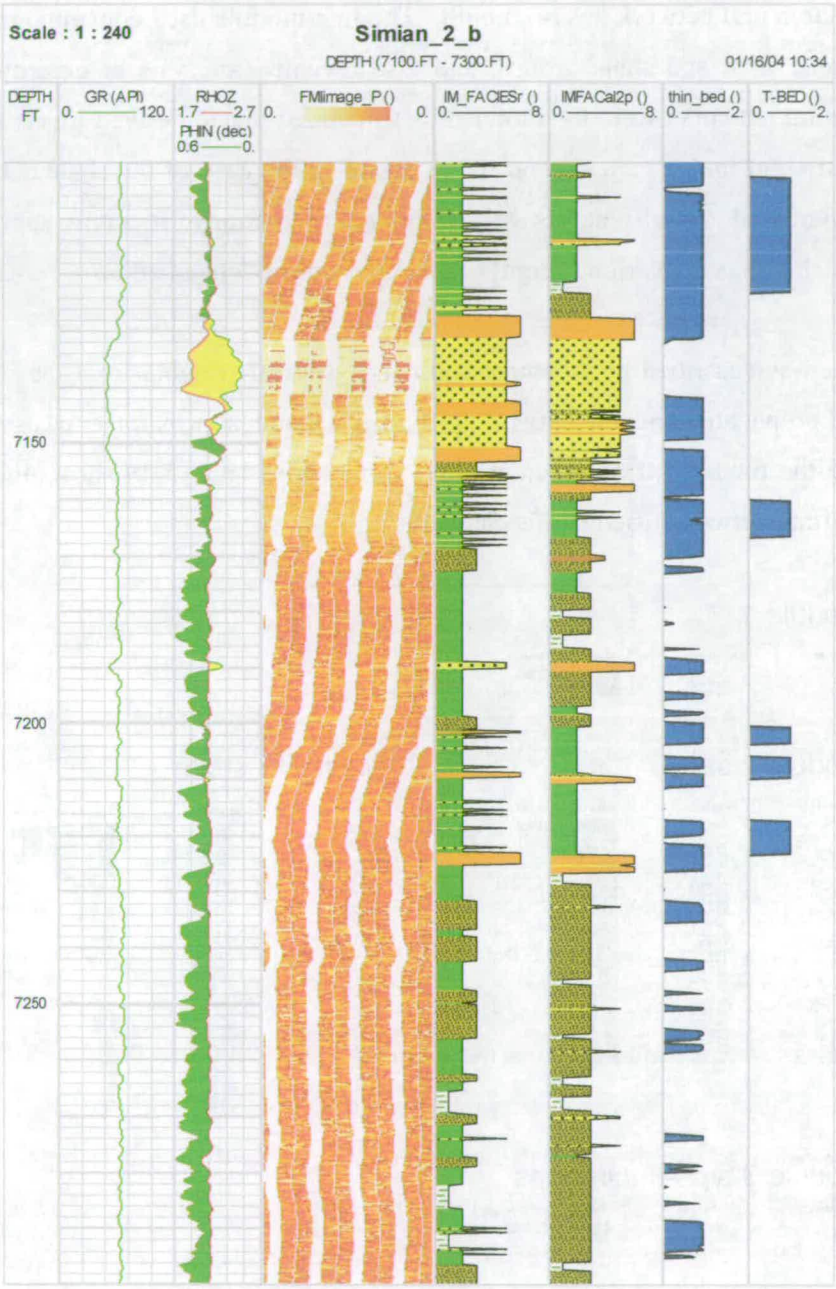



**Figure 5.48** An example of type-II thin-bed predictions from well Simian 3. Track 7 shows the raw predictions. These occur in almost all intervals. This could be for reasons described in the text. However if the thin-beds are only allowed to be predicted in facies 1 and 2 and only allowed to occur in intervals greater than 2 ft the results describe only the main levee deposits, shown in track 8.

The results of the modular system in all three wells are discussed further in Chapter 6. In these results type-II thin-beds are only shown if they occur in the principal facies (1 & 2).

### 5.6.5 Neural network dependence

So far a modular neural network has been built. The first module used conventional log data to describe broad sand and shale groups, and also revealed intervals of cemented facies. Subsequent neural networks were then trained that included image derived inputs that could differentiate different image facies – and it was found in the case of the shale network that using the conventional logs also at this stage improved predictions. It is now appropriate to investigate which inputs the various neural networks are most dependent on.

In Chapter 4 it was described how comparison of the sum of weights from the input layer *only* in a backpropagation neural network provides a good approximate measure of the contribution to the final result of different input variables. Figure 5.49 shows the relevant weights in the final networks used in this chapter.

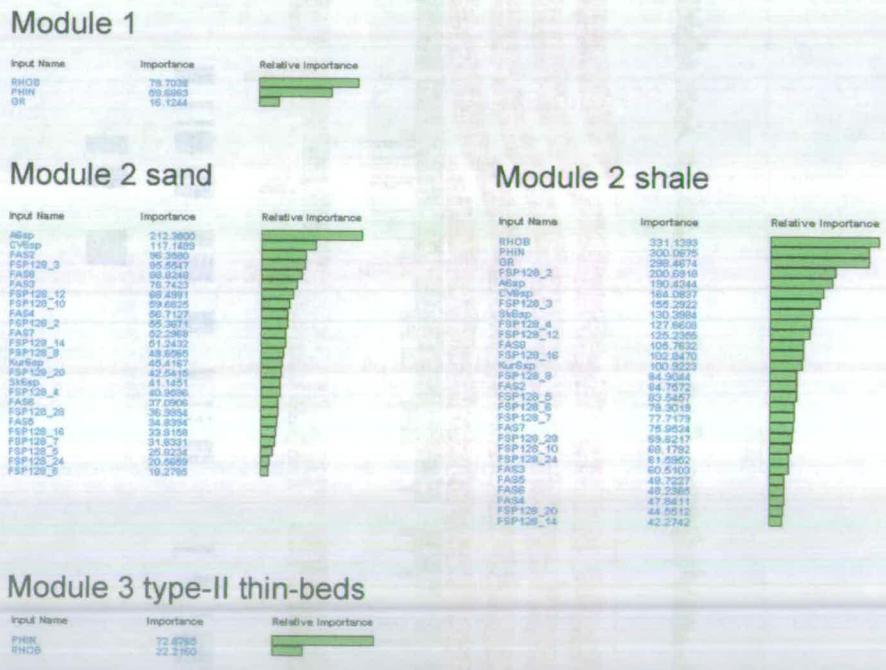



**Figure 5.49** Bar graphs to show the dependency of the various neural networks on the different inputs. The relative importance column shows the modular sum of the final weights attached to each input node, as described in Chapter 4. The input names can be found in the notations and conventions section that precedes Chapter 1. Note though that FSP128_8 for instance, refers to the **8**th lowest frequency from the **F**ourier spectrum from a **S**ingle **P**ad of data over a 128 point vertical moving window; FAS3 for instance, refers to the **3**rd lowest of the frequencies selected from the **F**ourier spectrum **A**cross a **S**ingle pad of data.

It is seen that in module 1 the neutron and density logs are more important than the gamma-ray log in discriminating sand from shale. This could be due to the higher resolution of these logs. The fact that the density log is most important could be due to the fact that this is important in discriminating facies 7 (cemented / conglomerate zones).

In the module 2 sand network the average button response is the most important input variable, and the coefficient of variation is the second most important. This is what was expected, as it was shown in Figure 5.12 that the average is a very good discriminator of facies 5 (resistive sand). It has also been shown in various other figures that this facies usually has a plain image and this is reflected in the importance of the coefficient of variation. The next most important variables are various power spectral curves from both the vertical and horizontal analysis. These were shown to be important in discriminating the different sand types (Figures 5.18 and 5.20).

In the module 2 shale network the three conventional logs are the most important discriminators, followed by a number of the spectral power curves and the average and coefficient of variation. It may be surprising that the three conventional logs are the most important in distinguishing the different types of shale. This could be because of facies 4 (debris flows) having a distinct neutron and density signature. However this is probably only part of the answer. These logs were interpolated to be the same resolution as the image logs, and if one imagines what is taking place during training of the neural network (Figure 5.50) then it is possible to understand why this occurs. The actual number of measured values of the conventional logs in the training set is far less then the image derived components. Therefore interpolating essentially boosts the restricted set artificially. The actual effect of this is mitigated to some extent by the averaging of the image derived components, and the training data coming from many different intervals. Also since there are more image derived inputs the total influence of these is greater than the conventional logs. However the use of the conventional logs was justified by experimentation, as it was shown in Figures 5.34, 5.35, and 5.36 that actual results are better when both image derived inputs and conventional logs are included in the shale network. This aspect of the research is discussed further in Chapters 6 and 7. Although the conventional logs are important in the module 2 shale network, the average and coefficient of variation are also very important too. This was expected (especially the coefficient of variation), from earlier analysis (Figure 5.13). Previous analysis also showed that the lowest frequencies in the vertical spectrum were

expected to be more important than their higher frequency counterparts for distinguishing different types of shales. Figure 5.49 shows the second, third, and fourth lowest frequencies to be important in the model. The twenty-eighth, twenty-fourth, tenth, twentieth, and fourteenth all appear less important in analysis. This illustrates that the algorithm is capable of sorting the input variables during training. Spectral analysis also took place horizontally, and it was expected that these power curves would be useful in distinguishing facies 3 (slumped shale). Although two of these curves do occur fairly high in the ranking, the majority are near the bottom. Either the relationships that it was thought existed do not exist throughout the whole data set, or the network has failed to learn this relationship. The network dependence is also discussed further in Chapter 6, when the results are viewed alongside the various input logs.

For the module 3 network that predicted thin-bed packages the neutron log is more important than the density log. This may indicate that these packages contain gas (it is known that such intervals are productive), which may affect the neutron log more. The influence of fluid type on any results was discussed in Chapter 4 - this would need to be considered before any further application to other wells in the concession area.

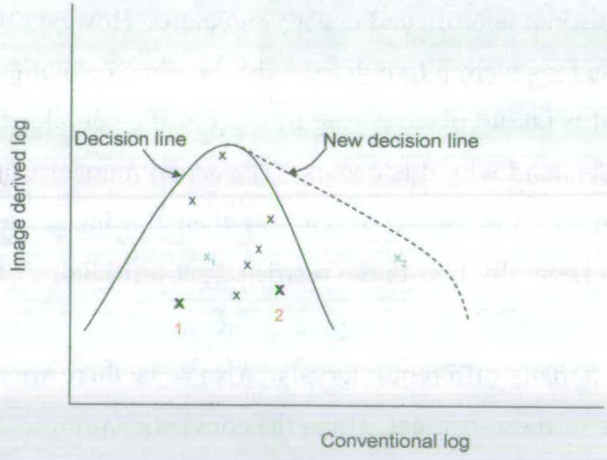



**Figure 5.50** Schematic of a two-dimensional cross section of the hypothesis space in which the neural network is searching for a solution. A conventional log is plotted on the abscissa axis, an image derived component on the ordinate. The two bold crosses (labelled 1 and 2) are actual measured values. The small black crosses (and $X_1$) are interpolated data. Therefore the positions of the small crosses on the abscissa are defined by the measured values, whereas their position on the ordinate can take on any value. If the points sit as they are shown then the network may draw the decision line indicated. However, if one of the interpolated points e.g. $X_1$ has a different abscissa value and isn't restricted by the measured points i.e. is in position $X_2$, then the resulting decision line could be very different (dashed). Thus the interpolated values of the conventional logs restrict the position of the decision line and therefore become artificially important during neural network training.

## 5.7 Chapter summary

This chapter described methodologies for integrating microresistivity image log data into the neural network process for 'image facies' prediction. Initially the geological setting and sedimentology of the West Delta Deep Marine Concession area were discussed and the image facies scheme developed by Baker Atlas (2000 & 2001) was presented. Section 5.3 described how the image data were processed before any interpretation took place.

In order to quantify aspects of the textures that could be seen in the images, various statistics of the image tool button responses were calculated. Spectral analysis of the data also took place both horizontally and vertically. It was shown how these criteria could potentially differentiate different textures on the image logs. In particular the coefficient of variation appeared a good discriminator of bioturbated shale and structureless sandstone. The average of button responses also appeared a good discriminator of structureless sandstone. The different spectra appeared to differentiate laminated and slumped shale. In all cases better discrimination was found if analysis took place on a single pad of data rather than over all the data at once. Also it was shown how some facies such as chaotic and slumped shale, and laminated, intraclastic, and irregular sand could not be discriminated. Debris flows were shown to have a very specific lithological signature that was seen by the neutron and density tools. On the basis of this work the image facies scheme was simplified before analysis with the neural network. In Chapter 3 it was discussed how transformation of data, and inter-well normalisation are important to ensure successful interpretation. This was investigated in Section 5.5. Finally training and validation sets were carefully designed.

Preliminary analysis of the data then took place. This initially involved the building of a modular system. The first module separated the well data into specific lithological groups using conventional logs. The second module contained two networks that were trained to predict different types of sand and shale. The sand network was trained successfully with only image-derived inputs. It was undecided whether to include the conventional logs along with the image-derived inputs in the shale network, and therefore two different networks were trained, one with conventional logs, and one without. The network trained with the conventional logs appeared to give better results. In particular facies 4 (debris flows) was predicted more successfully, as expected from previous analysis. The modular system was then compared to a single network that was trained to predict all facies. Although

theoretically the two systems should be able to predict with similar degrees of accuracy, it was shown that the modular system produced better results. Thin sandy beds exist within thicker shaly units and these could not be discriminated by the networks trained so far as the various inputs were averaged over a moving window. Therefore more networks were trained to predict these. One network used the average button response (but not averaged vertically) to predict those thin-beds that were resolved by the image. Many thin-beds were not resolved by the image. However where these occurred in dense packages the coarse logs such as the neutron and density appeared to respond to the increase in the bulk sand content. Therefore a separate network was trained to predict these packages.

Weight analysis of the networks revealed which input parameters were most important in the different models. These illustrated how the algorithm is capable of sorting input parameters into their importance during the training phase. It was also noted how combining interpolated coarser logs with higher resolution logs can artificially promote the coarse logs to be more important in model building.

The results from the modular system and the thin-bed predictions are illustrated further in Chapter 6. The conclusions drawn from this chapter are discussed in more detail in Chapter 7.

# Chapter 6 : Further analysis of image lithofacies results

## *6.1 Introduction*

This chapter presents further results from the modular neural network system developed in Chapter 5 for predicting images lithofacies. Various sections of the wells are shown that display the network results alongside the images. Description and discussion of these (Section 6.2) compliments analysis that took place in Chapter 5, by confirming what the network is actually responding to and whether the results are justified by the logs. Since the use of the thin-bed repair program to improve results was implemented in the previous chapter, no further discussion of this process takes place here. Since some of the absolute measurements used during analysis are affected by fluid saturation (even the measured image conductivity values are affected by reservoir fluid (Rider *et al.* 1999)) it is expected that the developed model will only be applicable in gas zones. All three well intervals in the data set occur in the gas leg and there are no obvious transition zones. For these reasons no further analysis is attempted (as in Chapter 4) to create a model applicable to transition and water zones.

In contrast to the detailed analysis of Section 6.2, Section 6.3 illustrates how network predictions can aid the interpretation of large-scale sedimentary environments and assist in depositional modelling. The chapter is then summarised in Section 6.4.

## *6.2 Detailed analysis of network predictions*

### *6.2.1 Introduction*

This section compares image facies predictions to the actual images on a well by well basis. Figure 6.1 shows an overview of Simian 1, 2 and 3. Black boxes indicate the intervals that are shown in subsequent figures.

### *6.2.2 Detailed well analysis*

Figure 6.2 shows an interval from a higher section of Simian 1. Tracks 2, 3 and 4 show the gamma-ray, neutron, density, average button response, and coefficient of variation that were all used as inputs into the model. The image log (dynamic) is then shown in track 5. Since

statistical and spectral analysis took place across a single pad of data the pad that was used for this is shown on its own in track 6 (this is actually a mirror image of the pad used, but it still shows the texture recorded by the tool). Tracks 7 and 8 show the horizontal and vertical spectra, as described in Chapter 5. Track 9 shows the 'real' image facies (a simplified version of the Baker Atlas scheme) and a black bar indicating where training data was taken from. Track 10 is the neural network prediction after application of the thin-bed repair program. Track 11 shows a thin-bed flag that records the possible presence of type-II thin-beds. Tracks 12-18 show the activation levels of the different output nodes for module 2 only, apart from where facies 7 (cemented) exists then the activation level from that output node in module 1 is shown. Although the raw un-repaired predicted image facies column is not shown this can be inferred from the activation levels. All other subsequent figures in Section 6.2 are set-up a similar way.

The Figure captions describe in detail the main features present in each figure. Although this is not repeated in the main text some discussion and general conclusions are presented.

The rest of this page is deliberately left blank.

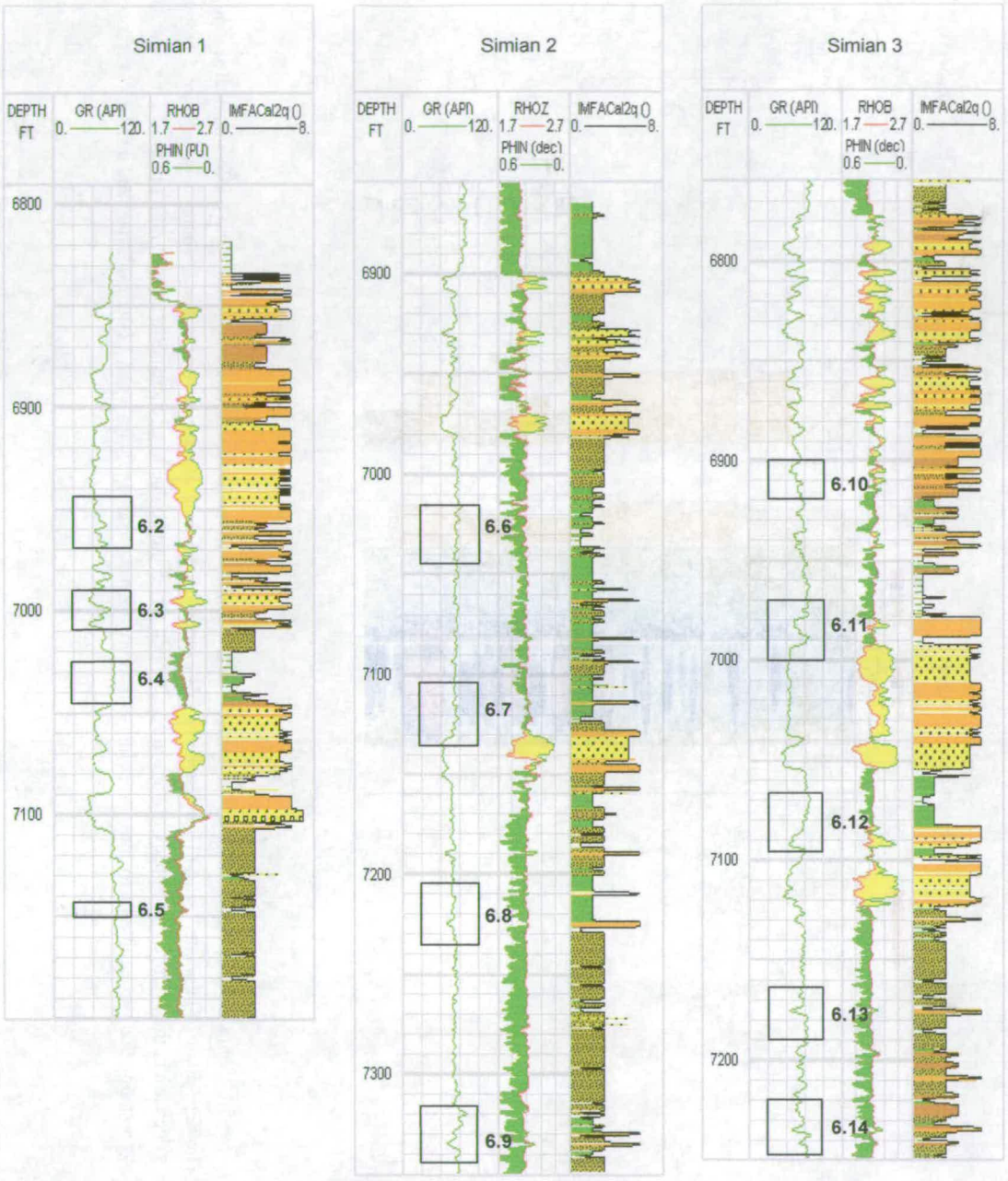



**Figure 6.1** Overview of the three wells that make up the data set. From the left the gamma-ray, neutron and density, and predicted image facies are shown. The black boxes indicate the position of subsequent figures in this chapter.

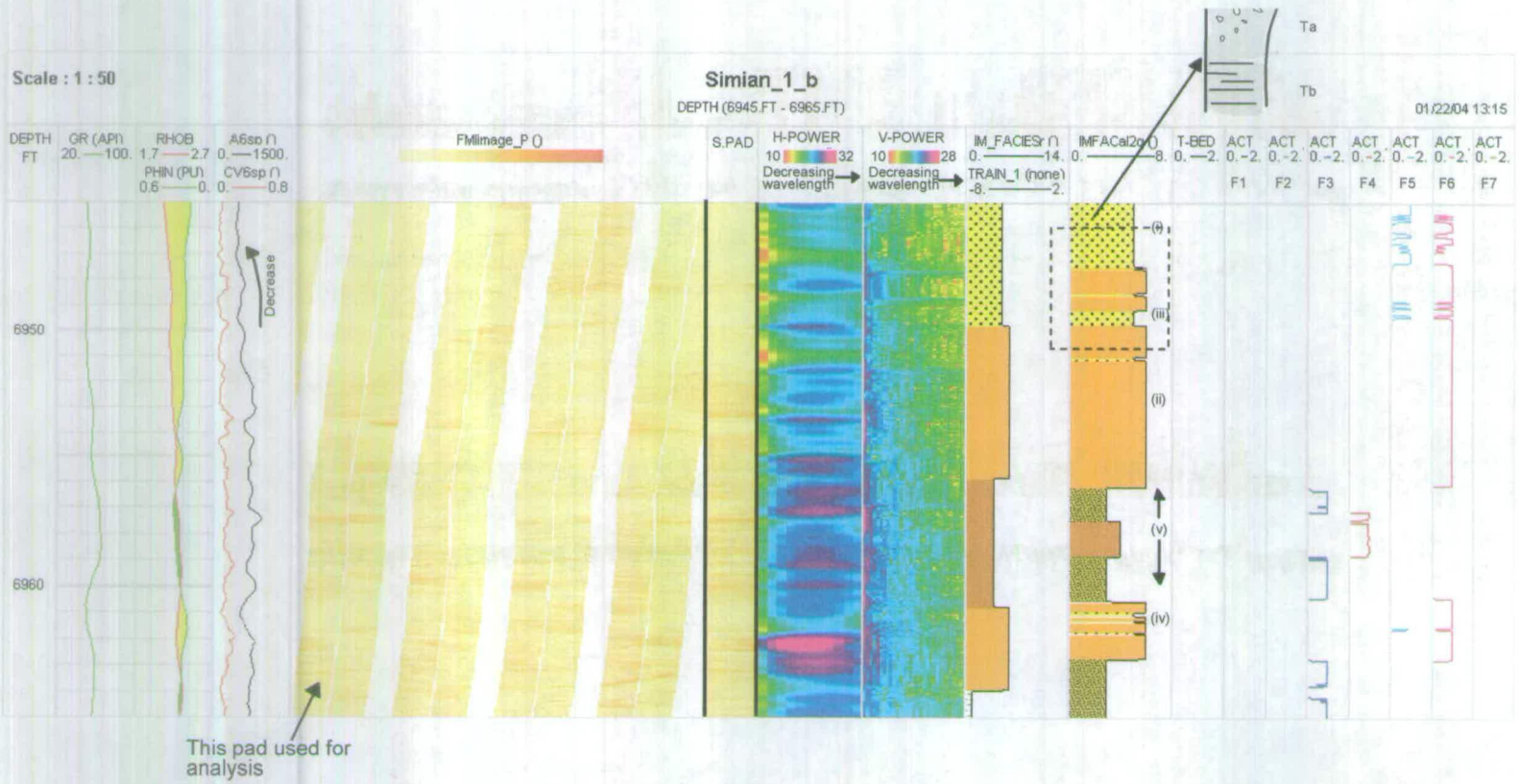



**Figure 6.2** Section from well Simian 1 6945-6965ft. Sands are predicted correctly at points (i) – (iv). The thin interbedded occurrence of facies 5 and 6 infers laminated sand - part of a classic Bouma sequence (Bouma 1962). The deposition of laminated sand (Tb division) in this example is followed by the start of another sequence with facies 5 associated with division Ta. This transition corresponds to a decrease in the average button response upwards, although this could be due to an increase in gas saturation in the Ta division sands. This interpretation agrees with the Baker Atlas interpretation that was calibrated to core. At point (v) the network has mixed up facies 3 and 4 (slumped shale and debris flow respectively).

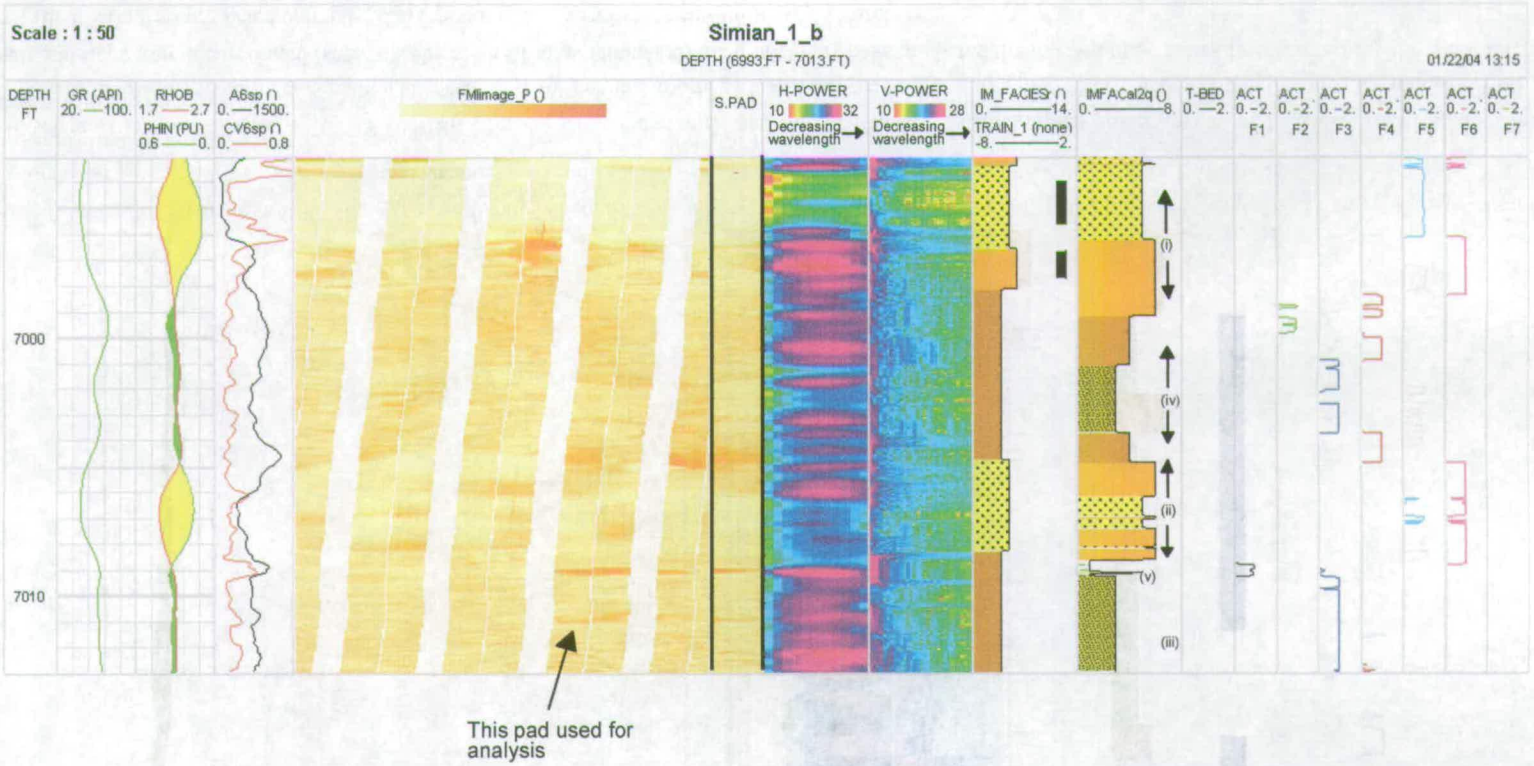



**Figure 6.3** Section from well Simian 1 6993- 7013ft. At (i) image facies are predicted correctly (although this is expected as they do form part of the training set, indicated by the black bar in track 9). The interval of facies 5 (structureless sand) at the top of this section is clearly distinguished by its very low average conductivity value and represents a Bouma Ta division. At (ii) although the predicted facies doesn't match the 'real' interpretation it certainly follows texture recorded by the single pad, with a more conductive component at the top. At (iii) and (iv) facies 3 and 4 (slumped shale and debris flow) are mixed up. This is probably due to high power in the horizontal spectrum that usually is associated with facies 3. There are extremely strong laminations at (v) that are detected by the vertical power spectrum. Therefore a small section of laminated shale is predicted. These laminations are not present across all pads and flaps. Therefore incorporation of other pads and flaps in the model may have produced a different result.

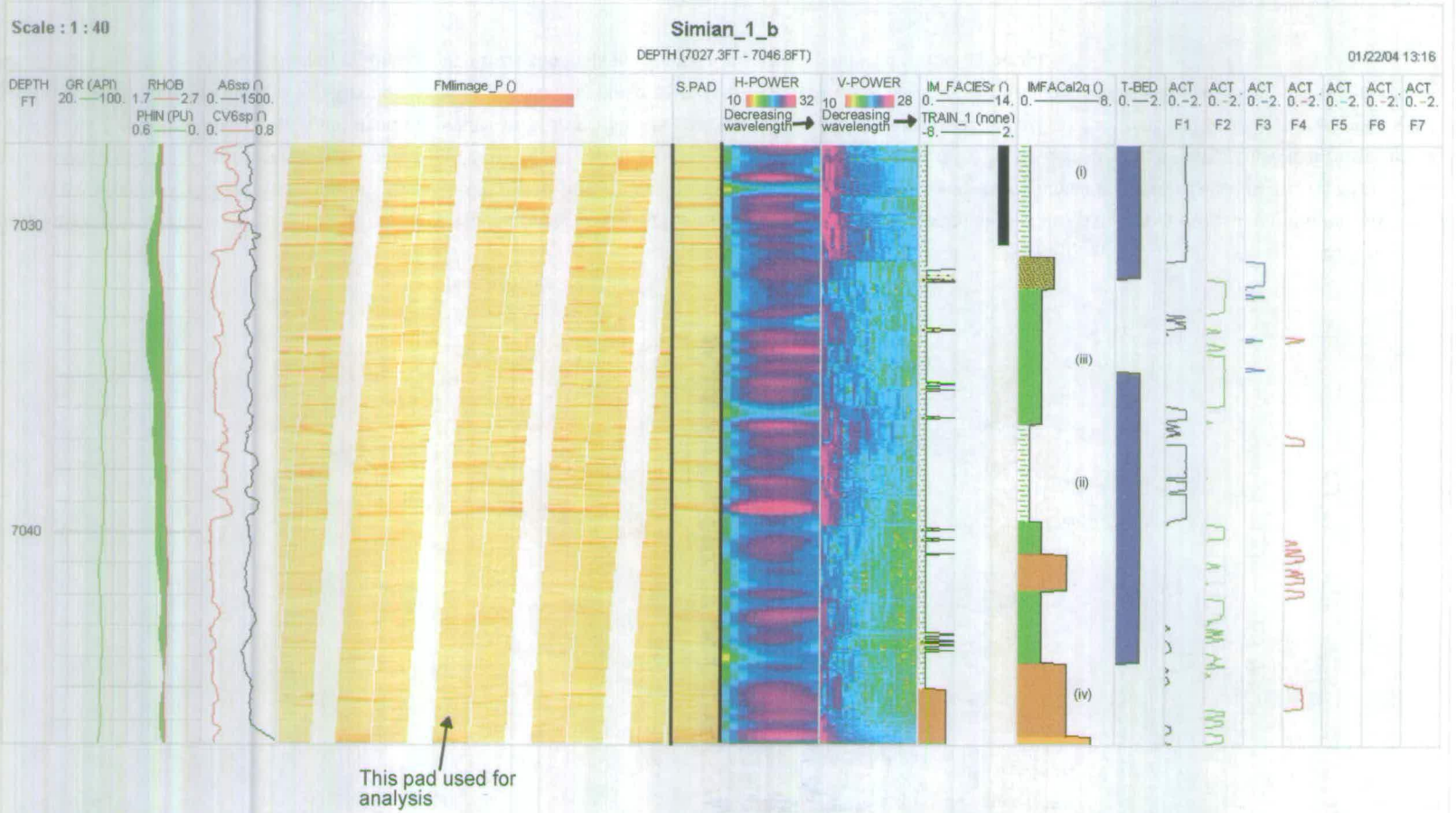



**Figure 6.4** Section from well Simian 1 7027.3-7046.8ft. Strong laminations at (i) and (ii) are detected by the vertical power spectra and facies 1 (laminated shale) is predicted correctly. At (iii) the single pad of data is plain and speckled corresponding to image facies 2 (often representing bioturbated shale). So in this area the model is working correctly. If other pads and flaps were incorporated (some of which are strongly laminated) the model may have predicted the interval to be facies 1, thus matching the 'real' interpretation. At (iv) facies 4 (debris flow) is predicted correctly, corresponding to a very close neutron-density separation.

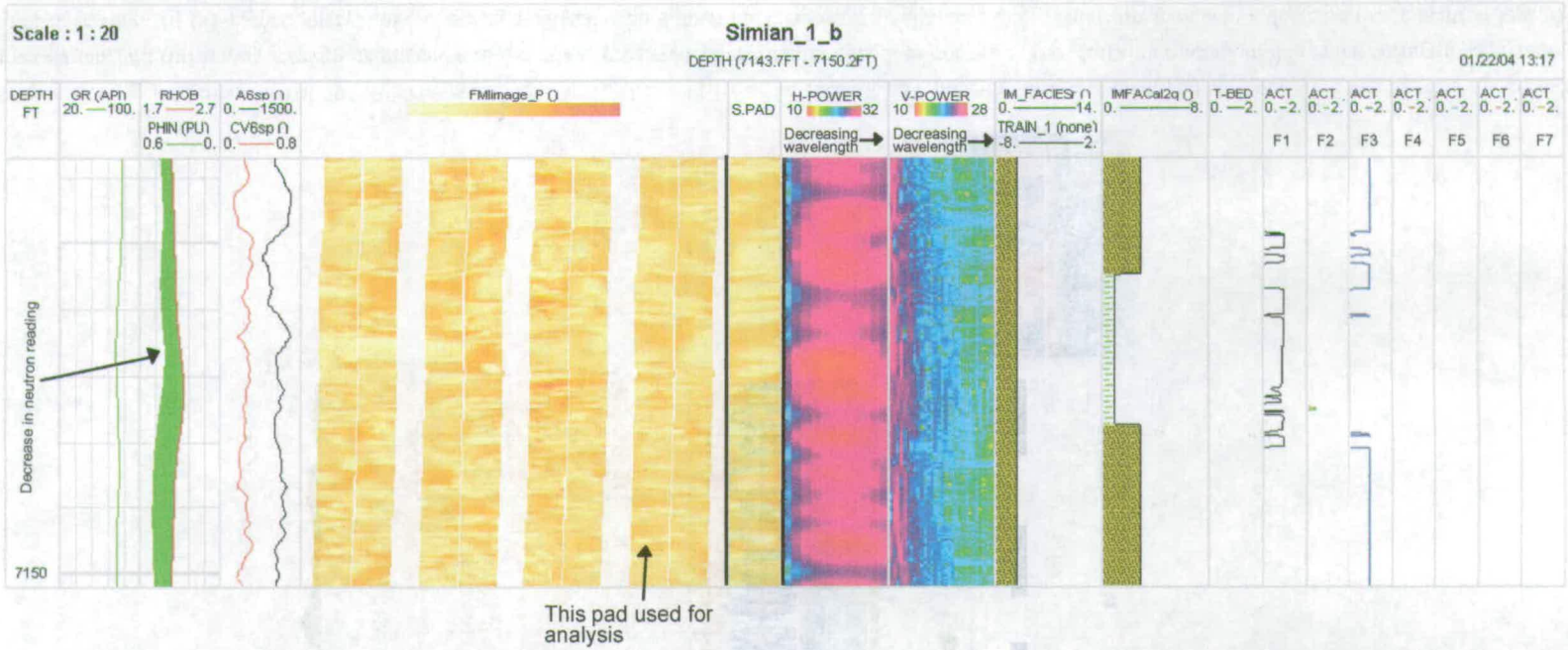



**Figure 6.5** Section from well Simian 1 7143.7-7150.2. There is a lot of variation in the image both vertically and horizontally, and this is detected by both power spectra. The coefficient of variation and average button response are both fairly high. This interval possibly represents data that is borderline between two facies types in the neural network high dimensional space. It is possible that the small decrease in the neutron values is why laminated shale has been predicted. This corresponds with the analysis undertaken in Chapter 5 that showed the conventional logs to be important discriminators in the model. Note that 1 vertical box represents 1ft.

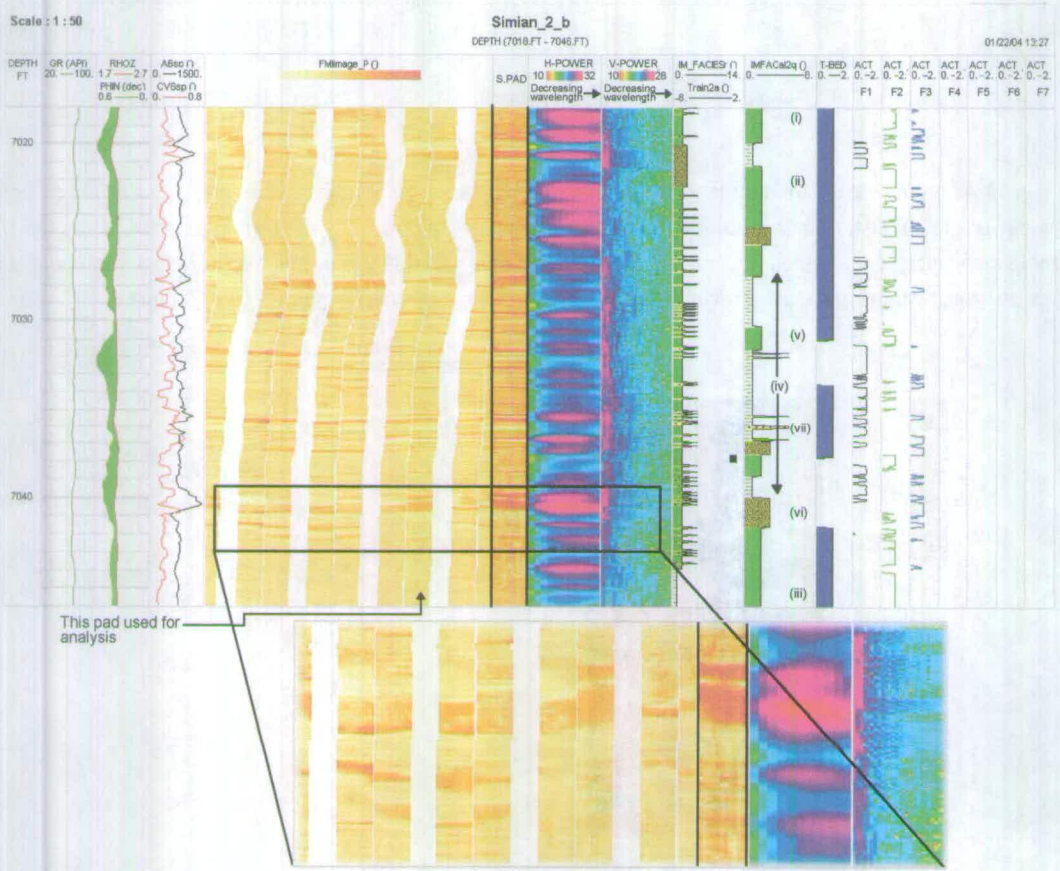



**Figure 6.6** Section from well Simian 2 7018-7046ft. The predictions at (i), (ii) and (iii) are of facies 2 and since the image is plain and speckled then this appears the correct result. The interval labelled (iv) is very strongly laminated and facies 1 is predicted. Even though this does not match the 'real' interpretation, this is the correct interpretation based on the image texture. At (v) a small interval of facies 2 is predicted even though the image is strongly laminated. This corresponds to a decrease in the neutron log. At (vi) the image is out of focus and this corresponds with very high values in the horizontal power spectra. Consequently facies 3 (slumped shale) is predicted. Note also that type-I thin-beds are predicted correctly at (vii) and much of this entire interval contains predicted type-II thin-beds (track 11 blue flag) which are correct.

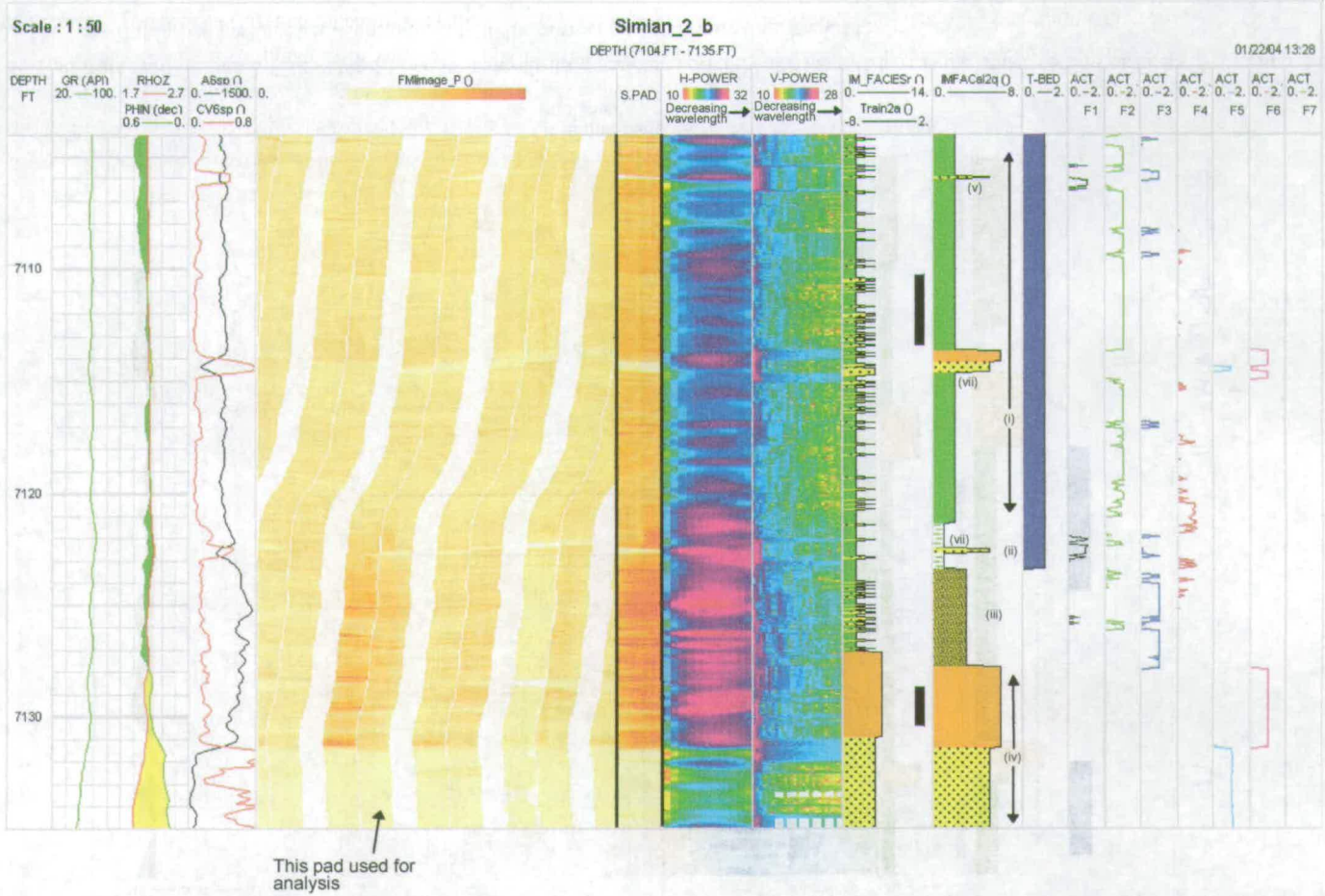



**Figure 6.7** Section from well Simian 2 7104-7135ft. Interval (i) represents a good interpretation of the image, facies 2 is predicted correctly. At (ii) the sandy thin-bed has been detected as a lamination by the vertical spectra and consequently facies 1 is predicted. At (iii) more facies 3 (slumped shale) is confused with facies 2 (bioturbated shale), although there is some heterogeneity in the image at this interval. Incorporation of other pads could have produced a different result. At (iv) sand is predicted correctly. Note also that type-I thin-beds are imaged very well and subsequently predicted correctly at (v), (vi) and (vii). Type-II thin-beds are also predicted in the correct place (blue flag, track 11).

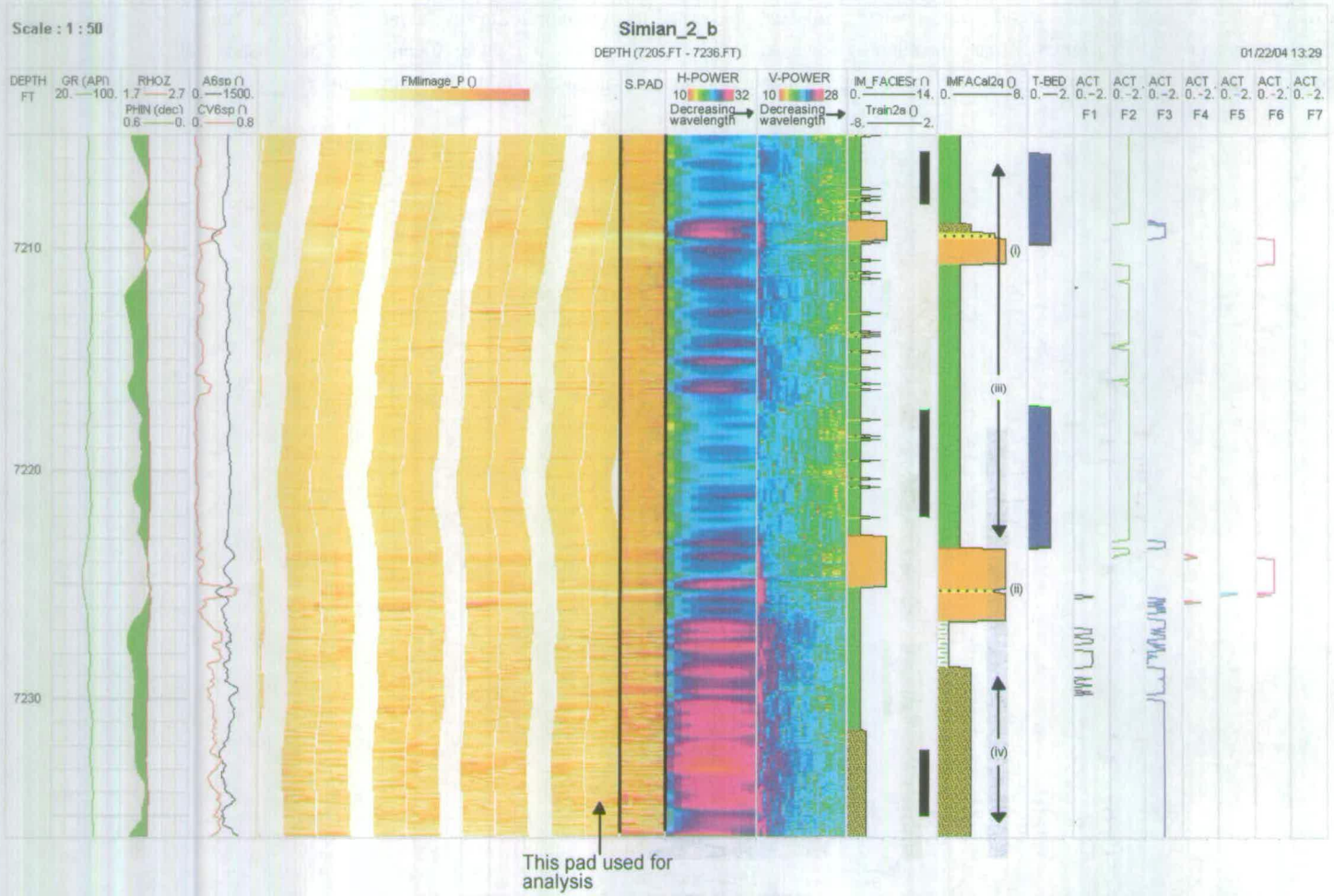



**Figure 6.8** Section from well Simian 2 7205-7236ft. Sandy intervals are predicted correctly at (i) and (ii), as is the upper section of facies 2 (iii), and the lower section of facies 3 (iv). The type-II thin-bed packages are approximately in the correct position (blue flag, track 11)

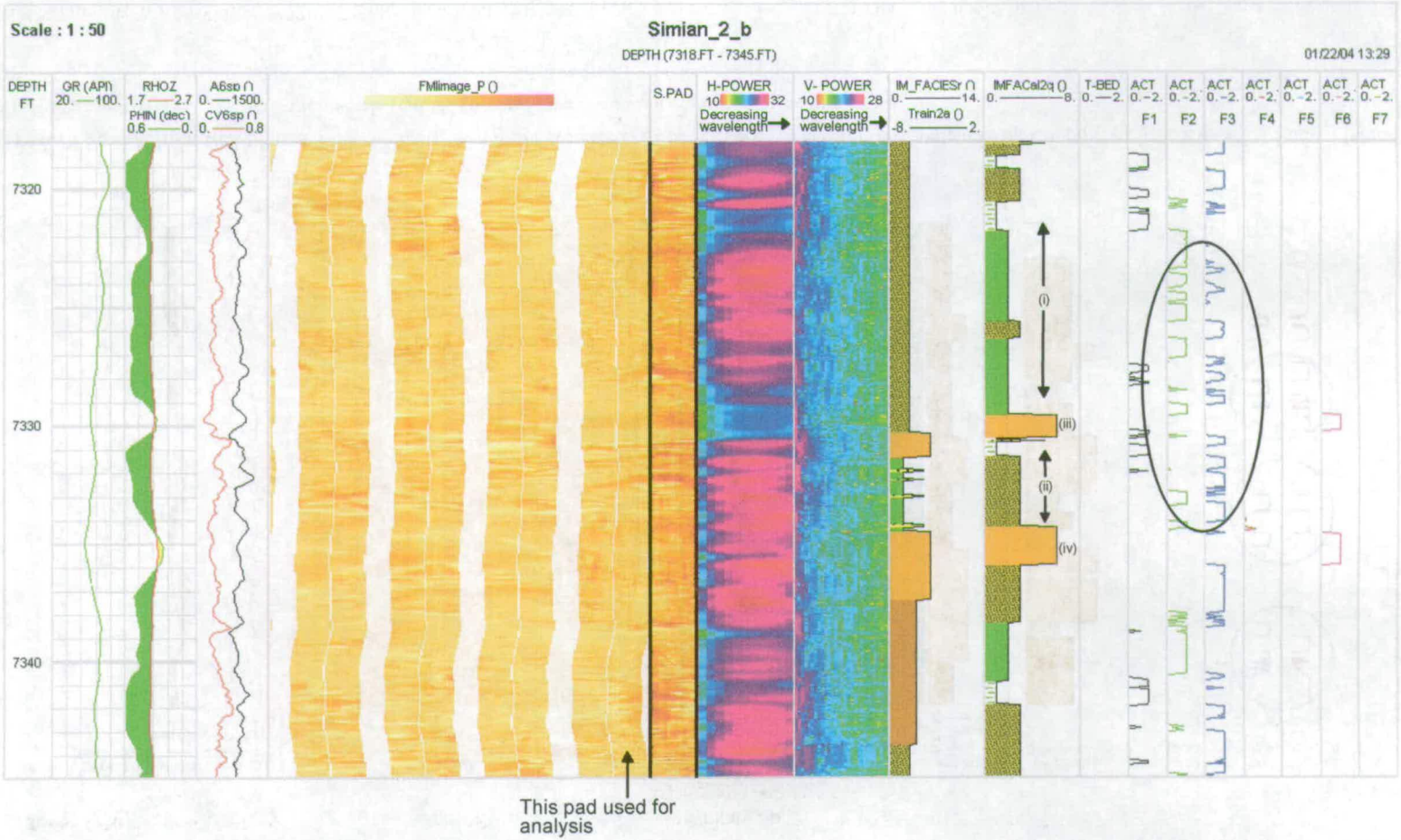



**Figure 6.9** Section from well Simian 2 7318-7345ft. At (i) and (ii) facies 2 and 3 are mixed up once again. However it is possible to tell that the network is uncertain by the activation levels - both output nodes for facies 2 and 3 are highly active (circled). At (iii) and (iv) sandy beds are predicted correctly even though they do not match up exactly with the 'real' facies.

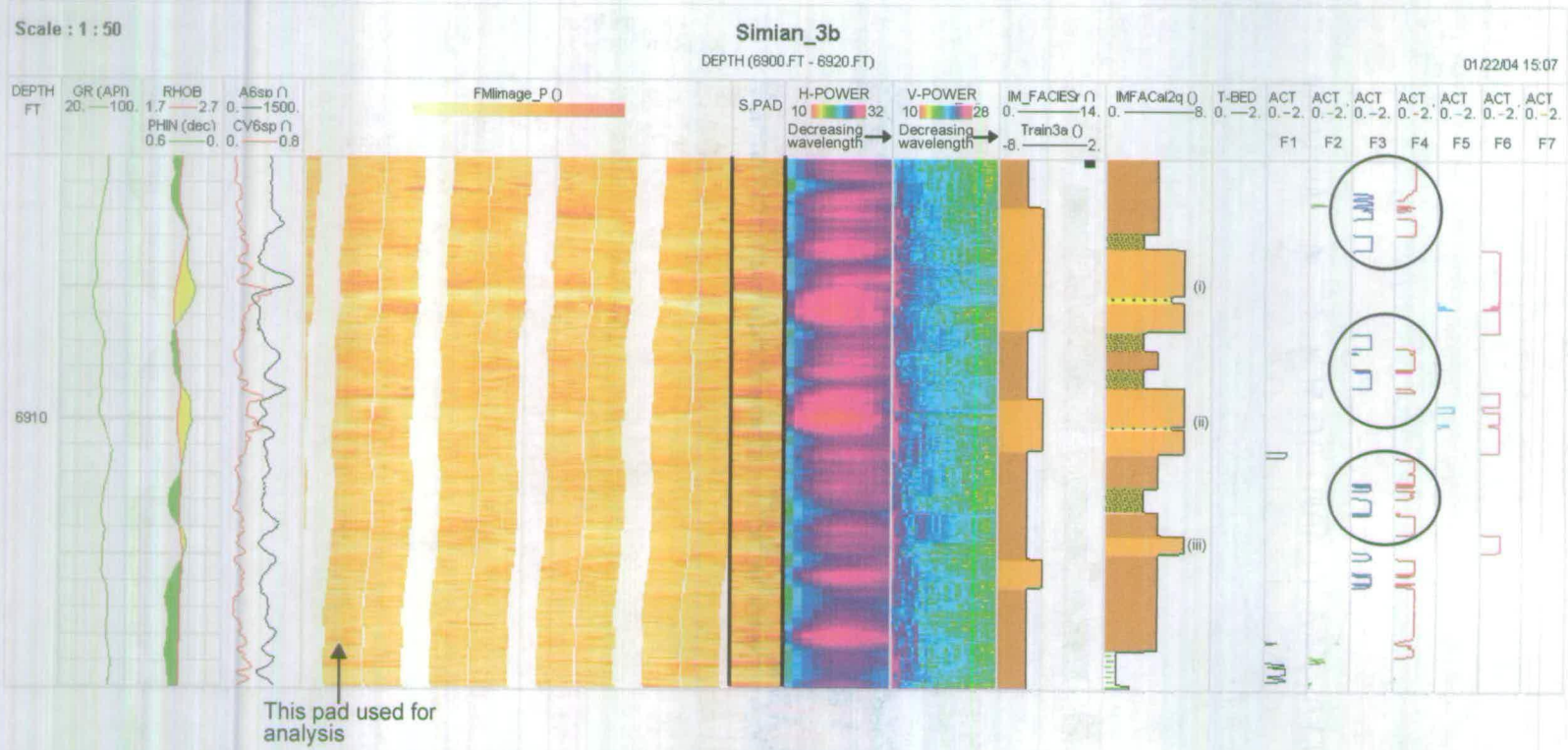



**Figure 6.10** Section from well Simian 3 6900-6920ft. Sands are predicted correctly at (i), (ii) and (iii) but some mix up can be seen between facies 3 and 4 (slump shale and debris flow respectively). The activation levels (circled) describe the uncertainty between these two facies.

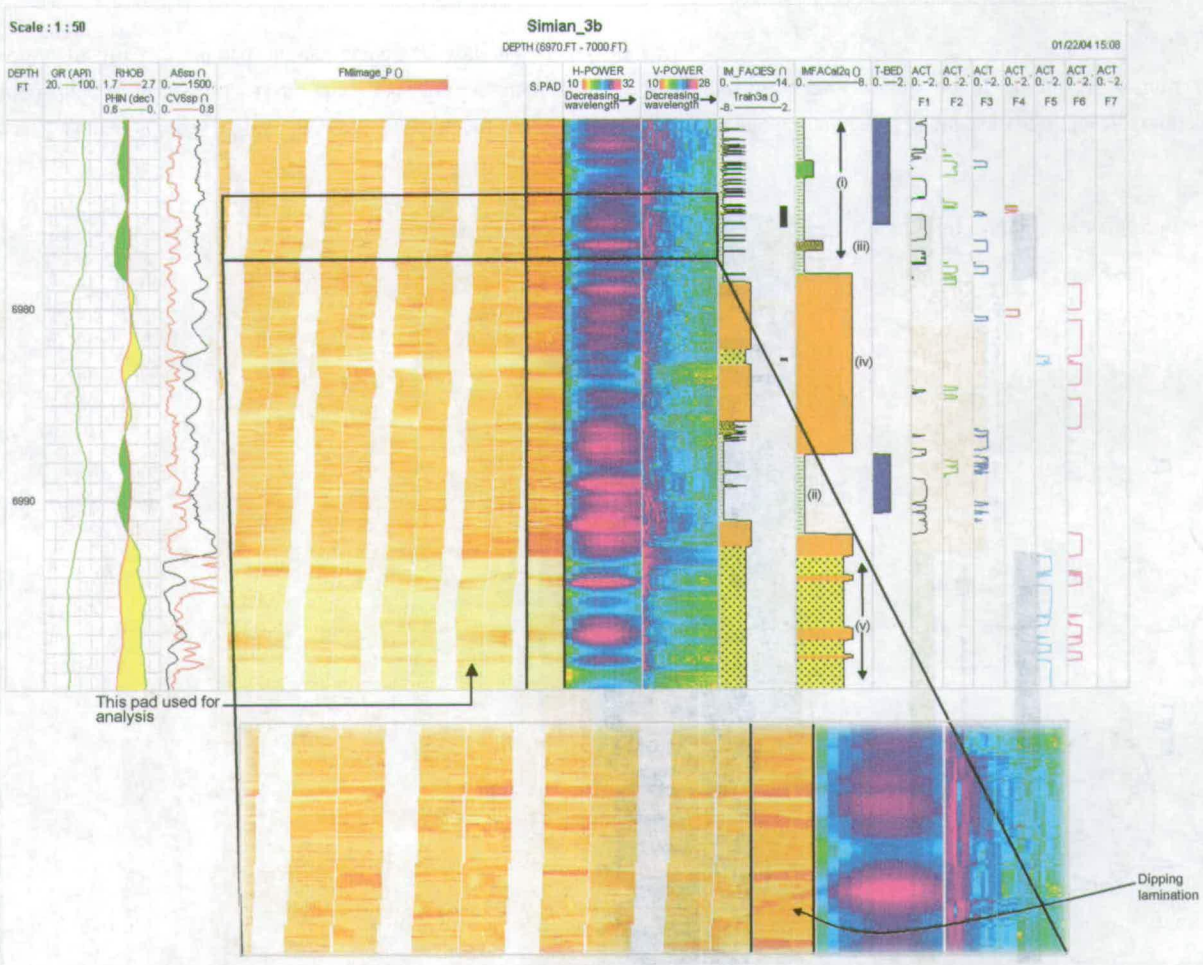



**Figure 6.11** Section from well Simian 3 6970-7000ft. The intervals of shale at (i) and (ii) are predicted correctly as both are strongly laminated. At (iii) a single dipping lamination produces high power in the horizontal spectra and consequently a small bed of facies 3 is predicted. This demonstrates how sensitive the model can be to single textural features. At (iv) conductive sand is predicted correctly but the thin bed of resistive sand (facies 5) is not predicted even though it is very clear on the image. The average button response for the particular pad that underwent analysis is not low enough for a prediction to be made. At (v) more detail is predicted that matches the image log. This detail is not included in the manual interpretation.

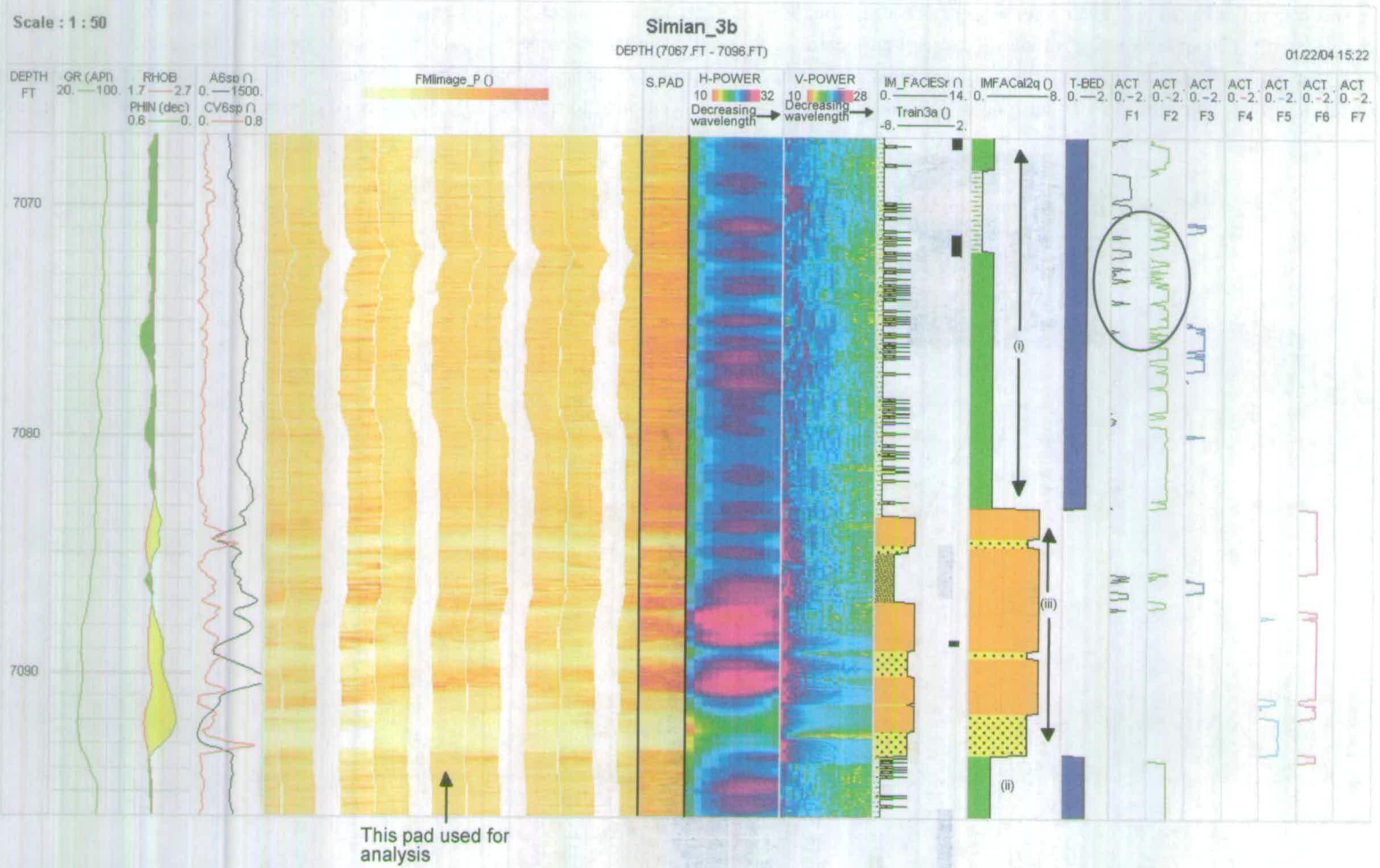



**Figure 6.12** Section from well Simian 3 7067-7096ft. In interval (i) and (ii) there is confusion by the model, indicated by the activation levels (circled), between facies 1 and 2 (laminated and bioturbated shale respectively). There are some faint laminations in the image but these are certainly not as prominent as those in Figure 6.6. Thus the interpretation by the network is justified. Sand beds are predicted very well at (iii).

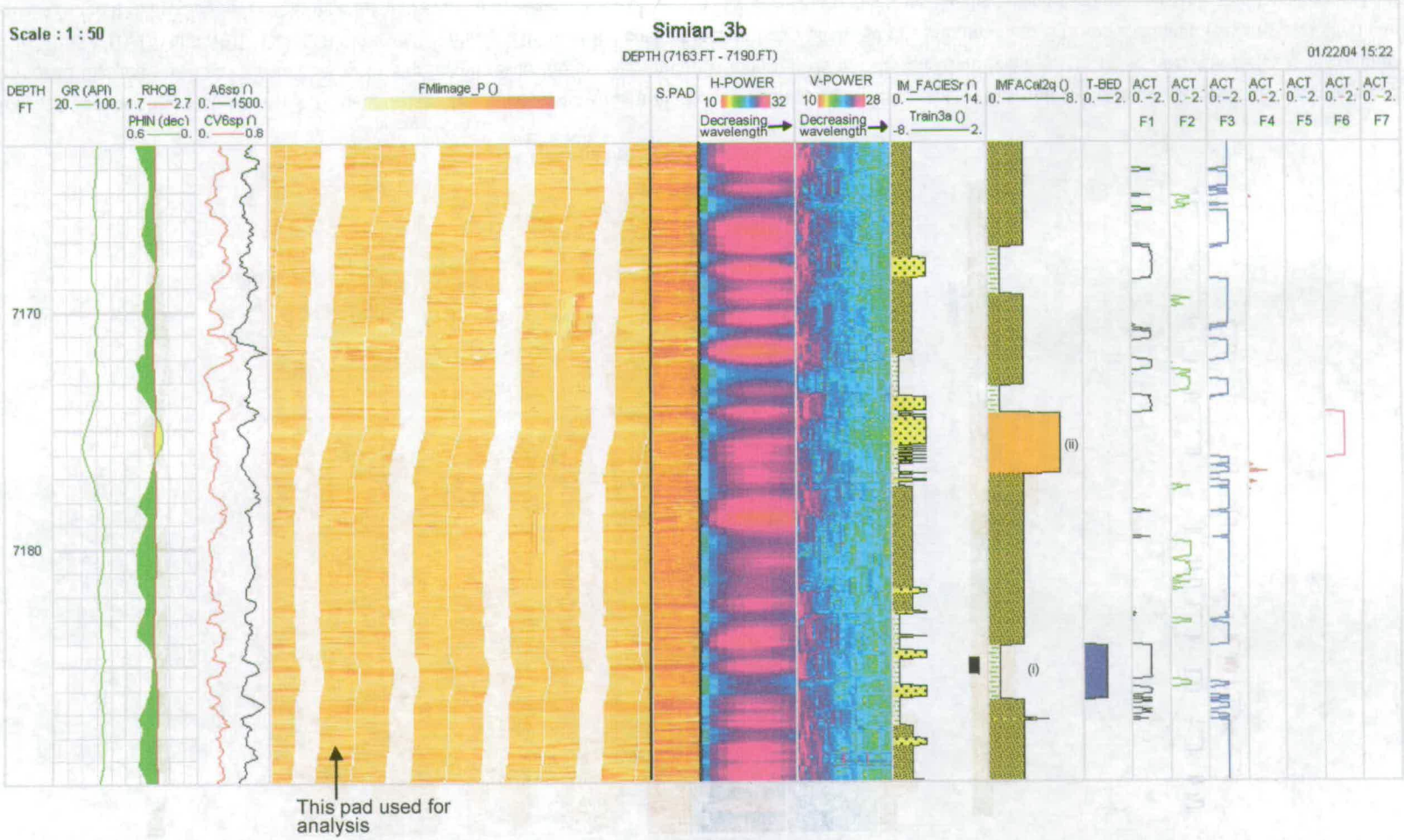



**Figure 6.13** Section from well Simian 3 7163-7190ft. In general the interval is predicted successfully with intervals of facies 1 and 3, depending on the strength of the laminations and the value of the neutron log. A thin-bedded sand package is detected at (i). At (ii) an amalgamation of thin-beds means that a thick bed of conductive sand (facies 7) is predicted.

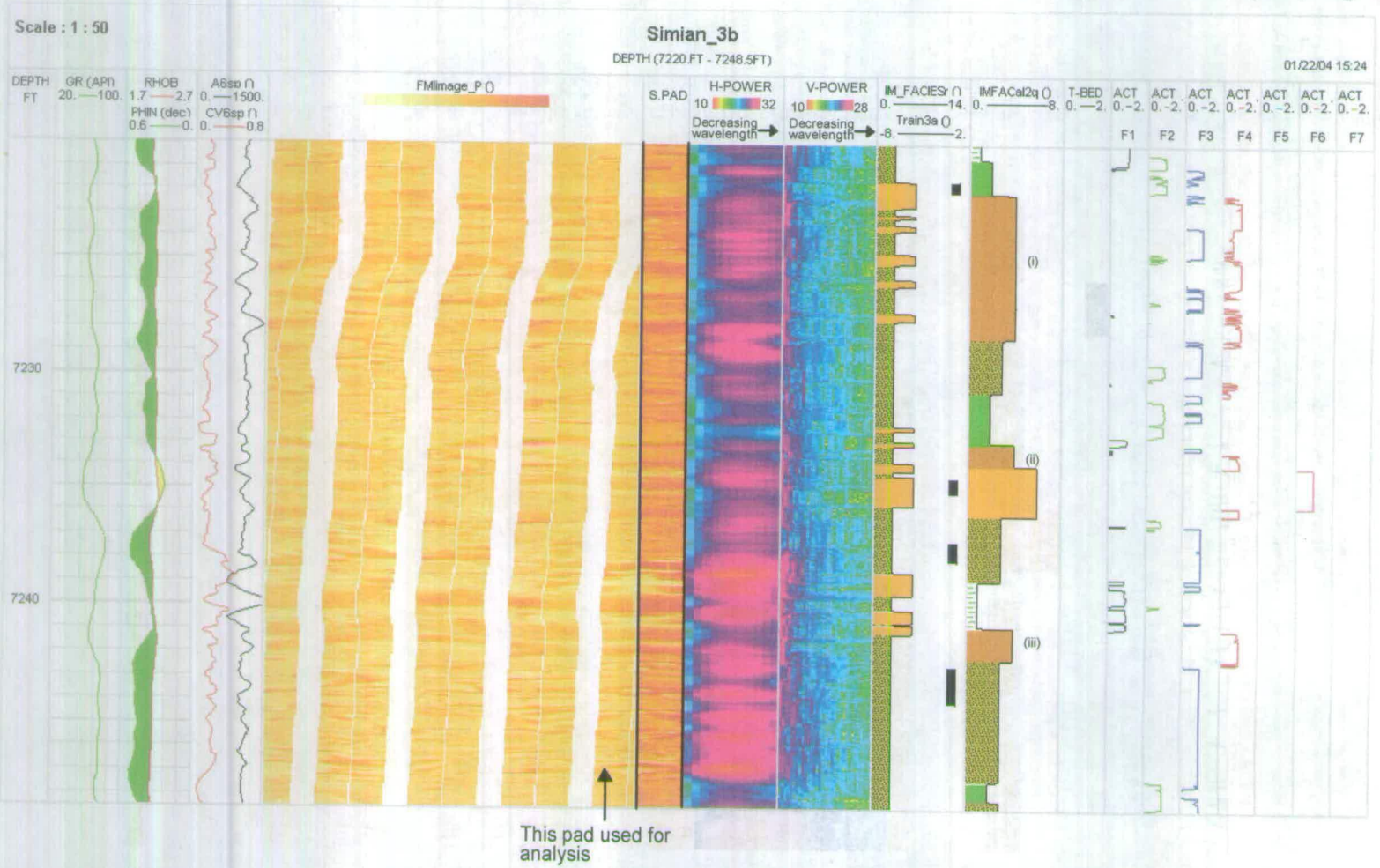



**Figure 6.14** Section from well Simian 3 7220-7248.5ft. The interval shown is from the lower slumped shale horizon in this well. Within the slumped shale are conductive beds of sand that are not discriminated easily by the image (even the average button response does not deviate significantly). In these intervals facies 4 is commonly predicted (e.g. at (i), (ii) and (iii)). Debris flows usually contain a higher sand content than ordinary shale, so this interpretation is to some extent a realistic one. Predictions of facies 4 in thick shaly sections (rather than the more common association with in-channel deposition) therefore, can be taken to indicate possible thin-beds of conductive sand.

In general the predictions by the modular neural network are good, the main intervals of different facies correspond to the texture shown by the image and the lithology indicated by the conventional logs. A direct comparison of the neural network defined image lithofacies with the Baker Atlas interpretation is difficult to assess. This is in part because some of the Baker Atlas interpretation was thought ambiguous (discussed in Chapter 5) and because some sections of their interpretation were also calibrated to core, whereas the analysis presented in this thesis is based only on the image logs. However there are specific places where the neural network interpretation appears more realistic than the Baker Atlas interpretation (e.g. section (iii) and below section (ii) in Figure 6.4 where the image is plain and facies 2 is predicted). This illustrates the consistency that this type of analysis can offer.

From the different image lithofacies it is shown how in many places the different associations can provide detailed sedimentological information. Finely interbedded intervals of facies 5 and 6 (resistive and conductive sand) represent laminated sand that make up part of a typical Bouma sequence (Bouma 1962). This interpretation agrees with the Baker Atlas interpretation (2000) which was calibrated to core. Facies 4 is usually associated with debris flows that generally represent in-channel deposition. Since these typically are resolved by their very close neutron-density signature when they occur in much thicker shaly intervals they appear to represent conductive sand horizons - the tools have responded to an increase in sand content and a prediction of facies 4 is the result. Therefore it is clearly very important to understand exactly what the model is responding to and what the different associations indicate. This knowledge should lead to an update of the facies associations described in Table 5.2 that could then be used to *assist* in a detailed sedimentological analysis of the images and/or core.

What is also shown is that the model created does appear to mix up some of the shaly facies. Specifically facies 1, 2, and 4 sometimes are predicted as facies 3. This could be a result of the make up of the training set. Although partial boosting took place facies 3 did occur more frequently than the other shaly facies (see Table 5.6). However in many places where a mix up of these facies occurs there is a significant deviation of the neutron log (for instance in Figure 6.5 where the neutron log decreases and facies 1 rather than facies 3 is predicted). This confirms the analysis that took place in Chapter 5 indicating the conventional logs to be important discriminators. In cases where this does occur though it is common for the image

to show borderline texture between the two facies and the activation levels to indicate uncertainty in the network's output (for a given interval rather then a specific data value).

It was also illustrated how the model is very sensitive to specific single textural elements. This is a result of the sensitivity of the spectral analysis (and why it was necessary to carry out this type of analysis over a single pad of data rather than all the data at once). If other pads and flaps could be incorporated into the methodology then this could reduce the overall sensitivity of the model to such specific features. Indeed a number of examples have been shown where the model prediction is deemed correct, but does not match the real interpretation simply because the texture of the pad used for analysis is not typical of the entire image. In a shale interval if the analysed pad is plain but the other 7 are laminated (as in Figure 6.4 (iii)) and bioturbated shale (facies 2) is predicted then this is a good result (since the network has recognised the plain nature of the image). If other pads and flaps could be incorporated in some way then one would hope that the output might be laminated shale (facies 1). The incorporation of more data into the analysis is discussed further in Chapter 7. Sensitivity of the model is also illustrated when the image is out of focus. This results in a large variation in the image and consequently very high power in the horizontal spectrum. In all such cases if the interval is shaly, then facies 3 is predicted. Success of the model is therefore (somewhat obviously) dependent on the quality of the actual data.

Where individual sandy thin-beds (type-I) are fully resolved by the image logs (usually this means that they contain gas and therefore have very low conductivity values) they are predicted correctly. Type-II thin-beds also appear to be predicted very well with the main packages occurring in the correct intervals (it must be recalled though that these were previously filtered in Chapter 5 to retain only the thickest intervals).

How thin-sandy beds influence the image texture also merits discussion. The model developed in this thesis assumes that the overall image texture characterises the primary image facies and that sandy thin-beds are essentially a 'separate element' of the texture. In Figure 6.7 (ii) a resolved thin-bed is detected as a lamination and consequently facies 1 is predicted. If an interval occurred that had repeating resolved sandy thin-beds in a shaly interval then the vertical power spectrum would detect these as laminations and predict the rock to be facies 1. The thin-beds would then be added to the interpretation in module 3. There is no particular solution to this problem. The model can only respond to the different

features that it has encountered during training. In this data set resolved type-I thin-beds never occur repeatedly in a single section, when thin-beds do occur in packages then they are thinner and not fully resolved (these being type-II thin-beds). In all cases where very strong laminations are present these represent laminated shale and are interpreted from core as being a consequence of fine-scale grain size variations in detrital clay (Baker Atlas 2000 & 2001). Thus when the model is applied to new wells then it is assumed that any strong laminations present are a result of the same process of formation. If a model is to be applied to new wells then the fundamental underlying assumption is that only features that exist in the training data should expect to be encountered in the new well.

## *6.3 Large scale analysis of image facies predictions*

### *6.3.1 Introduction*

This section describes how image facies can be used to interpret large-scale sedimentary environments and assist in integrating newly drilled wells into any assumed geological model.

### *6.3.2 Large-scale analysis*

Figure 6.15 shows the position of the three Simian wells on a seismic amplitude map from the top of the Simian channel system. Figure 6.16 shows an interpretation of the main intervals of the wells based on the neural network image facies predictions (track 6). The three wells are also broadly correlated. For comparison Figure 6.17 shows interpretation and correlation of the three wells by Baker Atlas (2001) based on image facies that were interpreted manually.

In the lower part of the three wells the slumped interval at (i) can be correlated across all three wells. This interval is interpreted by Baker Atlas (2001) to represent the basal unit of the channel system. This unit is thought to infill the deepest incision surface, the slumping representing re-equilibrium deposits corresponding to stage 1 in Figure 5.2. At (ii) the cemented zone in Simian 1 can be taken to indicate a conglomerate. This represents the coarsest fraction of a turbulant flow that possibly underwent tractional transport before forming a channel lag (Baker Atlas 2001). The levee deposits at (iii) are not interpreted as such in Figure 6.17 but are identified on a 1:40 sedimentological interpretation of the images

(Baker Atlas 2000). These broadly correlate with levee deposits occurring above the initial channel section in Simian 3, at (iv), and above the lower slumped interval in Simian 2, at (v). At (vi) the association of facies 4, 5 and 6 (debris flow, structureless sand, and conductive sand) indicates a channel complex. Similar facies associations at (vii) and (viii) also indicate in-channel deposition. This deposition corresponds to stages 2 and 3b in Figure 5.2. The main packages of levee deposits are found at (iii), (iv), (v), (ix) and (x). In all cases these packages match those identified in Figure 6.17. Some of the thin sand beds (not levees), that are actually predicted in the main column (e.g. at 7230ft in Simian 2) are interpreted by Baker Atlas (2001) as representing sheet sands because of their limited thickness corresponding to stage 2 of the geological evolution of the area (Figure 5.2). Note also that the main canyon fill, the boundaries of which are easily detected by the neural network predictions, is within seismic resolution and represents a single seismic facies.

The interpretation from the neural network predictions match very closely those derived by Baker Atlas (2001) from the image facies that were interpreted manually. Boundaries can be drawn between different facies associations to create broad geological units. If these units were to be included in any reservoir model then the facies predictions could be used to define them. The detail within the units could then be modelled stochastically or the detailed interpretation by the network could be included. The predictions can also assist in net/gross evaluation. For instance the amount of sand predicted by the neural network and the thickness of the individual beds can be seen to decrease downslope. This agrees with the interpretation of Baker Atlas (2001), shown in Figure 6.18.

Since the use of FMI logs is now routine in the West Delta Deep Concession area if a new well was drilled this type of analysis could take place within a few days of logging. Therefore the image facies associations could be interpreted and integrated into a field-wide geological model very quickly providing information on potential test intervals or a net/gross evaluation. This could take place prior to any detailed analysis of the images and/or core. Alternatively if FMI logs exist but no image facies have been interpreted the neural network model could produce one, providing further constraints on any geological model.

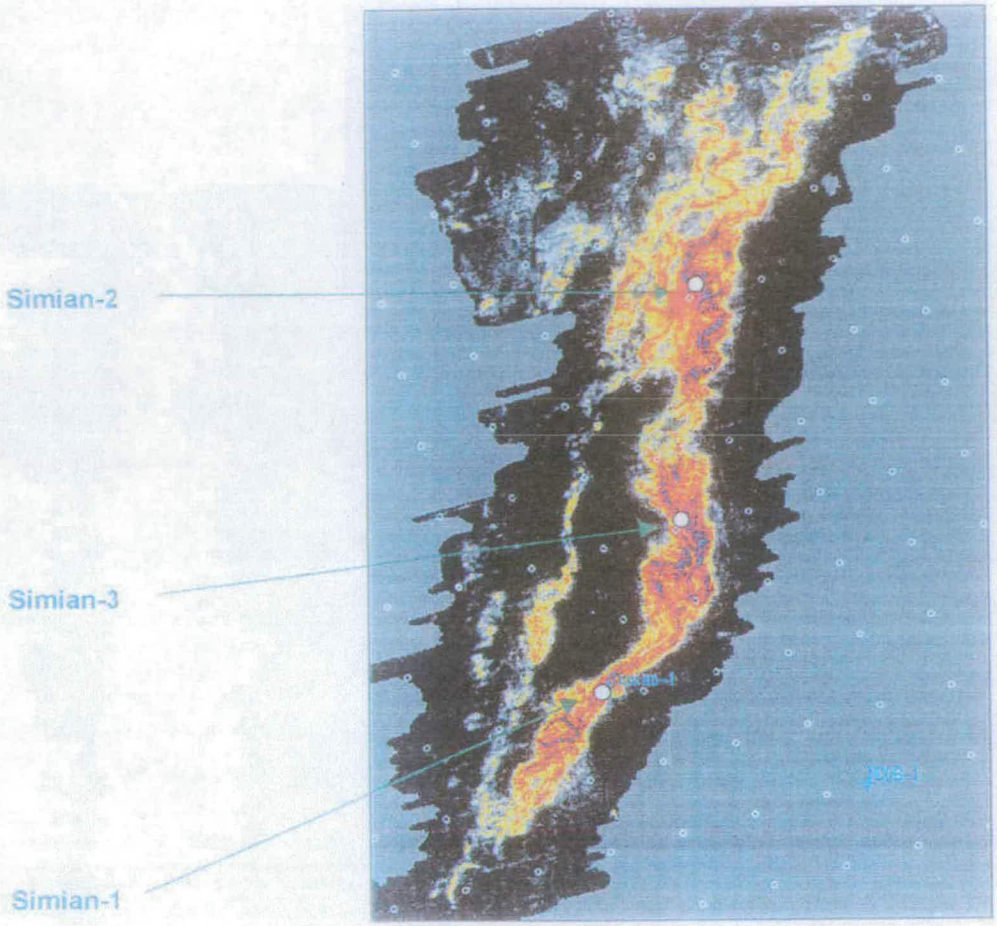



**Figure 6.15** Seismic amplitude map of the Simian prospect (top of the main canyon) with well positions. From Baker Atlas (2001).

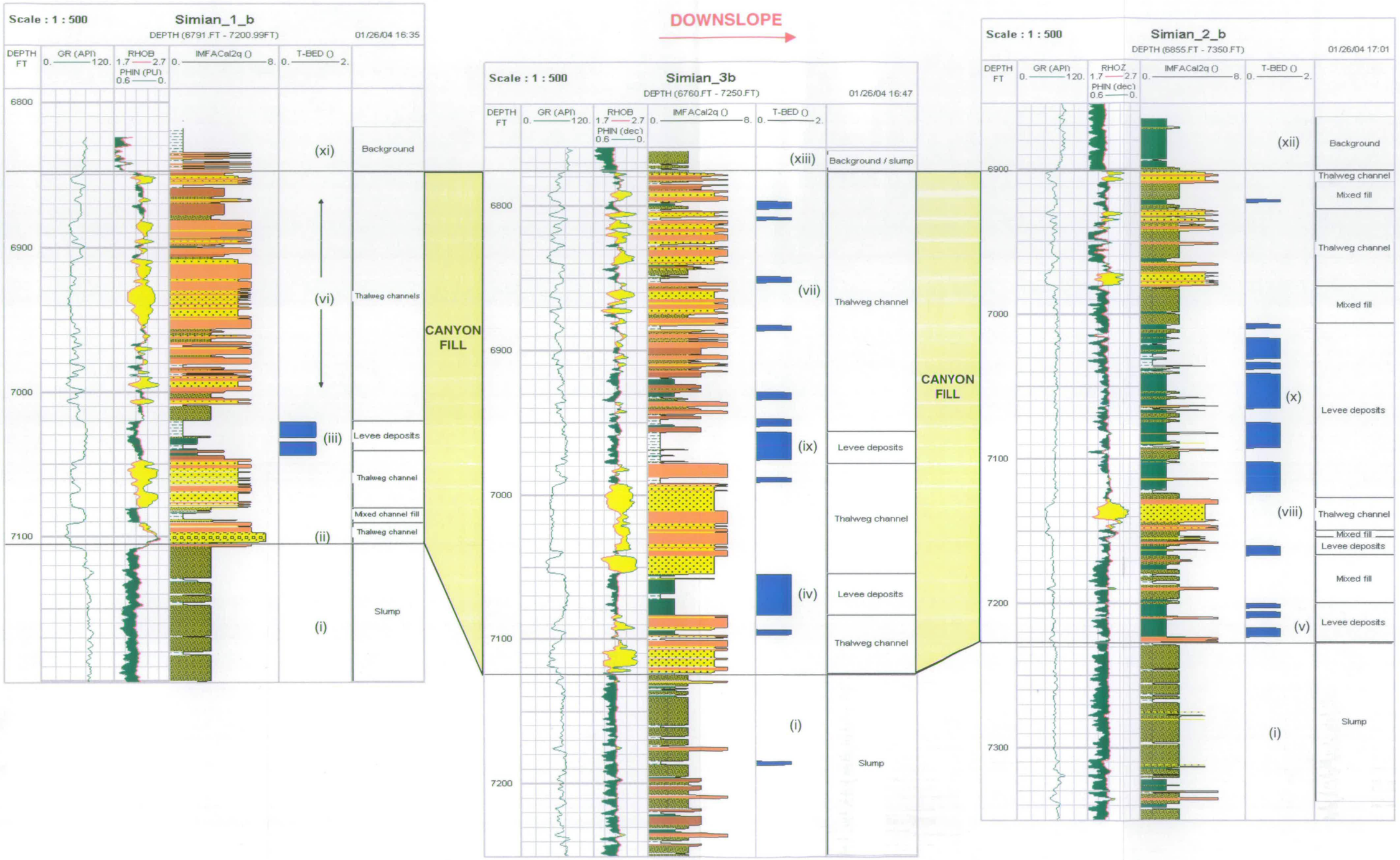



**Figure 6.16** Interpretation of the main depositional environments of the Simian channel system from image facies associations that were derived from neural network analysis. See text for more details.

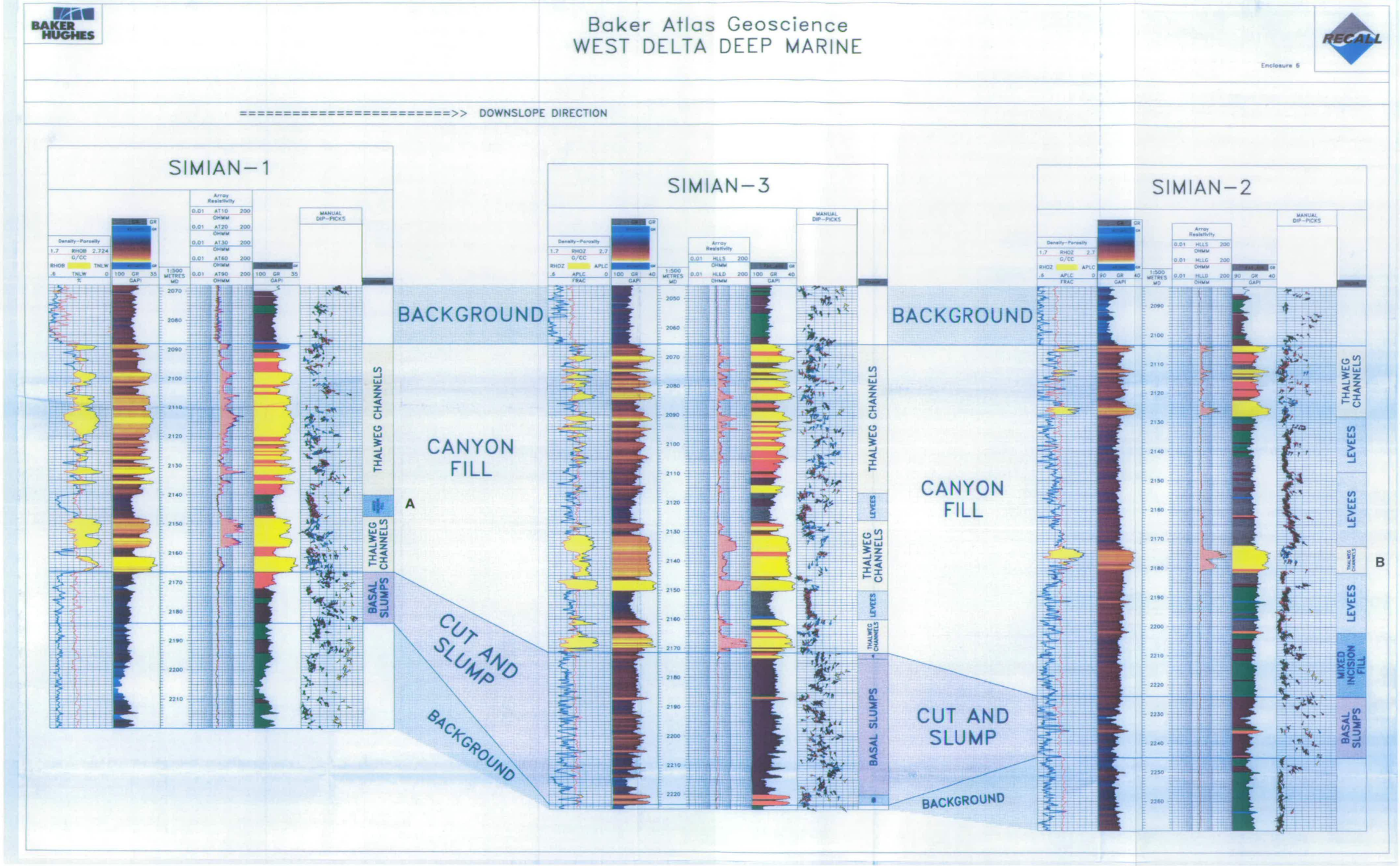



**Figure 6.17** Interpretation of the main depositional environments of the Simian channel system from image facies associations that were derived manually, from Baker Atlas (2001). In each well track 1 shows the neutron and density logs; track 2 the gamma-ray log that is shaded to indicate the more sandy horizons (yellow); track 4 various array resistivity logs shaded to indicated gas; track 5 manual dip picks, and; track 6 interpretation of sedimentary environment. Note that at A and B the text is small. At A the text reads 'Mixed Incision Fill' and at B 'Thalweg channels'.

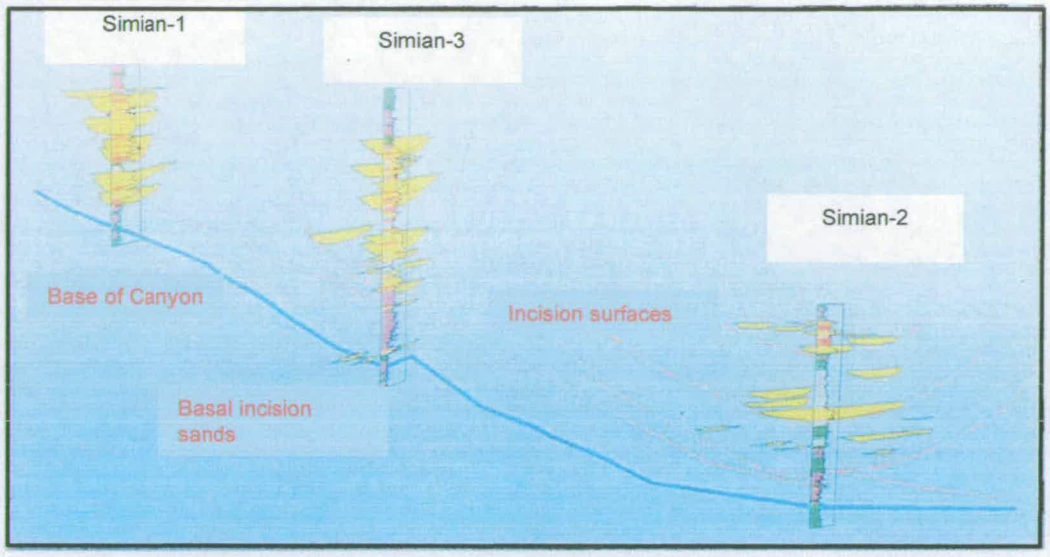



**Figure 6.18** Cartoon showing the widening of the Simian channel system and the possible lower net/gross in the downslope direction. From Baker Atlas (2001).

## *6.4 Chapter summary*

This chapter illustrated results from the modular neural network developed in Chapter 5. The results are good, when viewed in detail or at a larger scale and thus have the potential to assist detailed sedimentological analysis of specific wells or be integrated into broader field-wide studies. Analysis of the results confirmed that the model was responding to those discriminators expected from analysis that took place prior to model building. Where the model interpretation did not match the expected one, this was found to be due to the influence of the conventional logs or individual pads having different textures to other pads and flaps. Possible methods to overcome these limitations are described in an overall discussion of the thesis in Chapter 7.

# Chapter 7 : Discussion and conclusions

## *7.1 Introduction*

This thesis set out with the goal of testing the capability of a neural network, specifically the backpropagation algorithm, to predict lithofacies and image lithofacies from digital well log data. In Chapter 1 the objectives were stated as:

- To what extent can lithofacies be evaluated using a neural network from wireline log data recorded in deep marine clastic sediments?
- What are the most important parameters that influence the outcome? Are they the input data, the output demanded, or the methodology? How is it best to interpret any outcome from a neural network? Can the methodology express uncertainty in the results?
- Can image log data be incorporated into a neural network model to predict image lithofacies and produce a more acceptable result?

Two data sets were utilised to carry out these objectives, the first one contained ordinary log data, and the second microresistivity image data too. The investigation included an analysis of the training strategy employed for such an algorithm and testing of how various training parameters affect learning. Once results were obtained the ability of the model to predict lithofacies was documented by comparison directly to core. The limitations of applying a model to new wells were also recorded. In Chapter 5 it was shown how textures present in microresistivity image logs can be quantified and a method was developed to integrate these into the neural network workflow. Whilst some of the observations in the thesis are specific to the actual data used, the interpretation and conclusions have important implications in the wider context of the methodology. Each of the various aspects of the research presented can be divided into a number of key areas that are discussed in Section 7.2 below.

## 7.2 Categories for discussion in this thesis

### 7.2.1 Neural network methodology

Table 7.1 summarises the different sizes of networks used in this thesis and compares them to other authors. It can be seen that the network size required appears not to be affected by the number of inputs. The networks in this thesis that were trained on image derived components had many inputs yet the size of the networks needed for classification were not larger than those trained to predict lithofacies in the Lomond Field that only had seven inputs. The size of the network needed however does appear to be determined by the number of outputs required and, importantly, the distinction of each of the outputs. For instance in Chapter 5 module 1 of the modular system predicted sand, shale and cemented lithologies that were previously known to be very distinct. Only 2 hidden nodes in 1 hidden layer were required for classification. In module 2 for the sand network there were only 2 outputs which were also known to be fairly distinct. Only 3 nodes in 1 layer were required for classification. When five lithofacies were predicted in the Lomond Field (with some known overlap between lithofacies) 11 nodes were needed in 1 layer. For the shale network in module 2 (Chapter 5), 9 and 11 nodes were needed, depending on whether conventional logs were included as inputs. The other studies shown in Table 7.1 all utilise small networks, the maximum being 5 nodes in 1 hidden layer (Derek *et al.* 1990). However in all of these cases the target classes appear very distinct. For instance, in the study of Rogers *et al.* (1992) the target data is limestone, dolomite, sandstone and shale. These are known to have distinct log signatures and indeed a standard neutron-density cross-plot is commonly used to distinguish them. Although the target by Bhatt & Helle (2002b) is described as facies rather than lithology, because they represent specific parts of the sedimentary environment, the classes are fairly distinct. The four facies are channel sandstone, 'lake' facies, crevasse, and coal. These essentially equate to sandstone, shale, shaly sand, and coal. Although there is some obvious overlap between the sandstone, shaly sand and shale, the sand and shale are essentially end members of a lithological spectrum, and coal is known to have a very distinct log signature (especially a very low density). The lithofacies scheme developed for prediction in the Lomond Field was based on a number of different criteria - sedimentary facies type and architecture, petrophysical properties, and log separability. The scheme contained two different types of sand, a shaly sand, a very heterogeneous lithofacies that can consist of a variety of lithologies, and shale. What the network subsequently did was to find the *typical* log signatures of each of the lithofacies. When the results were compared to core

| No | Author | Problem | No of inputs | No of outputs | Optimum network size | Claimed % hit-rate | Other comments |
|---|---|---|---|---|---|---|---|
| 1 | **This thesis (Martin 2004)** | To classify five lithofacies, deep marine environment (turbidites mostly). | 7 | 5 | 1 layer 11 nodes | ~60% but thought to be higher when compared to core (75%?) | 5 conventional logs as inputs and 2 derivative logs. |
| 2 | **This thesis (Martin 2004)** | To classify three lithologies, deep marine environment (turbidites mostly). | 3 | 3 | 1layer 2 nodes | Near 100% | Each lithology (sand, shale, cemented) known to be very distinct. Conventional logs as inputs. |
| 3 | **This thesis (Martin 2004)** | To classify two image lithofacies, deep marine environment (turbibites mostly). | 25 | 2 | 1layer 3 nodes | Appeared very high (close to 100%). | Image logs inputs only. Both image lithofacies appeared distinct. |
| 4 | **This thesis (Martin 2004)** | To classify four image lithofacies, deep marine environment (turbibites mostly). | 28 | 4 | 1 layer 9 nodes | Not assessed | Conventional and image logs as inputs. |
| 5 | **This thesis (Martin 2004)** | To classify four image lithofacies, deep marine environment (turbibites mostly). | 25 | 4 | 1 layer 11 nodes | Not assessed | Image log inputs only. |
| 6 | **This thesis (Martin 2004)** | To classify seven image lithofacies, deep marine environment (turbibites mostly). | 28 | 7 | 1 layer 4 nodes | Not assessed, but much poorer than modular equivalent. | Both conventional and image logs as inputs. |
| 7 | **Derek *et al* (1990)** | To classify 5 lithofacies, but optimised to predict reservoir rock. Possibly shallow marine (siliclastic) environment. | 3 | 5 | 1 layer 5 nodes | 90.5% for reservoir rock. | Conventional logs only. Network was selected on the basis of its ability to classify a single lithofacies only (reservoir rock). |
| 8 | **Rogers *et al* (1992)** | To classify 4 lithologies (lmst, dol, sst, sh). | 3 | 4 | 1 layer 3 nodes & 1 layer 4 nodes for different training sets. | Not given | Conventional logs only (gamma, neutron and density). |
| 9 | **Wong *et al* (1995a)** | To classify 4 lithofacies (sst, sh, sst/sh, cemented). | 3 | 4 | 1 layer 4 nodes | 94.50% | 2 conventional logs (density and sonic) and 1 derivative log (acoustic impedance). |
| 10 | **Bhatt & Helle (2002b)** | To classify 4 facies in fluvial / lacustrine environment (coal, channel sst, lake, crevasse). | 5 | 1 | 1 layer 4 nodes | ~90% | Committee machine (see Chapter 2) means that networks are trained to classify a single facies at once - i.e. one output. |

**Table 7.1** Comparison of different backpropagation networks used by various authors.

in many cases the network interpretation appeared to match, even if it did not match the interpreted lithofacies. Indeed in many cases the network's interpretation questioned the validity of the manual interpretation (manual interpretation involves inspection of the images by eye before the interpreter assigns their specific facies interpretation; this sometimes involves inspection of core too). This meant that the actual capability of the network was greater than that indicated by the measured hit-rate (~60%). Bhatt & Helle (2002b) compare their results to similar studies and discuss them in terms of the absolute hit-

rate and the number of output classes. This is a simplification of the problem. Comparison must also take into account the distinction of the output classes and the sedimentary environment in which they occur. The sediments in the Forties Formation of the Lomond Field were deposited by a variety of gravity flow processes and from suspension and represent specific turbidite sub-environments (Cullen 1993d). Many of the sediments were deposited by coherent slumping and sliding resulting in very heterogeneous sediments. Lithofacies 3 (slumps sheets and debris flows) in particular can express a wide range of log signatures that overlap with other lithofacies. This is in part why the measured hit-rate calculated in Chapter 4 is lower than that of other published studies (none of which attempt to classify rocks from this type of sedimentary environment). Thus the most important factors in the size of network required for classification are the distinction of the lithofacies (which is related to the design of the scheme and the sedimentary environment from which they come) *as well as* the number of lithofacies. This is supported by the theory of the backpropagation algorithm and its representation in the multi-dimensional space - see Chapter 2. This is why the networks used in this thesis were larger than those utilised in other studies. Although larger networks are more susceptible to overtraining, in each case the networks developed were validated correctly and the results viewed alongside the logs before application to the entire well set.

The results of experimentation in Chapter 3 (Figures 3.24 and 3.25) also support the view that 2 hidden layers of nodes are rarely required for classification (Mitchell 1997, Gurney 1997).

Experimentation with momentum and learning parameters (Chapter 3) showed that these did not appear to conclusively affect the results. Few authors document their use of these parameters. One exception is Derek *et al.* (1990). They found that their network converged over a broad range of momentum values. However a momentum parameter above 0.9 gave sub-optimal solutions, and a value above 0.5 for the learning rate also inhibited performance. Since experiments in Chapter 3 did not involve a momentum parameter above 0.9 it is not possible to dispute these findings. However the networks trained in this thesis were not inhibited by a learning rate above 0.5. Selection of the learning rate in 'theory' is a compromise between training time, ability to step over local minima and precision of finding the global minimum. In practice these parameters may be less influential than the actual data itself and the specific problem to be solved.

This thesis also showed that pruning (in the way described in Chapter 3) cannot substitute exhaustive experimentation with different topologies to find the optimum size. When pruning algorithms are implemented then they appear to benefit from a starting topology that is not too far from the optimum one. This conclusion agrees with the view of Mitchell (1997) that 'techniques for dynamically modifying network structure have met with mixed success. It remains to be seen whether they can reliably improve on the generalisation accuracy of backpropagation'.

When derivative logs were incorporated into the methodology (also Chapter 3) these did not result in poorer classification, and indeed it was thought that including them might have increased the success of the network. However it was also thought that enough trials were not carried out to test whether the performance difference was significant. In theory there is no reason why derivative logs should increase performance of a neural network since all the information contained in the derivative logs should also be contained in the raw logs. This does not mean though, that inclusion of these logs cannot assist the network by increasing the number of degrees of freedom resulting in an easier path to the global minimum. Wong *et al.* (1995a) showed that the use of acoustic impedance as well as sonic and density logs decreased the training time of his backpropagation network trained to predict lithofacies. When predicting porosity from the same three logs the inclusion of lithofacies (i.e. a fourth input) decreased the error of the final network. When permeability was predicted improvement was seen when predicted lithofacies and porosity were included as inputs as well as the three original logs. Since lithofacies and porosity and acoustic impedance were calculated from the two raw logs all the information needed to predict permeability and porosity should have been contained in these. Thus our results support the results of Wong *et al.* (1995a). In this paper Wong also records that permeability was more successfully predicted if the log of permeability was used as the output rather than raw permeability values. The reasons for Wong's results were explained in Chapter 3. It is simply because permeability is a non-linear measurement (like resistivity). By taking the log of the measurement the resulting values fill the hypothesis space more fully and patterns in the data are more easily distinguished (Figure 3.18). This is also noted by Bhatt & Helle (2002a).

It was described in Chapter 2 the most recently published work (whilst the research in this thesis was taking place) regarding the methodology of using backpropagation neural networks in petroleum geology was carried out by Hans Helle and Alphana Bhatt (Bhatt &

Helle 2002a, Helle & Bhatt 2002, Bhatt & Helle 2002b). Bhatt & Helle (2002a) attempt to show that a committee of networks (Figure 2.15) reduces the bias and variance of the output. However their results for porosity prediction (on synthetic data) show that the committee actually produces a very similar result to the best performing network in the committee (the difference in standard deviation is less than the $2.5x10^{-5}$ porosity units). When applied to real data the bias and variance of the committee were not smaller then the best performing individual network in the committee. This indicates that the training of a number of networks and the selection of the best performing one (as in this thesis) would have produced similar results as the committee. It is the author's opinion that the generality of the results shown regarding the use of a committee rather than an individual network needs to be tested further. In the same paper permeability is predicted and in this case small committees were used to predict individual permeability ranges (known as a modular committee machine – Figure 2.16). This was shown to reduce the standard deviation but did not appear to have reduced the bias (single neural network bias 0.08 and standard deviation 1.3, modular committee bias -0.11, standard deviation 1.10 – all measurements in log permeability units). In this thesis a modular system was used in Chapter 5 to predict image lithofacies. The system used was different from the modular system of Bhatt & Helle (2002a) in that a network was initially trained to predict lithological groups. Then more networks were trained to subdivide the lithologies into image lithofacies, and further networks to predict thin-beds. A system similar to that described in Bhatt & Helle (2002a) would involve the training of a network (or committee) to predict a single image lithofacies i.e. the first module would predict 'resistive sand' or 'not resistive sand'. However the principle is the same – the task has been subdivided into smaller ones. As Bhatt & Helle (2002a) point out, since smaller tasks have fewer output nodes and are more likely to need smaller architectures for classification they therefore theoretically require less data for successful training. Results of the modular system were compared in Chapter 5 with a single network that was trained to predict all image facies. Even though in theory the single network should have been capable of predicting the image lithofacies with the same degree of accuracy as the modular system it did not appear to do so, in fact it mixed up some very clear textures on the image. Although a criticism of our comparison is that only one single network is compared to the modular system and the comparison is based on only a limited number of sections this result does support the view of Bhatt & Helle (2002a). Bhatt & Helle (2002a) also state in their conclusion that 'there are other advantages in decomposing a task into modular components, which may simplify and improve log analysis, and the

geological interpretation of well data in general'. Indeed it is the author's view that a modular arrangement could be a potential solution to incorporating multiple pads and flaps of image data into the neural network process (see Section 7.2.4 & 7.3).

Bhatt & Helle (2002b) introduce recurrent networks into the neural network methodology when predicting facies from well logs (Figure 2.17). Individual networks are trained with log data from different depth levels in the borehole. The outputs from these networks are then combined by another network. The combination of these creates the 'recurrent network'. Many recurrent networks are then combined to make a committee of recurrent networks. Each system can then predict a single facies so essentially is a single module in a modular system. The use of training values from different depths along the borehole is to take into account the fact that the logging tools actually read a volume of rock. Jenner & Baldwin (1994), Yang *et al.* (1996) and Goncalves, Harvey & Lovell (1997) also used a similar type of approach. It should be noted though that the term recurrent network used here is different from a classical recurrent network, in which the output nodes are connected directly to the inputs (described in Mitchell (1997)). This method is an alternative to that used in this thesis that uses logic to essentially 'repair' thin beds that commonly occur at log inflexion points at bed boundaries. The earlier papers do not compare using a windowing approach to a network without windowing. Bhatt & Helle (2002b) experiment with synthetic data and compare their recurrent network to a non-recurrent one. The predictions do appear to improve – the number of miss-hits reduces from 6.74% to 2.89% (for a three-layer model). However it is possible that these miss-classifications could have been repaired using the logic program ('thin-bed repair' program) from this thesis. It was shown that this type of logic increased the success of the network by an average of 3.7%, and improved the geological continuity of the predictions. The logic program also has the potential to incorporate geological knowledge. For instance the prediction of multiple thin-beds of lithofacies 3 and 4 could be defaulted to lithofacies 4, if this is thought to be more likely. In all cases the raw predictions are preserved and can be viewed alongside the repaired column. The comparison of Bhatt & Helle (2002b) is only on synthetic data. To solve this problem a much more comprehensive comparison of these two alternative techniques is required. For instance if a very thin sandy bed existed that wasn't fully resolved by the logs would the windowing of log data eliminate any prediction of this bed at all? If the use of a single network would allow a prediction (even if wrong) at least this would be providing useful information.

Although this thesis and all of the authors in Table 7.1 devote a substantial amount of effort to finding the optimum network design and methodology for classification an important conclusion of this study is that the biggest limiting factors in the successful application of a neural network model across a multi-well database are likely to be much more fundamental. Important factors that influence the results are the amount of training data available, and variation in the data due to fluid type, tool design, or depth interval. These issues are discussed in Section 7.2.2.

### *7.2.2 Limitations of the methodology due to data*

In Chapter 3 a comparison was made between networks trained with balanced data, unbalanced data, and unbalanced data with a known distinct lithofacies artificially reduced. It was shown that training with unbalanced data could produce an increased hit rate if the majority lithofacies occur more frequently in the test set. Also even if a very distinct lithofacies is in the minority in the training set then it still can be predicted correctly. It was concluded that the ability of a network to predict a lithofacies depends on its occurrence in the training set and its distinction – implying that partial boosting is a compromise (this was subsequently carried out in Chapter 5). This work agrees with that of Garden (2001) that partial boosting is more favourable than full boosting or no boosting of lower abundance facies. Bhatt & Helle (2002b), when they experimented with synthetic data, compared the hit-rate with the different number of examples used for training and different activation thresholds. A threshold of 0.5 (generally used as standard, and used in this thesis) required the minimum number of training parameters, and with 2 facies as outputs and 5 inputs the number required was approximately 20 - using more did not improve the hit-rate further. As already stated in Chapter 2 the number of training examples needed depends on the number of inputs and it has been shown that it depends ultimately on the distinction of the output classes. Unfortunately when their model is applied to real data this type of analysis does not take place.

In Chapter 3 experimentation took place with different training sets. Smaller training sets produced poorer classification. It was noted how the limitation of the training set in model development could be determined not by the number of mis-classifications but by the number of test examples that activated multiple nodes or no nodes. In terms of the absolute amount of data needed, since there is much more data recorded by image logs than

conventional logs then when these are incorporated into the analysis it is satisfactory to have many inputs.

When a model appears suitably trained and it has been tested on unseen data, the question remains how to spot if predictions in a well may be erroneous. When the optimum model developed in Chapter 4 was applied to well 23/21-T4 there were a number of output nodes that were activated at the same depth level indicating that the model may not be suitable for data in this well. In the same way it is also possible to tell when a model is not trained properly due to a small training set. In the case of well 23/21-T4 the reasons for this could be very practical such as the tool types used, calibration of the tools, depth interval, or the fluid saturation in the reservoir. When a datum shift was applied to the well data this did improve results. Therefore where known reasons for data variability exist calibration is an important step of the neural network process.

It was also shown that the model developed was strongly dependent on the resistivity log and did not appear to predict the correct lithofacies in transition zones or wells where the reservoir intervals appeared to have a lower gas saturation than similar intervals in the training wells. This was an unavoidable consequence of the training data being taken from the gas zone. When a model was trained without the resistivity log the results were much poorer. However when a correction was made to account for the fluid saturation a new model trained on this data did show improvement compared to the model trained without the resistivity log. Although it did not perform better than the original optimum model it did perform better in transition zones and reservoir sections with lower gas saturation (compared to the training wells). Helle *et al.* (2001) show that a backpropagation network is capable of predicting porosity and permeability independently of pore fluid type (and this is stated in Jenner & Baldwin 1994 but not illustrated). However this relies on the existence of training examples from water, oil and gas zones. Close inspection of their results indicates that for the permeability network very few data points (5) were included from gas zones with the majority taken from water and oil zones. The results show some of the biggest errors in a test well that contained gas, thus confirming the sensitivity of their model to the reservoir fluid. In most wells drilled core is always cut in the main reservoir interval, and this usually equates to the hydrocarbon zone. Thus, a common limitation of most data sets is that there are insufficient training examples from the different fluid zones. Even when such training examples are present then it could prove problematic to predict over a large transition zone.

The work carried out in this thesis shows that in unseen wells the optimum model trained with the resistivity log should be applied to the gas zone (as this model performed best in these regions). Where water or transition zones exist or intervals where the gas saturation is known to be lower than equivalent intervals in the training set then the model that was trained on data corrected for fluid should be applied (as this was shown to perform better in these regions).

Moss 1997 illustrates an example of a neural network used for predicting porosity, permeability, grain-size class and lithofacies. A subsection of the interval shown was used for training. Moss states that 'of particular interest would be to see how robust such a result proves to be in step-out wells'. Predictions in multiple wells where models do not classify with a high degree of success are rarely documented. For the Lomond data set used in this thesis, 9 wells were available in total and 3 were used for training. After calibration to the training set good results were reported in gas intervals of 7 wells (23/21-T1, T2, T3, T5, T8, T9 and T10). The transition zones of wells 23/21-T1 and T5 and the reservoir interval of 23/21-T6 required normalisation for fluid. Well 23/21-T4 required a datum shift to improve predictions, and even then classification did not appear as high as in other wells. This illustrates that a severe limitation in the use of neural network models is not the methodology and training but much more fundamental issues such as fluid variability, tool type, tool calibration, or depth interval. Which of these issues is the most important will depend on the specific data set being analysed. However, a single model cannot be applied at will to multiple wells without prior inspection and calibration of the data contained in them.

### *7.2.3 Neural network analysis of deep marine clastic sediments*

In Chapter 3 a lithofacies scheme was developed to describe sediments encountered in the Lomond Field. This took into account various parameters including sedimentary facies and their occurrence, porosity and permeability relationships and log separability. In fact it was shown that various sedimentary facies had specific porosity and permeability profiles and log signatures (albeit with some overlap). Thus the term 'lithofacies' was kept as the model predicted lithological signatures that were genetically related to the sedimentary facies. One would not expect a very high hit-rate if simply sedimentary facies were predicted, since the defining factors (e.g. sedimentary structures) are not 'seen' by conventional logs. The degree of overlap in the defined lithofacies was a result of the heterogeneous nature of the

rocks which is linked to their environment of deposition; rocks are interpreted as being deposited from turbidity currents, slumps, slides, and debris flows. In particular lithofacies 3 showed a range of log signatures. This was why the overall hit-rate was only approximately 60%, fairly low when compared to other authors. However other sedimentary environments are simpler with specific sub-environments having very specific lithological signatures. However the network trained in Chapter 3 managed to find the *typical* log signature of the lithofacies, and this is why after comparison to core the success of the network was considered to be higher than the hit-rate initially suggested. Data from the West Delta Deep Marine Concession area also showed a wide range of facies with variable log signatures. However the integration of image logs allowed attributes that are closer to those used to define sedimentary facies (i.e. texture) to be integrated into the methodology. Shale (facies 5 in the Lomond data set) could now be differentiated into laminated, slumped or bioturbated. This is essentially an image facies (although the term image lithofacies was used) – and is much closer to a sedimentary facies than the lithofacies predicted in the Lomond data set. The wider variety of components present in image data allows more facies to be predicted. This would certainly apply to other sedimentary environments too.

### *7.2.4 Neural network use with image logs*

The key to the use of microresistivity images in multivariant analysis is the extraction of components that describe various elements of the images. This can be analysis that quantifies textural elements of the image, or more simple components such as the continuous log of a single button. As Luthi (2001) states, 'many of the documented developments in this field are largely conceptual'. This is partly because the development of the tools and methodologies are fairly recent, but also because some of the studies are very complex and specific to certain rock types.

The techniques described in this thesis enabled the textures identified in the West Delta Deep data set to be characterised, and the methods were shown to work consistently through all three wells in the data set. This is in itself a step forward as some of above studies are limited to very small well sections (e.g. Luthi (1994) is restricted to a 10m section). It has already been discussed above how inter-well variability can be a limiting factor in this type of study. Spectral analysis of image data has also been independently shown to be useful tool for the quantification of textures. However in this thesis (compared with Luthi (1994)) a

horizontal spectrum was also incorporated enabling the quantification of directional heterogeneity. It was also shown how a sample of frequencies rather than an average frequency from a specific spectrum could be incorporated into the methodology if there are sufficient training examples (to take into account the increased number of inputs). This will produce a more accurate classification as redundant power curves can be relegated without directly affecting any useful power curves. This study also highlighted how very simple statistics (of the images) are useful in discriminating facies and should never be overlooked. The average of a pad was an exceptionally good discriminator of resistive sands, and at resolving sandy thin-beds. The coefficient of variation was important at quantifying the bulk variation in the images, thus assisting the identification of resistive sand and bioturbated shale. The importance of these logs as discriminators was confirmed by weight analysis of the trained network and this confirms the conclusions of Garden (2001) concerning their importance. Incorporation of these curves though when carrying out multi-well analysis means that the processing of the images becomes more important. The processing steps in Chapter 5 vastly changed the absolute value of the conductivity values. Therefore each well must be processed in exactly the same way. Finally another conclusion of this thesis is that textural analysis is best carried out over individual pads and flaps of data. This is because of the specific methods used in this thesis - both the vertical and horizontal spectra were sensitive to very slight changes between pads and flaps and pad/flap pairs. Thin-beds were also much more easily resolved via analysis of a single pad, and the need for an automatic dip compensation step was removed. A limitation of single pad analysis was illustrated when different pads and flaps showed different textures. Clearly there is a need for integration of all the data. This is discussed further in Section 7.3. The incorporation of features described by other authors could potentially increase the sophistication of the model developed in this thesis. Some of these may require interpretation of the whole image at once – e.g. if resistive and conductive spots are large and cover more than one pad. This is also discussed further in section 7.3.

The integration of conventional logs and image logs is a problem of reconciling data with different resolutions. This is a common problem in the integration of log, core, and seismic data in reservoir characterisation (Fryman & Deutsch 2002). The specific problem in this study is to prevent bias during neural network training whilst preserving the information contained within the whole data set. In the model developed in Chapter 5, for the shale network in module 2 since there were many more image derived inputs in the model than

conventional logs it could be argued that the image derived components are more important despite what the weight analysis indicates. However the results showed that the model was sensitive to slight variations in the neutron and density log and so this was cited as an important limitation of the model developed. Possible ways to overcome this are discussed in Section 7.3.

### *7.2.5 Interpretation of neural network results*

The majority of studies involving lithofacies predictions from well logs assess the quality of the results by comparing them to a manually derived interpretation and calculating the hit-rate (e.g. Derek *et al.* (1990), Bhatt & Helle (2002b)). This is usually quoted as a percentage. It has already been described in Section 7.2.1 how the hit-rate should always be explained with reference to the sedimentary environment and the expected distinction of the lithofacies. When the results from the Lomond Field were compared to sedimentary logs that described the core it was found that in many cases the neural network interpretation provided a close match, even in places where it did not match the manual interpretation. Thus the success of the network was not reflected in the hit-rate. An important part of the interpretation lay in the use of the activation levels. If for instance an interval showed areas where the output nodes of lithofacies 2 and 3 were activated (reservoir quality sand with minor slumping and deformed interbedded sandstones and mudstones respectively) clearly the interval could be interpreted as slumped sand, possibly with minor mudstones. Activation levels were useful when interpreting image outputs too (e.g. Figure 6.12). The use of the activation levels is similar to analysis using fuzzy logic (Cuddy 2000), where each output has an associated probability. In the case of the activation levels they do not represent probabilities but do show areas of uncertainty. The activation levels could also aid in the use of any predictions – a well section in a reservoir model could be populated with properties that relate to two lithofacies for instance. Rogers *et al.* (1992) use the activation levels in their network to describe different lithologies e.g. a shaly sand rather then a sand or shale. Bhatt & Helle (2002b) use activation levels to compare different types of network – for instance if activation levels are all close to 0 or 1 then the network should be performing well. As discussed in the above sections activation levels can also play an important role in analysing results in uncored wells. If no core is present it is impossible to quantify the neural network. But if the activation levels are low or if there are many places where all activation levels are zero this indicates the data in that well were not recognised and the

model should not be used. Another essential part of the interpretation of any network is weight analysis. It is vital not to treat the network as simply a black box with no idea how it is working. Wong (1995b) illustrates a method to calculate the contribution of each of the inputs to a trained network and in this thesis it is shown that it is the weights from the input layer to the hidden layer that are the most important contributors to the output. Weight analysis should be seen as an important step in the methodology. As in this study weight analysis can indicate dependence on certain logs. Is the gamma ray log important – if so then it is probably the shale volume that is important in lithofacies discrimination; if resistivity is important fluid type may be a discriminating factor. The model can then be applied more carefully. A major limitation in the use of this type of analysis (outside the academic community) is available software. For instance Schlumberger's RockCell program does not allow the network weights to be analysed after training.

## *7.3 Outstanding questions / further work*

Further research in this field falls into three main areas:

- Backpropagation neural network technique.
- Methodologies for integrating image data into the neural network process.
- Interpretation and use of neural network predictions especially in multi-well databases.

### *7.3.1 Backpropagation neural network technique*

How to use and train backpropagation neural networks properly is now well documented. However it is the author's opinion that using committee's of networks needs to be investigated further. Although using committees may (very slightly) reduce the bias and variance of the output, do they *significantly* improve the actual classification of the output classes thus justifying the extra training and data handling time required for their use? Comparisons should be made from neural networks trained on real data.

### *7.3.2 Methodologies for integrating image log data*

There still remains much research to be carried out on the integration of the image logs into the neural network process. For the specific data used in this thesis (the West Delta Deep

Marine Concession) good image lithofacies discrimination was achieved that matched the texture of the images. This enabled the determination of sedimentary environment and the correlation of major packages of sediment between wells. However, where predictions were wrong this was shown in Chapter 6 in most cases to be due to different pads showing different texture and because of the network responding to very slight changes in the conventional logs. The textures analysed in this thesis were quantified more easily when analysis took place over a single pad. So, even though good discrimination was found even better results would be expected if more data could be integrated into the technique. This would also increase the confidence of any predictions. Since lithological signatures from conventional logs were shown to be very important discriminators of specific facies these must be included. Interpolation of these logs to the same resolution as the image derived components artificially promoted them to be very important in the final network (analysis of the network weights illustrated this), although in this study it was mitigated partly by windowing of the image components. A modular approach has been shown to aid discrimination and it is the author's view that this arrangement could help overcome both of the above limitations. Figure 7.1 shows a possible arrangement that should be tested. Textures that are best analysed on a single pad of data should be trained via a single network (or a committee if these are proven to be a worthwhile step). This network would produce an image facies output (a discrete number) or a continuum of texture. For instance if the textures were capable of quantifying vertical and horizontal heterogeneity then there could be two outputs that both provide a continuous measure of these quantities. This though would require these parameters to be manually interpreted beforehand to create training sets. Other pads or flaps could be analysed with different neural networks in the same way. Conventional logs could also be trained independently to create a lithological signature. This too could be a discrete number or a continuum of compositions (shale volume, fluid, and cementation factor?) The training of networks in this way would keep textures from single pads and flaps separate yet incorporate all the data into the analysis and should prevent artificial dependence on the conventional logs. There is also the potential to include other authors' textural attributes. Specifically the work of Delhomme (1992) that quantifies spots on the images (to detect vugs in carbonate) could be potentially used to help discriminate intraclastic sand and debris flows. If this analysis took place across the whole image a 'whole image texture' network could be trained and included in the modular system. A final network would combine all the data to predict the final image lithofacies. This could make predictions at the scale of the conventional logs or the image logs. A disadvantage of

such a system is that weight analysis is much more complex. An alternative is to analyse individual pads and use the resulting components as individual inputs into a single network (Figure 7.2). The connections between the conventional log inputs and the hidden layer could be restricted in order to effectively add extra weighting to the image derived inputs (although this may not be necessary as there would be so many of them) – see Figure 7.2. Although weight analysis of this network would be easier it is the author's view that the modular system would offer the greatest potential. In the network trained in module 2 (Chapter 5) there were 28 inputs. The system in Figure 7.2 would have many more (possible >100). Although this is not unreasonable (e.g. Pomerleau (1993) utilises more than 100 inputs) it theoretically greatly increases the amount of training data required. In each case a further network would need to be trained to predict sandy thin-beds.

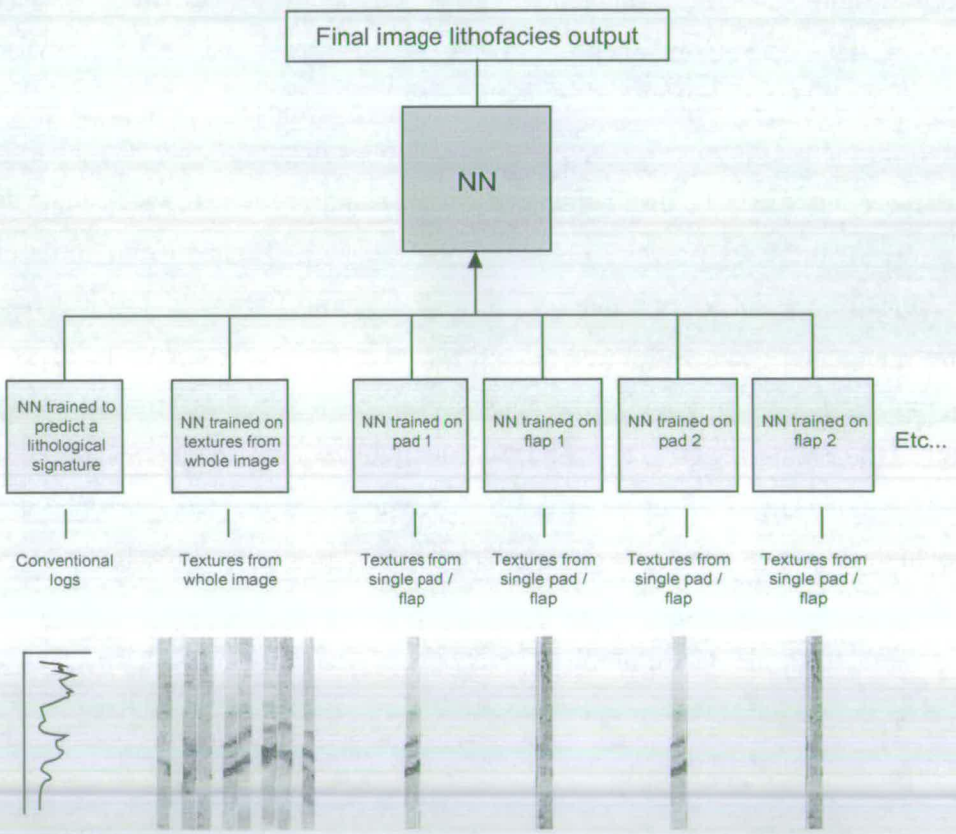



**Figure 7.1** An advanced modular system for predicting image lithofacies. See text for further details.

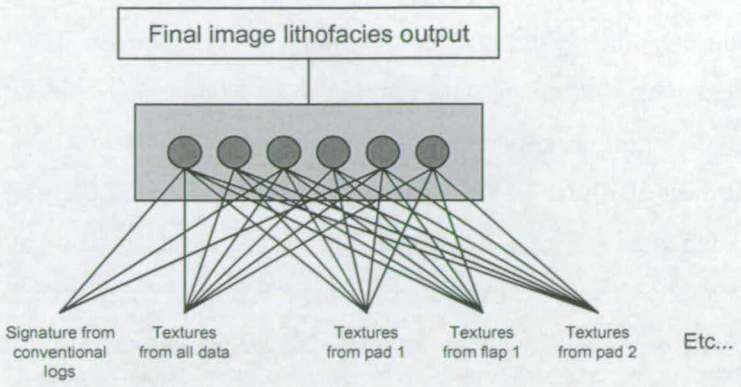



**Figure 7.2** An alternative system to that of Figure 7.1. Analysis of pads still takes place on an individual basis. However a single network is trained with many more inputs. Weight analysis would be a simpler task for this network compared to that of Figure 7.1. Note how the conventional log inputs are weighted so that they automatically become less important during training – these logs are only connected to three rather than all 6 hidden nodes. See text for further details.

In this thesis spectral analysis of the image logs both vertically and horizontally allowed the quantification of directional heterogeneity. All the wells were near vertical, so the same type of analysis was valid across all wells. However if a new well was drilled in a horizontal position then analysis may not be valid. For instance, the laminations that defined 'laminated shale' were normally 'flat' across the borehole. If these were dipping (thus seen as a sine wave on the image log) the vertical spectrum applied to a single pad could still be used. However, the use of the horizontal spectrum may need to be adapted. In this study some of the lower frequencies were sampled. These would always be present in dipping beds. Thus a different sample may be required for distinguishing for instance, slumped shale. A much more sophisticated application of this technique could utilise a full 2-D spectrum to quantify directional heterogeneity.

### *7.3.3 Use of predictions*

Once lithofacies or image lithofacies have been established, the next step in research should involve the integration of the results into reservoir models. Results from the Lomond field were compared to core (this was what the training data was based on). However the image lithofacies were only partly calibrated (since they were loosely based on an image facies scheme (Baker Atlas 2000 & 2001) that was calibrated to core). As Lovell *et al.* (1998)

describes - image data generally lacks precise calibration in terms of textural detail and lithological responses and is based on electrical not visual responses. Core and image data would be complementary the image data helping to overcome any biases in core recovery such as preferential sampling and incomplete recovery. Calibration of the *results* (as in Chapter 4) would describe how well the image lithofacies describe the real rocks. Network interpretations could then be used to populate reservoir models. How would any model differ from that built already? Can such a model provide a better history match to production data? If these questions can be answered neural networks are more likely to be routinely used in digital well log analysis.

## *7.4 Applications & use*

### *7.4.1 Classification*

As well as the estimation of various properties from wells logs neural networks have been used to solve a large range of problems such as seismic attributes for porosity prediction (e.g. Trapp & Hellmich 2000); classification of surface geochemical data to detect reservoir boundaries (Doraisamy, Vice & Halleck 2000); inversion of surface wave velocities to estimate Eurasian crustal thickness (Deville, Curtis & Roy-Chowdhury, 1999); ore grade estimation from shallow borehole data (Wu & Zhou 1993); steering a moving vehicle (Pomerleau 1993); recognition of vowel sounds from spectral analysis of the sound (Haung & Lippman 1988); Stock market forecasting (e.g. Refenes *et al.* 1994); medical diagnosis that predicts the length of stay in hospitals (Davis *et al.* 1993). Conclusions involving the neural network methodology, data handling and interpretation of the results are applicable to these types of studies.

### *7.4.2 Reservoir modelling (both static and dynamic)*

A major use of the results from neural network prediction of lithofacies (and in part the original motivation for the research) is the population of both static and dynamic geological models. In hydrocarbon fields where there are many wells (some have more than 100) the technique has the potential to efficiently populate all of these with many different attributes. Models can be executed quickly to predict lithofacies, porosity, permeability, and water saturation allowing rapid integration of all these into reservoir models. The use of the output

node activation levels can assess uncertainty in predictions providing understanding and reliability of the results.

However the applicability of the ease with which this can be achieved was questioned in this thesis. Limitations of the technique lie in the variation of the data across the field, and this can be due to elements such as fluid content and type, tool type & calibration, and depth interval. All of these variables need to be understood before a model can be successfully applied.

### *7.4.3 Interpretation of newly drilled wells*

A major use of the neural network methodology is in the prediction of properties in a newly drilled well. If a field already contains a large number of wells a model may already be trained and therefore implemented immediately after inspection and calibration (if necessary) of the logs. The model could be generic and trained on all wells in a field or it could be more specific and trained only on wells close to the location of the new well. If a particular part of a field is known to have a particular diagenetic overprint a model could be developed specifically to account for this feature. Since conventional log interpretation in a single well can take place quickly by an experienced petrophysicist this utilisation may be most applicable when used with image logs. As Hall *et al.* (1996) states 'the acquisition of borehole image data demands a high commitment in costs of acquisition, rig time, processing and often extensive interpretation time. Interpretation can tie up a highly experienced geologist or log analyst for a considerable period.' If a model was already trained that could predict image lithofacies this could be applied within days of acquisition. The real benefit of using such models is that they represent a rapid, consistent and objective interpretation of the data. The results can then be used to guide interpretation of the core or manual interpretation of specific log intervals.

### *7.4.4 Measurement whilst drilling (MWD)*

Helle *et al.* (2001) notes the application of this technique to real-time data. This is a natural extension of the use discussed above in Section 7.4.3. The user of any model in this situation must be confident that it can handle all features that might be encountered, such as changes in fluid type or quantity.

### 7.4.5 Fractures

Image data is commonly used to identify and characterise fractures. These can be important in reservoir performance (e.g. the Clair Field, West of Shetland). Spectral analysis of images in a way similar to that described in this thesis could be used to quantify the volume/density of fractures and possibly the orientation of them. Neural network modelling could then be used for classification.

## 7.5 Main conclusions

In reply to the original objectives of the thesis the main conclusions are now stated.

### 7.5.1 Prediction of lithofacies and image lithofacies

The backpropagation neural network is capable of discriminating lithofacies and image lithofacies from conventional and image log data in deep-sea clastic reservoirs. The model can provide a rapid, consistent and objective interpretation. Any model is capable of finding the 'typical' log signatures of each class and therefore offers an unbiased estimate of the rock type. In many cases the neural network interpretation can be more correct than a manually derived, simplified lithofacies scheme. Neural network results when deemed wrong (i.e. do not match a simplified lithofacies scheme that has been deemed the 'target data') in this way should not be dismissed as incorrect.

### 7.5.2 Limitations and interpretation

Classification is affected by network topology, the quantities of each class in the training set, and the distinction of each class.

A major limitation in the use of neural network modelling to predict lithofacies or image lithofacies is practical elements such as tool type and calibration, fluid type and content, and the depth interval investigated.

A neural network model is sensitive to the data it is trained on. If the majority of training examples are taken from zones containing a single fluid type the network will only be capable of predicting successfully in wells that contain that fluid. Where insufficient training data is available to comprehensively describe all possible fluids that may be

encountered, standardisation of the logs to represent a single fluid type before training can overcome this limitation.

A model that is not applicable to a particular well or interval can be identified by measuring the ambiguity in the results – the number of instances where there are multiple predictions or no predictions. When this occurs calibration of the data in that well to the training set can improve predictions.

Raw lithofacies predictions commonly contain thin-beds that occur at the edge of thicker beds due to log inflexion points and thin beds that occur within thicker units - a result of beds that are not fully resolved. These beds can be repaired using simple logic, resulting in a much more consistent geological column. In all cases the new repaired column should be interpreted in conjunction with the raw predictions.

Output node activation levels are important in interpretation of neural network results and indicate potential areas of uncertainty in the network predictions.

Weight analysis of a trained neural network indicates the dependence of the network on the various input parameters. Assessing the weights from the input layer *only* can provide a good measure of this dependence.

### *7.5.1 Incorporation of image data*

Statistics and spectral analysis can quantify lithological signatures and texture from borehole images. This analysis is more successful if applied to single pads and flaps of data rather than the whole image. Quantification in this way allows classification of 'image lithofacies' by a supervised neural network.

Improved results are obtained when the task of image lithofacies prediction by a neural network is divided into sub-tasks. The division of the logs into lithological groups prior to division into image lithofacies aids discrimination.

The interpolation of conventional logs to be the same resolution as the image derived components can result in these becoming artificially important in network analysis.

Where sandy thin-beds exist in thicker beds of shale then different inputs to those used to detect the above image lithofacies are required for discrimination.

The backpropagation algorithm is capable of sorting input parameters into their importance during training. Consequently where many input parameters exist this can potentially aid future neural network model development.

# References

Ali, J. K. 1994. Neural Networks: A New Tool for the Petroleum Industry? *Society of Petroleum Engineers paper number 27561.*

Allaby, A. & Allaby, M. 1996. *The Concise Oxford Dictionary of Earth Sciences*. Oxford University Press.

Amaefule, J. O., Altunbay, M., Tiab, D., Kersey, D. G., and Keelan, D. K. 1993. Enhanced Reservoir Description: Using Core and Log Data to Identify Hydraulic (Flow) Units and Predict Permeability in Uncored Intervals/Wells. *68th SPE Annual Conference and Exhibition, Houston, Texas, 3-6 October 1993. Society of Petroleum Engineers paper number 26436.*

Archie, G. E. 1942. The Electrical Resistivity Log as an Aid in Determining some Reservoir Characteristics. *Transactions of AIME,* **146,** 54-62.

Baker Atlas 2000. *West Delta Deep Marine Saffron-1, Saffron-2, Scarab-1, Scarab-2, WDDE-5 & Simian 2 FMI Processing, Quality Assessment, Structural and Sedimentological Interpretation.* BG Group plc internal report.

Baker Atlas 2001. *West Delta Deep Marine Simian Prospect. Interpretation of FMI Borehole Images for Wells Simian-2 & Simian-3, and Integration with Data from Simian-1.* BG Group plc internal report.

Baum, E. & Haussler, D. 1989. What Size Net Gives General Validation? *Neural Computation,* **1,** 151-160.

Bhatt, A. & Helle, H. B. 2002a. Committee Neural Networks for Porosity and Permeability Prediction from Well Logs. *Geophysical Prospecting,* **50,** 645-660.

Bhatt, A. & Helle, H. B. 2002b. Determination of Facies from Well Logs using Modular Neural Networks. *Petroleum Geoscience,* **8,** 217-228.

Bischof H., Schneider W., and Pinz, A. J. 1992. Multispectral Classification of Landsat-Images Using Neural Networks. *IEEE Trans. Geosci. Remote Sensing,* **30**, 482-490.

Bishop, C. M. 1996. *Neural Networks for Pattern Recognition*. Oxford University Press.

Bouma, A. H. 1962. *Sedimentology of some Flysch Deposits: A Graphic Approach to Facies Interpretation.* Elsevier, Amsterdam.

Burke, J. A., Campbell, R. L. and Schmidt, A. W. 1969. The Lithoporosity Cross Plot. *Society of Professional Well Log Analysts $10^{TH}$ Annual Symposium Transactions,* 1-29.

Carpenter, G. A. & Grossberg, S. 1987a. A Massive Parallel Architecture for a Self-Organising Neural Pattern Recognition Machine. *Computer Vision, Graphics, and Image Processing,* **37**, 54-115.

Carpenter, G. A. & Grossberg, S. 1987b. ART-2: Self-Organisation of Stable Category Recognition Codes for Analogue Input Parameters. *Applied Optics,* **26**, 4919-4930.

Carpenter, G. A. & Grossberg, S. 1990. ART3: Hierarchical Search using Chemical Transmitters in Self-Organising Pattern Recognition Architectures. *Neural Networks,* **3**, 129-152.

Carpenter, G. A., Grossberg, S., and Reynolds J. H. 1991. ARTMAP: Supervised Real-Time Learning and Classification of Nonstationary Data by a Self-Organising Neural Network. *Neural Networks,* **4**, 565-588.

Chan, D. S. K. 1984. Accurate Depth Determination in Well Logging. *IEEE Transactions on Acoustics, Speech and Signal Processing,* **32**, no.1, 42-48.

Cheung, P. S. 1999. Microresistivity and Ultrasonic Imagers: Tool Operations and Processing Principles with reference to commonly encountered Image Artefacts. *In:* Lovell, M. A., Williamson, G. and Harvey, P. K. (eds.), 1999, *Borehole Imaging: Applications and Case Histories,* Geological Society Special Publication No. 159, 45-57.

Clavier, C. & Rust, D. H. 1976. MID plot: A new lithology technique. *The Log Analyst*, **17**, no.6, 16-24.

Cook, S. 2000. *Lomond Field Geological Model Update Post Development wells T9 and T10.* BG Group plc internal report.

Cuddy, S. 2000. Lithofacies and permeability prediction from electrical logs using fuzzy logic. *Society of Petroleum Engineers Reservoir Evaluation and Engineering,* **3**, no.4 319-324.

Cullen, B. 1993a. *Sedimentological Evaluation of Cores from the 23/21-T3 Well, Lomond Field, UK, North Sea.* BG Group plc internal report.

*Cullen, B. 1993b.* Sedimentological Evaluation of Cores from the 23/21-T4 Well, Lomond Field, UK, North Sea. *BG Group plc internal report.*

Cullen, B. 1993c. *Sedimentological Evaluation of Cores from the 23/21-T5 Well, Lomond Field, UK, North Sea.* BG Group plc internal report.

Cullen, B. 1993d. *Sedimentological Evaluation of Cores from the 23/21-T8 Well, Lomond Field, UK, North Sea.* BG Group plc internal report.

Cybenko, G. 1988. *Continuous Valued Neural Network with Two Hidden Layers are Sufficient.* Technical Report, Department of Computer Science, Tufts University, Medford, MA.

Cybenko, G. 1989. Approximation by Superpositions of a Sigmoidal Function. *Mathematics of Control, Signals, and Systems*, **2**, 303-314.

Davis, J. C. 1986. *Statistics and data analysis in geology.* New York, John Wily & Sons.

Davis, G. E., Lowell, W. E., and Davis, G. L. 1993. A Neural Network that Predicts Psychiatric Length of Stay. *MD Computing,* **10**, 87-92.

Deegan, C. E. & Scull, B. J. 1977. *A standard lithostratigraphic nomenclature for the Central and Northern North Sea.* Institute of Geological Sciences Report 77/25. NPD-Bulletin No. 1

Delhomme, J. P. 1992. A Quantitative Characterisation of Formation Heterogeneities based on Borehole Image Analysis. *Society of Professional Well Log Analysts 33$^{RD}$ Annual Logging Symposium, June 14-17,* Paper T.

Delhomme, J. P., Bedford, J., Colley, N. M. and Kennedy, M. C. 1996. Permeability and Porosity Upscaling in the Near-Wellbore Domain: The contribution of Borehole Electrical Images. *Society of Petroleum Engineers Annual Conference and Exhibition, Milan, Italy, 22-24 October 1996. SPE paper number 36822.*

Derek, H., Johns, R. and Pasternack, E. 1990. Comparative Study of a Backpropagation Neural Network and Statistical Pattern Recognition Techniques in Identifying Sandstone Lithofacies. *Conference on Artificial Intelligence in Exploration and Production A&M,* 41-49.

Devilee, R. J. R., Curtis, A. and Roy-Chowdhury, K. 1999. An Efficient, Probabilistic Neural Network approach to solving Inverse Problems: Inverting Surface Wave Velocities for Eurasian Crustal Thickness. *Journal of Geophysical Research,* **104**, no. B12, 28841-28857.

Doraisamy, H., Vive, D. H. and Halleck, M. 2000. Detection of Hydrocarbon Reservoir Boundaries using Neural Network analysis of Surface Geochemical Data. *American Association of Petroleum Geologists' Bulletin*, **84**, no.12, 1893-1904.

Doveton, J. H., 1986. *Log Analysis of Subsurface Geology – Concepts and Computer Methods*. New York, John Wily & Sons.

Doveton, J. H., 1994. *Geologic log analysis using computer methods*. American Association of Petroleum Geology Computer Applications in Geology, no. 2.

Ellis, D. V. 2003. Formation Porosity Estimation from Density Logs. *Petrophysics,* **44,** no.5, 306-315.

Ellis, D. V., Case, C. R., and Chiaramonte, J. C. 2004. Porosity from Neutron Logs I: Measurement. *Petrophysics,* **44,** no.6, 383-395.

Fahlman, S., & Lebiere, C. 1990. *The Cascade-Correlation learning architecture.* Technical Report CMU-CS-90-100. Computer Science Department, Carnegie Mellon University, Pittsburgh, PA.

Fryman, P. & Deutsch, C. V. 2002. Practical Application of Geostatistical Scaling Laws for Data Integration. *Petrophysics*, **43**, no.3, 153-171.

Garden, R. 2001. *Application of Neural Networks for Facies Characterisation in Thin-Bedded Sandstones as applied to Gaza Marine-1 and –2.* BG Group plc internal report.

Goldberg, D. E. 1989. *Genetic Algorithms in Search, Optimisation and Machine Learning.* Addison-Wesley, Reading, MA.

Gonclaves, C. A., Harvey, P. K., and Lovell, M. A. 1997. Prediction of Petrophysical Parameter Logs using a Multilayer Backpropagation Neural Network. *In:* Lovell, M. A. & Harvey, P. K. (eds.), 1997, *Developments in Petrophysics,* Geological Society Special Publication No. 122, 169-180.

Gruping 1999, T. 1998. Introduction to Formation Evaluation. *Course notes for MSc, Aberdeen University.*

Gupta, R. & Johnson, H. D. 2001. Characterization of Heterolithic Deposits using Electrofacies Analysis in the Tide-Dominated Lower Jurassic Cook Formation (Gullfaks Field, offshore Norway). *Petroleum Geoscience,* **7**, 321-330.

Gurney, K. 1997. *An Introduction to Neural Networks*. UCL Press.

Hall, J., Ponzi, M., Gonfalini, M. and Maletti, G. 1996. Automatic Extraction and Characterisation of Geological Features and Textures from Borehole Images and Core Photographs. *Society of Professional Well Log Analysts 37$^{TH}$ Annual logging symposium,* Paper CCC.

Haller, D., & Porturas, F. 1998. How to Characterise Fractures in Reservoirs using Borehole and Core Images: Case Studies. *In:* Harvey, P. K. & Lovell, M. A. (eds.), 1998, *Core-Log Integration,* Geological Society Special Publication No. 136, 249-259.

Hartmann, D. J., 1975. Effect of Bed Thickness and Pore Geometry on Log Response. *Society of Professional Well Log Analysts 16$^{TH}$ Annual Symposium. Transactions,* Paper Y, 1-14.

Hashem S. 1997. Optimal Linear Combination of Neural Networks. *Neural Networks,* **10**, 599-614.

Huang, W. Y. & Lippmann, R. P. 1988. Neural Net and Traditional Classifiers. *In:* Andersen (ed.), *Neural Information Processing Systems*, 387-396.

Hazeu, G. J. A., Krakstad, O. S., Rlan, D. T. and Skaug, M. 1988. The Application of New Approaches for the Shale Management in a Three-Dimensional Simulation Study of the Frigg Field. *Society of Petroleum Engineers Formation Evaluation*, **3**, 493-502.

Helle H. B., Bhatt, A. and Ursin, B. 2001. Porosity and Permeability prediction from Wireline Logs using Artificial Neural Networks: a North Sea case study. *Geophysical Prospecting,* **49,** 431-444.

Helle, H. B. & Bhatt, A. 2002. Fluid Saturation from Well Logs using Committee Neural Networks. *Petroleum Geoscience* **8,** 109-118.

Hodgson, N. A., Farnsworth, J. and Fraser, A. J. 1992. Salt related Tectonics, Sedimentation, and Hydrocarbon Plays in the Central Graben, North Sea, UKCS. *In:* Hardman R. F. P. (ed.) 1992, *Exploration Britain: Geological insights for the next decade*, Geological Society Special Publication No. 67, 31-63.

Hopfield, J. J. 1982. Neural Networks and Physical Systems with Emergent Collective Computational Properties. *Proceedings of the National Academy of Sciences of the USA,* **79**, 2554-2588.

Hossack, W. 2003. School of Physics, Edinburgh University, personal communication.

Jenner, R. & Baldwin J. L. 1994. Application of an Artificial Neural Network to Obtain an Improved Permeability Profile. *Society of Professional Well Log Analysts 16th European Formation Evaluation Symposium*, Aberdeen, Scotland, paper M.

Kleverlaan, K. & Cossey, S. P. J. 1993. Permeability Barriers within Sand-Rich Submarine Fans: Outcrop Studies of the Tabernas Basin, SE Spain. *In:* Eschard, R. and Doligez (eds.) 1993, *Subsurface Reservoir Characterisation from Outcrop Observations*. Editions Techniq, Paris 161-164.

Kohonen, T. 1982. Self-Organised Formation of Topologically Correct Feature Maps. *Biological Cybernetics,* **43,** 59-69.

Kohonen, T. 1984. *Self-organisation and associative memory.* Berlin: Springer Verlag.

Knox, R. W. O'B & Cordey, W. G. 1992. Paleogene of the Central and Northern North Sea. *In:* Knox, R. W. O'B. & Holloway, S. 1992. *Lithostratigraphic nomenclature of the UK North Sea.* British Geological Survey on behalf of the UK Offshore Operators Association.

LeCun, Y., Denker, J. S. and Solla, S. A. 1990. Optimal Brain Damage. *In*: Touretzky, D. (ed.), *Advances in Neural Information Processing Systems,* **2**, 598-605. San Mateo, CA: Morgan Kaufmann.

Lofts, J. C. & Bourke, L. T. 1999. The Recognition of Artefacts from Acoustic and Resistivity Borehole Imaging Devices. *In:* Lovell, M. A., Williamson, G. and Harvey, P. K. (eds.), 1999, *Borehole Imaging: Applications and Case Histories,* Geological Society Special Publication No. 159, 59-76.

Lovell, M. A., Harvey, P. K., Brewer, T. S., Williams, C., Jackson, P. D. and Williamson, G. 1998. Application of FMS Images in the Ocean Drilling Program: an overview. *In:* Cramp, A., MacLeod, C. J., Lee, S. V. and Jones, E. J. W. (eds.), *Geological Evolution of Ocean Basins: Results from the Ocean Drilling Program.* Geological Society Special Publication No. 131, 287-303.

Lovell, M. A., Harvey, P. K., Jackson, P. D., Brewer, D., Williamson, G. and Williams, C. G. 1998. Integration of Core and Log Data – Integration or Calibration? *In:* Harvey, P. K. & Lovell, M. A. (eds.), 1998, *Core-Log Integration,* Geological Society Special Publication No. 136, 39-51.

Luthi, S. M. 1990. Sedimentary Structures of Clastic Rocks Identified from Electrical Borehole Images. *In:* Hurst, A., Lovell, M. A. and Morton, A. (eds.), 1990, *Geological Applications of Wireline Logs,* Geological Society Special Publication Classic, 3-10.

Luthi, S. M. 1994. Textural Segmentation of Digital Rock Images into Bedding Units using Texture and Cluster Labels. *Mathematical Geology,* **26**, no.2, 181-196.

Luthi, S. M. 2001. *Geological Well Logs Their Use in Geological Modelling.* Springer-Verlag Berlin and Heidelberg.

McCulloch, N. 2001. BG Group plc, personal communication.

McCulloch, W. & Pitts, W. 1943. A Logical Calculus of the ideas Imminent in Nervous Activity. *Bulletin of Mathematical Biophysics,* **7**, 115-33.

Macgregor, J. R. 1965. Quantitative Determination of Reservoir Pressures from Conductivity Log. *Bulletin American Society of Petroleum Geologists',* **49**, no.9, 1502-1511.

Masters, T. 1993. *Practical Neural Network Recipes in C+.* Academic Press.

Minsky, M. & Papert, S. 1969. *Perceptrons.* Cambridge MA: MIT Press.

Mitchell, T. 1997. *Machine Learning.* McGraw-Hill international publishing.

Mohaghegh, S. & Ameri, S. 1996. Virtual Measurement of Heterogeneous Formation Permeability using Geophysical Well Log Responses. *The Log Analyst*, **37**, no.2, 32-39.

Moss, B. P. 1997. The Partitioning of Petrophysical Data: A Review. *In:* Lovell, M. A. & Harvey, P. K. (eds.), 1997, *Developments in Petrophysics,* Geological Society Special Publication No. 122, 181-251.

Mudge, D. C. & Copesake, P. 1992a. Revised Lower Palaeogene Lithostratigraphy for the Outer Moray Firth, North Sea. *Marine and Petroleum Geology,* **9**, 53-69.

Mudge, D. C. & Copesake, P. 1992b. Lower Palaeogene Stratigraphy of the Northern North Sea. *Marine and Petroleum Geology,* **9**, 287-301.

Mutti, E. 1985. Turbidite Systems and their Relations to Depositional Sequences. *In:* Zuffa, G. G. (ed.), *Provenance of Arenites*, 65-93. Reidel, Amsterdam.

Mutti, E. & Ricci Lucchi, F. 1972. *Le torbiditi dell'Appennino settentrionale: introduzione all'analisi di facies:* Mem. Soc. Geol. It., **11** 161-199.

Osborne, D. A. 1992. Neural Networks Provide More Accurate Reservoir Permeability. *Oil & Gas Journal*. September, 80-83.

Parker, B. 1985. *Learning logic.* (MIT Technical Report TR-47). MIT Centre for Research in Computational Economics and Management Science.

Pomerleau, D. A. 1993. Knowledge-Based Training of Artificial Neural Networks for Autonomous Robot Driving. *In:* Connell, J. & Mahadevan, S. (eds.), 1993, *Robot Learning: Applications and Case Histories,* Boston Kluwer Academic Publishers, 19-43.

Poulton, M. M. 2001. Computational Neural Networks for Geophysical Data Processing. *In:* Helbig, K. & Treitel, S. (eds.) *Handbook of Geophysical Exploration,* **30,** Pergamon.

Poupon, A., Hoyle, W. R. and Schmidt, A. W. 1971. Log Analysis in Formations with Complex Lithologies. *Journal of Petroleum Technology,* 995-1005.

Prensky, S. E. 1999. Advances in Borehole Technology and Applications. *In:* Lovell, M. A., Williamson, G. and Harvey, P. K. (eds.), 1999, *Borehole Imaging: Applications and Case Histories,* Geological Society Special Publication No. 159, 1-43.

Press, H., Teukolsky, S. A., Vetterling, W. T. and Flannery, B. P. 1992. *Numerical Recipes in Fortran, The Art of Scientific Computing*. Cambridge University Press.

Reading, H. G. 1996. *Sedimentary Environments: Processes, Facies and Stratigraphy.* Blackwell Science.

Refenes, A. N., Zapranis, A., Francis, G. 1994. Stock Market Performance Modelling using Neural Networks: A Comparative Study with Regression Models. *Neural Networks*, **7**, 375-388.

Rider, M. 1996. *The Geological Interpretation of Well Logs*. Whittles Publishing.

Rider, M., Goodall, T. and Dodson T. 1999. A Pre-Development Turbidite Reservoir Evaluation using FMS Electrical Images. *In:* Lovell, M. A., Williamson, G. and Harvey, P. K. (eds.), 1999, *Borehole Imaging: Applications and Case Histories,* Geological Society Special Publication No. 159, 123-137.

Rider, M. 2003. Rider-French Consulting, personal communication.

Robinson, R. 1991. Neural Networks Offer an Alternative to Traditional Regression. *Geobyte*, February, 14-19.

Rogers, S. J., Fang, J. H., Karr, C. L. and Stanley, D. A. 1992. Determination of Lithology from Wireline Well Logs using a Neural Network. *American Association of Petroleum Geologists' Bulletin*, **76**, no. 5, 731-739.

Rosenblatt, F. 1958. The Perceptron: A Probabilistic Model for Information Storage and Organisation in the Brain. *Psychological Review,* **65**, 386-408.

Rosenblatt, F. 1962. *Principles of Neurodynamics*. New York: Spartan Books.

Rumelhart, D. E., & McCelland, J. L. 1986. *Parallel Distributed Processing: Exploration in the Microstructure of Cognition (Vols. 1 & 2)*. Cambridge MA: MIT Press.

Russell, S. D., Akbar, M., Vissapragada, B. and Walkden, G. M. 2002. Rock Types and Permeability Prediction from Dipmeter and Image Logs: Shuaiba Reservoir (Aptian), Abu Dhabi. *American Association of Petroleum Geologists' Bulletin*, **86**, no.10, 1709-1732.

Saggaf, M. M. & Nebrija, E. L. 2000. Estimation of Lithologies and Depositional Facies from Wireline Logs. *American Association of Petroleum Geologists' Bulletin,* **84**, no.10, 1633-1646.

Samuel, A., Kneller, B., Raslan, S., Sharp, A. and Parsons, C. 2003. Prolific Deep-Marine Channels of the Nile Delta, Egypt. *American Association of Petroleum Geologists' Bulletin*, **87**, no.4, 541-560.

Savre, W. C. 1963. Determination of a more Accurate Porosity and Mineral Composition in Complex Lithologies with the use of Sonic, Neutron, and Density surveys. *Journal of Petroleum Technology*, **15**, no.6, 945-959.

Schlumberger 1972. *The Essentials of Log Interpretation Practice.* Schlumberger Publication.

Schlumberger 1987. *Log Interpretation Principles/Applications.* Schlumberger Publication.

Schlumberger 1990. *Formation MicroScanner Image Interpretation.* Schlumberger Publication.

Schuppers, J. D. 1993. Quantification of Turbidite Facies in a Reservoir-Analogous Submarine-Fan Channel Sand body, South Central Pyrenees, Spain. *In:* Flint S. S. & Bryant, I. D. (eds.), *The Geological Modelling of Hydrocarbon Reservoir and Outcrop Analogues,* Spec. Publs int. Ass. Sediment. No.15, Blackwell Scientific Publications, 99-112.

Serra, O. 1979. Diagraphies Différées. Bases de l'interprétation. Tome : Acquisition des données Diagraphiques. *Bull. Centre Rech. Expl.-Prod. Elf Aquitaine,* Mem. **1**, Technip, Paris, 328.

Serra, O. & Abbott, H. T. 1980. The Contribution of Logging data to Sedimentology and Stratigraphy. *55th Annual Conference Dallas,* 1-19, SP 9270.

TerraSciences 2002. *TerraStation II software manual.*

Trappe, H. & Hellmich, C. 1998. Seismic Characterisation of Rotliegend Reservoirs – from Bright Spot to Stochastic Simulation. *First Break*, **16**, 79-87.

Trappe, H. & Hellmich, C. 2000. Using Neural Networks to Predict Porosity Thickness from 3D Seismic. *First Break*, September, 377-384.

Vaughan, A., Hansen, T., Cardon, H., and Radcliffe, N. 1999. Litho-Flow Facies Prediction in an Alluvial Fan/Fluvial System, Central North Sea. *Petroleum Geoscience,* **5**, 409-419.

Wadge, G., Benaouda, D., Ferrier, G., Whitmarsh, R. B, Rothwell, R. G., and Macleod, C. 1998. Lithological Classification within ODP Holes using Neural Networks trained from Integrated Core-Log Data. *In:* Harvey, P. K. & Lovell, M. A. (eds.), 1998, *Core-Log Integration,* Geological Society Special Publication No. 136, 129-140.

Wakefield, M. 2001. BG Group plc, personal communication.

Walsgrove, T. 1996. *Lomond Field Petrophysical Re-Study.* BG Group plc internal report.

Wardell, J. R., Hayes, M. R., Burford, S. J., McGuckin, J. J. and Hurst, A. R. 1996. A 3-D Geostatistical Model of a Turbidite Reservoir and Validation by Pressure Transient Analysis. *Society of Petroleum Engineers' Conference on 3-D Reservoir Modelling, Stavanger, Norway, 16-17 April. SPE paper number* 35538.

Werbos, P. 1974. *Beyond Regression: New tools for Prediction and Analysis in the Behavioural Sciences.* Ph.D. dissertation, Harvard University.

Widrow, B. &. Hoff, M. E. Jr 1960. Adaptive Switching Circuits. *In*: *IRE WESCON convention record, 96-104.* New York: IRE. (Reprinted in Anderson, A. & Rosenfeld, E. (eds.) 1988. *Neurocomputing – foundations of research.* Cambridge, MA: MIT Press.)

Widrow, B. & Stearns, S. D. 1985. *Adaptive Signal Processing.* Englewood Cliffs, NJ: Prentice-Hall.

Widrow, B., Winter, R. G. and Baxter, R. A. 1987. Learning Phenomena in Layered Neural Networks. *In: 1st IEEE International Conference on Neural Networks,* **II**, 411-29, San Diego.

Wiener, J. M., Rogers, J. A., Rogers, J. R. and Moll, R. F. 1991. Predicting Carbonate Permeabilities from Wireline Logs using a Backpropagation Neural Network. *Society of Exploration Geophysicists, expanded abstracts and biographies*, **1**, 285-288.

Wolstenhulme, S. 2003. EasyNN help, personal communication.

Wong, S. A., Startzman, R. A. and Kuo, T. B. 1989. Enhancing Borehole Image Data on a High-Resolution PC. *Society of Petroleum Engineers Petroleum Computer Conference, June 26-28*, Society of Petroleum Engineers Paper 19124.

Wong, P. M., Jian, F. X. and Taggart, I. J. 1995a. A Critical Comparison of Neural Networks and Discriminant Analysis in Lithofacies, Porosity and Permeability Predictions. *Journal of Petroleum Geology,* **18,** no.2, 191-206.

Wong, P. M., Gedeon, T. D. and Taggart, I. J. 1995b. An Improved Technique in Porosity Prediction: A Neural Network Approach. *IEEE Transactions on Geoscience and Remote Sensing,* **33,** no.4, 971-980.

Wong, P. M., Gedeon, T. D. and Taggart, I. J. 1995c. Use of Fuzzy ARTMAP for Lithofacies Classification: A Comparison Study. *Society of Professional Well Log Analysts 36th Annual Logging Symposium, June 26-29.*

Wong, P. M., Tamhane, D. and Wang, L. 1997. A Neural Network approach to Knowledge-Based Well Interpolation: A case study of a Fluvial Sandstone Reservoir. *Journal of Petroleum Geology,* **20,** no.3, 363-372.

Worthington, P. F. 1990. Sediment Cyclicity from Well Logs. *In:* Hurst, A., Lovell, M. A. and Morton, A. (eds.), 1990, *Geological Applications of Wireline Logs,* Geological Society Special Publication Classic, 123-132.

Wu, X. & Zhou, Y. 1993. Reserve Estimation Using Neural Network Techniques. *Computers & Geoscience*, **19,** no.4, 567-575.

Wu, T. & Berg, R. R. 2003. Relationship of Reservoir Properties for Shaly Sandstones Based on Effective Porosity. *Petrophysics,* **44,** no.5, 328-341.

Wyllie, M. R. J. & Rose, W. D. 1950. Some Theoretical Considerations related to the Quantitative Evaluation of the Physical Characteristics of Reservoir Rocks from Electrical Log Data. *Journal of Petroleum Technology,* **189,** April.

Wyllie, M. R. J., Gregory, A. R. and Gardener, L.W. 1956. Elastic Wave Velocities in Heterogeneous and Porous Media. *Geophysics,* **21**, no.1, 41-70.

Yang, H., Chen, H. C. and Fang, J. H. 1996. Determination of carbonate lithofacies using hierarchical neural networks. *Intelligent Engineering Systems Through Artificial Neural Networks,* **6,** 481-486.

**INTERNET REFERENCES**

http://faculty.washington.edu/chudler/cells.html, last accessed February 2004.

http://www.easynn.com, last accessed February 2004.

http://www.trajan-software.demon.co.uk/, last accessed February 2004

# Appendix 1 : Tool design and limitations & derivative log calculations

## *A1.1 Introduction*

This appendix begins by briefly outlining some of the principles behind the acquisition of conventional well log data and documents some of the limitations of the technique. The principles behind the acquisition of image logs are discussed in Chapter 5. A short discussion follows on the differences between acquisition in horizontal and vertical wells. Finally Section A1.3 illustrates how the derivative logs used in this thesis were calculated.

## *A1.2 Data acquisition and limitations*

### *A1.2.1 The gamma ray log*

The simple gamma-ray log records a formation's radioactivity. The radioactivity originates predominantly from naturally occurring uranium, thorium and potassium. The actual tool consists of a sensitive gamma-ray detector that is made up of a scintillation counter and a photomultiplier. The counter is usually a sodium iodide crystal. When gamma rays pass through the crystal a flash occurs. These are recorded by the photo-multiplier over a set period of time. When the tool detects radiation it has already passed through the formation and the drilling mud both of which cause scattering. Thus the volume of mud in the borehole and consequently the borehole diameter affects the value recorded by the tool. For the same reason gamma ray logs are affected by borehole washouts. The vertical bed resolution is approximately 8"-10" and the depth of investigation approximately 10cm.

### *A1.2.2 The sonic log*

The sonic log measures a formations interval transit time – the formation's capacity to transmit sound waves. This is related to porosity and rock texture. The tool consists of a number of emitters and receivers positioned on the main tool body. Emitters send a pulse of sound into the rock at set intervals that are subsequently detected by the receivers. The sonic curves used in this study derive from the pulse that represents the compressional or p-wave (the first arrival). The use of more than one emitter-receiver pair increases the accuracy of

the measurement and effectively eliminates unwanted borehole effects. Even when the borehole is in a poor condition the measurement can still be reliable, unlike the density tool (Rider, 1996). The sonic tool is generally run in the centre of the borehole, thus the pulse travels through the mud, along the borehole wall (it is refracted at the borehole-mud interface) and back through the mud again. Therefore the depth of investigation of the sonic tool is very shallow. The mud effect is eliminated by the use of multiple transmitter-receiver pairs. The vertical resolution is approximately 2ft. Sonic log values are affected by depth, generally showing a regular increase due to compaction.

### *A1.2.3 The density log*

The main use of the density log is to calculate porosity. Measurement is made by bombardment of the formation with gamma rays (from a source) and then by measuring their attenuation (via a detector). Attenuation is a measure of the electron density of the formation that is closely related to its true density. In dense formations attenuation is extreme and few gamma rays reach the detector. When hydrogen (in the form of water or hydrocarbon) is present there is a greater difference between the electron and true density. Therefore this log is always calibrated to the density of calcite (2.71g/cm3) and pure water (1.00g/cm3) and presented in g/cm3.

Tools consist of a single gamma ray source and two detectors (that help to compensate for borehole effects) which are mounted on a single plough shaped pad. The pad is pressed against the borehole wall during logging. Density logs are therefore specific to a sector of the borehole. The vertical resolution is good at approximately 2ft, but the depth of investigation is shallow, typically less then 5". Because of the very shallow investigation measurement is very much affected by bad-hole conditions. The pad can also in some circumstances cause the tool to stick. The density log is affected by depth with density increasing with compaction.

### *A1.2.4 The neutron log*

Neutron logs record the formation's response to bombardment by neutrons. The tool consists of a neutron source and two detectors that are attached to a skid that is pushed against the borehole wall. The source bombards the formation with neutrons and the detectors measure their loss in energy as they pass through it. Most energy loss is through

collision with particles that have the same mass as the neutrons – in logging this is mainly hydrogen. Therefore the log is essentially a measure of the hydrogen content of the formation – be it as pore or bound water (in clay) or hydrocarbon. The hydrogen richness is called the hydrogen Index (HI). The HI is equal to 1 in pure water. The main use of the log is as a porosity index so it is always presented in neutron porosity units. Neutron porosity is the same as real porosity in clean limestone. The depth of investigation of the neutron tool is 6"-10"; the vertical resolution is 3ft. Because of the skid (as opposed to a pad) and the fact that investigation is deeper, the neutron tool is less affected by borehole washouts than the density log. The neutron log is also less affected by depth then the neutron or sonic log.

### *A1.2.5 The resistivity log*

This log is a measure of a formation's resistivity. The main use of the log is in the identification of hydrocarbon in porous formations. Simply, hydrocarbons are insulators whereas saline water is very conductive. The tools used in both data sets were inductive logs that actually measure conductivity. Conductivity is directly inverted and plotted as resistivity on log plots. In induction logs a current is induced in the formation, and the capacity of that formation to carry the current is observed. Induction logs consist of emitting and receiving coils separated by an insulated section of the tool. A current is applied to the emitting coil that creates a magnetic field around the tool. This induces eddy currents in the formation that flow around the tool. These currents create their own magnetic field that induces an alternating current in the receiver coil. The separation of the coils in a deep induction log is approximately 1m and thus the induced currents derive from between 1m and 5m away from the borehole. This means that the deep induction log is not affected by the invaded or flushed zone – it is a measurement of the virgin formation. Consequently bed resolution is poor, being of the order of 2m. Deep induction logs are affected by depth (resistivity increases with depth). Log readings are also affected by temperature, although this is generally the temperature of the mud rather than the formation (Rider, pers. comm.).

In this data set the caliper curve was used to identify areas of borehole washout. Data in these regions were subsequently excluded from any training sets.

### *A1.2 Horizontal wells*

Wells from the WDDM concession are all vertical or sub-vertical. However wells in the Lomond Field are all deviated. Some tool measurements are affected by the attitude of the well. In horizontal wells the invasion profile of the mud is different to that of vertical wells due to gravity. Drilling mud will penetrate further into the formation at the base of the borehole than at the top. Compared with a vertical well this will affect some log readings. The pad on a density tool is much more likely to measure the lower section of the borehole and thus may measure a different value than an equivalent section in a vertical well. Newer azimuthal density tools measure the density in different sections of the borehole, and in horizontal wells these are more likely to be different. It is also possible that drilling debris could gather along the borehole of a horizontal well and this could also affect measurement. Logs such as the neutron, sonic and resistivity are thought to be less affected than the density tool because they do not utilise a pad mechanism.

Although the Lomond wells are deviated, they are not fully horizontal and so it is thought that the above effects on the density tool are not highly significant.

### *A1.3 Derivative log calculation*

Three derivative logs were calculated over the Lomond data set: shale volume, neutron density separation and total porosity. Neutron-density separation and total porosity were used as inputs for neural network analysis, as explained in Chapter 3. Shale volume was used in the standardisation of logs to a single fluid saturation, as explained in Chapter 4 and Appendix 3. The way in which these were calculated is described below.

#### *A1.3.1 Neutron-density separation*

This log was calculated in the same way as that described by Gupta & Johnson (2001). The density log can be scaled in neutron porosity units where:

0pu $\equiv 2.7 gcm^{-3}$ which is equivalent to a log value representing 100% carbonate.

100pu $\equiv 1 gcm^{-3}$ equivalent to a log value representing pure water.

Using these equivalent values the density log was scaled in neutron porosity units, and the resulting neutron-density separation curve calculated as:

NPHI – RHOB (scaled in porosity units)

This tends to produce a small or negative value in sand horizons and a larger positive value in shale sections.

### *A1.3.2 Shale volume*

Shale volume was calculated from a normalisation of the gamma-ray log:

$$V_{sh} = \frac{GR_{\log} - GR_{\min}}{GR_{\max} - GR_{\min}} \qquad \text{(A 1.1)}$$

Since the gamma-ray curve is sensitive to borehole size, if the borehole was greater than 10" (normally 8.5") as indicated by the caliper log then the shale volume was set to a null value.

### *A1.3.3 Total porosity*

A simple total porosity was calculated as follows:

$$\phi_T = \frac{\rho_{mat} - \rho_b}{\rho_{mat} - \rho_{fl}} \qquad \text{A 1.2}$$

Where:

$\phi_T$ = total porosity;

$\rho_{mat}$ = matrix density;

$\rho_b$ = bulk density read by the density tool;

$\rho_{fl}$ = density of the 'fluid' in the invaded zone.

The values used were taken from Walsgrove (1996) who computed both the matrix and fluid values from cross-plots with core plug values (after a correction to reservoir temperature and pressure):

Well 23/21-T4:

gas zone 1: $\rho_{fl} = 0.354$g/cm3 (13098-13148) and (13682-13734);

gas zone 2: $\rho_{fl} = 0.514$g/cm3 (13194-13428);

water zone: $\rho_{fl} = 1.284$g/cm3

All other wells:

gas zones: $\rho_{fl} = 0.855$g/cm3

water zones: $\rho_{fl} = 1.038$g/cm3

Note Ellis (2003) gives a useful account of formation porosity estimation from the density log.

# Appendix 2 : Programs used in this thesis

The following program is the thin-bed repair program (written in FORTRAN 90) used in thesis. The program shown repairs beds if they are less than 2ft and 1.5 ft in thickness. In total four 'repaired' columns are output - each specified thickness has a fully repaired column (where thick beds if they have null values are repaired) and a column that is partially repaired where these thick beds remain. Also this program defaults sections with multiple thin-beds to specific lithofacies – this is stage 2 of the program. This was the program that was used for analysis in Chapter 4. The program was also used in Chapter 5, however facies columns were repaired over 20 data points (2"). This involved the single change to the variable C3, C4, CX3 and CX4 to C20, etc. Also stage 2 was removed for analysis in Chapter 5.

Other programs used in this thesis are:

- A program to calculate the moving statistics of image array data as described in Chapter 5;
- A program to calculate the vertical power spectra of the average button response over a moving window of 128 data points, (courtesy of Roger Hipkin at the School of GeoSciences, Edinburgh University);
- A program to calculate the horizontal power spectra across a single pad of image data, (courtesy of Roger Hipkin at the School of GeoSciences, Edinburgh University);
- A post-processing program that aligns depth tags with the results of the moving power spectra.

These programs are not shown as these represent standard implementation of well-known equations or techniques.

***Thin-bed repair program***

```
PROGRAM thin_bed_corr
 !! Post processing program to correct for thin beds

IMPLICIT NONE

! List variables
CHARACTER (len=16) :: file_name,fnamc,fnamo,Header
CHARACTER (len= 4) :: dat,out

INTEGER :: imax,i,fnamlen,L_999
 INTEGER :: j,q,list_start,list_end,test,next,length,no_cells
 INTEGER :: Facies,Facies_1,Facies_2,half,L_test,L_next

INTEGER, DIMENSION(:) ,ALLOCATABLE :: A
INTEGER, DIMENSION(:) ,ALLOCATABLE :: A_ini
INTEGER, DIMENSION(:) ,ALLOCATABLE :: B
INTEGER, DIMENSION(:) ,ALLOCATABLE :: B2
INTEGER, DIMENSION(:) ,ALLOCATABLE :: C
INTEGER, DIMENSION(:) ,ALLOCATABLE :: C3
INTEGER, DIMENSION(:) ,ALLOCATABLE :: C4
INTEGER, DIMENSION(:) ,ALLOCATABLE :: C3X
INTEGER, DIMENSION(:) ,ALLOCATABLE :: C4X
INTEGER, DIMENSION(:) ,ALLOCATABLE :: D
REAL, DIMENSION(:) ,ALLOCATABLE :: Depth

dat='.txt' ; out='.out'
WRITE (*,*) 'Enter data filename :' ; READ (*,*) file_name
fnamlen=SCAN(file_name,' ')-1
fnamc=file_name(1:fnamlen)//dat(1:4)          ! Variable
fnamo=file_name(1:fnamlen)//out(1:4)          ! Output filenames

 !! Parameters
 length=4        ! Minimum bed length not to correct

!! Open file and read in data
OPEN(UNIT=7,FILE=fnamc ,ACCESS='sequential' ,STATUS='old')
  READ(7,*) imax
    ALLOCATE(A_ini(imax),A(imax),B(imax),B2(imax))
```

```
ALLOCATE(C(imax),C3(imax),C4(imax),C3X(imax),C4X(imax),D(imax),Depth(imax))
      READ(7,*) Header
      DO i=1,imax
         READ (7,*) Depth(i),A_ini(i)
      ENDDO
    CLOSE(UNIT=7,STATUS='KEEP')

   DO length=3,4
   A=A_ini

!!-- Stage 1 ----------How many adjacent alike values?

     !! Initalise variables
     q=1
     list_start=1
     list_end=1
     test=A(1)

     !! Do over all list
     DO i=2,imax
     IF(test==A(i))THEN          !! If A(i) is same as last cell
        q=q+1                  !! Increment no. of alike cells
        list_end=i                  !! Move end of alike list

      ELSE                  !! Else
                                !! Write last list of alike cells to B
         DO j=list_start,list_end ; B(j)=q ; ENDDO

         !! Re-initialise variables
        q=1
        list_start=i
         list_end=i
         test=A(i)
      ENDIF
     ENDDO

     !! Finish end of list
     DO j=list_start,imax
       B(j)=q
```

```
    ENDDO

!!-- Stage 2 ----------How are pairings grouped and correct

    D=A
    i=1

    DO
      IF(i>imax)EXIT
      test=D(i)
      next=D(i+B(i))
      L_test=B(i)
      L_next=B(i+B(i))

      write(*,*)i,test,next

     IF((L_test<length).OR.(L_next<length))THEN

        IF(((test==3).AND.(next==2)).OR.((test==2).AND.(next==3)))THEN
         IF((L_test<length).AND.(L_next>=length))THEN
            Facies=next
         ELSEIF((L_test>=length).AND.(L_next<length))THEN
            Facies=test
         ELSEIF((L_test<length).AND.(L_next<length))THEN
            Facies = 2
         ENDIF

          DO j=i,i+B(i)+B(i+B(i))-1
              D(j)=Facies
          ENDDO

        ELSEIF(((test==5).AND.(next==4)).OR.((test==4).AND.(next==5)))THEN
         IF((L_test<length).AND.(L_next>=length))THEN
            Facies=next
         ELSEIF((L_test>=length).AND.(L_next<length))THEN
            Facies=test
         ELSEIF((L_test<length).AND.(L_next<length))THEN
            Facies = 4
         ENDIF
```

```
            DO j=i,i+B(i)+B(i+B(i))-1
                D(j)=Facies
            ENDDO

          ELSEIF(((test==5).AND.(next==6)).OR.((test==6).AND.(next==5)))THEN
            IF((L_test<length).AND.(L_next>=length))THEN
              Facies=next
            ELSEIF((L_test>=length).AND.(L_next<length))THEN
              Facies=test
            ELSEIF((L_test<length).AND.(L_next<length))THEN
              Facies = 6
            ENDIF

            DO j=i,i+B(i)+B(i+B(i))-1
                D(j)=Facies
            ENDDO

          ELSE
            DO j=i,i+B(i)-1
                D(j)=test
            ENDDO
          ENDIF
        ENDIF

      i=i+B(i)

      ENDDO

!!-- Stage 3 ----------How many adjacent alike values in corrected?

      !! Initalise variables
      q=1
      list_start=1
      list_end=1
      test=D(1)

      !! Do over all list
      DO i=2,imax
      IF(test==D(i))THEN          !! If A(i) is same as last cell
        q=q+1                  !! Increment no. of alike cells
```

```
        list_end=i                    !! Move end of alike list

      ELSE                  !! Else
                                    !! Write last list of alike cells to B
        DO j=list_start,list_end ; B2(j)=q ; ENDDO

          !! Re-initialise variables
        q=1
        list_start=i
         list_end=i
         test=D(i)
      ENDIF
    ENDDO

    !! Finish end of list
    DO j=list_start,imax
      B2(j)=q
   ENDDO

!!-- Stage 4 ----------Sort through alike list and remove variable beds
!!--- Correct upto end of first normal bed
   DO i=1,imax
      test=B2(i)
     list_end=i
      IF (test>=length) EXIT
    ENDDO

    DO i=1,list_end+test-1
      C(i)=D(list_end)
    ENDDO

!!--- Inital parameter from end of first normal bed
    i=list_end+test
    list_start=i
    Facies_1=D(list_end)

!!--- Loop over main list and correct for thin beds
    DO
     IF (i>imax) EXIT          !--- Don't run past end of list
```

```
IF (B2(i)<length)THEN     !--- Check for thin beds
    i=i+1                 !! If bed not thin, check next cell

ELSE                  !! Correct thin
   list_end=i
    no_cells=list_end-list_start
    Facies_2=D(i)

!! Correct thin beds
 IF(Facies_1==-999)THEN
   DO j=list_start,list_end
    C(j)=Facies_2
   ENDDO

 ELSEIF(Facies_2==-999)THEN
   DO j=list_start,list_end
    C(j)=Facies_1
   ENDDO

 ELSE
   DO j=list_start,list_end
      half=List_start+INT(no_cells/2)
   IF(j<half)THEN
        C(j)=Facies_1
      ELSE
      C(j)=Facies_2
      ENDIF
   ENDDO
  ENDIF

!! Output normal beds
    DO j=i,i+B2(i)-1
      C(j)=D(i)
    ENDDO

!! Re-initialise variables
    i=i+B2(i)
    list_start=i
    Facies_1=Facies_2
 ENDIF
```

```
      ENDDO

!!--- Finish end of corrected list
      DO i=list_start,imax
        C(i)=Facies_1
      ENDDO

      IF(length==3)THEN;C3=C;ELSE;C4=C;ENDIF
      ENDDO


!!!!!!!!!!!!! Remove all -999
     DO length=3,4
     IF(length==3)THEN;C=C3;ELSE;C=C4;ENDIF
!!-- Stage 1 ----------How many adjacent alike values?


      !! Initalise variables
      q=1
      list_start=1
      list_end=1
      test=A(1)

      !! Do over all list
      DO i=2,imax
      IF(test==C(i))THEN          !! If A(i) is same as last cell
         q=q+1                  !! Increment no. of alike cells
         list_end=i                  !! Move end of alike list

       ELSE                  !! Else
                                 !! Write last list of alike cells to B
          DO j=list_start,list_end ; B(j)=q ; ENDDO

          !! Re-initialise variables
         q=1
         list_start=i
          list_end=i
          test=C(i)
       ENDIF
      ENDDO
```

```
      !! Finish end of list
      DO j=list_start,imax
        B(j)=q
      ENDDO

      i=1
      DO
        IF(i>imax)EXIT
        IF(C(i)==-999)THEN
          L_999=B(i)
          half=i+INT(B(i)/2)
          Facies_1=C(i-1)
          Facies_2=C(i+B(i))
          DO j=i,i+B(i)-1
            IF(j<half)THEN
              C(j)=Facies_1
            ELSE
              C(j)=Facies_2
            ENDIF
          ENDDO
        ENDIF
        i=i+B(i)
      ENDDO

      IF(length==3)THEN;C3X=C;ELSE;C4X=C;ENDIF
      ENDDO

!!--- Write solution to screen
      OPEN(UNIT=8,FILE=fnamo ,ACCESS='sequential' ,STATUS='new')
      WRITE(8,*)'DEPTH  PLith0_3_A  PLith0_3_B  PLith0_4_A  PLith0_4_B'
      DO i=1,imax
!     WRITE(*,*)A(i),C(i),D(i),'    ',B(i)
!     WRITE(8,*)A(i),C(i),D(i),'    ',B(i)
      WRITE(8,*)Depth(i),C3(i),C3X(i),C4(i),C4X(i)
      WRITE(*,*)Depth(i),C(i)
      ENDDO
      CLOSE(8,STATUS='KEEP')

      ENDPROGRAM
```

# Appendix 3 : Correction for fluid

## *A3.1 Introduction*

In Chapter 4 it was explained how the sonic, density and neutron logs were recalculated to represent a single fluid type. They were recalculated to represent the effective porosity being filled with gas. The following method gives a summary of the calculations carried out and describes any assumptions made. Note this document initially describes the process with reference to well 23/21-T3.

## *A3.2 Logs affected by fluid*

The following logs in the Lomond data set are affected by fluid:
Sonic
Density
Neutron
Resistivity
Sonic, density, and neutron calculations depend on *Sxo* (water saturation in the invaded zone) as these tools measure the volume of rock very close to the borehole. There exist no shallow resisitvity curves in any of the four Lomond wells that are being investigated initially. Therefore no direct measurement can be made of *Sxo*, it can only be estimated. Since the reservoir is to be filled with gas (with no invasion by the mud filtrate), *Sxo* will be 0.

## *A3.3 Sonic*

The Wyllie time average equation is (Wyllie *et al.* 1956):

$$\Delta t = \phi_S . \Delta t_{fl} + (1 - \phi_S) . \Delta t_{mat} \qquad \text{(A 3.1)}$$

Where:

$\Delta t$ = sonic log reading;

$\Delta t_{fl}$ = travel time in invaded zone fluid (mud filtrate, residual water and gas);

$\Delta t_{mat}$ = travel time in matrix;

$\phi_S$ = sonic derived porosity.

This equation can incorporate a shale correction:

$$\Delta t = \phi_S . \Delta t_{fl} + V_{sh}(\Delta t_{sh}) + (1 - V_{sh} - \phi_S).\Delta t_{mat} \qquad \text{(A 3.2)}$$

Where:

$V_{sh}$ = shale volume from the gamma ray tool;

$\Delta t_{sh}$ = sonic transit time in shale.

The introduction of the shale parameter means that the calculation is a shale corrected porosity. A density porosity can be corrected for shale in a similar way (see later) and this approximates an effective porosity. Note a clay correction is not used, as no petrographic point counts were available for calibration. Shale volume was calculated from the gamma ray log (explained in Appendix 1). A cross-plot was taken (Figure A3.1) of sonic values against core porosities corrected to reservoir conditions (equation for correction from Walsgrove (1996)). Values were only plotted if shale content was less then 10% (to obtain a clean matrix point). A linear regression line (the most common type where we take an average y for specific x) yields a matrix point of 50.53. This is slightly less than the expected 55.1 for quartz, and maybe because the matrix is not pure quartz but contains some lithic fragments. The fluid point of 251.83 appears reasonable given that oil is 238, and the fluid is mostly oil-based mud with some gas and residual water.

Using the transit times for matrix and fluid, porosity was calculated using the equation above re-arranged:

$$\phi_S = \frac{\Delta t - \Delta t_{mat} + V_{sh}(\Delta t_{mat} - \Delta t_{sh})}{\Delta t_{fl} - \Delta t_{mat}} \qquad \text{(A 3.3)}$$

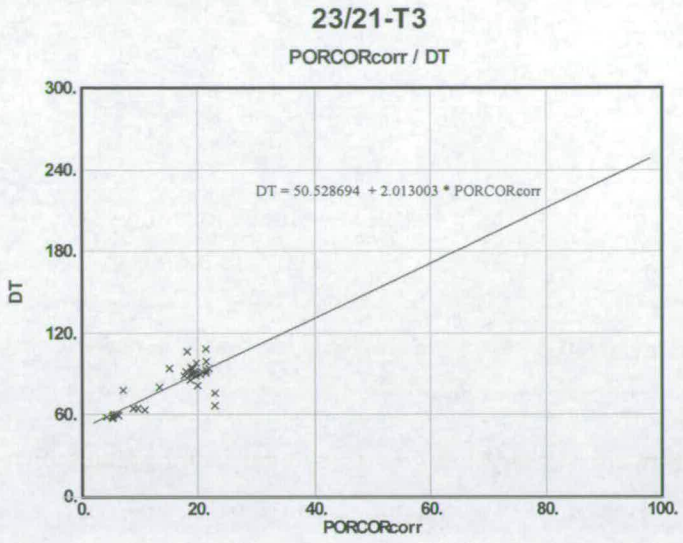



**Figure A3.1** A plot of core porosity corrected to reservoir conditions plotted against sonic values in order to measure average sonic transit times in fluid and matrix. Points only plotted if shale content was less than 10% (thus only finding the matrix value).

A value of 90usec/ft for shale was used. This was found by inspection of logs in pure shale horizons. A sonic transit time for pure gas was taken to be 626usec/ft (Gruping 1998). This represents the sonic transit time in methane at 15psi. No available conversion to reservoir conditions was available for the transit time of gas.

By taking the above parameters it is possible to calculate the sonic transit time for a given fluid content:

$$\Delta t = \phi_S(\Delta t_{fl} - \Delta t_{mat}) + \Delta t_{mat} - V_{sh}(\Delta t_{mat} - \Delta t_{sh}) \qquad \text{(A 3.4)}$$

### *A3.4 Density*

The equation used to calculate an effective porosity is (Mark Bowers pers. comm.):

$$\phi_E = \frac{\rho_{mat} - \rho_b - V_{sh}(\rho_{mat} - \rho_{sh})}{\rho_{mat} - \rho_{fl}} \qquad \text{(A 3.5)}$$

Where:

$\phi_E$ = effective porosity;

$V_{sh}$ = shale volume from the gamma ray log;

$\rho_{mat}$ = matrix density;

$\rho_{fl}$ = invaded zone fluid density (mud filtrate, residual water and gas);

$\rho_b$ = bulk density

$\rho_{sh}$ = an average shale density.

Effective porosity from the density log was calculated using parameters from the Amoco 1996 report. A fluid value of 0.855g/cm3 and a matrix value of 2.65g/cm3 (for well 23/21-T3) were used. A shale density of 2.42g/cm3 was used from inspection of the logs in pure shale horizons.

The equation for calculating a new density curve becomes:

$$\rho_b = \rho_{mat} - \phi_E(\rho_{mat} - \rho_{fl}) - V_{sh}(\rho_{mat} - \rho_{sh}) \qquad \text{(A 3.6)}$$

For recalculation of the log to an all-gas reservoir a fluid value of 0.17g/cm3 was assumed (representing gas slightly denser than methane at the reservoir temperature and pressure, Schlumberger (1987)). However the density tool reads the apparent density. The apparent density of a gas with this density is approximately 0.04 (Schlumberger 1987). This was the value used.

### *A3.5 Neutron*

The neutron log is affected by all hydrogen in the formation. Therefore it is affected by water, oil, gas, mud filtrate and shale (that contains clay which consists of hydrogen in the crystal lattice or as bound water). Relevant equations that describe the neutron tool's response to a formation are:

$$\phi_N = \phi_E\left[HI_{mf}.S_{xo} + HI_{hc}(1 - S_{xo})\right] \qquad \text{(Gruping 1998)} \qquad \text{(A 3.7)}$$

$$\phi_N = \phi_E + V_{sh}\phi.N_{shale} \qquad \text{(Schlumberger 1972)} \qquad \text{(A 3.8)}$$

Where:

$\phi_N$ = porosity as read by the neutron log;

$S_{xo}$ = water saturation in the invaded zone;

$\phi_E$ = effective porosity;

$HI_{mf}$ = hydrogen index of the fluid (mud filtrate, gas and residual water);

$HI_{hc}$ = hydrogen index of the hydrocarbon;

$\phi.N_{shale}$ = the neutron reading when $V_{sh}$ is equal to 1.

Equation A3.7 ignores any lithology or shale effects and describes the contribution of the hydrocarbon and mud filtrate only. Equation A3.8 ignores all lithology and hydrocarbon effects and explains the contribution of shale to the neutron reading. These equations essentially explain that the neutron response is made up of the hydrogen index of the mud filtrate multiplied by the volume of this material, summed with the volume of shale multiplied by the hydrogen index of shale, summed with the hydrogen index of the hydrocarbon multiplied by the volume of hydrocarbon. This is valid for limestone formations as the hydrogen index of limestone is zero (Rider 1996). Since matrix is not limestone neutron readings must be corrected. The hydrogen index of quartz is 0.01 (Rider 1996). Therefore the above equations can be re-written to express the mud filtrate, gas and residual water as 'fluid', and for a quartz matrix:

$$\phi_N = 0.01V_{mat} + \phi_e HI_{fl} + V_{sh} HI_{shale} \qquad \text{(A 3.9)}$$

In general when gas is present the hydrogen content per unit volume is lower than in water. Accordingly the neutron log calibrated for water filled formations reads porosities that are too low. The reduction in neutron porosity is substantially greater than would be expected if the hydrogen content alone is taken into consideration. This is because for an equivalent water filled formation (of equal hydrogen content), there will be more solids per unit volume of formation – and the solids contribute to the slowing down of neutrons (Schlumberger 1972). This is known as the 'excavation effect'. If it is assumed that close to the borehole wall (where the neutron log reads) there is little gas (it is possible to say this because the density of the fluid in the invaded zone is close to that expected for oil based mud), then the

HI of the 'fluid' from the above equation can be estimated. For clean formations the $V_{sh}$ part of the equation drops to zero. The above equation can be rearranged so that:

$$\phi_N - 0.01 = \phi_e\left(HI_{fl} - 0.01\right) \qquad \text{(A 3.10)}$$

So a graph (Figure A3.2) of neutron-0.01 against core porosities will for clean formations (e.g. $V_{sh}$ <0.1 and where effective and total porosities are similar) reveal the hydrogen index of the fluid. The average hydrogen index of the fluid in the gas zone for all wells came to 0.718. For well T3 the hydrogen index of shale used was 0.306 (from a shale point picked on a neutron-density cross-plot and by studying shaly intervals in the well). Therefore it is possible to estimate porosity from the neutron tool:

$$\phi_N = 0.01(1-\phi_e - V_{sh}) + 0.718\phi_e + 0.306V_{sh}$$

$$\phi_N - 0.306V_{sh} = 0.01 - 0.01\phi_e - 0.01V_{sh} + 0.718\phi_e$$

$$\phi_N - 0.306V_{sh} + 0.01V_{sh} - 0.01 = +0.717\phi_e \qquad \text{(A 3.10)}$$

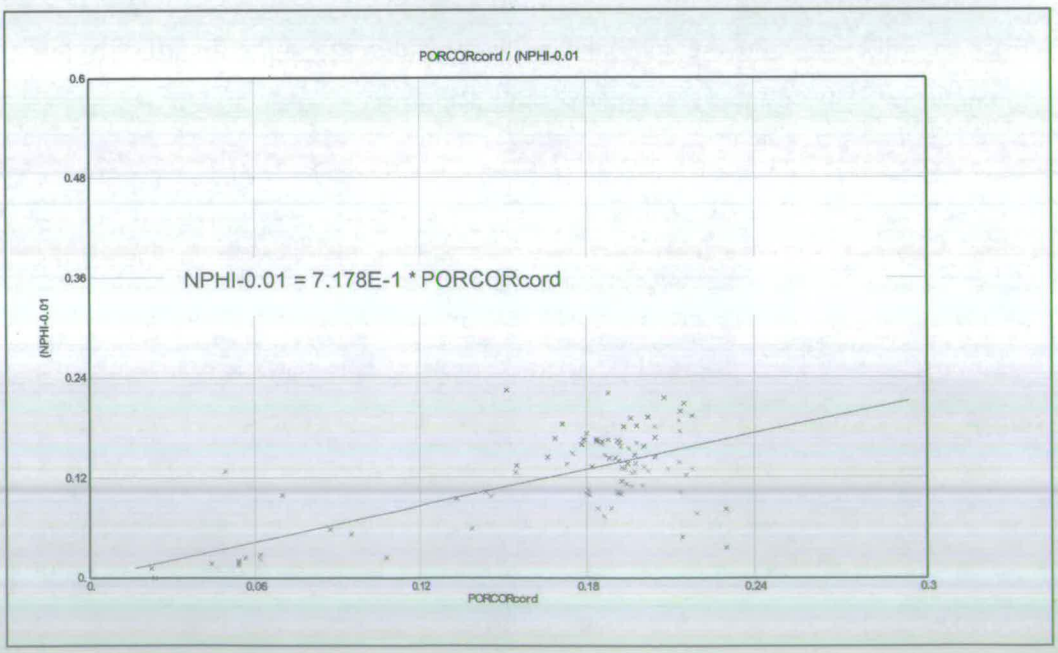



**Figure A.3.2** Plot of (NPHI –0.01) v core porosities (PORCORcord) for the gas zones for all wells with core. All points are 'clean' having a shale volume of less than 10%.

The equation if the invaded zone is filled with gas becomes:

$$\phi_N = \phi_e \lfloor HI_{gas} \rfloor + 0.306V_{sh} + 0.01(1 - \phi_e - V_{sh}) \qquad \text{(A 3.11)}$$

Where:

$HI_{hc}$ = hydrogen index of gas, value taken as 0.38 (Schlumberger 1987).

### *A3.6 Parameters used for other wells*

The above explanation used well 23/21-T3 as the 'type' well in order to establish the technique (although Figure A3.2 was for all core plugs for all wells except 23/21-T4). This analysis was also applied to wells 23/21-T1, T2, T5, T6 and T8. For these a composite plot utilising all available core plugs were used to calculate the relevant fluid and matrix values. Different values were used for the gas and water zones. Fluid contacts were taken from Cook (2000).

#### *A3.6.2 Sonic*

Sonic values for the matrix and fluid were obtained using a composite plot of all available core data, except from 23/21-T4 (the same as in Walsgrove (1996) for calculating porosity from the density log). All core plugs were corrected to reservoir temperature and pressure using the formula given in Walsgrove (1996).

The resulting sonic cross-plots were taken from wells T1, T2, T3, T5, T8 (i.e. all those with core) and have a clay volume of less than 10%. Figure A3.3 shows the cross-plot for the gas zone, Figure A3.4 the cross-plot for the water zone. Note in the water zone a shale volume cut-off of 20% was used instead of 10%, as using 10% resulted in only 2 points on the graph. Because of the lack of points, it was decided to us the matrix point in the gas zone as the matrix point in the water zone, the underlying assumption being that the average matrix constituents all the way through the reservoir is the same. Therefore the regression to find the fluid point in the water zone was fixed through the point (0, 55.93). The subsequent regression analysis reveals the following parameters:

matrix point in the gas zone: 55.93usec/ft;
fluid point in gas zone: 236.88usec/ft;
matrix point in the water zone: 55.93usec/ft;

fluid point in water zone: 197.88usec/ft.

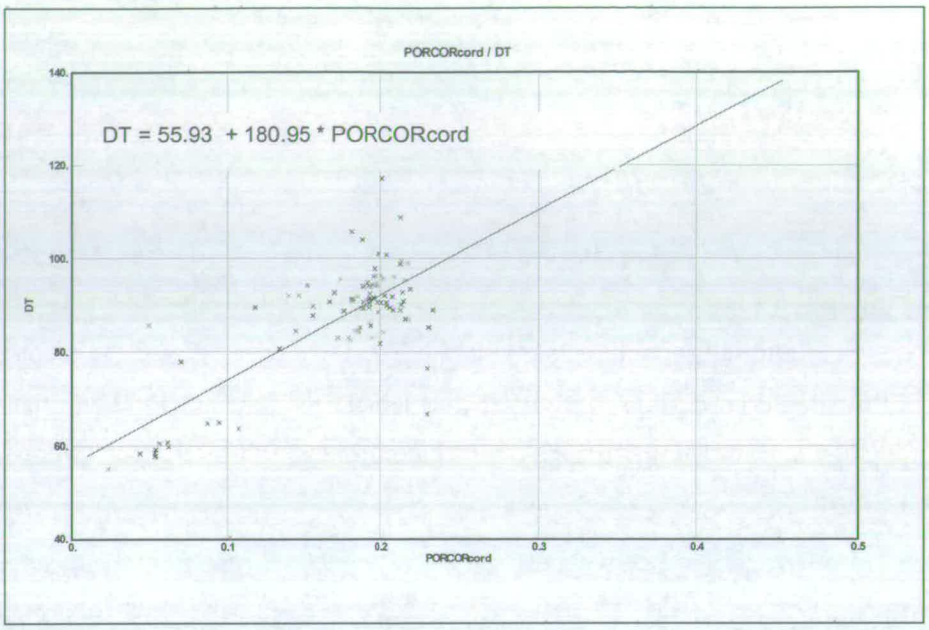



**Figure A.3.3** Plot of sonic values (DT) v core porosities (PORCORcord) for the gas zones for all wells with core. All points are 'clean' having a shale volume of less then 10%.

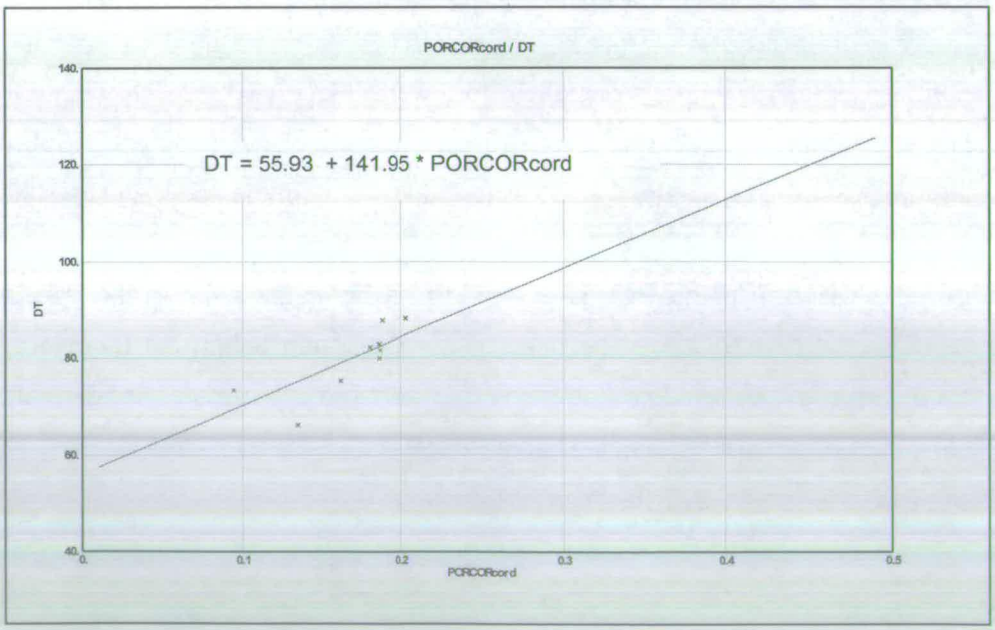



**Figure A.3.4** Plot of sonic values (DT) v core porosities (PORCORcord) for the water zones for all wells with core. All points are 'clean' having a shale volume of less then 20%. See text for further details.

The sonic value for pure water is 189usec/ft (Gruping 1998). The slightly higher value for the fluid in the water zone may be the influence of the oil-based mud.

The sonic value of shale was taken as 90usec/ft from inspection of the logs for both the gas and water zones.

The equations and parameters as specified in Section A3.3 were then used to calculate the new sonic log, corrected for gas.

### *A3.6.3 Density*

Walsgrove (1996) shows all wells except 23/21-T4 to have similar cross-plots when determining the fluid point in the water and gas zone. From Walsgrove (1996) the following parameters were extracted:

fluid density in the gas zone: 0.855g/cm3;
fluid density in the water zone: 1.038g/cm3;
grain modal density: 2.65g/cm3.

Note these are for clean sandstone – an acceptance expression of 'net sand' only was used. Thus shale is eliminated, and the fluid values only apply to the effective porosity.

The density of gas water specified in Section A3.4 was used to calculate a gas corrected porosity.

### *A3.6.4 Neutron*

The method followed that described in Section A3.5. The graph for the corresponding gas column in all the wells is shown as Figure A3.5, and for the water column Figure A3.6. As for the sonic log there are very few points (core points) in the water leg to constrain the HI index of the fluid. Therefore as for the sonic log a shale volume cut-off of less than 20% was used, instead of 10%.

Both equations (that indicate the hydrogen index of the 'fluid') are very similar (as expected).

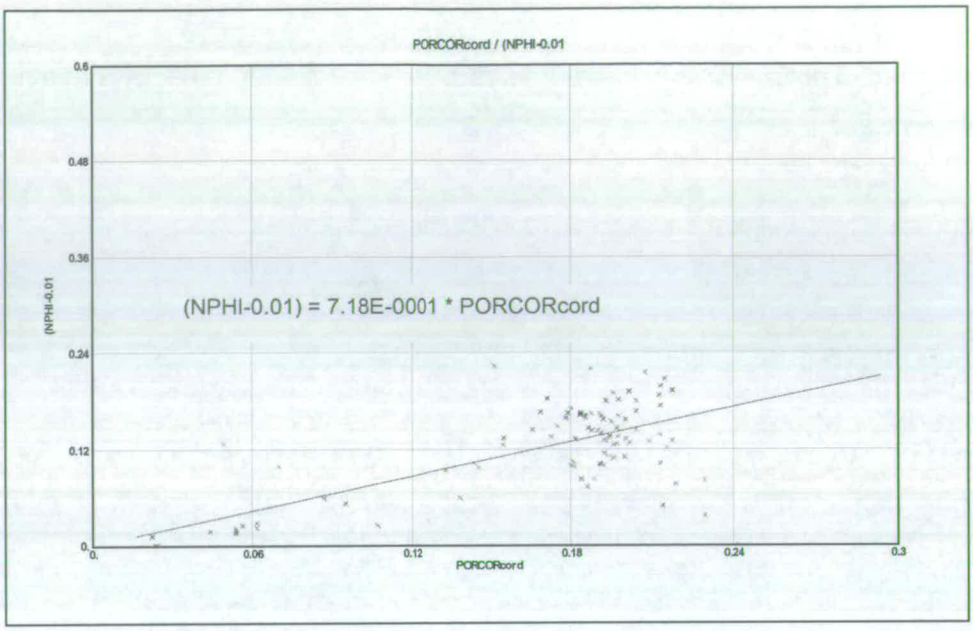



**Figure A.3.5** Plot of (NPHI –0.01) v core porosities (PORCORcord) for the gas zones for all wells with core. All points are 'clean' having a shale volume of less than 10%.

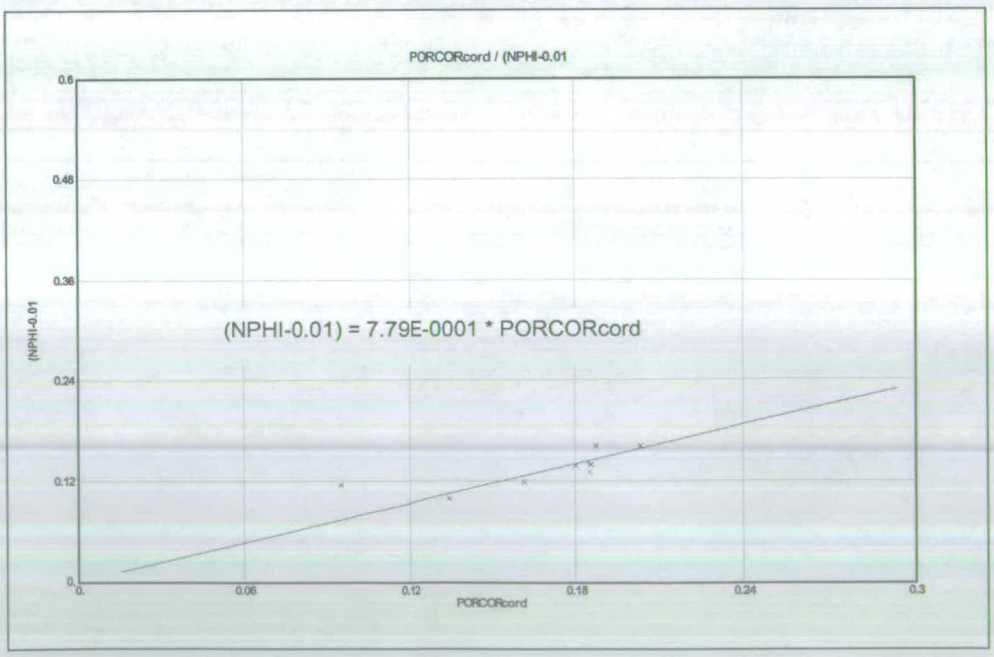



**Figure A.3.6** Plot of (NPHI –0.01) v core porosities (PORCORcord) for the water zones for all wells with core. All points are 'clean' having a shale volume of less than 10%.

The neutron shale point was read from a standard neutron-density cross-plot. A value of 0.314 was selected for all wells.

Note, Ellis (2003) gives a useful account of formation porosity estimation from the density log, and Ellis *et al.* (2004) gives a useful overview of neutron tool measurement.

# Appendix 4 : Training intervals for thin-beds

## *4.1 Introduction*

This Appendix lists the training intervals used to train neural network models (in Chapter 5) to predict type-I and type-II thin-beds.

## *4.2 Type-I thin-beds*

From well Simian 1 (1 point from each depth), thin-beds:
6853.7, 6867.1, 6992.9, 7033.3

From well Simian 1, not thin-beds:
6871.4-6871.6, 7029.4-7030.1, 7112.8-7113.8

From well Simian 2 (1 point from each depth), thin-beds:
7054.4, 7122.6, 7162.3, 7209.4

From well Simian 2, not thin-beds:
7161-7161.4, 7256.4-7256.8

From well Simian 3 (1 point from each depth, unless an interval), thin-beds:
6791.3-6791.6, 6798.4, 6803.1, 6803.2, 6803.8, 6811.1, 6875.1, 6905.4, 6975.4, 7060.0

From well Simian 3, not thin-beds:
7140-2-7141, 7129.7-7130, 7126.6-7126.9, 7095.4-7095.6

## *4.3 Type-II thin-beds*

From well Simian 2 (1 point from each depth, unless specified), thin-beds:
7201.7 (x2), 7166.6 (x2), 7160.8 (x2), 7156.1, 7112.0 (x2), 6938.2

From well Simian 2, (1 point from each depth) not thin-beds:

7346.4, 7303.4, 7283.3, 7263.3, 7236.9, 7204.8, 7182.2, 7184.2, 7032.1, 6882.7

From well Simian 3 (1 point from each depth, unless specified), thin-beds:
6852.2, 6973.8 (x2), 6962.6 (x2), 7057.3 (x2), 7078.1 (x2), 7095.1 (x2), 6949.8

From well Simian 3, (1 point from each depth) not thin-beds:
7245.2, 7147, 7156.8, 7139.1, 7126.3, 7063.5, 6977.0, 6931.4, 6774.3, 6990.1, 7148.6, 7180.6

# Appendix 5 : Full logs and electronic thesis

An enclosure to this thesis is a CD-ROM containing:

- Contained in the folder 'Lomond' - a full suite of logs and lithofacies predictions from the optimum neural network (trained in Chapter 3) for wells 23/21-T1 – T10, excluding 23/21-T7;
- Contained in the folder 'WDDM_Egypt' - a full suite of logs and images and image lithofacies predictions from the optimum neural network (trained in Chapter 5) for wells Simian 1, 2, and 3;
- In the folder 'Thesis' a copy of this thesis as a single pdf file.

Log acronyms can be found in the notations and conventions section preceding Chapter 1, and in the additional enclosures.

# Enclosure 1 - notations & conventions, Chapters 3 & 4.

*Log acronyms*

| | |
|---|---|
| GR | gamma ray log |
| DT | sonic log |
| DT4P | p-sonic (as DT) |
| ILD | deep induction log (resistivity) |
| ILM | medium induction log (resistivity) |
| AHT90 | deep resistivity (from Array Tool) |
| RHOB | density log |
| NPHI | neutron log |
| PORCOR | laboratory measured core plug porosity value |
| KAH (cor) | laboratory measured core plug horizontal permeability value |
| NDSEP | neutron density separation (see Appendix 1) |
| PORLOGT | calculated total porosity (see Appendix) |
| DTgas | sonic log corrected to represent a full gas reservoir |
| RHOBgas | density log corrected to represent a full gas reservoir |
| NPHIgas | neutron log corrected to represent a full gas reservoir |
| P-Train | interval in primary training set (always shown as black flag/bar) |
| Train | interval in primary training set (always shown as black flag/bar) |
| ACT_1 - ACT_5 | activation of output node representing lithofacies 1-5 (from optimum network) |
| ACT_1n - ACT_5n | activation of output node representing lithofacies 1-5 (input data calibrated to training set) |
| ACT_1a - ACT_5a | activation of output node representing lithofacies 1-5 (model not trained with resistivity log) |
| ACT_1G - ACT_5G | activation of output node representing lithofacies 1-5 (when trained with gas corrected logs and no resistivity) |

*Lithofacies columns*

| | |
|---|---|
| Lithofacie | core defined lithofacies |
| B | best performing network from topological experiments |
| C | best performing network from experiments with different learning rates and momentum parameters |
| D | best performing network from experiments with pruning algorithm starting with 23 nodes |
| E | best performing network from experiments with pruning algorithm starting with 14 nodes |
| F | best performing network from experiments with unbalanced data |
| G | best performing network from experiments with unbalanced data and lithofacies 1 reduced further |
| H | best performing network from training without derivative logs |
| I | best performing network from training with Training Set 2 |
| J | best performing network from training with Training Set 3 |
| LF_PR | best performing of all networks 'optimum network' (actually same as 'B') |
| PLF_Rep3 | LF_PR after application of thin-bed repair program (with thin-bed defined as 1.5ft) |
| PLF_Rep4 | LF_PR after application of thin-bed repair program (with thin-bed defined as 2ft) |
| PLF_Repair | LF_PR after application of thin-bed repair program (with thin-bed defined as 1.5ft) |
| LF_PRmax | raw lithofacies predictions with maximum activation taken as the output |
| PLF_Rep_m | LF_PRmax but after application of thin-bed repair program |
| LF_PRn | raw lithofacies predicted from normalised data |
| LF_PRmaxn | raw lithofacies predicted from normalised data with maximum activation taken as the output |
| LF_PRmaxnR | LF_PRmaxn but after application of the thin-bed repair program |
| LF_PRa | lithofacies output from model trained with no resistivity log and the highest activated node as the prediction |
| LF_PRg | lithofacies output from model trained with gas corrected logs with the highest activated node taken as prediction |

## Sedimentary facies codes (Figures 4.8 - 4.12)

- Sandstone
- Claystone / mudstone
- Siltstone
- Calcite cemented
- Mud clasts
- Calcareous
- Dolomitic
- Massive / structureless
- Horizontal lamination
- Cross stratification
- Trough cross stratification
- Climbing ripple lamination
- Current ripple lamination
- Contorted / deformed bedding
- Dish structures
- Water escape pipes
- Fractures
- Plant fragments / rootlets

## Lithofacies colour-code

1 2 3 4 5

Descriptions in Table 3.2

# Enclosure 2a - notations & conventions, Chapters 5 & 6.

*Log acronyms*

| | |
|---|---|
| GR | gamma ray log |
| RHOB | density log |
| RHOZ | density log |
| NPHI | neutron log |
| PHIN | neutron log |
| FMIimage | microresistivity image log, unprocessed |
| FMIimage_P | microresistivity image log, processed (steps described in Chapter 5) |
| C1 | first caliper curve from image tool |
| C2 | second caliper curve from image tool |
| S-PAD | Single pad of data used for analysis |
| AVsp | continuous vertical average of resistivity button responses over a single pad of data |
| A2 | vertical moving average of all button data over 2" |
| A2sp | vertical moving average of a single pad of data over 2" |
| A6sp | vertical moving average of a single pad of data over 6" |
| CV05sp | moving coefficient of variation of a single pad of data over 0.5" |
| CV6 | moving coefficient of variation of all button data over 6" |
| CV6sp | moving coefficient of variation of a single pad of data over 6" |
| Sk6sp | moving skewness of a single pad of data over 6" |
| Kur6sp | moving kurtosis of a single pad of data over 6" |
| Stack_ssp | stacked button response over a single pad of data |
| ARRAY-H | synthetic vertical stripes that can be identified by a horizontal spectral analysis |
| ARRAY-V | synthetic horizontal stripes that can be identified by a vertical spectral analysis |
| POWER-V *or* V-POWER | spectral power from the vertical power spectral analysis, wavelength decreases to the right |
| POWER-H *or* H-POWER | spectral power from the horizontal power spectral analysis, wavelength decreases to the right |
| FAS2 – FAS12 | individual horizontal power spectral curves; the 2nd lowest frequency sampled – 12th lowest frequency sampled |
| FSP128_2 – FSP128_64 | individual vertical power spectral curves; the 2nd lowest frequency 64th lowest frequency |
| TRAIN_1 | sections from well Simian 1 used for training (black bar) |
| Train2a | sections from well Simian 2 used for training (black bar) |
| Train3a | sections from well Simian 3 used for training (black bar) |
| ACT F1 – ACT F7 | activation levels for image lithofacies 1-7 (activation levels come from module 1 for image lithofacies 7, from module 2 for other facies) |
| thin_bed | raw prediction of type-II thin-beds (packages) |
| T-BED | as for thin_bed except filtered to leave only packages of thin-beds greater than 2ft thickness and those occurring in image lithofacies 1 and 2 |

*Log acronyms- Baker Atlas (in Figure 6.18 only)*

| | |
|---|---|
| TNLW | neutron log |
| RHOB | density log |
| RHOZ | density log |
| AT10 – AT90 | Array resistivity tool (with depth of investigation shown in cm) |
| HLLS | high resolution laterolog shallow |
| HLLD | high resolution laterolog deep |

*Lithofacies columns*

| | |
|---|---|
| Imfacds *or* Image_fa | image facies defined by Baker Atlas (2000 & 2001) – see key below |
| IMFACIESr | facies scheme that the neural networks were trained to predict, this is a simplified version of the Baker Atlas scheme – see key below |
| Mod1_com | raw results of module 1, used to predict sand, shale and cemented lithofacies |
| Mod1_comb | results of module 1, used to predict sand, shale and cemented lithofacies after thin-bed repair |
| IM_FACall | results from modular system when the shale network in module 2 utilised both conventional and image derived logs as inputs |
| IM_FACal2b | as IM_FACall but after thin-bed repair |
| IM_FACim | results from modular system when the shale network in module 2 utilised only image derived logs as inputs |
| IMFACim2b | as IM_FACim but after thin-bed repair |
| IM_FAC_S | results from a single network trained to predict all 7 image lithofacies at once (non-modular system) |
| IM_FAC_S2 | as IM_FAC_S but after thin-bed repair |
| IMFACal2p | as IM_FACal2b but with type-I thin-beds added |
| IMFACal2q | as IMFACal2p but with type-I thin-beds removed if caliper curve was above a specific threshold - these are the final results shown in Chapter 6 |

# Enclosure 2b - notations & conventions, Chapters 5 & 6.

Key - Baker Atlas image facies scheme (Baker Atlas 2000 & 2001) defined in Table 5.1
[Imfacds *or* Image_fa columns]

- Laminated shale
- Bioturbated shale
- Slumped shale
- Chaotic shale
- Debris flow
- Structureless sand
- Laminated sand
- Irregular sand
- Slumped sand
- Structureless and intraclastic sand
- Conglomerate
- Cross-bedded sand

Key - simplified image lithofacies scheme defined in Table 5.3
[IMFACIESr column]

- 1 - Laminated shale
- 2 - Bioturbated shale
- 3 - Slumped and chaotic shale
- 4 - Shaly SST, debris flow
- 5 - resistive sand (structureless sand)
- 6 - Conductive sand (irregular, slumped, intraclastic)
- 7 - Cemented intervals / conglomerate